1-1-2014

# Evaluation Of Nozzle Geometry On High Pressure Gasoline Direct Injection Spray Atomization

Mark Shost
*Wayne State University,*

# EVALUATION OF NOZZLE GEOMETRY ON HIGH PRESSURE GASOLINE DIRECT INJECTION SPRAY ATOMIZATION

by

**MARK ANTHONY SHOST**

**DISSERTATION**

Submitted to the Graduate School

of Wayne State University,

Detroit, Michigan

in partial fulfillment of the requirements

for the degree of

**DOCTOR OF PHILOSOPHY**

2014

MAJOR: MECHANICAL ENGINEERING

Approved by:

________________________________________
Advisor                                                            Date

________________________________________

________________________________________

________________________________________

# DEDICATION

I dedicate my dissertation work to my family. First to my loving parents, John and Pauline Shost, who supported me in every pursuit in my youth, including disassembling, sandblasting, welding, and painting my first car in their garage, and who always promoted education as a worthy pursuit. To my sister Sharon and to my late brother John Shost Jr. who was my model for an engineer's inquisitive mind.

I also dedicate this work to my wife Denise, who has been my partner in this and every challenge of my life, always supportive and encouraging including encouraging finishing this dissertation a few times. To my daughter Jessica who shares my love of history and science and was born during my business school classes and twenty years later always knew a dad taking classes, and to my son Michael who shares my love of math and science. I hope to have passed to my children my parents' value of education and my love of learning and scientific research as part of a rewarding and happy life.

# ACKNOWLEDGEMENTS

It was a tremendous experience to study under my thesis advisor, Professor Ming-Chia Lai at Wayne State University, over the past eight years, his support and encouragement and his recognized knowledge in the injector spray field was invaluable.  I also recognize and appreciate the time and effort of my dissertation committee of Professor Singh and Professor Bryzik of the mechanical engineering department and especially recognize Associate Professor Lebiedzik from the math department for joining my committee.

I want to express my gratitude to Delphi Powertrain management for their support, foremost Scott Bailey and Skip Wagner who sponsored my degree pursuit as well as engineering management Jim Zizelman and Walter Piock for supporting this work over the past four years and recognize injector team member Dan Varble for his efforts in coordinating hardware design and prototyping. I also recognize and thank Dr. Bizhan Befrui for his coordination of simulation & testing in Luxembourg.  My discussions with Bizhan as the project and our learning progressed and his generous sharing of time and insights helped guide the overall success of the work.

# TABLE OF CONTENTS

# LIST OF TABLES

# LIST OF FIGURES

# CHAPTER 1 BACKGROUND

## *1.1 Gasoline engine and fuel system evolution*

The gasoline-fueled spark-ignited internal combustion engine has long dominated as the powertrain of choice for passenger car and light duty truck applications. Over history, fuel systems have gone through three major technological changes starting with mechanical carburetion transitioning to electronic port fuel injection and recently to today's high-pressure direct fuel injection. Early applications, dating back to Karl Benz, Gottlieb Daimler, and Henry Ford's model T, utilized carburetors, like shown in Figure 1, to meter fuel with intake air. Carburetors work on the Bernoulli principle by funneling air through a venturi whose restriction increases the air velocity while decreasing its static pressure. The resulting reduction in static pressure provides the opportunity to introduce gasoline at a low pressure port. Fuel is then metered into the air stream as a function of vacuum, which itself is a function of mass airflow. This effect maintains a relatively constant air to fuel ratio across the varying mass airflows required for engine operation. To vary the airflow, a throttle valve is connected by linkage to the driver's pedal for engine load demand control, and the proper targeted fueling mix is controlled by the carburetor design. The desired air to fuel mixture varies slightly based on engine operating conditions, but is targeted around the stoichiometric air/fuel

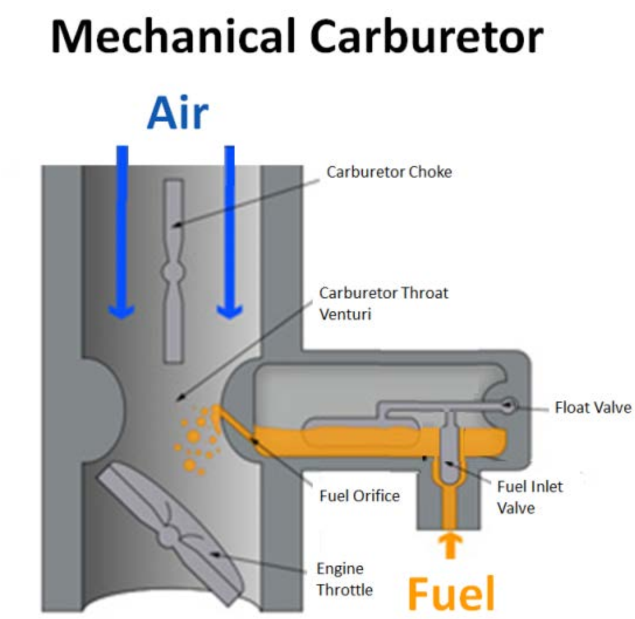


Figure 1 Carburetor from 1st generation of gasoline fuel systems

ratio of 14.7/1 where the combustion reaction in the engine will fully consume the gasoline reagent with the air oxidizer. To provide the best vehicle drivability, carburetors evolved with additional mechanisms to vary the air/fuel ratio based on conditions. For example, when the driver wants more power to the wheels, he depresses the pedal or “tips-in” to the throttle. To adjust more quickly to the increased air-flow, accelerator pumps were added to the carburetor to add extra fuel for tip-in conditions so no lag would be experienced by the driver as the fuel would adjust to the increased air-flow condition. Likewise, to aid in start-up an additional function was added, called a “choke”, to limit airflow in the carburetor throat, thus providing a lower air to fuel ratio thereby operating more rich to aid in initial engine firing, especially at cold temperatures. In the 1970’s, internal combustion engines further developed to improve the exhaust emission characteristics. A phenomenon called “smog” was being experienced, especially prevalent in cities like Los Angeles where air inversion caused by mountains produced an unhealthy haze. Early research identified incomplete combustion of gasoline fuel, resulting in high levels of hydrocarbon and carbon monoxide, to be a main cause. Automakers solved this problem with the adoption of engine after-treatment devices called catalytic converters. In 1974, General Motors introduced oxidation catalysts, which promoted the complete oxidation of engine out hydrocarbons and the conversion of carbon monoxide to carbon dioxide. Within a few years, reduction catalysts were also added to the engine aftertreatment to reduce the oxides of nitrogen ($NO_x$), the ozone affecting gas. This culminated in the invention of the three-way catalyst, which provided both the oxidation function for hydrocarbons and the reduction of $NO_x$. The three-way catalyst was a major breakthrough in providing the clean emission operation of gasoline engines. The caveat to maintain optimum performance with the three-way catalysts is precise control of the air-fuel mixture around the stoichiometric point. To aid in this control, a closed-loop feedback was added to the engine management system with the adoption of an exhaust oxygen sensor. Oxygen sensors located in the engine exhaust stream measure the partial pressure of oxygen in the exhaust gas. The presence of oxygen, or lean operation, indicates more fuel is necessary to reach stoichiometric operation. The absence of oxygen means the engine is operating at the stoichiometric point or in a rich regime with excess fuel. The engine management system adjusts the fueling command based on the output of the switching-style oxygen sensor around the switching voltage, which indicates the stoichiometric combustion desired for efficient catalytic converter operation. These demands for more precise fueling that could be dynamically adjusted led to "electronic" carburetors, but cost and complexity soon gave way to the next era in fuel control, the electronic fuel injector in the 1980s. Fuel injectors have the advantage of not relying on the air flow to set the fuel flow, instead using the engine control module to operate an electric solenoid to open a fuel flow orifice. With the adoption of fuel injection, engine management systems could now provide any fuel flow desired for engine operation based on vehicle drivability, performance, or exhaust emission after-treat requirements. Early systems were either throttle body injection, which maintained a central injector for the entire engine, or multi-point injection where individual injectors are located closer to the intake port of each cylinder. This multi-point fuel injection (MPFI) scheme, as shown in Figure 2, became the norm in the 1990's. Since its introduction, MPFI development focused on improved atomization of the fuel to

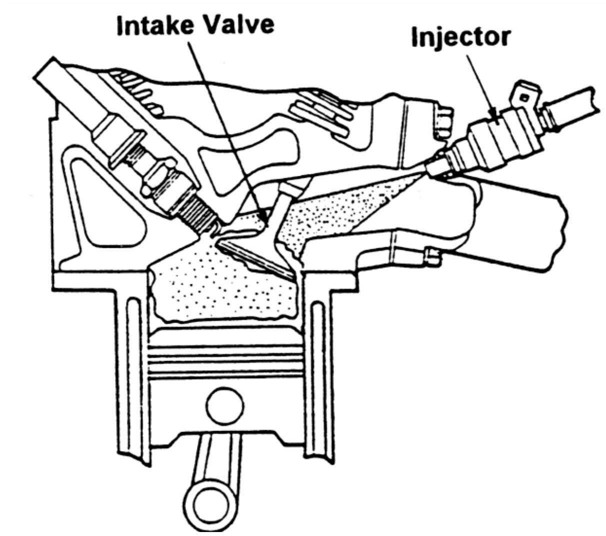


Figure 2 Multi-point Fuel Injector, MPFI, the 2nd generation of gasoline fuel systems

promote air and fuel mixing for enhanced combustion and emission characteristics. Generally, the quest for smaller fuel droplet sizes drove the desire for higher fuel pressures or reduced fuel orifice diameters achieved by additional director plate holes for the given fuel flow rate. Injector targeting was also improved to avoid fuel impinging on surfaces, however, the fueling operated as closed-intake valve injection, and as such, still relied on the vacuum caused by the piston motion to pull the air and fuel mixture into the cylinder during the intake stroke for naturally aspirated engines. The pursuit of improved fuel economy driven by consumer's reaction to higher fuel prices, Corporate Average Fuel Economy, CAFE, regulations in the US, and $CO_2$ regulations in Europe drove automakers to search for alternatives to the naturally aspirated MPFI gasoline engine. The 1990s saw a large penetration of turbocharged direct-injected common rail diesel engines in Europe. The new common rail injection technology provided for split injection, which dramatically improved the Noise, Vibration, and Harshness (NVH) characteristics of the diesel powertrain, and combined with turbocharging, provided the vehicle excellent drivability due to the high cylinder pressures achievable, hence high levels of engine torque. However, diesel engines still suffered somewhat compared to gasoline engines for noise, vibration, and harshness, and since diesel combustion has excess air, exhaust aftertreatment is more costly as

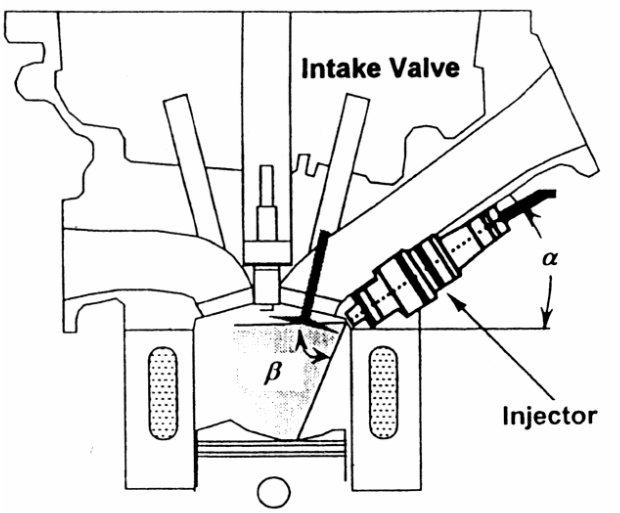


Figure 3 Gasoline Direct Injection, GDi, the 3rd generation of gasoline fuel systems

three way catalysts cannot be applied. An alternative technology, Gasoline Direct Injection (GDi), shown in Figure 3, was introduced by Mitsubishi in 1996 where the fuel injection point moved from the intake port to the combustion chamber. This direct means of injection improves volumetric efficiency since the intake port and gas exchange process only has to transfer air to the combustion chamber. Another benefit of direct injection into the chamber is the charge cooling effect due to fuel evaporation that acts to boost the effective engine knock tolerance. Lastly, direct injection decoupled the timing of the fuel injection from the intake valve timing. This permits techniques, like demonstrated in diesel engines, where multiple injections could be provided, even during the compression stroke when the intake valve is closed, to affect combustion. In order to achieve proper atomization of the fuel, direct injection requires that the injection pressures are raised to 100 bar, 1,450 PSI, and above. This represents a 30 fold increase over port fuel injectors, but still 1/10 of the pressures utilized by diesel injectors. To produce and accommodate the higher pressures, a high pressure pump, typically cam lobe driven, and strengthened fuel lines and rails are adopted in GDi systems, as shown in Figure 4. GDi technology is also well suited for use in combination with turbocharging since cylinder

Figure 4 Gasoline Direct Injection System comprised of high-pressure pump, fuel rail, and side or center mount injector

scavenging could be increased without a hydrocarbon issue and much higher levels of cylinder pressure achieved. This allows smaller engines to provide the maximum Brake Mean Effective Pressure, BMEP, or torque of larger engines when power is demanded, while maintaining the fuel saving characteristics of a smaller engine for lower demand driving. The charge cooling effect of direct injection also works well with turbocharging where engine knock limits spark advance for fuel efficiency or boost levels for power. Therefore, this technology employed with down-sizing of engine displacement, can realize fuel economy gains of 12% as demonstrated by Ford's roll-out of their "EcoBoost" Powertrain brand in a 3.5L V6 [1]. A trend starting in Europe currently is the development of 3-cylinder turbocharged GDi engines to replace the turbo-diesel powertrains, while offering similar low fuel consumption and good low-end torque characteristics, but without the need for costly exhaust after-treatment for $NO_x$ and particulate matter. The new Turbocharged GDi engine technology using the down sized and down speeded concept is more costly than the MPFI technology it replaces due to the higher pressure fuel system and turbocharger additions, but is still significantly cheaper than the diesel alternative. The GDi engine has higher injection and cylinder pressures, and can provide additional vehicle packaging advantages since no complex diesel aftertreatment is required.

Figure 5 Side-mount and Center-mount GDi systems

Vehicle segments with the most cost sensitivity, like compacts under 1,400 kilograms, are expected to adopt Turbocharged GDi Powertrains to meet the $CO_2$ challenge, while maintaining an attractive customer offering [2]. This work will focus on the spray characteristics of GDi injectors that are the foundation for achieving the combustion required to meet the demands on modern gasoline engines. GDi systems are configured either as side-mount, where the injector is located below the intake port, or as has been the industry trend, central-mount, where the injector is located in the center of the combustion chamber near the spark plug location, as shown on the right in Figure 5. The trend to center-mount is due to the fuel/air mixing advantages the location can provide, especially important for any lean operation where air/fuel mixture concentrations near the spark electrode are critical for reliable ignition and flame front propagation of the combustion system. Although the center-mount location requires a longer injector than side mount, as shown in Figure 4, the valve group's seat and nozzle geometry are similar, but require adjustments to spray plume targeting to match the application combustion chamber.

### *1.2 Understanding of turbulence*

Given the dominant influence of fuel atomization and mixing on engine performance and emissions, it is expected that this physical mechanism has been well-studied. In fact, observations on fluid turbulence and flow of liquid jets date back more than 500 years to Leonardo da Vinci's studies of water and blood flow in an effort to determine the underlying physical laws, see Figure 6. Leonardo da Vinci in 1507 named the phenomenon he observed in swirling flow "la turbolenza" and described the following:

"Observe the motion of the surface of the water, which resembles that of hair, which has two motions, of which one is caused by the weight of the hair, the other by the direction of the curls; thus the water has eddying motions, one part of which is due to the principal current, the other to random and reverse motion."

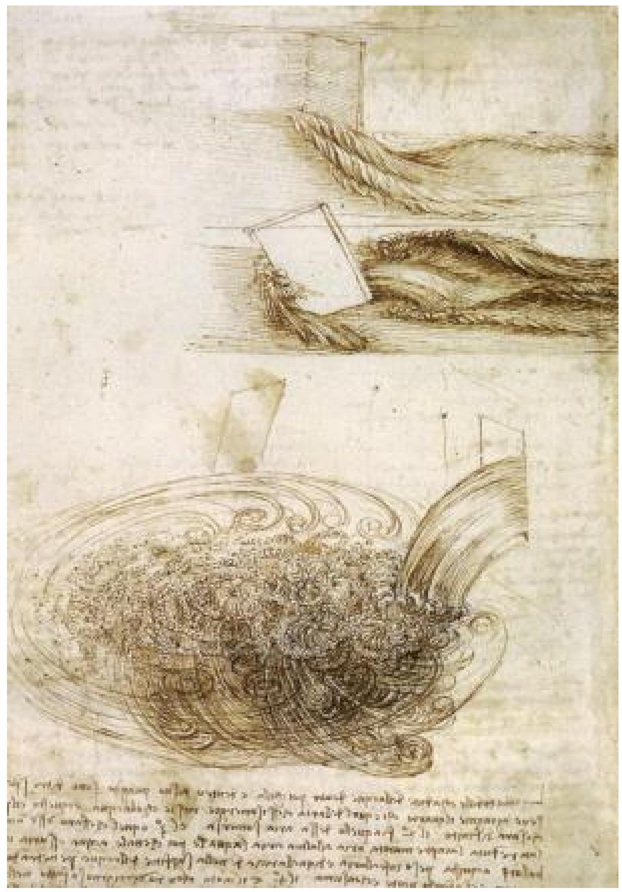

Figure 6 Studies of Water passing Obstacles and Falling, notes and drawings by Leonardo da Vinci (circa 1507)

Formal definitions of turbulence are surprisingly difficult for a readily observable natural phenomenon, but da Vinci noted two key characteristics the curls or eddies form, they have the velocity components of the main current and another component to a random motion. Although a concise definition is elusive, most researchers note the characteristics of turbulent flow, Bakker [3] does a comprehensive list as follows:

- One characteristic of turbulent flows is their irregularity or randomness. A full deterministic approach is very difficult. Turbulent flows are usually described statistically. Turbulent flows are always chaotic, but not all chaotic flows are turbulent.
- The diffusivity of turbulence causes rapid mixing and increased rates of momentum, heat, and mass transfer. A flow that looks random, but does not exhibit the spreading of velocity fluctuations through the surrounding fluid is not turbulent. If a flow is chaotic, but not diffusive, it is not turbulent. The trail left behind a jet plane that seems chaotic, but does not diffuse for miles is then not turbulent.
- Turbulent flows always occur at high Reynolds numbers. They are caused by the complex interaction between the viscous terms and the inertia terms in the momentum equations.
- Turbulent flows are rotational; that is, they have non-zero vorticity. Mechanisms such as the stretching of three-dimensional vortices play a key role in turbulence.
- Turbulent flows are dissipative. Kinetic energy gets converted into heat due to viscous shear stresses. Turbulent flows die out quickly when no energy is supplied. Random motions that have insignificant viscous losses, such as random sound waves, are not turbulent.
- Turbulence is a continuum phenomenon. Even the smallest eddies are significantly larger than the molecular scales. Turbulence is therefore governed by the equations of fluid mechanics.
- Turbulence is a feature of fluid flow, not of the fluid. When the Reynolds number is high enough, most of the dynamics of turbulence are the same whether the fluid is an actual fluid or a gas. Most of the dynamics are then independent of the properties of the fluid.

Osborne Reynolds (1883) was the first to systematically investigate the transition from laminar to turbulent flow in pipes by injecting a dye streak into flow through a pipe having smooth transparent walls [4]. His observations led to identification of a single dimensionless parameter representing the ratio of fluid inertial forces to viscous forces, now known as the Reynolds number.

$$Re = \frac{\rho U L}{\mu} \quad where \; \substack{\rho = density, \;\; \mu = kinematic\ viscosity \\ U = velocity, \;\; L = length\ scale}$$

His experiments showed that the distinction between laminar and turbulent flow depended on a relationship between the dimensions of space and velocity, see Figure 7. Reynolds determined the transition to turbulent flow inside a pipe occurred when the Reynolds number exceeded a certain range ( $2{,}000 \leq Re \leq 2{,}300$). Reynolds also noted that the transition from the streamline (laminar) flow to the sinuous (turbulent) flow was quite abrupt. Reynolds went on to decompose the velocities of turbulent flow in terms of components representing its mean and eddying parts, a concept that will serve as the core for future fluid dynamic modeling.

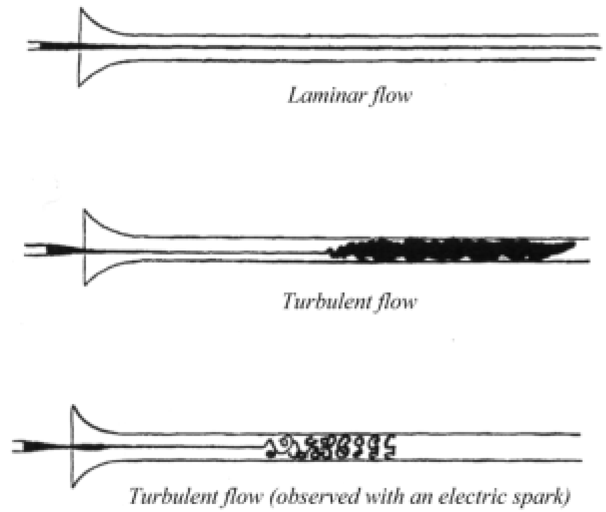


Figure 7 Drawings from Reynolds' investigation of circumstances which determine whether the motion of water in parallel channels shall be direct or sinuous

The study of turbulence is of primary interest in several scientific fields, one of which is meteorology. In 1922 Lewis Richardson, an English mathematician, developed a novel method of weather forecasting by solution of differential equations [5]. Richardson laid out a method where discrete calculations would be performed in subsections based on local instantaneous data. Calculations of the subsections were used by surrounding subsections and all activity was coordinated by a supervisor to maintain the timing of all calculations. The described method, predating computing machines, represented well the method of turbulent flow modeling, using finite differences, which would be made practical with the advent of modern computers. Richardson is best remembered for his rhyme in this work to describe the turbulent cascade.

"When making a drawing of a rising cumulus from a fixed point; the details change before the sketch can be completed.'

We realize thus that:

Big whirls have little whirls
Which feed on their velocity;
And little whirls have lesser whirls,
And so on to viscosity
in the molecular sense."

The concept of turbulent energy and its transition from large eddies to smaller eddies, the turbulent cascade, represent another key concept for representing turbulent flow in fluid models.

Russian mathematician Andrei Nikolaevich Kolmogorov in 1941 proposed a mathematical theory for Turbulent Cascades, see Figure 8, defining a mechanism to calculate turbulent scales for length, velocity, and time [6]. His theory is based on the premise that the unstable large eddies breakup and transfer energy to smaller eddies, which in turn breakup and transfer to even smaller eddies. This cascading of energy continues until a small enough scale is reached where the eddy motion is stable and viscous dissipation converts the kinetic energy into thermal energy. Turbulent Cascade theory requires the energy transfer is in only one direction from large eddies to smaller eddies. Although evidence exists to show smaller eddies

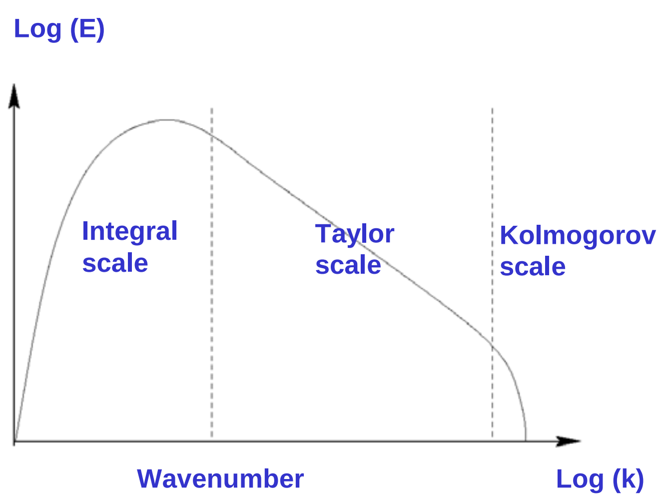

Figure 8 Theory of Turbulent Cascades from Integral to Taylor to Kolmogorov scale

can interact to form larger eddies, a process known as backscatter, the forward progression from large to small energy cascade accounts for the vast majority of energy transfer. Kolmogorov noted that no closed mathematical solution would exist, but that a method involving random functions of several variables would be needed to match the irregularities seen in experimental data.

### *1.3 Understanding of primary atomization*

Qualitative study of jets and their breakup dates back to Savart in 1833 noting that liquid atomization drops come from the rupture of objects having the form of threads or ligaments, where the liquid jet eventually ends in a train of droplets. In 1873, Plateau explained why the initial jet state is unstable, thus recognizing the crucial role of surface tension in the breakup phenomena. The liquid jet is unstable to any perturbation that reduces its surface area. This can be visualized as drops form from a slow flowing sink faucet stream. As the liquid column velocity is reduced, the liquid inertial and surface tension forces converge in magnitude. Drops are formed as the surface tension tries to minimize the surface area of the liquid mass, the liquid column narrows and subsequently "pinches-off" the spherical drop. Plateau showed the perturbations were unstable if their wavelength exceeded $\lambda$ critical / nozzle radius = $2\pi \approx 6.28$. Lord Rayleigh (1879) applying acoustic excitation to the jet, found among all the unstable wavelengths the one with the fastest growth rate will dominate and determined:

$$\lambda \text{ optimal} = 9.01 * \text{nozzle radius}$$

Further, he described the theory of linear stability analysis of a liquid jet using these physical relationships. Wolfgang von Ohnesorge completed a PhD thesis "Application of a cinematographic high frequency apparatus with mechanical control of exposure for photographing the formation of drops and the breakup of liquid jets" in 1937. This work was instrumental in documenting the jet breakup phenomena with high temporal resolution. Ohnesorge varied the fluid properties experimentally using water, aniline, glycerin, and two hydrocarbon fuels in his study. From his work he noted four distinct breakup regimes:

I. Slow dripping from the nozzle under gravity with no jet formation

II. Breakup of a cylindrical jet by axisymmetric perturbations, according to Rayleigh

III. Breakup by screw-like perturbations of the jet, according to Weber-Haenlein

IV. Atomization of the jet

A review of dimensional analysis evaluating the relative contributions of fluid viscosity, inertia, surface tension, and nozzle diameter led to a new dimensionless parameter to clearly define the four breakup regimes now referred to as the Ohnesorge number:

$$Oh = \frac{\mu}{\sqrt{\rho\sigma d}} \quad where \; {}^{\mu=viscosity, \quad \rho=density}_{\sigma=surface\ tension, \quad d=nozzle\ diameter}$$

$$Oh = \frac{\sqrt{We}}{Re} \quad where \; {}^{We=Weber\ number}_{Re=Reynolds\ number}$$

# CHAPTER 2 PREVIOUSLY RELATED RESEARCHES

## *2.1 Blob or Stripping-Rate Model*

In many applications, such as ink jet printing, powder metallurgy, or fuel spray considered here, it is sometimes advantageous to hasten breakup, for fuel spray plumes to avoid liquid impingement on a surface like the cylinder wall or piston. While other times it is desirable to suppress the jet breakup mechanism, for instance, in fuel spray to target air/fuel mixture in a specific region of the combustion chamber. Therefore, a rigorous understanding of the mechanism and the ability to model or predict atomization is desired. Since the combustion efficiency and exhaust particle emissions are dominated by the effectiveness of atomization, an understanding of the nozzle design parameters on the spray plume and the resulting particle size and distribution is desired. The classic Kelvin-Helmholtz instability model by Reitz, [7] [8] [9] still cited today, also known as the blob or stripping rate model, shown in Figure 9, used viscosity, surface tension, and aerodynamic forces to predict the primary atomization. Reitz defined the jet breakup in four main regimes, as shown in Figure 10, and provided equations to predict the maximum growth wavelength and jet breakup length based on different

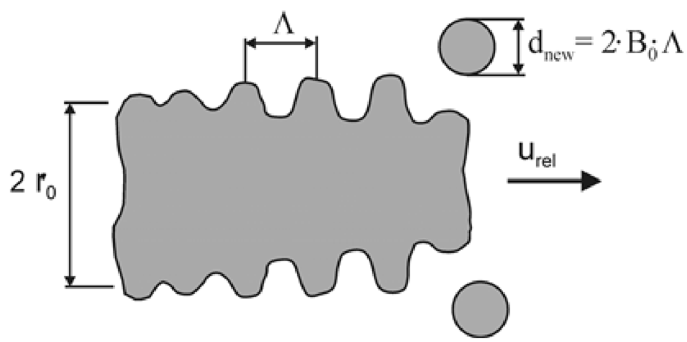

Figure 10 Reitz blob model showing Kelvin-Helmholtz instabilities on the liquid surface

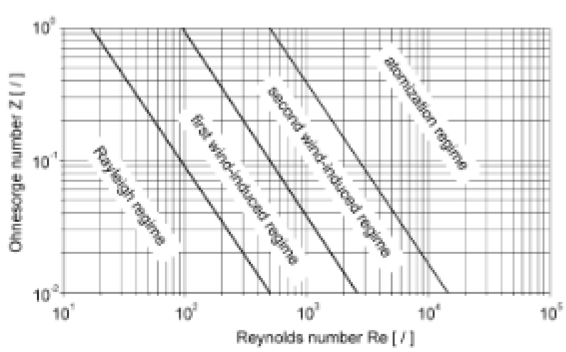

Figure 9 Droplet breakup regimes: Rayleigh, First wind-induced, Second wind-induced and Atomization

combinations of liquid inertia, surface tension, and aerodynamic forces acting on the jet. The Rayleigh breakup regime, dominated by growth of capillary waves along the jet surface, is characterized by drops larger than nozzle diameter initiating many nozzle diameters downstream. As velocity increases, interaction with aerodynamic forces yields the first wind-induced regime with drops on the order of the nozzle diameter with breakup occurring earlier, but still many nozzle diameters downstream. As velocity increases still further, the breakup shifts to the breakup characteristic of the second wind-induced regime with drops smaller than nozzle diameter, starting some nozzle diameters downstream. Finally, highest velocity jets operate in the Atomization Regime with droplets much smaller than nozzle diameter starting at the nozzle exit. Reitz also derived empirical relations for the jet-interface maximum growth-rate wave and its wave-length, based on the round-jet linear stability analysis:

$$\frac{\Lambda}{a} = 9.02\frac{(1.+0.45Z^{0.5})(1.+0.4T^{0.7})}{(1.+0.87We_{gas}{}^{1.67})^{0.6}}$$

$$\Omega.[\frac{\rho_{liquid}a^3}{\sigma}]^{0.5} = \frac{(0.34+0.38We_{gas}{}^{1.5})}{(1.+Z)(1.+1.4T^{0.6})}$$

With the dimensionless parameters defined as:

$$Z = \frac{\sqrt{We_{liquid}}}{Re_{liquid}}, \quad T = Z\sqrt{We_{air}}, \quad We_{air} = \frac{\rho_{air}a}{\sigma}, \quad Re_{liquid}\frac{Ua}{\vartheta_{liquid}}$$

Where U is the liquid jet relative velocity and $a(=0.5d)$ is the jet radius.

The relations the round jet breakup length (in a quiescent ambient) $L/a$ are derived from the Taylor's analysis of high-speed liquid jet breakup, as:

$$\frac{L}{a} = \frac{B\sqrt{\frac{\rho_{liquid}}{\rho_{gas}}}}{f(T)}$$

With the parameter B = 4.04, recommended for typical diesel spray nozzles.

The Taylor's parameter $T$ and $f(T)$ defined as:

$$T = \left(\frac{\rho_{liquid}}{\rho_{gas}}\right)\left(\frac{Re_{liquid}}{We_{liquid}}\right)^2$$

$$f(T) = \frac{\sqrt{3}}{6}[1 - e^{-10T}]$$

Reitz and other researchers showed these relationships correlated well to diesel sprays under study. It is not clear if they would expect to translate well to the GDi injector with a factor lower pressure, since there is no explicit account for internal jet turbulence, vortices, or cavitation, but rather semi-empirical coefficients. Investigation in this work will evaluate predicted breakup length and droplet size as well as calculate indicated coefficients based physical spray experimental results.

### *2.2 Taylor Analogy Breakup (TAB) Model*

A second major development in jet modeling was the Taylor Analogy Breakup (TAB) model proposed by O'Rourke [10]. The analogy suggested originally by Taylor was between an oscillating and distorting droplet and a spring mass system where the restoring force is the surface tension force and the external force is the aerodynamic force, as depicted in Figure 11. This method seems intuitively well suited to secondary breakup where larger droplets or ligaments are breaking to form smaller particles.

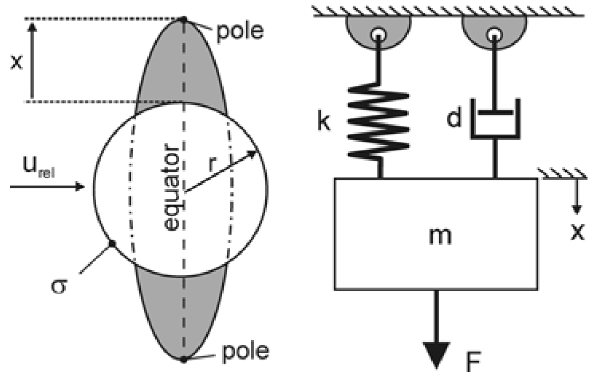

Figure 11 O'Rourke's Taylor Analogy Breakup (TAB) model applies a spring-mass system to predict breakup

This provides several advantages over Reitz's KH Instability model. First, there is not one unique critical Weber number for breakup, which is consistent with experimental evidence. Second, liquid viscosity effects are included, which can significantly affect the oscillations of small drops. Third, the model predicts the droplet state of oscillation and distortion, which can be used in calculation of exchange rates for mass, momentum, and energy between the droplet and the gas. Fourth, the model has shown better correlation with experimental data for drop size and spray angle. The model is based on the equation of a damped, forced harmonic oscillator:

$$m\ddot{x} = F - kx - d\dot{x} \quad where \quad \begin{matrix} m{=}drop\ mass,\ \ F{=}aerodynamic\ force \\ kx{=}restoring\ surface\ tension\ force,\ \ d\dot{x}{=}liquid\ viscous\ damping\ force \end{matrix}$$

$$\frac{F}{m} = C_F \frac{\rho_g W^2}{\rho_l r_p}, \qquad \frac{k}{m} = C_k \frac{\sigma}{\rho_l r_p^3}, \qquad \frac{d}{m} = C_d \frac{\mu_l}{\rho_l r_p^2}$$

We assume the drop breakup only occurs if $x > C_b r$ and then nondimensionalize by setting $y = {}^{x}/_{C_b r}$ gives:

$\ddot{y} = \frac{C_F}{C_b}\frac{\rho_g}{\rho_l}\frac{U^2}{r_p^2} - C_k\frac{\sigma}{\rho_l r_p^3}y - C_d\frac{\mu_l}{\rho_l r_p^2}\dot{y}$ This linear, nonhomogeneous, second-order differential equation has an exact solution

$$y(t) = \frac{C_F}{C_k\,C_b}We + e^{-t/t_d}\left[\left(y_0 - \frac{C_F}{C_k\,C_b}We\right)cos\omega t + \frac{1}{\omega}\left(\dot{y}_0 + \frac{y_0 - \frac{C_F}{C_k\,C_b}We}{t_d}\right)sin\omega t\right]$$

Where $We = \frac{\rho_g U^2 r_p}{\sigma}$, $\frac{1}{t_d} = \frac{C_d}{2}\frac{\mu_l}{\rho_l r_p^2}$, $\omega^2 = C_k\frac{\sigma}{\rho_l r_p^3} - \frac{1}{t_d^2}$, $y_0 = y(0)$, $\dot{y}_0 = \frac{dy}{dt}(0)$

Experimental data suggests $C_F = \frac{1}{3}, C_b = \frac{1}{2}, C_k = 8,\ C_d = 5,\ t_d = \infty,\ y_0 = \dot{y}_0 = 0$

Substituting into $y(t)$ and solving for Weber Number critical for breakup $We_{crit} \approx 6$

The breakup time is defined when Weber Number is close to its critical value as:

$t_{bu} = U\sqrt{\frac{\rho_l\, r^3}{8\sigma}}$ $where\ We \approx We_{crit}$ and Drop normal velocity $\dot{y} \approx \frac{C_F}{C_k\,C_b}We\,\omega^2 t_{bu}$

Spray angle θ can be found as $tan\frac{\theta}{2} = C_v\frac{\sqrt{3}}{3}\sqrt{\frac{\rho_g}{\rho_l}}$ the experimental result was found as $tan\frac{\theta}{2} = \frac{\sqrt{3}}{3}\frac{2U}{3+\frac{L/d}{3.6}}\sqrt{\frac{\rho_g}{\rho_l}}$ these agree when $C_v = 1, hole\ length\ to\ diamter\ {}^{L}/_{d} = 11.8$ to predict the drop size, the energy of the parent drop, the sum of its minimum surface energy, and the oscillation and distortion energy:

$E_{surf} = (4\pi r^2\sigma)$

$$E_{osc} = K\frac{4\pi}{5}\rho_l r_p^3(\dot{x} + \omega^2 x^2) = K\frac{\pi}{5}\rho_l r_p^5(\dot{y}^2 + \omega^2 y^2)$$

$E_{parent} = E_{surf} + E_{osc} = (4\pi r^2\sigma) + K\frac{\pi}{5}\rho_l r_p^5(\dot{y}^2 + \omega^2 y^2)$ After breakup, assuming the product drops are not oscillating, the energy becomes the sum of the minimum surface energy and the kinetic energy of the product drops.

$E_{product} = 4\pi r^2\sigma\frac{r}{r_{32}} + \frac{U}{6}r^5\rho_l\,\dot{y}^2$ Where $r_{32}$ is the Sauter-Mean Radius (SMR) after secondary atomization, equating energy of parent to energy of product and rearranging we get:

$$r_{32} = \frac{4\pi r^3\sigma}{E_{parent} - \frac{\pi}{6}r^5\rho_l\,\dot{y}^2}$$

Another approach is a combined model, as depicted in Figure 12, where near-field primary breakup is modeled using the Blob method and TAB is utilized for secondary atomization. These works are still phenomenological based on certain relevant conditions and not broad general solutions to the fluid dynamics of interest. The difficulty in a robust solution to the primary jet atomization problem is the competition of forces acting on the jet surface between cohesive and disruptive forces. It is also heavily influenced by the jet's turbulence, which itself is a function of conditions upstream of the nozzle exit.

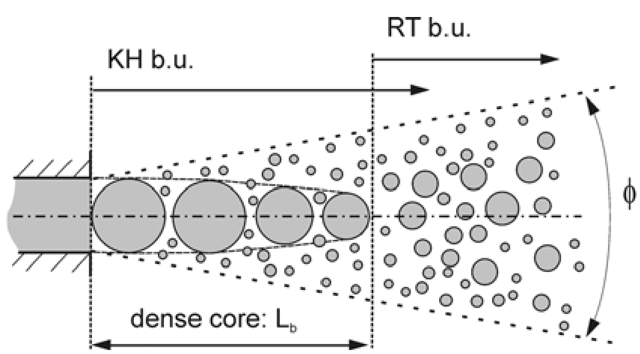

Figure 12 Combined model uses Blob method for primary atomization and TAB for secondary atomization

### *2.3 Computational Fluid Dynamics (CFD) Models*

The last twenty years have seen new approaches to the Navier Stokes closure problem using computational fluid dynamic (CFD) methods. Given the increase in computing power and CFD methodologies, researchers aspired to solve the Navier-Stokes equations directly, a method referred to as direct numerical simulation (DNS), avoiding the need for any empirical coefficients. In order to accomplish a fully resolved solution, we apply the Navier Stokes equations, simplified in this example for incompressible flow.

In Cartesian coordinates ($x$, $y$, $z$) with the components of the velocity given by u = ($u$, $v$, $w$) the conservation of mass is defined as:

$$\nabla \mathrm{u} = 0 \qquad \text{or} \qquad \frac{\partial u}{\partial x} + \frac{\partial v}{\partial y} + \frac{\partial w}{\partial z} = 0$$

We can apply the same treatment to Navier Stokes or the x, y, and z momentum equations:

$$\frac{\partial \mathrm{u}}{\partial t} + \mathrm{u}\nabla \mathrm{u} = \frac{-1}{\rho}\nabla \mathrm{p} + \vartheta \nabla^2 \mathrm{u}$$

$$\frac{\partial u}{\partial t} + u\frac{\partial}{\partial x}(u) + v\frac{\partial}{\partial y}(u) + w\frac{\partial}{\partial z}(u) = \frac{-1}{\rho}\frac{\partial \mathrm{p}}{\partial x} + \vartheta\left(\frac{\partial^2 u}{\partial x^2} + \frac{\partial^2 u}{\partial y^2} + \frac{\partial^2 u}{\partial z^2}\right)$$

$$\frac{\partial v}{\partial t} + v\frac{\partial}{\partial x}(v) + v\frac{\partial}{\partial y}(v) + w\frac{\partial}{\partial z}(v) = \frac{-1}{\rho}\frac{\partial \mathrm{p}}{\partial y} + \vartheta\left(\frac{\partial^2 v}{\partial x^2} + \frac{\partial^2 v}{\partial y^2} + \frac{\partial^2 v}{\partial z^2}\right)$$

$$\frac{\partial w}{\partial t} + u\frac{\partial}{\partial x}(w) + v\frac{\partial}{\partial y}(w) + w\frac{\partial}{\partial z}(w) = \frac{-1}{\rho}\frac{\partial \mathrm{p}}{\partial z} + \vartheta\left(\frac{\partial^2 w}{\partial x^2} + \frac{\partial^2 w}{\partial y^2} + \frac{\partial^2 w}{\partial z^2}\right)$$

We can identify the characteristics of each term

$$\frac{\partial \mathrm{u}}{\partial t} \quad + \quad \mathrm{u}\nabla\mathrm{u} \quad = \quad \frac{-1}{\rho}\nabla\mathrm{p} \quad + \quad \vartheta\nabla^2\mathrm{u}$$

The terms are: unsteady acceleration, convective acceleration, pressure-gradient, and turbulent viscosity. Several observations can be made on the equations; first, the equations are expressed in velocity terms rather than position. The unsteady acceleration indicates the velocity is a function of time. The convective acceleration term is nonlinear, representing a change in velocity with position not just time, and the dependent variables appear in each equation yielding, at any given time, 4 coupled equations (continuity and x, y, and z momentum) with 4 unknowns (*u, v, w, p*) requiring an iterative solution for time step. The complication is that the model's grid size needs to account for the smallest eddies in the turbulent flow field, therefore reducing the uncertainty imposed by simplified models that estimate unresolved scales comes at the expense of extremely challenging computational requirements. The goal of resolving all the length and time scales is reasonably attainable when the flow is a single phase jet, but as the breakup process progresses, the smallest length scale approaches zero as the droplet is pinched-off the ligament to form an independent body. To deal with this limitation, modeling is introduced to facilitate a practical solution while still maintaining sufficient solution fidelity. The two dominate methods for turbulent modeling are Large-Eddy Simulation (LES) proposed by Smagorinsky [11] and Deardorff [12] and Reynolds-Averaged Navier-Stokes Equations (RANS) proposed by Deardorff [12] in the 1970's. A graphical representation of the solution techniques is provided in Figure 13, showing both the resolved and modeled portions of the DNS, LES, and RANS closures to Navier Stokes equations from Bakker [13].

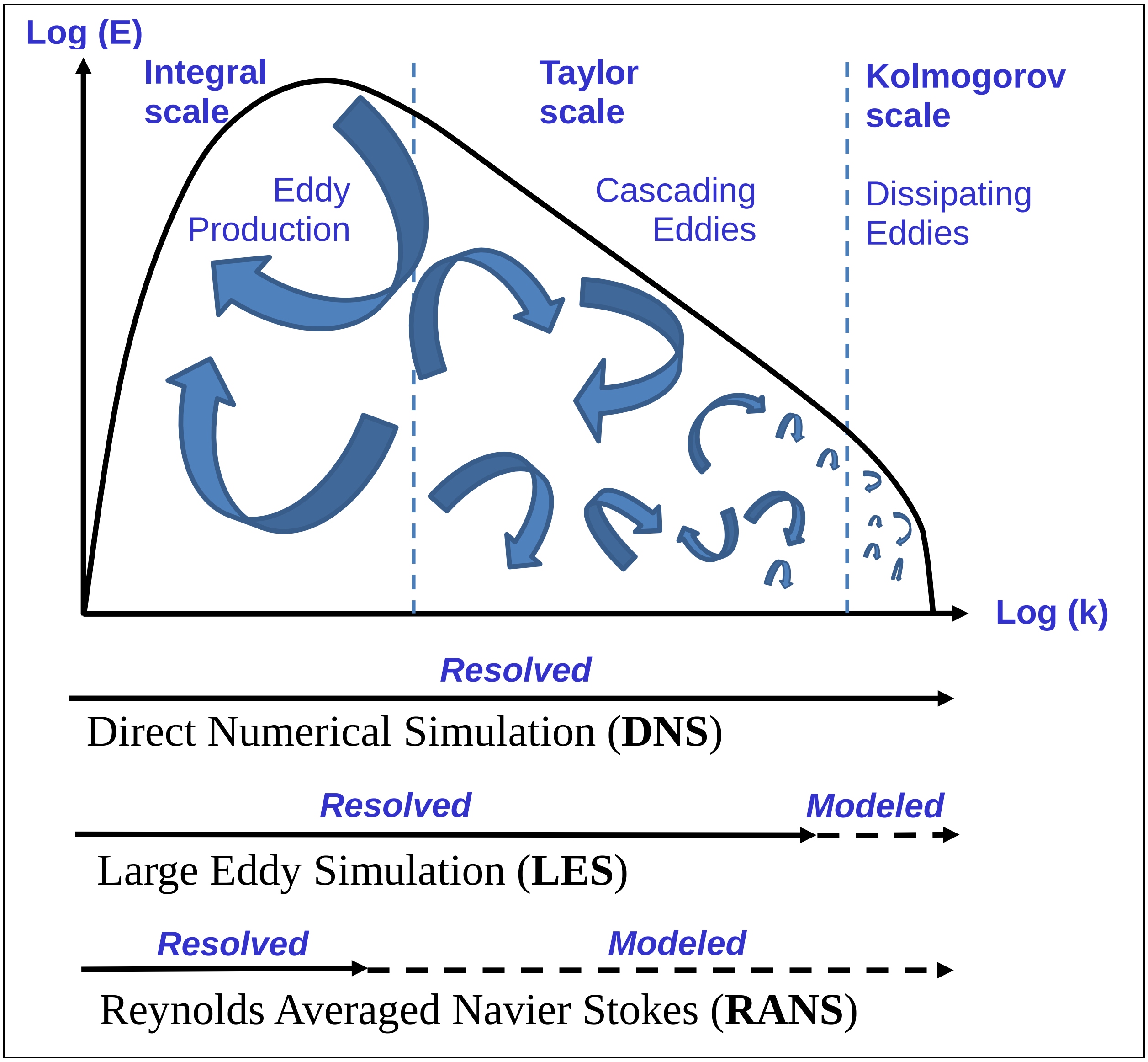


Figure 13 Graphic Representation of Solutions: DNS, LES, and RANS

### 2.3.1 Reynolds-Averaged Navier-Stokes Equations (RANS)

Modeling by use of Reynolds-Averaged Navier-Stokes Equations (RANS) is an attempt to close the Navier-Stokes equations by splitting them into averaged ($\overline{\mu}$) and varying ($\mu'$) parts. If we define a velocity $\mu\ (x)$ varying in time this can be viewed as:

$$\mu\ (x,t) = \overline{\mu}(x,t) + \mu'(x,t)$$

The splitting, or decomposition, concept is shown in Figure 14, where the variable Velocity is decomposed into an average and fluctuating signal. Likewise, this approach can be applied to pressure and other properties of the fluid field.

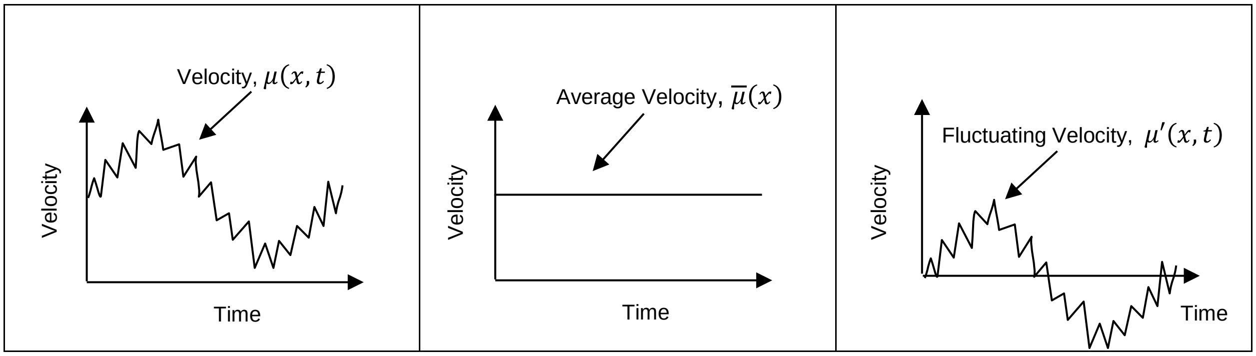

Figure 14 Velocity decomposed into Average Velocity and Fluctuating Velocity

The averaging operation is associated with time averaging:

$\overline{\mu}(x,t) \approx \overline{\mu}(x) = \lim_{T\to\infty} \frac{1}{T}\int_0^T \mu(x,t)\,dt$ , and the decomposition is: $u = \overline{u} + u'$

From this we see $\overline{u}$ is constant over time and therefore $\overline{\overline{u}} = \overline{u}$ and by definition $\overline{u'} = 0$

If we apply the concept of average and fluctuating components to the continuity equation we get:

$$\frac{\partial u}{\partial x} + \frac{\partial v}{\partial y} + \frac{\partial w}{\partial z} = \frac{\partial(\overline{u} + u')}{\partial x} + \frac{\partial(\overline{v} + v')}{\partial y} + \frac{\partial(\overline{w} + w')}{\partial z} = 0$$

Distributing the partial differentiation:

$$\frac{\partial \overline{u}}{\partial x} + \frac{\partial u'}{\partial x} + \frac{\partial \overline{v}}{\partial y} + \frac{\partial v'}{\partial y} + \frac{\partial \overline{w}}{\partial z} + \frac{\partial w'}{\partial z} = 0$$

Now if we take the average of the equation we get:

$$\overline{\frac{\partial \overline{u}}{\partial x} + \frac{\partial u'}{\partial x} + \frac{\partial \overline{v}}{\partial y} + \frac{\partial v'}{\partial y} + \frac{\partial \overline{w}}{\partial z} + \frac{\partial w'}{\partial z}} = \overline{0}$$

And from our earlier identities we can substitute since the averages of the average part $\overline{\overline{u}} = \overline{u}$ and the average of the fluctuating part $\overline{u'} = 0$ resulting in **the averaged continuity equation:**

$$\boxed{\frac{\partial \overline{u}}{\partial x} + \frac{\partial \overline{v}}{\partial y} + \frac{\partial \overline{w}}{\partial z} = 0} \qquad (1)$$

We can apply the same treatment to the x-momentum equation:

$$\frac{\partial u}{\partial t} + \frac{\partial}{\partial x}(u^2) + \frac{\partial}{\partial y}(uv) + \frac{\partial}{\partial z}(uw) = \frac{-1}{\rho}\frac{\partial \text{p}}{\partial x} + \vartheta\left(\frac{\partial^2 u}{\partial x^2} + \frac{\partial^2 u}{\partial y^2} + \frac{\partial^2 u}{\partial z^2}\right)$$

Again we take the average of both sides of the equation

$$\overline{\frac{\partial u}{\partial t} + \frac{\partial}{\partial x}(u^2) + \frac{\partial}{\partial y}(uv) + \frac{\partial}{\partial z}(uw)} = \overline{\frac{-1}{\rho}\frac{\partial \text{p}}{\partial x} + \vartheta\left(\frac{\partial^2 u}{\partial x^2} + \frac{\partial^2 u}{\partial y^2} + \frac{\partial^2 u}{\partial z^2}\right)}$$

Applying the properties of averaging to addition and multiplication we get:

$$\frac{\partial \overline{u}}{\partial t} + \frac{\partial}{\partial x}\left(\overline{u^2}\right) + \frac{\partial}{\partial y}(\overline{uv}) + \frac{\partial}{\partial z}(\overline{uw}) = \frac{-1}{\rho}\frac{\partial \overline{\text{p}}}{\partial x} + \vartheta\left(\frac{\partial^2 \overline{u}}{\partial x^2} + \frac{\partial^2 \overline{u}}{\partial y^2} + \frac{\partial^2 \overline{u}}{\partial z^2}\right)$$

Substituting the decomposition, $u = \overline{u} + u'$ we get:

$$\frac{\partial \overline{u}}{\partial t} + \frac{\partial}{\partial x}\left(\overline{u^2} + \overline{u'u'}\right) + \frac{\partial}{\partial y}\left(\overline{uv} + \overline{u'v'}\right) + \frac{\partial}{\partial z}\left(\overline{uw} + \overline{u'w'}\right)$$

$$= \frac{-1}{\rho}\frac{\partial \overline{\text{p}}}{\partial x} + \vartheta\left(\frac{\partial^2 \overline{u}}{\partial x^2} + \frac{\partial^2 \overline{u}}{\partial y^2} + \frac{\partial^2 \overline{u}}{\partial z^2}\right)$$

Next we can rearrange the equation by moving the fluctuating part to the right hand side generating **the averaged x-momentum equation:**

$$\frac{\partial \overline{u}}{\partial t} + \frac{\partial}{\partial x}\left(\overline{u^2}\right) + \frac{\partial}{\partial y}\left(\overline{uv}\right) + \frac{\partial}{\partial z}\left(\overline{uw}\right)$$
$$= \frac{-1}{\rho}\frac{\partial \overline{\mathrm{p}}}{\partial x} + \vartheta\left(\frac{\partial^2 \overline{u}}{\partial x^2} + \frac{\partial^2 \overline{u}}{\partial y^2} + \frac{\partial^2 \overline{u}}{\partial z^2}\right) + \frac{\partial}{\partial x}\left(\overline{u'u'}\right) + \frac{\partial}{\partial y}\left(\overline{u'v'}\right) + \frac{\partial}{\partial z}\left(\overline{u'w'}\right) \tag{2}$$

We can add **the averaged y-momentum equation:**

$$\frac{\partial \overline{v}}{\partial t} + \frac{\partial}{\partial x}\left(\overline{uv}\right) + \frac{\partial}{\partial y}\left(\overline{v^2}\right) + \frac{\partial}{\partial z}\left(\overline{vw}\right)$$
$$= \frac{-1}{\rho}\frac{\partial \overline{\mathrm{p}}}{\partial y} + \vartheta\left(\frac{\partial^2 \overline{v}}{\partial x^2} + \frac{\partial^2 \overline{v}}{\partial y^2} + \frac{\partial^2 \overline{v}}{\partial z^2}\right) + \frac{\partial}{\partial x}\left(\overline{u'v'}\right) + \frac{\partial}{\partial y}\left(\overline{v'v'}\right) + \frac{\partial}{\partial z}\left(\overline{v'w'}\right) \tag{3}$$

And **the averaged z-momentum equation:**

$$\frac{\partial \overline{w}}{\partial t} + \frac{\partial}{\partial x}\left(\overline{uw}\right) + \frac{\partial}{\partial y}\left(\overline{vw}\right) + \frac{\partial}{\partial z}\left(\overline{w^2}\right)$$
$$= \frac{-1}{\rho}\frac{\partial \overline{\mathrm{p}}}{\partial y} + \vartheta\left(\frac{\partial^2 \overline{w}}{\partial x^2} + \frac{\partial^2 \overline{w}}{\partial y^2} + \frac{\partial^2 \overline{w}}{\partial z^2}\right) + \frac{\partial}{\partial x}\left(\overline{u'w'}\right) + \frac{\partial}{\partial y}\left(\overline{v'w'}\right) + \frac{\partial}{\partial z}\left(\overline{w'w'}\right) \tag{4}$$

We now have derived the Reynolds-Averaged Navier-Stokes Equations (RANS). We started with 4 equations (continuity and x, y, z momentum) and 4 unknowns $(u, v, w, p)$ after applying decomposition into average $(\overline{u}, \overline{v}, \overline{w}, \overline{p})$ and fluctuating parts $(u', v', w', p')$ we have 10 unknowns $\left(\overline{u},\ \overline{v},\ \overline{w},\ \overline{p},\ \overline{u'u'},\ \overline{u'v'},\ \overline{u'w'},\ \overline{v'v'},\ \overline{v'w'},\ \overline{w'w'}\right)$ It should be noted that the fluctuating parts $(u', v', w', p')$ do not appear directly, but as the averaged products of fluctuating parts $\left(\overline{u'u'},\ \overline{u'v'},\ \overline{u'w'},\ \overline{v'v'},\ \overline{v'w'},\ \overline{w'w'}\right)$.

So closure of the Navier-Stokes equations is not possible unless some simplification or substitution is provided to eliminate some of the 10 unknowns. The 6 fluctuating products could be of magnitudes that are positive, negative, or zero value. First, let us consider if any of the 6 fluctuating products could be ignored or considered as zero or of negligible value. By definition of having turbulent flow, the turbulent flux terms $\left(\overline{u'u'},\ \overline{v'v'}\ ,\ \overline{w'w'}\right)$ are non-zero, since then the flow would be laminar not turbulent, nor are they negative, since the terms are squared. Experimentally, we find the magnitude of the turbulent term at times is similar to the averaged magnitude; therefore, the terms cannot be ignored as negligible. The Reynold stress cross product terms $\left(\overline{u'v'},\ \overline{u'w'},\ \overline{v'w'}\right)$ can be positive or negative, but cannot be assumed of zero magnitude. In 1877, French mathematician Joseph Valentin Boussinesq proposed the "Boussinesq Hypothesis" [13] defining a turbulent shear stress that is proportional to the mean flow strain rate, or "gradient transport":

$$\overline{u'v'} \approx \frac{1}{2}\left(\frac{\partial\,\overline{u}}{\partial\,y} + \frac{\partial\,\overline{v}}{\partial\,x}\right) \quad \text{or} \quad -\overline{u'v'} \approx \vartheta_t\left(\frac{\partial\,\overline{u}}{\partial\,y} + \frac{\partial\,\overline{v}}{\partial\,x}\right),\ \vartheta_t = \frac{-\overline{u'v'}}{\frac{1}{2}\left(\frac{\partial\,\overline{u}}{\partial\,y} + \frac{\partial\,\overline{v}}{\partial\,x}\right)}$$

The premise of the hypothesis is Newton's law for laminar flow where viscosity is the proportional constant of shear stress to strain rate. The value of the hypothesis is clear since it allows for closure of the RANS equation by giving turbulent averaged substitutions for the turbulent fluctuating terms. Now the validity of the hypothesis is challenged on several fronts as well discussed in the literature [15]. Unlike viscosity, which is a function of the fluid, turbulent eddy viscosity, $\vartheta_t$, like turbulence itself, is a function of the flow, and even with the hypothesis would be more properly defined as a vector rather than a scalar to match the local flow characteristics. Second, the hypothesis is based on a relation of small scale behavior, $\overline{u'}, \overline{v'}, \overline{w'}$, to large scale behavior, $\overline{u}, \overline{v}, \overline{w}$, contradicting our energy cascade framework for energy input, transfer, and dissipation. With serious reservations aside, the hypothesis does provide a pathway to closure if we have an estimate for turbulent viscosity, $\vartheta_t$ , which Boussinesq himself warned might be very difficult.

### 2.3.1.1 Zero dimensional model, mixing length model or algebraic model

The simplest solution is to define $\vartheta_t$ as a constant, meaning the turbulent contribution would vary in proportion to the mean flow velocity. We can construct this problem by evaluating our solution to flow between two parallel plates of infinite length as shown in Figure 15.

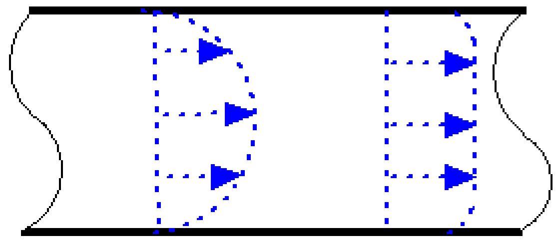

Figure 15 Field velocity profile for Laminar and Turbulent flows between plates

The averaged continuity and momentum equations in 2-D are:

$$\frac{\partial \bar{u}}{\partial x} + \frac{\partial \bar{v}}{\partial y} = 0$$

$$0 = \frac{-1}{\rho}\frac{\partial \bar{p}}{\partial x} + \vartheta_t\left(\frac{\partial \bar{u}}{\partial y} + \frac{\partial \bar{v}}{\partial x}\right) - \frac{\partial \overline{u'^2}}{\partial x} - \frac{\partial \overline{u'v'}}{\partial y}$$

If $\overline{u'v'} = 0$ then the velocity profile would be identical to that of laminar flow, therefore $\vartheta_t$ must be some non-zero value as defined as:

$$-\overline{u'v'} = \vartheta_t\left(\frac{\partial \bar{u}}{\partial y} + \frac{\partial \bar{v}}{\partial x}\right)$$

$$0 = C + \frac{\partial}{\partial y}\left(\vartheta\frac{\partial \bar{u}}{\partial y} + \vartheta_T\frac{\partial \bar{u}}{\partial y}\right)$$

$$\mathrm{C} = \frac{\partial}{\partial y}(\vartheta + \vartheta_T)\frac{\partial \bar{u}}{\partial y}$$

$$\mathrm{C} = \frac{\partial}{\partial y}\big(\vartheta\,(1 + c_1)\big)\frac{\partial \bar{u}}{\partial y} \quad where \quad \vartheta_T = c_1\vartheta$$

$$\vartheta_T = \; C\vartheta \frac{\partial^2 \overline{u}}{\partial y^2}$$

If $\vartheta_T$ is related to $\vartheta$ by a constant, while the velocity itself may vary in magnitude, the shape of the velocity profile must remain consistent with laminar flow adjusted by a scalar multiple, which is not the case. In order to affect the velocity profile in our simple flow between infinite plates example, we see that $\vartheta_t$ must vary for the flow as a function of distance from the plate or $\vartheta_t = f(y)$. Starting with our continuity and x-momentum equation:

$$\frac{\partial \overline{u}}{\partial x} + \frac{\partial \overline{v}}{\partial y} = 0$$

$$\frac{\partial \overline{u}^2}{\partial x} + \frac{\partial \overline{uv}}{\partial y} = \frac{-1}{\rho}\frac{\partial \overline{\mathrm{p}}}{\partial x} + \vartheta\left(\frac{\partial \overline{u}}{\partial y}\right) - \frac{\partial \overline{u'^2}}{\partial \mathrm{x}} - \frac{\partial \overline{u'v'}}{\partial \mathrm{y}}$$

our y-momentum equation:

$$\frac{\partial \overline{uv}}{\partial x} + \frac{\partial \overline{v^2}}{\partial y} = \frac{-1}{\rho}\frac{\partial \overline{\mathrm{p}}}{\partial y} + \vartheta\left(\frac{\partial \overline{v}}{\partial x}\right) - \frac{\partial \overline{u'v'}}{\partial \mathrm{x}} - \frac{\partial \overline{v'^2}}{\partial \mathrm{y}}$$

Substitution yields:

$$\vartheta\left(\frac{\partial \overline{u}}{\partial y}\right) = \vartheta\left(\frac{\partial^2 \overline{u}}{\partial x^2} + \frac{\partial^2 \overline{u}}{\partial y^2}\right) = \frac{\partial}{\partial x}\left(\vartheta\frac{\partial \overline{u}}{\partial x}\right) + \frac{\partial}{\partial y}\left(\vartheta\frac{\partial \overline{u}}{\partial y}\right)$$

Applying the Boussinesq hypothesis:

$$-\overline{u'^2} = \vartheta_t\left(\frac{\partial\,\overline{u}}{\partial\,x}\right), \qquad -\overline{u'v'} = \vartheta_t\left(\frac{\partial\,\overline{u}}{\partial\,y}\right), \qquad -\overline{v'^2} = \vartheta_t\left(\frac{\partial\,\overline{v}}{\partial\,y}\right)$$

We can express the RANS equation as:

$$\frac{\partial\,\overline{u}^2}{\partial\,x} + \frac{\partial\,\overline{uv}}{\partial\,y} = \frac{-1}{\rho}\frac{\partial\,\overline{\mathrm{p}}}{\partial\,x} + \frac{\partial}{\partial\,x}\left((\vartheta\ +\ \vartheta_T)\frac{\partial\,\overline{u}}{\partial\,x}\right) + \frac{\partial}{\partial\,y}\left((\vartheta\ +\ \vartheta_T)\frac{\partial\,\overline{u}}{\partial\,y}\right)$$

In 1925, Prandtl [16] suggested considering the flow a collection of fluid particles where each fluid particle has influence on surrounding particles. This influence is important as by definition $\overline{u'v'}\ \neq 0$ since $u'$and $v'$ are not independent. So visualizing an eddy of swirling motion, the effect of the mean flow velocity $\overline{u'}$ has effect on the adjacent flow velocity $\overline{v'}$ as eddy convection. High rates of convection yield increased rates of heat exchange and mixing of turbulent flow. These eddies vary in size across the broad range of length scales as illustrated in Figure 16 so mixing is well distributed. If we consider the full spectrum of kinetic turbulent energy, *E*, it is defined as:

$$E = \frac{1}{2}\left(\overline{u^2} + \overline{v^2} + \overline{w^2}\right)$$

$$\vartheta_t = \left|-\overline{u'v'}\right|, \left|\quad\right| + coefficient$$

$$\left|-\overline{u'v'}\right| \approx \left|\left(l\frac{\partial\,\overline{u}}{\partial\,y}\right)\left(l\frac{\partial\,\overline{u}}{\partial\,y}\right)\right|$$

$$\approx\ l^2\left|\frac{\partial\,\overline{u}}{\partial\,y}\right|\left|\frac{\partial\,\overline{u}}{\partial\,y}\right|$$

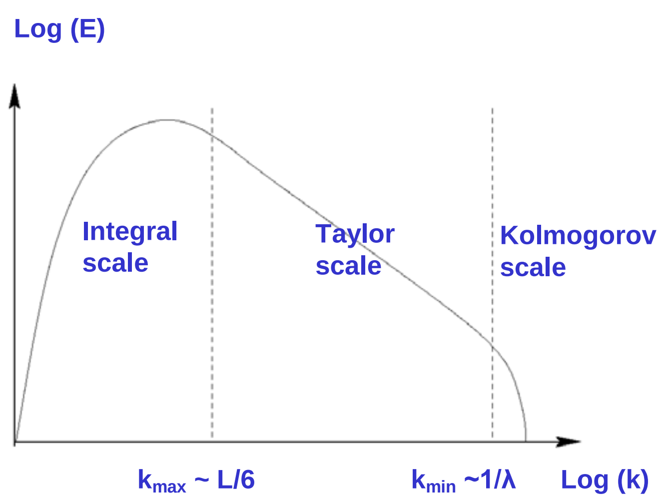


Figure 16 Turbulent energy across the length scale

Prandtl used experimental data to determine if a coefficient could be found such that mixing length $l_{mix}$ could be simply determined.

$l_{mix} = C\delta(x)$ *where* $\delta$ *is the characteristic length, like jet diameter*

A range of cases have been explored in literature and the value of the constant varied from 0.08 for a round jet to 0.18 for a far wave [17]. The value for $k_{max}$ is established by the geometry, the distance between the two plates in our example, and the ratio of $k_{max}/k_{min} \sim 10^3$ where $k_{min}$ represents geometry-independent dissipating length scales in the Kolmogorov range. The mixing length model's main advantage is ease of application to represent wall effects for the turbulent flow, providing a proper velocity profile, but it lacks time history effects in fully local solutions for the modeled turbulence yielding poor results for complex flows.

#### 2.3.1.2 One-Equation Model,

One-equation model family includes Spalart-Allmaras, Smagorinsky, Baldwin-Barth, and Prandtl. One-equation RANS models are mostly used in the aerospace industry where boundary effects are negligible. The Prandtl model defines the kinematic eddy viscosity as:

$$\vartheta_t = k^{\frac{1}{2}} l = C_D \frac{k^2}{\varepsilon} \ \text{where}\ \varepsilon = C_D \frac{k^{\frac{2}{3}}}{l}$$

Where the coefficient $C_D$=0.08

The main advantage of the one-equation model is it adds history effects to the RANS solution.

#### 2.3.1.3 Two-Equation Model, *k-ε* model

The two-equation model family attempts to better match the physical characteristics of turbulence with the addition of two additional transport equations (partial differential equations) representing the turbulent energy cascade with turbulent energy production, turbulent energy transfer, and turbulent energy dissipation. The most widely utilized model with excellent solution convergence characteristics is the *k-ε* model where the term k represents the turbulent kinetic energy and ε represents the turbulent kinetic energy dissipation rate given by:

$$k = \frac{1}{2}\left(\overline{u'^2} + \overline{v'^2} + \overline{w'^2}\right)$$

$$\varepsilon = 2\vartheta\overline{s'_{ij}s'_{ij}} \;\; where\; fluctuating\; strain\; rate\; tensor \;\; s'_{ij} = \frac{1}{2}\left(\frac{\partial u'_i}{\partial x_j} + \frac{\partial u'_j}{\partial x_i}\right)$$

$$\frac{\partial (k)}{\partial t} + \frac{\partial \left(k\overline{u_j}\right)}{\partial x_j} = \frac{\partial}{\partial x_j}\left(\frac{\vartheta_t}{\sigma_k}\frac{\partial k}{\partial x_j}\right) + 2\vartheta_t S_{ij} S_{ij} - \rho\varepsilon, \qquad where \;\; \vartheta_t = C_\vartheta \frac{k^2}{\varepsilon}$$

$$\frac{\partial (\varepsilon)}{\partial t} + \frac{\partial \left(\varepsilon\overline{u_j}\right)}{\partial x_j} = \frac{\partial}{\partial x_j}\left(\frac{\vartheta_t}{\sigma_\varepsilon}\frac{\partial \varepsilon}{\partial x_j}\right) + C_{1\varepsilon}\frac{\varepsilon}{k} 2\vartheta_t S_{ij} S_{ij} - 2C_{2\varepsilon}\frac{\varepsilon^2}{k}$$

$with\; widely\; used\; constants: C_\vartheta = 0.09, \sigma_k = 1.0, \sigma_\varepsilon = 1.3, C_{1\varepsilon} = 1.44, C_{2\varepsilon} = 1.92,$

With this closure, our RANS solution is expressed in 6 equations with 6 unknowns, $\overline{u}, \overline{v}, \overline{w}, \overline{p}, k, \varepsilon$ but with the addition of 5 constants, which must be determined empirically. Industry experience has shown *k-ε* model to be the most popular as the finite element solution is stable, converges quickly, and results have shown a fair representation of experimental data. There are several limits of the model as it does not accurately capture the effects of wall or boundary surfaces, so separate wall models are applied in practice. The *k-ε* model also does not perform well in swirling flows or flows with large separation, and in general the solutions are overly dissipative, thus eliminating turbulent effects more quickly than experimental data suggests appropriate.

## 2.3.2 Large Eddy Simulation (LES)

Modeling by use of Large Eddy Simulation (LES) is an attempt to close the Navier-Stokes equations by splitting, or decomposing, turbulent kinetic energy into large scale resolved portions and small scale modeled parts. If we define a velocity $\mu\ (x)$ varying in time, this can be decomposed into filtered Large Scale $(\tilde{\mu})$ and Small Scale $(\mu')$ parts through the application of a spatial filter. If we define a velocity $\mu\ (x,t)$ varying in time this can be viewed as:

$\mu\ (x,t)\ =\ \tilde{\mu}(x,t) +\ \mu'(x,t)$

The decomposition concept is illustrated in Figure 17 where the low-frequency

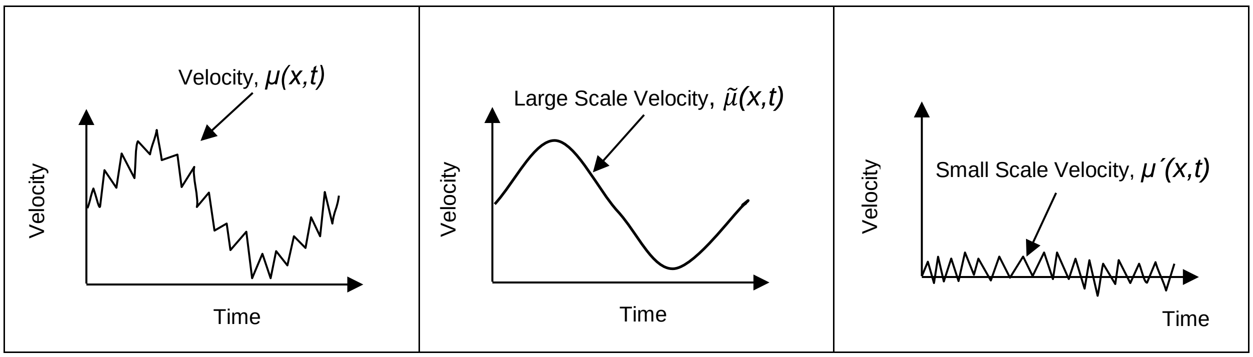


Figure 17 Velocity decomposed into Large Scale and Small Scale components

content of the Velocity signal is retained and directly resolved in the simulation, while the high frequency content, termed Sub-Grid-Stress (SGS), can be modeled. The filtering operation is associated with spatial averaging defined over domain Ω:

$\tilde{\mu}(x,t)\ =\ \frac{1}{V_\Omega}\int_\Omega \mu(x,t)\ dx\ , where\ V_\Omega\ represents\ Volume$, and the decomposition is:

$u = \tilde{\mu} +\ u'$

From Figure 17 we see that unlike RANS, time averaging $\tilde{u}$ is not constant over time and therefore $\tilde{\tilde{u}} \neq\ \tilde{u}$ and $\widetilde{u'} \neq 0$

As shown by Sagaut [18], we can also consider function $\mu(x,t)$ decomposition by defining the spatially-filtered function:

$$\tilde{\mu}(x,t) \equiv \frac{1}{V_{\Omega}} \int_{\Omega} G(x,x',|\Delta)\, x'dx' \;\; where\ G(x,x',|\Delta)\ is\ the\ kernel\ of\ the\ filter$$

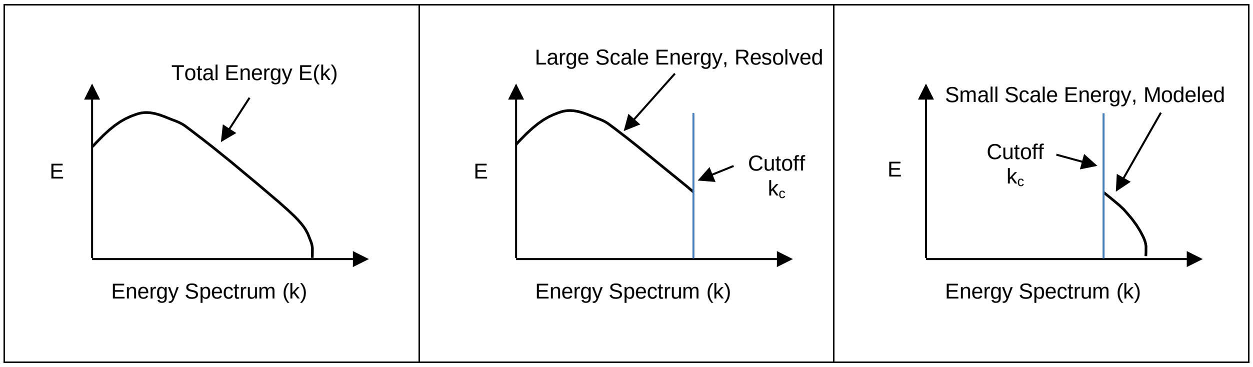


Figure 18 Spectral Decomposition of Total Energy into Large Scale and Small Scale components

Performing the decomposition, a low-pass filter provides the large-scale content to be resolved, and the high-pass filter portion yields the small-scale energy to be modeled, as illustrated in Figure 18. Various filter types: Gaussian, Box or Top-hat, or Sharp cutoff have been used and their specific filter characteristic impact the transformation.

The Gaussian filter is smooth where:

$$G(x,\Delta) = \sqrt{\frac{6}{\pi\Delta^2}}\, e^{\left(-\frac{6x^2}{\Delta^2}\right)}$$

The Box or Top-hat filter commonly applied to FE where the grid establishes Δ:

$$G(x,\Delta) = \begin{cases} \frac{1}{\Delta} where & \left(|x'| \le \frac{\Delta}{2}\right) \\ 0 & otherwise \end{cases}$$

The Sharp cutoff filter can be thought of as a Fourier space transformation (FFT) removing wave numbers above a cutoff value, $k_c$, the sharp cutoff filter is the only true projection filter:

$$\dot{G}(k,\Delta) = \begin{cases} 1\ where & \left(k \le \frac{\pi}{\Delta}\right) \\ 0 & otherwise \end{cases}$$

The cutoff length, Δ(x), establishes the cutoff frequency $k_c$ for the scale separation. Any cutoff length can be chosen, but a value smaller than the mesh size in the finite element model would be meaningless.

$$\Delta = \sqrt[3]{\Delta_x \Delta_y \Delta_z}$$

The filtered velocity is represented as:

$$\widetilde{u_i}(x,t) \equiv \int G(x,x',\Delta) u_i(x',t)\, dx'$$

If we apply the concept to the conservation of mass we get **the filtered continuity equation:**

$$\boxed{\frac{\partial \tilde{u}}{\partial x} + \frac{\partial \tilde{v}}{\partial y} + \frac{\partial \tilde{w}}{\partial z} = 0} \quad (1)$$

We can apply the same filtered component to the x-momentum equation:

$$\frac{\partial \tilde{u}}{\partial t} + \frac{\partial (\widetilde{uv})}{\partial y} = \frac{-1}{\rho}\frac{\partial \tilde{p}}{\partial x} + \vartheta \frac{\partial}{\partial y}\left(\frac{\partial \tilde{u}}{\partial y} + \frac{\partial \tilde{y}}{\partial x}\right) = \frac{-1}{\rho}\frac{\partial \tilde{p}}{\partial x} + 2\vartheta \frac{\partial}{\partial y}\tilde{S}_{xy}$$

$$where\ fluctuating\ strain\ rate\ tensor\quad \tilde{S}_{xy} = \frac{1}{2}\left(\frac{\partial \tilde{u}}{\partial y} + \frac{\partial \tilde{y}}{\partial x}\right)$$

The non-linear term $\widetilde{uv}$ must be expressed in terms of filtered variables for a solution.

#### 2.3.2.1 Leonard's Decomposition for the non-linear term $\widetilde{uv}$

An approach for decomposing the non-linear term $\widetilde{uv}$ was proposed by Leonard [19] as:

$$\widetilde{uv} = \widetilde{(\tilde{u} + u')(\tilde{v} + v')}$$

$$= \widetilde{\tilde{u}\tilde{v}} + \widetilde{\tilde{u}v'} + \widetilde{\tilde{v}u'} + \widetilde{u'v'}$$

Grouping the fluctuating terms per Germano [20] we can define a subgrid tensor $\tau_{ij}$, as:

$$\tau_{xy} = \widetilde{\tilde{u}v'} + \widetilde{\tilde{v}u'} + \widetilde{u'v'} = \widetilde{uv} - \widetilde{\tilde{u}\tilde{v}}$$

The $\widetilde{\tilde{u}\tilde{v}}$ term requires a second application of the filter. Leonard proposed to express it in components that could be grouped to provide context to the physics of turbulence starting with the Leonard Tensor $L_{ij}$ , which represents the interaction of the large scales:

$$\widetilde{\tilde{u}\tilde{v}} = \left(\widetilde{\tilde{u}\tilde{v}} - \tilde{u}\tilde{v}\right) + \tilde{u}\tilde{v}$$

$$= L_{ij} + \tilde{u}\tilde{v} \quad or \;\; L_{xy} = \widetilde{\tilde{u}\tilde{v}} - \tilde{u}\tilde{v}$$

The Cross term tensor $C_{ij}$ represents the interactions between the large and small scales, and the Reynolds subgrid scale tensor $R_{ij}$ represents the subgrid scale interactions.

$$C_{ij} = \widetilde{\tilde{u}v'} + \widetilde{\tilde{v}u'}$$

$$R_{ij} = \widetilde{u'v'}$$

The resulting subgrid tensor as defined is a function of the grid size, and as $\Delta \to 0$ the stress tensor $\tau \to 0$, therefore the LES model approaches the DNS solution. The Leonard tensor and Cross tensor are not Galilean invariant, although the entire SGS tensor $\tau$ is, leading to modeling of the entire SGS tensor as the preferred solution.

Now substituting $\widetilde{uv} = \tau_{xy} + \tilde{u}\tilde{v}$ we get **the filtered x-momentum equation**:

$$\frac{\partial \tilde{u}}{\partial t} + \frac{\partial (\widetilde{uv})}{\partial y} = -\frac{1}{\rho}\frac{\partial \tilde{p}}{\partial x} + 2\vartheta \frac{\partial}{\partial y}\tilde{S}_{xy}$$

$$\frac{\partial \tilde{u}}{\partial t} + \frac{\partial \left(\tau_{xy} + \tilde{u}\tilde{v}\right)}{\partial y} = -\frac{1}{\rho}\frac{\partial \tilde{p}}{\partial x} + 2\vartheta \frac{\partial}{\partial y}\tilde{S}_{xy}$$

$$\frac{\partial \tilde{u}}{\partial t} + \frac{\partial (\tilde{u}\tilde{v})}{\partial y} = -\frac{1}{\rho}\frac{\partial \tilde{p}}{\partial x} + 2\vartheta \frac{\partial}{\partial y}\tilde{S}_{xy} - \frac{\partial \tau_{xy}}{\partial y}$$

$$\boxed{\frac{\partial \tilde{u}}{\partial t} + \frac{\partial (\tilde{u}\tilde{v})}{\partial y} = -\frac{1}{\rho}\frac{\partial \tilde{p}}{\partial x} + 2\vartheta \frac{\partial}{\partial y}\tilde{S}_{xy} - \frac{\partial \tau_{xy}}{\partial y}} \qquad (2)$$

Similarly **the filtered y-momentum equation:**

$$\boxed{\frac{\partial \tilde{v}}{\partial t} + \frac{\partial (\tilde{v}\tilde{w})}{\partial z} = -\frac{1}{\rho}\frac{\partial \tilde{p}}{\partial y} + 2\vartheta \frac{\partial}{\partial z}\tilde{S}_{yz} - \frac{\partial \tau_{yz}}{\partial z}} \qquad (3)$$

Similarly **the filtered z-momentum equation:**

$$\boxed{\frac{\partial \tilde{w}}{\partial t} + \frac{\partial (\tilde{w}\tilde{z})}{\partial x} = -\frac{1}{\rho}\frac{\partial \tilde{p}}{\partial z} + 2\vartheta \frac{\partial}{\partial x}\tilde{S}_{zx} - \frac{\partial \tau_{zx}}{\partial x}} \qquad (4)$$

Therefore, we now have 4 filtered equations with 4 filtered unknowns $(\tilde{u}, \tilde{v}, \tilde{w}, \tilde{p})$ plus Subgrid

Stress Tensor terms$(\tau_{xy}, \tau_{yz}, \tau_{zx})$, which must be modeled.

### 2.3.2.2 Smagorinsky Model

The Smagorinsky Model [11] was first used by Deardorff [12] in his original work for closure of LES equations. This occurred in the same time period of RANS work, and not surprisingly, the Smagorinsky or Smagorinsky-Lilly [21] closure is based on the Boussinesq hypothesis used in RANS closure work of the same time period. It should be noted, however, one significant difference in LES solutions is that the SGS models represent a smaller portion of the turbulent solution than the RANS closure counterpart, resulting in a comparably smaller error being introduced. The essence of the Smagorinsky model is the assumption that the small scales are in equilibrium and thus entirely dissipate all the energy transferred from the resolved larger scales.

The SGS Tensor is defined as:

$$\tau_{SGSij} = -2\vartheta_{SGS}\tilde{S}_{ij}, \qquad and\ \ \vartheta_{SGS} = (C_S\Delta)^2|\tilde{S}|$$

Experimental data supports a turbulent deceleration coefficient range where $0.18 \le C_S \le 0.23$ , but empirical data also indicate the model is overly dissipative and in many situations near walls, which results in high shear rates, the constant must be decreased.

### 2.3.2.3 one-equation eddy viscosity SGS Model

Given the shortcomings of the algebraic model closure, alternative solutions add complexity to the simulation to better reflect the experimental data. As done earlier for the RANS closure, the first choice is a one-dimensional model like Spalart-Allmaras. A one-equation model was defined by Yoshizawa [22] defining a transport term where $\varepsilon$ is the turbulent dissipation rate and $\Delta$ is the SGS length scale.

$$\frac{\partial K}{\partial t} + \nabla(K\tilde{u}) = \nabla[(\vartheta + \vartheta_{SGS})\nabla K] - \varepsilon - \tau\tilde{S} \quad where\ \vartheta_{SGS} = C_k K^{\frac{1}{2}}\Delta\,, \qquad \varepsilon = \frac{C_\varepsilon K^{\frac{3}{2}}}{\Delta}$$

Empirical data suggests Model constants $C_k \approx 0.07$ and $C_\varepsilon \approx 1.05$

### 2.3.2.4 Scale Similarity SGS Model

Scale similarity models provide for additional interactions across turbulent scales by introducing a second level of filtering where:

$$\tau_{SGSij} = L_{ij} + C_{ij} + R_{ij}$$

$$where\ L_{ij} = \widetilde{\tilde{u}\tilde{v}} - \tilde{u}\tilde{v}\,, C_{ij} = (\tilde{u} - \tilde{\tilde{u}})\tilde{\tilde{v}} + (\tilde{v} - \tilde{\tilde{v}})\tilde{\tilde{u}}, R_{ij} = (\tilde{u} - \tilde{\tilde{u}})(\tilde{v} - \tilde{\tilde{v}})$$

This simplifies to:

$\tau_{SGSij} = \widetilde{\tilde{u}\tilde{v}} - \tilde{\tilde{u}}\tilde{\tilde{v}}$ Allowing for direct approximation based on filtered properties

### 2.3.2.5 SGS Model study

A study of the SGS closure methods: Smagorinski, one-equation eddy viscosity, and scale similarity was conducted by Weller [23] using a C++ based open source finite element code named FOAM (field operation and manipulation). The study case involved bluff bodies where the comparison was to a RANS *k-ε* model, RANS Launder-Gibson Reynolds stress model and RNG model. The results showed the RANS *k-ε* model performed poorly and the RANS Launder-Gibson Reynolds as well as the LES one-equation eddy viscosity models predicted flow near the obstacle well. Based on this conclusion, Delphi CFD analysis using open FOAM formulation is based on LES one-equation eddy viscosity model for closure according to Yoshizawa [22]

$$\frac{\partial K}{\partial t} + \nabla(K\tilde{u}) = \nabla[(\vartheta + \vartheta_{SGS})\nabla K] - \varepsilon - \tau\tilde{S} \qquad (7)$$

$$where\ \vartheta_{SGS} = C_k K^{\frac{1}{2}}\Delta\,,\ \varepsilon = \frac{C_\varepsilon K^{\frac{3}{2}}}{\Delta}$$

Where ε is the SGS turbulence dissipation rate, $\vartheta_{SGS}$ the SGS turbulent viscosity, and Δ is the SGS length scale (equivalent to the local computational cell size). The turbulence model constants have the values $C_K$ =0.07 and Cε = 1.05, in accordance with Yoshizawa.

### 2.3.3 Injector Nozzle Studies

Over the recent two decades, there has been significant recognition of the influence of the injector valve group design on the flow structure within the injector nozzle and the subsequent liquid jet primary breakup and atomization characteristics of the spray. The nozzles representative of the diesel fuel injectors have received extensive R&D attention, leading to identification of multiple fluid dynamic phenomena as influential factors that affect the spray primary breakup, including the cavitation [24] [25] [26] [27], turbulence [7] [28] [9], and vortices [29] [30] [31] that form after nozzle exit, upstream of the breakup, or within the valve group with subsequent breakup immediately at nozzle exit. It is notable that often these phenomena are concurrent and coupled; for instance, cavitation or separation can markedly influence the nozzle jet velocity distribution as well as impact jet turbulence levels.

The GDi multi-hole injector valve-group and spray atomization is receiving more attention [32] [33] [34] in line with the broad adoption of direct injection for gasoline engines as well as advances of the GDi combustion system, including the application of center-mount injectors for well-mixed homogenous charge combustion systems, and the more stringent requirements on fuel economy and emissions, especially the particulate number emission targets implemented in Europe. The experimental data indicates dependence of the spray plume structure and atomization on the GDi nozzle geometry, in addition to expected influence of the pintle-sac volume, due to its influence on the flow velocity field and formation of turbulent eddies. In this respect, despite the conceptual similarity with the diesel injectors, it is expected that the differences in the GDi nozzle geometry, in particular the nozzle thru-hole, length-to-diameter ratio, and injection pressure modify the profile of the velocity field, rate of acceleration, and nozzle-exit liquid jet velocity, are significant to render the key nozzle fluid dynamic and breakup features different than diesel injector nozzles. For example, it is expected that the short nozzle l/d renders the jet breakup characteristics more sensitive to the nozzle thru-hole entrance conditions and provides the potential occurrence of the hydraulic flip phenomenon [25]. The implication is that an accurate computational analysis of the flow within the injector valve group is an integral component of the analysis of the spray near-field breakup and atomization characteristics.

The VOF-LES method for analysis of the jet breakup process has been under development and verification over the past decade. The capability of the method has been broadly demonstrated [35] [36] [37] [38], although in all cases, the injector internal flow domain was excluded and the liquid jet VOF-LES simulations were performed with assumed nozzle-exit flow conditions or with imposed disturbances to represent turbulent fluctuations. The importance of the nozzle-exit flow condition on the jet breakup was investigated in the DNS "numerical experiments" of Sander and Weigand [38] [39] that demonstrated significant influence of the issuing jet velocity profile and turbulence disturbances on the jet primary breakup. The recent combined VOF-LES and spray imaging studies of the GDi conical [40] and planar-sheet [41] liquid jet atomization incorporated the injector valve group into the computational domain in order to couple the injector internal flow with the jet primary breakup process and to alleviate uncertainty or complexity associated with prescribing the nozzle-exit spatial and temporal initial conditions. These simulations provided good quantitative predictions of the jet breakup process, including the prediction of the Kelvin-Helmholtz instability wave length, and demonstrated both the strong dependence of the spray geometry and atomization characteristics on the details of the nozzle geometry, as well as the capability of the VOF-LES method to capture the effect of nozzle design on the jet primary breakup structure. Therefore, the VOF-LES of the injector valve-group internal flow and near-field primary breakup offers a useful tool for the investigation of the GDi multi-hole specific nozzle design geometry and the associated effect on the liquid plume structure and its primary breakup to be analyzed in this work.

# CHAPTER 3 OBJECTIVES OF THE STUDY

The optimization of the multi-hole GDi injector spray characteristics: atomization, spray plume angle, spray plume penetration, and spray targeting within the constraints imposed by engine geometry, to avoid spray impingement on all solid surfaces, is a crucial component of the combustion system optimization to meet the fuel consumption and emission objectives.

The GDi multi-hole injector must fulfill several requirements:

1) Precise fuel metering with a uniform or defined hole-to-hole flow rate distribution to promote proper charge mixing for combustion
2) Precise spray plume targeting geometry and defined plume penetration to avoid impingement on surfaces
3) Required atomization characteristics of plume angle and spray droplet-size distribution to promote evaporation and clean combustion

The simultaneous fulfillment of these requirements renders design optimization of the GDi injector valve group for specific combustion chamber geometry a non-trivial, and often iterative, process. This complexity owes to the inherent coupling of the injector fuel metering, spray targeting, and atomization characteristics as a result of the influence of the nozzle geometry on

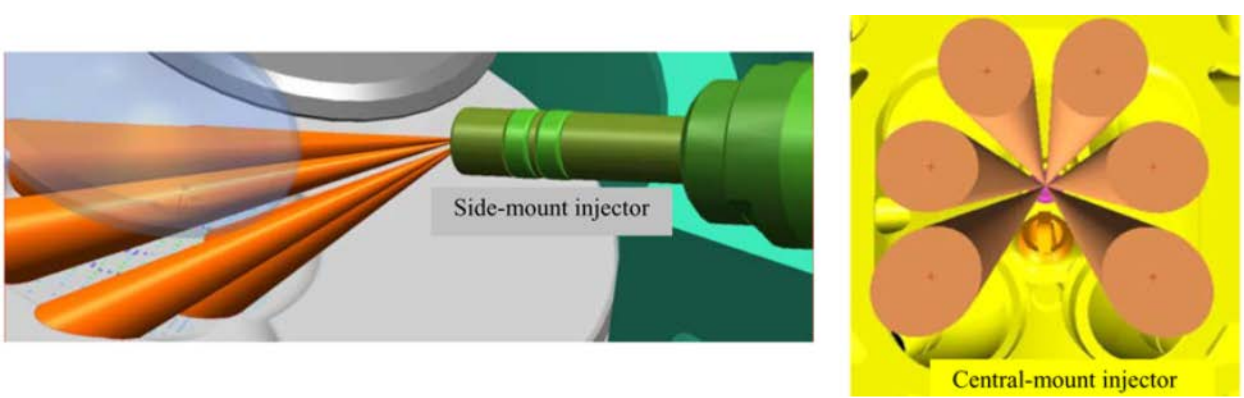


Figure 19 Application of side-mount and central-mount GDi injectors

all features of the spray. Although the physical packaging of the injector may vary for side or central-mount applications, the targeting goal of the spray plumes is consistent: targeting specific locations to avoid impingement on the valves, piston, and cylinder bore wall while providing excellent mixture distribution, especially near the spark plug electrode for proper emissions, as shown on Figure 19. These plume targets are typically defined relative to a downstream target, see Figure 20, and confirmed in a spray lab with a patternator (described in 4.3 Test Equipment), which calculates the mass centroid of each spray plume.

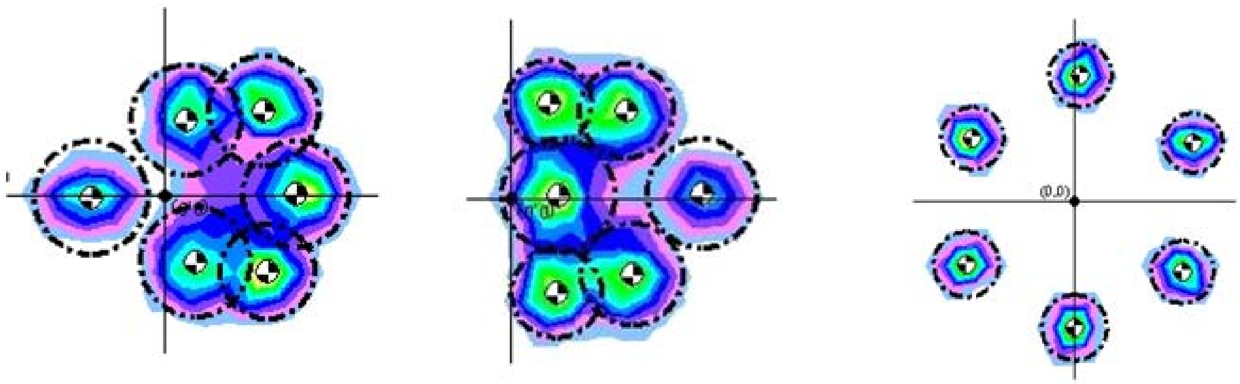

Figure 20 Visualization of spray plume targeting in side and central-mount GDi injectors

Currently, the GDi injector seat and nozzle design draws on significant empirical knowledge, developed through experimental valve-group hardware design and test programs. The major drawback of this method, apart from the cost and time requirement, is the difficulty to investigate one aspect of the spray characteristics in isolation (without affecting other spray features) in order to establish a direct and conclusive correlation of nozzle geometry to spray characteristics. One approach to address this complexity and establish a fundamental understanding of the relationship between the seat nozzle geometry and the spray characteristics is through application of advanced computational fluid dynamic (CFD) methods. In order to establish model verification, physical hardware and appropriate test methodology will be applied.

The fundamental geometry of interest for the nozzle, as defined in Figure 21 is:

1) Thru-hole length to diameter ratio (l/d)
2) Counterbore interaction with spray (D/d), (l+L)/d
3) Spray plume skew angle for targeting (β)

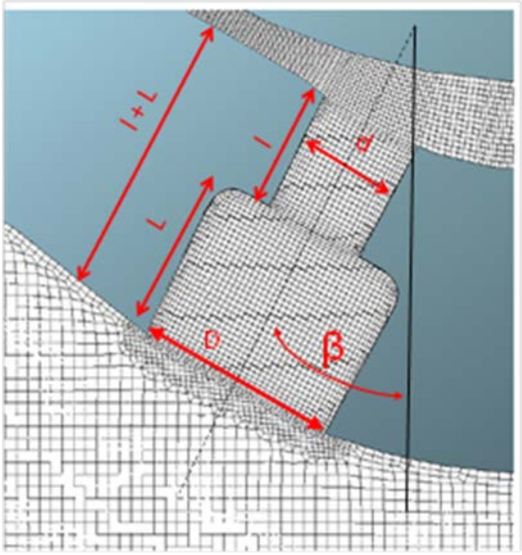


Figure 21 Definition of thru-hole, counterbore and skew angle geometry

# CHAPTER 4 OUTLINE OF THE STUDY METHODOLOGY

## *4.1 Defined Terms*

ASIE - after the start of injector energizing

ASOS - after the start of simulation

SOF - start of fuel, visual jet exiting the nozzle

d – nozzle thru-hole diameter

l – nozzle thru-hole length of diameter d

(l/d) – thru-hole length to diameter ratio

D – nozzle counterbore diameter

L – nozzle counterbore length of counterbore diameter D

(D/d) – ratio of counterbore diameter to thru-hole diameter

(l+L)/d – ratio of thru-hole length plus counterbore length to thru-hole diameter

β - spray plume skew angle for targeting

$D_{V90}$ – The drop diameter value that is a statistical indicator of the largest drops in the spray. 90% of the spray liquid volume and mass is contained within drops that have a diameter less than or equal to $D_{V90}$

$D_{V50}$ – The drop diameter value that is a statistical indicator of the median drop size. Half the spray volume and mass is contained in smaller, while half in larger drops. $D_{V50}$ is also sometimes referred to as the Mass Median Diameter (MMD) or Volume Mean Diameter (VMD)

Sauter Mean Diameter (SMD) – The drop diameter, which has the same ratio of the volume to surface area as that of the entire spray. This diameter is particularly useful for spray combustion modeling, can also be expressed at $D_{V32}$

u, U - fluid velocity field

($u$, $v$, $w$) the (x, y, z) components of the fluid velocity u

$\overline{\mathrm{u}}$ - averaged fluid velocity, where $\mathrm{u} = \overline{\mathrm{u}} + \mathrm{u}'$ applies to pressure and other averaged variables

u' - fluctuating fluid velocity

$(\overline{u}, \overline{v}, \overline{w})$ - the averaged (x, y, z) components of the fluid velocity averaged fluid velocity $\overline{\mathrm{u}}$

$\tilde{\mathrm{u}}$ - filtered fluid velocity, where $\mathrm{u} = \tilde{\mathrm{u}} + \mathrm{u}'$ applies to pressure and other filtered variables

$(\tilde{u}, \tilde{v}, \tilde{w})$ - the filtered (x, y, z) components of the fluid velocity filtered fluid velocity $\tilde{\mathrm{u}}$

$\vartheta$ – kinematic viscosity

$\vartheta_t$ - turbulent kinematic viscosity

Re - Reynolds number, = ρliquidULs / μ

We – Weber number, = ρliquidU2Ls/σ

Oh – Ohnesorge number, = μ / √(ρσLs)

Ma – Mach number, = U / speed sound

ρ - density

μ – viscosity

Ls – Length scale

σ – surface tension

τ - stress tensor

LES - Large Eddy Simulation

RANS - Reynolds Averaged Navier Stokes

DNS - Direct Numerical Simulation

This work will follow the SAE standard J2715 for spray nomenclature and measurement specification [42] terminology. Since fuel spray measurement and characterization is critical to the automotive industry, a comprehensive industry-wide set of measurement and reporting procedures and nomenclature was established to correct a situation where many spray parameters and test procedures had been created and utilized within individual automotive manufacturers, tier-one fuel system manufacturers, and third-party testing laboratories and universities. The SAE standard provides very detailed procedures and test specifications for all of the spray parameters, and establishes a neutral, unbiased test for each defined spray parameter. The adoption of a standard permits researchers to compare results from various published works with expectation of consistent definition and measure.

Table 1 Overview of Primary Spray Characterization Variables

| | TYPE OF TEST PROCEDURE IN SAE J2715 | | | |
|---|---|---|---|---|
| SPRAY CHARACTERIZATION PARAMETER (SAE Primary Set) | Spray Imaging | High-Res Patternation | Phase-Doppler Interferometry | Laser Diffraction |
| Spray Angle | ✓ (G-DI) | × | × | × |
| Main Spray Tip Penetration | ✓ (G-DI) | × | × | × |
| Sac Spray Tip Penetration | ✓ (G-DI) | × | × | × |
| Cone Angle | × | ✓ (PFI) | × | × |
| Separation Angle (Dual Spray Injector) | × | ✓ (PFI) | × | × |
| Cone Bend Angle (Bent Spray Injector) | × | ✓ (PFI) | × | × |
| Centroid Angle | × | ✓ (PFI) | × | × |
| Sauter Mean Diameter | × | × | ✓ (PFI & G-DI) | ✓ (PFI & G-DI) |
| Dv90 | × | × | ✓ (PFI & G-DI) | ✓ (PFI & G-DI) |
| Dv50 | × | × | × | ✓ (PFI & G-DI) |

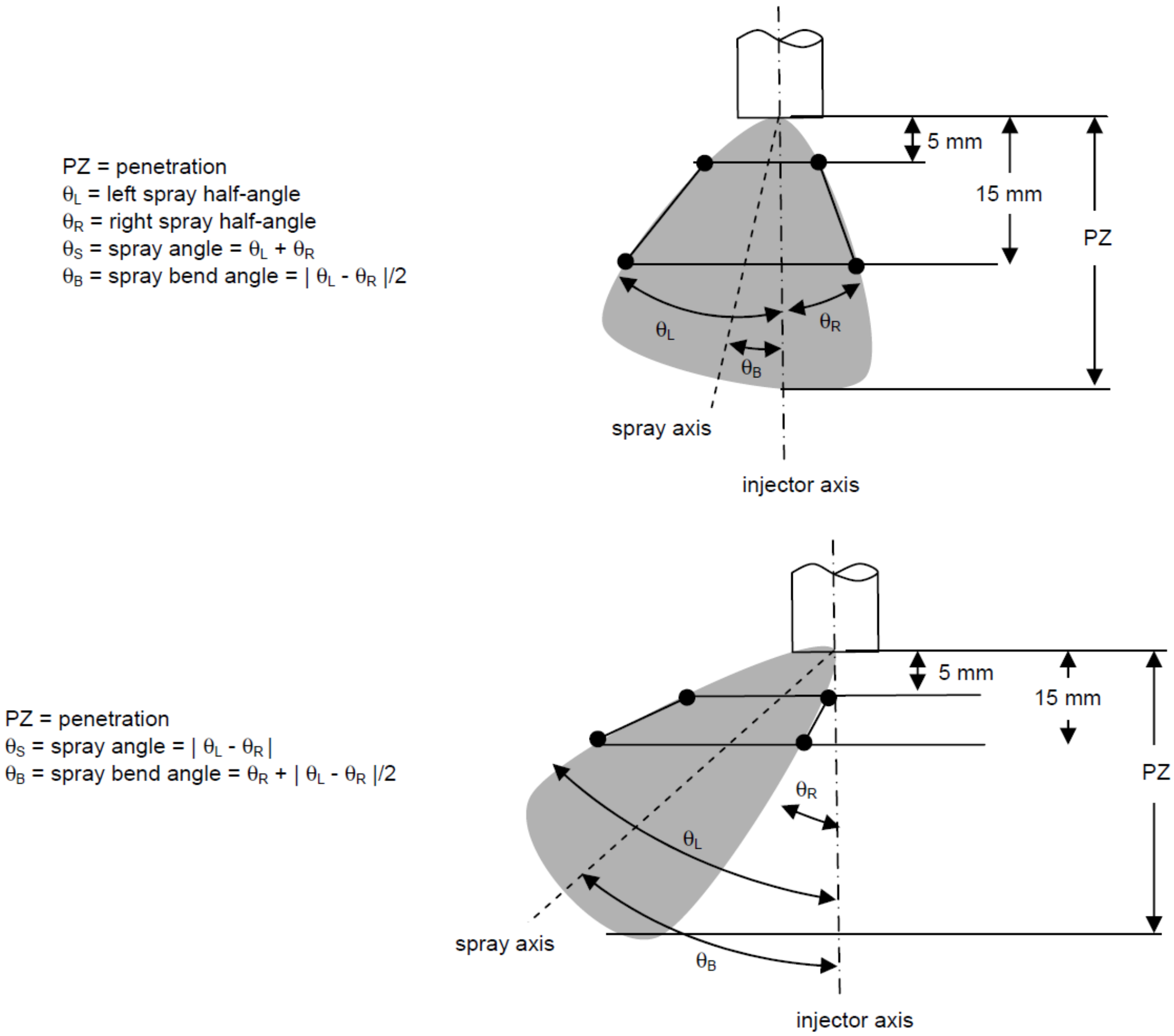


Figure 23 Determination of the SAE J2715 Spray Angle and Spray Bend Angle from a Digital Image of the Spray

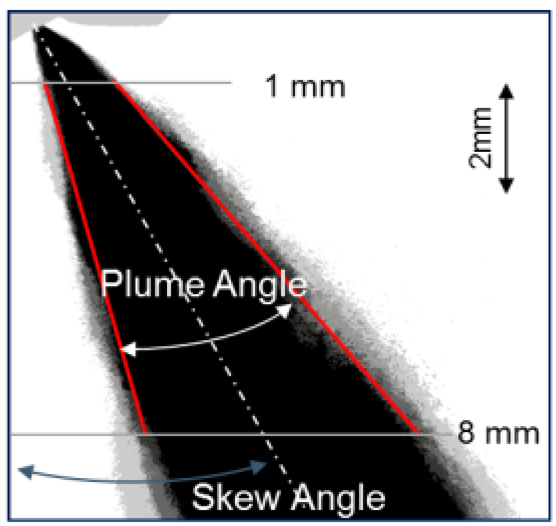


Figure 24 Nomenclature for near-field Plume angle

The spray angle is a measure of the angular extent of a GDi fuel spray, and is determined by backlit imaging. It is defined as the angle between the spray edges at 5mm and 15mm axially downstream from the injector tip at 1.5ms after the start of fuel (SOF). This angle is denoted as θs, and is illustrated schematically in Figure 23. The details of how the test for spray angle is to be conducted and reported are provided in Section 6.1 of the SAE standard. For the purpose of this paper, some measures of individual plumes in the near-field are desired. The nomenclature used will be plume angle, as shown in Figure 24. It is important to note that the spray angle, represented and described for GDi injectors, differs conceptually from the cone angle of a PFI spray, which is not calculated by imaging, but by a patternation test. Some literature still refers to cone angle when discussing GDi sprays; however, since the spray angle for GDi is determined by optical spray imaging, it will provide only a measure of the angular extent between spray edges, not the mass distribution between them. Hence, the distinctly different and non-interchangeable names, spray angle (GDi) and cone angle (PFI), describing two different metrics should *not* be interchanged.

### *4.2 Test Hardware*

GDi injector and special seats for study are based on production applications of the side-mount and center-mount type shown in Figure 4. The design of the product was developed using a Design for Six Sigma innovation methodology [43]. Several unique features resulted from the methodology including a decoupled armature, providing for low bounce thus minimizing audible noise and after-closing injections, a valve group optimized for fast response and low shot-to-shot flow variation, and a valve group designed for accurate spray targeting. A cross-section of the injector showing the actuator coil and armature details and valve seat group is presented in Figure 25.

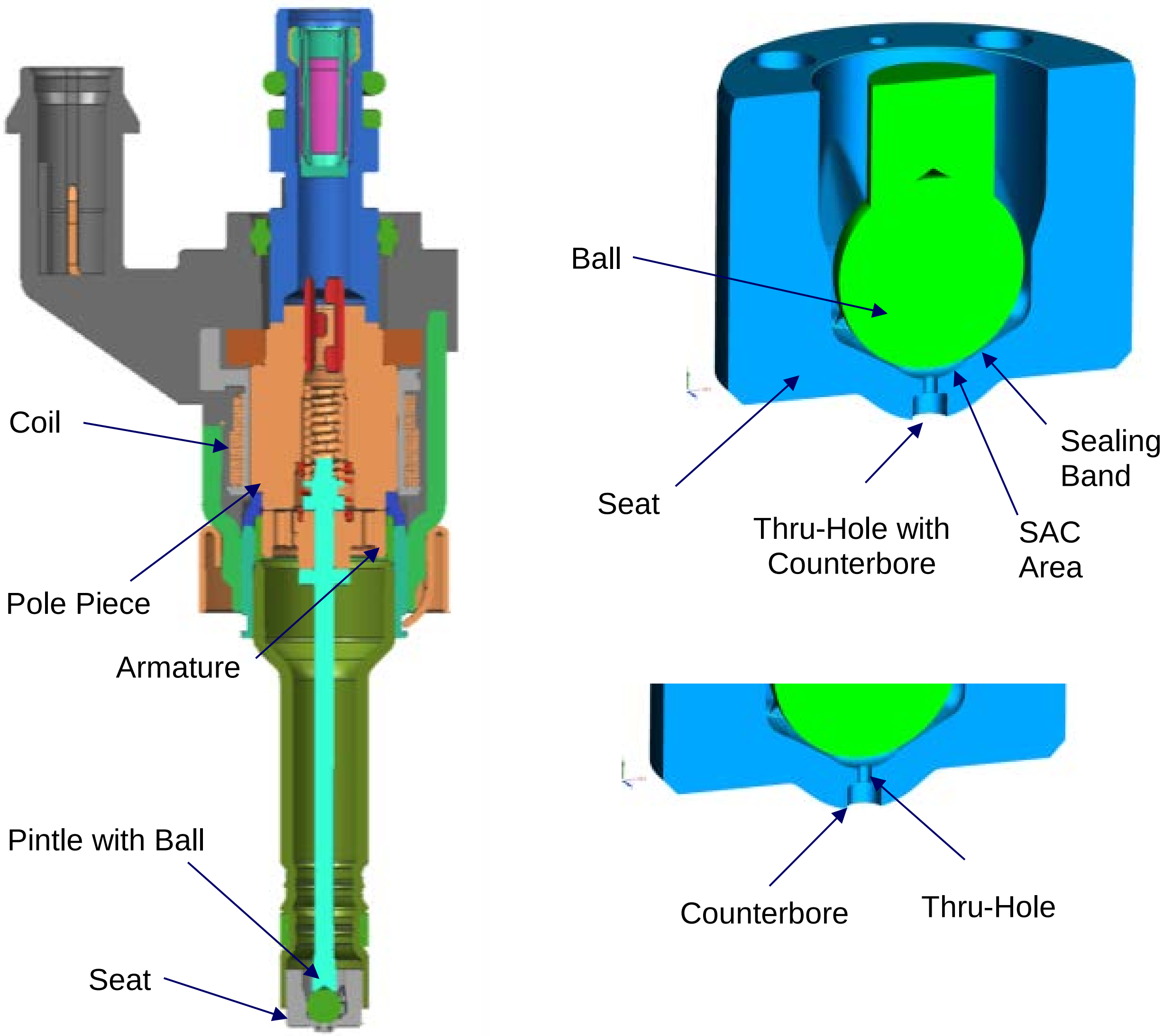


Figure 25 Cross-section views of GDi injector and Seat Nozzle geometry

To facilitate the study of nozzle parameter design on spray characteristics, a series of special seats were designed incorporating the desired geometry per the definition provided in Figure 26, as shown in Table 2, Injector spray study prototype seat definition. The initial study focused on axis-symmetric single-hole nozzles, seats 1-6, and 10-12. This direction followed previous work on diesel nozzles with the desired benefit of a clearer view of the spray morphology by focusing on a single spray plume downstream unaffected by other plumes. A typical GDi injector application has 5 to 6 spray plumes and a temporal spray study would be difficult due to the high liquid density, especially at the higher 20MPa injection pressure test conditions. The baseline nozzle is typical of production GDi injectors with a ≈0.20mm diameter thru-hole of ≈0.22mm length exiting in a ≈0.50mm diameter counterbore of ≈0.37mm length. More specific values are not included at the request of Delphi to maintain proprietary information; however, all listed approximations are scaled to the ≈.20mm reference, and therefore the calculations for ratios that are key to this work, are accurately represented. The counterbore serves several functions; first it allows the thru-hole l/d to be in a practical range for manufacture while maintaining the overall seat thickness of l+L to maintain structural integrity for the high pressure. The counterbore also provides a buffer for the thru-hole exit from the high temperatures of the combustion chamber. One critical design requirement is robustness to buildup of deposits at the nozzle exit since they directly impact spray morphology and hence combustion performance. The defined baseline geometry for seat 1 is then defined as:

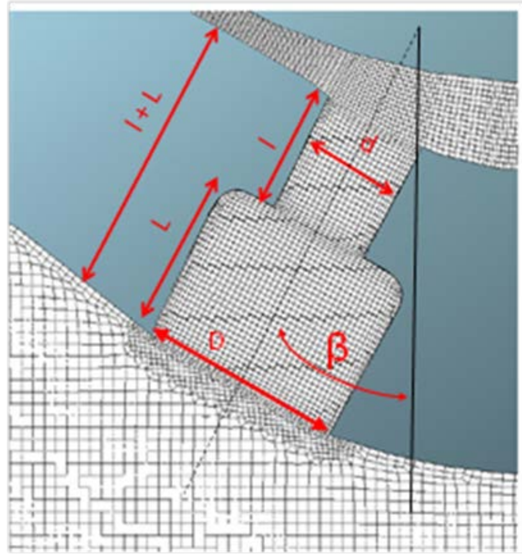

Figure 26 Definition of thru-hole, Counterbore and skew angle geometry

$$\frac{l}{d} = \frac{\approx.2}{\approx.22} = 1.10 \qquad \frac{(l+L)}{d} = \frac{(\approx.22+\approx.37)}{\approx.22} = 2.95 \qquad \frac{D}{d} = \frac{\approx.5}{\approx.2} = 2.50$$

Seat 2 targeting a long l/d is produced by elimination of the majority of the counterbore increasing l to ≈0.60mm. Seat 3 was defined as the baseline with the counterbore ground off generating the same l/d to isolate the effect of the counterbore. Seats 4-6 repeated the sequence, but with a different thru-hole diameter also indicative of production GDi injectors, to isolate the effect of d independently of ratio l/d. Seats 10-12 duplicated the geometry , but with a skew angle of 30º, typical of application where each spray plume is defined to target areas in the combustion chamber for optimized atomization and mixing, while avoiding impingement on surfaces of the valves, piston, or cylinder wall. Seats 7-9, derived from the baseline geometry, also included a skew angle, and as well added additional thru-holes to understand the effects that multi-hole fluid motion has on spray morphology.

Table 2 Injector spray study prototype seat definition

| AK29 | 01 | 02 | 03 | 04 | 05 | 06 | 07 | 08 | 09 | 10 | 11 | 12 |
|---|---|---|---|---|---|---|---|---|---|---|---|---|
| test nozzles | SHN(baseline) | SHN2(Long) | SHN3(short) | SHN4(small) | SHN5(s-L) | SHN6(s-s) | 3HN(baseline) | 3HN2(long) | 3HN3(short) | SHN4(small) | SHN5(s-L) | SHN6(s-s) |
| d(mm) | ≈0.20 | ≈0.20 | ≈0.20 | ≈ 0.15 | ≈ 0.15 | ≈ 0.15 | ≈0.20 | ≈0.20 | ≈0.20 | ≈ 0.15 | ≈ 0.15 | ≈ 0.15 |
| l (mm) | ≈0.22 | ≈0.60 | ≈0.22 | ≈0.16 | ≈0.60 | ≈0.16 | ≈0.22 | ≈0.60 | ≈0.22 | ≈0.16 | ≈0.60 | ≈0.16 |
| D(mm) | ≈0.50 | ≈0.22 | ground | ≈0.37 | ≈0.15 | ground | ≈0.55 | ≈0.22 | ground | ≈0.37 | ≈0.15 | ground |
| L (mm) | ≈0.37 | na | na | ≈0.43 | na | na | ≈0.407 | na | na | ≈0.43 | na | na |
| β | 0° | 0° | 0° | 0° | 0° | 0° | ~30° | ~30° | ~30° | ~30° | ~30° | ~30° |
| l+L (mm) | ≈0.60 | ≈0.60 | ≈0.22 | ≈0.60 | ≈0.60 | ≈0.16 | ≈0.60 | ≈0.60 | ≈0.22 | ≈0.60 | ≈0.60 | ≈0.16 |
| **l/d** | **1.10** | **2.95** | **1.10** | **1.10** | **3.96** | **1.10** | **1.10** | **2.95** | **1.10** | **1.10** | **3.96** | **1.10** |
| **(l+L)/d** | **2.95** | **na** | **na** | **3.96** | **na** | **na** | **2.95** | **na** | **1.10** | **3.96** | **na** | **na** |
| **D/d** | **2.50** | **na** | **na** | **2.50** | **na** | **na** | **2.50** | **na** | | **2.50** | **na** | **na** |
| **Effects of** | | **l/d** | **c-bore** | | **l/d** | | **multi-hole** | **l/d** | **c-bore** | | | |
| **# of Holes** | **1** | **1** | **1** | **1** | **1** | **1** | **3** | **3** | **3** | **1** | **1** | **1** |
| | | | This is the same as #2, but grind flat on tip just to the bottom of the CB | | | This is the same as #5, but grind flat on tip just to the bottom of the CB | | | This is the same as #7, but grind flat on tip just to the bottom of the CB | | | This is the same as #11, but grind flat on tip to bottom of the CB |
| **Qty of Seats** | 5 | 5 | 5 | 5 | 5 | 5 | 5 | 5 | 5 | 5 | 5 | 5 |
| Seat P/N | 28331614A | 28331614B | 28331614C | 28331614D | 28331614E | 28331614F | 28331614G | 28331614H | 28331614I | 28331614J | 28331614K | 28331614L |
| Solid Model | 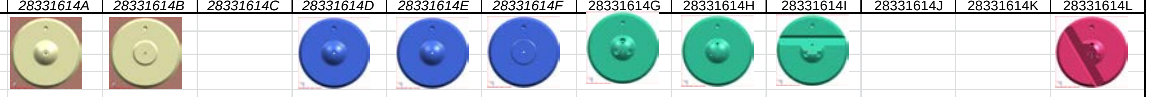 | | | | | | | | | | | |
| Seat Prototype | 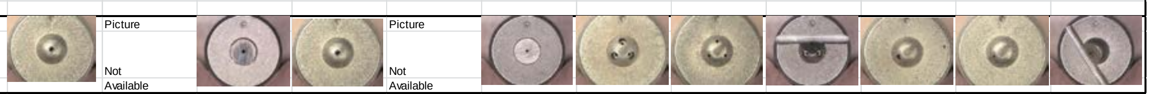 | Picture Not Available | | | Picture Not Available | | | | | | | |

| EWO | Proposed 2012 round of seats | | | | | | | | | | Added to order 11JUL12 | | |
|---|---|---|---|---|---|---|---|---|---|---|---|---|---|
| **AK29** | **13** | **14** | **15** | **16** | **17** | **18** | **19** | **20** | **21** | **22** | **23** | **24** | **07** |
| | | | | | | | | | | | | | 1-Aug-11 |
| | SHN(baseline) | l/d short | l/d mid | mid c/b | m c/b w/ 30 angle | narrow c/b | n c/b w 30angle | B w/ 10 angle | B w/ 20 angle | B w/ 30 angle | B w/ 10 angle | B w/ 20 angle | 3HN(baseline) |
| d(mm) | ≈0.20 | ≈0.20 | ≈0.20 | ≈0.20 | ≈0.20 | ≈0.20 | ≈0.20 | ≈0.20 | ≈0.20 | ≈0.20 | ≈0.20 | ≈0.20 | ≈0.20 |
| l (mm) | ≈0.22 | ≈0.11 | ≈0.33 | ≈0.22 | ≈0.22 | ≈0.22 | ≈0.22 | ≈0.22 | ≈0.22 | ≈0.22 | ≈0.22 | ≈0.22 | ≈0.22 |
| D(mm) | ≈0.50 | ≈0.50 | ≈0.50 | ≈0.40 | ≈0.40 | ≈0.30 | ≈0.30 | ≈0.50 | ≈0.50 | ≈0.50 | ≈0.50 | ≈0.50 | ≈0.50 |
| L (mm) | ≈0.37 | ≈0.48 | ≈0.26 | ≈0.37 | ≈0.37 | ≈0.37 | ≈0.37 | ≈0.37 | ≈0.37 | ≈0.37 | ≈0.37 | ≈0.37 | ≈0.37 |
| β | 0° | 0 ° | 0 ° | 0 ° | 30 ° | 0 ° | 30 ° | 10 ° | 20 ° | 30 ° | 10 ° | 20 ° | ~30° |
| l+L (mm) | ≈0.60 | ≈0.60 | ≈0.60 | ≈0.60 | ≈0.60 | ≈0.60 | ≈0.60 | ≈0.60 | ≈0.60 | ≈0.60 | ≈0.60 | ≈0.60 | ≈0.60 |
| **l/d** | **1.10** | **0.55** | **1.65** | **1.10** | **1.10** | **1.10** | **1.10** | **1.10** | **1.10** | **1.10** | **1.10** | **1.10** | **1.10** |
| **(l+L)/d** | **2.95** | **2.95** | **2.95** | **2.95** | **2.95** | **2.95** | **2.95** | **2.95** | **2.95** | **2.95** | **2.95** | **2.95** | **2.95** |
| **D/d** | **2.50** | **2.50** | **2.50** | **2.00** | **2.00** | **1.50** | **1.50** | **2.50** | **2.50** | **2.50** | **2.50** | **2.50** | **2.50** |
| **Effects of** | | l/d | l/d | D/d | D/d & β | D/d | D/d & β | β | β | β | β | β | multi-hole |
| **# of Holes** | 1 | 1 | 1 | 1 | 1 | 1 | 1 | 1 | 1 | 1 | 3 | 3 | 3 |
| **Qty of Seats** | 5 | 5 | 5 | 5 | 5 | 5 | 5 | 5 | 5 | 5 | 5 | 5 | 5 |
| **seat P/N** | 28331614M | 28331614N | 28331614O | 28331614P | 28331614Q | 28331614R | 28331614S | 28331614T | 28331614U | 28331614V | 28331614T | 28331614U | 28331614G |
| **Seat Prototype** | 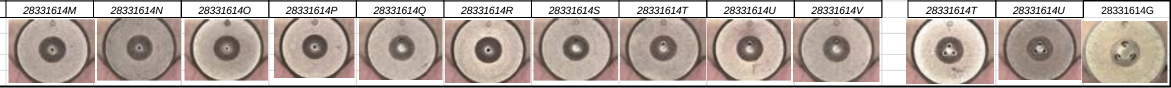 | | | | | | | | | | | | |

An additional seat added to the study was a tapered nozzle similar to those used in diesel injectors. The geometry was defined to have an identical exit diameter as the comparable cylindrical seat and an 8º taper to the thru-hole inlet at the injector sac, as shown in Figure 27.

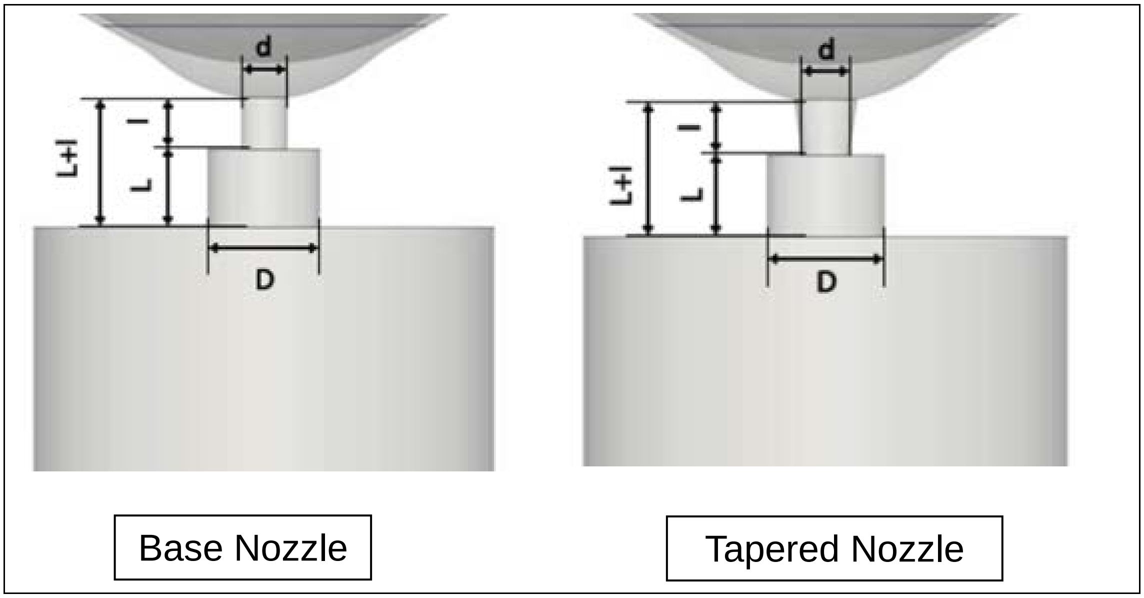


Figure 27 Tapered Nozzle definitions with common exit diameter

Following the first year of study, an adjusted prototype seat matrix was selected based on initial spray analysis at Technical Center Rochester for evaluation in the Spray Lab at Customer Technical Centre Luxembourg, these seats are listed in Table 3.

Table 3 Injectors for Spray Characterization Luxembourg Spray Laboratory

| EWO | AK29-3 | AK29-3 | AK29-6 | AK29-9 | | | AK29-10 | AK29-11 |
|---|---|---|---|---|---|---|---|---|
| suffix | -001 | -002 | -002 | -001 | | | -3-003 | -2-002 |
| Feature | Single hole | Single hole | Single hole | hole 1 | hole2 | hole 3 | 3-hole | 3-hole |
| d(mm) | ≈0.20 | ≈0.20 | ≈0.15 | ≈0.20 | ≈0.20 | ≈0.20 | ≈0.15 | ≈0.15 |
| l (mm) | ≈0.22 | ≈0.22 | ≈0.16 | ≈0.22 | ≈0.22 | ≈0.22 | ≈0.16 | ≈0.60 |
| D(mm) | ground | ground | ground | ground | ≈0.55 | ≈0.55 | ≈0.37 | na |
| L (mm) | na | na | na | na | ≈0.407 | ≈0.407 | ≈0.43 | na |
| β | 0° | 0° | 0° | ~30° | ~30° | ~30° | ~30° | ~30° |
| l+L (mm) | na | na | na | na | ≈0.60 | ≈0.60 | ≈0.60 | na |
| **l/d** | **1.10** | **1.10** | **1.10** | **1.10** | **1.10** | **1.10** | **1.10** | **3.96** |
| **(l+L)/d** | **1.10** | **1.10** | **1.10** | **na** | **2.95** | **2.95** | **3.96** | **na** |
| **D/d** | **na** | **na** | **na** | **na** | **2.50** | **2.50** | **2.50** | **na** |
| **Effects of** | **Baseline** | **Baseline** | **small d** | **CB** | **CB** | **CB** | **small d, CB** | **Long l/d** |
| **# of Holes** | **1** | **1** | **1** | **3** | **3** | **3** | **3** | **3** |
| **g/s @ 10MPa** | **3.34** | **3.14** | **1.86** | **7.69** | **7.69** | **7.69** | **5.29** | **5.46** |
| **g/s @ 10MPa** | **3.34** | **3.14** | **1.86** | **2.56** | **2.56** | **2.56** | **1.76** | **1.82** |
| | | | identical l/d with smaller d | Seat with 1 hole ground to eliminate CB | | | identical l/d with smaller d | Long l/d no CB |
| **Seat S/N** | **28331614** | **28331614** | **28331614** | **28331614** | **28331614** | **28331614** | **28331614** | **28331614** |
| **Injector S/n** | **1304** | **1304** | **1306** | **1308** | **1308** | **1308** | **1313** | **1315** |
| Solid Model |  | 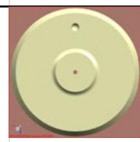 | 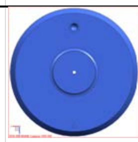 | |  | |  | 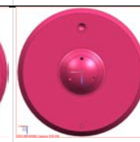 |
| Seat Prototype |  |  |  | |  | |  |  |

### *4.3 Test Equipment and Data Acquisition Systems*

#### 4.3.1 Shadowgraph Optical Imaging

The experimental spray bench at Delphi Customer Technical Centre Luxembourg comprises of the fuel supply, test injector fixture, illumination source, camera mounting, and additional spray measurement equipment. It incorporates a multi-functional capability that enables complementary laser diagnostic techniques. The spray imaging investigations utilize a shadowgraph imaging technique for visualization of the spray development, which with the aid of data analysis software, enables automatic extraction of the relevant spray spatial-temporal development data. In the optical investigations, the spray “side” imaging arrangements is used to capture the spray breakup structure, trajectory (especially deviation from the nozzle skew angle), and plume angle. The imaging utilizes laser illumination and a macroscopic zoom lens in order to capture the structure of the high-speed spray in close proximity of the nozzle exit. The Shadowgraph Optical Imaging experimental setup, shown in Figure 28, employs a laser light source, fluorescence screen dye diffuser plate, target injector for spray with pressurized fuel supply, and CCD camera. Synchronization of the camera, light source, and injector actuation is realized by the imaging system.

Analysis of the image is performed by an automated image capture program using parameters defined per SAE [42], as shown in Figure 29. It should be noted that Spray angle, as defined by SAE, envelopes all spray plumes in each view. In this work, we will focus only on single plume structures, and when evaluating near field spray, alternative measurement lengths of 1mm and 8mm downstream from the nozzle tip will be utilized, as documented in 4.1 Defined Terms.

**Shadowgraph Optical Image acquisition instrumentation & set-up:**

CCD-Camera: LaVision Flow Master
Camera lens: Nikon 50mm, f#1.8 (retro mounting)
Camera lens aperture: 4
Back light: ND-YAG Laser combined with Dye Diffuser Plate
Fluorescence screen: LaVision Dye Diffuser Plate
[Light output pulse duration (@ 5 ns input): 20 ns, 580nm)]

ND YAG Laser: Quantel Big Sky Laser Twins Ultra (25mJ per cavity)
Image size: 9 x 8mm (width x height)
Camera Orientation: 0° & 120° to Injector
Image acquisition: shot imaging (one spray image per injection)

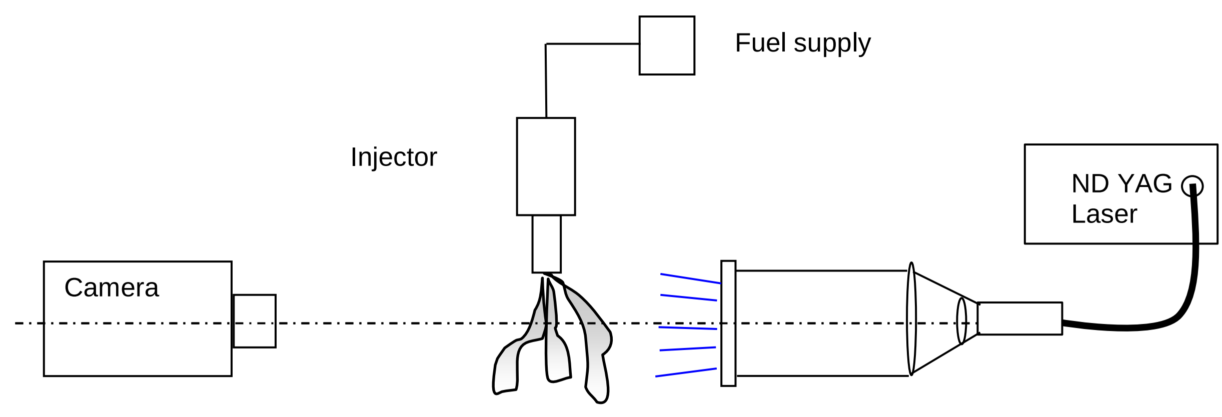


Figure 28 Test Configurations for Shadowgraph Optical Image Capture

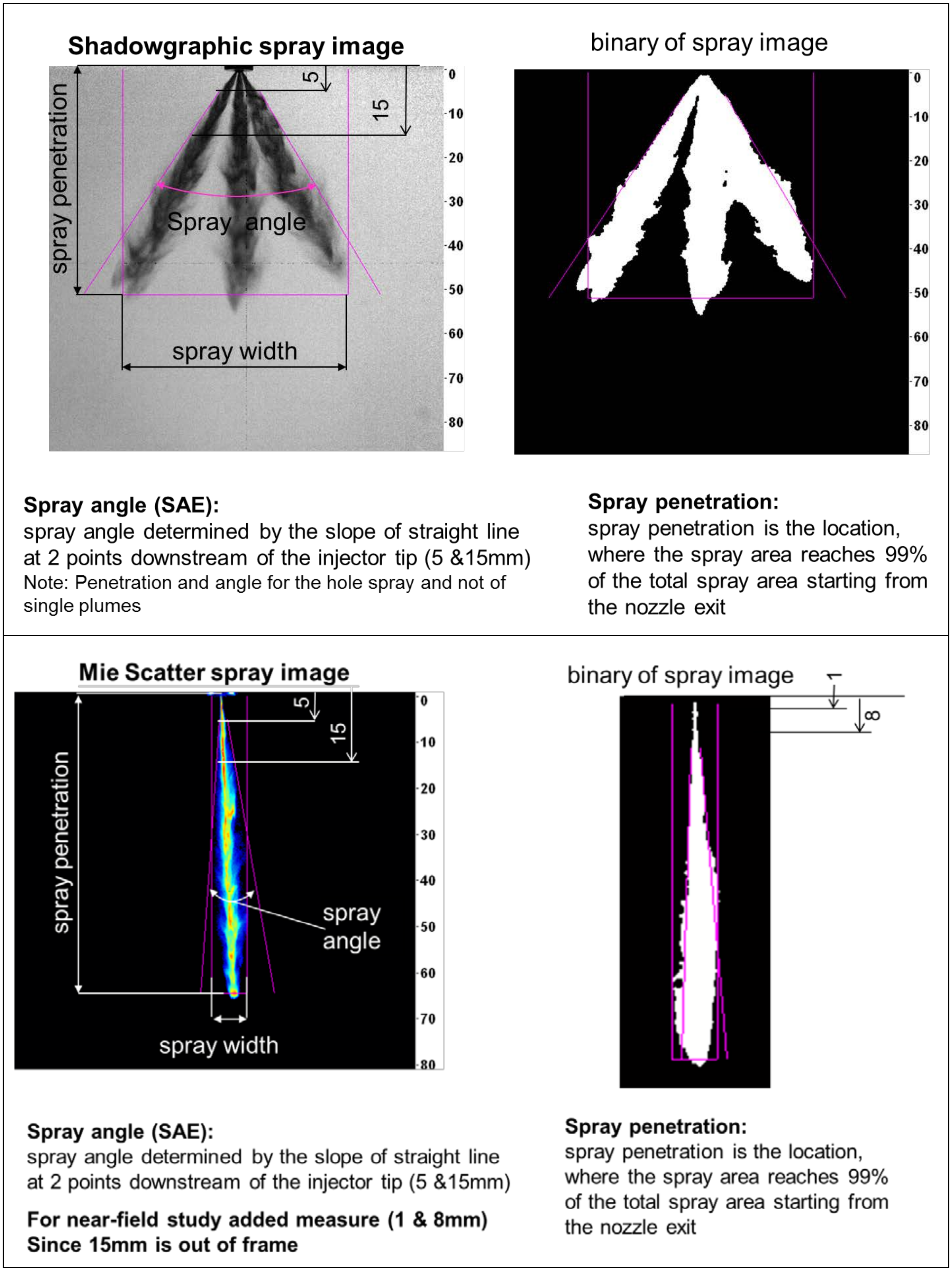


Figure 29 Spray Image Capture definitions for Single Spray Plumes and Complete Sprays

### 4.3.2 High Speed Integral Mie Imaging

An alternative to shadowgraph imaging is high speed integral Mie imaging to capture spray morphology. LED flash panels provide the light source and a special CCD camera captures the image. The bench setup for front and side views is shown in Figure 30, the configuration can also rotate to capture spray progression from below the injector. Similar to shadowgraph imaging, analysis of the image is performed by an automated image capture program using parameters defined per SAE [42], as shown in Figure 29. A comparison of sprays for injector AK29-11-3-002 captured in both techniques is shown in Figure 31. It can be seen there were plume issues for this injector and both imaging techniques capture the phenomena.

**Image acquisition instrumentation/set-up:**

HS-Camera: Phantom v711
Camera lens: Nikon 50mm, f#1.8, 28mm f#2.8 bottom view
Camera lens aperture: 11, 2.8 bottom view
Light Source: 2 LED Flash Panels operated at 25 kHz
Image size: 90 x 90mm (width x height)
Orientation of injector to camera: 0° & 90° side view
**Image acquisition:** 25 kHz frame rate, exposure time 5 micro seconds

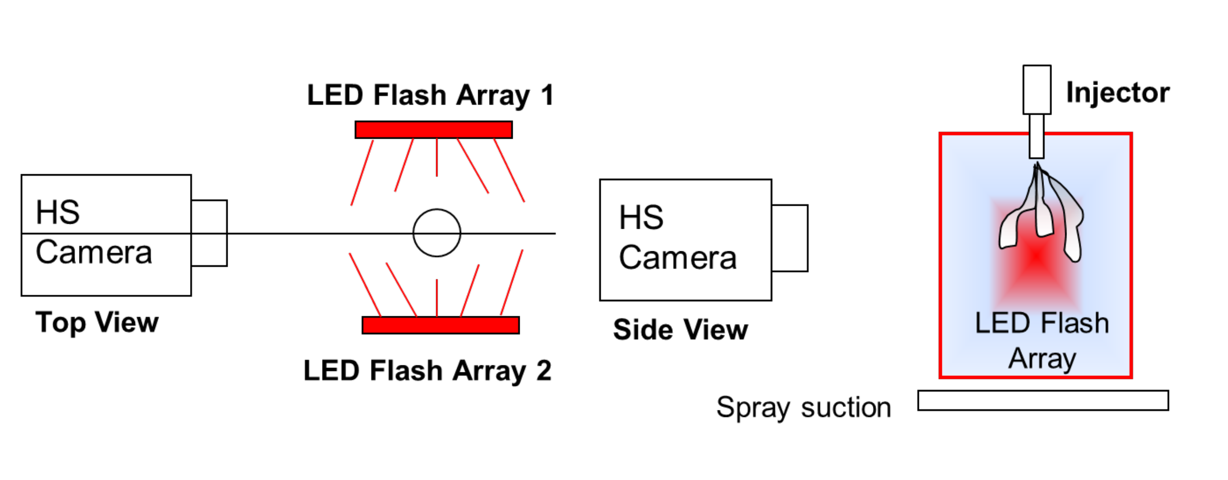


Figure 30 Test Configurations for High Speed integral Mie Image Capture

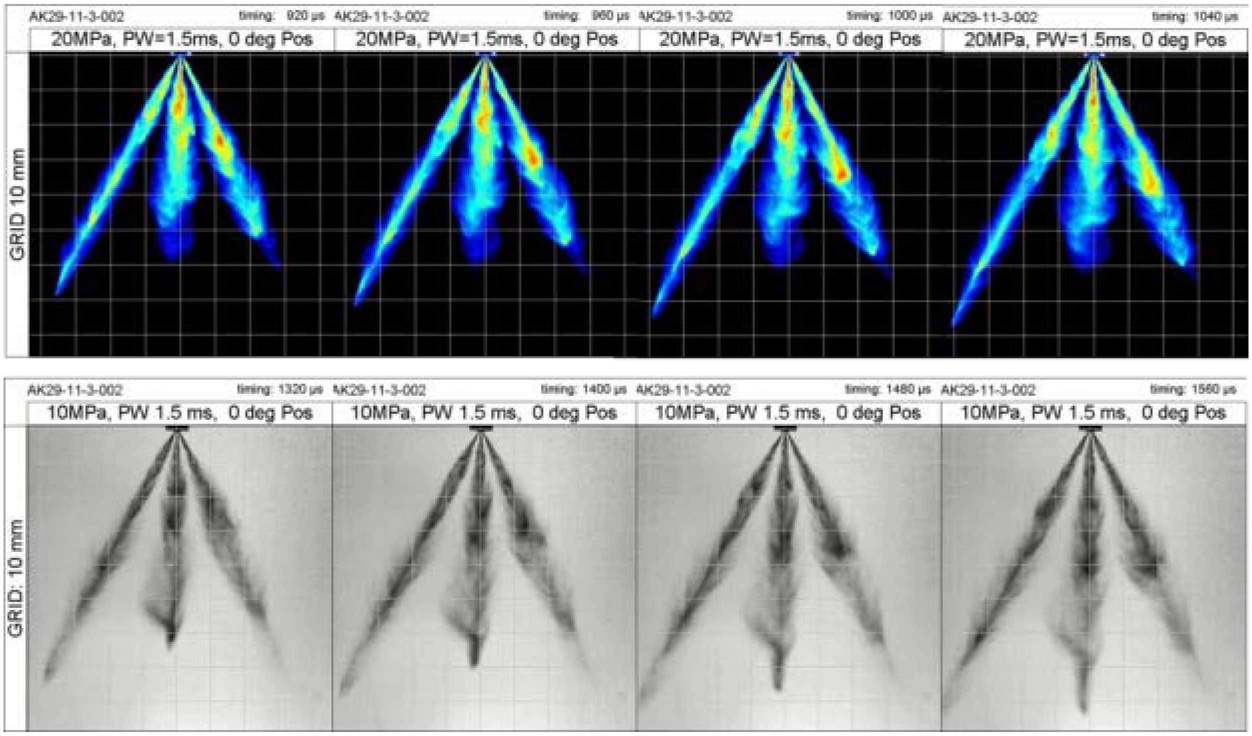


Figure 31 Comparisons of Shadowgraph and High Speed Mie Imaging for Injector AK29-11-3-002

### 4.3.3 Laser Diffraction Technique

A key characteristic of injector spray is spray particle, or droplet size, determination. The Delphi spray lab test bench, shown in Figure 32, uses a commercially available Laser Diffraction product, the Malvern Spraytec 2000 [44], which measures droplet size distributions using the technique of laser diffraction. The technique is Fraunhofer diffraction where the scattering of light around particles produces varying intensities of wavelengths proportional to the particle size. Malvern can also use Mie theory diffraction, which provides for better small particle resolution when reference data for the fluid is available. Diffraction requires the angular intensity of light scattered from a spray to be measured as it passes through a laser beam. The recorded scattering pattern is then analyzed using a proprietary multiple scattering algorithm to yield a size distribution. The angular range where scattering measurements are made has been optimized to ensure diverse size distributions are fully resolved. This ensures accurate particle size distributions can be measured at up to 98% obscuration. The test setup shows the laser passes through the spray at 50mm distance per the SAE standard, as shown in Figure 33. For this work, the 3-hole injectors were rotated so direct comparisons to the single-hole injectors could be made.

**Malvern Spraytec 2000**

- Method: Frauenhofer diffraction of parallel monochromatic light
  diffraction angle ~ $1/d_{particle}$
- Line of sight measurement
  limited by dense sprays: extinction of beam < 8 %
- Sampling frequence: 20 kHz
  Scan interval: 30µs at 20 kHz

| | |
|---|---|
| Focal length | 200mm |
| Laser beam diameter | 15mm |
| Injection Frequency | 10Hz |
| No. of repetitions | 20 |
| Integration time: | 0-7 ms after ASOI |

- Size range (focal length lense)

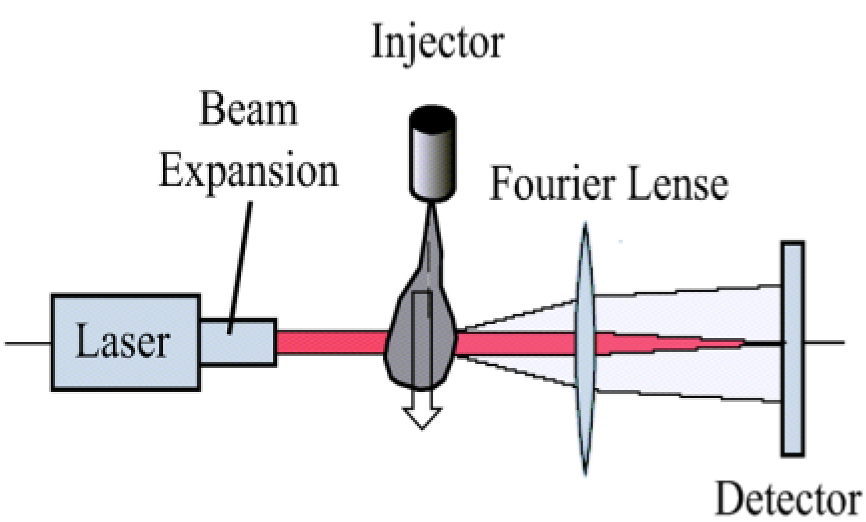


Figure 32 Particle Size Distribution determined using Laser Diffraction Technique

For the 3-hole injectors the spray plume has been oriented, so that the spray is vertical, similar to the single-hole injectors

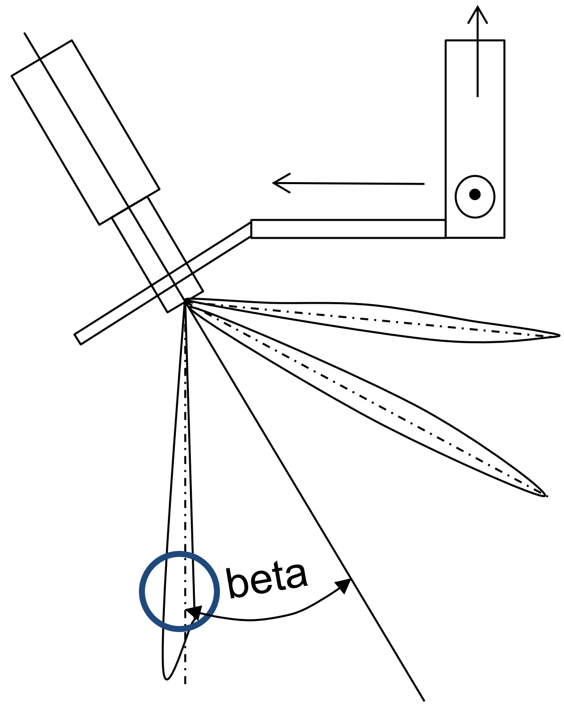


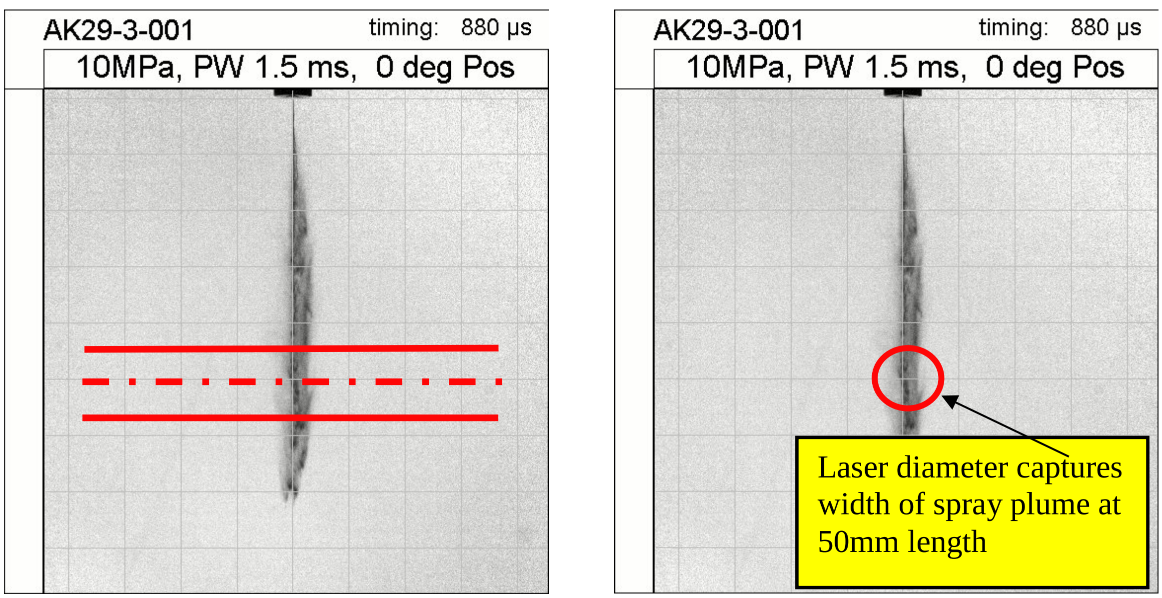


The laser beam center line is located at 50mm vertical distance from the tip
The laser beam (diameter 15mm) is perpendicular to the spray axis, therefore almost of the spray is captured by the measurement system

Figure 33 Test Configurations for Spray Particle Size Measurement

### 4.3.4 High Speed Near Nozzle Spray Imaging by Mie Scatter

For the purpose of this study, the ability to capture near field spray development in the immediate vicinity of the nozzle exit was desired. A technique similar to the high speed Mie shadowgraph technique is high speed near-nozzle imaging, applied with changes to the CCD camera and the replacement of the LED flash banks with a continuous monochromatic white light source. Videos are captured at 300 frames per second, providing analysis of the near field spray development. The test setup is shown in Figure 34.

**High Speed Near-Nozzle Spray Image acquisition instrumentation/set-up:**

| | |
|---|---|
| HS-Camera: | Phantom v711 |
| Camera lens: | Nikon 85mm, f#1.4 |
| Light Source: | Continuous white light source |
| Image size: | 2.5 x 2.5mm (88x 80 pixel) |

**Image acquisition:**
- 300 kHz frame rate
- exposure time 0.3µs

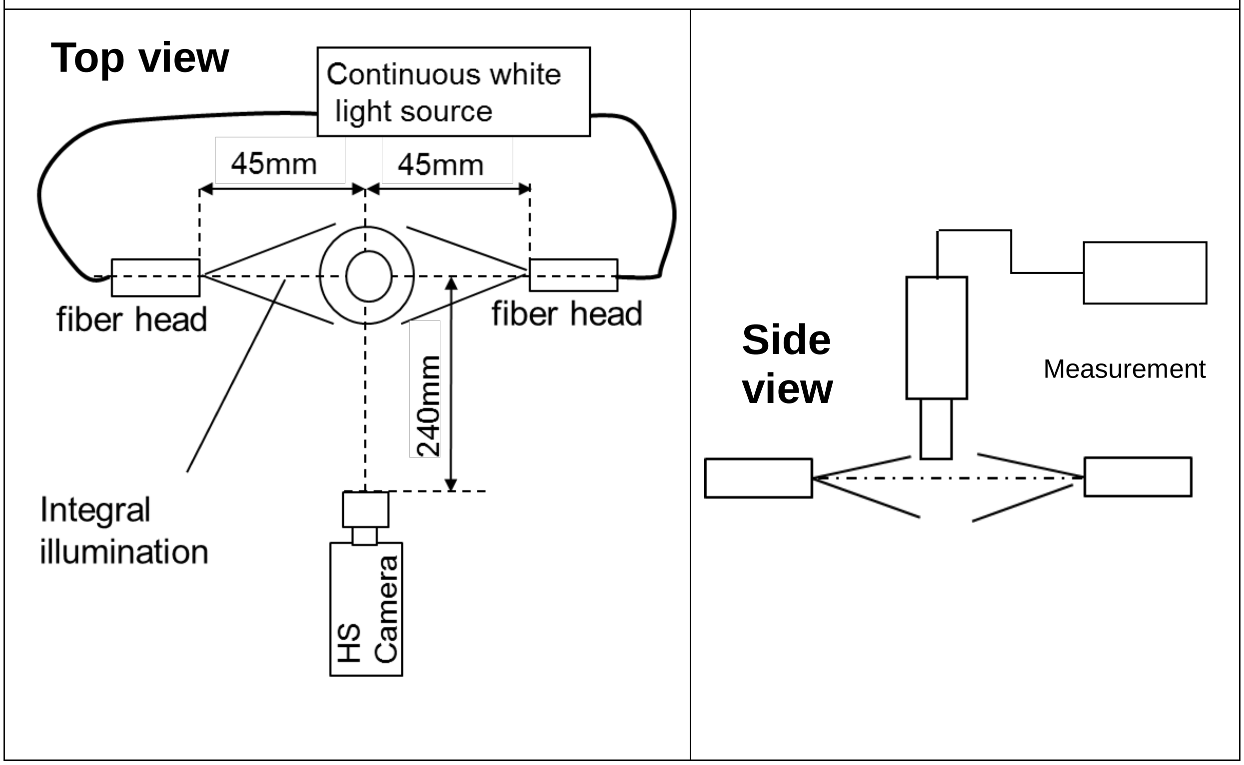


Figure 34 Test Configurations for High Speed Near-Nozzle Spray Image Capture

### 4.3.5 Phase-contrast X-ray Imaging

The Advanced Photon Source (APS) at the Argonne National Lab experimental bench, shown in Figure 35, utilizes slow and fast shutters, an injector fixture with variable pressure fuel supply, scintillator crystal to convert signal to visible light, and a 45° mirror to direct light to a CCD camera. The X-ray beam is generated from an insertion device (undulator) in the APS electron storage ring. The special beam pattern (hybrid singlet mode), shown in Figure 35, was used in this experiment. This pattern contains a single electron bunch (150ps duration and carrying 16 mA current) isolated from the remaining electron train bunch (472 ns long, 96 mA) by symmetrical 1.594μs gaps. To reduce the heat power, the X-ray beam is gated by two mechanical shutters: the slow shutter operating at 1Hz frequency with 10ms opening duration and the fast shutter operating at 2kHz frequency with 9μs opening duration. Synchronized operation of these two shutters cuts-off more than 99% of the beam heat power. After being transmitted through the spray, the X-ray beam generates the phase-contrasted image on the scintillator crystal (LYSO:Ce), which converts the transmitted X-ray beam into the visible light spectrum (432nm). This image is reflected by a 45° mirror and then captured by a charge coupled device (CCD) camera (Sensicam, 1376x1040 pixels, from Cooke). The camera was gated at the timing when only the singlet electron bunch passed through the shutters. The remaining electron bunches were cut-off by closing the camera gate at 1.5μs after the gate opening (yielding exposure time of 1.5μs). The field of view of the camera was 1.75mm x 1.32mm when a 10x objective lens (NA=0.14) was used. The fuel was injected into a spray chamber using a high pressure rail GDi injection system composed of fuel tank, motor, high-pressure pump, pressure control valve, and high-pressure rail. The pressure inside the rail was controlled via feedback control of measured pressure inside the rail and bleeding fuel flow rate of the pressure valve. The spray chamber has two Kapton windows, which allow the X-ray beam to pass through this without loss of intensity. Synchronization of the camera, the shutters, and the injector actuation is realized by the imaging system.

**Phase-Contrast X-ray Image acquisition instrumentation & set-up:**

CCD-Camera: Cooke Sensicam, 1376×1040 pixels,
Scintillator crystal: (LYSO:Ce), converts X-ray beam into visible light (432 nm).

Synchrotron X-ray: 150 ps duration from a single 16mA electron bunch
Image size: 1.74×1.32mm
Camera Orientation: 0° to injector (normal to spray)
Image acquisition: 1.26μm/pixel with 5x objective lens

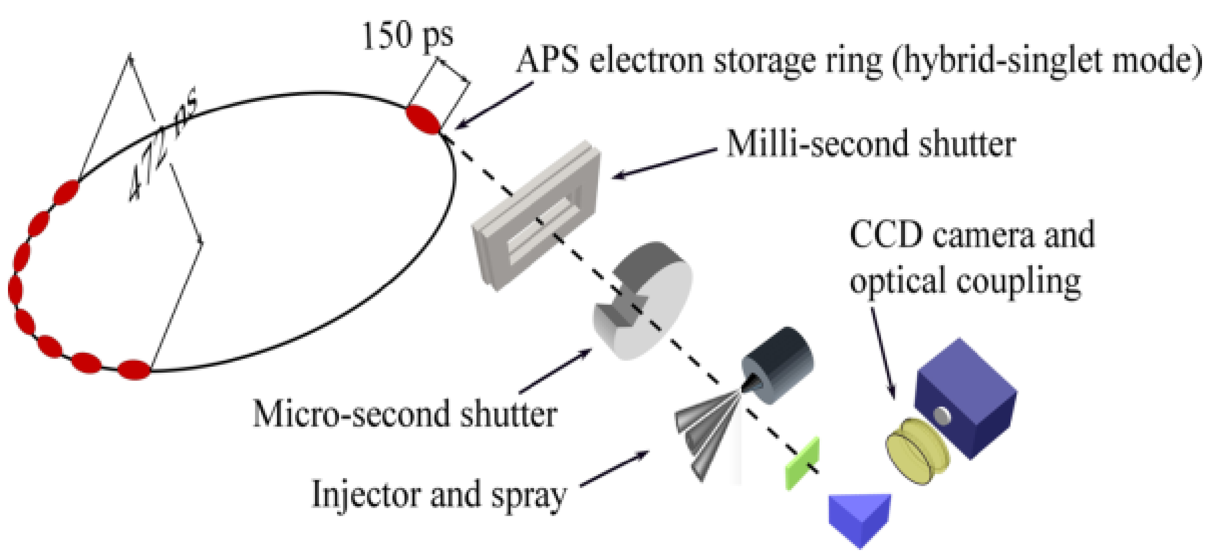


Figure 35 Test Configurations for Phase-Contrast X-ray Image Capture

### *4.4 Simulation and Modeling*

#### 4.4.1 Conservation Equations of Multi-Phase System

The mathematical modeling practice is similar to de Villiers [44] [45], based on the transport equations for the conservation of mass and momentum of a two-phase flow system, comprised of two immiscible, incompressible Newtonian fluids, including the surface tension. The single set of conservation equations that describe the flow of a two-phase mixture are:

$$\frac{\partial \rho}{\partial t} + \nabla \cdot (\rho U) = 0 \qquad (1)$$

$$\frac{\partial \rho U}{\partial t} + \nabla \cdot (\rho U \otimes U) = -\nabla P + \nabla \cdot \tau + \int_{S(t)} \sigma \kappa' n' \delta (x - x') ds \qquad (2)$$

Where, U is the velocity, $\rho$ is the density, $\sigma$ is the surface tension coefficient, $\tau$ is the stress tensor, $\kappa$ is the curvature of the liquid surface, $n$ represents a unit vector normal to the liquid surface, and $\nabla$ ( ) and $\nabla$ . ( ) denote the gradient and the divergence operations, respectively.

The integral term in equation (2) represents the momentum source due to surface tension: it is effective at the interface of the liquid surface $S$ (t) over the entire liquid volume. This is an important source term in the numerical simulation of the liquid jet breakup process. The evaluation of this term is achieved through the Continuum Surface Force (CSF) model of Brackbill [46] as:

$$\int_{S(t)} \sigma \kappa' n' \delta (x - x') ds \approx \sigma \kappa \nabla \alpha \qquad (3)$$

Where α is the "volume-of-liquid" phase-fraction, which is obtained from solution of a transport equation, and $\kappa$ is the "curvature of the interface", estimated from the solution of the phase-fraction α as:

$$\kappa = \nabla \cdot \left( \frac{\nabla \alpha}{|\nabla \alpha|} \right) \tag{4}$$

Equation (4) is valid for cases with constant surface tension, as in the case of the present study. In case of variable surface tension, e.g. in case of spatially non-uniform composition or temperature distribution, surface tension gradients are encountered that generate additional shear stress at the interface that must be taken into account.

### 4.4.2 Large-Eddy-Simulation Method

The VOF-LES equations are derived from equations (1) to (3), through a process of local volume averaging of the phase-weighted hydrodynamic variables. This entails decomposition of the dependent variables into resolvable and computational sub-grid scales of turbulent fluctuations, and application of a filter that removes the sub-grid scale fluctuations from the direct numerical simulation. The filtering process, in conjunction with the non-linear term in equation (2), produces additional terms, involving correlations of the hydrodynamic variable fluctuations at sub-grid scales that require closure with the aid of mathematical models. The most notable of these terms is the Sub-Grid-Scale (SGS) stress tensor that represents the effect of unresolved scales of turbulence on the momentum transport process and its viscous dissipation.

The Sub-Grid-Scale (SGS) stress is defined as:

$$\tau_{sgs} = \left(\widetilde{U}\widetilde{U}\right) - \widetilde{U}\widetilde{U} \tag{5}$$

Where $\widetilde{U}$ is the filtered instantaneous velocity field. The closure of the SGS stress is provided through a sub-grid-scale "eddy-viscosity" model as:

$$\tau_{sgs} = \frac{2}{3}\kappa \mathrm{I} - \frac{\mu_{sgs}}{\rho}\left(\nabla\widetilde{U} + \nabla\widetilde{U}^{T}\right) \tag{6}$$

Where Κ is the SGS turbulence kinetic energy and $\mu_{sgs}$ is the SGS turbulent viscosity. These SGS turbulence parameters are obtained through solution of a transport equation for the SGS turbulence kinetic energy, according to Yoshizawa [21].

$$\frac{\partial \kappa}{\partial t} + \nabla \cdot (\kappa \tilde{U}) = -\nabla \cdot \left[ (\nu + \nu_{sgs}) \nabla \kappa + \tau_{sgs} \cdot \tilde{U} \right] - \frac{1}{2} \tau_{sgs} : \left( \nabla \tilde{U} + \nabla \tilde{U}^T \right) - \varepsilon \qquad (7)$$

Where $\varepsilon = C\varepsilon\ K^{3/2} / \Delta$ is the SGS turbulence dissipation rate, $\nu sgs = C_K\ K^{1/2} \Delta$, and Δ is the SGS length scale (equivalent to the local computational cell size). The turbulence model constants have the values $C_K = 0.07$ and $C_\varepsilon = 1.05$, in accordance with Yoshizawa [22].

The additional SGS terms associated with the transport equations involve correlations of the sub-grid fluctuations of the phase-fraction, density, surface tension, etc., that are neglected in the absence of mathematical closure models, following the work of de Villiers et al [45].

### 4.4.3 VOF-Based Interface-Tracking Method

The principle of the "Volume of Fluid" (VOF) approach is that a two- (or indeed multi-) phase system can be represented as a mixture of phases where the phase-fraction distribution includes sharp, yet resolvable, transitions between the phases. Accordingly, the interface in a two-phase flow system is computed with the aid of the transport equation for the liquid volume fraction as the indicator function to locate the interface. The transport equation for the phase fraction α, for two incompressible fluids, is:

$$\frac{\partial \rho \alpha}{\partial t} + \nabla \cdot (\rho U \alpha) = 0 \qquad (8)$$

According to the definition of α, the mixture thermo-physical properties are calculated as:

$$\rho = \alpha \rho_f + (1 - \alpha) \rho_g \qquad (9)$$

$$\mu = \alpha \mu_f + (1 - \alpha) \mu_g \qquad (10)$$

The VOF interface capture and tracking method is a simple and flexible approach for simulation of multi-phase systems with free surfaces, especially for circumstances where the surface tension effects are not dominant. The main challenge of the VOF methodology relates to the accuracy of the numerical scheme, in order to assure that it simultaneously provides the boundedness and conservation of the flow variables, and that the interface remains sharp, yet is not affected by numerical dispersion and mesh alignment bias [48]. In the present simulations, an advanced method formulated by Open-FOAM Ltd. [49] that adopts a two-fluid formulation of the conventional volume-of-fluid concept, within the frame-work of the finite-volume method, is used. The method employs a formulation of the phase transport equation that includes a “compression velocity” term [50], which acts to “compress” the VOF interface and maintain a sharp interface resolution. Appropriate numerical schemes are employed to ensure the bounded temporal and spatial discretization with minimum mesh biasing of the compression term and convection of the phase fraction transport equation, but without numerical diffusion or dispersion of the liquid-gas interface.

A comparison of the VOF interface capturing, and tracking, and the numerical solution method in the Open-FOAM code with the alternative "Interface Reconstruction" scheme [51] for prediction of a Rayleigh jet breakup, provides closely similar predictions of the jet structure, breakup length, and droplet size between the two computational methods, in close agreement with the measurements and theoretical analysis [51].

### 4.4.4 Vortex Identification Method

Identification of vortical coherent structure is an important component of LES allowing for flow visualization or rotating velocity fields. In this work, the term Q will be used for quantified rotation energy of vortex cores following the most cited convention in the literature [52] [53].The quantity Q is defined as:

$$Q = \frac{1}{2}(\|W\|^2 - \|S\|^2)$$

Where W is defined as the anti-symmetric part of the velocity gradient tensor:

$$\|W\| = (W{:}W)^{\frac{1}{2}}$$

$$W = \frac{1}{2}(\nabla\widetilde{U} - (\nabla\widetilde{U})^T)$$

Where S is the local rate of strain tensor

$$\|S\| = \frac{1}{2}(S{:}S)^{\frac{1}{2}}$$

$$S = \frac{1}{2}(\nabla\widetilde{U} + (\nabla\widetilde{U})^T)$$

A large value for Q represents a flow region where the rate of strain is dominated by the rate of rotation.

### 4.4.5 The Numerical Solution Method

The simulations are performed using Open-FOAM, an open-source finite-volume CFD tool-box [54]. The solution method for the VOF-LES conservation equations in Open-FOAM incorporates a “compressive” formulation of the phase-fraction transport equation, employs special NVD/TVD and a blend of central/upwind schemes for spatial discretization of the transport terms, and a combination of the Crank-Nicholson and Euler-implicit integration schemes for the phase-fraction and the governing conservation equations. The numerical method is intended to afford second-order spatial and temporal discretization maintaining integration accuracy and to assure that the schemes are bounded and preserve the proper physical limits of the fluid dynamic variables.

The "pressure implicit with splitting of operators" (PISO) [55] algorithm, specifically suited to transient flows, is employed for coupled solution of the mass and momentum conservation equations through coupling of the velocity and the pressure fields. The method starts with an initial estimate for the pressure field based on the last time step result. The momentum equation is then used to yield the approximate matching velocity field. The pressure Poisson equation is applied with the divergence of the partial velocity flux as a source term to estimate the pressure field. The corrected pressure field is then used to correct the velocity field. These steps are repeated until convergence criteria are met. In the calculations, the numerical integration time-step is dynamically adjusted according to various stability criteria, and is of the order 1 E-10 to 1 E-9 second.

### 4.4.6 Computational Domain and Mesh

Figure 36 presents the three-dimensional computational domain that comprises the injector valve-group flow domain and its immediate near-field ambient. The computational mesh is of the order 5 M cells (1 M cells within the injector domain and 4 M cells within the ambient) and affords a spatial resolution in the range 2-5 µm (within the injector seat-nozzle) to 10 µm (within the ambient domain). The effective filter is 2 times the grid size, therefore, 4-10 E-6 m suggests resolved scales will include the Integral scale eddy production range and cascading eddies into the Taylor microscale range and smaller than 4-10 E-6 m will be modeled as Kolmogorov dissipating eddies in the Sub-Grid-Scale (SGS) term.

Table 4 Turbulent Length Scales for 3-hole skew-angled nozzle

| ***Turbulent Reynolds number*** $Re_L = k^2/\varepsilon\nu$ | ***Integral Scale Eddy production*** $l_0 = \eta\, Re_L^{3/4}$ | ***Taylor microscale Cascading eddy*** $\lambda = (15\nu u^2/\varepsilon)^{1/2}$ | ***Kolmogorov scale Dissipating eddy*** $\eta = (\nu^3/\varepsilon)^{1/4}$ |
|---|---|---|---|
| 1.5 E3 | 3.3 E-5 m | 4 E-6 m | 2 E-7 m |

The simulation run time for this model of 5M cells, covering into the Taylor microscale range, running on a HP Z800 workstation with 2 CPUs each CPU with 6 cores operating at clock speed of 2.4GHz, is listed in Table 5 for 3-hole injector geometry. The CPU execution time depends on the conditions as the simulation time step adjusts dynamically to meet the convergence criteria, generally, 1µs of flow simulation required between 2.8 to 3.9 hours of CPU run time.

Table 5 CPU runtime for Flow Simulation of the 5M cell grid

| ***Flow Simulation*** | ***CPU time*** | ***CPU time*** |
|---|---|---|
| 1µs | 14,000 sec | 10,000 sec |
| | 3.9 hours | 2.8 hours |
| 100µs | 389 hours | 278 hours |
| | 16.2 days | 11.6 days |
| 120µs | 467 hours | 333 hours |
| | 19.5 days | 13.9 days |

Skew-angled 3-hole nozzles converged with average simulation time step ~ 1.e-9s – 4.e-9s of simulation, and required 100µs to reach steady state conditions. Axis-symmetric hole were more time consuming due to the long physical-time to evacuate the air in the sac volume, the calculations required a time step of order 1e-10s, and at least120µs to reach steady state, or more than one month of execution runtime.

The pintle motion is not included in the simulation due to severe requirements of the VOF-LES method for mesh geometric quality (e.g. orthogonal arrangement, aspect ratio, etc.) that would not permit the extensive mesh deformation required to accommodate the pintle displacement of approximately 45µm. Hence, the transient simulation of the seat-nozzle flow development is performed on a fixed geometry mesh with the pintle at the nominal open stroke position. The initial condition fills the nozzle from the inlet to the pintle sealing band with liquid at rest, while the remainder of the computational domain, downstream of the sealing band, is filled with stagnant air at ambient conditions of the near field. At the start of the calculation, the liquid phase at the inlet boundary is instantaneously accelerated to its nominal velocity corresponding to the static flow for the fuel injection pressure being evaluated.

### 4.4.7 Boundary Conditions

In the present calculations, the liquid is n-Heptane at T=293°K temperature. The following boundary conditions are employed:

- Inlet: Uniform inlet velocity, corresponding to the nozzle static flow for injection fuel pressure, without imposition of any artificial velocity disturbances
- Outlets : Non-reflective, uniform static ambient pressure
- Walls: zero-slip velocity condition, with law-of-the-wall treatment of the wall shear stress

The outlet boundaries are at sufficient distance from the nozzle to ensure minimum reflection of pressure disturbances that may influence the jet breakup process.

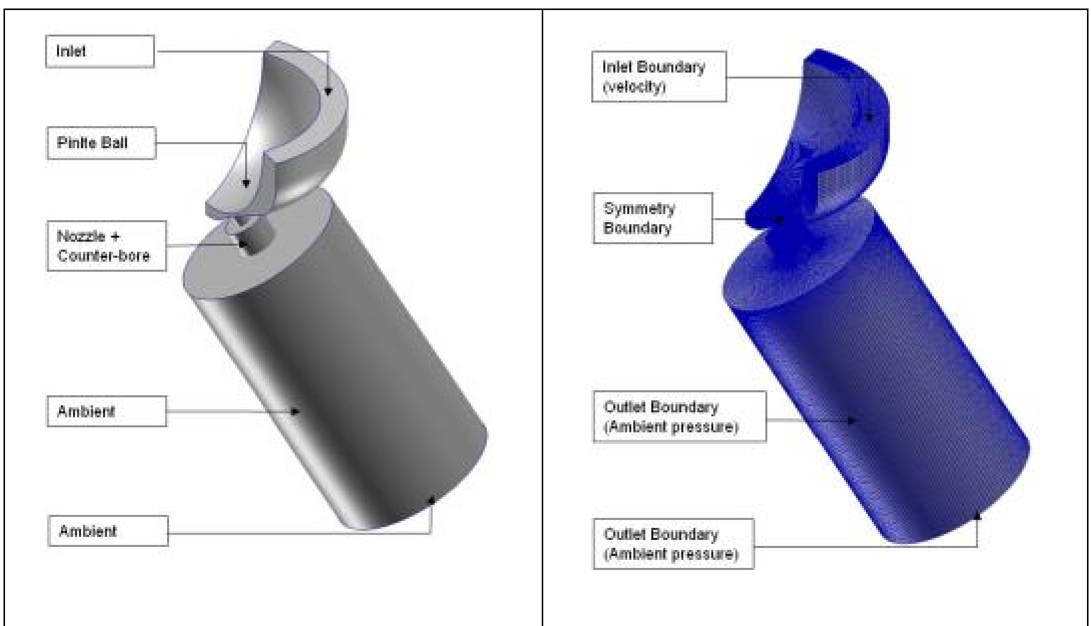


**(a) Geometry** | **(b) Computational mesh, 5M cells**

Figure 36 Computational domain, mesh, and boundaries

# CHAPTER 5 OUTLINE OF THE RESULTS

## *5.1 Large Eddy Simulation of GDi Axis-symmetric single-hole Nozzles*

The results of this section were published [56] and presented at the SAE World Congress in Detroit in April of 2012. This section summarizes a Large Eddy Simulation of 4 case studies using single-hole axis-symmetric nozzles, as shown in Figure 37. The contrast between the baseline nozzle and nozzle without counterbore should help to understand the effect of the counterbore on spray. Likewise, comparison of the nozzle without counterbore and the long l/d nozzle should show influence of l/d. Lastly, a tapered nozzle similar to those used in diesel applications is introduced to understand its impact on spray.

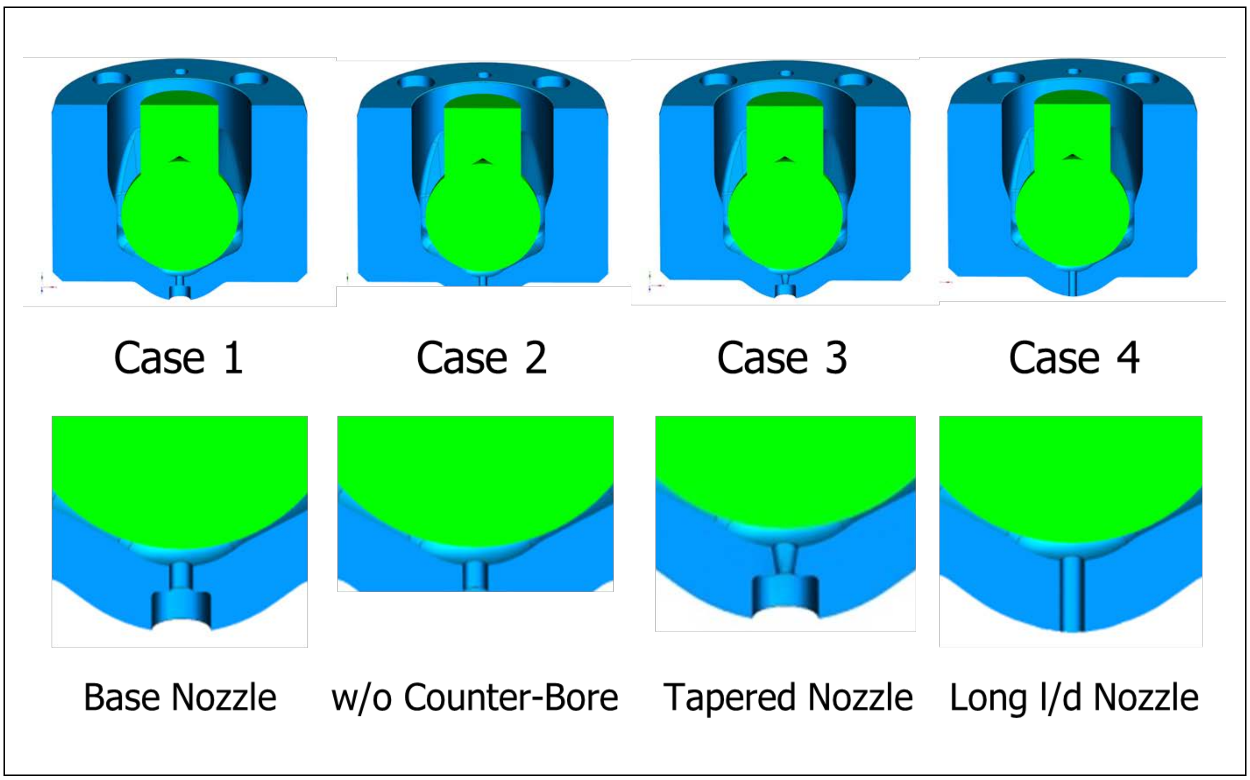


Figure 37 Case studies using axis-symmetric injector nozzles: Base Nozzle, Nozzle w/o Counterbore, Tapered Nozzle, and Long l/d Nozzle

# THE SIMULATION RESULTS

## 5.1.1 Base Nozzle Geometry

The geometry and nozzle dimensions of the Base GDi nozzle are presented in Figure 38. The nozzle diameter, d, is of order 0.2mm. This geometry is representative of the design features of the current production GDi nozzles that incorporate a counterbore to achieve a small nozzle l/d ratio, irrespective of the seat thickness imposed by the structural integrity considerations.

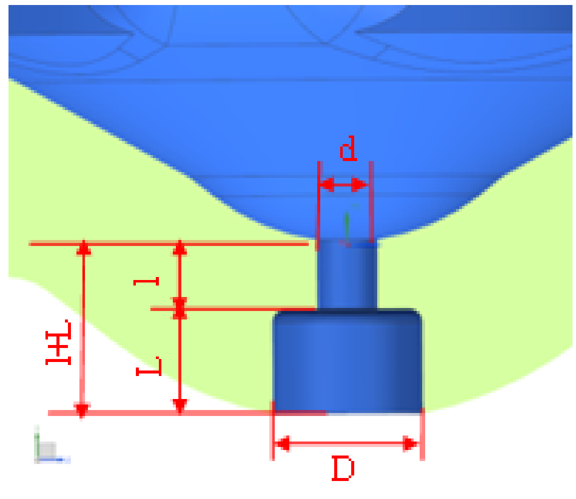


| l/d | (l+L)/d | D/d |
|---|---|---|
| 1.10 | 2.95 | 2.50 |

Figure 38 Nozzle geometry and dimensional parameters

The transient development of the flow within the injector seat and nozzle is illustrated by the evolution of the iso-surface plots of VOF=0.5, colored by the instantaneous velocity at selected times after the start of simulation, as shown in Figure 39. Figure 40 presents the corresponding VOF contour plots on a symmetry cut-plane through the geometry.

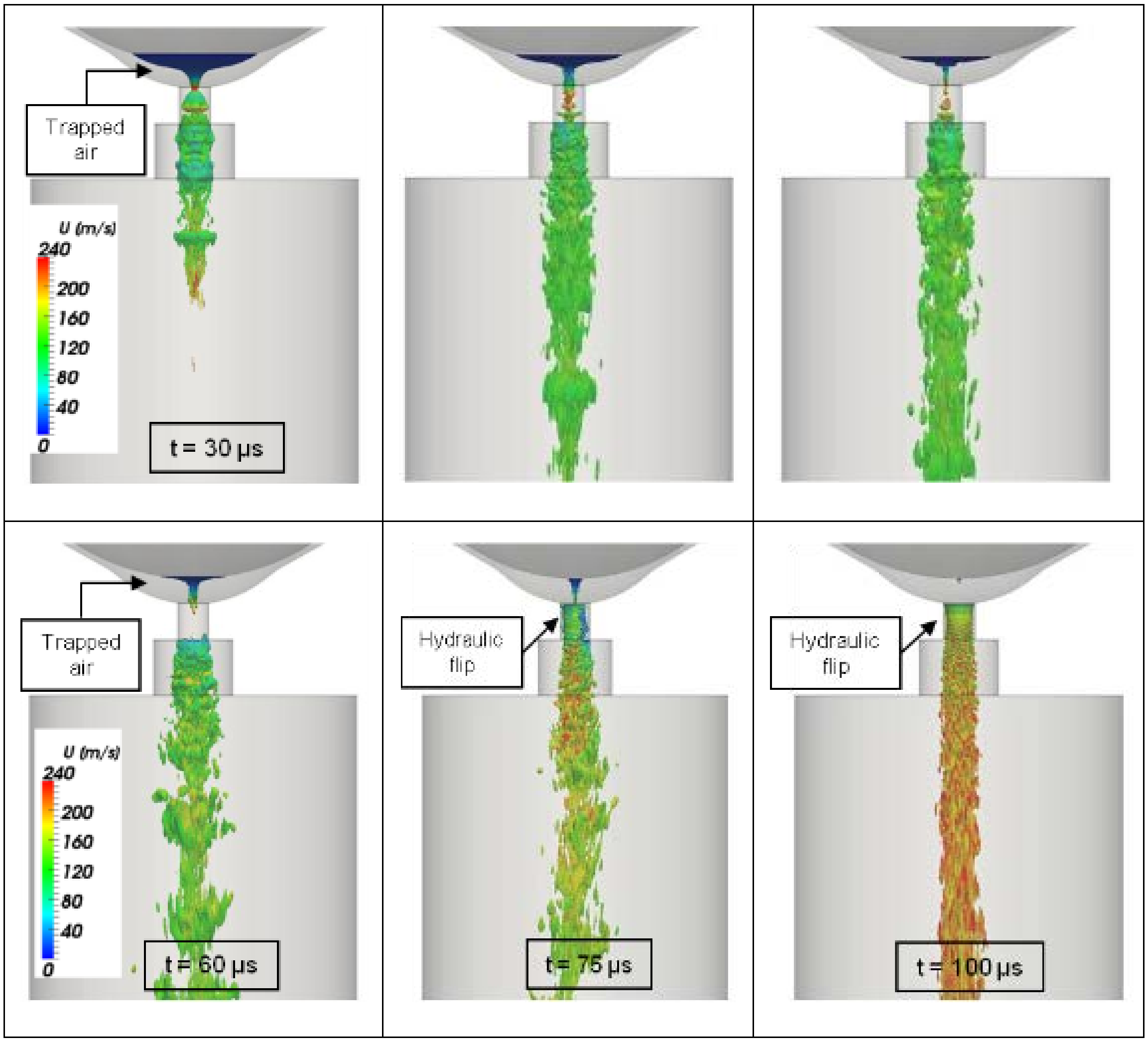


Figure 39 Iso-surface plots of VOF= 0.5, colored by instantaneous local velocity

The transient nozzle flow is markedly affected by the entrapped air in the sac volume, beneath the pintle. The initial liquid jet is fully attached at the nozzle entrance. The entrapment and discharge of the trapped air by the liquid causes formation of an attached liquid jet with an unsteady air core, as illustrated by the VOF iso-surface contour plots for t = 30µs, 40µs, and 50µs. Also notable is the perfect axisymmetric structure of the flow within the nozzle, which is indicative of the high level of resolution and numerical accuracy of the solution. The VOF plots at 40µs already show the development of the liquid jet irregular instabilities within the immediate downstream of the nozzle exit.

With diminishing of the sac volume entrapped air and reduction of the jet core air volume flow rate, the liquid jet separates at the nozzle entrance edge and, owing to the short nozzle l/d, the separation extends through the nozzle exit. This causes ingestion of the ambient air into the nozzle, thus forming an air annulus that separates the liquid jet from the nozzle wall. The phenomenon is known as “hydraulic flip” and its occurrence is indicated in Figure 39 by the VOF plot at $t = 75\mu s$. The full establishment of the hydraulic flip takes between 75μs and 100μs; thereafter, the liquid jet is fully detached at the nozzle entrance and the ingested air penetrates the full nozzle length, thus completing the hydraulic flip. This is the structure of the steady-state stationary turbulent jet that prevails for $t > 100\mu s$. This structure is very stable, without temporal or cyclic variation of the jet separation, yielding consistent jet velocity profile, and downstream Kelvin-Helmholtz interface waves.

It must be underlined that the present simulation method excludes a cavitation model; hence, the hydraulic flip is engendered solely due to liquid flow separation at the nozzle entrance. It is expected that inclusion of cavitation, causing formation of a cavitation ring at the nozzle entrance, would promote separation and the hydraulic flip process, as well as augmentation of the jet inertial instabilities and impact on the breakup process.

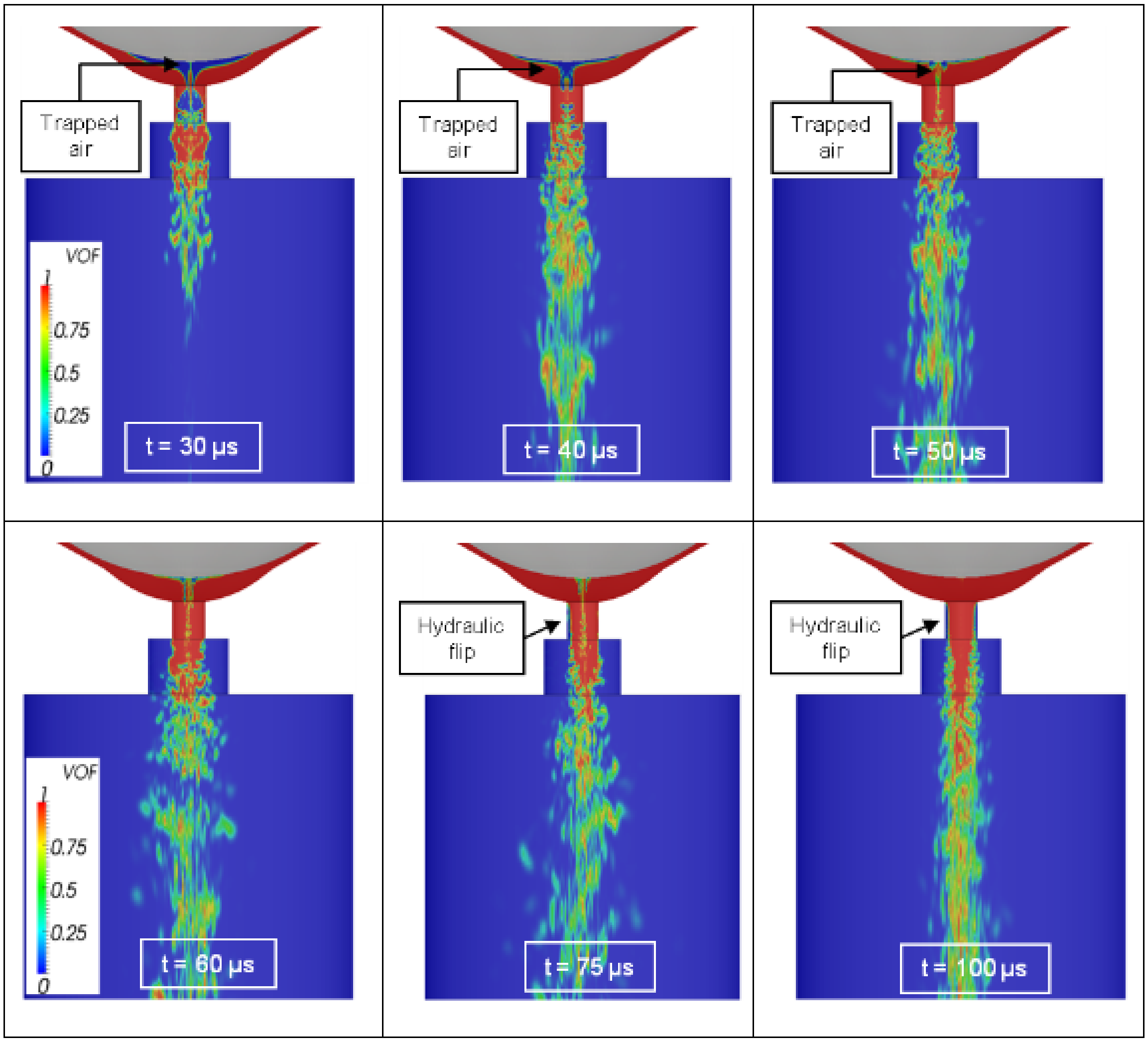


Figure 40 VOF Contour plots on a cut-plane across the nozzle diameter

Stationary Liquid Jet Breakup Structure

The structure of the stationary liquid jet, including the Kelvin-Helmholtz interface waves, is remarkably stable, as shown by the VOF = 0.5 iso-surface plots of the nozzle flow with separated liquid jet at t = 100µs, 110µs, and 120µs in Figure 41. It is worth mention that presence of a disturbance at the nozzle entrance, due to velocity perturbation or edge irregularity, is expected to engender an asymmetric and instationary Kelvin-Helmholtz wave development, although jet breakup 'mean' features, trajectory, spray plume angle, etc., remain stationary.

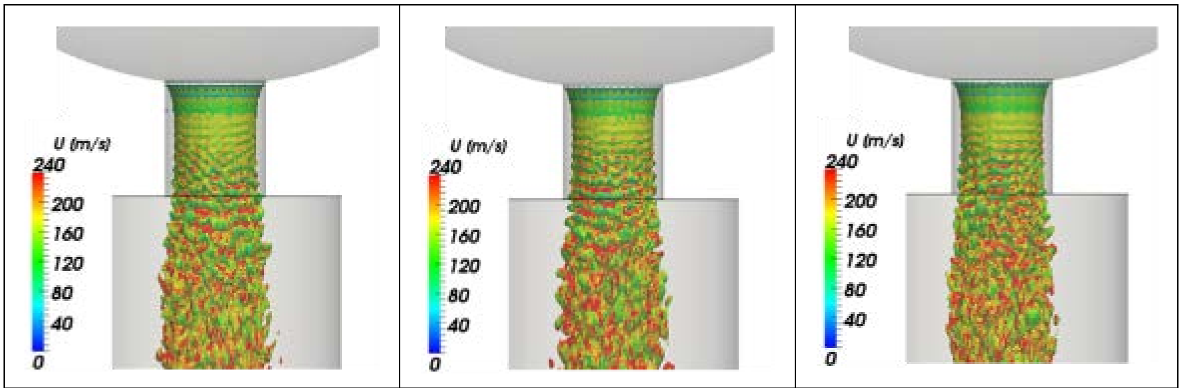


| t =100 µs | t =110 µs | t =120 µs |
|---|---|---|

Figure 41 Stationary nozzle flow and liquid jet breakup structure (depicted by VOF =0.5 iso-surface plots) at t=100,110,120 µs after SOI

As further illustrated in Figure 42, the nozzle flow is characterized by the full circumferential flow separation at the nozzle entry and formation of a liquid jet accompanied by the full hydraulic flip and resulting detachment of the liquid jet from the nozzle wall, shielded by the air

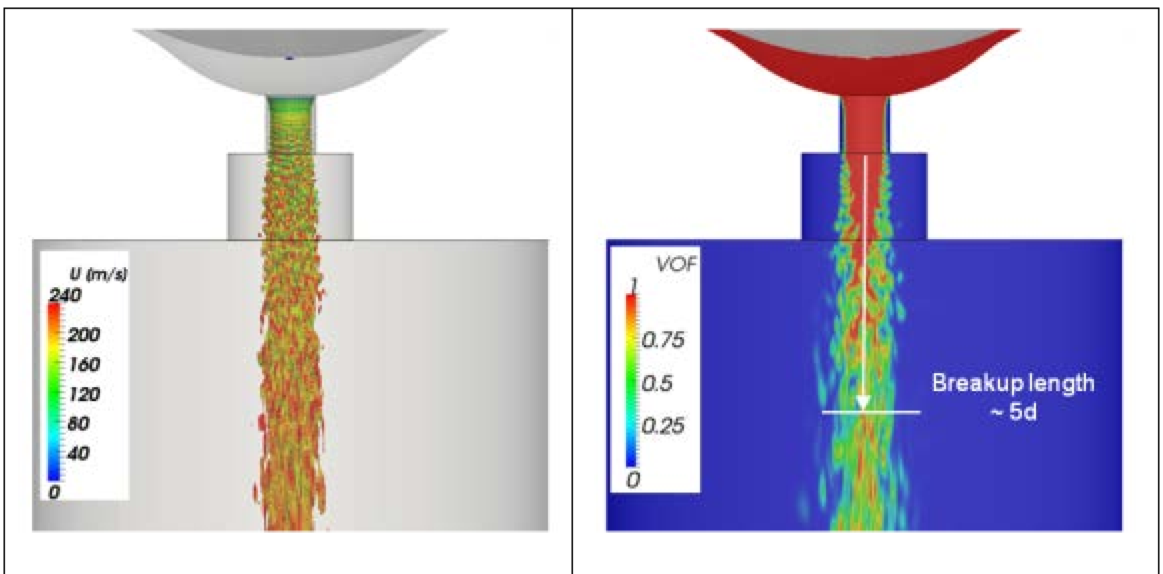


| (a) Iso-surface VOF=0.5(colored by instantaneous local velocity) | (b) VOF contour plot (nozzle-diameter cross-section) |
|---|---|

Figure 42 Stationary jet breakup structure (depicted by VOF iso-surface and contour plot) at t=110 µs after SOI

ingested from the spray ambient. The VOF contour plots show initiation and growth of the Kelvin-Helmholtz jet interface instabilities within the nozzle hole. The amplification and transformation of the ring-vortex Kelvin-Helmholtz structures, also shown in the plot of Q in

Figure 42, in the counterbore space and turbulence leads to liquid jet primary breakup at a distance of ~5d downstream of the nozzle hole exit plane. Figure 43 displays the VOF=0.5 iso-surface and the VOF contour plots at four cut-planes at locations z =l/2, z = l, z = l+L/2, and z = l+L. The results show the uniform circumferential separation of the liquid jet at the nozzle-hole entrance. The separated liquid jet within the nozzle-hole exhibits a remarkable circumferential

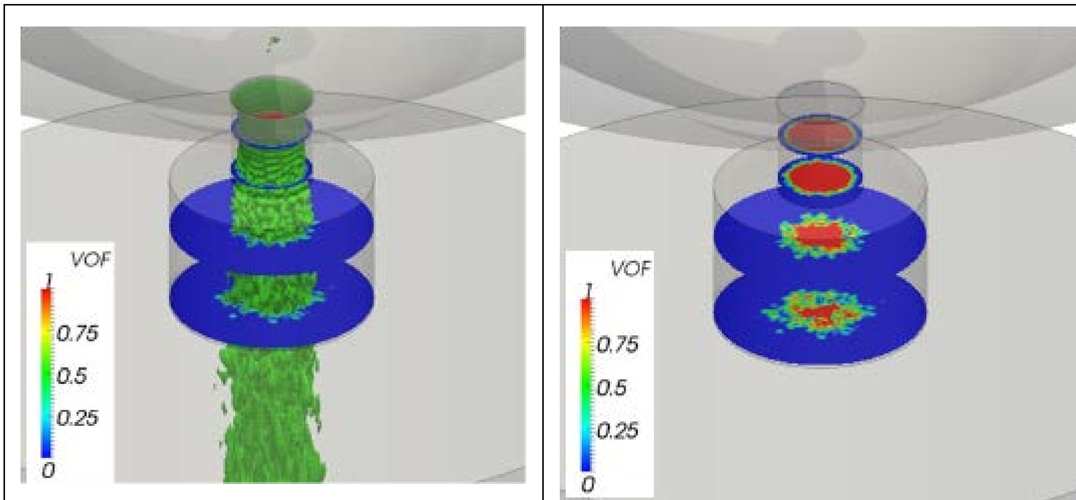


(a) Iso-surface VOF=0.5

(b) VOF contour plot (nozzle and counterbore cross-sections)

Figure 43 Stationary jet breakup structure (depicted by VOF iso- surface and contour plots) at t=110 μs after SOI

symmetry and temporal consistency, with the evidence of perturbation of its interface by the Kelvin-Helmholtz waves. The progression of the Kelvin-Helmholtz circumferentially-symmetric ring-vortex instabilities into three-dimensional instabilities within the counterbore space engenders the irregular primary breakup of the liquid jet, as clearly shown by the VOF contour plots (at z = l+L/2 and z = l+L). This phenomenon is similar to that observed in the VOF-LES simulations of the primary breakup of the accelerated planar-sheet liquid jets [41].

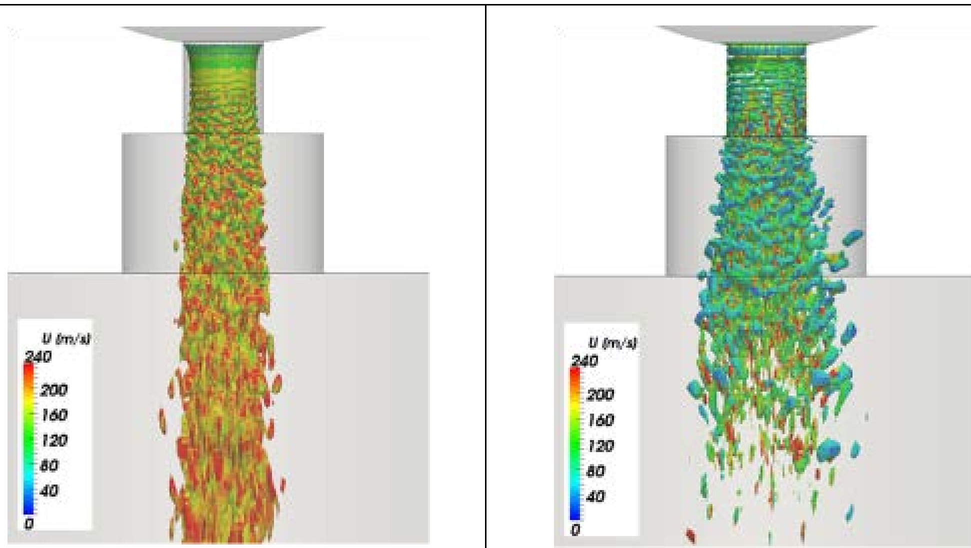


| a) Iso-surface VOF=0.5(colored by instantaneous local velocity) | (b) Iso-surface Q=1.E+13 (colored by instantaneous local velocity) |
|---|---|

Figure 44 Stationary jet breakup structure (depicted by VOF =0.5 and Q =1.E+13 iso- surfaces) at t=110μs after SOI

Figure 44 displays the structure of the liquid jet-air interface instabilities with the aid of the VOF = 0.5 and the Q = 1.E+13 iso-surfaces. The Q plot in Figure 44 shows imparting of high levels of vorticity onto the liquid jet at the nozzle entrance and formation of vortex-ring structures along the nozzle length at the liquid jet to air interface extending to the nozzle wall, that corresponds to the Kelvin-Helmholtz interface waves. The Q vortex-ring structures extend to the nozzle wall and indicate merging of the vorticity at the liquid jet to air interface with that of the surrounding air boundary layer, although the structure underlines the prominence of the jet interface instability in vorticity formation.

The deformation and breakup of the regular ring-vortex structures, concurrent with similar circumferential deformation of KH interface waves, along the nozzle hole is evident. In the immediate vicinity downstream of the nozzle hole, Q is enhanced by the amplification of the three-dimensional KH interface instabilities that diffuse vorticity into the surrounding air. The level of Q rapidly diminishes with the jet primary breakup as the linear motion of the stretched liquid ligaments forms droplets.

### 5.1.2 Influence of Counterbore

The influence of counterbore on the liquid jet atomization is of special interest, as it provides a practical means to affect the atomization features; plume angle, droplet-size distribution, penetration, etc., of the individual spray plumes of the GDi multi-hole injector without resorting to complex and restrictive nozzle-hole geometry modifications, which simultaneously affect other features of the spray plume, such as the flow rate or targeting. The effect of counterbore geometry on the spray plume features is investigated through hardware experiments conducted on varying designs that have provided indication of its influence on the plume angle and penetration. Therefore, it is of particular interest to investigate the mechanism of this influence with the aid of VOF-LES.

Figure 45 presents the stationary nozzle flow and the liquid jet primary breakup structure for the base nozzle geometry without the counterbore. The transient nozzle flow development is identical to that of base geometry since it is dependent on features of the seat-nozzle geometry that determine the flow upstream of the nozzle hole, and is not presented. The VOF plots in Figure 45 depict a fully detached liquid jet within the nozzle with a jet surface corrugated by growth of the KH interface instability waves within the nozzle, and a jet breakup length of ~5.5d, almost identical to ~5d of the base geometry.

| | |
|---|---|
| 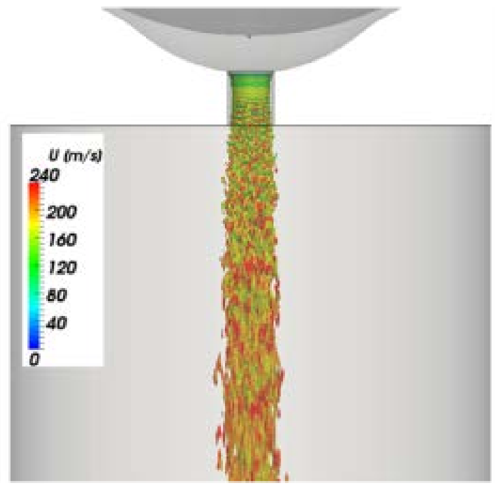 | 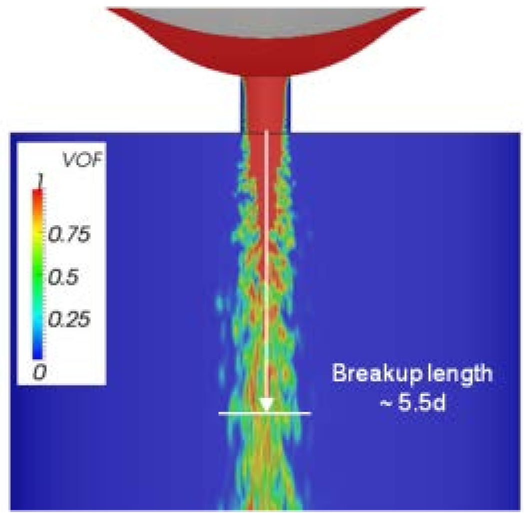 |
| (a) Iso-surface VOF=0.5(colored by instantaneous local velocity) | (b) VOF contour plot (nozzle-diameter cross-section) |

Figure 45 Stationary jet breakup structure (depicted by VOF and Q iso-surfaces) at t=110 μs after SOI

Figure 46 displays a direct comparison of the liquid jet interface structure and Q levels for the base geometry and without the counterbore. The structure of the liquid jet within and downstream of the nozzle, including the features of the development of the KH interface instabilities, are practically identical for the two cases, which is remarkable considering that they display instantaneous and not statistically averaged field values. Also, as illustrated by the super-positioned lines that mark the spray interface for Case 1, there is no discernible difference between the spray plume angles for Case 1 and Case 2. However, there is noticeable difference in the Q iso-surface plots between the two cases, as seen in Figure 46 (a.2) vs. (b.2), with Case 1 showing a noticeable spread of vorticity from the jet into the surrounding air within and downstream of the counterbore, which is absent in Case 2. The explanation is that the combination of jet-induced air motion and pressure disturbances, engendered by the Kelvin-Helmholtz instabilities, excites the air within the counterbore with the effect of generating energetic vortex structures within the surrounding air. However, as shown by the plots of VOF and Q, especially the location of decay of Q, the phenomenon does not have a marked influence

| | |
|---|---|
| 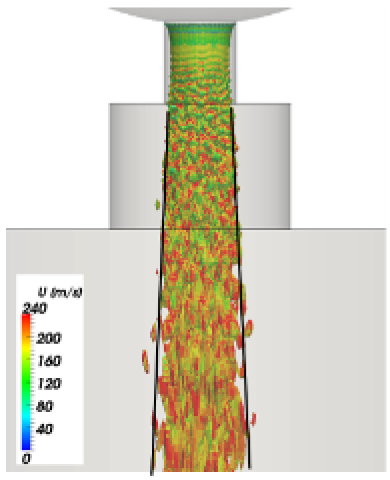  | 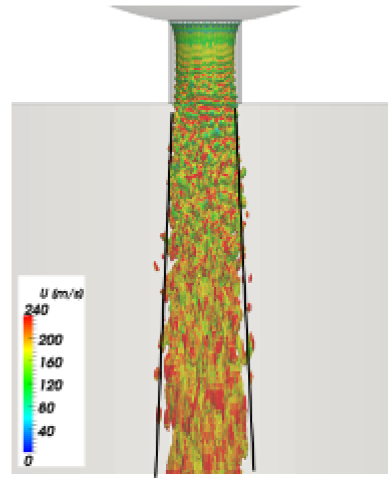  |
| (a.1) Iso-surface VOF=0.5(colored by instantaneous local velocity) | (b.1) Iso-surface VOF=0.5(colored by instantaneous local velocity) |
| 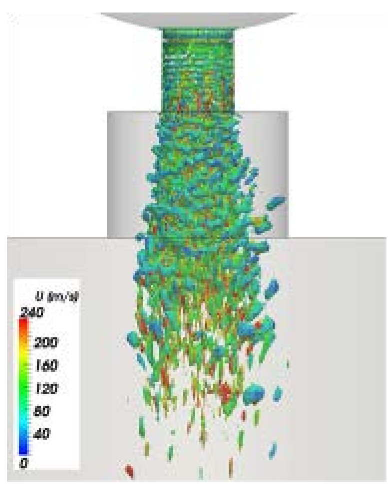  | 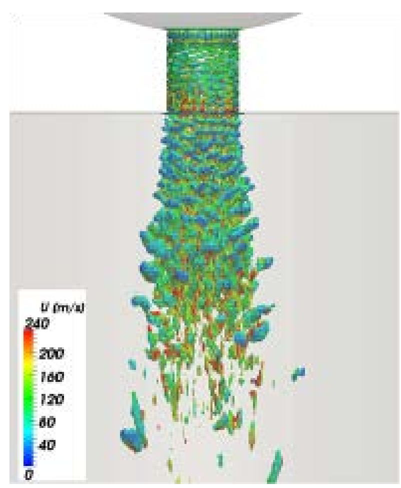  |
| (a.2)Iso-surface Q=1.E+13 (colored by instantaneous local velocity) | (b.2) Iso-surface Q=1.E+13 (colored by instantaneous local velocity) |
| (a) Case 1: base nozzle geometry | (b) Case 2: base nozzle geometry without the counterbore |

Figure 46 Comparison of jet breakup structure (depicted by VOF=0.5 and Q=1.E+13 iso- surfaces) for base nozzle with/without counterbore, at t=110μs after SOI

on the liquid jet breakup process. The possible explanations are 1) the jet breakup is an inertial process that is predominantly controlled by the instabilities of the liquid jet and the air disturbances do not play a major role due to the large density ratio, or 2) the counterbore dimensions are outside the range that could influence the jet breakup. Further investigation is required to understand the underlying mechanism.

#### 5.1.3 Influence of Nozzle Taper

One practical method to influence the flow structure within the nozzle hole is through tapered nozzle geometry. The 'positive tapered', or convergent nozzle, is considered to be advantageous as it enables reduction of the nozzle entrance losses, thus increasing nozzle Cd in addition to a reduction of the flow cavitation potential. However, it has a disadvantage that the flow acceleration tends to suppress turbulence within the nozzle and consequently adversely impacts the initiation and growth-rate of the KH instabilities. This subject has been the focus of attention in the field of diesel injector nozzle development [26] [57] [58] [59], and received significant consideration for the GDi multi-hole injectors. Therefore, it is of special interest to investigate the potential benefits of the GDi multi-hole tapered nozzle geometry with respect to the spray atomization characteristics. Figure 47 present the stationary nozzle flow and spray near-field breakup structure for a tapered nozzle with same flow-metering nozzle exit diameter as the base nozzle geometry. The most notable feature of the simulation results are:

- Fully attached flow in the nozzle hole,
- Initiation and growth of the KH interface waves downstream of the nozzle exit, with the consequent significant increase of the jet breakup length.
- Significant increase of the nozzle discharge coefficient (Cd ~ 0.9) for the tapered versus that of the cylindrical nozzle hole (Cd ~ 0.6).

- Significant increase in jet breakup length and deterioration of the jet breakup process.

Therefore, the pressure loss characteristic of a nozzle is not necessarily a negative feature of its design, as it contributes the energy for the atomization process. An energy budget of the nozzle flow losses from pressure fluctuations, Reynolds stresses, etc., is necessary to establish the linkage between the nozzle entrance losses and the jet breakup enhancement.

| | |
|---|---|
| 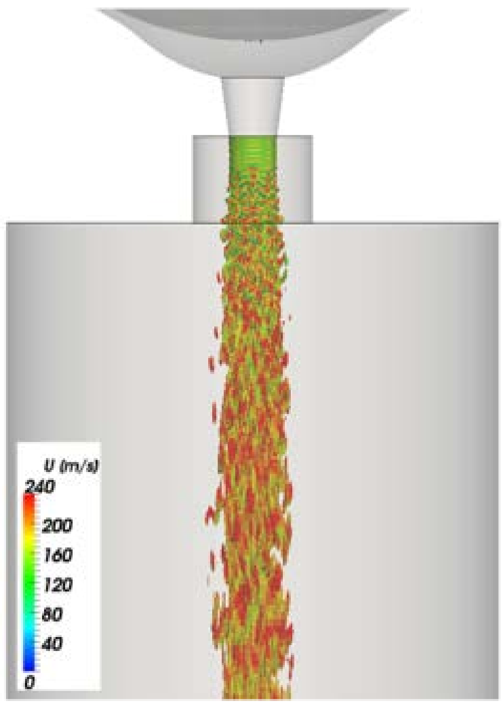 | 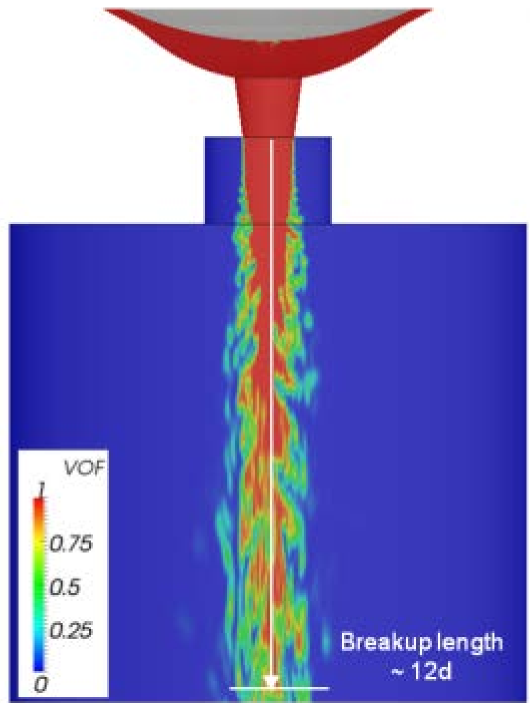 |
| (a) Iso-surface VOF=0.5(colored by instantaneous local velocity) | (b) VOF contour plot (nozzle-diameter cross-section) |

Figure 47 Stationary jet breakup structure for the tapered nozzle (depicted by the VOF=0.5 iso-surfaces and the VOF contour plot) at t=110 μs after SOI

Figure 48 provides a direct comparison of the nozzle flow, liquid jet instability, and breakup for the cylindrical and the tapered nozzles with the aid of the VOF iso-surface contour-plots at several locations downstream of the nozzle and the iso-surface plots of the quantity Q, representative of the magnitude of the jet interface vortical structures.

| | |
|---|---|
| 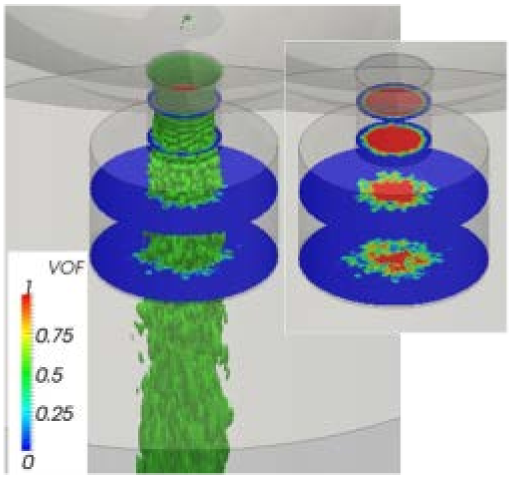  | 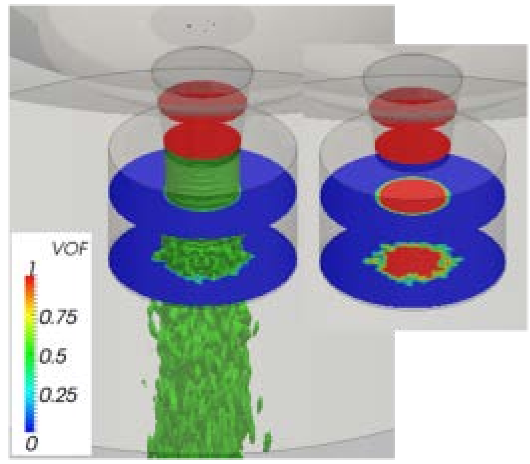  |
| (a.1) Iso-surface VOF=0.5 and VOF contour plots (cross-sections) | (b.1) Iso-surface VOF=0.5 and VOF contour plots (cross-sections) |
| 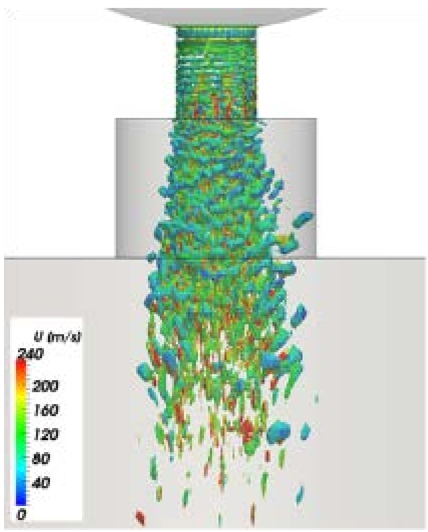  | 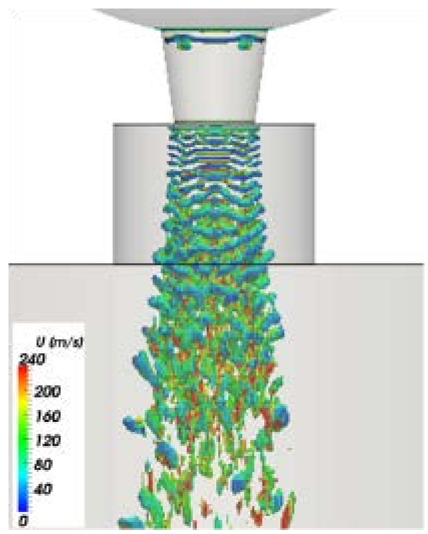  |
| (a.2) Iso-surface Q=1.E+13 (colored by instantaneous local velocity) | (b.2) Iso-surface Q=1.E+13 (colored by instantaneous local velocity) |
| (a) Case 1: base nozzle geometry | (b) Case 3: tapered nozzle geometry |

Figure 48 Comparison of jet breakup structures (depicted by the VOF =0.5 iso-surface, VOF contours, and the Q=1.E+13 iso- surface plots) for the base and tapered nozzles, at t=110 μs after SOI

The VOF contour plots in Figure 48 illustrate the attached flow within the tapered nozzle and the consequent effect on the temporal and spatial development of the KH jet interface instabilities and the jet breakup. The Q iso-surface plots show the retarded formation of the jet-air interface vorticity, in spatial correspondence with the development of the KH waves, downstream of the nozzle. Notably, the Q iso-plot indicates formation of vorticity at the nozzle entrance edge, but this is not amplified by the nozzle wall boundary layer likely due to the suppression effect of acceleration on turbulence.

### 5.1.4 Influence of Nozzle l/d Ratio

The GDi multi-hole nozzle has a short l/d ratio, of the order 0.8-1.5, compared with the diesel nozzles. It is of interest to investigate the flow and spray structure from a GDi multi-hole seat without a counterbore. Figure 49 presents the stationary spray near-field breakup structure for the long nozzle, with l/d ~ 3, and illustrates the effect of large nozzle l/d on the nozzle flow and the spray breakup process. The most notable features of the simulation results are:

- Absence of flow separation at nozzle entrance and the associated hydraulic flip
- Initiation and growth of the KH interface waves downstream of the nozzle exit, with the consequent significant increase of the jet breakup length.
- Significant increase of the nozzle discharge coefficient (Cd ~0.8) for the large l/d (~3) nozzle versus that of the small l/d (~1.1) nozzle hole (Cd ~ 0.6). Similar to the simulations for the tapered-hole geometry, the gain in the discharge coefficient is at the expense of deterioration of the jet breakup process.

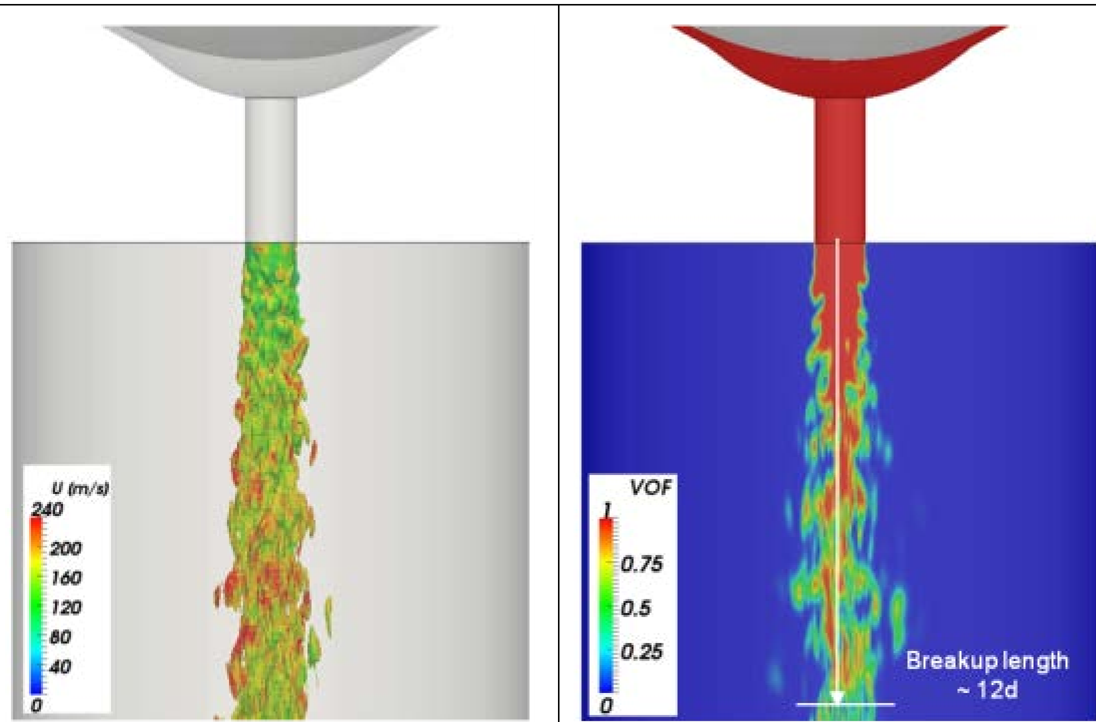


| (a) Iso-surface VOF=0.5(colored by instantaneous local velocity) | (b) VOF contour plot (nozzle-diameter cross-section) |
|---|---|

Figure 49 Stationary jet breakup structure for the large nozzle l/d (depicted by the VOF=0.5 iso-surfaces and the VOF contour plot) at t=110 μs after SOI

Figure 50 provides a direct comparison of the nozzle flow and the liquid jet breakup structure for the long and short l/d nozzles with the aid of the VOF iso-surface contour-plots at several locations downstream of the nozzle entrance and iso-surface plots of the quantity Q, representative of the magnitude of the jet interface vorticity.

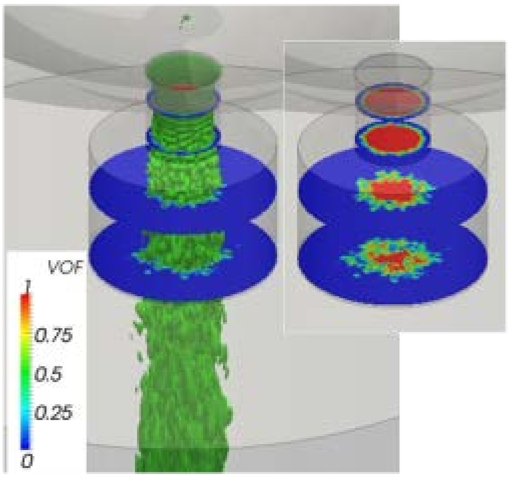


(a.1) Iso-surface VOF=0.5 and VOF contour plots (cross-sections)

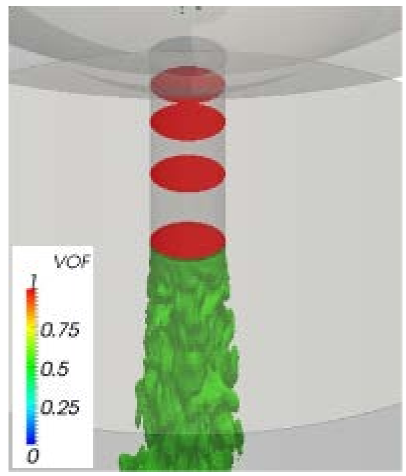


(b.1) Iso-surface VOF=0.5 and VOF contour plots (cross-sections)

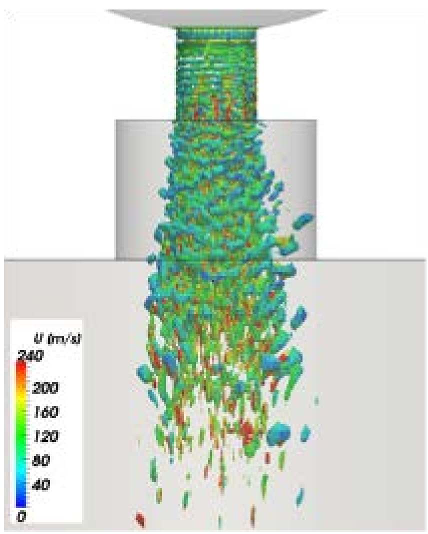


(a.2) Iso-surface Q=1.E+13 (colored by instantaneous local velocity)

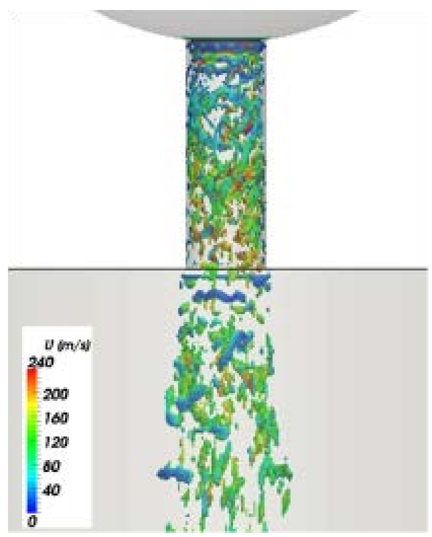


(b.2) Iso-surface Q=1.E+13 (colored by instantaneous local velocity)

(a) Case 1: base nozzle geometry

(b) Case 4: Large l/d nozzle geometry

Figure 50 Comparison of jet breakup structures (depicted by the VOF =0.5 iso-surface, VOF contours, and Q=1.E+13 iso- surface plot) for the base and large l/d nozzles, at t=110 μs after SOI

The VOF contour plots in Figure 50 illustrate the attached flow within the long nozzle, and the consequent effect on the downstream development of the KH jet interface instabilities and the jet breakup. It is noteworthy that the jet momentum is significantly larger for the long nozzle, which is due to its superior flow discharge coefficient. Most notably, the Q iso-plot for the large l/d nozzle shows formation of vorticity at the nozzle entrance edge and its amplification within the nozzle due to turbulent flow development. The Q iso-surface highlights the distinct difference in the mechanisms of vorticity production between the short and the long nozzle, and that the vorticity production by KH interface instability of short nozzle is markedly more effective.

It must be underscored that the present VOF-LES method does not include a cavitation modeling capability. In the case of the long nozzle, the cavitation inception at the nozzle entrance is expected to play a significant influence on the flow field and turbulence within the nozzle and the subsequent jet breakup process. The present simulations primarily serve to highlight the significant difference between the nozzle flow and atomization features of typical GDi multi-hole and diesel injector nozzles.

### 5.1.5 Theoretical Jet Breakup Comparison

The VOF-LES simulations provide evidence of Kelvin-Helmholtz instability as the primary jet breakup mechanism for the GDi representative nozzle geometry and fuel pressure, as well as notable influence of nozzle-hole geometry on the jet primary breakup process. A comparison of the VOF-LES predictions with the jet breakup relations derived from the linear stability theory and semi-empirical analysis of the round-jet atomization [7] [9] [55] is of interest, especially since these relations take no account of the nozzle geometry and the nozzle internal flow. The important jet hydrodynamic parameters for the base nozzle geometry are presented in Table 6.

Table 6 The base nozzle liquid jet non-dimensional parameters

| ReL = $\rho_{liquid} Ua / \mu$ | WeL = $\rho_{liquid} U^2 a/\sigma$ | WeG = $\rho_{gas} U^2 a/\sigma$ | Oh = $\mu / \sqrt{(\rho\sigma a)}$ |
|---|---|---|---|
| 2.70E+04 | 8.10E+04 | 1.40E+02 | 1.00E-02 |

Where U is the nozzle-exit jet superficial velocity, a (=0.5d) is the nozzle radius, and the liquid properties pertain to n-Heptane. It must be noted that ReL, WeL, and WeG are larger for the tapered and long nozzles, due to their superior discharge coefficients. The WeG value is significantly larger than 40.3, the upper limit for the second wind-induced breakup regime [9], and so the atomization regime prevails, whereby the primary atomization mechanism is the Kelvin-Helmholtz liquid to air interface instability, and the start of atomization is expected at the nozzle exit [9]. The VOF-LES simulations reveal that, for all the nozzle geometries, Kelvin-Helmholtz waves are seen immediately at the nozzle exit consistent with primary jet breakup mechanism due to KH instability, but they indicate a much shorter jet breakup length range of L/a ~ 10- 24 (note l/d = 5-12) than predicted. Some of this apparent discrepancy can be attributed to the jet divergent plume angle obscuring the visual criterion used for determining the jet atomization regime that is caused by the Kelvin-Helmholtz wave deformation of the jet surface in the immediate vicinity of the nozzle, as evident in Figure 45 and Figure 49, in spite of the presence of a core liquid jet. The corresponding jet atomization parameters, calculated from the relations shown in section 2.1 Blob or Stripping-Rate Model, are presented in Table 7.

Table 7 The base nozzle liquid jet atomization parameters, based on the jet linear stability / breakup theories

| $\Lambda / a$ | $\Omega$ [1/s] | $T$ (Taylor's Parameter) | $f$ (T) | $L_{breakup} / a$ |
|---|---|---|---|---|
| 8.00E-02 | 2.00E+08 | 6.30E+01 | 2.90E-01 | 3.40E+02 |

The jet breakup characteristics are defined by the frequency, Ω, and the associated wave-length Λ of the maximum growth-rate wave, produced by an infinitesimal axisymmetric disturbance on the liquid jet interface at the nozzle exit. The VOF-LES simulations indicate the KH wave-length values in the range Λ/a ~ 0.2 (base nozzle) – 1. (l/d ~3 nozzle), which are notably larger than the value predicted by the linear stability theory. Conversely, VOF-LES simulations of the jet breakup length are in the range L/a ~ 10 (base nozzle) - 24 (l/d ~ 3 nozzle), which are significantly smaller than provided by linear stability theory. In this regard, it is likely that the value of parameter B = 4.04, pertinent to the sprays from diesel nozzles, is inappropriate for the GDi nozzle's small l/d nozzle geometry. The VOF-LES simulations indicate a suitable value for the GDi nozzles is in the range B ~ 0.1 – 0.3.

It should be noted that the present VOF-LES simulations exclude in-flow disturbances and nozzle geometry imperfections, like those at the nozzle inlet edge. These are expected to be present and influential in the jet breakup experiments, and hence assimilated into the semi-empirical atomization models. With regards to the influential computational factors, the computational mesh resolution of the current VOF-LES simulations has been shown to be sufficient for quantitatively reliable simulation of the jet breakup from GDi-representative nozzle geometries [40] [41]. Nevertheless, the predicted results require confirmation through comparison with experimental data.

### 5.1.6 Summary/Conclusions

The VOF-LES simulations provide insight into the salient nozzle flow and jet-breakup features of the current GDi nozzle design and the important influences of the nozzle geometry. The simulations highlight for the axis-symmetric single-hole nozzles:

- The full flow detachment, caused by flow separation at the nozzle entrance, accompanied by hydraulic flip, is a major feature of the GDi nozzle geometry (l/d ~ 0.8-1.5).
- Initiation and growth of the Kelvin-Helmholtz instabilities within the nozzle, engendered by the flow separation at nozzle entrance, with jet primary breakup within a short nozzle downstream distance (~ 5* nozzle diameter).

- Formation of unsteady vortical flow within the counterbore volume, induced by the Kelvin-Helmholtz instabilities. However, these do not augment the jet breakup process. The likely explanation is that the liquid jet breakup is controlled by the jet inertial instabilities and the kinetic energy of the surrounding air disturbances is insufficient to influence the process.

In the case of a tapered nozzle, the attached nozzle flow yields a significant increase of the nozzle discharge coefficient (Cd ~0.9 vs ~0.6 for the detached cylindrical nozzle). However, vorticity is reduced, and therefore the initiation and growth of KH interface instabilities are arrested, thus resulting in a marked increase of the jet primary breakup length.

The LES predictions of the KH wave-length and the jet breakup length are not in quantitative conformity with the values obtained from the jet stability and breakup theories [9] [55]. The empirical parameters in the jet breakup relations may require modification for spray predictions with GDi multi-hole injector nozzle geometry.

Simulation results for the large l/d (~3) nozzle highlight the marked influence of the flow separation at the nozzle entrance on the mechanism for production of vorticity and the jet breakup process. This is, in conjunction with the nozzle-entrance cavitation, a distinction between the GDi multi-hole and the diesel injector nozzle flow and breakup processes.

The stationary nozzle flow structure and the liquid jet breakup process are remarkably stable: there is no transient instability of the nozzle flow detachment, the liquid jet trajectory, or the development of the Kelvin-Helmholtz instabilities (including transition to irregular waves) in the jet breakup structure.

Overall, the VOF-LES results reveal that the nozzle flow characteristics of GDi nozzle holes are markedly different from the diesel nozzles, owing to the relatively short nozzle l/d (of order 1, vs. 6 - 7 for the diesel nozzles). This renders the hydraulic flip an important feature of the nozzle flow and the jet primary breakup process.

It is worth mentioning that the higher nozzle discharge coefficients of the tapered and large l/d nozzles enable smaller nozzle sizes for the same static flow as the base GDi nozzle geometry.

This study highlights the potential capability of the VOF-LES method for analysis of the liquid to air interface dynamics of the jet breakup and influence of the GDi multi-hole injector valve-group specific design features. Experimental studies are required to quantitatively verify the VOF-LES simulations. Also, more realistic GDi multi-hole nozzle geometries, taking into account the nozzle hole skew angle, are subjects of investigation.

### *5.2 GDi Injector Spray Characterization*

#### 5.2.1 Prototype Injector Manufacture

Based on the test hardware defined in section 4.2 Test Hardware, injector seat drawings were generated to provide the l/d, counterbore, and skew angle geometry desired, the drawings are provided in Appendix A, and the solid model is shown in Figure 51. GDi Production seat blanks used in this study are manufactured by powder metal forming process and production blanks were sent to a supplier, Leer, with Electric Discharge Machining (EDM) equipment, to generate the nozzle thru-hole geometry and subsequently to a second supplier, Arnprior, to machine the counterbores. A grinding process was then used to create the short l/d and non-counterbored seats by removing material through surface grinding to achieve the desired geometry on the finished seat, as shown in Figure 52. This was viewed as the best method to achieve representative geometry, but the material removal does result in thinner seat material cross-section raising concerns for structural strength, however, assuring representative prototype injector nozzle thru-hole features. As can be partially seen in the interior of the seat has 5 internal ribs and thru-hole geometry was established to provide flow streamlines representative of production 5 and 6 hole injectors. It should be noted that if

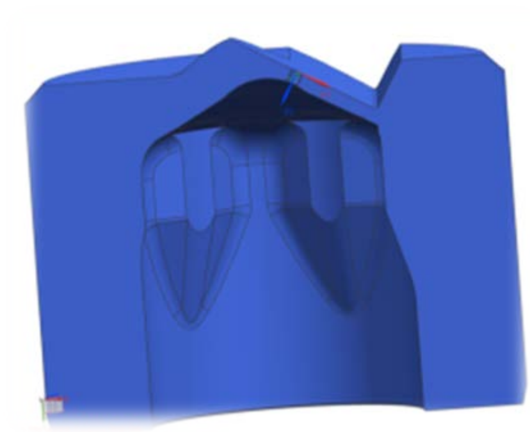

Figure 51 Injector Seat Solid Model

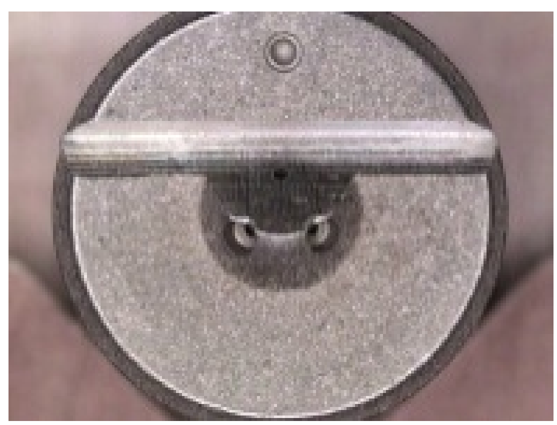

Figure 52 Finished Prototype seat with grind

the number of holes ≠ 5 some asymmetry is introduced affecting flow between ribs and thru-hole entrance.

Completed injector seats were inspected to assure resulting geometry was achieved. Due to the critical nature of the thru-hole inlet edge condition, a positive silicone mold was produced, shown in Figure 53, to analyze the transition from the seat sac volume to thru-hole inlet. The mold confirmed the thru-hole inlet transition to be a sharp corner, less than .002mm radius, desired for production of fluid turbulence. A study of the effects using LES was conducted and determined a rounded inlet radius had significant effect on the discharge coefficient for the nozzle confirming the importance the thru-hole inlet edge plays in engendering turbulent structures that aid atomization.

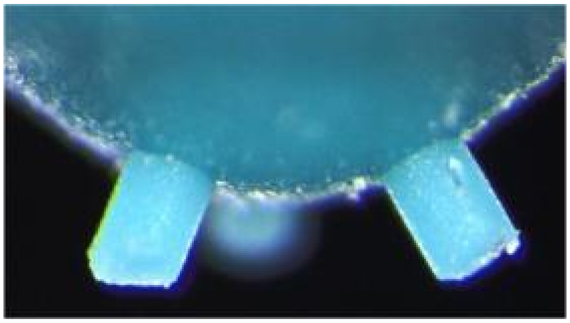

Figure 53 Silicone mold to reveal internal seat geometry

A list of initial prototype seats and their respective geometry is provided in Table 2. The matrix provided the range of l/d, counterbore, and skew angles outlined in Chapter 3 . Additionally, a tapered seat geometry, shown in Figure 54, was added to further the understanding of inlet geometry implications on spray formation as discussed in section 5.1.3 Influence of Nozzle Taper.

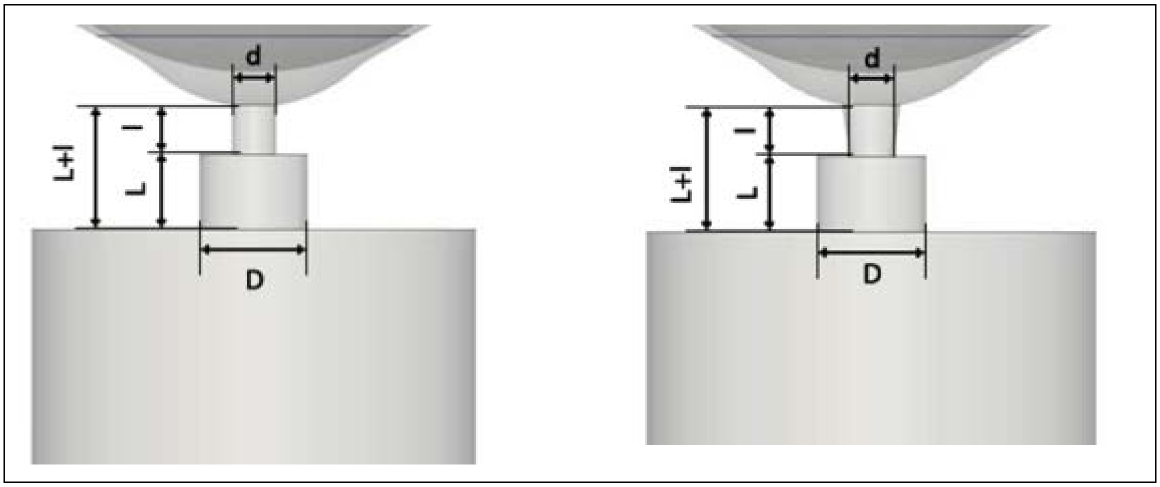


Figure 54 Prototype Cylindrical and Tapered thru-hole

### 5.2.2 Test Conditions

The spray imaging was performed using n-Heptane fuel, with system fuel pressure of 10MPa, and injection into the atmospheric ambient. In the case of the phase-contrast X-ray imaging, the Viscor calibration fluid 16B substitute was used [34]. Table 8 provides the relevant physical properties of the working liquids at 23°C for 10MPa injection pressure.

Table 8 Physical properties of the spray test liquids n-Heptane and Viscor-16B2

| ***Fluid*** | $\rho$ *[kg/m3]* | ***μ [cP]*** | **σ [N/m]** | ***P vapor [Pa]*** |
|---|---|---|---|---|
| n-Heptane | 684 | 0.41 | 0.02 | 5.3E+3 |
| Viscor 16B2 | 778 | 0.9 | 0.024 | - (low) |

The relevant spray plume non-dimensional parameters based on LES nozzle exit velocities and n-Heptane material properties are provided in Table 9.

Table 9 Non-dimensional parameters for the spray shadow-imaging experiments

| $Re = \rho_{liquid} UL / \mu$ | $We = \rho_{liquid} U^2 L/\sigma$ | $Oh = \mu / \sqrt{(\rho\sigma L)}$ | $Ma = U / a$ |
|---|---|---|---|
| 38,000 | 80,000 | 0.007 | 0.33 |

### 5.2.3 Injector Spray Characterization

Injector Spray Characterization was conducted per test request # 6500035516 listed in plume angle. The X-ray image does reveal extensive turbulent structures immediately at nozzle exit. The structures are also similar across injection pressures of 25, 50, and 75MPa. Following an initial evaluation discussed in section 5.2.4 Summary/Conclusion on Physical Test and Modified Project Scope Direction the injector series listed in Table 3 was selected and evaluated at the Delphi Luxembourg Spray laboratory Figure 55 according to the SAE standard J2715 for spray nomenclature and measurement specification [42]. To verify seat geometry, Hexcell Patternization was utilized to record plume centroid location and mass distribution for comparison to the target geometry and plume angle, as shown in Figure 56. For initial inspection of spray plume formation and penetration, backlight images were captured at 0º and 90º view angles as illustrated in Figure 57. The Hexcell Patternization and spray imaging conducted in the Rochester Spray lab for the complete seat matrix is provided in Appendix C. It should be noted in the table the seat # with red indicates that this portion of the label was omitted in the marked injector. Tests were also conducted at Argonne National Lab using the Advanced Photon Source (APS) to characterize the near-field spray turbulence. Testing conducted at Argonne National Lab (APS) focused on the single-hole injectors representing l/d of 2.95 and 3.96, and the series of image captures is presented in Appendix D. A typical time sequence is shown in Figure 58, and similar to the shadowgraph images for axis-symmetric single-hole nozzles, we see long penetration and spray plumes that contract as the penetration increases in contrast to the 30º skew angle nozzles typical of GDi injectors in application.

## REQUEST FOR TEST ENGINEERING

SAP IO #(s) 650035516

TEST REQUEST # PU927-AQ18 — REQUESTER Varble/Mergler

SUBJECT Spray Request for AK29 Injectors - Mark Shost Project — SUPERVISOR Dom Dalo

DEPT. 15640 — PHONE x6795 — DATE 12-Jan-2012

TDP/ADP/PDP Status

○ TDP ○ ADP ○ Analytical Design Confirmation ○ Design Confirmation

○ Design Validation ○ Product Validation ○ MCIP ◉ Other Spray angle

TEST CLOSURE METHOD:

○ REPORT/SUMMARY ◉ DATA ONLY

Test Sample Level

◉ Development Model Shop

○ Production Intent Model Shop

○ Production Equipment ○ MQ1 ○ MQ2

DATE SAMPLES AVAILABLE 12-Jan-2012 — DATE RESULTS REQUIRED 18-Jan-2012

SAMPLE DISPOSITION

○ RETAIN PER PROC 1001 ◉ RETURN TO Dan Varble

DESCRIPTION OF WHAT IS TO BE TESTED: — PART NAME: Beta Spray Mule — MODEL YEAR N/A

PART NO. AK29 Spray Mule — REV. — QTY. 3 ea of 12 TC's — SUPPLIER Leer/Arnprior

SERIAL NO. AK29-01, AK29-02….to AK29-12 plus 3 hole versions of AK10-3, AK11-3 & AK12-3

PPAP DATE — SOP DATE — BEN # — BEN TEST COMPLETION DATE

BACKGROUND INFORMATION & SPECIAL FEATURES

Seat Part No.: NA
Fuel Pressure: 10 Mpa
Static Flow Rate: 1 to 3 g/sec @ 10Mpa Stoddard (65 um stroke)
*Other Information (e.g. GDi injector driver, GDi spray orientation, special fixturing, etc.):*

Please use HMC nominal pressure waveform, "HMC_IDM3Lvl9_Nom30FFT_10-9-10"

TEST OBJECTIVE

Background:
(3) injectors of (12) different seat configurations for a total of (36) injectors. These seats were EDM'ed at Leer and spray mules built at Arnprior. (9) single hole seats and (3) three hole seats. Flow rates are very low on the order of 1-3 g/sec!

For flow: Please calibrate in Stoddard to 10% of SF using "SW9_Std65V_Nom_Beta_SprayMule.s28" drive waveform. Please record SF (in Stoddard) and stroke in spray mule file. Flow work was requested under AJ84.

Note first injectors (2&5) arrived 6/24, and were previously shipped, so not available for spray testing. Have Extra 3 hole Versions of 10,11&12. for testing.
Spray: Use N-Heptane.
HexCell / Patternation: all spray mules
Imaging / Penetration: all spray mules
LD / drop size all spray mules

Attachments? ◉ Yes ○ No

SUGGESTED PROCEDURE #:

PASS/FAIL CRITERIA

N/A

TEST COMPLETED WITH DATA ONLY - NO REPORT REQUIRED

RESULTS ____ (Quantity) ☐ Pages ☐ Files ☐ Disks — FORWARDED TO — METHOD ☐ Hard Copy ☐ E-Mail ☐ CD/Disks ☐ Network Drive — ON ____ (Date)

FORWARDED BY — TEST SUPERVISOR APPROVAL

Figure 55 Injector Test Request, for Hexcell Patternation, Backlight Imaging, and Laser drop size profile

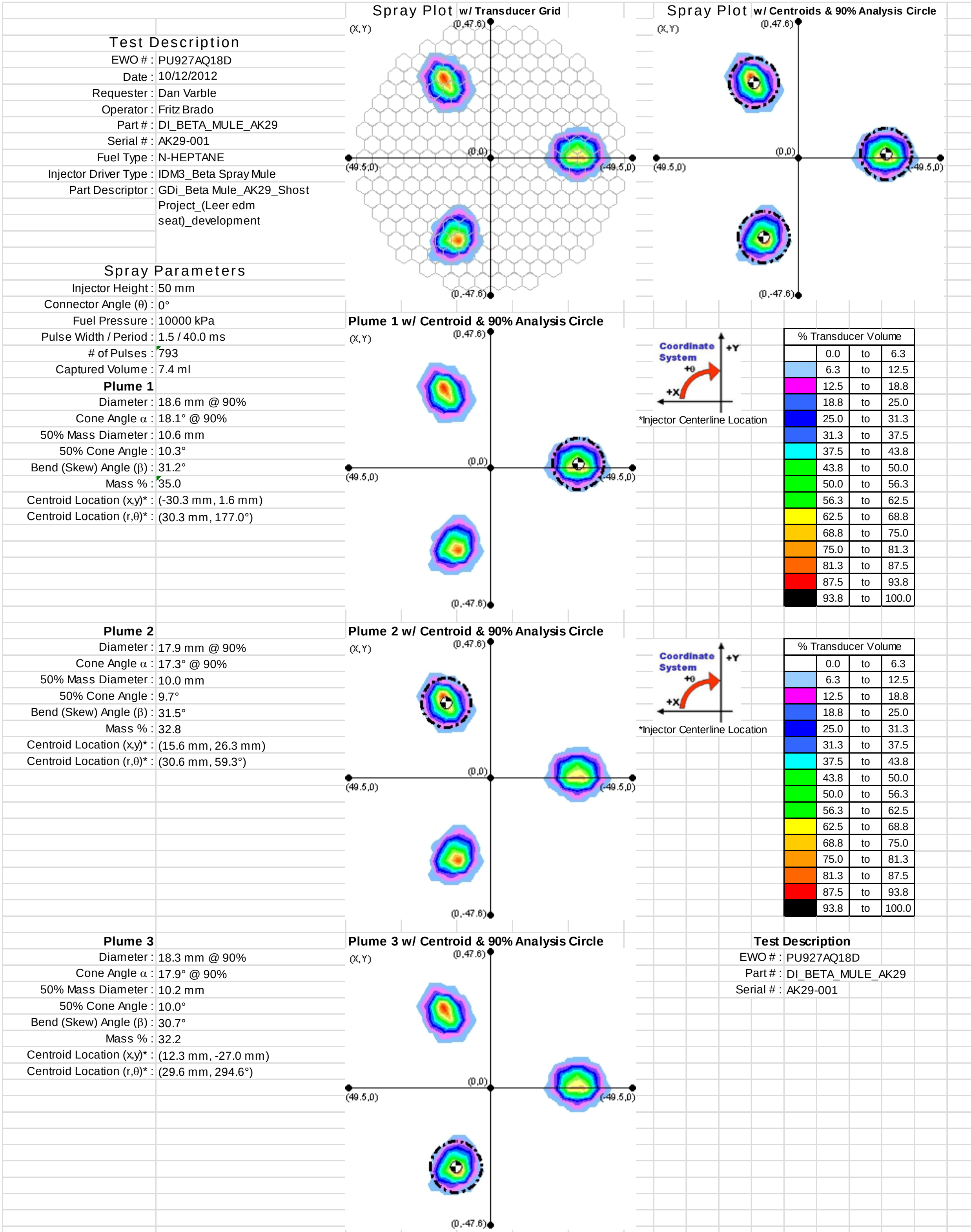


Figure 56 Spray Plume Characterization using Hexcell Patternator, S/N AK29-07-001

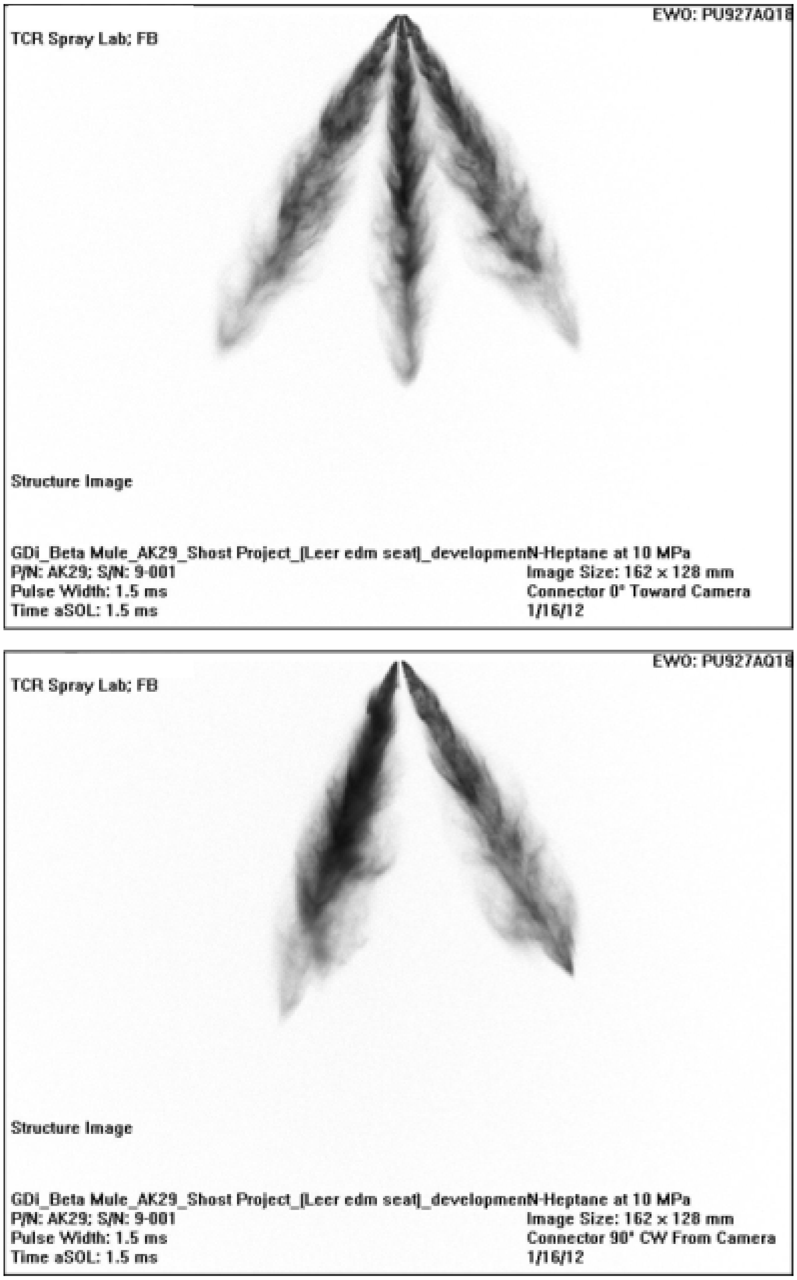


Figure 57 Shadowgraph Image at 0º and 90º for 3-hole seat injector

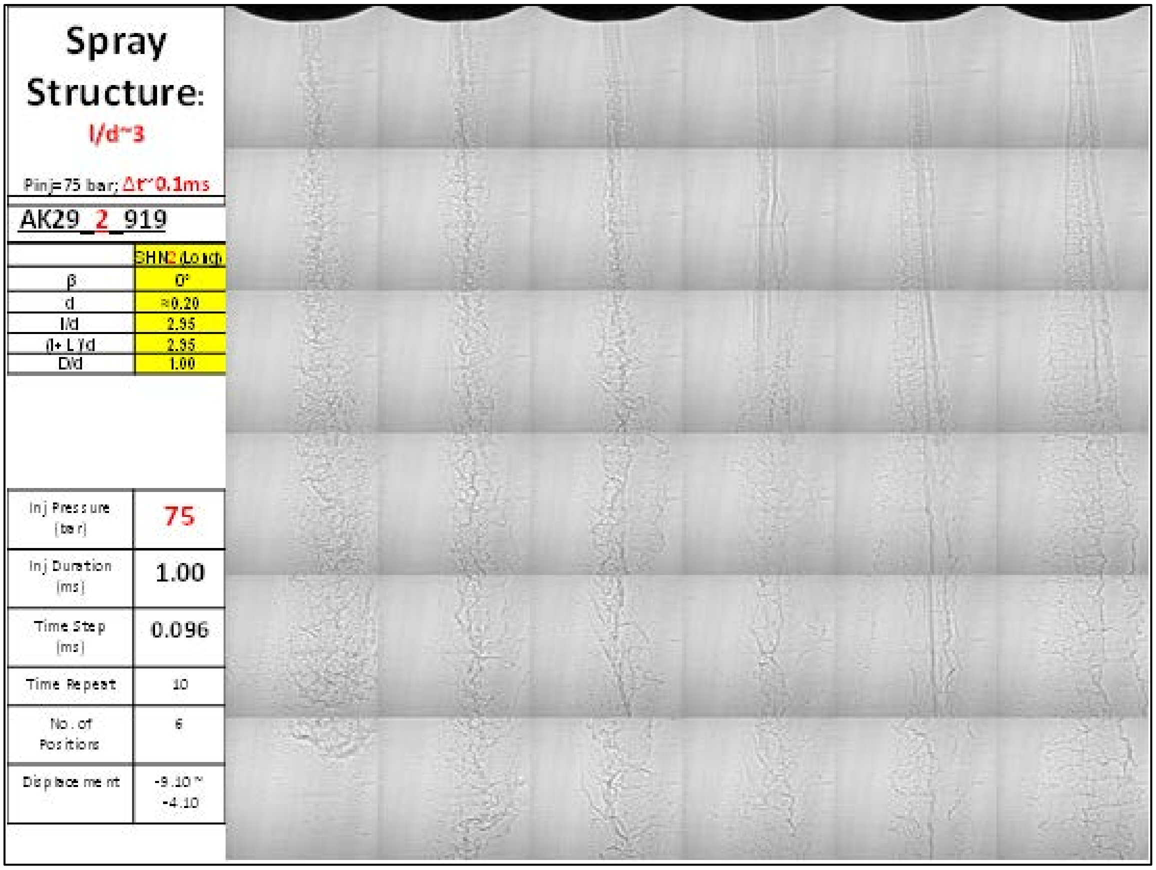


Figure 58 Phase-Contrast X-ray images revealing turbulent structure

Testing in the Delphi Luxembourg spray lab was conducted per the SAE standard documented in 4.1 Defined Terms. To understand the differences of methodology, calculations for plume angle and penetration were conducted using both Shadowgraph and Mie Images.

The following summarize the presented data:

- High speed shadowgraph images from the side view are presented in Appendix E
- High speed integral Mie Images from the side view are presented in Appendix F
- Bottom-view high speed integral Mie Images are presented in Appendix G
- Mie Scatter Images of near-field Spray are presented in Appendix H

Calculated spray penetration length for the axis-symmetric single-hole nozzles from the Shadowgraph images at 0° and 90° orientations, and 10 and 20MPa injection pressures, is shown in Figure 59 and indicates a consistent penetration ≈ 88mm across the range of pressure. While seat AK29-3 and AK29-6 both had an l/d = 1.1, the thru-hole diameters varied with AK29-3 ≈ .20mm and diameter of AK29-6 ≈ .15mm. A similar penetration calculation using the Mie Imaging data is presented in Figure 60. The data documents a slightly shorter penetration ≈ 86mm, again unaffected by injection pressure. Calculated spray angle for the axis-symmetric single-hole nozzles from the Shadowgraph images at 0º and 90º orientations, and 10 and 20MPa injection pressures, shown in Figure 61, reveals variation in the plume angle over time from 4-14º with a mean value ≈ 6-8º, while Figure 62 with Mie Scatter images indicate similar variability with a mean ≈ 8-10º. Analysis was also conducted on the 3-hole seats AK29-9, AK29-10, and AK29-11 with results presented on Figure 63 for the Shadowgraph images at 0º and 90º orientations, and 10 and 20MPa injection pressures. Similar results were found using Mie Scatter images, as shown in Figure 64. There is a noticeable anomaly for seat AK29-10 at the 90º orientation exhibiting a markedly lower penetration on the shadowgraph images. The lower penetration is also seen in the Mie Scatter image calculations, but to a somewhat reduced amount. Additionally seat AK29-11 shows some larger penetration rates at around 1000μs ASIE, this can be seen clearly in the Mie scatter image, presented in Appendix F, with one nozzle plume exhibiting far greater penetration and narrower plume angle. Spray angle is presented for the 3-hole seats in Figure 65 for the Shadowgraph images at 0º and 90 º orientations with 10 and 20MPa injection pressures. The results are more consistent than the single-hole nozzles with variation between 60-80º. In this case, the results are very similar for the Mie Scatter images provided in Figure 66. Spray droplet measurements were conducted using the Malvern Spraytec 2000, as defined in 4.3.3 Laser Diffraction Technique, at 10 and 20MPa with calculated key spray statistics for Dv10-Dv90, Dv32, and Sauter Mean Diameter

(SMD), listed in. Table 10 The results indicate similar droplet distribution for all nozzles with the tendency for smaller droplets at 20MPa injection pressure. This would indicate the deeper penetrating axis-symmetric single-hole nozzles showed no degradation in particle size as measured at 50mm from injector tip. Distributions of the droplet size for the single-hole and 3-hole injectors at 10 and 20MPa are presented in Figure 67 and Figure 68, show a tendency of a larger quantity of smaller droplets for 3-hole injectors, but with a similar mean characteristic. Figure 69 compares similar nozzles constructed with and without counterbores and the graph of nearly identical droplet size distributions indicates no discernable influence of the counterbore. The last comparison was for skew angle, as presented on Figure 70, where AK29-3, skew angle = 0º, showed a greater propensity of small droplets compared to AK29-3 with skew angle = 30º.

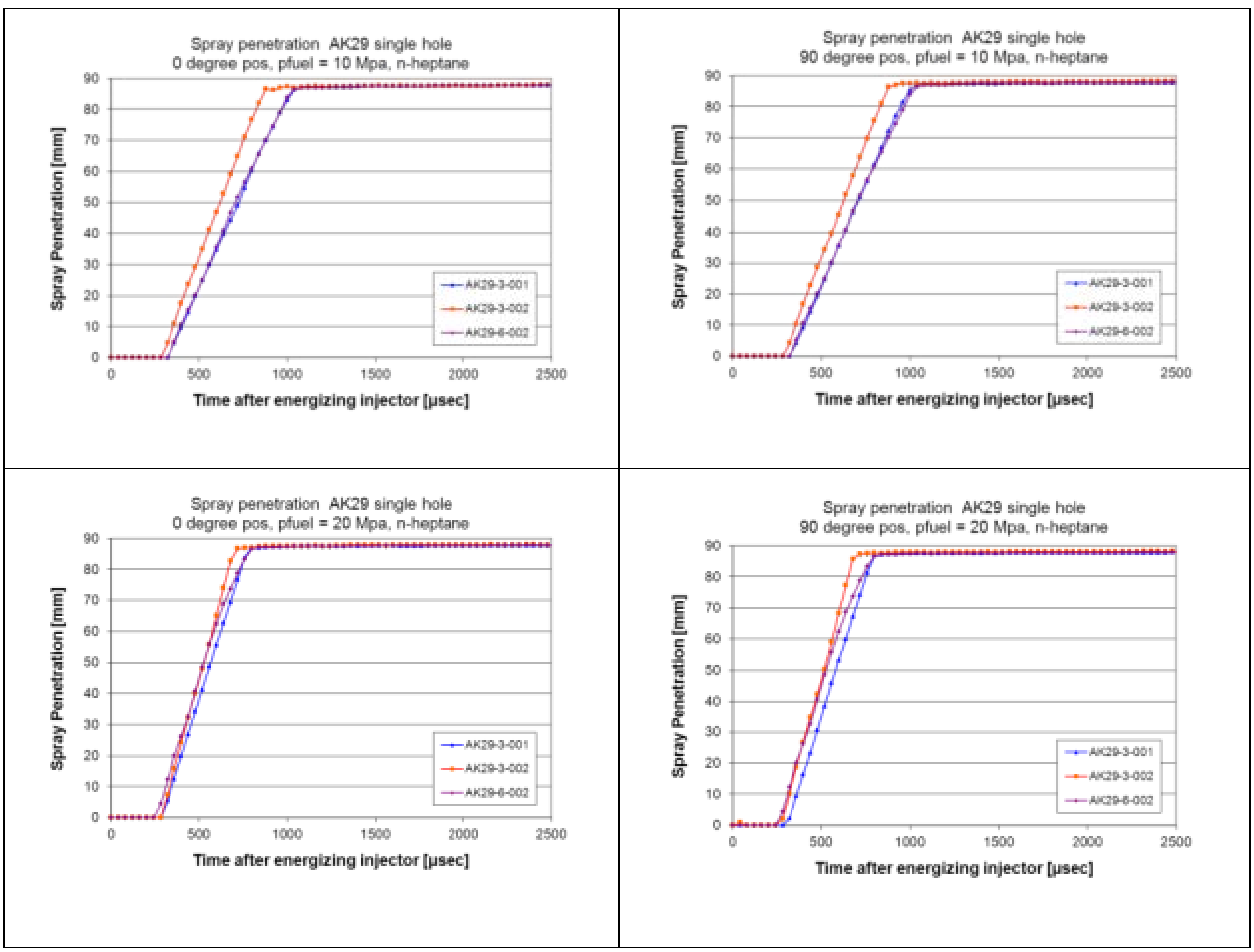


Figure 59 Spray Penetration after injection 0º, 90º at 10 and 20MPa calculated from Shadowgraph Images

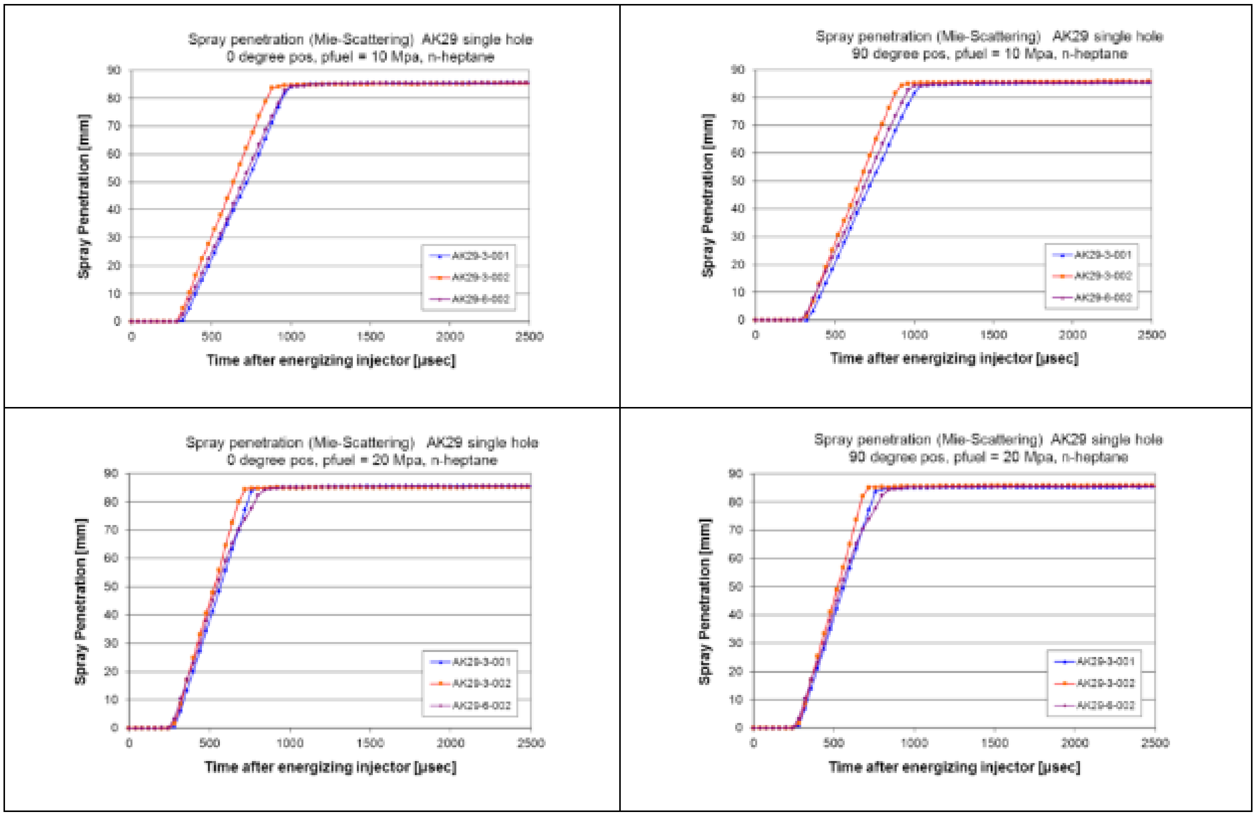


Figure 60 Spray Penetration after injection 0º, 90º at 10 and 20MPa calculated from Mie Scatter Images

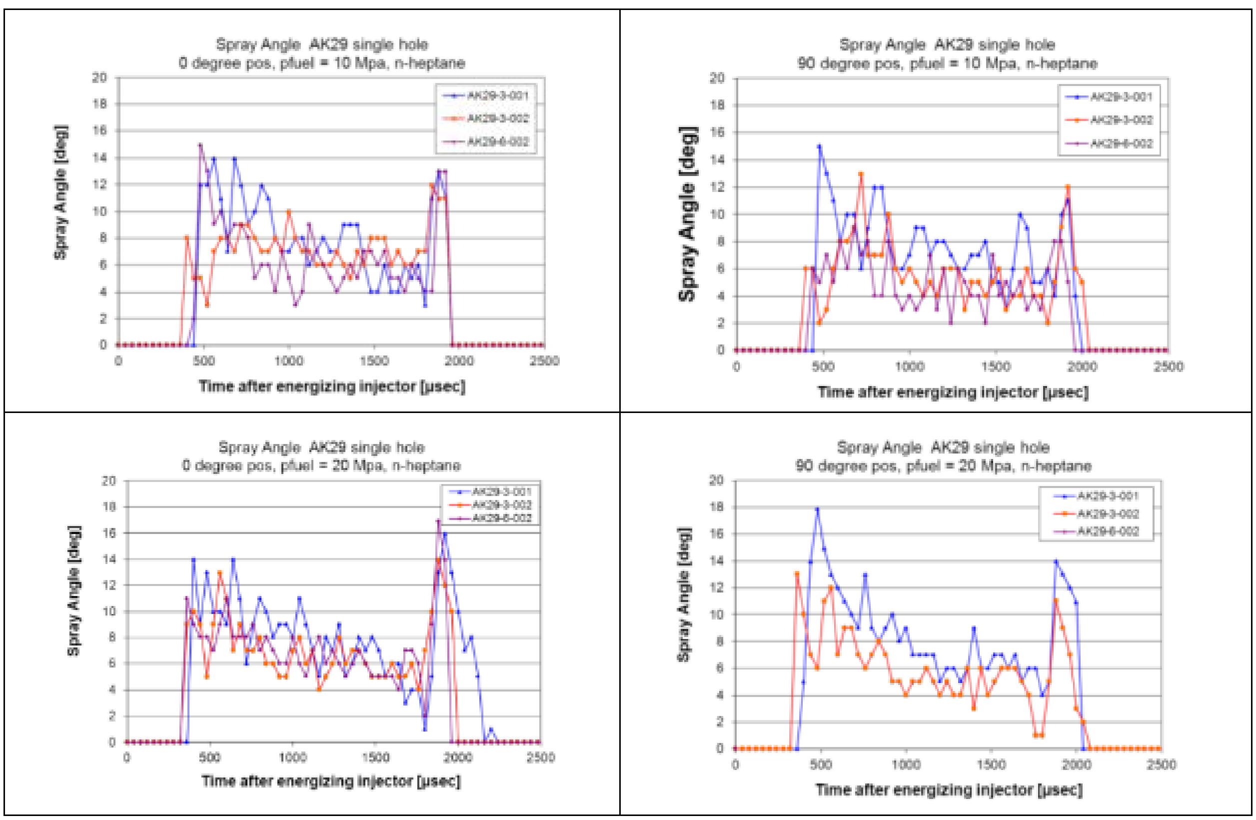


Figure 61 Spray Angle after injection 0º, 90º at 10 and 20MPa calculated from Shadowgraph Images

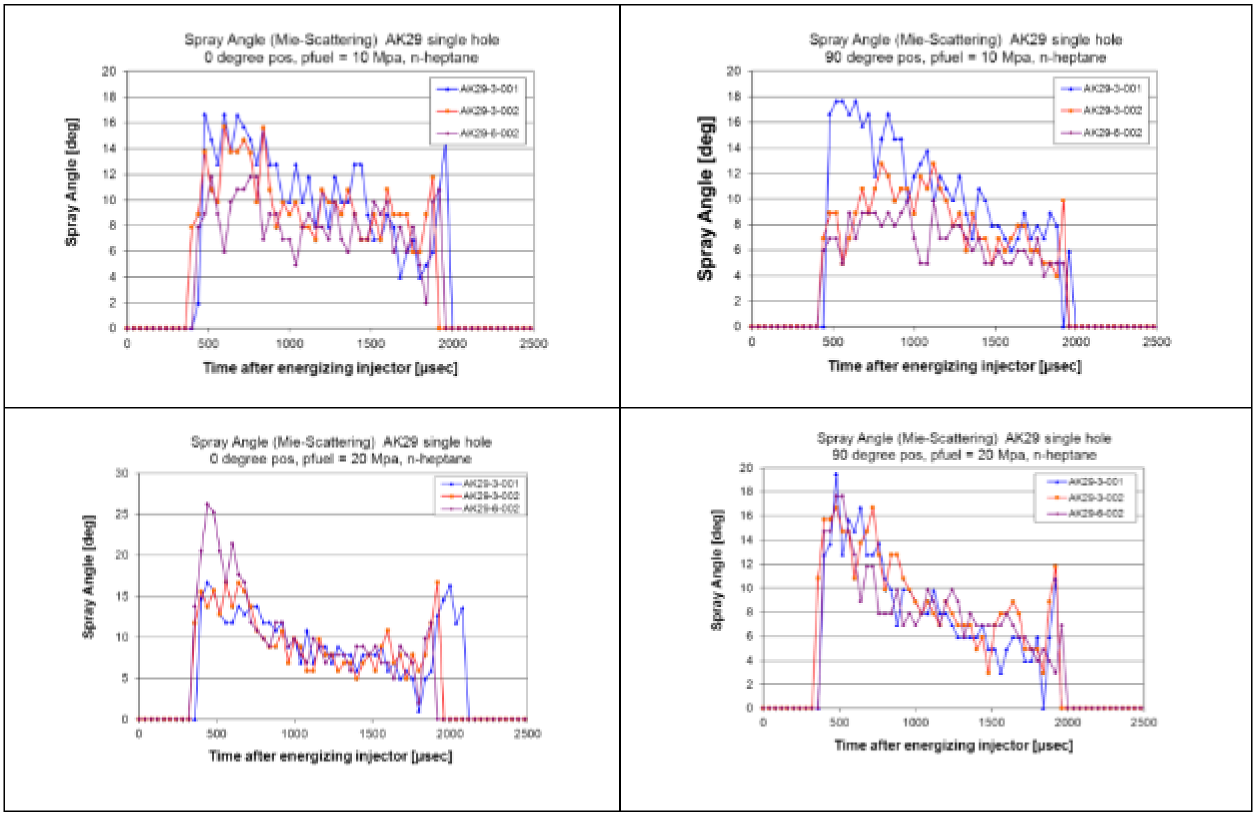


Figure 62 Spray Angle after injection 0º, 90º at 10 and 20MPa calculated from Mie Scatter Images

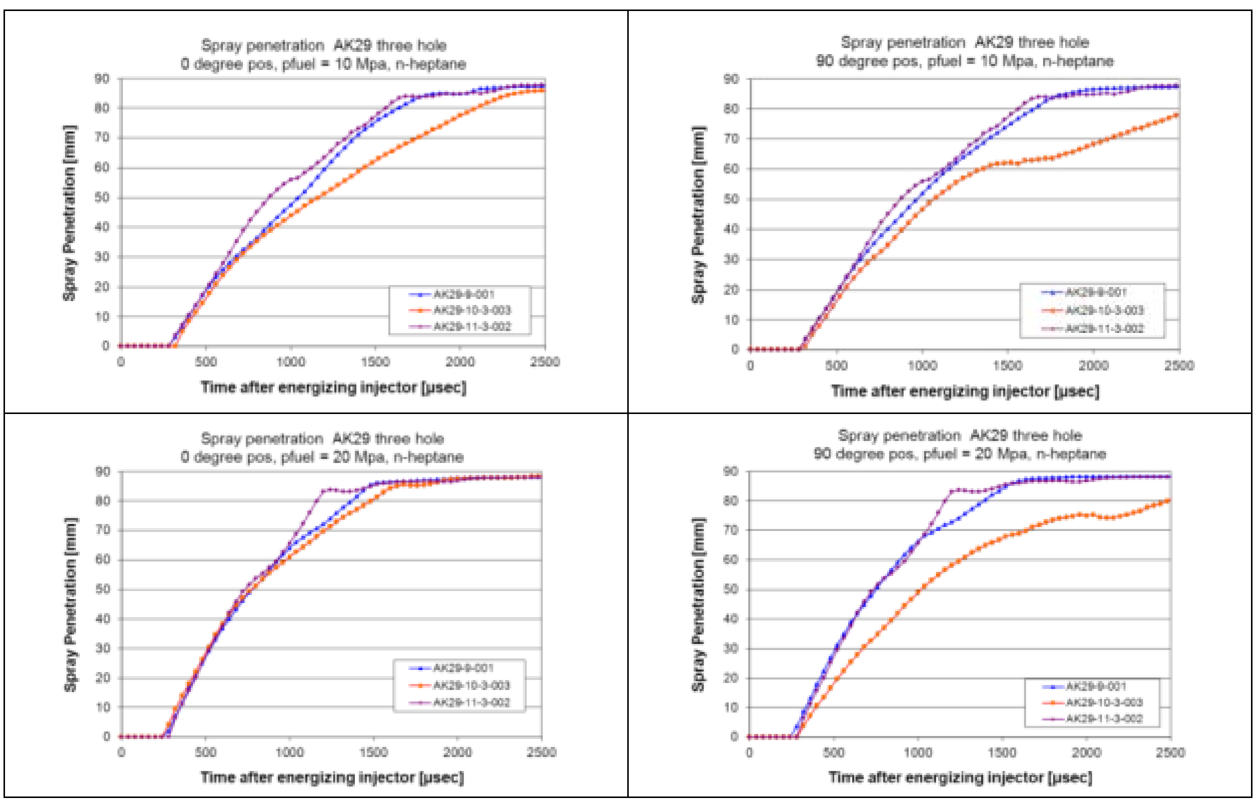


Figure 63 Spray Penetration after injection 0º, 90º at 10 and 20MPa calculated from Shadowgraph Images, 3-hole

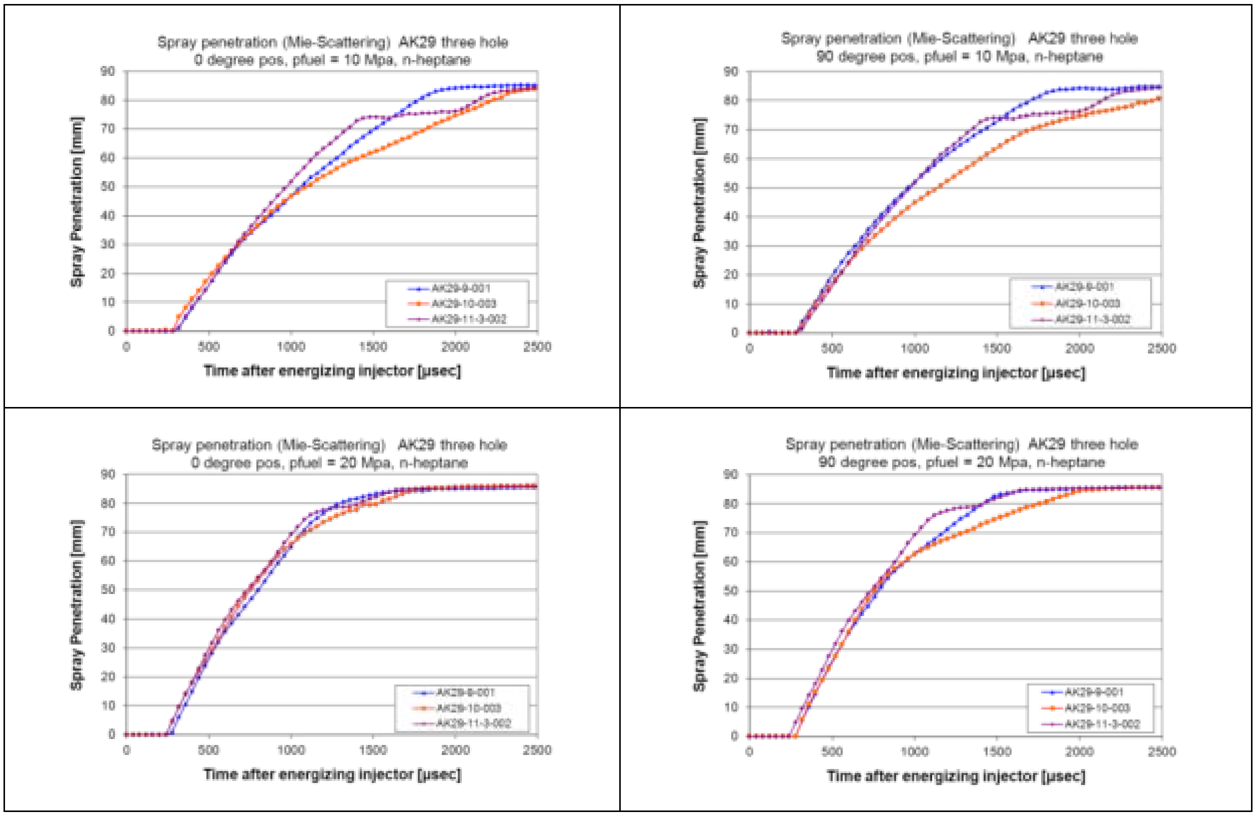


Figure 64 Spray penetration after injection at 10 and 20MPa calculated from Mie Scatter Images, 3-hole

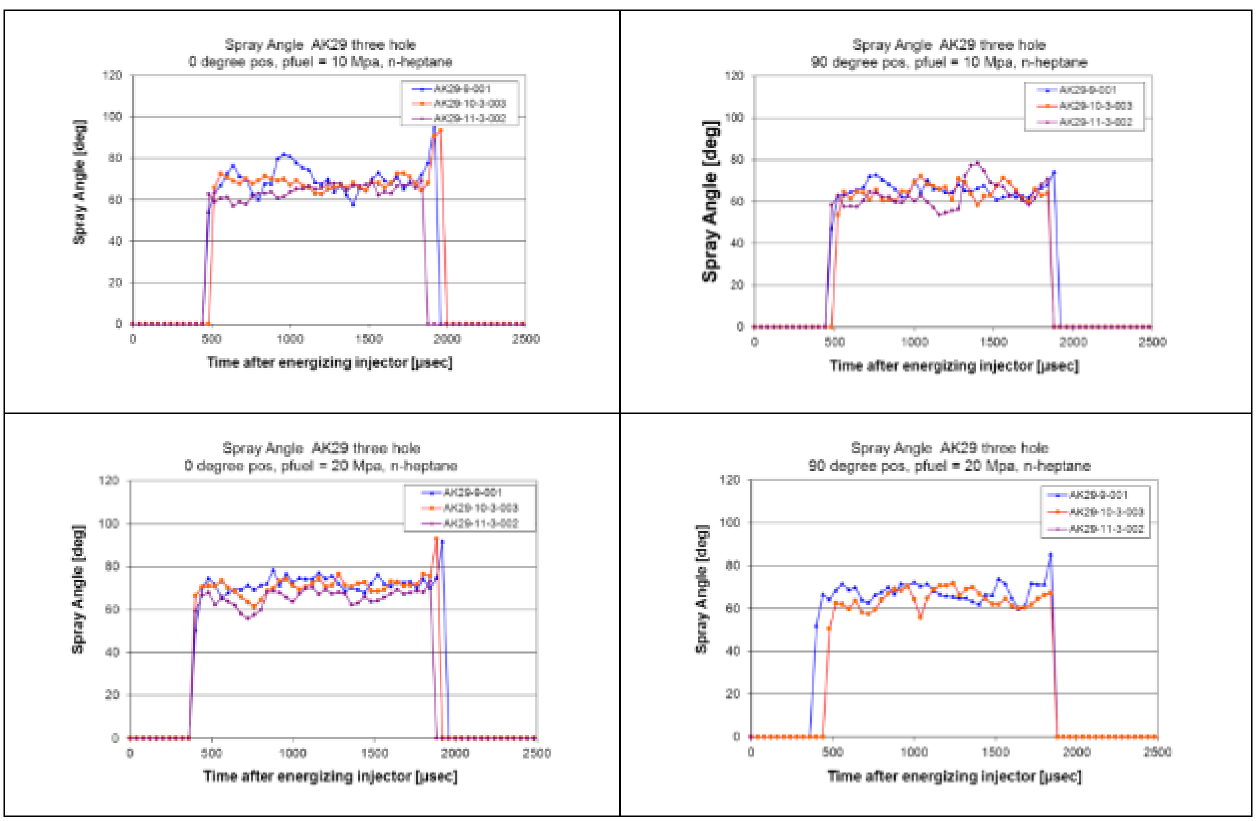


Figure 65 Spray angle after injection at 10 and 20MPa calculated from Shadowgraph Images, 3-hole injectors

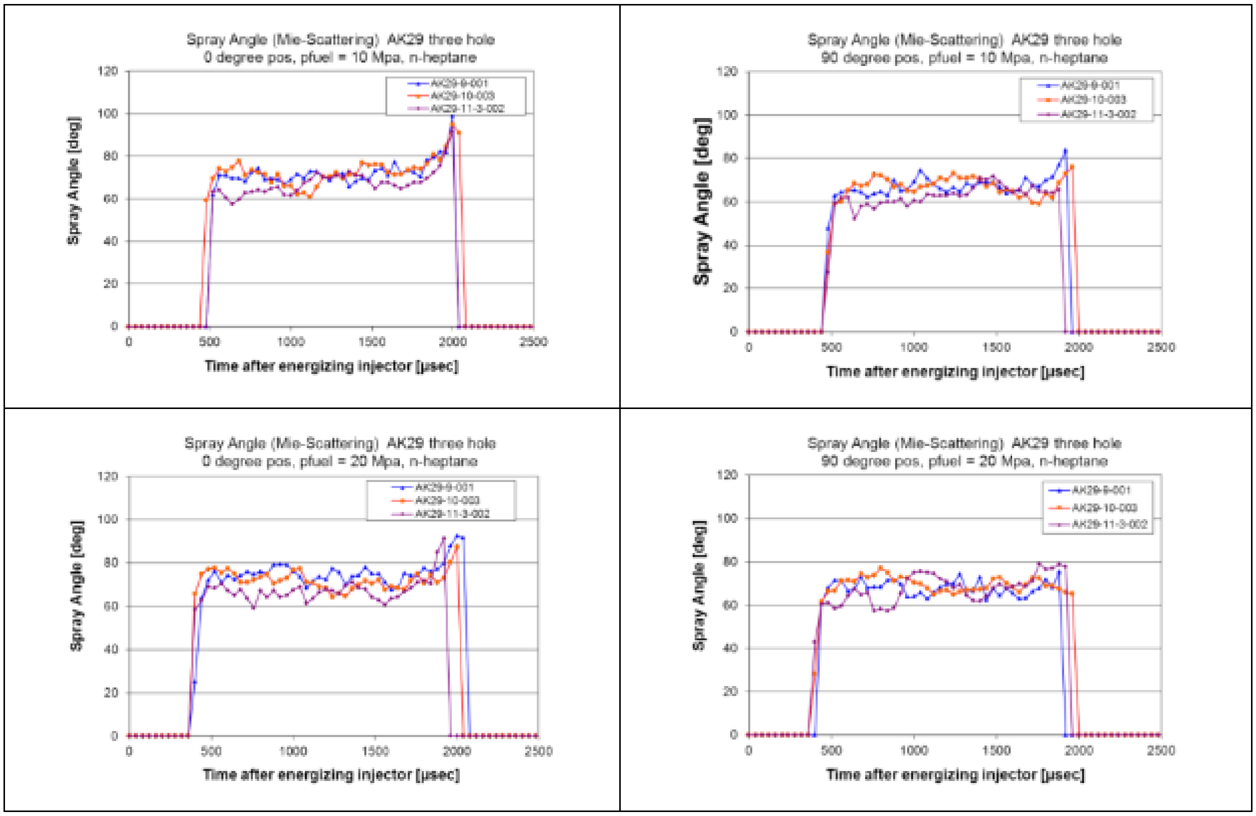

Figure 66 Spray angle after injection at 10 and 20MPa calculated from Mie Scatter Images, 3-hole injectors

Table 10 Injector Spray Droplet size distribution measured at 50mm from nozzle tip

| Injector | Nozzle holes | Nozzle Key Feature | Fuel pressure [Mpa] | Sauter mean Dv32 [µm] | Dv43 [µm] | Dv10 [µm] | Dv50 [µm] | Dv90 [µm] |
|---|---|---|---|---|---|---|---|---|
| AK29-3-001 | 1 | d≈.20, l/d=1.1 | 10 | 7.3 | 15.6 | 3.5 | 11.9 | 30.5 |
| AK29-3-002 | 1 | d≈.20, l/d=1.1 | 10 | 6.4 | 13.2 | 3.1 | 10.3 | 26.3 |
| AK29-6-002 | 1 | d≈.15, l/d=1.1 | 10 | 6.6 | 14.8 | 3.1 | 10.9 | 29.6 |
| AK29-9-001 | 3 | d≈.20, l/d=1.1 | 10 | 8.6 | 15.6 | 4.8 | 12.9 | 27.9 |
| AK29-10-3-003 | 3 | d≈.15, l/d=1.1 | 10 | 8.3 | 16.3 | 4.3 | 13.1 | 30.6 |
| AK29-11-3-002 | 3 | d≈.15, l/d=3.96 | 10 | 8.8 | 16.9 | 4.7 | 13.6 | 31.2 |
| Injector | Nozzle holes | Nozzle Key Feature | Fuel pressure [Mpa] | Dv32 [µm] | Dv43 [µm] | Dv10 [µm] | Dv50 [µm] | Dv90 [µm] |
| AK29-3-001 | 1 | d≈.20, l/d=1.1 | 20 | 4.4 | 8.9 | 2.0 | 6.9 | 17.7 |
| AK29-3-002 | 1 | d≈.20, l/d=1.1 | 20 | 4.4 | 8.6 | 2.0 | 6.8 | 17.1 |
| AK29-6-002 | 1 | d≈.15, l/d=1.1 | 20 | 3.8 | 8.0 | 1.6 | 5.8 | 16.5 |
| AK29-9-001 | 3 | d≈.20, l/d=1.1 | 20 | 5.6 | 10.2 | 2.8 | 8.5 | 18.8 |
| AK29-10-3-003 | 3 | d≈.15, l/d=1.1 | 20 | 5.2 | 10.1 | 2.5 | 8.1 | 19.1 |
| AK29-11-3-002 | 3 | d≈.15, l/d=3.96 | 20 | 5.6 | 10.6 | 2.7 | 8.7 | 19.6 |

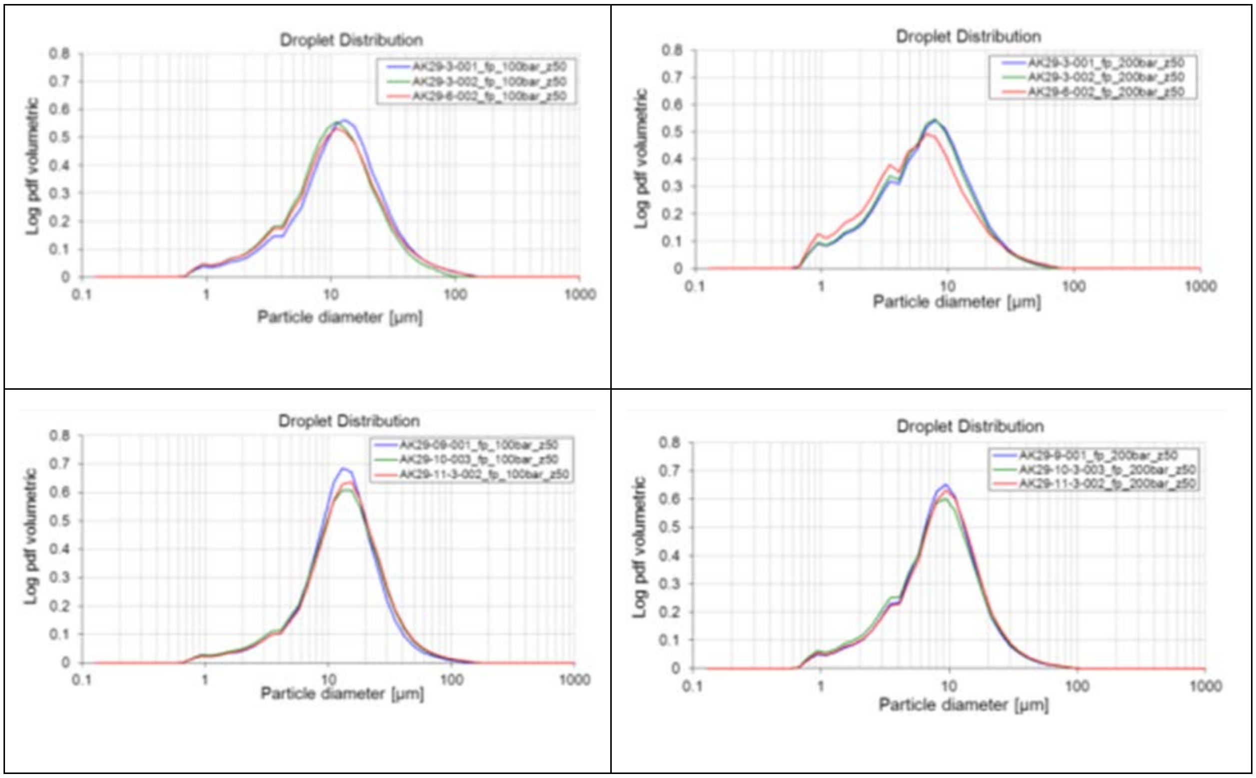


Figure 67 Spray Droplet size distributions for single and 3-hole injectors

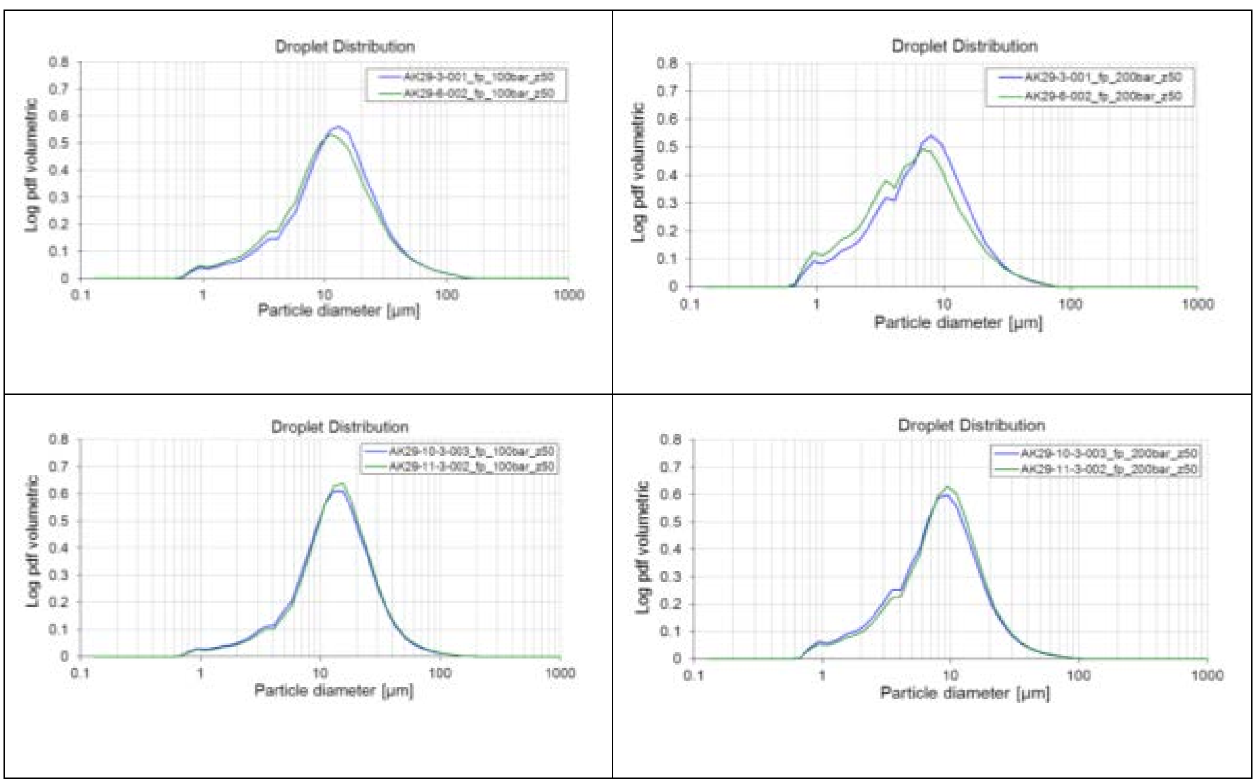


Figure 68 Spray Droplet size distributions single nozzle, d≈.20 & d≈.15, at 10 and 20MPa, and 3-hole nozzle, l/d=1.1 & l/d=3.96, at 10 and 20MPa

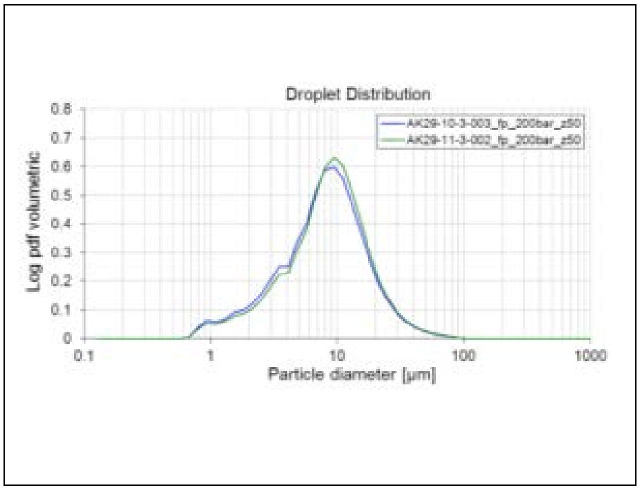


Figure 69 Spray Droplet size effect of Counterbore

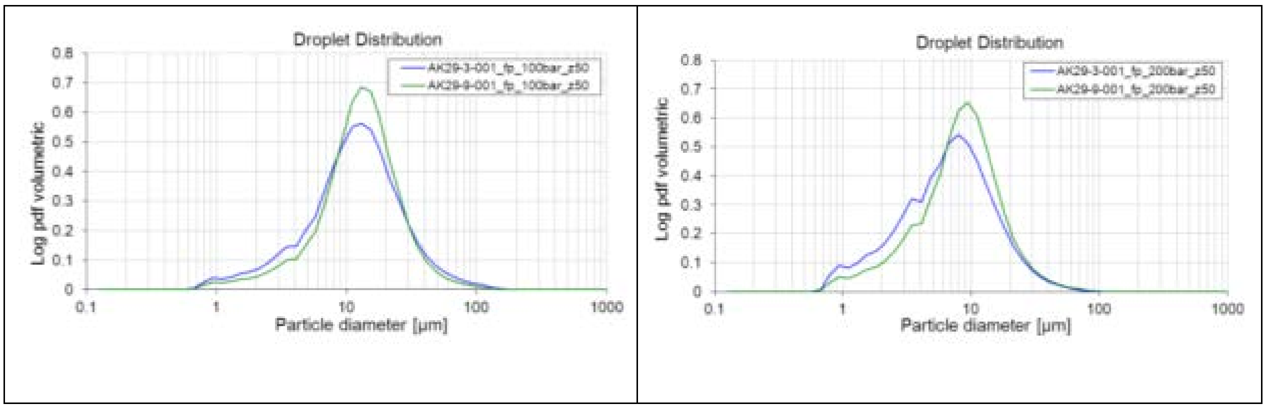


Figure 70 Spray Droplet size effect of Skew angle at 10, 20MPa

### 5.2.4 Summary/Conclusion on Physical Test and Modified Project Scope Direction

Review of the spray imaging revealed that axis-symmetric single-hole seats produced spray plumes with a slightly narrower plume angle and a much longer penetration than single-hole nozzles with a 30º skew angle or the 3-hole seats as shown in Figure 71. The spray morphology of seats with approximately a 30º skew angle more resemble production 5 or 6 hole injectors. Testing of 3-hole seats with 30º, 20º, and 10º skew angles, shown on Figure 72, revealed the same tendency. The 20º geometric skew angle injectors demonstrated a spray plume skew angle of approximately 17º and the 10º geometric skew angle nozzles collapsed into a single spray plume. Based on these findings, the prototype seats underway for calendar year 2012 testing were adjusted to add more focus on 3-hole seat configurations with 30° skew angles, which are expected to provide representative and thus more meaningful results for future GDi injector nozzle design. The injector test plan, injector solid models with FEA meshes, and LES simulations were

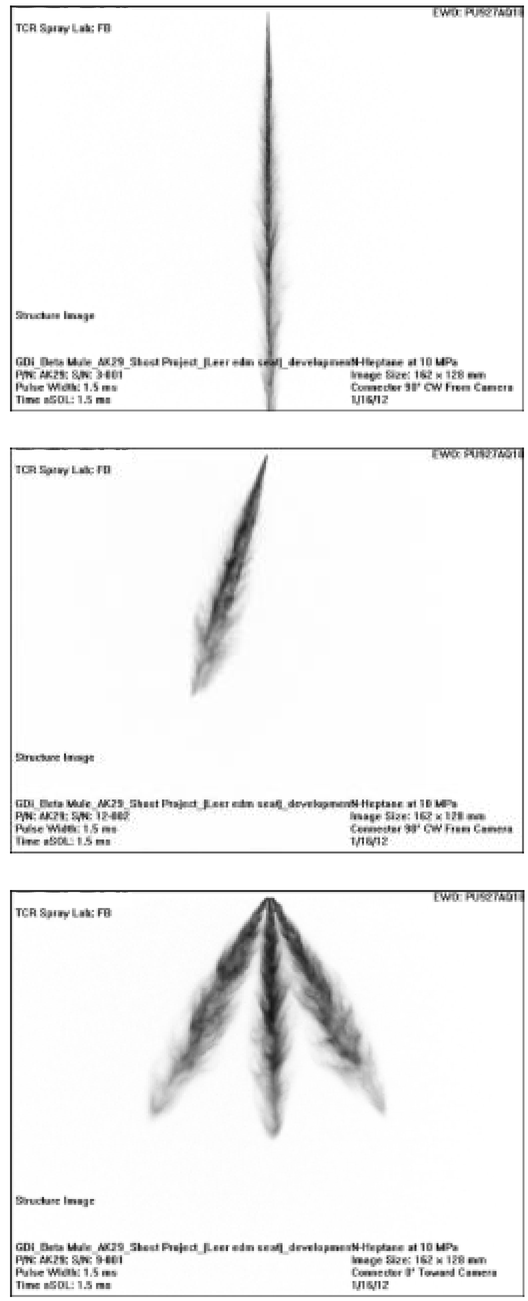


Figure 71 Shadowgraphic Spray Images for axis-symmetric, skewed angled and 3-hole seats

re-focused accordingly. The impact of this change would add approximately 1 year to the study, as previous modeling and testing would be redone. The intended second SAE paper expected to conclude this work, which was to focused on axis-symmetric single-hole nozzle test results, would be replaced by two future SAE papers each including LES simulation and experimental results focused on the injector design parameters established in Chapter 4 .

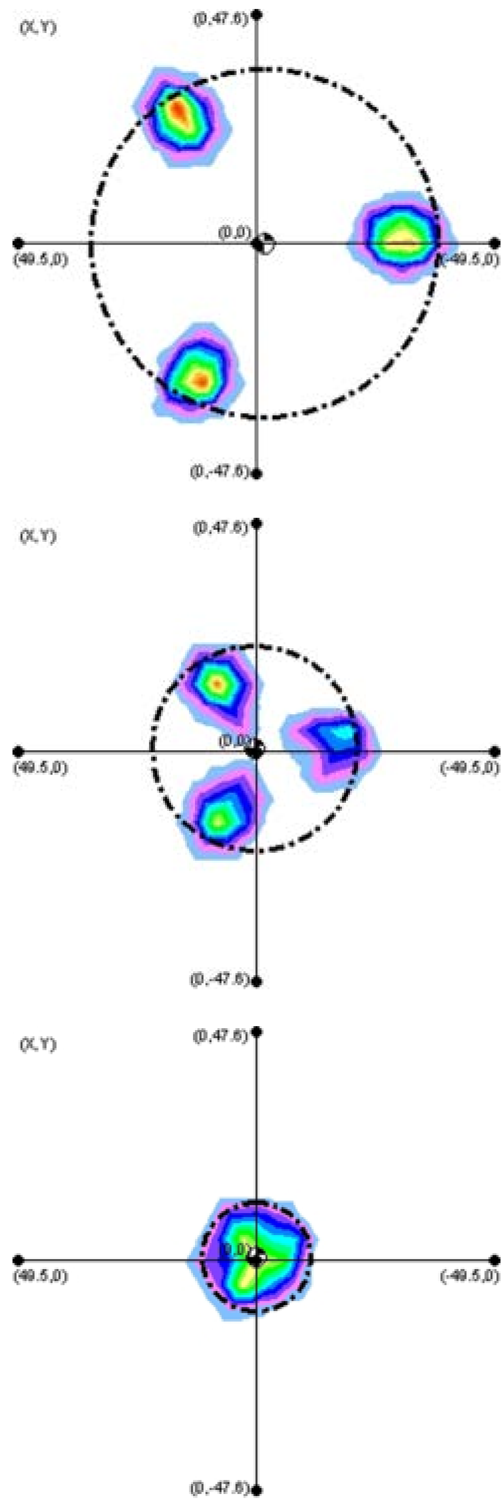


Figure 72 Patternization tests for 10º, 20º, and 30º sk

### *5.3 GDi Skew-Angled Nozzle Flow and Near-Field Spray Analysis using Optical and X-ray Imaging and VOF-LES Computational Fluid Dynamics*

The results of this section were published [60] and presented at the SAE World Congress held in Detroit in April of 2013. The objective of this study is optical imaging investigation of the nozzle near-field jet breakup structure and the influence of nozzle geometry on the spray primary atomization. Of specific interest, especially for comparison with the VOF-LES model, is the nozzle near-field spray primary breakup structure and relevant geometric parameters. The data is obtained with the aid of conventional shadowgraph optical imaging techniques at the Delphi Technology Centre Luxembourg and phase-contrast X-ray imaging using high-intensity and high-brilliance X-ray beams available at the Advanced Photon Source (APS) at Argonne National Lab.

#### 5.3.1 Nozzle Geometry

Figure 73 presents views of the purpose-built 3-hole GDi seat geometry. For this investigation, the same injector seat contained nozzle A and B geometry. This was accomplished by using a purpose-built seat containing 3 holes having identical thru-hole and counterbore dimensions arranged at 120° circumferential spacing. A secondary process was used on the seat of nozzle B geometry to precisely grind the seat of one hole to remove seat material to the depth of the counterbore, thus producing nozzle geometry as shown in the 4.2 Test Hardware. Figure 74 provides a view of the nozzle-hole

| | |
|---|---|
|  |  |
| Side view of fluid cavity for LES model | Bottom view of seat with CB machined |

Figure 73 Geometry of the GDi 3-hole seat and nozzles

geometry for nozzle A and B and their associated dimensional parameters. The thru-hole diameter (d) is of the order 0.2mm, and the skew-angle from the injector axis (β), thru-hole length (l), counterbore diameter (D), and counterbore length (L) is representative of modern multi-hole GDi seats. The skew-angle β=30° was particularly selected to precipitate nozzle flow separation and, thereby, enable predictive accuracy of the VOF-LES method for prediction of the deviation between the plume trajectory and the nozzle axis direction for typical production GDi nozzles.

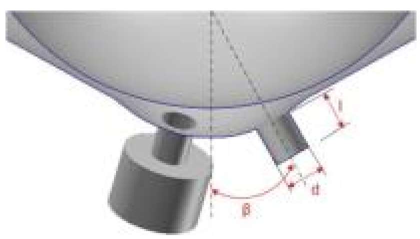

| β | l/d |
|---|---|
| 30° | 1.1 |

Nozzle Geometry A - Thru-hole (without Counterbore)

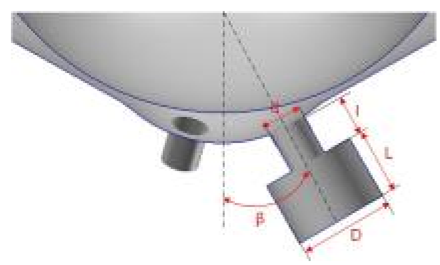

| β | l/d | (l+L)/d | D/d |
|---|---|---|---|
| 30° | 1.1 | 2.95 | 2.5 |

Nozzle Geometry B - Thru-hole and Counterbore

Figure 74 Nozzle Geometry A and B with associated dimensional parameters

### 5.3.2 Nozzle Geometry A, without Counterbore

Figure 75 presents the temporal development of the spray plume near-field with snapshot images at selected instances after the start of injector energizing (ASIE) for the fuel system pressure of 10MPa. The images provide evidence of an “atomization regime” turbulent jet breakup. The jet primary breakup happens within close vicinity of the nozzle, almost immediately after the injector opening and plume emergence. Remarkably, the development of the jet Kelvin-Helmholtz interface instabilities and primary breakup is detectable within 2mm vicinity of the nozzle exit. The most notable feature of the spray plume morphology is the intermittent jet breakup structure, which is evident in the wave pattern of spatial liquid mass distribution longitudinal with the plume propagation.

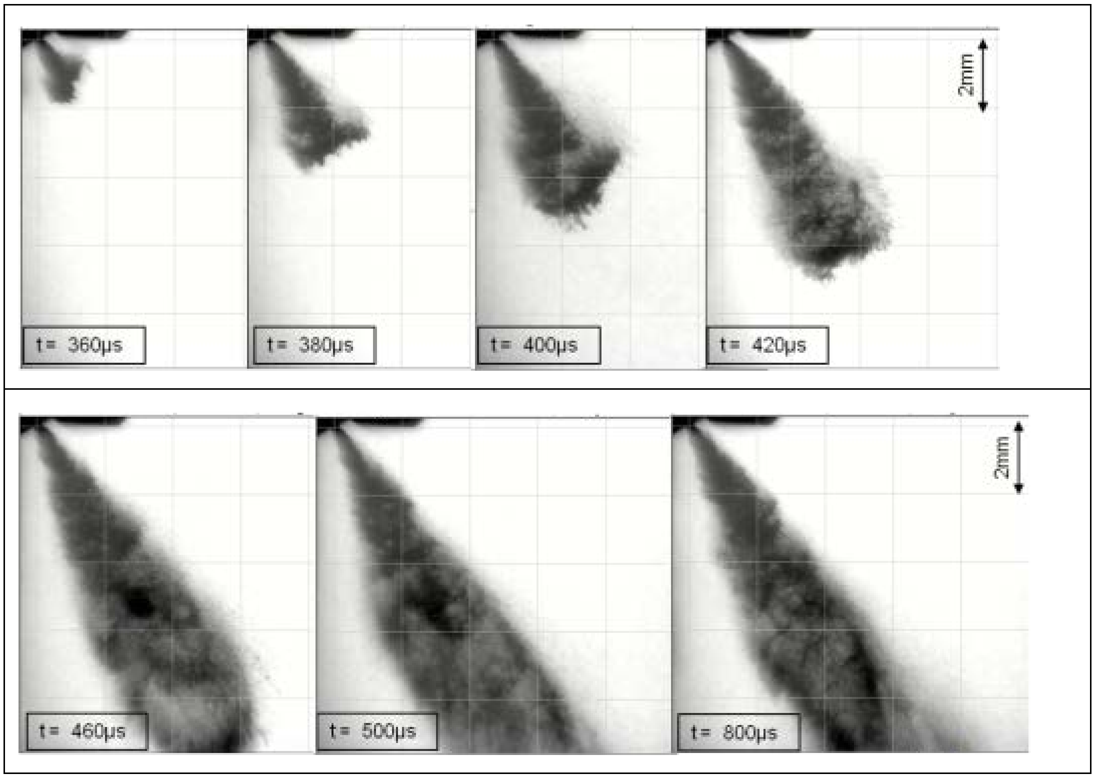

Figure 75 Shadowgraph imaging of the nozzle near-field spray plume (fuel pressure=10MPa, t=time ASIE)

The plume intermittent morphology is clearly discernible in Figure 76. This shows the concurrent development of the interface instabilities close to the nozzle exit, intermittent spatial mass distribution and associated wave-like jet breakup into concentrated ligament structures that subsequently atomize through interaction with the air. This plume morphology is caused by the injection rate pulsations that are induced by the high-frequency hydraulic pressure oscillations in the injector valve group. This structure is also attributed to unsteady vortex shedding and cavitation in the GDi multi-hole nozzles, although it shows correlation with the nozzle pressure

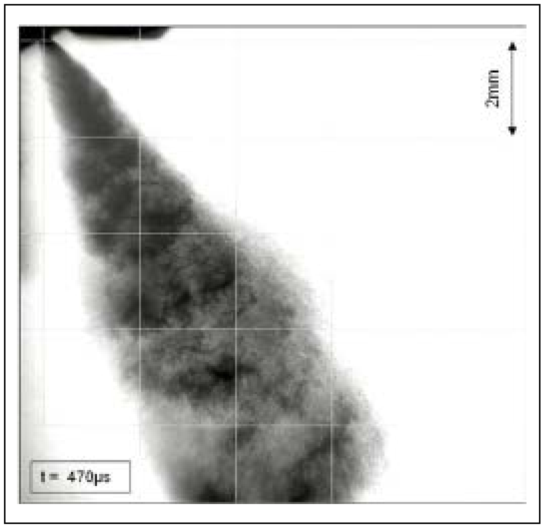


Figure 76 Nozzle near-field plume structure, primary breakup and atomization (fuel pressure=10MPa, t=470μs ASIE)

and the injection rate oscillations [61]. It is also detectable in the measurements of diesel sprays [62]. This morphology is notable, since it highlights the coupling of the injector design hydraulic features with the spray breakup structure and atomization. The concurrent plume breakup and the atomization of ligaments are through interactions with the ambient air accompanied by the spray lateral dispersion. It is expected that the plume intermittent structure influences all aspects the spray-air interactions, such as air entrainment rate, penetration, etc., that affect its mixture preparation characteristic.

Figure 77 provides an indication of the spray plume shot-to-shot variation, for five repetitions at t=700μs ASIE, and the associated statistical average (normalized liquid-phase probability density function) for the plume geometry. Since the SAE standard method for quantifying the plume geometry [42] is not applicable to the nozzle near-field, the plume angle is characterized per section 4.1 Defined Terms based on the plume width between 1mm and 8mm downstream of the nozzle along the injector axis. Figure 77 (a) shows that the intermittent formation and atomization of the massive ligaments, due to interactions with the ambient air, cause stochastic variations of the plume spatial structure, lateral dispersion, and trajectory. Figure 77 (b) shows the alignment of jet center-line with the nozzle axis and statistical variation of the plume angle in the range φ = 19° - 26° due to shot-to-shot plume breakup variability.

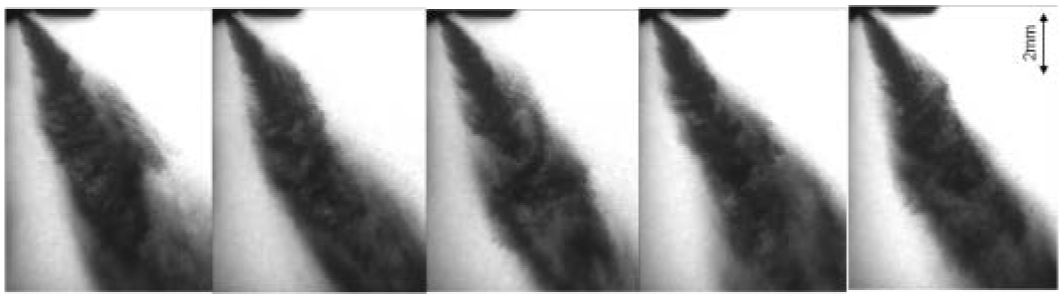


(a) Spray plume shot-to-shot variation over 5 spray events

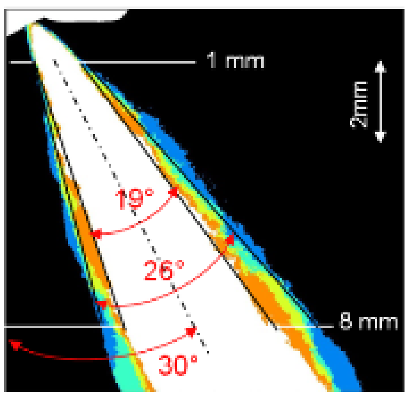


(b) Spray plume statistical average (liquid probability density function)

Figure 77 Spray plume shot-to-shot variation and statistical PDF (liquid–phase probability density function) (fuel pressure =10MPa, t =700μs ASIE)

The optical image shadowgraph provides good insight into the spray plume structure. However, the use of conventional optical techniques to provide information about the internal structure of high-speed jets in immediate vicinity of the nozzle exit has proven problematic due to the multiple scattering by droplets and interfaces, and the high density of the near-field jet. This problem becomes exacerbated as fuel pressures rise, as noted in the optical images at 20MPa, and spray masses yield a larger level of spatial liquid concentration and higher jet velocity, therefore the jet breakup structure is not as sharp and discernible. For this reason, researchers have often concentrated more on the leading edges of the spray field. In previous research, in order to provide more insight into the near field structures, ultrafast synchrotron X-ray full-field phase-contrast imaging has been used [63]. This technique reveals instantaneous velocity and internal structure of optically dense sprays with a combined spatial and time resolution. It is employed in this work to gain insight to the turbulent jet characteristics at the near-field of nozzle exit. The test fluid used in the X-ray visualization is Viscor-16B2, whose physical properties compared with n-heptane used in the shadowgraph tests are listed in Table 6. The spray field is captured in a series of 1.32mm tall by 1.74mm wide image blocks. In order to provide a view of the spray plume formation a series of five optical image panels, taken at the same time ASIE, are used to form a mosaic covering the spatial range of interest, as shown in Figure 78. In prior work done by the author for diesel sprays with injection pressures of 30-100MPa [63], good spatial coherence of the composite images resulted from excellent shot-to-shot repeatability of the structures. However, when this technique was extended to GDi multi-hole injectors operated at 5-10MPa, the spray was found to be highly temporally and spatially stochastic [34]. In order to construct a view of the developing spray, multiple pictures were taken for each panel, and then a collection of panels was selected to form the best spatially coherent composite picture, or mosaic, representative of a typical temporal event.

Figure 78 presents the phase-contrast X-ray imaging for nozzle geometry A at 10MPa. As shown in the figure, spray has enveloped the 4mm visual field by 430μs ASIE. Inspection of the image at 430μs reveals a stochastic pattern of waves that is consistent from nozzle exit through the spatial field, 0-4mm distance. The plume structure suggests breakup at the nozzle exit with established disturbances that originated inside the nozzle and turbulent dispersion perpendicular to the spray axis. The chaotic jet breakup structure and shot-to-shot variation of the plume angle is visible. There is substantial difference between the GDi plume morphology, shown in Figure 78, and the X-ray phase-contrast images of the diesel nozzle near-field plume breakup structure [64] [65]. The data signify the influence of the seat-nozzle geometry on the plume breakup mechanism and spray morphology.

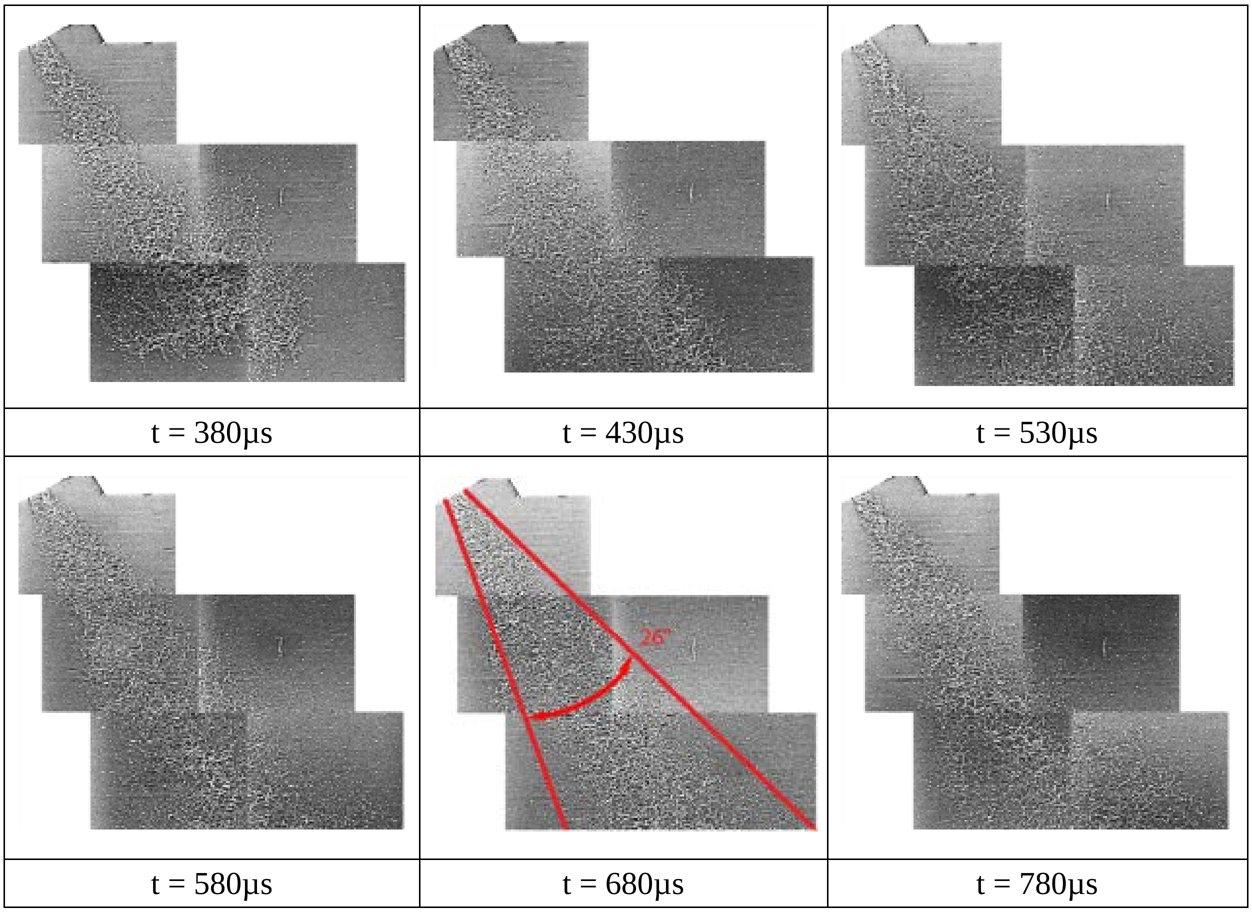


Figure 78 Nozzle A X-ray phase-contrast imaging (fuel pressure=10MPa, t=time ASIE)

A notable feature of the spray plume imaging data, in Figure 75 to Figure 78, is the alignment of the plume trajectory with the geometric nozzle axis direction. This differs from previous studies of the GDi nozzle internal flow and spray for different seat-nozzle geometry [33] that highlighted the liquid-phase flow separation in a skew-angle nozzle as a primary cause of the commonly observed deviation of the plume trajectory from the nozzle axis direction. The alignment in the present study suggests absence of a major liquid-phase flow separation within the nozzle, as indicated by the VOF-LES simulation. This dissimilarity is attributable to the differences in the seat-nozzle geometries of the two studies; notably the hole-to-hole circumferential separation, 120° in present study vs. 60° in Ref. [33], and the nozzle skew angle, β=30° simple vs. compound angle in Ref [33]. The geometric differences alter the nozzle-entrance velocity condition, which alters the structure of the nozzle flow and the jet velocity distribution and turbulence condition.

### 5.3.3 Nozzle Geometry B, with Counterbore

The imaging data for the nozzle geometry B provides a comparison of the influence of counterbore on the spray breakup structure. Figure 79 presents the temporal development of the

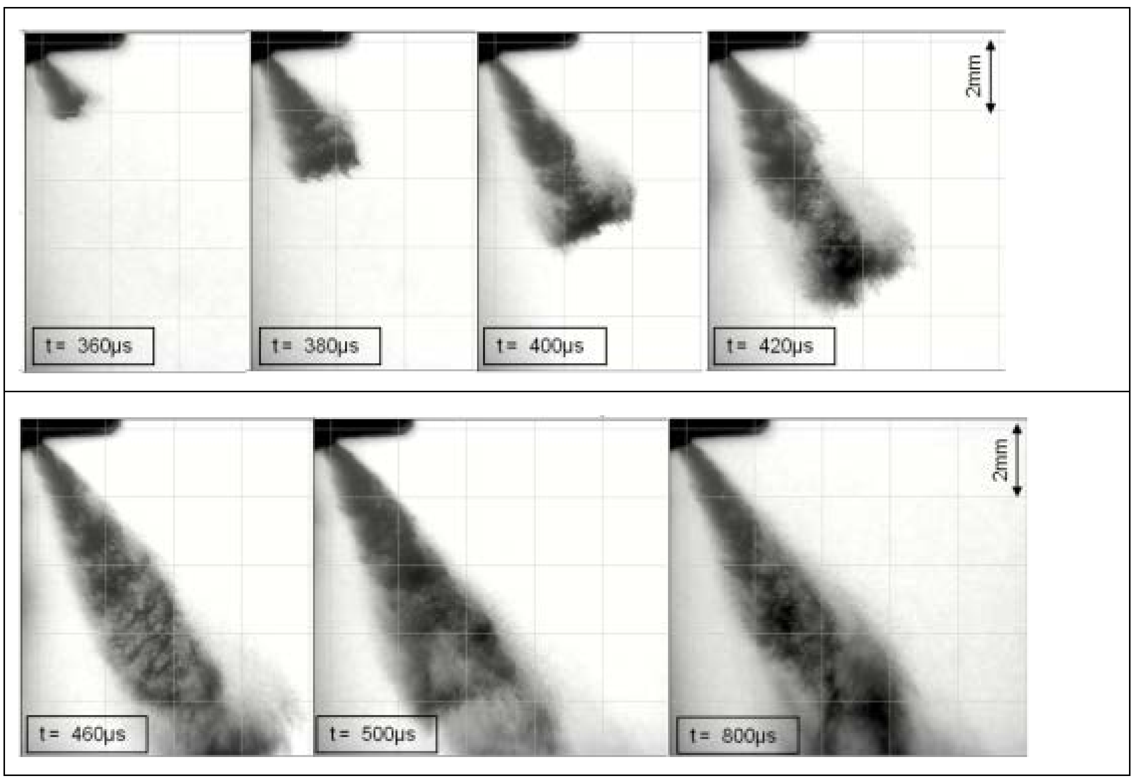


Figure 79 Shadowgraph imaging of the nozzle near-field spray plume (fuel pressure=10MPa, t=time ASIE)

spray plume near-field for the fuel system pressure of 10MPa. The images show evidence of the spray plume breakup and atomization, taking place immediately after the jet emergence, within close vicinity of the nozzle. As in the case of Nozzle A, the most notable feature of the temporal-spatial plume development is the intermittent jet breakup morphology induced by the hydraulic pressure oscillations in the injector valve group.

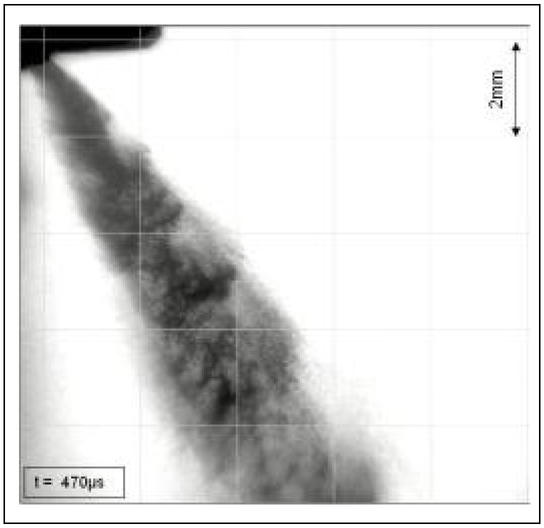


Figure 80 Nozzle near-field plume structure, primary breakup, and atomization (fuel pressure=10MPa, t=470μs ASIE)

Figure 80 displays the nozzle-near-field plume primary breakup and atomization structure. The jet morphology appears similar to that of nozzle A, shown in Figure 75, which illustrates the development of interface instabilities, intermittent liquid jet breakup, formation of large ligaments, which deform and spread the plume in the lateral direction and atomize through interaction with the ambient air.

Figure 81 provides an illustration of the extent of spray plume shot-to-shot variation. It presents five repetitions of the plume image at t =700μs ASIE and the associated statistical average (liquid-phase probability density function) for the fuel pressure of 10MPa. The plume trajectory is aligned with the nozzle axis, but there is notable reduction in plume angle compared to nozzle A. One likely explanation, provided by the VOF-LES simulation, is the physical plume interaction with the counterbore wall, which imposes restriction on the plume angle. This explanation is supported by the plume images in Figure 79 to Figure 82 that show spray plume at the nozzle exit emerges with the width of the counterbore, although this does not prove a preceding physical interaction.

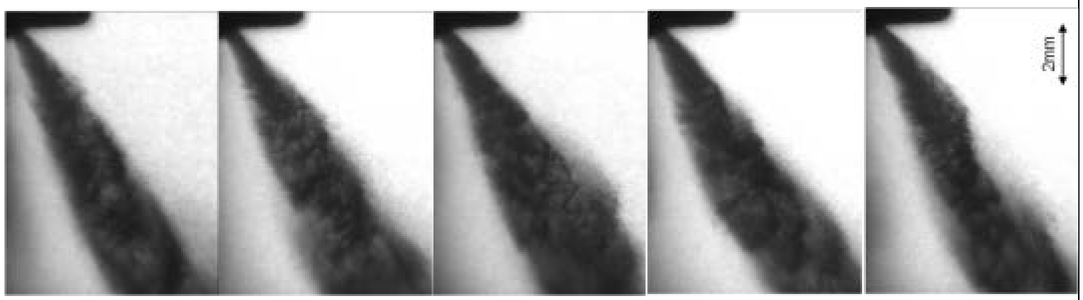


(a) Spray plume shot-to-shot variation

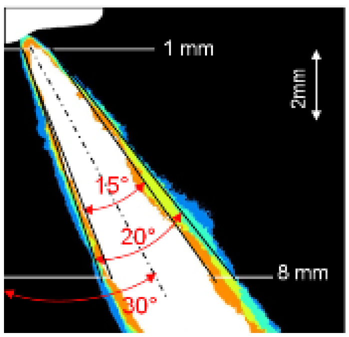


(b) Spray plume statistical average (liquid probability density function)

Figure 81 Spray plume shot-to-shot variation and statistical PDF (liquid –phase probability density function) fuel pressure=10MPa, t =700μs ASIE

Figure 82 presents the phase-contrast X-ray imaging for nozzle geometry B at 10MPa. Similar jet breakup morphology to that of nozzle A is evident throughout the temporal progression to 780μs ASIE. The notable characteristics are the jet breakup in the immediate vicinity of the nozzle with a stochastic pattern indicating transverse structures normal to the plume axis. Some discrete particles appear surrounding the structures in all of the time exposures. It is unclear whether these droplets result from breakup due to interaction of near-field spray ligaments and surrounding ambient air, or result from spray plume interaction with the counterbore wall. The quantity of droplets does appear qualitatively greater than evidenced in nozzle A.

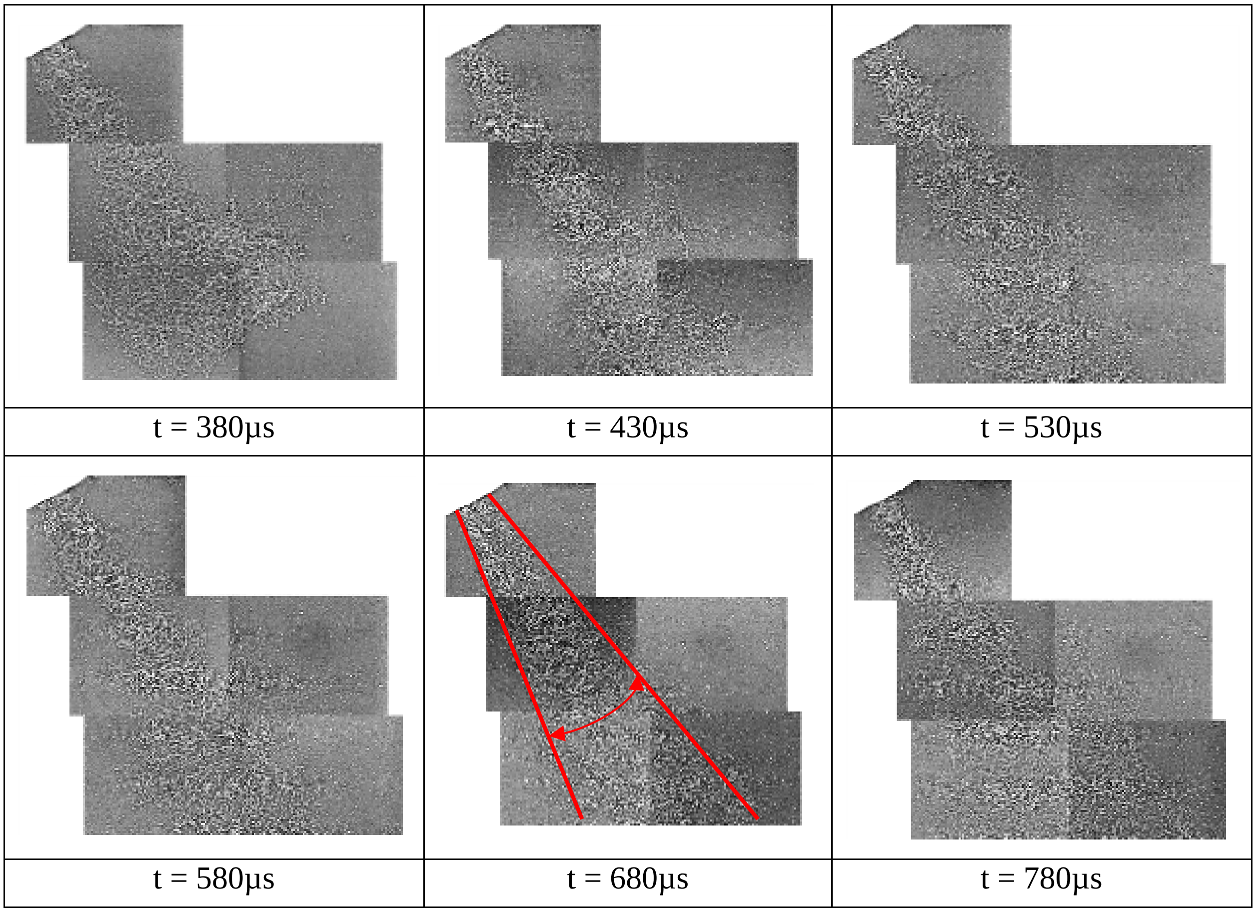


Figure 82 Nozzle B X-ray imaging of the nozzle near-field spray plume (fuel pressure=10MPa, t=time ASIE)

<u>Nozzle geometry A – w/o Counterbore</u>

The transient development of the flow within the injector seat and the nozzle near-field jet primary breakup structure is illustrated by the plots of evolution of the VOF=0.5 iso-surface, colored by the instantaneous velocity, at selected times after the start of simulation (ASOS), in Figure 83. The VOF=0.5 iso-surface is commonly used as the median value (Air =0 ≤ VOF ≤ 1 = Liquid) to present the liquid-air interface geometry. Figure 84 presents the corresponding VOF contour plots on the nozzle symmetry plane, and aids to elucidate the jet primary atomization structure.

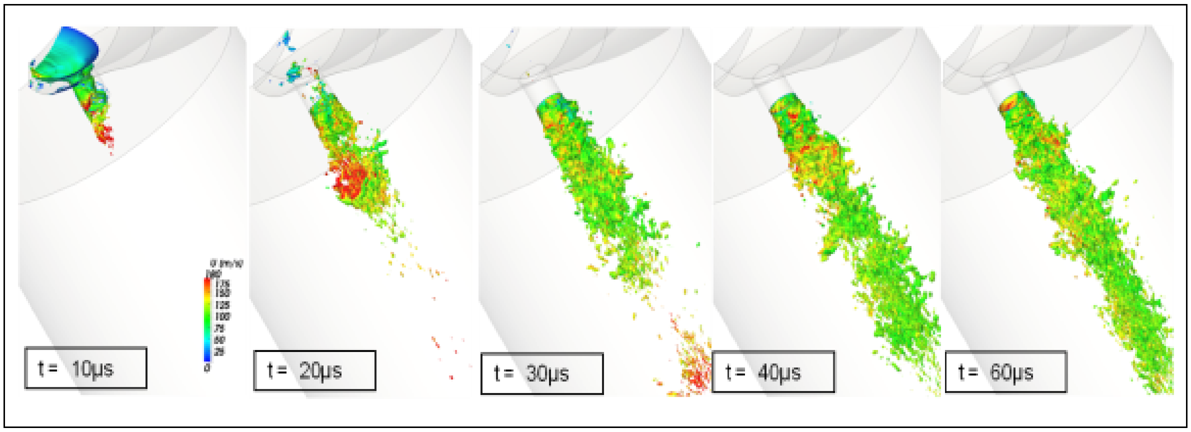


Figure 83 Iso-surface plots of VOF= 0.5, colored by the instantaneous local velocity magnitude, at selected times ASOS

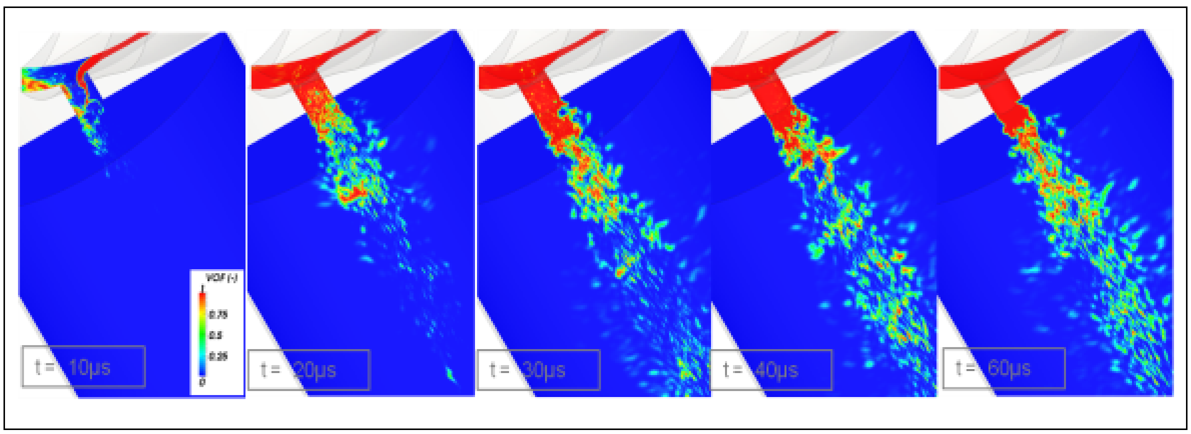


Figure 84 VOF Contour plots on the nozzle symmetry plane, at selected times ASOS

The initial stage of the transient nozzle flow is affected by the scavenging of the entrapped air within in the sac volume. This phase is characterized by transition of a separated liquid jet within the nozzle, concurrent with a ‘slug’ type two-phase flow, to a fully attached nozzle flow that produces a full-cone liquid jet. This is accompanied by the transient expelling of the air entrapped in the sac volume in the form of transition of the nozzle flow from the initial slug type two-phase flow to a dispersed bubble type flow. After complete discharge of the sac air, the nozzle flow and the liquid jet attain a stationary structure at t=40µs. Nevertheless, Figure 83 and Figure 84 illustrate the unsteady character of the jet primary breakup, caused by the nozzle turbulent velocity disturbances in addition to the boundary pressure oscillations induced by the imposed acceleration of the inlet velocity boundary condition.

The unsteady character of the jet primary breakup is further illustrated in Figure 85 by the VOF contour plots on the planes normal to the jet axis, within the nozzle, and at locations z= 0 (corresponding to the counterbore exit plane in Nozzle B), and z=5*d downstream of the injector.

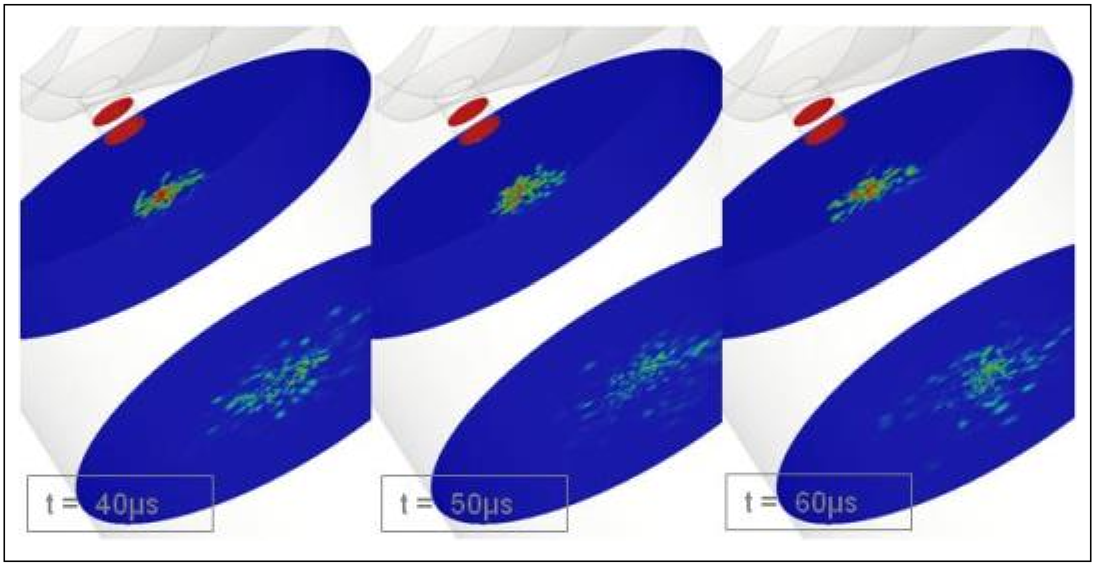


Figure 85 VOF Contour plots on planes normal to nozzle axis, in nozzle hole and at locations z=0 and 5*d (t = ASOS)

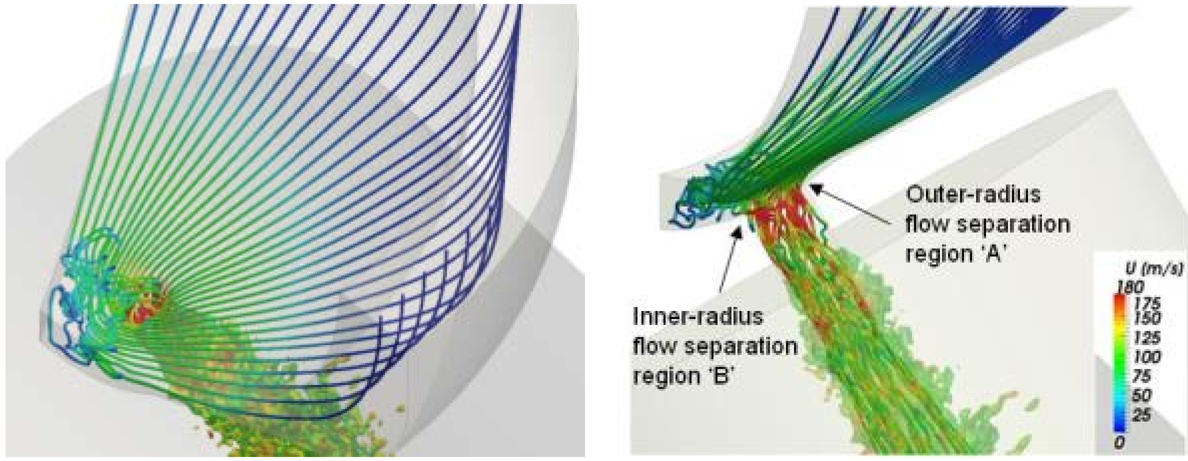


Figure 86 Flow stream-lines colored by local instantaneous velocity (t= 60 μs ASOS)

A notable feature of the VOF-LES predictions is the absence of flow separation at the nozzle entrance. Flow separation at nozzle entrance was predicted in a previous VOF-LES analysis of the GDi multi-hole skew-angled nozzle geometry [33] and identified as a cause of deviation of the liquid jet trajectory from the nozzle-hole axis. As noted earlier, the primary difference between the present VOF-LES analysis and that of reference [33] is associated with the seat-nozzle topology. Figure 86 presents flow stream-line plots that illustrate the effect of the three-hole 120° segment seat geometry on the circumferential distribution of the nozzle entrance flow, which inhibits flow separation at the outer and inner radius locations of the nozzle entrance.

The quantity Q is the 2$^{nd}$ invariant of the velocity gradient tensor, commonly adopted for vortex visualization in DNS and LES studies of wall-bounded flows [52]. Figure 87 presents the iso-surface plots of Q=5.E12, 1.E13, and 5.E13 colored with the magnitude of the instantaneous local velocity. It shows the cascade structure and intensity of the vortical flows within the nozzle, the near-field liquid jet, and the surrounding ambient air. The highest level of vorticity is found in vortex cores with dimension of the order 0.1*d (i.e. the order of length-scale of the energy-containing turbulent eddies). These high intensity vortical eddies induce a cascade of vortical flow structures, which extend upstream of the nozzle into the seat volume to cause formation of the ‘string cavitation’ [66] [67] and propagate downstream to engender the jet breakup through combined internal shear and temporal/spatial inertial and pressure perturbations.

| | | |
|---|---|---|
| 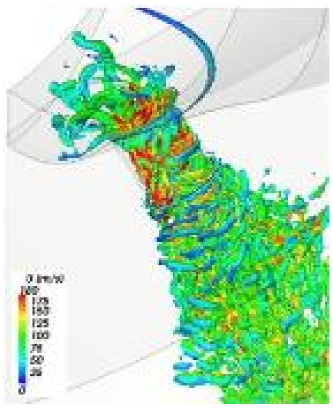 | 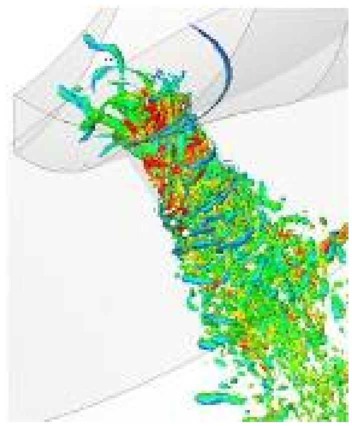 | 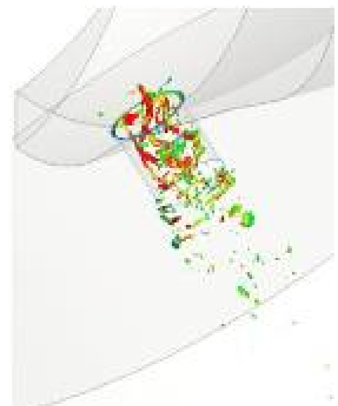 |
| ***Q=5 E12*** | ***Q=1 E13*** | ***Q=5 E13*** |

Figure 87 Iso-surface plots of Q=5E12, 1E13, and 5E13 (colored by the instantaneous local velocity magnitude) at t=60μs ASOS

<u>Nozzle geometry B – w/ Counterbore</u>

Figure 88 and Figure 89 illustrate the transient development of the flow within the injector seat, nozzle, and the near-field jet primary breakup structure, with the aid of plots of evolution of the VOF=0.5 iso-surface, colored by the instantaneous velocity, and corresponding VOF contour plots displayed on the nozzle symmetry plane at selected times after the start of simulation.

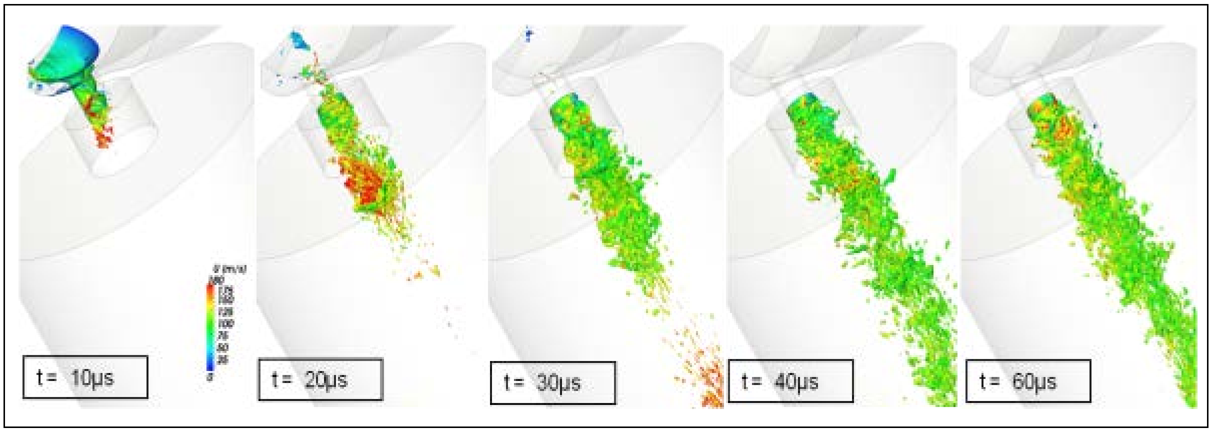

Figure 88 Iso-surface plots of VOF= 0.5, colored by instantaneous local velocity, at selected times ASOS

The transient development of seat-nozzle flow and morphology of the jet primary breakup is identical to the case of nozzle A. The exceptional feature of nozzle B plume is the indication of physical interaction of the jet primary breakup process with the counterbore wall which constraints the plume lateral dispersion as well as causing liquid splash from the surface.

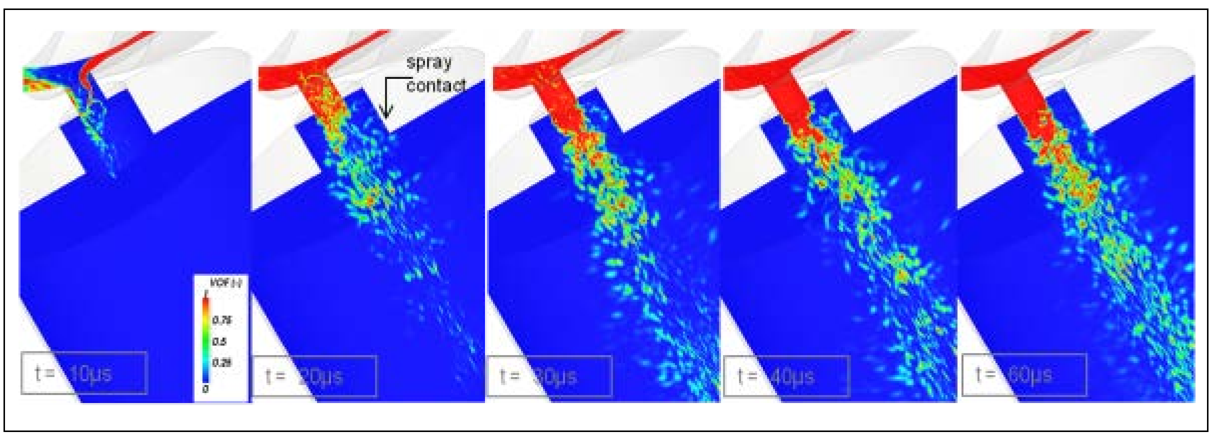

Figure 89 VOF Contour plots on the nozzle symmetry plane, at selected times ASOS

Figure 90 illustrates the unsteady character of the jet primary breakup and the spray contact with the counterbore wall with the aid of VOF contour plots on multiple display planes, normal to the jet axis, within the nozzle, the counterbore, and the location z=5*d downstream of the injector (z = 0 corresponds to the counterbore exit plane).

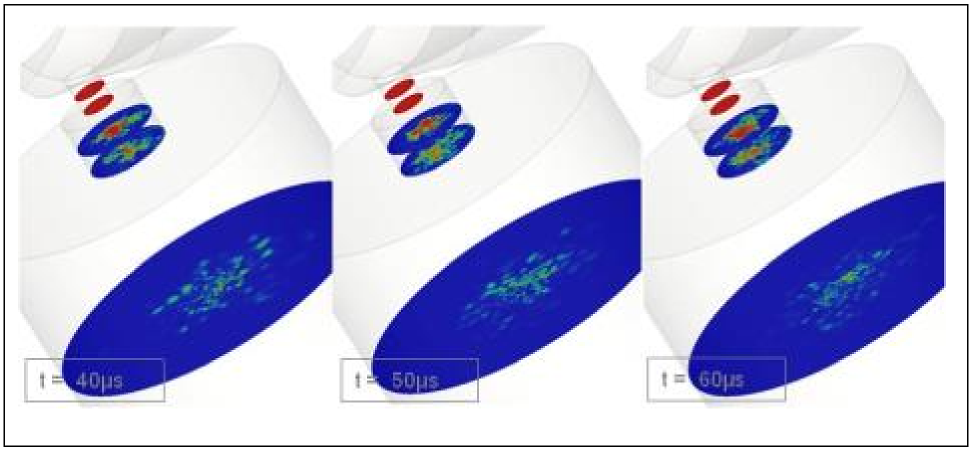


Figure 90 VOF Contour plots on planes normal to nozzle axis, within the nozzle-hole, counterbore, and location z = 5*d downstream of injector (t=ASOS)

Figure 91 presents the contour plots of Q=5.E12, 1.E13, and 5.E12 in order to illustrate the structure and intensity of vortical flows within the nozzle and the nozzle near-field liquid jet. The most notable aspect of the results is the evident suppression of the diffusion of vorticity into the surrounding air within the counterbore space compared with the nozzle A. This is in contrast

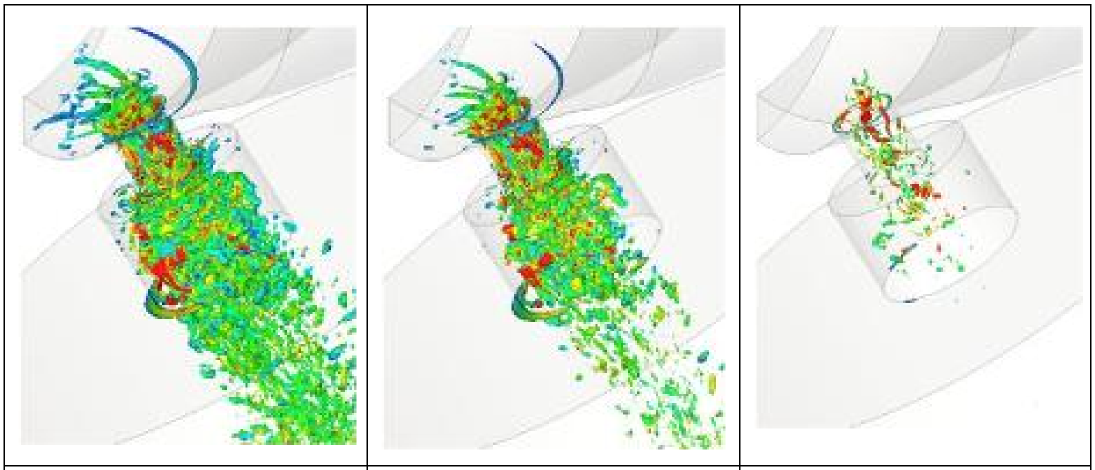

| ***Q=5.E12*** | ***Q=1.E13*** | ***Q=5.E13*** |
|---|---|---|

Figure 91 Iso-surface plots of Q=5E12, 1E13, and 5E13 (colored by the instantaneous local velocity magnitude) at t=60μs ASOS

with the enhancement of vorticity of the air in the counterbore observed in the VOF-LES simulations of the GDi axisymmetric nozzles [56], and underscores the significance of the nozzle geometric parameters on the hydrodynamic and aerodynamic of the jet primary atomization.

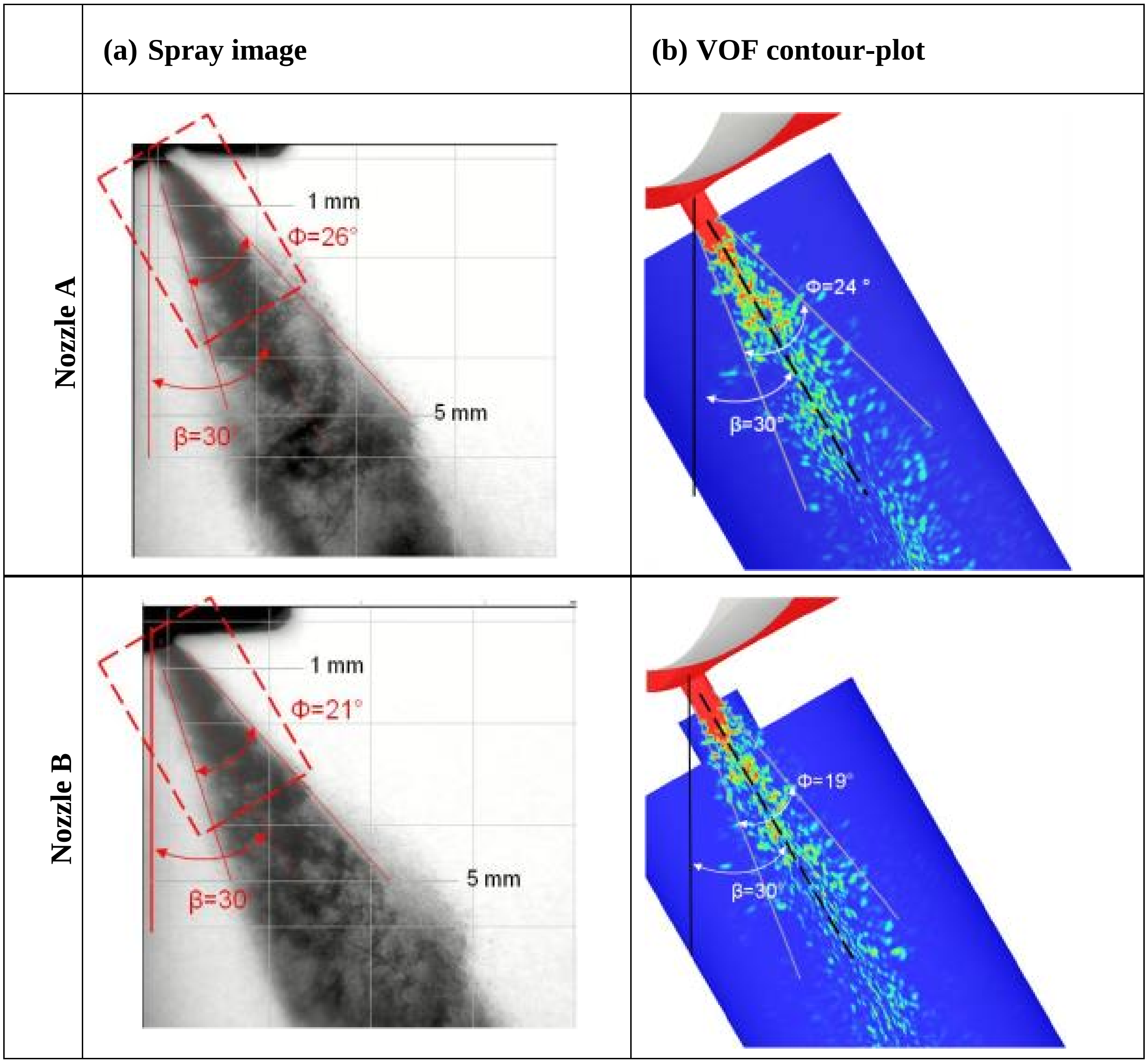


Figure 92 Nozzle A - Comparison of the plume images (at t=700µs ASIE) and VOF-LES simulations (at t=60µs ASOS) of the instantaneous plume near-field breakup structure

<u>Comparison with Imaging Data</u>

The comparison of the instantaneous VOF-LES simulation of the stationary jet primary breakup structure, at t=60µs ASOS, for the nozzles A and B with the respective single-shot images of the plume near-field, at t=700μs ASIE, is presented in Figure 92. The computational domain for the VOF-LES simulation is indicated by the dashed-line rectangles in Figure 92(a).

Figure 92 provides a side by side view of the effect of counterbore on the plume structure as quantified by the plume angle and quantitative comparison with the VOF-LES simulations. There is evidence of the good predictive accuracy of the VOF-LES method with respect to (a) the initiation of the jet primary breakup in the immediate vicinity of the nozzle exit, (b) the plume trajectory angle (β=30°), aligned with the nozzle axis, and (c) the near-field plume angle. The imaging data exhibits excellent correspondence of the single-shot plume macro scale geometry, center-line axis, and plume angle with that of the statistical plume analysis in Figure 77 and Figure 81. The agreement between the plume imaging data and the VOF-LES prediction of the plume angle is good (Nozzle A: experimental φ=26° vs. VOF-LES prediction of φ=24°. Nozzle B: experimental φ=21° vs. VOF-LES prediction of φ=19°). It can be concluded that the predictive accuracy of the VOF-LES method is satisfactorily validated for analysis of the influence of nozzle design on the plume geometric features.

It is worth noting that the present VOF-LES method does not provide a cavitation simulation capability. Therefore, cavitation is excluded in the simulations. The good predictive accuracy of the VOF-LES jet primary breakup structure and plume macro scale parameters does not warrant concluding absence of flow cavitation in the nozzle flow experiments.

### 5.3.4 Summary/Conclusions on Counterbore effect

The conclusions of this experimental and computational study of the GDi multi-hole nozzle geometry can be summarized as:

- The near-field plume imaging provides evidence of the jet primary breakup in the immediate vicinity of the nozzle exit, almost immediately after start of injection. The GDi plume breakup morphology is indicative of the “atomization” regime.

- There is evidence of the influence of intermittent injector valve-group hydraulic pressure oscillations on the jet breakup structure. This is expected to influence the air entrainment, and associated combustion-relevant characteristics of the spray plume.

- There is evidence of the physical interaction and influence of counterbore on the jet primary breakup process, with consequent effects on the plume trajectory, plume angle, and atomization.

- The VOF-LES simulations of the plume near-field breakup structure are in good agreement with the imaging data. Specifically, the important plume near-field macro scale characteristics: plume trajectory, plume angle, and the trend of influence of nozzle geometry on the plume breakup structure are in satisfactory agreement with data.

- The VOF-LES simulations indicate the atomization effectiveness of the GDi nozzle is associated with the vorticity and turbulence imparted on the flow at nozzle entrance.

The VOF-LES results and corresponding plume imaging data, in conjunction with previous GDi multi-hole seat-nozzle flow and spray investigations, underscore the major importance of the seat-nozzle topology and geometry on the hydrodynamics of the nozzle flow and structure of the plume primary atomization. Further investigations of the GDi multi-hole nozzle design influence on the plume primary breakup structure and evaluation of the predictive accuracy of the VOF-LES method are in progress. The objective is to establish a key knowledge of the prominent features of the relationship of GDi nozzle design and the spray near-field and far-field characteristics.

### *5.4 GDi Nozzle Parameter Studies Using LES and Spray Imaging Methods*

The results of this section were published [68] and presented at the SAE World Congress held in Detroit in April of 2014. This study provides analyses of GDi skew-angled nozzles with β=30° skew (bend) angle and varying nozzle geometries. This work is an extension of previous work [56] [60] where the effect of counterbore geometry on spray was analyzed. In this current study, the effect of nozzle thru-hole length over diameter ratio (l/d = .55 and 1.10) and fuel pressure (5, 10, and 20MPa) on spray skew angle, spray plume angle, and primary breakup length is studied. The work is a combination of Large Eddy Simulation (LES) providing insight into physical mechanisms behind underlying spray results, validated by spray imaging testing using optical shadowgraph to evaluate spray plume geometry and phase-contrast X-ray imaging to focus on near-field structures within the dense spray plumes. Overall, the LES and spray imaging results are in qualitative and quantitative agreement and the model is successfully validated.

#### Nozzle Geometries

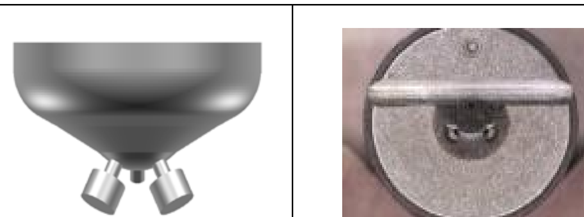

(a) Side view of fluid cavity for LES model | (b) Bottom view of seat as machined for l/d

Figure 93 Geometry of the GDi 3-hole seat and nozzle

Figure 93 presents the solid model and experimental hardware views of the purpose-built 3-hole GDi seat used in this study. Specific geometry was accomplished by using a purpose built seat containing 3 holes arranged at 120° circumferential spacing having identical thru-hole diameters. A secondary process was used on the seat to precisely grind the face of one hole, normal to the thru-hole, to remove seat material and vary the length of the thru-hole producing nozzle A and C geometry with varying length to diameter ratio (l/d), as shown in the Figure 93(b). Figure 94 provides a view of the nozzle-hole geometry for nozzle A and C, and their associated dimensional parameters. The thru-hole diameter (d) is of the order 0.2mm, and the skew-angle (β) is 30° from the injector axis.

<table>
<tr><td>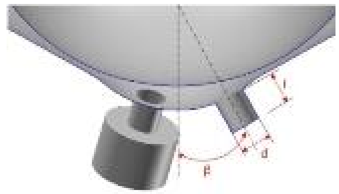</td><td>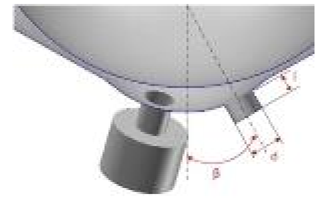</td></tr>
<tr><td><table><tr><td>β</td><td>l/d</td></tr><tr><td>30°</td><td>1.1</td></tr></table></td><td><table><tr><td>β</td><td>l/d</td></tr><tr><td>30°</td><td>0.55</td></tr></table></td></tr>
<tr><td>A Nozzle Geometry<br>l/d = 1.10</td><td>C Nozzle Geometry<br>l/d = 0.55</td></tr>
</table>

Figure 94 Nozzle Geometry A and C with associated dimensional parameters

A skew angle and varying l/d ratios representative of production injectors were selected to understand nozzle flow separation, and, thereby, enable evaluation of the accuracy of the VOF-LES method for prediction of the deviation between the plume trajectory and the nozzle thru-hole geometric axis direction.

## 5.4.1 Nozzle Geometry A, l/d = 1.1

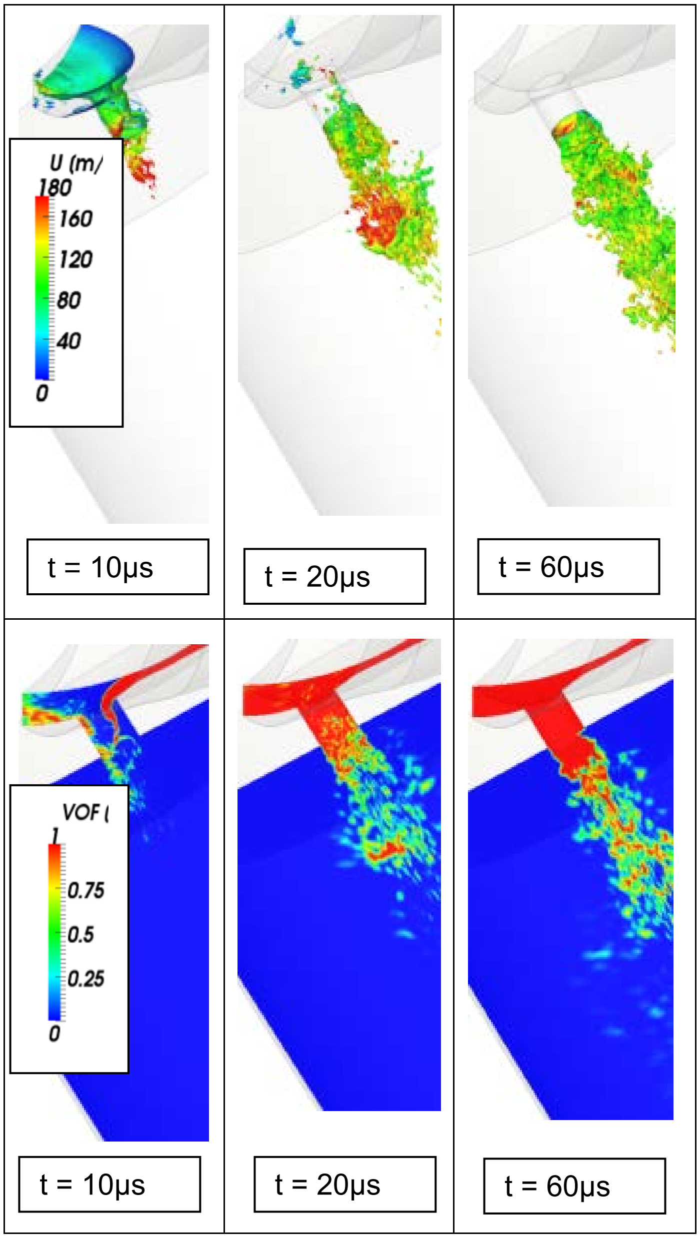


Figure 95 Spray velocity and VOF for Nozzle A at 10MPa at 10, 20, and 60µs

### 5.4.1.1 Simulation Results

Figure 95 shows the simulation results for Nozzle A, l/d = 1.1, as flow progresses after start of injector energizing. As can be seen in the VOF plot, the injector sac volume is initially filled with air and the liquid starts to enter the thru-hole at 10µs. Liquid completely fills the sac volume by 20µs, and fills the thru-hole by 60µs. It can be noted that there is no separation at the thru-hole entrance, and the spray plume jet follows the thru-hole geometry on exit. The velocity plot for VOF=.5 shows breakup of particles immediately at the nozzle exit and particle velocities in the range of 120m/s.

Fluid particle motion was tracked to provide a visualization of the flow path, specifically at the thru-hole inlet, and is presented in Figure 96. As can be seen in the plot, the flow lines start with well-defined axial travel at a velocity of 20m/s. The side view shows that the streamlines undulate at the thru-hole entrance and particles accelerate as they enter the thru-hole. Particle velocity reaches its maximum of approximately 180m/s in the thru-hole. The figure reveals that particle flow generally moves on axis of the thru-hole as expected, however, at some points, the figure reveals some streamlines move normal to the hole axis, which suggests turbulent vortices develop in the transition from the nozzle sac to the thru-hole inlet and are present in the thru-hole prior to the exit. The plot indicates attached flow in the thru-hole and at the nozzle exit and the particle streams exit the thru-hole following the nozzle seat thru-hole geometry. The particle stream decelerates upon exiting the injector traveling at approximately 120m/s.

#### 5.3.1.2 Shadowgraph Optical Imaging Results

Shadowgraph optical imaging spray plume progression from start of injector energizing is presented in Figure 97. The reference grid is 2 x 2mm at time snap shots taken for 20, 60, and 140µs. The test was performed at 5, 10, and 20MPa fuel pressures. As shown in the captured images, the spray plume penetration is 1-2mm at 20µs, and spray breakup is evident immediately at the exit of the nozzle at all fuel pressures. Spray penetration increases to between 4-6mm at 60µs, and evidence of a consistent spray plume angle of approximately 26º can be observed. The spray progression at 60µs also reveals optically more dense waves of droplets progressing at a regular spatial interval, at approximately 1.7mm spacing, across the plume penetration length, which indicates a dynamic disturbance in the nozzle or valve group at a given frequency is the likely cause. At 140µs the penetration the

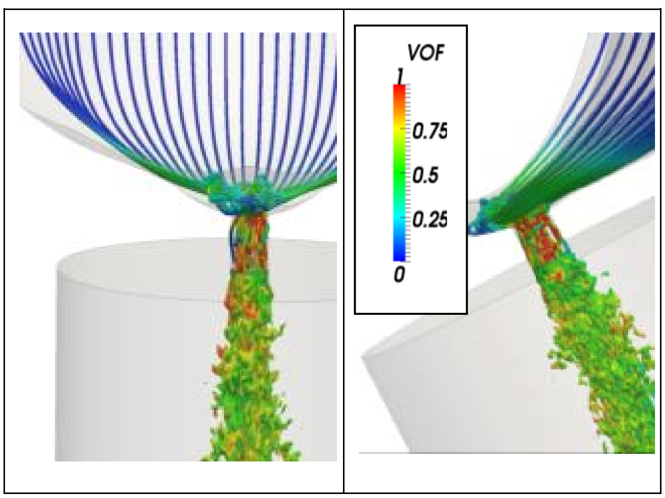

Figure 96 Particle Streamlines for Nozzle A

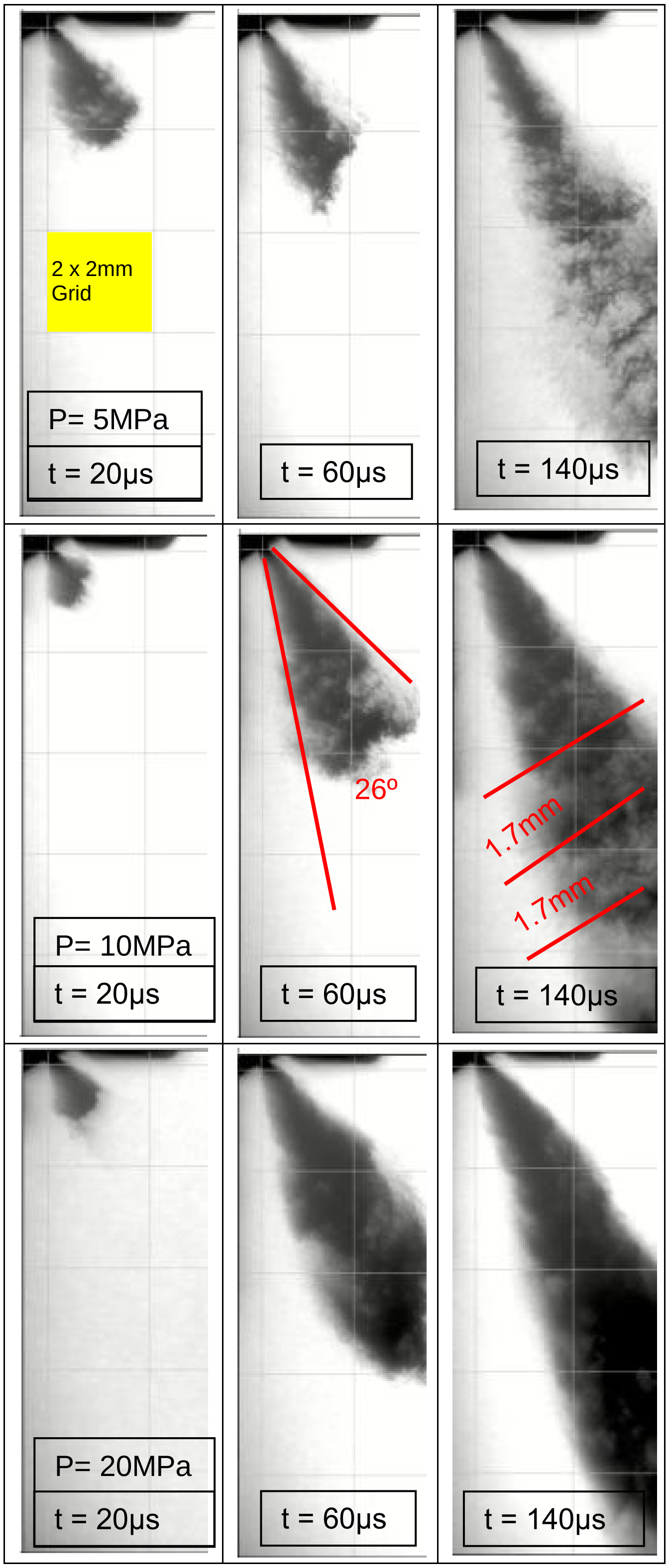


Figure 97 Spray for Nozzle A at 5, 10, & 20MPa at 20, 60 at time = 140µs, grid is 2 x 2mm

Spray plumes have exceeded 8mm of penetration and maintain characteristics of consistent spray plume angle and waves of heavier droplet density along the penetration length. The spray plumes also increase optical density with increasing injection pressures and at the highest pressure of 20MPa distinguishing droplets and waves is more difficult due to the high optical density. To better assess the spray plume geometry, a statistical PDF (liquid phase probability density function) is calculated for the 10MPa fuel pressure test point at 700µs, where the spray is fully developed, based on 5 spray plumes to account for any shot to shot variation. The results in Figure 98 indicate 100% liquid phase is captured at a spray plume angle of 19º and the majority of liquid is captured within a 26º plume angle. The spray plume skew axis is 30º matching the thru-hole geometry.

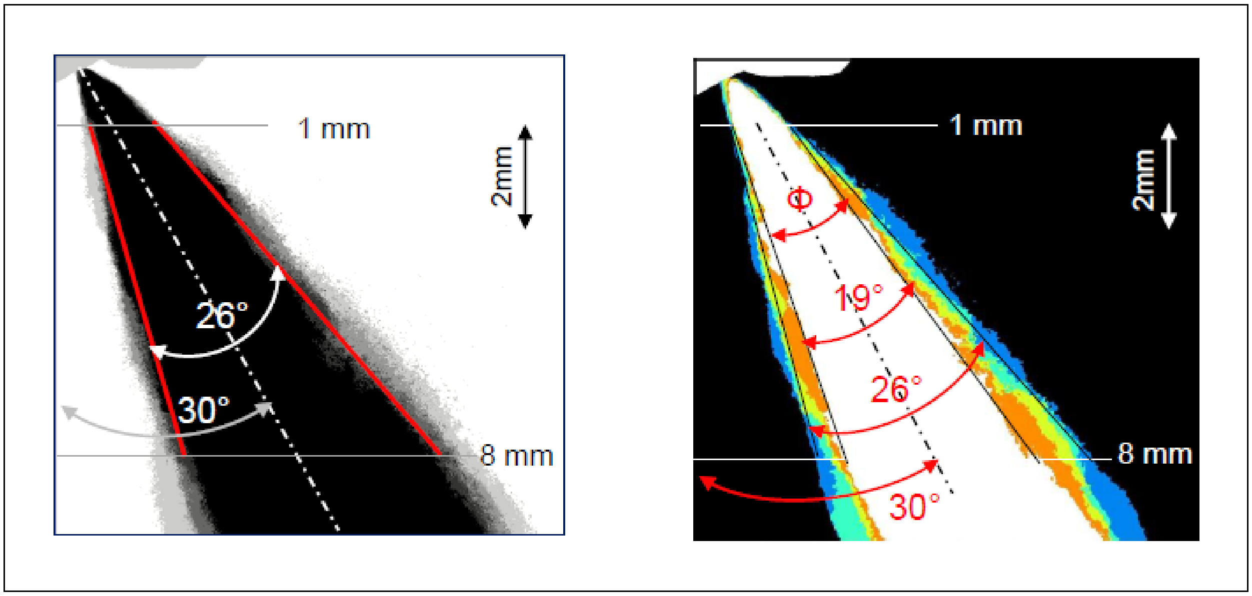


Figure 98 Spray plume statistical PDF (liquid phase probability density function) based on 5 injections for Nozzle A, l/d=1.1, Fuel Pressure = 10MPa, time = 700µs

The statistical PDF can also evaluate the plume geometry at 5, 10, and 20MPa fuel pressures tested to understand the effect of pressure on the geometry. As seen in Figure 99, fuel pressure did not show a significant effect over the range of 5-20MPa when tested, with the PDF indicating a plume angle between 19º-26º well captures the liquid phase spray. The statistical PDF can also be compared to the LES simulation as shown in Figure 100 where the spray is fully developed for 10MPa fuel pressure at 700µs.

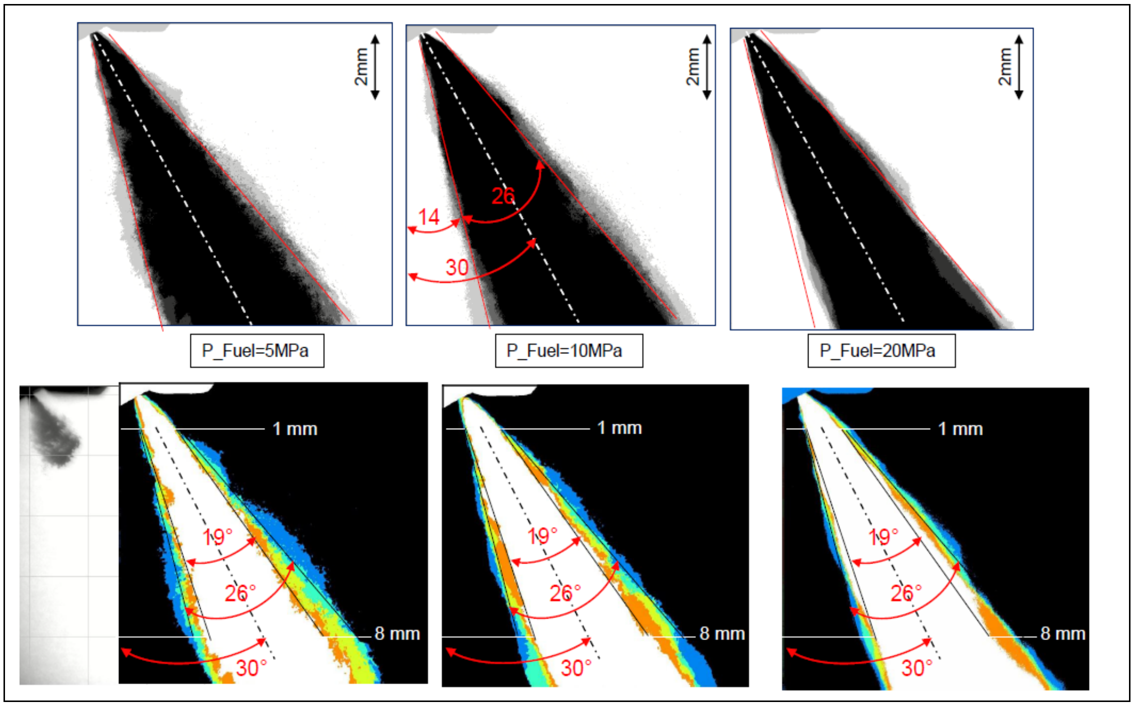


Figure 99 Spray plume statistical PDF versus injection pressure for Nozzle A, l/d=1.1, time =700μs

As shown in the figure, the LES confirms well the spray plume skew angle of 30º. The LES would indicate a spray plume angle of approximately 24º, well within the 19º-26º range indicated by the PDF. Overall, the LES and optical spray imaging are in excellent quantitative agreement for injector spray plume angle, spray plume skew angle, and particle breakup length. Previous work of the authors [69] showed the LES model predicted spray plume and skew angles were unaffected by injection pressure. The LES particle tracking streamlines also provide good insight into the role of the thru-hole inlet in developing turbulent eddies in the accelerating fluid flow in the thru-hole.

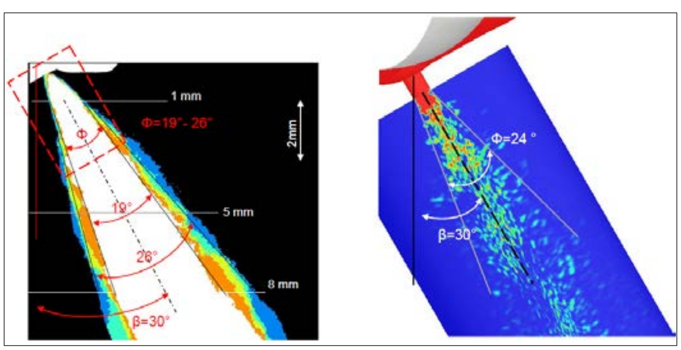


Figure 100 Spray plume statistical PDF compared to LES modeled spray plume for Nozzle A, l/d=1.1, Fuel Pressure =10MPa, time = 700μs image, 60μs simulation

#### 5.3.1.3 Phase contrast X-ray Optical imaging

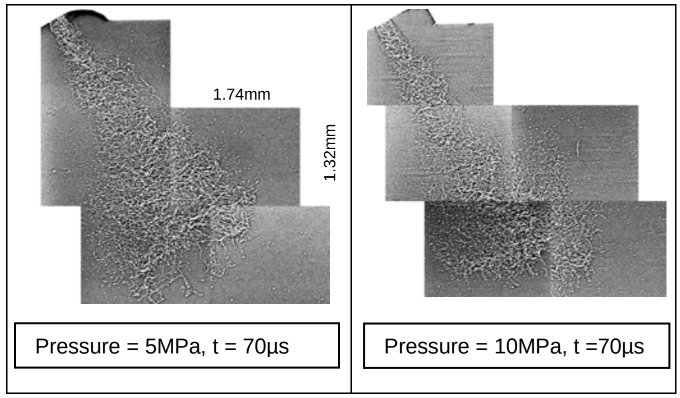


Figure 101 Spray plume X-ray optical imaging for varying injection pressure Nozzle A, l/d = 1.1, time = 60µs

As was evidenced in Figure 97, it is difficult to discern spray morphology near the nozzle exit due to the optical density of the GDi spray using a shadowgraph method. This condition is only exacerbated with increasing fuel pressures, as seen in the 20MPa optical image. It is important to understand this structure to help confirm whether the primary driver of spray breakup occurs in the nozzle or in friction interactions with the air through Kelvin-Helmholtz mechanism. X-ray optical images for nozzle A are presented in Figure 101 at varying injection pressure. At 70µs the spray plume has penetrated approximately 5mm into the chamber. The X-ray passes through the dense spray and reveals a stochastic pattern of waves that is consistent from nozzle exit through the spatial field. The plume structure breakup at the nozzle exit suggests disturbances originated inside the nozzle, and turbulent dispersion perpendicular to the spray axis can be seen similar to that predicted within the thru-hole by the particle streamlines. The chaotic jet breakup structures appear similar for 5 and 10MPa operating pressures with turbulence evident immediately at nozzle exit prior to any interaction with ambient air in the chamber.

## 5.4.2 Nozzle Geometry C, l/d = 0.55

### 5.4.2.1 Simulation Results

Figure 102 shows the simulation results for Nozzle C, l/d = 0.55, as flow progresses after start of injector energizing. As can be seen in the VOF plot the injector sac volume is initially filled with air and the liquid starts to enter the thru-hole at approximately 10µs. Liquid completely fills the sac volume by 20µs and the thru-hole by 60µs. However, in contrast to nozzle A there is evidence of unsteady flow separation at the thru-hole outboard edge. The separation starts at the thru-hole inlet, and the distance of separation increases as the flow in the thru-hole progress, thus causing a deviation of the spray plume jet from the thru-hole geometry on exit. The implication of flow separation is that the observed spray plume skew (bend) will be

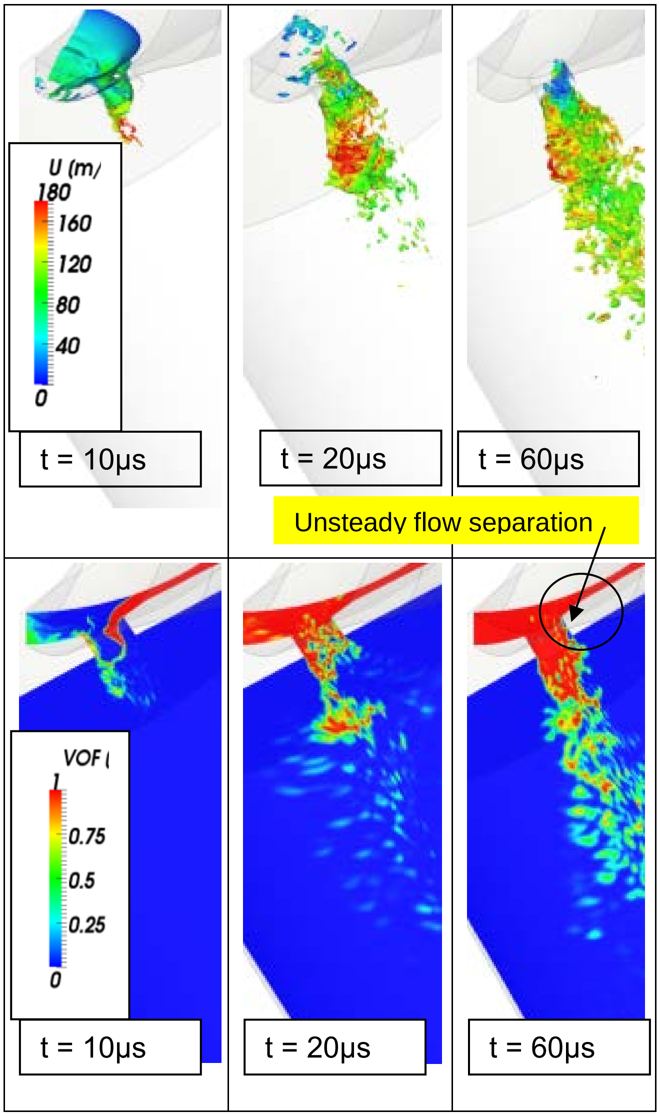


Figure 102 Spray velocity and VOF for Nozzle C at 10MPa at 10, 20, and 60µs

narrower than the geometric angle. The velocity plot for VOF=.5 shows the fluid starts at approximately 20m/s and accelerates to 40m/s in the sac volume and to 120-160m/s in the thru-hole with breakup to particles immediately at the nozzle exit and particle velocities in the range of 120m/s.

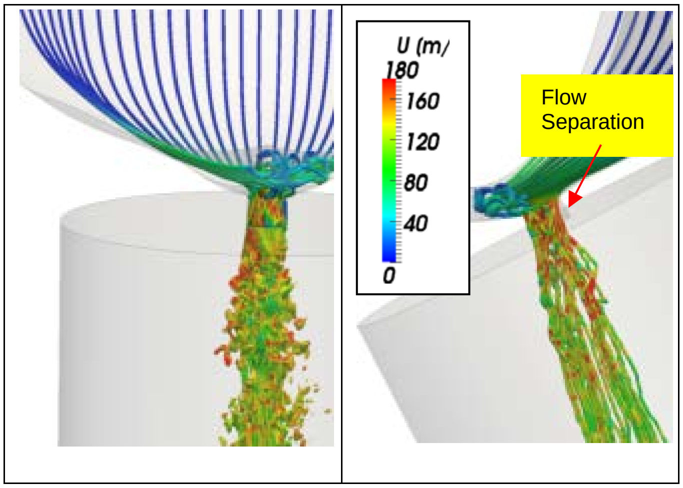


Figure 103 Particle Streamlines for Nozzle C

Fluid particle motion tracking is presented in Figure 103. As can be seen in the plot, the flow lines start with well-defined axial travel at a velocity of 20m/s. As the side view shows, the flow lines undulate as they wrap around the far edge of the thru-hole, but enter the near edge with minimum deviation. Thereby, maintaining the streamline momentum passing through the nozzle and exiting at an angle narrower than the geometric skew angle. The particles accelerate with velocity reaching its maximum in the thru-hole moving up to 180m/s. Particle flow is bi-modal with near edge streamlines leaving the nozzle at a narrower than geometric skew angle, while far edge streamlines show evidence of turbulent vortices deviating the path of travel and impacting the relative near edge streamlines. The plot indicates unsteady flow separation starting at the near edge inlet to the thru-hole and separation distance from the wall growing as the streamline progresses due to the deviation of streamline angle to the geometric angle.

### 5.4.2.2 Shadowgraph Optical Imaging Results

Shadowgraph optical imaging of spray plume progression from the start of injector energizing is presented in Figure 104. The reference grid is 1 x 1mm (note smaller grid than Nozzle A imaging) at time snap shots taken for 20, 60, and 140µs. The test was performed at 5, 10, and 20MPa fuel pressures. As shown in the captured images, the spray plume penetration is 1-2mm at 20µs, and spray breakup is evident immediately at the exit of the nozzle at all fuel pressures. Spray penetration increases to between 4-6mm at 60µs and evidence of a consistent spray plume angle of approximately 33° can be observed. Again, similar to Nozzle A, the spray progression at 60µs also reveals optically more dense waves of droplets progressing at a regular spatial interval, approximately 1.7mm in length, across the plume penetration length, likely indicating

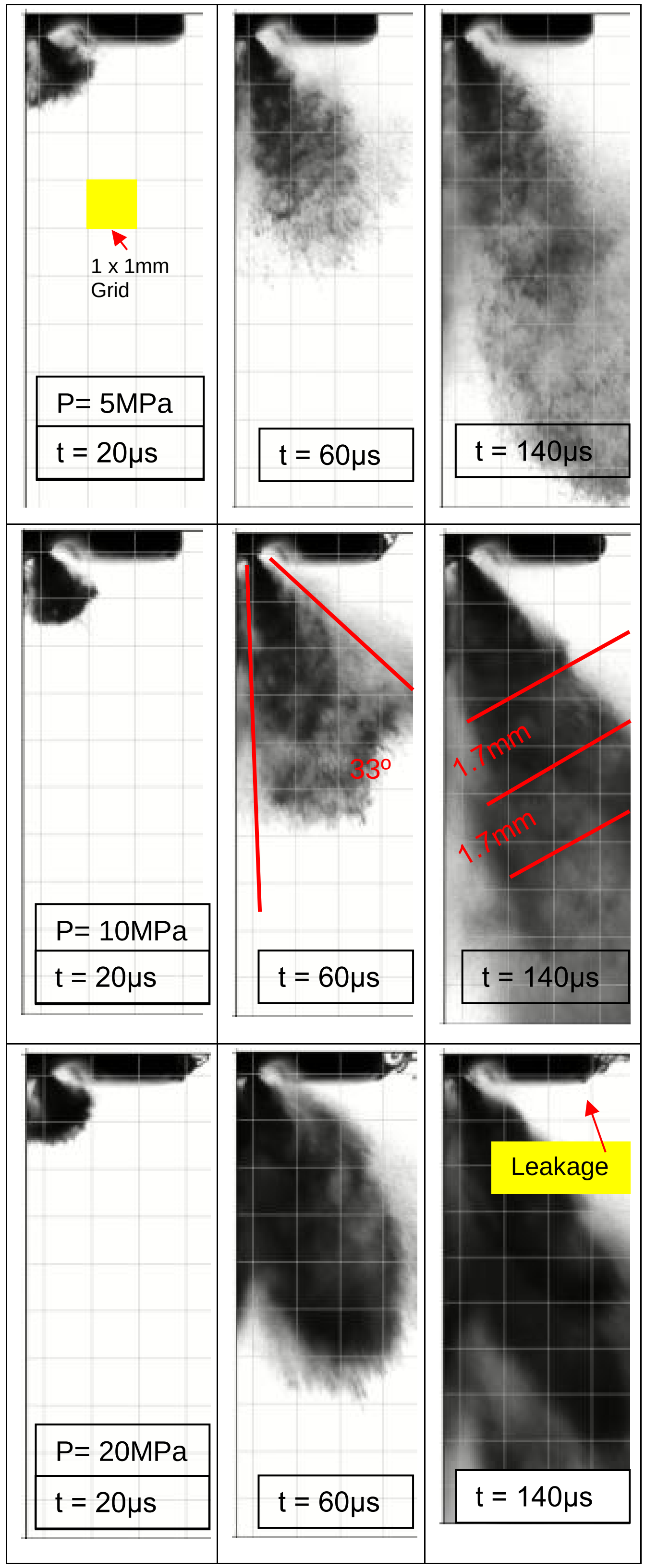


Figure 104 Spray Shadowgraph for Nozzle C at 5, 10, & 20MPa at 20, 60 & 140µs

a dynamic disturbance in the nozzle or valve group at a given frequency. At 140µs, the spray plumes have exceeded 8mm of penetration and maintain characteristics of consistent spray plume angle and waves of heavier droplet density along the penetration length. The spray plumes also increase optical density with increasing injection pressures, and at the highest pressure of 20MPa distinguishing droplets and waves is more difficult due to the high optical density. Significant seat leakage is also visible at 20MPa, forming a film on the seat surface and large droplets shedding from the seat edge.

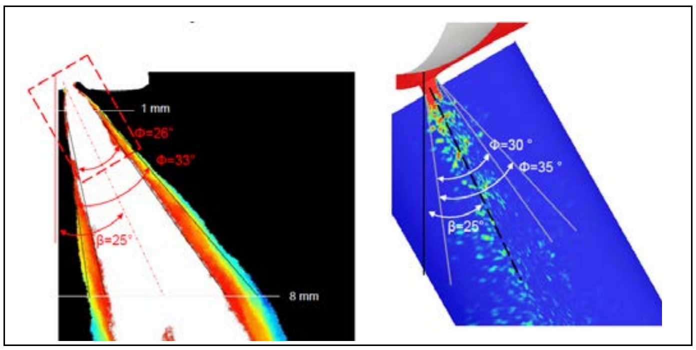

Figure 105 Spray plume statistical PDF compared to LES modeled spray plume for Nozzle C, l/d=0.55, Fuel Pressure =10MPa, time = 740µs image, 60µs simulation

To better assess the spray plume geometry, a statistical PDF (liquid phase probability density function) is calculated for the 10MPa fuel pressure test point at 700µs, where the spray is fully developed, based on 5 spray plumes to account for any shot to shot variation. The results, shown in Figure 105, indicate 100% liquid phase is captured at a spray plume angle of 26º, and the majority of liquid is captured within a 33º plume angle. The plume skew axis is 25º, narrower than the thru-hole geometry.

Similar to Nozzle A, the statistical PDF can also be compared to the LES simulation. This comparison at 10MPa fuel pressure test point and 700µs, where the spray is fully developed, is provided in Figure 105. As shown in the figure, the LES confirms well the narrowed spray plume skew angle of 25º. The LES would indicate a spray plume angle of approximately 30º-35º, slightly greater than the 26º-33º range indicated by the PDF. Overall, the LES and optical spray imaging are in excellent quantitative agreement for injector spray plume angle, spray plume skew angle, and particle breakup length. The LES particle tracking streamlines in the case of Nozzle C illustrated the mechanism of how near edge streamlines separated, starting at the thru-hole inlet edge and followed a trajectory exiting the nozzle resulting in a reduction of the skew angle. Like Nozzle A, the entrance of the fluid into the thru-hole created turbulent eddies.

The statistical PDF comparing optical imaging to the LES simulation is provided in Figure 106 at 700μs where the spray is fully developed for 20MPa fuel pressure. The LES would indicate a spray plume angle of approximately 30º-35º, slightly greater than the 21º-29º range indicated by the PDF. In case of l/d = 0.55, simulation and imaging data indicates there is no effect of fuel pressure on the plume skew angle trajectory. As in the case of l/d = 1.1, simulations predict no effect of pressure on spray plume angle, however, the imaging data suggest the effect is notable and complex. Figure 106 shows a significant increase of plume spray angle as pressure increases from 5MPa (24º-28°) to 10MPa (28º-33°), followed by a reduction of the plume spray angle, concurrent with marked increase of shot-to-shot variations, as pressure is further increased from 10MPa (28º-33°) to 20MPa (21º-29°). The author’s hypothesis is that the observed effect of fuel pressure increase was associated with deformation of the cracked seat, a result of machining, which caused a disproportionate increase of fuel leakage with increased pressure that substantially interacted with and influenced the spray development.

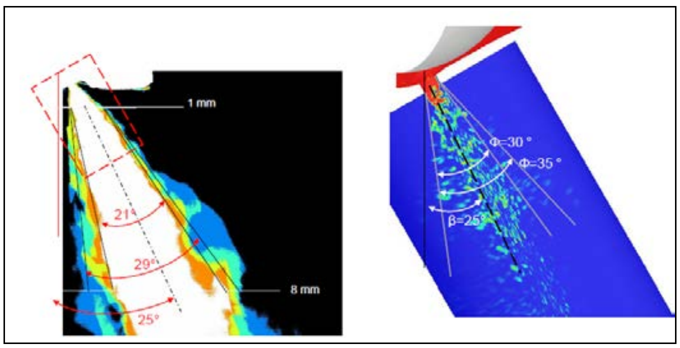

Figure 106 Spray plume statistical PDF (liquid phase density function) compared to LES modeled spray plume for Nozzle C, l/d=0.55, Fuel Pressure =20MPa, time = 740μs image, 60μs simulation

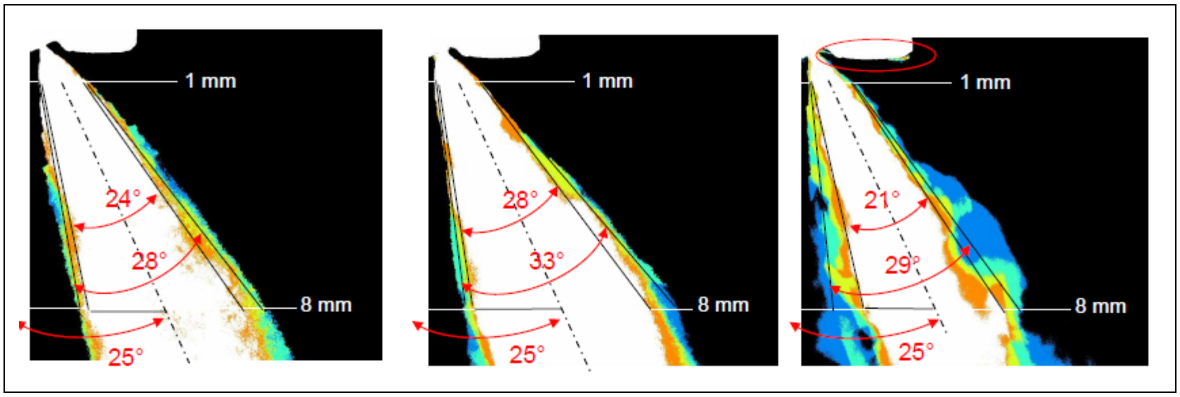


Figure 107 Spray plume statistical PDF (liquid phase probability density function) versus injection pressure for Nozzle C, l/d=0.55, time =740µs

#### 5.3.2.3 Phase contrast X-ray Optical imaging

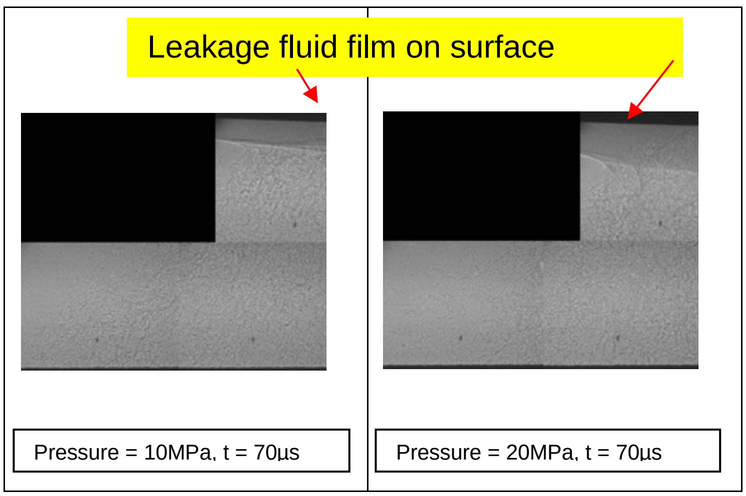


Figure 108 Spray plume X-ray optical imaging for varying injection pressure Nozzle A, l/d = 0.55, time = 70µs

X-ray images for nozzle C are presented in Figure 108 at varying injection pressure. At 70µs, the spray plume has penetrated approximately 5mm into the chamber. The X-ray passes through the dense spray and reveals a stochastic pattern of waves that is consistent from nozzle exit through the spatial field. The X-ray also shows the injector leakage leaves a deposit of fluid on the seat surface that the spray plume penetrates (limited contrast of particles in image). It can also be seen that the film thickness increased with increasing pressure. The plume structure breakup at the nozzle exit suggests disturbances originated inside the nozzle, and turbulent dispersion perpendicular to the spray axis can be seen similar to that predicted within the thru-hole by the particle streamlines. The chaotic jet breakup structures appear similar for 10 and 20MPa operating pressures with turbulence evident in both immediately at nozzle exit prior to any interaction with ambient air in the chamber.

### 5.4.3 Summary/Conclusions on l/d and Pressure effects

Overall, the GDi nozzle parameter studies using LES and spray imaging methods were very successful. LES and optical spray imaging are in agreement for injector spray plume angle, spray plume skew angle, and jet breakup length. There exists some imprecision in the assessments as plume angle and breakup length are visually based on the droplet distribution in the instantaneous VOF field and the VOF field, like the experimental images, have temporal variations. The LES particle tracking streamlines also provide good insight into the role of the thru-hole inlet in developing turbulent eddies with the accelerating fluid flow in the thru-hole as well as the mechanism of flow separation and resulting narrower skew angle for shorter l/d nozzles. The X-ray imaging revealed a stochastic pattern of waves that is consistent from nozzle exit through the spatial field and turbulent dispersion perpendicular to the spray axis similar to that predicted within the thru-hole by the particle streamlines. The complementary analysis of CFD methods and empirical data supported definitive conclusions on parameter effects as well as provided an understanding of the underlying physical mechanism involved. The conclusions of the LES and experimental spray imaging study of GDi nozzle parameters can be summarized as:

***Spray Breakup Structure:***

Simulation, shadowgraph imaging, and X-ray imaging all reveal jet primary atomization in close vicinity of the nozzle exit, evidenced immediately after start of fueling at all fuel pressures evaluated, even in the 5MPa case. The simulation and optical imaging data suggests that nozzle induced vorticity/turbulence is the primary cause of jet breakup. X-ray imaging confirms the turbulence is present at nozzle exit prior to any interaction with ambient air.

***The effect nozzle l/d reduction:***

Simulation and optical imaging showed spray plume angle increased approximately 7º as nozzle thru-hole l/d was reduced:

l/d = 1.1 spray plume angle = 19º-26°
l/d = 0.55 spray plume angle = 26º-33°

The plume skew angle deviated approximately 5º from thru-hole nozzle geometric axis for the shorter l/d due to separation at the nozzle inlet as follows:

l/d = 1.1 skew angle = 30º, deviation angle= 0°
l/d = 0.55 skew angle = 25º, deviation angle= -5°

***Effect of Fuel pressure:***

In the case of l/d=1.1, simulation and imaging data show the absence of a significant, and consistent, effect of fuel pressure on the near-field plume breakup, spray plume angle, and plume skew angle.

In the case of l/d=0.55, simulation and imaging data indicates there is no effect of fuel pressure on the plume skew angle trajectory. As in the case of l/d = 1.1, simulations predict no effect of pressure on spray plume angle; however, the imaging data suggested a notable and complex effect. The hypothesis is that the observed effect of fuel pressure increase was associated with deformation of the cracked seat, a result of machining, which caused a disproportionate increase of fuel leakage with increased pressure that substantially interacted with and influenced the spray development.

# CHAPTER 6 SUMMARY

## *6.1 Summary of Conclusions*

Overall, the GDi nozzle parameter studies using LES and spray imaging methods were very successful. LES was validated by optical spray imaging for injector spray plume angle, spray plume skew angle, and jet breakup length. There exists some imprecision in the assessments as spray angle and breakup length are visually based on the droplet distribution in the instantaneous VOF field and, like the experimental images, the VOF field have temporal variations. The success of the VOF-LES model is noteworthy given the varying flow conditions accurately predicted: separation with full hydraulic flip without influence of counterbore for axis symmetric nozzles, fully attached flow following geometric skew angle with spray plume angle counterbore influence for skew angled nozzles of l/d ~ 1, and detached flow with separation on the leading edge with effect on spray skew angle and spray plume angle for small l/d ~ .6 skew angled nozzles. All of these effects were predicted without model coefficients or other adjustment parameters but solely on the nozzle geometry and imposed initial velocity of the flow field without any disturbances. The LES particle tracking streamlines also provided good insight into the role of the thru-hole entrance in development of turbulent eddies within the accelerating fluid flow in the thru-hole as well as the mechanism of flow separation and resulting narrower skew angle for shorter l/d nozzles. The X-ray imaging revealed a stochastic pattern of turbulent waves that is consistent from the immediate nozzle exit through the spatial field, as well as turbulent dispersion perpendicular to the spray axis similar to that predicted within the thru-hole by the particle streamlines. The complementary analysis of CFD methods and empirical data supported definitive conclusions on parameter effects as well as provided an understanding of the underlying physical mechanism involved. Several findings changed the "understanding of spray formation" that existed at the start of this work. Overall, the study reveals that the nozzle flow characteristics of GDi nozzle holes are markedly different from the diesel nozzles, owing to the relatively short nozzle l/d~1 versus l/d~6-7 for the diesel nozzles. The VOF-LES simulations of the plume near-field breakup structure are in good agreement with the shadowgraph, Mie scatter, and X-ray imaging data. Specifically, the important plume near-field macro-scale characteristics of plume trajectory, plume spray angle, plume penetration, and the trend of influence of nozzle geometry on the plume breakup structure are in satisfactory agreement with data to validate the model. The summary of key findings with an index to relevant VOF-LES Figures and Test Images are presented in Table 11.

Table 11 Summary of key findings with index to VOF Figures and Spray Images Index

| Evaluation | VOF-LES Figures | Test Images | Spray Morphology Conclusion |
|---|---|---|---|
| axis-symmetric single-hole nozzles | 39-44 | Appendix C 157,158<br>Appendix E 187-193<br>Appendix F 120-131 | Separation at inlet<br>full hydraulic flip<br>Narrowed spray plume at exit<br>No counterbore contact<br>Extremely long penetration |
| Skew-angled Nozzle with and without counterbore | 83-92 | Appendix E 199-205<br>Appendix F 232-238 | Spray contact with counterbore narrows spray plume ≈ 5° |
| Injection pressures 5, 10 and 20Mpa | 95 | Figure 97, 99<br>Appendix E 205-211<br>Appendix F 238-244 | No change in plume angle<br>No change in skew angle |
| Nozzle l/d reduced from 1.1 to 0.55 | 95, 102, 103 | Figure 97, 104 | Separation at top-of inlet edge<br>Spray plume angle increases ≈ 7°<br>Spray skew angle deviates ≈ 5° from geometric |

In summary, the supported conclusions are:

**GDi plume breakup morphology is indicative of the "Atomization" regime**

The near-field plume imaging provides evidence of the jet primary breakup in the immediate vicinity of the nozzle exit, almost immediately after start of injection.

There is evidence of the influence of injector valve-group hydraulic pressure oscillations on the near-field jet breakup structure, revealed in regular waves of optically dense spray.

Evidence of Kelvin-Helmholtz interface instability waves was shown in both VOF-LES modeling and spray imaging; however, the ligament formation stemming from vorticity internal to the jet dominated as the breakup mechanism occurring immediately at nozzle exit.

The VOF-LES simulations indicate the atomization effectiveness of the GDi nozzle is associated with the vorticity and turbulence imparted on the flow at nozzle thru-hole entrance.

- **Effect of Nozzle Counterbore:**

There is evidence of the physical interaction and influence of counterbore on the jet primary breakup process with consequent effects on the plume trajectory, plume angle, and atomization. This counterbore interaction yields smaller spray plume angles for nozzle geometry typical for GDi production. It should be noted, as the geometric skew angle approaches 0º, the effect of the counterbore will diminish as was demonstrated with axis-symmetric nozzles.

- **Effect of Nozzle l/d:**

Simulation and optical imaging showed spray plume angle increased approximately 7º as nozzle thru-hole l/d was reduced:

  - l/d = 1.1 spray plume angle = 19º-26°
  - l/d = 0.55 spray plume angle = 26º-33°

The observed plume skew angle deviated approximately 5º from thru-hole nozzle geometric axis for the shorter l/d due to separation at the nozzle inlet as follows:

  - l/d = 1.1 skew angle = 30º, deviation angle= 0°
  - l/d = 0.55 skew angle = 25º, deviation angle= -5°

- **Effect of Nozzle d:**

The plume angle was shown to be a function of l/d and nozzles of d≈.20mm and d≈.15mm demonstrated similar plume angle.

- **Effect of Fuel Pressure:**

  In the case of l/d=1.1, typical of production GDi injectors, simulation and imaging data show the absence of a significant, and consistent, effect of fuel pressure on the near-field plume breakup, spray plume angle, and plume skew angle.

### *6.2 Recommendations for Future Work*

While this work provided new insights into the turbulent dynamics of GDi nozzle flow and validated a methodology for use in GDi nozzle design, it also opens several areas of research focus for future work. The first of these is already being pursued, the extension of the VOF-LES modeling of internal injector flow and near-field jet breakup analysis to spray droplet formation [70] and predicted droplet distribution developed in the far field. It will be interesting to understand the nozzle design variable influences since the laser diffraction measurement of this work indicated droplet distribution was fairly independent of nozzle l/d or counterbore presence. Another area of interest that was observed in the experimental images of this work was the clear and consistent pulsed frequency of optically dense spray plume waves, future work incorporating pintle movement in the simulation is recommended to confirm the interaction of the injector valve group dynamics, non-ideal asymmetries as exist with internal seat features and nozzle hole placements, and seat sac volume on spray plume morphology. Likewise, as this work excluded cavitation which is known to significantly contribute to turbulent structure as l/d increases, future work to develop stable CFD solutions that permit inclusion of cavitation in the analysis is desired. Finally, a study of element mesh size impact on the simulation result to understand the effect of LES resolved versus modeled scales as the solution ranges from near Reynolds Averaged Navier Stokes solution to Direct Numerical Simulation for the GDi nozzle could establish guidelines for predictive accuracy and computational expense so that future work may target an appropriate compromise required for injector development.

# APPENDIX A PROTOTYPE INJECTOR SEAT DRAWING

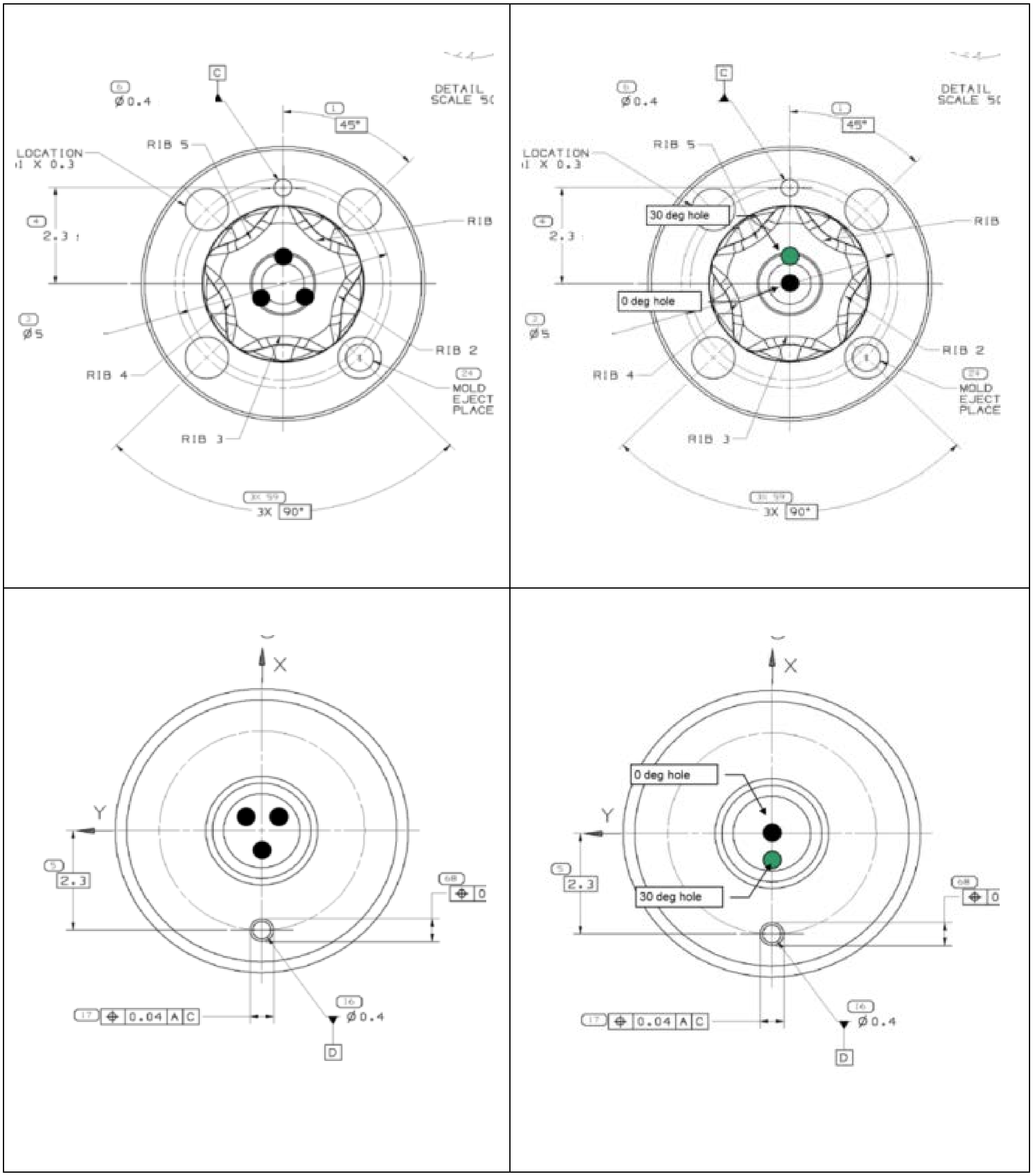

## HOLE POSITIONS ON BOLT CIRCLE (x,y)-COORDINATE SYSTEM

Comments — input in green cells

| | | | |
|---|---|---|---|
| number of holes | 3 | | |
| position of Hole #1 | 180 | deg | (Typically 180 deg or less) |
| Posalux EDM Hole position Offset | 180 | deg | (Typically 180 deg for the posalux) |
| Equaly distributed spacing calc | 120.00 | deg between holes | |

Hole Location — Bolt Circle [mm]: 0.75; Z Coordinate [mm]: -0.16

| Hole # | Print Bolt Circle Angular Hole Position | Coordinates [mm] x | y | z | EDM Hole Pos. | sizes for bubble plot |
|---|---|---|---|---|---|---|
| 1 | 180.0 | -0.375 | 0.000 | -0.160 | 0.0 | 1.01 |
| 2 | 60.0 | 0.188 | 0.325 | -0.160 | 120.0 | 1.02 |
| 3 | -60.0 | 0.188 | -0.325 | -0.160 | 240.0 | 1.03 |
| 4 | -180.0 | 10.000 | 0.000 | -0.160 | 360.0 | 1.04 |
| 5 | -300.0 | 10.000 | 0.325 | -0.160 | 480.0 | 1.05 |
| 6 | -420.0 | 10.000 | -0.325 | -0.160 | 600.0 | 1.06 |
| 7 | -540.0 | 10.000 | 0.000 | -0.160 | 720.0 | 1.07 |
| 8 | -660.0 | 10.000 | 0.325 | -0.160 | 840.0 | 1.08 |

| For Reference | | bolt circle | Z-coord |
|---|---|---|---|
| BRAVO | | 0.65 | -0.13 |
| BETA3.175 | | 0.75 | -0.186 |
| BETA 3.0 | X | 0.75 | -0.16 |

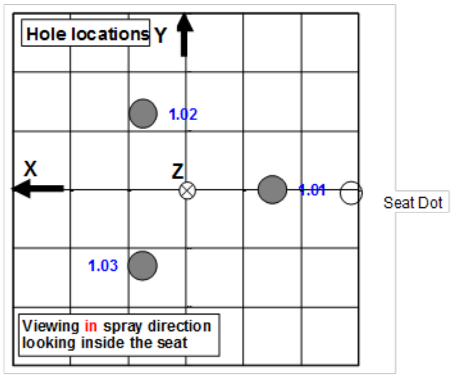


Hole Numbering System
Hole # 1 on X-axis closest to seat dot
View from Inside Seat
Hole's ordered CCW– starting at seat dot or CCW from seat dot
View from Outside Seat
Hole's ordered CW – starting seat dot or CW from seat dot

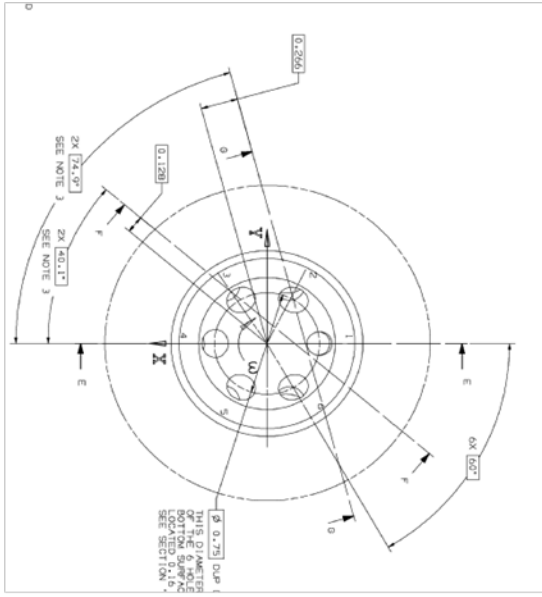

Reference coordinate system
X axis identified by Seat Dot - on negative X
Y axis 90 degrees to X axis
Z axis in direction of spray

# APPENDIX B INJECTOR FLOW RATE

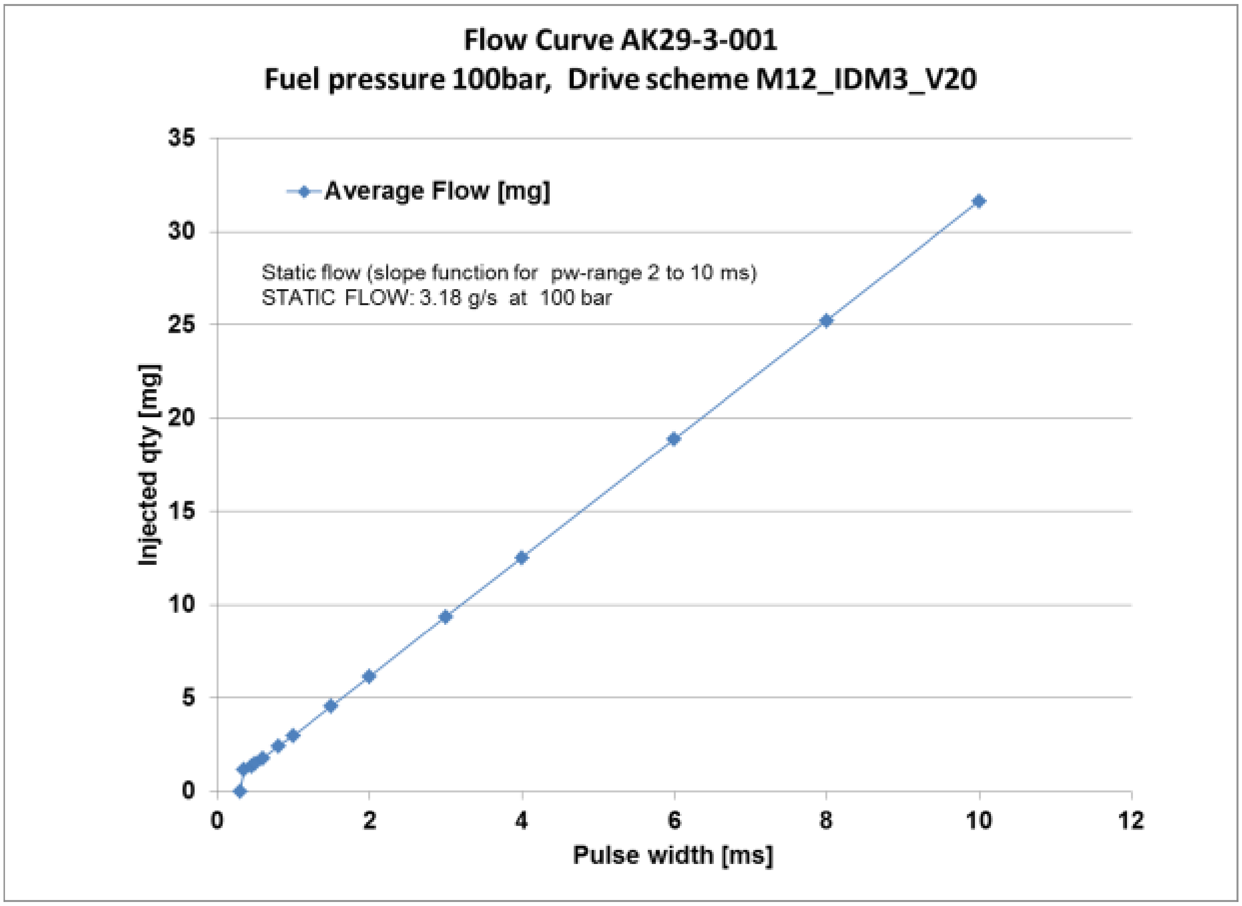


| | |
|---|---|
| Injector | AK29-3-001 |
| Drive Scheme | M12_IDM3_V20 |
| Fuel pressure [bar] | |
| Test Number | 29475 |

| Pulse width [ms] | Average Flow [mg] | Pulse width [ms] | Average Flow [mg] |
|---|---|---|---|
| 0.30 | 0.00 | 8.00 | 25.22 |
| 0.35 | 1.17 | 10.00 | 31.64 |
| 0.45 | 1.37 | | |
| 0.50 | 1.50 | | |
| 0.60 | 1.79 | | |
| 0.80 | 2.42 | | |
| 1.00 | 2.99 | | |
| 1.50 | 4.57 | | |
| 2.00 | 6.15 | | |

| | | |
|---|---|---|
| Slope | 3.18 | g/s |
| Intercept | -0.21 | |

# APPENDIX C ROCHESTER SPRAY LAB RESULTS

Injector Patternization for targeting centroid, plume angle and shadowgraphic image from Rochester spray lab, seat # xx- indicates number omitted in s/n label

| Sheet # | Seat # | # holes | d (mm) | β | l/d | (l+L) /d | D/d | Inj. Pres. | Plume Angle | View Angle |
|---|---|---|---|---|---|---|---|---|---|---|
| 1 | AK29-03-001 | 1 | ≈.20 | 0° | 1.1 | na | na | 10MPa | 13.5° | 0°, 90° |
| 1 | AK29-03-002 | 1 | ≈.20 | 0° | 1.1 | na | na | 10MPa | 17.1° | 0°, 90° |
| 1 | AK29-03-003 | 1 | ≈.20 | 0° | 1.1 | na | na | 10MPa | 16.1° | 0°, 90° |
| 2 | AK29-06-001 | 1 | ≈.15 | 0° | 1.1 | na | na | 10MPa | 17.6° | 0°, 90° |
| 2 | AK29-06-002 | 1 | ≈.15 | 0° | 1.1 | na | na | 10MPa | 17.4° | 0°, 90° |
| 2 | AK29-06-003 | 1 | ≈.15 | 0° | 1.1 | na | na | 10MPa | 14.9° | 0°, 90° |
| 3 | AK29-09-001 | 3 | ≈.20 | 30° | 1.1 | na | na | 10MPa | 16.6° | 0°, 90° |
| 3 | AK29-09-002 | 3 | ≈.20 | 30° | 1.1 | na | na | 10MPa | 16.2° | 0°, 90° |
| 3 | AK29-09-003 | 3 | ≈.20 | 30° | 1.1 | na | na | 10MPa | 17.5° | 0°, 90° |
| 4 | AK29-10-3-001 | 3 | ≈.15 | 30° | 3.96 | na | na | 10MPa | 16.0° | 0°, 90° |
| 4 | AK29-10-3-002 | 3 | ≈.15 | 30° | 3.96 | na | na | 10MPa | 17.2° | 0°, 90° |
| 4 | AK29-10-3-003 | 3 | ≈.15 | 30° | 3.96 | na | na | 10MPa | 16.2° | 0°, 90° |
| 5 | AK29-11-3-001 | 3 | ≈.15 | 30° | 1.1 | na | na | 10MPa | 13.4° | 0°, 90° |
| 5 | AK29-11-3-002 | 3 | ≈.15 | 30° | 1.1 | na | na | 10MPa | 14.2° | 0°, 90° |
| 5 | AK29-11-3-003 | 3 | ≈.15 | 30° | 1.1 | na | na | 10MPa | 15.5° | 0°, 90° |
| 6 | AK29-12-3-002 | 3 | ≈.15 | 30° | 1.1 | na | na | 10MPa | 13.2° | 0°, 90° |
| 6 | AK29-12-3-003 | 3 | ≈.15 | 30° | 1.1 | na | na | 10MPa | 15.1° | 0°, 90° |
| 6 | AK29-12-3-004 | 3 | ≈.15 | 30° | 1.1 | na | na | 10MPa | 13.0° | 0°, 90° |
| 7 | AK29-12-001 | 1 | ≈.15 | 30° | 1.1 | na | na | 10MPa | 13.7° | 0°, 90° |
| 7 | AK29-12-002 | 1 | ≈.15 | 30° | 1.1 | na | na | 10MPa | 15.8° | 0°, 90° |
| 7 | AK29-12-003 | 1 | ≈.15 | 30° | 1.1 | na | na | 10MPa | 13.5° | 0°, 90° |
| 8 | AK29-13-003 | 1 | ≈.20 | 0° | 1.1 | 2.95 | 2.5 | 10MPa | 18.5° | |
| 8 | AK29-13-004 | 1 | ≈.20 | 0° | 1.1 | 2.95 | 2.5 | 10MPa | 21.7° | |
| 9 | AK29-14-005 | 1 | ≈.20 | 0° | .55 | 2.95 | 2.5 | 10MPa | 18.3° | |
| 9 | AK29-14-006 | 1 | ≈.20 | 0° | .55 | 2.95 | 2.5 | 10MPa | 18.1° | |
| 10 | AK29-15-007 | 1 | ≈.20 | 0° | 1.65 | 2.95 | 2.5 | 10MPa | 17.9° | |
| 10 | AK29-15-008 | 1 | ≈.20 | 0° | 1.65 | 2.95 | 2.5 | 10MPa | 18.3° | |
| 11 | AK29-16-009 | 1 | ≈.20 | 0° | 1.1 | 2.95 | 2.0 | 10MPa | 21.5° | |
| 11 | AK29-16-010 | 1 | ≈.20 | 0° | 1.1 | 2.95 | 2.0 | 10MPa | 18.1° | |
| 12 | AK29-17-011 | 1 | ≈.20 | 30° | 1.1 | 2.95 | 2.0 | 10MPa | 17.6° | |
| 12 | AK29-17-012 | 1 | ≈.20 | 30° | 1.1 | 2.95 | 2.0 | 10MPa | 18.9° | |
| 13 | AK29-18-013 | 1 | ≈.20 | 0° | 1.1 | 2.95 | 1.5 | 10MPa | 18.1° | |
| 13 | AK29-18-014 | 1 | ≈.20 | 0° | 1.1 | 2.95 | 1.5 | 10MPa | 18.0° | |
| 14 | AK29-19-015 | 1 | ≈.20 | 30° | 1.1 | 2.95 | 1.5 | 10MPa | 14.7° | |
| 14 | AK29-19-016 | 1 | ≈.20 | 30° | 1.1 | 2.95 | 1.5 | 10MPa | 14.4° | |
| 15 | AK29-20-017 | 1 | ≈.20 | 10° | 1.1 | 2.95 | 2.5 | 10MPa | 23.3° | |
| 15 | AK29-20-018 | 1 | ≈.20 | 10° | 1.1 | 2.95 | 2.5 | 10MPa | 21.9° | |
| 16 | AK29-21-019 | 1 | ≈.20 | 20° | 1.1 | 2.95 | 2.5 | 10MPa | 17.6° | |
| 16 | AK29-21-020 | 1 | ≈.20 | 20° | 1.1 | 2.95 | 2.5 | 10MPa | 18.1° | |
| 17 | AK29-22-021 | 1 | ≈.20 | 30° | 1.1 | 2.95 | 2.5 | 10MPa | 19.5° | |
| 17 | AK29-22-022 | 1 | ≈.20 | 30° | 1.1 | 2.95 | 2.5 | 10MPa | 20.1° | |
| 18 | AK29-23-023 | 3 | ≈.20 | 10° | 1.1 | 2.95 | 2.5 | 10MPa | 26.0° | |
| 19 | AK29-24-024 | 3 | ≈.20 | 20° | 1.1 | 2.95 | 2.5 | 10MPa | 20.9° | |
| 19 | AK29-24-025 | 3 | ≈.20 | 20° | 1.1 | 2.95 | 2.5 | 10MPa | 21.5° | |
| 20 | AK29-07-001 | 3 | ≈.20 | 30° | 1.1 | 2.95 | 2.5 | 10MPa | 18.1° | |
| 20 | AK29-07-002 | 3 | ≈.20 | 30° | 1.1 | 2.95 | 2.5 | 10MPa | 18.7° | |

| | AK29-03-001 | AK29-03-002 | AK29-03-003 | Average | St. Dev. | | | |
|---|---|---|---|---|---|---|---|---|
| Spray Parameters | Spray Parameters | Spray Parameters | Spray Parameters | | | | | |
| Injector Height : | 50 mm | 50 mm | 50 mm | | | | | |
| Connector Angle (θ) : | 0° | 0° | 0° | | | | | |
| Fuel Pressure : | 10000 kPa | 10000 kPa | 10000 kPa | | | | | |
| Pulse Width / Period : | 1.5 / 40.0 ms | 1.5 / 40.0 ms | 1.5 / 40.0 ms | | | | | |
| # of Pulses : | 183 | 193 | 218 | **198** | **18.03** | 183 | 11.9 | 13.5 |
| Captured Volume : | 1.0 ml | 1.3 ml | 1.3 ml | | | 193 | 15.1 | 17.1 |
| **Plume 1** | | | | | | 218 | 14.2 | 16.1 |
| Diameter : | 11.9 mm @ 90% | 15.1 mm @ 90% | 14.2 mm @ 90% | **13.73** | **1.65** | 198 | 13.73333 | 15.56667 |
| Cone Angle α : | 13.5° @ 90% | 17.1° @ 90% | 16.1° @ 90% | **15.57** | **1.86** | 18.02776 | 1.650253 | 1.858315 |
| 50% Mass Diameter : | 6.8 mm | 7.8 mm | 7.3 mm | | | | | |
| 50% Cone Angle : | 7.8° | 8.9° | 8.4° | | | | | |
| Bend (Skew) Angle (β) : | 2.0° | 2.2° | 1.7° | | | | | |
| Mass % : | 100.0 | 100.0 | 100.0 | | | | | |
| Centroid Location (x,y)* : | (-1.1 mm, 1.4 mm) | (-0.9 mm, 1.7 mm) | (-0.9 mm, 1.2 mm) | | | | | |
| Centroid Location (r,θ)* : | (1.8 mm, 130.4°) | (1.9 mm, 117.4°) | (1.5 mm, 128.6°) | | | | | |
| Static Flow [g/s] per hole @ 10 Mpa | 3.14 | 3.34 | 3.25 | | | | | |
| **Plume 1 w/ Centroid & 90% Analysis Circle** | **Plume 1 w/ Centroid & 90% Analysis Circle** | **Plume 1 w/ Centroid & 90% Analysis Circle** | **Plume 1 w/ Centroid & 90% Analysis Circle** | | | | | |

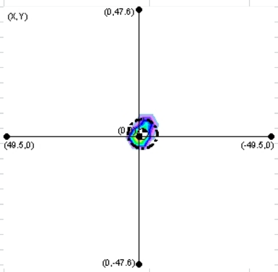


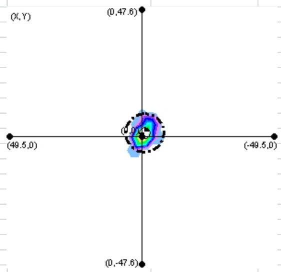


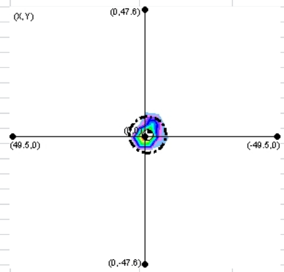


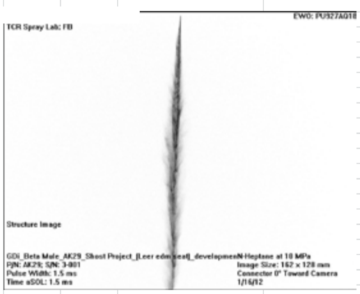

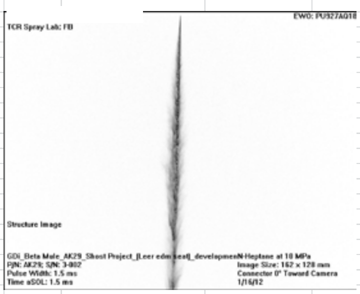

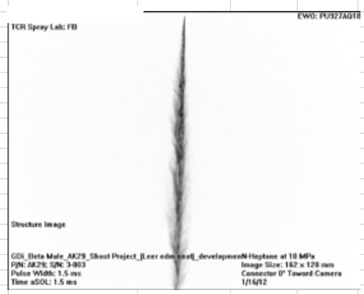

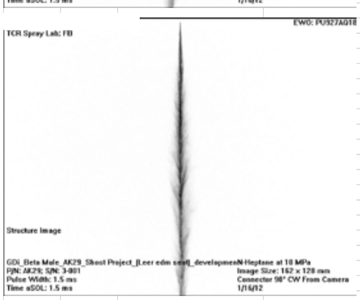

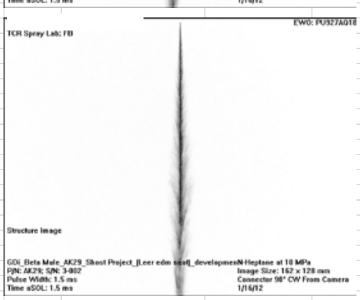

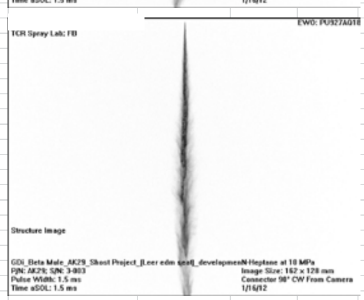

| | | | | | | | | | | |
|---|---|---|---|---|---|---|---|---|---|---|
| AK29-06-001 | | AK29-06-002 | | AK29-06-003 | | | | | | |
| Spray Parameters | | Spray Parameters | | Spray Parameters | | **Average** | **St. Dev.** | | | |
| Injector Height : | 50 mm | Injector Height : | 50 mm | Injector Height : | 50 mm | | | | | |
| Connector Angle (θ) : | 0° | Connector Angle (θ) : | 0° | Connector Angle (θ) : | 0° | | | | | |
| Fuel Pressure : | 10000 kPa | Fuel Pressure : | 10000 kPa | Fuel Pressure : | 10000 kPa | | | | | |
| Pulse Width / Period : | 1.5 / 40.0 ms | Pulse Width / Period : | 1.5 / 40.0 ms | Pulse Width / Period : | 1.5 / 40.0 ms | | | | | |
| # of Pulses : | 335 | # of Pulses : | 398 | # of Pulses : | 288 | **340.33** | **55.19** | 335 | 15.5 | 17.6 |
| Captured Volume : | 1.5 ml | Captured Volume : | 1.7 ml | Captured Volume : | 0.9 ml | | | 398 | 15.3 | 17.4 |
| **Plume 1** | | **Plume 1** | | **Plume 1** | | | | 288 | 13.1 | 14.9 |
| Diameter : | 15.5 mm @ 90% | Diameter : | 15.3 mm @ 90% | Diameter : | 13.1 mm @ 90% | **14.63** | **1.33** | 340.3333 | 14.63333 | 16.63333 |
| Cone Angle α : | 17.6° @ 90% | Cone Angle α : | 17.4° @ 90% | Cone Angle α : | 14.9° @ 90% | **16.63** | **1.50** | 55.1936 | 1.331666 | 1.504438 |
| 50% Mass Diameter : | 8.3 mm | 50% Mass Diameter : | 8.4 mm | 50% Mass Diameter : | 6.1 mm | | | | | |
| 50% Cone Angle : | 9.5° | 50% Cone Angle : | 9.6° | 50% Cone Angle : | 6.9° | | | | | |
| Bend (Skew) Angle (β) : | 0.7° | Bend (Skew) Angle (β) : | 1.5° | Bend (Skew) Angle (β) : | 0.2° | | | | | |
| Mass % : | 100.0 | Mass % : | 100.0 | Mass % : | 100.0 | | | | | |
| Centroid Location (x,y)* : | (-0.5 mm, 0.2 mm) | Centroid Location (x,y)* : | (-1.0 mm, 0.9 mm) | Centroid Location (x,y)* : | (0.2 mm, 0.0 mm) | | | | | |
| Centroid Location (r,θ)* : | (0.6 mm, 160.9°) | Centroid Location (r,θ)* : | (1.3 mm, 135.4°) | Centroid Location (r,θ)* : | (0.2 mm, 346.0°) | | | | | |
| Static Flow [g/s] per hole @ 10 Mpa | 1.87 | Static Flow [g/s] per hole @ 10 Mpa | 1.86 | Static Flow [g/s] per hole @ 10 Mpa | 1.89 | | Note no relation SF vs. cone angle | | | |
| **Plume 1 w/ Centroid & 90% Analysis Circle** | | **Plume 1 w/ Centroid & 90% Analysis Circle** | | **Plume 1 w/ Centroid & 90% Analysis Circle** | | | | | | |

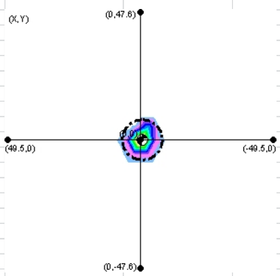


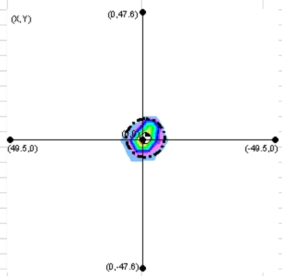


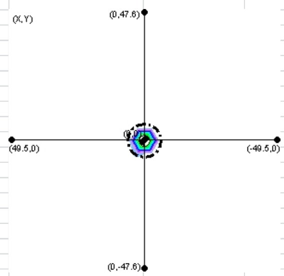


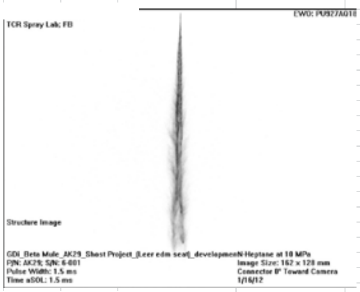

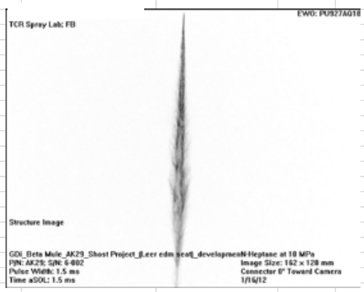

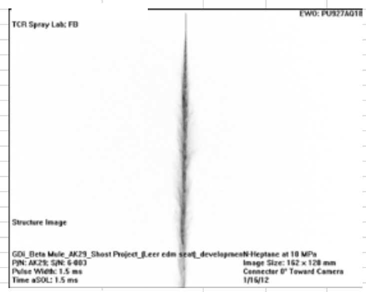

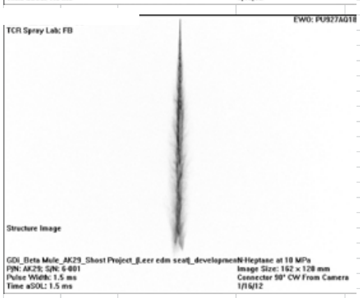

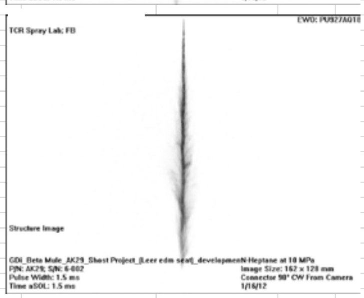

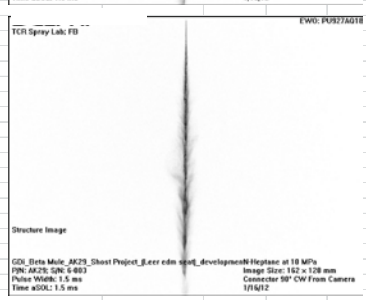

| | | | | | | | | | | |
|---|---|---|---|---|---|---|---|---|---|---|
| AK29-09-001 | | AK29-09-002 | | AK29-09-003 | | | | | | |
| Spray Parameters | | Spray Parameters | | Spray Parameters | | Average | St. Dev. | | | |
| Injector Height : | 50 mm | Injector Height : | 50 mm | Injector Height : | 50 mm | | | | | |
| Connector Angle (θ) : | 0° | Connector Angle (θ) : | 0° | Connector Angle (θ) : | 0° | | | | | |
| Fuel Pressure : | 10000 kPa | Fuel Pressure : | 10000 kPa | Fuel Pressure : | 10000 kPa | | | | | |
| Pulse Width / Period : | 1.5 / 40.0 ms | Pulse Width / Period : | 1.5 / 40.0 ms | Pulse Width / Period : | 1.5 / 40.0 ms | | | | | |
| # of Pulses : | 523 | # of Pulses : | 468 | # of Pulses : | 560 | **517.00** | **46.29** | 523 | 17 | 16.6 |
| Captured Volume : | 6.1 ml | Captured Volume : | 5.4 ml | Captured Volume : | 6.7 ml | | | 468 | 17 | 16.2 |
| **Plume 1** | | **Plume 1** | | **Plume 1** | | | | 560 | 17.9 | 17.5 |
| Diameter : | 17.0 mm @ 90% | Diameter : | 17.0 mm @ 90% | Diameter : | 17.9 mm @ 90% | **17.30** | **0.52** | 517 | 17.3 | 16.76667 |
| Cone Angle α : | 16.6° @ 90% | Cone Angle α : | 16.2° @ 90% | Cone Angle α : | 17.5° @ 90% | **16.77** | **0.67** | 46.29255 | 0.519615 | 0.665833 |
| 50% Mass Diameter : | 9.5 mm | 50% Mass Diameter : | 9.6 mm | 50% Mass Diameter : | 10.3 mm | | | | | |
| 50% Cone Angle : | 9.3° | 50% Cone Angle : | 9.2° | 50% Cone Angle : | 10.1° | | | | | |
| Bend (Skew) Angle (β) : | 30.8° | Bend (Skew) Angle (β) : | 33.0° | Bend (Skew) Angle (β) : | 30.5° | | | | | |
| Mass % : | 35.3 | Mass % : | 35.2 | Mass % : | 33.8 | | | | | |
| Centroid Location (x,y)* : | (-29.8 mm, 0.8 mm) | Centroid Location (x,y)* : | (-32.5 mm, 0.8 mm) | Centroid Location (x,y)* : | (-29.4 mm, 0.1 mm) | | | | | |
| Centroid Location (r,θ)* : | (29.8 mm, 178.5°) | Centroid Location (r,θ)* : | (32.5 mm, 178.6°) | Centroid Location (r,θ)* : | (29.4 mm, 179.8°) | | | | | |
| Static Flow [g/s] per hole @ 10 Mpa | 2.56 | Static Flow [g/s] per hole @ 10 Mpa | 2.41 | Static Flow [g/s] per hole @ 10 Mpa | 2.55 | | | | | |
| **Plume 1 w/ Centroid & 90% Analysis Circle** | | **Plume 1 w/ Centroid & 90% Analysis Circle** | | **Plume 1 w/ Centroid & 90% Analysis Circle** | | | | | | |

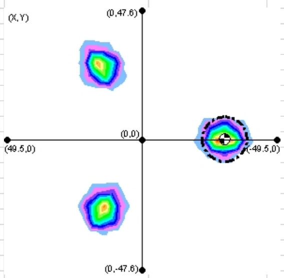


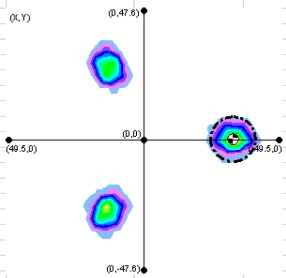


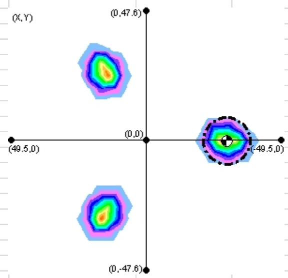


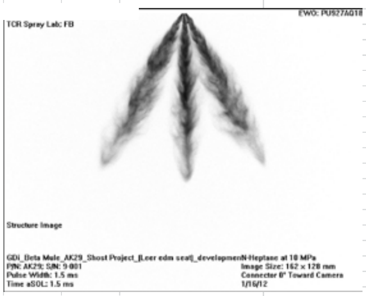

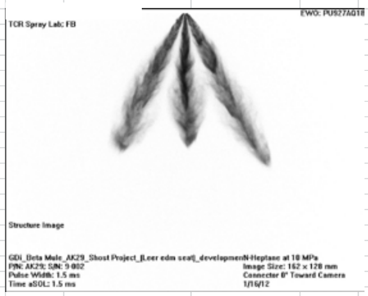

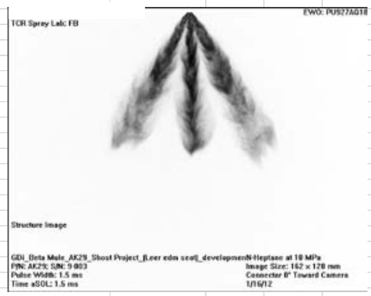

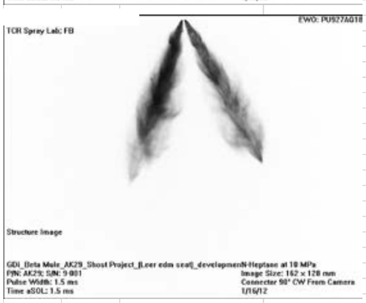

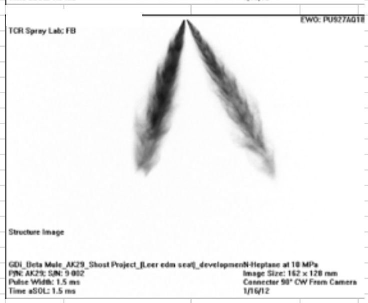

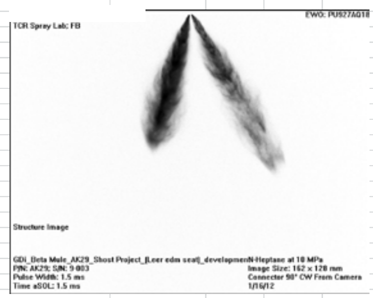

| | AK29-10-3-001 | AK29-10-3-002 | AK29-10-3-003 | Average | St. Dev. | | | |
|---|---|---|---|---|---|---|---|---|
| Spray Parameters | | | | | | | | |
| Injector Height : | 50 mm | 50 mm | 50 mm | | | | | |
| Connector Angle (θ) : | 0° | 0° | 0° | | | | | |
| Fuel Pressure : | 10000 kPa | 10000 kPa | 10000 kPa | | | | | |
| Pulse Width / Period : | 1.5 / 40.0 ms | 1.5 / 40.0 ms | 1.5 / 40.0 ms | | | | | |
| # of Pulses : | 813 | 923 | 720 | **818.67** | **101.62** | 813 | 16.4 | 16 |
| Captured Volume : | 6.6 ml | 6.7 ml | 5.9 ml | | | 923 | 17.7 | 17.2 |
| **Plume 1** | | | | | | 720 | 16.6 | 16.2 |
| Diameter : | 16.4 mm @ 90% | 17.7 mm @ 90% | 16.6 mm @ 90% | **16.90** | **0.70** | 818.6667 | 16.9 | 16.46667 |
| Cone Angle α : | 16.0° @ 90% | 17.2° @ 90% | 16.2° @ 90% | **16.47** | **0.64** | 101.6186 | 0.7 | 0.64291 |
| 50% Mass Diameter : | 9.3 mm | 9.9 mm | 9.4 mm | | | | | |
| 50% Cone Angle : | 9.1° | 9.7° | 9.2° | | | | | |
| Bend (Skew) Angle (β) : | 30.9° | 31.2° | 30.8° | | | | | |
| Mass % : | 34.6 | 36.3 | 37.0 | | | | | |
| Centroid Location (x,y)* : | (-29.9 mm, 0.9 mm) | (-30.3 mm, 0.0 mm) | (-29.7 mm, 1.1 mm) | | | | | |
| Centroid Location (r,θ)* : | (29.9 mm, 178.3°) | (30.3 mm, 179.9°) | (29.8 mm, 177.9°) | | | | | |
| Static Flow [g/s] per hole @ 10 Mpa | 1.69 | 1.76 | 1.76 | | | | | |

**Plume 1 w/ Centroid & 90% Analysis Circle** (AK29-10-3-001)

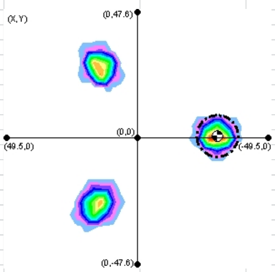


**Plume 1 w/ Centroid & 90% Analysis Circle** (AK29-10-3-002)

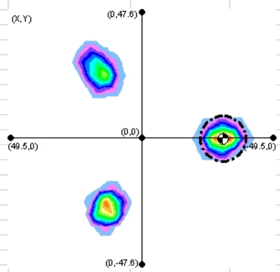


**Plume 1 w/ Centroid & 90% Analysis Circle** (AK29-10-3-003)

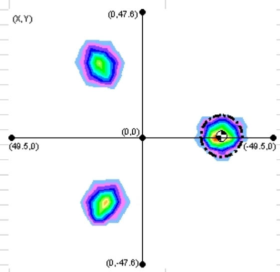


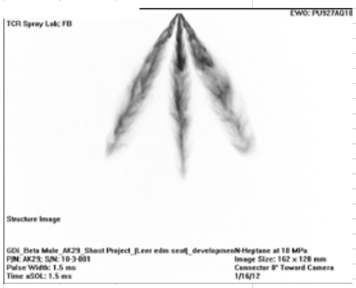


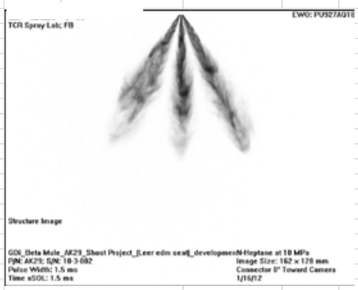


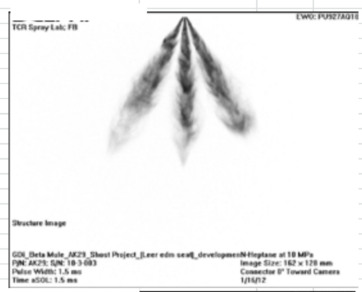


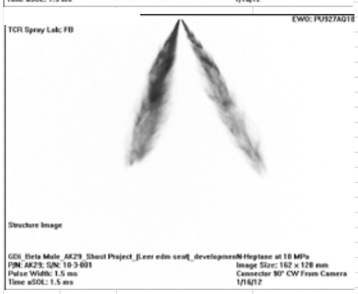



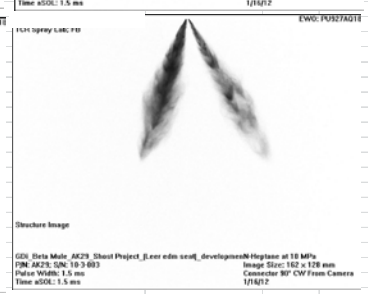

| AK29-11-3-001 | | AK29-11-3-002 | | AK29-11-3-003 | | | | | | |
|---|---|---|---|---|---|---|---|---|---|---|
| Spray Parameters | | Spray Parameters | | Spray Parameters | | Average | St. Dev. | | | |
| Injector Height : | 50 mm | Injector Height : | 50 mm | Injector Height : | 50 mm | | | | | |
| Connector Angle (θ) : | 0° | Connector Angle (θ) : | 0° | Connector Angle (θ) : | 0° | | | | | |
| Fuel Pressure : | 10000 kPa | Fuel Pressure : | 10000 kPa | Fuel Pressure : | 10000 kPa | | | | | |
| Pulse Width / Period : | 1.5 / 40.0 ms | Pulse Width / Period : | 1.5 / 40.0 ms | Pulse Width / Period : | 1.5 / 40.0 ms | | | | | |
| # of Pulses : | 440 | # of Pulses : | 478 | # of Pulses : | 638 | **518.67** | **105.08** | 440 | 13.9 | 13.4 |
| Captured Volume : | 4.1 ml | Captured Volume : | 4.7 ml | Captured Volume : | 5.5 ml | | | 478 | 14.6 | 14.2 |
| **Plume 1** | | **Plume 1** | | **Plume 1** | | | | 638 | 15.7 | 15.5 |
| Diameter : | 13.9 mm @ 90% | Diameter : | 14.6 mm @ 90% | Diameter : | 15.7 mm @ 90% | **14.73** | **0.91** | 518.6667 | 14.73333 | 14.36667 |
| Cone Angle α : | 13.4° @ 90% | Cone Angle α : | 14.2° @ 90% | Cone Angle α : | 15.5° @ 90% | **14.37** | **1.06** | 105.0777 | 0.907377 | 1.059874 |
| 50% Mass Diameter : | 7.9 mm | 50% Mass Diameter : | 8.6 mm | 50% Mass Diameter : | 9.1 mm | | | | | |
| 50% Cone Angle : | 7.7° | 50% Cone Angle : | 8.4° | 50% Cone Angle : | 9.0° | | | | | |
| Bend (Skew) Angle (β) : | 31.9° | Bend (Skew) Angle (β) : | 31.1° | Bend (Skew) Angle (β) : | 29.8° | | | | | |
| Mass % : | 32.4 | Mass % : | 32.7 | Mass % : | 35.8 | | | | | |
| Centroid Location (x,y)* : | (-31.1 mm, 0.8 mm) | Centroid Location (x,y)* : | (-30.2 mm, 1.1 mm) | Centroid Location (x,y)* : | (-28.6 mm, -0.2 mm) | | | | | |
| Centroid Location (r,θ)* : | (31.1 mm, 178.5°) | Centroid Location (r,θ)* : | (30.2 mm, 177.9°) | Centroid Location (r,θ)* : | (28.6 mm, 180.5°) | | | | | |
| Static Flow [g/s] per hole @ 10 Mpa | 1.76 | Static Flow [g/s] per hole @ 10 Mpa | 1.82 | Static Flow [g/s] per hole @ 10 Mpa | 1.68 | | | | | |

**Plume 1 w/ Centroid & 90% Analysis Circle**

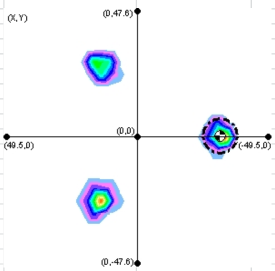


**Plume 1 w/ Centroid & 90% Analysis Circle**

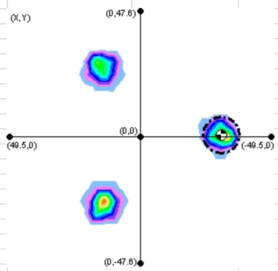


**Plume 1 w/ Centroid & 90% Analysis Circle**

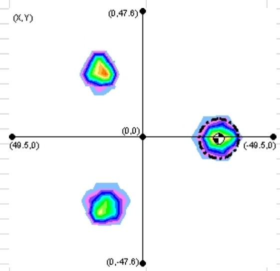


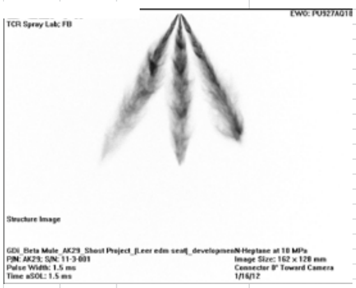


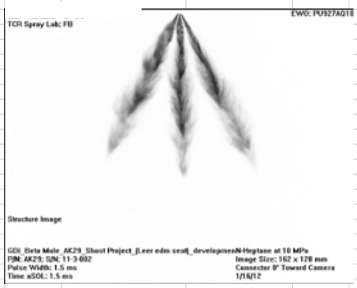


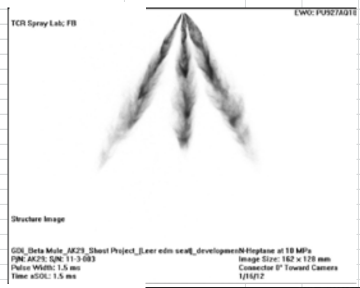


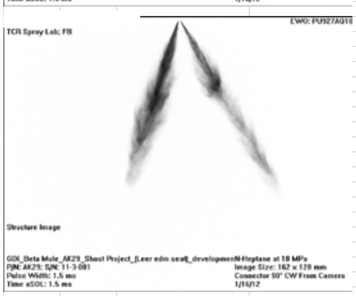


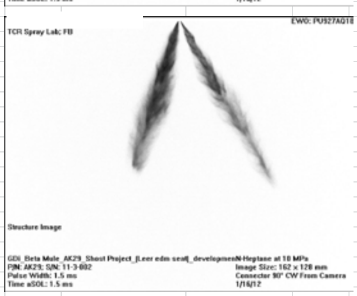


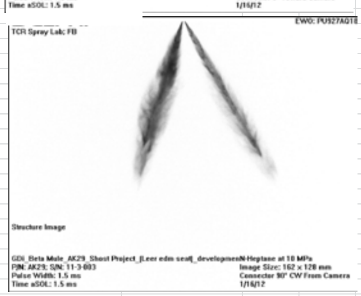

| | AK29-12-3-002 | | AK29-12-3-003 | | AK29-12-3-004 | | | | | |
|---|---|---|---|---|---|---|---|---|---|---|
| Spray Parameters | | Spray Parameters | | Spray Parameters | | Average | St. Dev. | | | |
| Injector Height : | 50 mm | Injector Height : | 50 mm | Injector Height : | 50 mm | | | | | |
| Connector Angle (θ) : | 0° | Connector Angle (θ) : | 0° | Connector Angle (θ) : | 0° | | | | | |
| Fuel Pressure : | 10000 kPa | Fuel Pressure : | 10000 kPa | Fuel Pressure : | 10000 kPa | | | | | |
| Pulse Width / Period : | 1.5 / 40.0 ms | Pulse Width / Period : | 1.5 / 40.0 ms | Pulse Width / Period : | 1.5 / 40.0 ms | | | | | |
| # of Pulses : | 570 | # of Pulses : | 765 | # of Pulses : | 388 | **574.33** | **188.54** | 570 | 13.6 | 13.2 |
| Captured Volume : | 4.4 ml | Captured Volume : | 5.1 ml | Captured Volume : | 3.5 ml | | | 765 | 15.4 | 15.1 |
| **Plume 1** | | **Plume 1** | | **Plume 1** | | | | 388 | 13.3 | 13 |
| Diameter : | 13.6 mm @ 90% | Diameter : | 15.4 mm @ 90% | Diameter : | 13.3 mm @ 90% | **14.10** | **1.14** | 574.3333 | 14.1 | 13.76667 |
| Cone Angle α : | 13.2° @ 90% | Cone Angle α : | 15.1° @ 90% | Cone Angle α : | 13.0° @ 90% | **13.77** | **1.16** | 188.5374 | 1.135782 | 1.159023 |
| 50% Mass Diameter : | 8.1 mm | 50% Mass Diameter : | 8.9 mm | 50% Mass Diameter : | 8.0 mm | | | | | |
| 50% Cone Angle : | 7.8° | 50% Cone Angle : | 8.7° | 50% Cone Angle : | 7.8° | | | | | |
| Bend (Skew) Angle (β) : | 31.8° | Bend (Skew) Angle (β) : | 31.0° | Bend (Skew) Angle (β) : | 31.2° | | | | | |
| Mass % : | 35.9 | Mass % : | 35.4 | Mass % : | 37.3 | | | | | |
| Centroid Location (x,y)* : | (-30.9 mm, 1.9 mm) | Centroid Location (x,y)* : | (-30.0 mm, 1.3 mm) | Centroid Location (x,y)* : | (-30.2 mm, 1.3 mm) | | | | | |
| Centroid Location (r,θ)* : | (30.9 mm, 176.6°) | Centroid Location (r,θ)* : | (30.1 mm, 177.4°) | Centroid Location (r,θ)* : | (30.3 mm, 177.5°) | | | | | |

**Plume 1 w/ Centroid & 90% Analysis Circle**

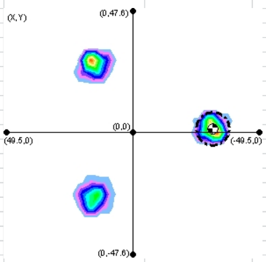


**Plume 1 w/ Centroid & 90% Analysis Circle**

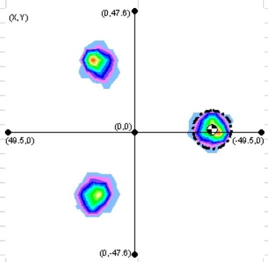


**Plume 1 w/ Centroid & 90% Analysis Circle**

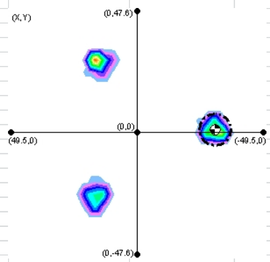


g model

model




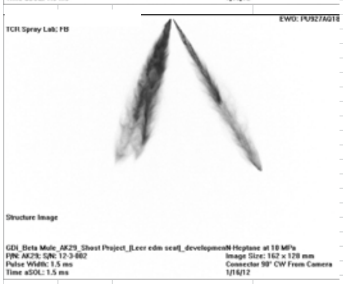


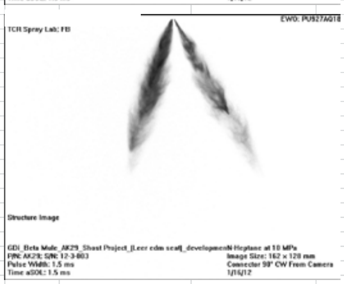


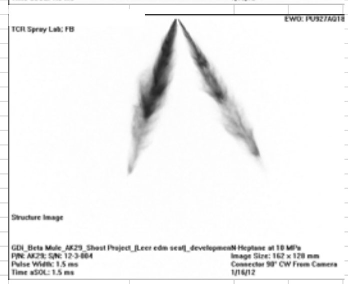

| Parameter | AK29-12-001 | AK29-12-002 | AK29-12-003 | Average | St. Dev. | | | |
|---|---|---|---|---|---|---|---|---|
| | Spray Parameters | Spray Parameters | Spray Parameters | | | | | |
| Injector Height : | 50 mm | 50 mm | 50 mm | | | | | |
| Connector Angle (θ) : | 0° | 0° | 0° | | | | | |
| Fuel Pressure : | 10000 kPa | 10000 kPa | 10000 kPa | | | | | |
| Pulse Width / Period : | 1.5 / 40.0 ms | 1.5 / 40.0 ms | 1.5 / 40.0 ms | | | | | |
| # of Pulses : | 510 | 575 | 480 | **521.67** | **48.56** | 510 | 13.9 | 13.7 |
| Captured Volume : | 1.6 ml | 2.1 ml | 1.5 ml | | | 575 | 16 | 15.8 |
| **Plume 1** | | | | | | 480 | 13.8 | 13.5 |
| Diameter : | 13.9 mm @ 90% | 16.0 mm @ 90% | 13.8 mm @ 90% | **14.57** | **1.24** | 521.6667 | 14.56667 | 14.33333 |
| Cone Angle α : | 13.7° @ 90% | 15.8° @ 90% | 13.5° @ 90% | **14.33** | **1.27** | 48.56267 | 1.24231 | 1.274101 |
| 50% Mass Diameter : | 8.3 mm | 9.5 mm | 7.9 mm | | | | | |
| 50% Cone Angle : | 8.2° | 9.4° | 7.8° | | | | | |
| Bend (Skew) Angle (β) : | 30.3° | 29.6° | 30.8° | | | | | |
| Mass % : | 100.0 | 100.0 | 100.0 | | | | | |
| Centroid Location (x,y)* : | (13.3 mm, -26.0 mm) | (13.3 mm, -25.0 mm) | (14.9 mm, -25.8 mm) | | | | | |
| Centroid Location (r,θ)* : | (29.2 mm, 297.1°) | (28.4 mm, 298.0°) | (29.8 mm, 300.1°) | | | | | |

**Plume 1 w/ Centroid & 90% Analysis Circle** | **Plume 1 w/ Centroid & 90% Analysis Circle** | **Plume 1 w/ Centroid & 90% Analysis Circle**

g model

model

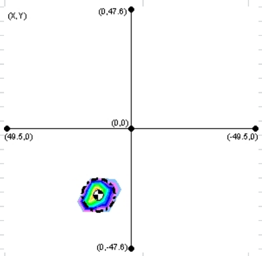


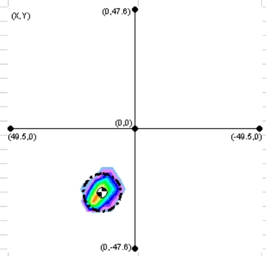


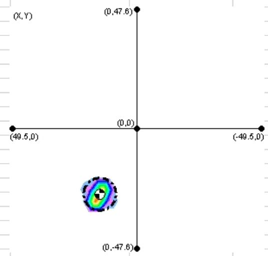


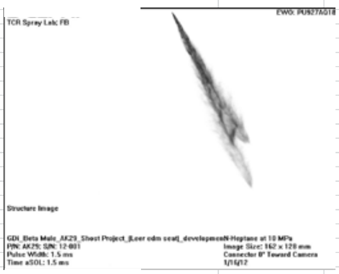


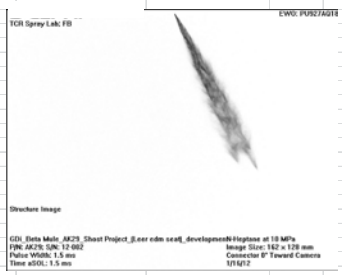


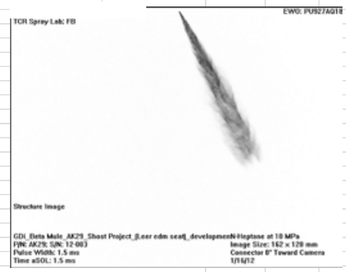



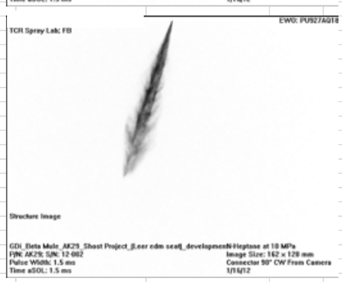


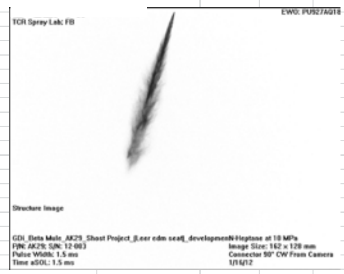

| | AK29-003 | | AK29-004 |
|---|---|---|---|
| Spray Parameters | | Spray Parameters | |
| Injector Height : | 50 mm | Injector Height : | 50 mm |
| Connector Angle (θ) : | 0° | Connector Angle (θ) : | 0° |
| Fuel Pressure : | 10000 kPa | Fuel Pressure : | 10000 kPa |
| Pulse Width / Period : | 1.5 / 40.0 ms | Pulse Width / Period : | 1.5 / 40.0 ms |
| # of Pulses : | 600 | # of Pulses : | 495 |
| Captured Volume : | 2.0 ml | Captured Volume : | 2.0 ml |
| **Plume 1** | | **Plume 1** | |
| Diameter : | 16.3 mm @ 90% | Diameter : | 19.2 mm @ 90% |
| Cone Angle α : | 18.5° @ 90% | Cone Angle α : | 21.7° @ 90% |
| 50% Mass Diameter : | 10.2 mm | 50% Mass Diameter : | 11.6 mm |
| 50% Cone Angle : | 11.7° | 50% Cone Angle : | 13.2° |
| Bend (Skew) Angle (β) : | 0.4° | Bend (Skew) Angle (β) : | 1.5° |
| Centroid Location (x,y)* : | (0.2 mm, -0.3 mm) | Centroid Location (x,y)* : | (1.0 mm, 0.8 mm) |
| Centroid Location (r,θ)* : | (0.4 mm, 297.0°) | Centroid Location (r,θ)* : | (1.3 mm, 37.3°) |

**Plume 1 w/ Centroid & 90% Analysis Circle**

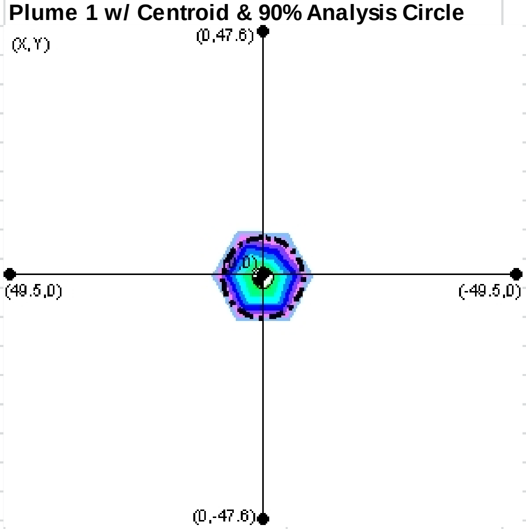


**Plume 1 w/ Centroid & 90% Analysis Circle**

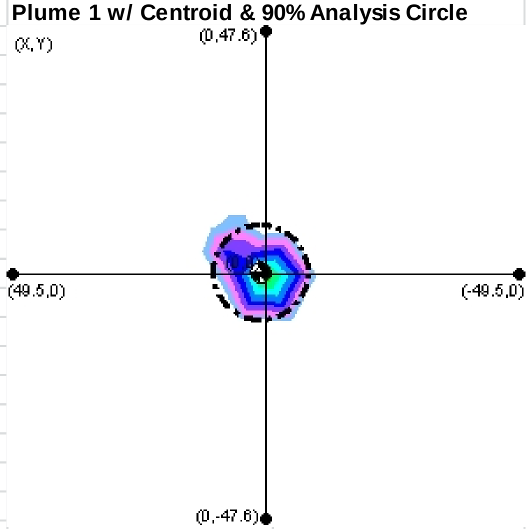

| AK29-005 | |
|---|---|
| **Spray Parameters** | |
| Injector Height : | 50 mm |
| Connector Angle (θ) : | 0° |
| Fuel Pressure : | 10000 kPa |
| Pulse Width / Period : | 1.5 / 40.0 ms |
| # of Pulses : | 358 |
| Captured Volume : | 1.4 ml |
| **Plume 1** | |
| Diameter : | 16.1 mm @ 90% |
| Cone Angle α : | 18.3° @ 90% |
| 50% Mass Diameter : | 9.9 mm |
| 50% Cone Angle : | 11.3° |
| Bend (Skew) Angle (β) : | 0.4° |
| Centroid Location (x,y)* : | (0.2 mm, -0.3 mm) |
| Centroid Location (r,θ)* : | (0.4 mm, 309.3°) |

**Plume 1 w/ Centroid & 90% Analysis Circle**

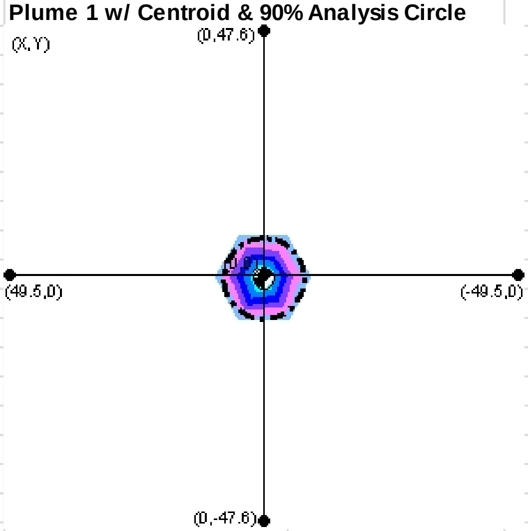


| AK29-006 | |
|---|---|
| **Spray Parameters** | |
| Injector Height : | 50 mm |
| Connector Angle (θ) : | 0° |
| Fuel Pressure : | 10000 kPa |
| Pulse Width / Period : | 1.5 / 40.0 ms |
| # of Pulses : | 555 |
| Captured Volume : | 1.9 ml |
| **Plume 1** | |
| Diameter : | 15.9 mm @ 90% |
| Cone Angle α : | 18.1° @ 90% |
| 50% Mass Diameter : | 9.5 mm |
| 50% Cone Angle : | 10.8° |
| Bend (Skew) Angle (β) : | 0.3° |
| Centroid Location (x,y)* : | (0.1 mm, -0.3 mm) |
| Centroid Location (r,θ)* : | (0.3 mm, 283.4°) |

**Plume 1 w/ Centroid & 90% Analysis Circle**

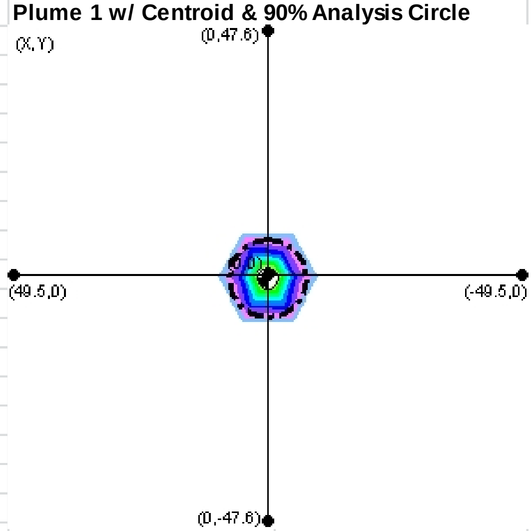

| AK29-007 | |
|---|---|
| Spray Parameters | |
| Injector Height : | 50 mm |
| Connector Angle (θ) : | 0° |
| Fuel Pressure : | 10000 kPa |
| Pulse Width / Period : | 1.5 / 40.0 ms |
| # of Pulses : | 538 |
| Captured Volume : | 1.5 ml |
| **Plume 1** | |
| Diameter : | 15.7 mm @ 90% |
| Cone Angle α : | 17.9° @ 90% |
| 50% Mass Diameter : | 9.0 mm |
| 50% Cone Angle : | 10.3° |
| Bend (Skew) Angle (β) : | 0.9° |
| Centroid Location (x,y)* : | (0.1 mm, -0.7 mm) |
| Centroid Location (r,θ)* : | (0.7 mm, 281.4°) |

**Plume 1 w/ Centroid & 90% Analysis Circle**

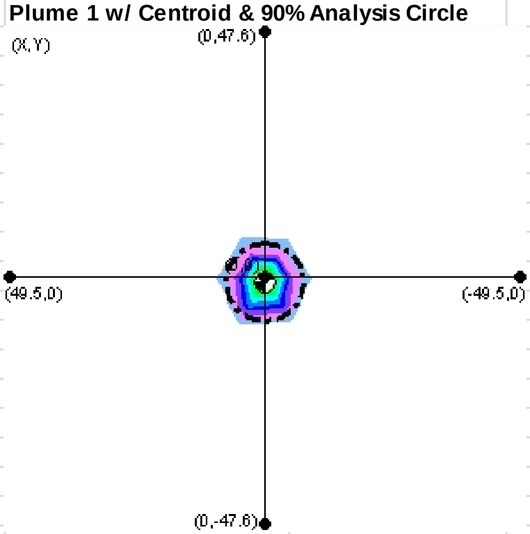


| AK29-008 | |
|---|---|
| Spray Parameters | |
| Injector Height : | 50 mm |
| Connector Angle (θ) : | 0° |
| Fuel Pressure : | 10000 kPa |
| Pulse Width / Period : | 1.5 / 40.0 ms |
| # of Pulses : | 455 |
| Captured Volume : | 1.5 ml |
| **Plume 1** | |
| Diameter : | 16.1 mm @ 90% |
| Cone Angle α : | 18.3° @ 90% |
| 50% Mass Diameter : | 9.9 mm |
| 50% Cone Angle : | 11.3° |
| Bend (Skew) Angle (β) : | 0.3° |
| Centroid Location (x,y)* : | (0.0 mm, -0.3 mm) |
| Centroid Location (r,θ)* : | (0.3 mm, 279.2°) |

**Plume 1 w/ Centroid & 90% Analysis Circle**

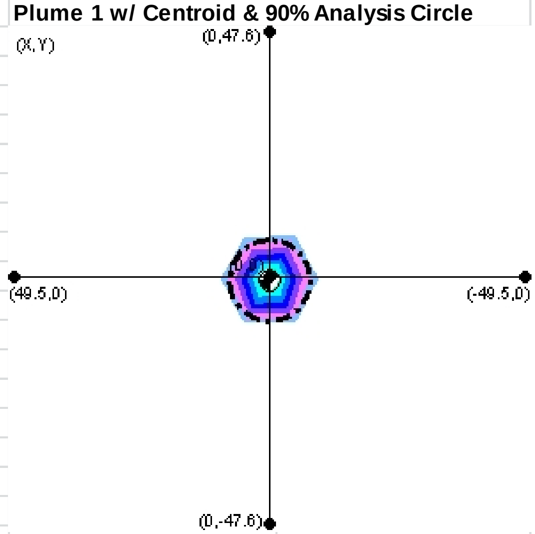

| AK29-009 | |
| --- | --- |
| Spray Parameters | |
| Injector Height : | 50 mm |
| Connector Angle (θ) : | 0° |
| Fuel Pressure : | 10000 kPa |
| Pulse Width / Period : | 1.5 / 40.0 ms |
| # of Pulses : | 458 |
| Captured Volume : | 1.7 ml |
| **Plume 1** | |
| Diameter : | 19.0 mm @ 90% |
| Cone Angle α : | 21.5° @ 90% |
| 50% Mass Diameter : | 11.1 mm |
| 50% Cone Angle : | 12.7° |
| Bend (Skew) Angle (β) : | 1.1° |
| Centroid Location (x,y)* : | (0.4 mm, 0.9 mm) |
| Centroid Location (r,θ)* : | (1.0 mm, 65.7°) |

**Plume 1 w/ Centroid & 90% Analysis Circle**

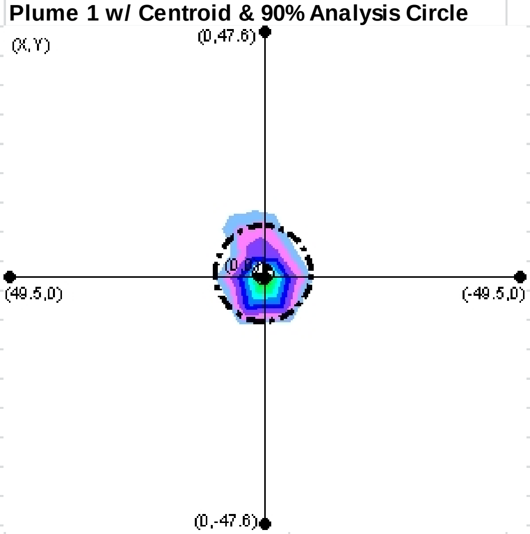


| AK29-010 | |
| --- | --- |
| Spray Parameters | |
| Injector Height : | 50 mm |
| Connector Angle (θ) : | 0° |
| Fuel Pressure : | 10000 kPa |
| Pulse Width / Period : | 1.5 / 40.0 ms |
| # of Pulses : | 305 |
| Captured Volume : | 1.2 ml |
| **Plume 1** | |
| Diameter : | 15.9 mm @ 90% |
| Cone Angle α : | 18.1° @ 90% |
| 50% Mass Diameter : | 9.4 mm |
| 50% Cone Angle : | 10.8° |
| Bend (Skew) Angle (β) : | 0.4° |
| Centroid Location (x,y)* : | (0.0 mm, -0.3 mm) |
| Centroid Location (r,θ)* : | (0.3 mm, 261.7°) |

**Plume 1 w/ Centroid & 90% Analysis Circle**

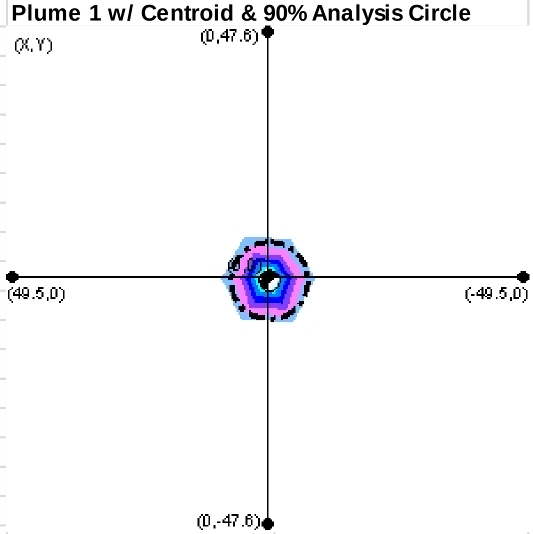

| AK29-011 | |
|---|---|
| Spray Parameters | |
| Injector Height : | 50 mm |
| Connector Angle (θ) : | 0° |
| Fuel Pressure : | 10000 kPa |
| Pulse Width / Period : | 1.5 / 40.0 ms |
| # of Pulses : | 588 |
| Captured Volume : | 2.3 ml |
| **Plume 1** | |
| Diameter : | 18.1 mm @ 90% |
| Cone Angle α : | 17.6° @ 90% |
| 50% Mass Diameter : | 10.1 mm |
| 50% Cone Angle : | 9.9° |
| Bend (Skew) Angle (β) : | 31.4° |
| Centroid Location (x,y)* : | (-30.5 mm, 0.8 mm) |
| Centroid Location (r,θ)* : | (30.5 mm, 178.4°) |

**Plume 1 w/ Centroid & 90% Analysis Circle**

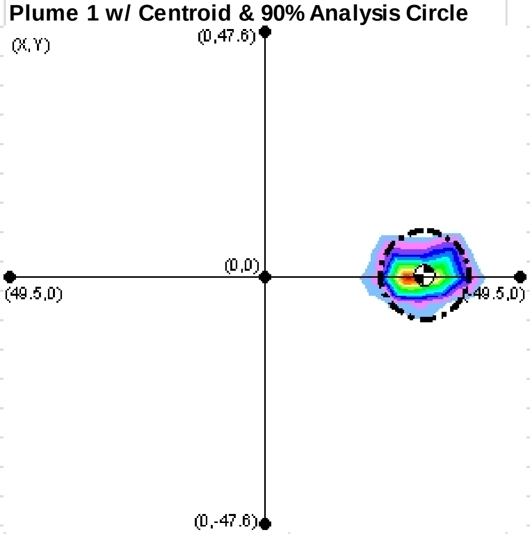


| AK29-012 | |
|---|---|
| Spray Parameters | |
| Injector Height : | 50 mm |
| Connector Angle (θ) : | 0° |
| Fuel Pressure : | 10000 kPa |
| Pulse Width / Period : | 1.5 / 40.0 ms |
| # of Pulses : | 770 |
| Captured Volume : | 3.2 ml |
| **Plume 1** | |
| Diameter : | 19.6 mm @ 90% |
| Cone Angle α : | 18.9° @ 90% |
| 50% Mass Diameter : | 11.4 mm |
| 50% Cone Angle : | 11.1° |
| Bend (Skew) Angle (β) : | 32.1° |
| Centroid Location (x,y)* : | (-31.3 mm, 2.3 mm) |
| Centroid Location (r,θ)* : | (31.4 mm, 175.7°) |

**Plume 1 w/ Centroid & 90% Analysis Circle**

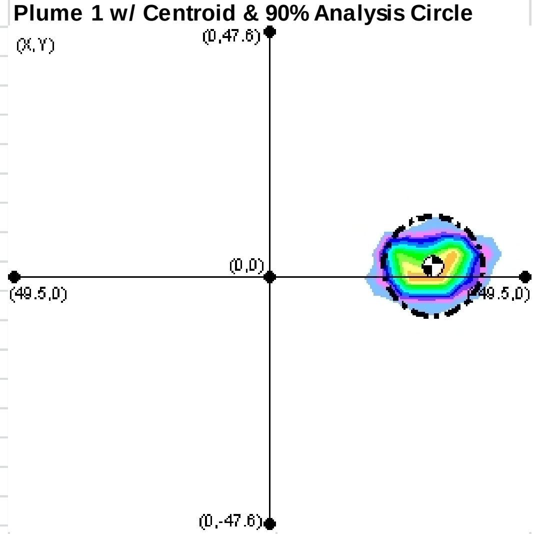

| AK29-013 | |
|---|---|
| **Spray Parameters** | |
| Injector Height : | 50 mm |
| Connector Angle (θ) : | 0° |
| Fuel Pressure : | 10000 kPa |
| Pulse Width / Period : | 1.5 / 40.0 ms |
| # of Pulses : | 375 |
| Captured Volume : | 1.3 ml |
| **Plume 1** | |
| Diameter : | 15.9 mm @ 90% |
| Cone Angle α : | 18.1° @ 90% |
| 50% Mass Diameter : | 9.4 mm |
| 50% Cone Angle : | 10.7° |
| Bend (Skew) Angle (β) : | 0.6° |
| Centroid Location (x,y)* : | (0.0 mm, -0.5 mm) |
| Centroid Location (r,θ)* : | (0.5 mm, 270.4°) |

**Plume 1 w/ Centroid & 90% Analysis Circle**

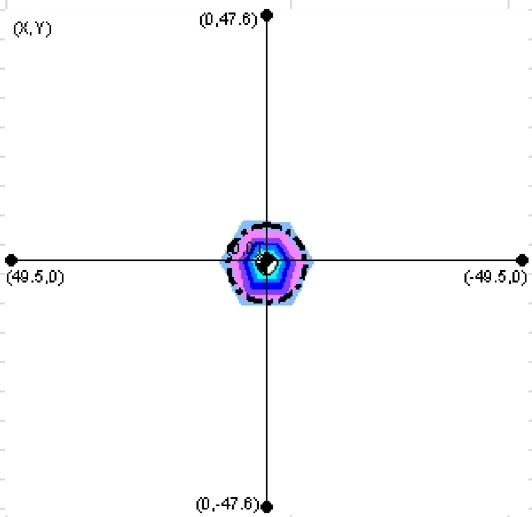


| AK29-014 | |
|---|---|
| **Spray Parameters** | |
| Injector Height : | 50 mm |
| Connector Angle (θ) : | 0° |
| Fuel Pressure : | 10000 kPa |
| Pulse Width / Period : | 1.5 / 40.0 ms |
| # of Pulses : | 275 |
| Captured Volume : | 1.1 ml |
| **Plume 1** | |
| Diameter : | 15.8 mm @ 90% |
| Cone Angle α : | 18.0° @ 90% |
| 50% Mass Diameter : | 9.2 mm |
| 50% Cone Angle : | 10.5° |
| Bend (Skew) Angle (β) : | 0.6° |
| Centroid Location (x,y)* : | (0.0 mm, -0.6 mm) |
| Centroid Location (r,θ)* : | (0.6 mm, 269.6°) |

**Plume 1 w/ Centroid & 90% Analysis Circle**

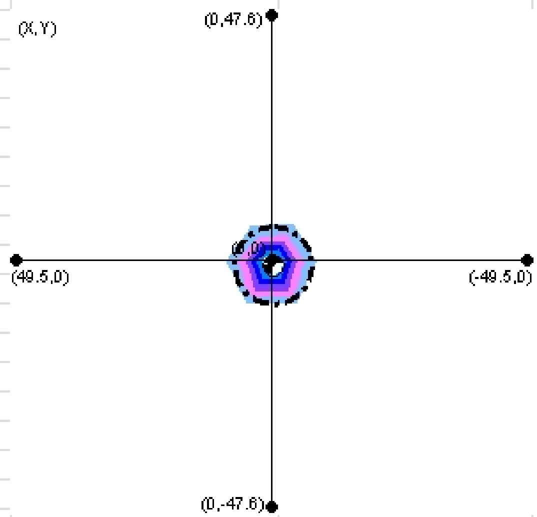

| AK29-15 | | AK29-16 | |
|---|---|---|---|
| Spray Parameters | | Spray Parameters | |
| Injector Height : | 50 mm | Injector Height : | 50 mm |
| Connector Angle (θ) : | 0° | Connector Angle (θ) : | 0° |
| Fuel Pressure : | 10000 kPa | Fuel Pressure : | 10000 kPa |
| Pulse Width / Period : | 1.5 / 40.0 ms | Pulse Width / Period : | 1.5 / 40.0 ms |
| # of Pulses : | 413 | # of Pulses : | 375 |
| Captured Volume : | 1.9 ml | Captured Volume : | 1.7 ml |
| **Plume 1** | | **Plume 1** | |
| Diameter : | 14.8 mm @ 90% | Diameter : | 15.1 mm @ 90% |
| Cone Angle α : | 14.7° @ 90% | Cone Angle α : | 14.4° @ 90% |
| 50% Mass Diameter : | 8.6 mm | 50% Mass Diameter : | 8.5 mm |
| 50% Cone Angle : | 8.6° | 50% Cone Angle : | 8.2° |
| Bend (Skew) Angle (β) : | 29.6° | Bend (Skew) Angle (β) : | 32.8° |
| Centroid Location (x,y)* : | (-28.2 mm, 2.6 mm) | Centroid Location (x,y)* : | (-32.1 mm, 2.2 mm) |
| Centroid Location (r,θ)* : | (28.4 mm, 174.6°) | Centroid Location (r,θ)* : | (32.2 mm, 176.0°) |

**Plume 1 w/ Centroid & 90% Analysis Circle**

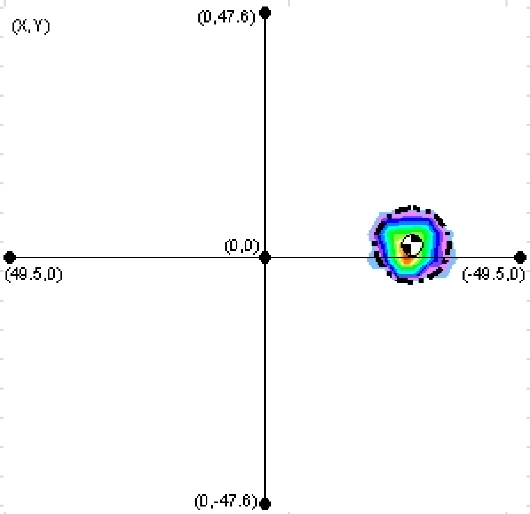


**Plume 1 w/ Centroid & 90% Analysis Circle**

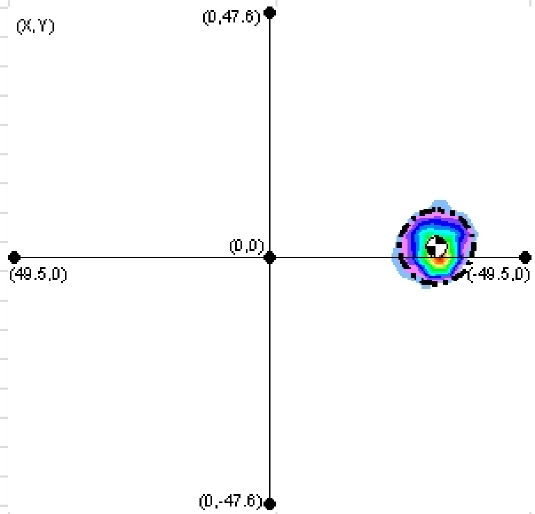

| AK29-17 | |
|---|---|
| Spray Parameters | |
| Injector Height : | 50 mm |
| Connector Angle (θ) : | 0° |
| Fuel Pressure : | 10000 kPa |
| Pulse Width / Period : | 1.5 / 40.0 ms |
| # of Pulses : | 938 |
| Captured Volume : | 2.7 ml |
| **Plume 1** | |
| Diameter : | 21.2 mm @ 90% |
| Cone Angle α : | 23.3° @ 90% |
| 50% Mass Diameter : | 12.6 mm |
| 50% Cone Angle : | 13.9° |
| Bend (Skew) Angle (β) : | 13.6° |
| Centroid Location (x,y)* : | (-12.0 mm, 0.9 mm) |
| Centroid Location (r,θ)* : | (12.1 mm, 175.5°) |

**Plume 1 w/ Centroid & 90% Analysis Circle**

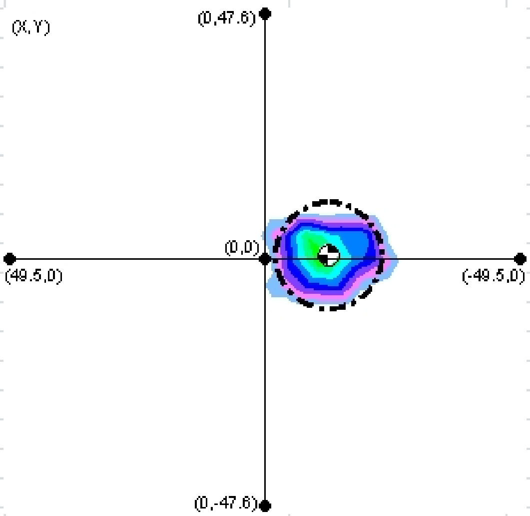


| AK29-18 | |
|---|---|
| Spray Parameters | |
| Injector Height : | 50 mm |
| Connector Angle (θ) : | 0° |
| Fuel Pressure : | 10000 kPa |
| Pulse Width / Period : | 1.5 / 40.0 ms |
| # of Pulses : | 848 |
| Captured Volume : | 2.6 ml |
| **Plume 1** | |
| Diameter : | 20.0 mm @ 90% |
| Cone Angle α : | 21.9° @ 90% |
| 50% Mass Diameter : | 12.6 mm |
| 50% Cone Angle : | 13.9° |
| Bend (Skew) Angle (β) : | 15.2° |
| Centroid Location (x,y)* : | (-13.5 mm, 0.9 mm) |
| Centroid Location (r,θ)* : | (13.6 mm, 176.1°) |

**Plume 1 w/ Centroid & 90% Analysis Circle**

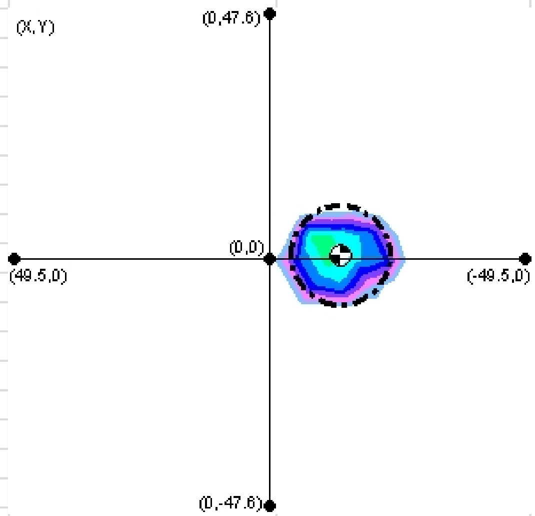

| AK29-19 | |
|---|---|
| Spray Parameters | |
| Injector Height : | 50 mm |
| Connector Angle (θ) : | 0° |
| Fuel Pressure : | 10000 kPa |
| Pulse Width / Period : | 1.5 / 40.0 ms |
| # of Pulses : | 315 |
| Captured Volume : | 1.3 ml |
| **Plume 1** | |
| Diameter : | 17.0 mm @ 90% |
| Cone Angle α : | 17.6° @ 90% |
| 50% Mass Diameter : | 9.5 mm |
| 50% Cone Angle : | 9.8° |
| Bend (Skew) Angle (β) : | 24.4° |
| Centroid Location (x,y)* : | (-22.5 mm, 3.1 mm) |
| Centroid Location (r,θ)* : | (22.7 mm, 172.3°) |

**Plume 1 w/ Centroid & 90% Analysis Circle**

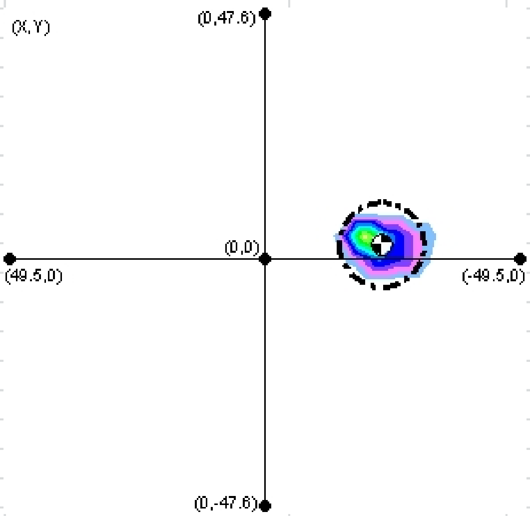


| AK29-20 | |
|---|---|
| Spray Parameters | |
| Injector Height : | 50 mm |
| Connector Angle (θ) : | 0° |
| Fuel Pressure : | 10000 kPa |
| Pulse Width / Period : | 1.5 / 40.0 ms |
| # of Pulses : | 435 |
| Captured Volume : | 1.6 ml |
| **Plume 1** | |
| Diameter : | 17.6 mm @ 90% |
| Cone Angle α : | 18.1° @ 90% |
| 50% Mass Diameter : | 9.8 mm |
| 50% Cone Angle : | 10.2° |
| Bend (Skew) Angle (β) : | 24.8° |
| Centroid Location (x,y)* : | (-23.0 mm, 2.1 mm) |
| Centroid Location (r,θ)* : | (23.1 mm, 174.8°) |

**Plume 1 w/ Centroid & 90% Analysis Circle**

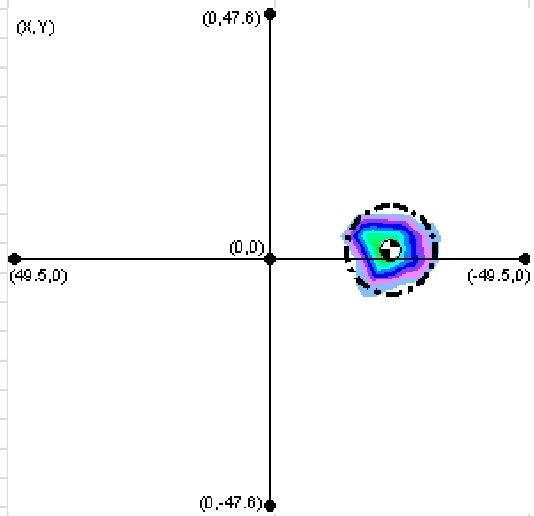

| AK29-21 | |
|---|---|
| Spray Parameters | |
| Injector Height : | 50 mm |
| Connector Angle (θ) : | 0° |
| Fuel Pressure : | 10000 kPa |
| Pulse Width / Period : | 1.5 / 40.0 ms |
| # of Pulses : | 688 |
| Captured Volume : | 2.9 ml |
| **Plume 1** | |
| Diameter : | 20.2 mm @ 90% |
| Cone Angle α : | 19.5° @ 90% |
| 50% Mass Diameter : | 11.5 mm |
| 50% Cone Angle : | 11.2° |
| Bend (Skew) Angle (β) : | 31.6° |
| Centroid Location (x,y)* : | (-30.8 mm, 1.2 mm) |
| Centroid Location (r,θ)* : | (30.8 mm, 177.8°) |

**Plume 1 w/ Centroid & 90% Analysis Circle**

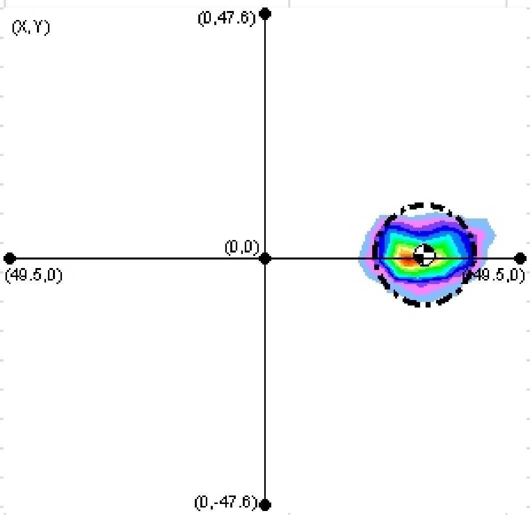


| AK29-22 | |
|---|---|
| Spray Parameters | |
| Injector Height : | 50 mm |
| Connector Angle (θ) : | 0° |
| Fuel Pressure : | 10000 kPa |
| Pulse Width / Period : | 1.5 / 40.0 ms |
| # of Pulses : | 650 |
| Captured Volume : | 2.7 ml |
| **Plume 1** | |
| Diameter : | 20.9 mm @ 90% |
| Cone Angle α : | 20.1° @ 90% |
| 50% Mass Diameter : | 11.7 mm |
| 50% Cone Angle : | 11.4° |
| Bend (Skew) Angle (β) : | 31.7° |
| Centroid Location (x,y)* : | (-30.9 mm, 1.1 mm) |
| Centroid Location (r,θ)* : | (30.9 mm, 178.0°) |

**Plume 1 w/ Centroid & 90% Analysis Circle**

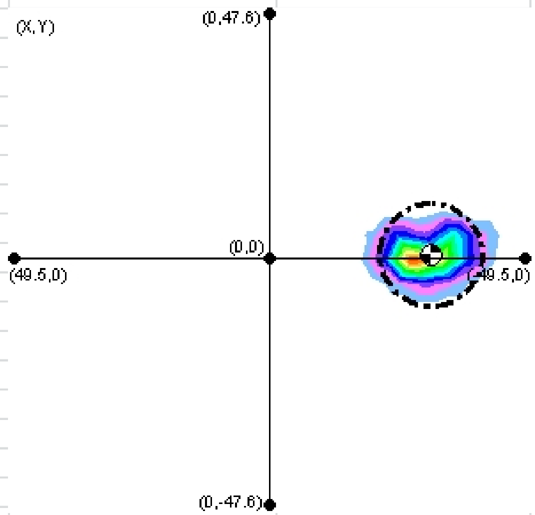

| | |
|---|---|
| AK29-23 | |
| Spray Parameters | |
| Injector Height : | 50 mm |
| Connector Angle (θ) : | 0° |
| Fuel Pressure : | 10000 kPa |
| Pulse Width / Period : | 1.5 / 40.0 ms |
| # of Pulses : | 383 |
| Captured Volume : | 4.3 ml |
| **Plume 1** | |
| Diameter : | 23.1 mm @ 90% |
| Cone Angle α : | 26.0° @ 90% |
| 50% Mass Diameter : | 14.1 mm |
| 50% Cone Angle : | 16.0° |
| Bend (Skew) Angle (β) : | 1.2° |
| Centroid Location (x,y)* : | (0.2 mm, 1.0 mm) |
| Centroid Location (r,θ)* : | (1.0 mm, 78.3°) |

Likely the 3 plumes have coallesced into 1.

**Plume 1 w/ Centroid & 90% Analysis Circle**

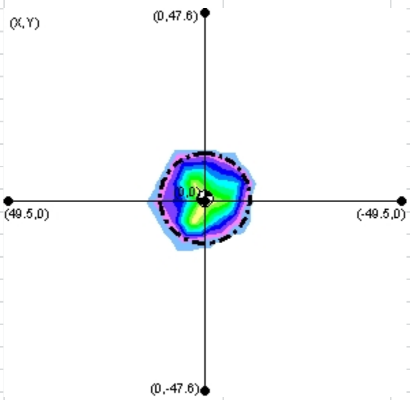

AK29-24

**Spray Parameters**

| | |
|---|---|
| Injector Height : | 50 mm |
| Connector Angle (θ) : | 0° |
| Fuel Pressure : | 10000 kPa |
| Pulse Width / Period : | 1.5 / 40.0 ms |
| # of Pulses : | 543 |
| Captured Volume : | 5.4 ml |
| **Spray** | |
| Diameter : | 43.3 mm @ 90% |
| Cone Angle α : | 46.8° @ 90% |
| 50% Mass Diameter : | 31.7 mm |
| 50% Cone Angle : | 35.2° |
| Bend (Skew) Angle (β) : | 1.2° |
| Centroid Location (x,y)* : | (0.4 mm, 1.0 mm) |
| Centroid Location (r,θ)* : | (1.1 mm, 66.9°) |

**Plume 1 w/ Centroid & 90% Analysis Circle**

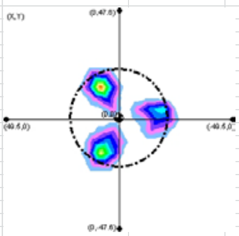

AK29-24

**Spray Parameters**

| | |
|---|---|
| Injector Height : | 50 mm |
| Connector Angle (θ) : | 0° |
| Fuel Pressure : | 10000 kPa |
| Pulse Width / Period : | 1.5 / 40.0 ms |
| # of Pulses : | 543 |
| Captured Volume : | 5.4 ml |
| **Plume 1** | |
| Diameter : | 19.4 mm @ 90% |
| Cone Angle α : | 20.9° @ 90% |
| 50% Mass Diameter : | 11.4 mm |
| 50% Cone Angle : | 12.4° |
| Bend (Skew) Angle (β) : | 17.8° |
| Mass % : | 28.7 |
| Centroid Location (x,y)* : | (-15.9 mm, 1.9 mm) |
| Centroid Location (r,θ)* : | (16.1 mm, 173.3°) |

**Plume 1 w/ Centroid & 90% Analysis Circle**

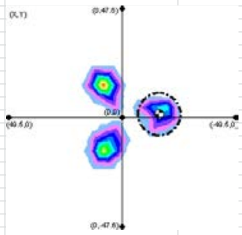

**Spray Parameters**

| | |
|---|---|
| **Plume 2** | |
| Diameter : | 18.3 mm @ 90% |
| Cone Angle α : | 19.8° @ 90% |
| 50% Mass Diameter : | 10.2 mm |
| 50% Cone Angle : | 11.1° |
| Bend (Skew) Angle (β) : | 17.1° |
| Mass % : | 35.8 |
| Centroid Location (x,y)* : | (7.4 mm, 13.5 mm) |
| Centroid Location (r,θ)* : | (15.4 mm, 61.0°) |

**Plume 2 w/ Centroid & 90% Analysis Circle**

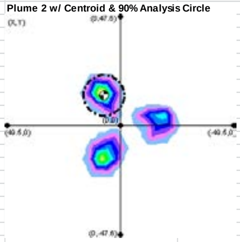

AK29-25

**Spray Parameters**

| | |
|---|---|
| Injector Height : | 50 mm |
| Connector Angle (θ) : | 0° |
| Fuel Pressure : | 10000 kPa |
| Pulse Width / Period : | 1.5 / 40.0 ms |
| # of Pulses : | 613 |
| Captured Volume : | 5.5 ml |
| **Spray** | |
| Diameter : | 42.7 mm @ 90% |
| Cone Angle α : | 46.2° @ 90% |
| 50% Mass Diameter : | 30.7 mm |
| 50% Cone Angle : | 34.1° |
| Bend (Skew) Angle (β) : | 1.7° |
| Centroid Location (x,y)* : | (0.6 mm, 1.3 mm) |
| Centroid Location (r,θ)* : | (1.5 mm, 65.2°) |

**Plume 1 w/ Centroid & 90% Analysis Circle**

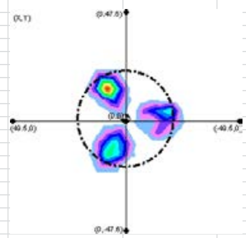

AK29-25

**Spray Parameters**

| | |
|---|---|
| Injector Height : | 50 mm |
| Connector Angle (θ) : | 0° |
| Fuel Pressure : | 10000 kPa |
| Pulse Width / Period : | 1.5 / 40.0 ms |
| # of Pulses : | 613 |
| Captured Volume : | 5.5 ml |
| **Plume 1** | |
| Diameter : | 19.9 mm @ 90% |
| Cone Angle α : | 21.5° @ 90% |
| 50% Mass Diameter : | 12.3 mm |
| 50% Cone Angle : | 13.4° |
| Bend (Skew) Angle (β) : | 17.0° |
| Mass % : | 27.6 |
| Centroid Location (x,y)* : | (-15.2 mm, 1.9 mm) |
| Centroid Location (r,θ)* : | (15.3 mm, 172.8°) |

**Plume 1 w/ Centroid & 90% Analysis Circle**

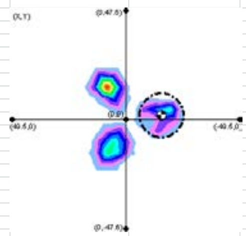

| | |
|---|---|
| **Plume 2** | |
| Diameter : | 18.0 mm @ 90% |
| Cone Angle α : | 19.5° @ 90% |
| 50% Mass Diameter : | 9.9 mm |
| 50% Cone Angle : | 10.9° |
| Bend (Skew) Angle (β) : | 17.3° |
| Mass % : | 36.5 |
| Centroid Location (x,y)* : | (7.4 mm, 13.7 mm) |
| Centroid Location (r,θ)* : | (15.5 mm, 61.6°) |

**Plume 2 w/ Centroid & 90% Analysis Circle**

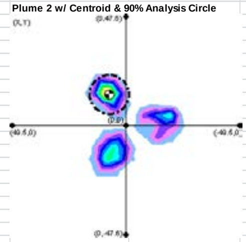

| AK29-001 | |
|---|---|
| **Spray Parameters** | |
| Injector Height : | 50 mm |
| Connector Angle (θ) : | 0° |
| Fuel Pressure : | 10000 kPa |
| Pulse Width / Period : | 1.5 / 40.0 ms |
| # of Pulses : | 793 |
| Captured Volume : | 7.4 ml |
| **Spray** | |
| Diameter : | 72.9 mm @ 90% |
| Cone Angle α : | 72.1° @ 90% |
| 50% Mass Diameter : | 61.0 mm |
| 50% Cone Angle : | 62.8° |
| Bend (Skew) Angle (β) : | 1.8° |
| Centroid Location (x,y)* : | (-1.5 mm, 0.5 mm) |
| Centroid Location (r,θ)* : | (1.6 mm, 161.9°) |

**Plume 1 w/ Centroid & 90% Analysis Circle**

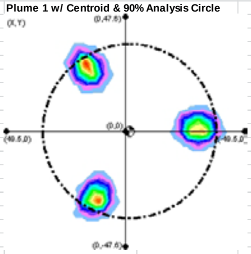

| AK29-001 | |
|---|---|
| **Spray Parameters** | |
| Injector Height : | 50 mm |
| Connector Angle (θ) : | 0° |
| Fuel Pressure : | 10000 kPa |
| Pulse Width / Period : | 1.5 / 40.0 ms |
| # of Pulses : | 793 |
| Captured Volume : | 7.4 ml |
| **Plume 1** | |
| Diameter : | 18.6 mm @ 90% |
| Cone Angle α : | 18.1° @ 90% |
| 50% Mass Diameter : | 10.6 mm |
| 50% Cone Angle : | 10.3° |
| Bend (Skew) Angle (β) : | 31.2° |
| Mass % : | 35.0 |
| Centroid Location (x,y)* : | (-30.3 mm, 1.6 mm) |
| Centroid Location (r,θ)* : | (30.3 mm, 177.0°) |

**Plume 1 w/ Centroid & 90% Analysis Circle**

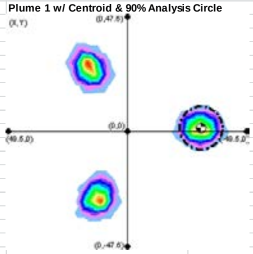

| Spray Parameters | |
|---|---|
| **Plume 2** | |
| Diameter : | 17.9 mm @ 90% |
| Cone Angle α : | 17.3° @ 90% |
| 50% Mass Diameter : | 10.0 mm |
| 50% Cone Angle : | 9.7° |
| Bend (Skew) Angle (β) : | 31.5° |
| Mass % : | 32.8 |
| Centroid Location (x,y)* : | (15.6 mm, 26.3 mm) |
| Centroid Location (r,θ)* : | (30.6 mm, 59.3°) |

**Plume 2 w/ Centroid & 90% Analysis Circle**

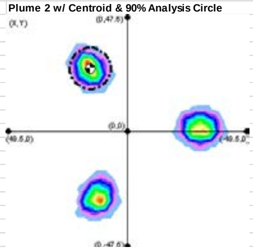

| AK29-002 | |
|---|---|
| **Spray Parameters** | |
| Injector Height : | 50 mm |
| Connector Angle (θ) : | 0° |
| Fuel Pressure : | 10000 kPa |
| Pulse Width / Period : | 1.5 / 40.0 ms |
| # of Pulses : | 898 |
| Captured Volume : | 7.8 ml |
| **Spray** | |
| Diameter : | 74.2 mm @ 90% |
| Cone Angle α : | 73.1° @ 90% |
| 50% Mass Diameter : | 61.1 mm |
| 50% Cone Angle : | 62.8° |
| Bend (Skew) Angle (β) : | 2.4° |
| Centroid Location (x,y)* : | (-1.7 mm, 1.3 mm) |
| Centroid Location (r,θ)* : | (2.1 mm, 141.9°) |

**Plume 1 w/ Centroid & 90% Analysis Circle**

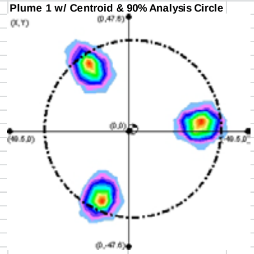

| AK29-002 | |
|---|---|
| **Spray Parameters** | |
| Injector Height : | 50 mm |
| Connector Angle (θ) : | 0° |
| Fuel Pressure : | 10000 kPa |
| Pulse Width / Period : | 1.5 / 40.0 ms |
| # of Pulses : | 898 |
| Captured Volume : | 7.8 ml |
| **Plume 1** | |
| Diameter : | 19.2 mm @ 90% |
| Cone Angle α : | 18.7° @ 90% |
| 50% Mass Diameter : | 10.7 mm |
| 50% Cone Angle : | 10.5° |
| Bend (Skew) Angle (β) : | 31.0° |
| Mass % : | 35.7 |
| Centroid Location (x,y)* : | (-29.9 mm, 3.0 mm) |
| Centroid Location (r,θ)* : | (30.0 mm, 174.2°) |

**Plume 1 w/ Centroid & 90% Analysis Circle**

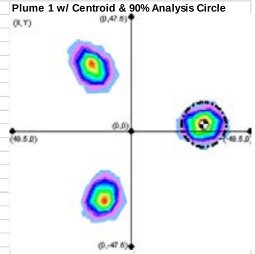

| Spray Parameters | |
|---|---|
| **Plume 2** | |
| Diameter : | 19.6 mm @ 90% |
| Cone Angle α : | 18.8° @ 90% |
| 50% Mass Diameter : | 10.7 mm |
| 50% Cone Angle : | 10.4° |
| Bend (Skew) Angle (β) : | 32.2° |
| Mass % : | 32.6 |
| Centroid Location (x,y)* : | (16.2 mm, 27.0 mm) |
| Centroid Location (r,θ)* : | (31.5 mm, 59.0°) |

**Plume 2 w/ Centroid & 90% Analysis Circle**

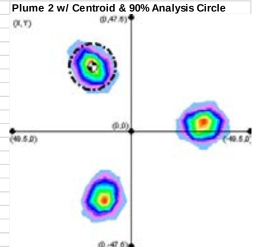

# APPENDIX D PHASE-CONTRAST X-RAY IMAGES

Phase Contrast X-ray images from Argonne testing for single-hole injectors

| Image # | Sequence # | d (mm) | β | l/d | (l+L)/d | D/d | Injection Pressure (Bar) |
|---|---|---|---|---|---|---|---|
| 1 | AK29-2-919 | ≈.20 | 0° | 2.95 | na | na | 75 |
| 2 | AK29-2-920 | ≈.20 | 0° | 2.95 | na | na | 75 |
| 3 | AK29-2-921 | ≈.20 | 0° | 2.95 | na | na | 75 |
| 4 | AK29-2-922 | ≈.15 | 0° | 3.96 | na | na | 75 |
| 5 | AK29-2-923 | ≈.15 | 0° | 3.96 | na | na | 75 |
| 6 | AK29-2-924 | ≈.15 | 0° | 3.96 | na | na | 75 |
| 7 | Start & end of Injection | | | | | | 75 |
| 8 | Varying Inj Pressure | | | | | Varying View angles | 25,50,75 |
| 9 | Needle motion | | | | | | 25,50,75 |

## Current Geometry Matrix (7'11):

Single-Hole Injectors : only two types, three each, **no counter-bore (L=0)**.

| | SHN2(Long) | SHN5(s-L) |
|---|---|---|
| d(mm) | **≈0.20** | **≈0.15** |
| β | 0° | 0° |
| **l/d** | **2.95** | **3.96** |
| **(l+L)/d** | **2.95** | **3.96** |
| **D/d** | **1.00** | **1.00** |
| **Effects of** | l/d | l/d |
| **# of Holes** | 1 | 1 |

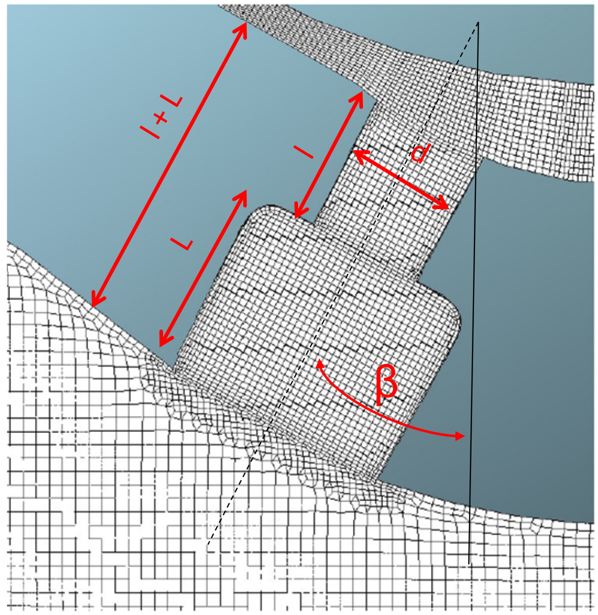


## Current Nozzle Matrix (7'11):

2 types of Single-Hole Injectors : d and l/d, three each, **no counter-bore**.

| **l/d** | | | |
|---|---|---|---|
| **2.95** | **AK29_2_919**<br>SF: 3.121<br>SP: **0.321** | AK29_2_920<br>**SF: 3.26**<br>SP: 0.329 | AK29_2_921<br>SF: **3.072**<br>SP: **0.332** |
| **3.96** | AK29_5_922<br>SF: **1.871**<br>SP: **0.248** (15%) | **AK29_5_923**<br>SF: 1.873<br>SP: 0.208 (15%) | AK29_5_924<br>SF: **1.92**<br>SP: **0.199** |

**NOTES:**

- **SF** is the Static flow of the injector is 3.121 grams/sec, at calibration point (10 Mpa, with stoddard solvent).
- **SP** is the dynamic flow (at calibration point) is 0.321 grams/sec of fuel with 1.0 msec pulse-width.

**Spray Structure:**

**l/d~3**

**Pinj=75 bar; Δt~0.1ms**

**AK29_2_919**

| | SHN2(Long) |
|---|---|
| β | 0° |
| d | ≈0.20 |
| l/d | 2.95 |
| (l+L)/d | 2.95 |
| D/d | 1.00 |

| | |
|---|---|
| Inj Pressure (bar) | 75 |
| Inj Duration (ms) | 1.00 |
| Time Step (ms) | 0.096 |
| Time Repeat | 10 |
| No. of Positions | 6 |
| Displacement | -9.10 ~ -4.10 |

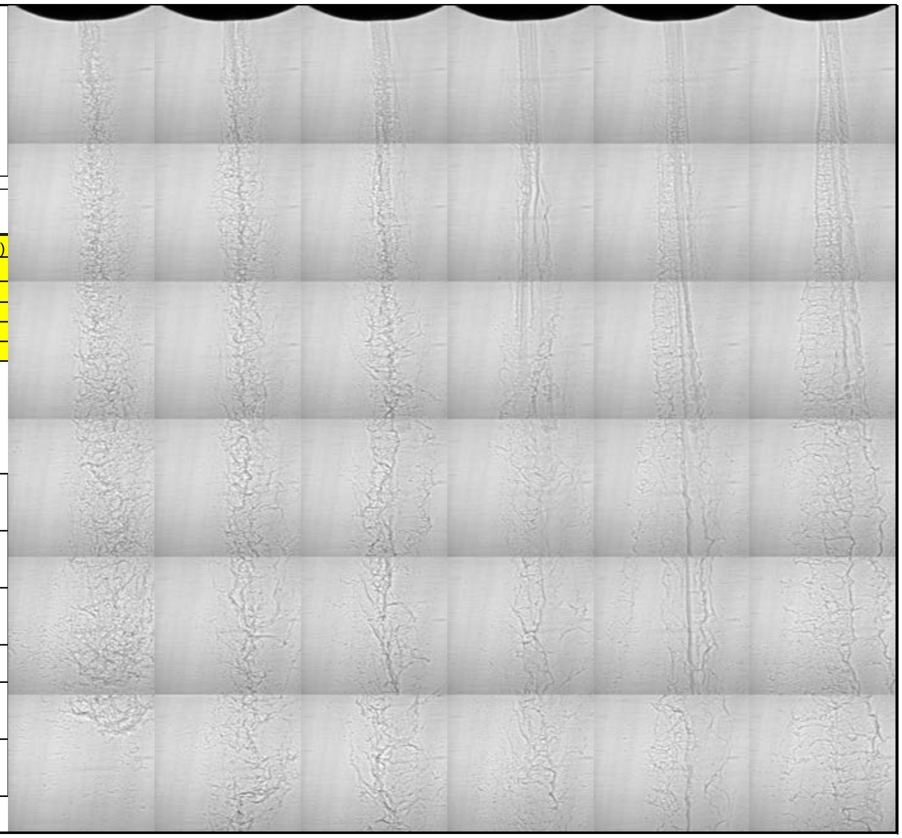

**Spray Structure:**

**l/d~3**

**Pinj=75 bar;**

**Δt~0.1ms**

AK29_2_**920**

| | SHN2(Long) |
|---|---|
| β | 0° |
| d | ≈0.20 |
| l/d | 2.95 |
| (l+L)/d | 2.95 |
| D/d | 1.00 |

| | |
|---|---|
| Inj Pressure (bar) | 75 |
| Inj Duration (ms) | 1.00 |
| Time Step (ms) | 0.096 |
| Time Repeat | 10 |
| No. of Positions | 6 |
| Displ. | -8.82 to -3.82 |

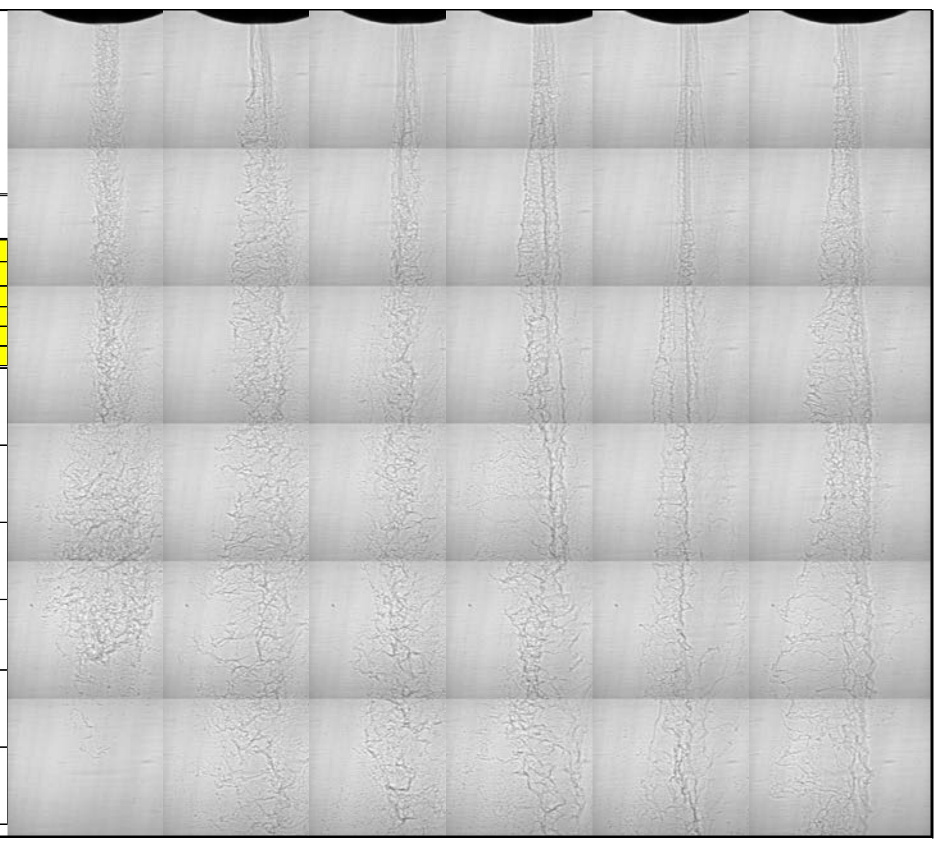

**Spray Structure : l/d~3**

**Pinj=75 bar;**

**Δt~0.1ms**

AK29_2_921

| | SHN2(Long) |
|---|---|
| β | 0° |
| d | ≈0.20 |
| l/d | 2.95 |
| (l+L)/d | 2.95 |
| D/d | 1.00 |

| | |
|---|---|
| Inj. P (bar) | 75 |
| Inj T(ms) | 1.00 |
| Time Step (ms) | 0.096 |
| Time Repeat | 10 |
| No. of Positions | 6 |
| Displ. | -9.10 to -4.10 |

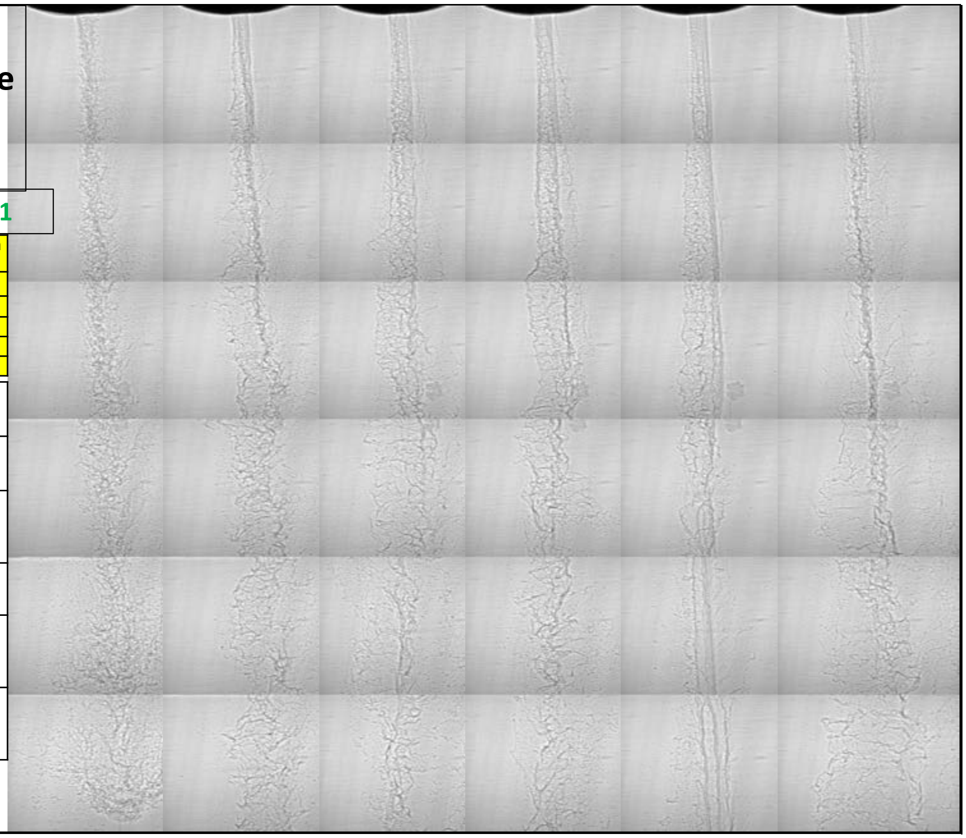

**Spray Structure l/d~4**

**Pinj=75 bar;**

**Δt~0.1ms**

AK29_2_922

| | SHN5(s-L) |
|---|---|
| β | 0° |
| d | ≈0.15 |
| l/d | 3.96 |
| (l+L)/d | 3.96 |
| D/d | 1.00 |

| | |
|---|---|
| Inj P.(bar) | 75 |
| Inj T ms) | 1.00 |
| Time Step (ms) | 0.096 |
| Time Repeat | 10 |
| Positions | 6 |
| Displ. | -8.62 to -3.62 |

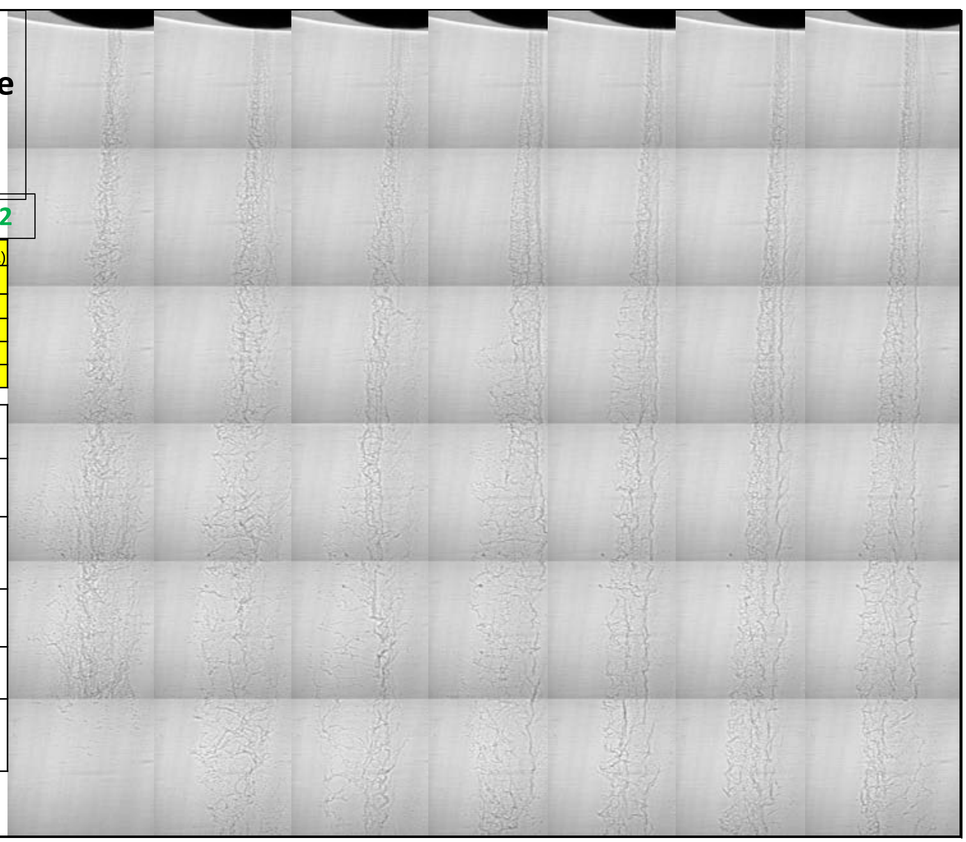

**Spray Structure**
**l/d~4**
**Pinj=75 bar;**
**Δt~0.1ms**

AK29_2_**923**

| | SHN5(s-L) |
|---|---|
| β | 0° |
| d | **≈0.15** |
| **l/d** | **3.96** |
| **(l+L)/d** | **3.96** |
| **D/d** | **1.00** |

| | |
|---|---|
| Inj P.(bar) | **75** |
| Inj T ms) | **1.00** |
| Time Step (ms) | **0.096** |
| Time Repeat | 10 |
| Positions | 6 |
| Displ. | -9.10 to -4.10 |

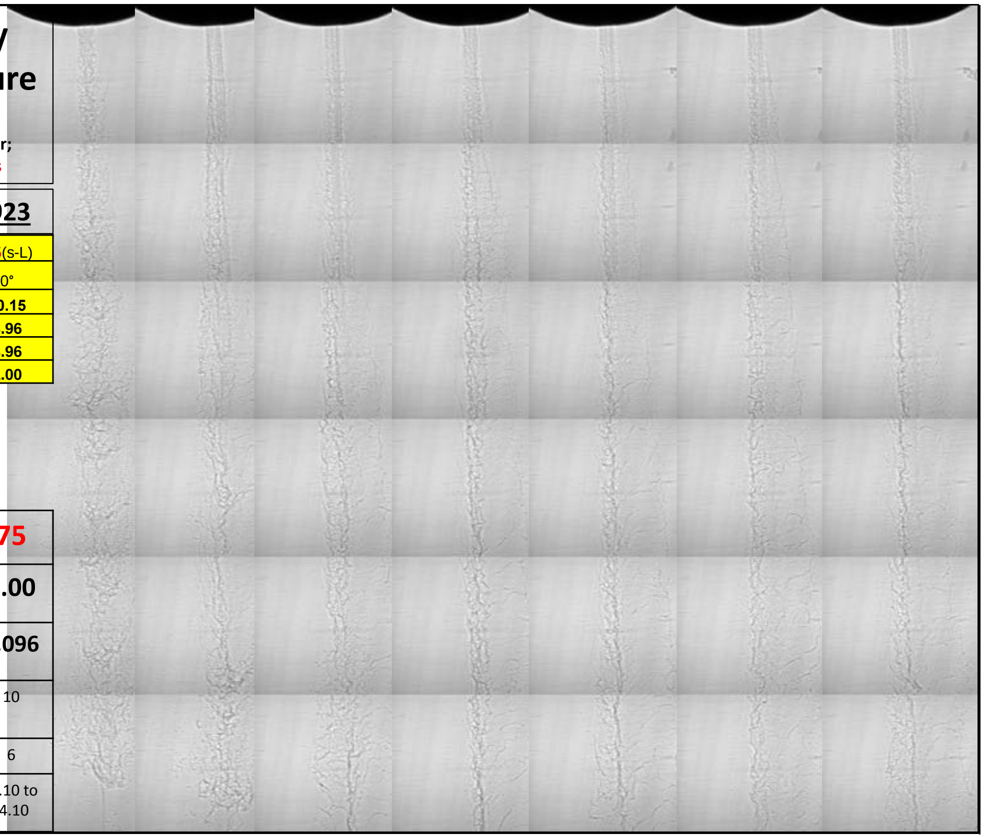

**Spray Structure**
**l/d~4**
**Pinj=75 bar;**
**Δt~0.1ms**

AK29_2_**924**

| | SHN5(s-L) |
|---|---|
| β | 0° |
| d | **≈0.20** |
| **l/d** | **3.96** |
| **(l+L)/d** | **3.96** |
| **D/d** | **1.00** |

| | |
|---|---|
| Inj P.(bar) | **75** |
| Inj T ms) | **1.00** |
| Time Step (ms) | **0.096** |
| Time Repeat | 10 |
| Positions | 6 |
| Displ. | -9.10 to -4.10 |

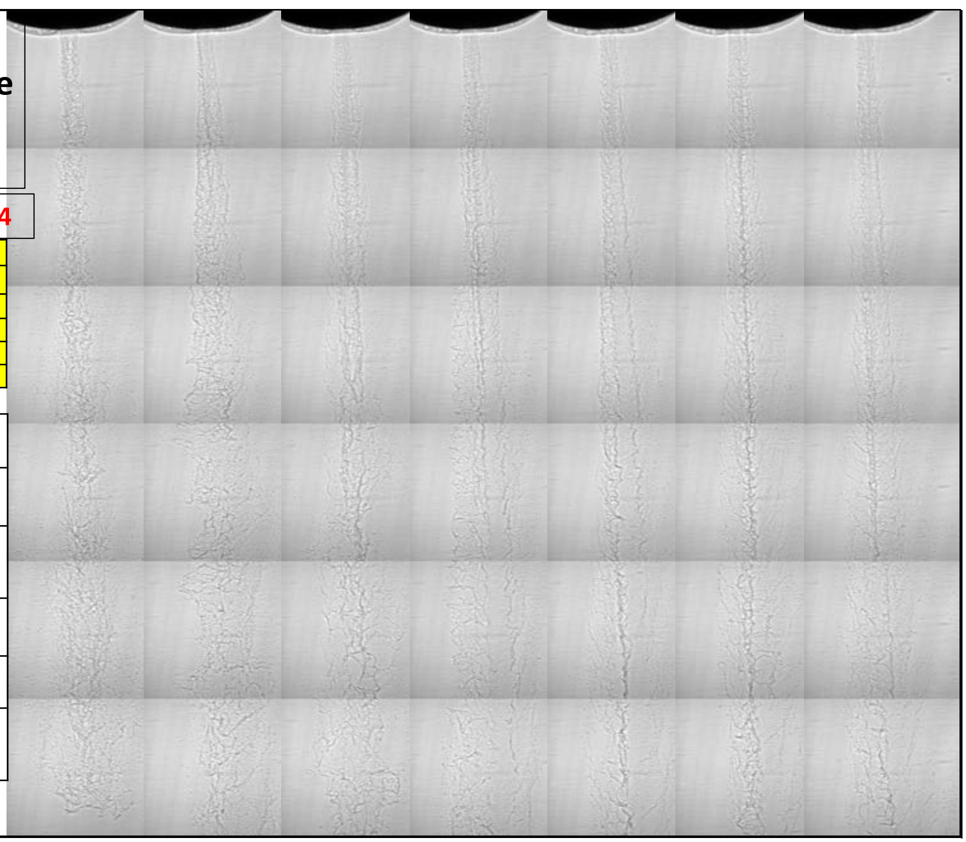

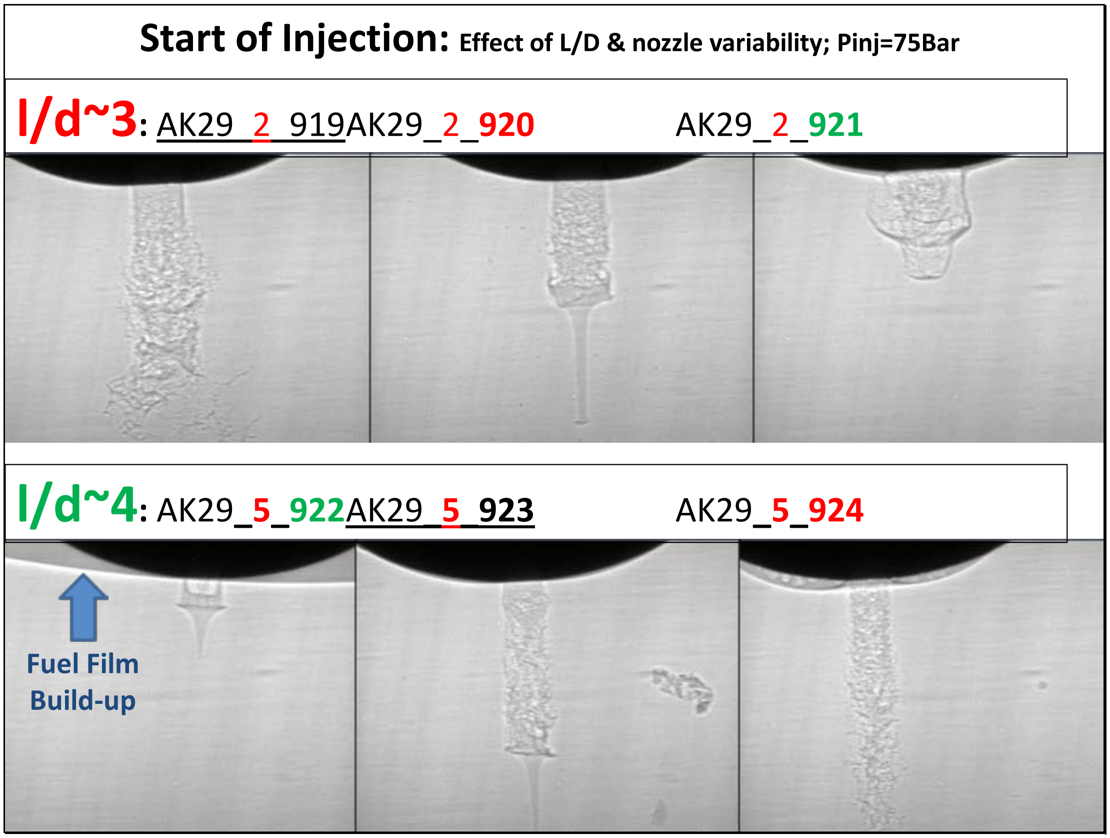
Start of Injection: Effect of L/D & nozzle variability; Pinj=75Bar
l/d~3: AK29_2_919 AK29_2_920 AK29_2_921
l/d~4: AK29_5_922 AK29_5_923 AK29_5_924
Fuel Film Build-up

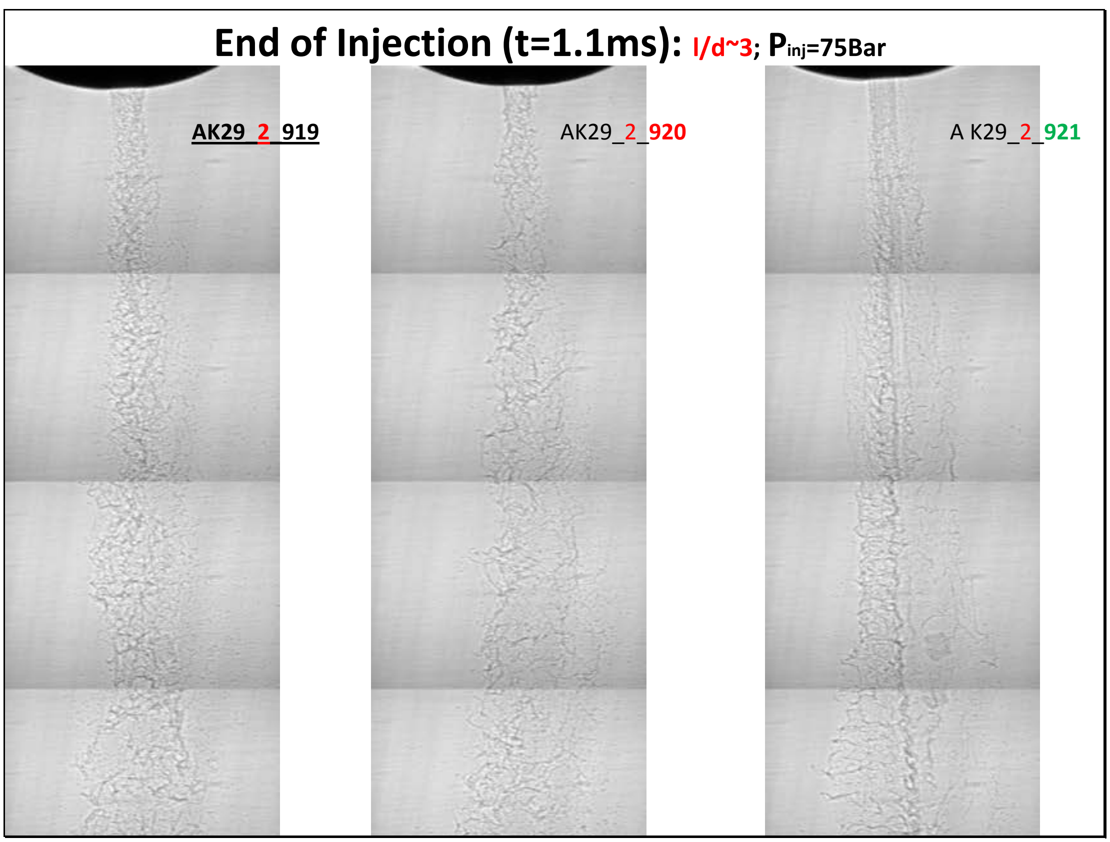
End of Injection (t=1.1ms): l/d~3; Pinj=75Bar
AK29_2_919
AK29_2_920
A K29_2_921

## Effect of Injection Pressure: t=0.62ms,

**$P_{inj}$=25<50<75Bar; l/d~3, #919 <> l/d~4, #923; 25<50<75Bar**

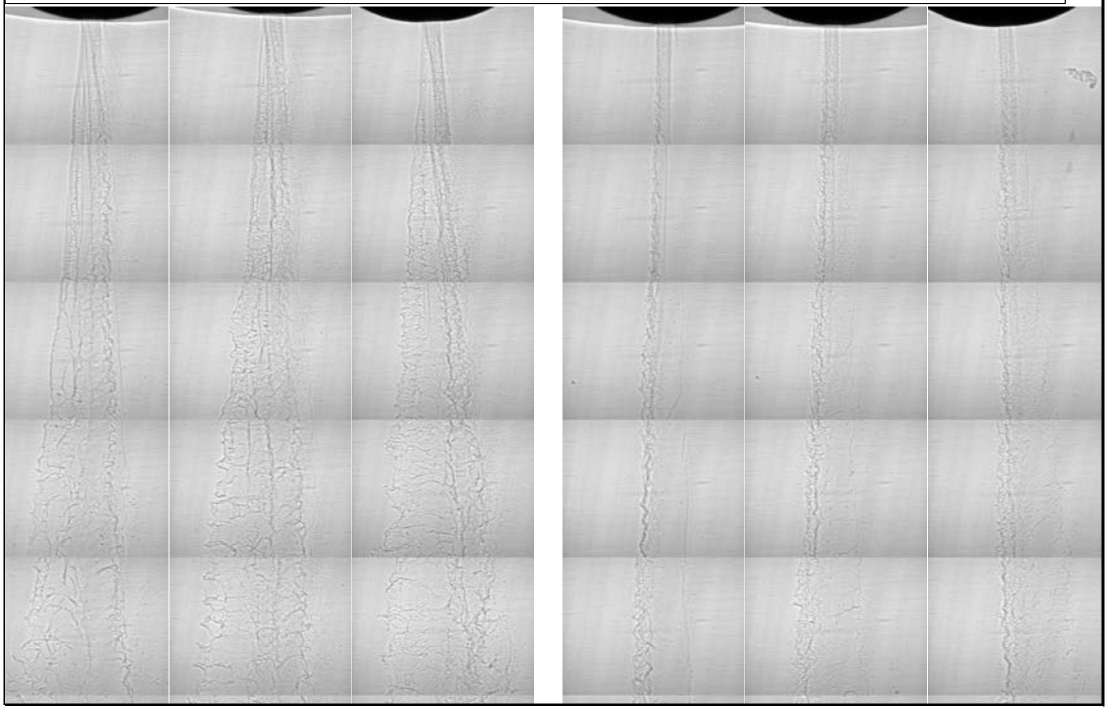

Different View Angle

AK29_2_919
SF: 3.121
SP: 0.321

| | SHN2(Long) |
|---|---|
| β | 0° |
| **l/d** | **2.95** |
| **(l+L)/d** | **2.95** |
| **D/d** | **1.00** |
| **Effects of** | l/d |
| **# of Holes** | 1 |

| | |
|---|---|
| Inj Pressure (bar) | **25** |
| Inj Duration (ms) | 1.00 |
| | (6.680 to 5.480) |
| Time Step (ms) | 0.048 |
| Time Repeat | 10 |
| No. of Positions | 6 |
| Displacement | -7.35 to -2.35 |

position #1

-45deg

-30deg

-15deg

0deg

15deg

30deg

45deg

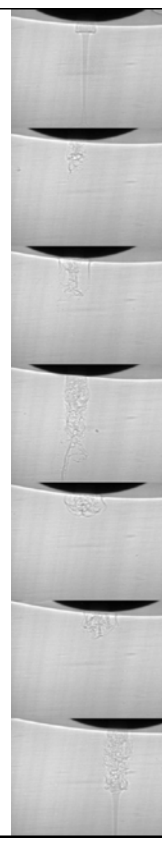

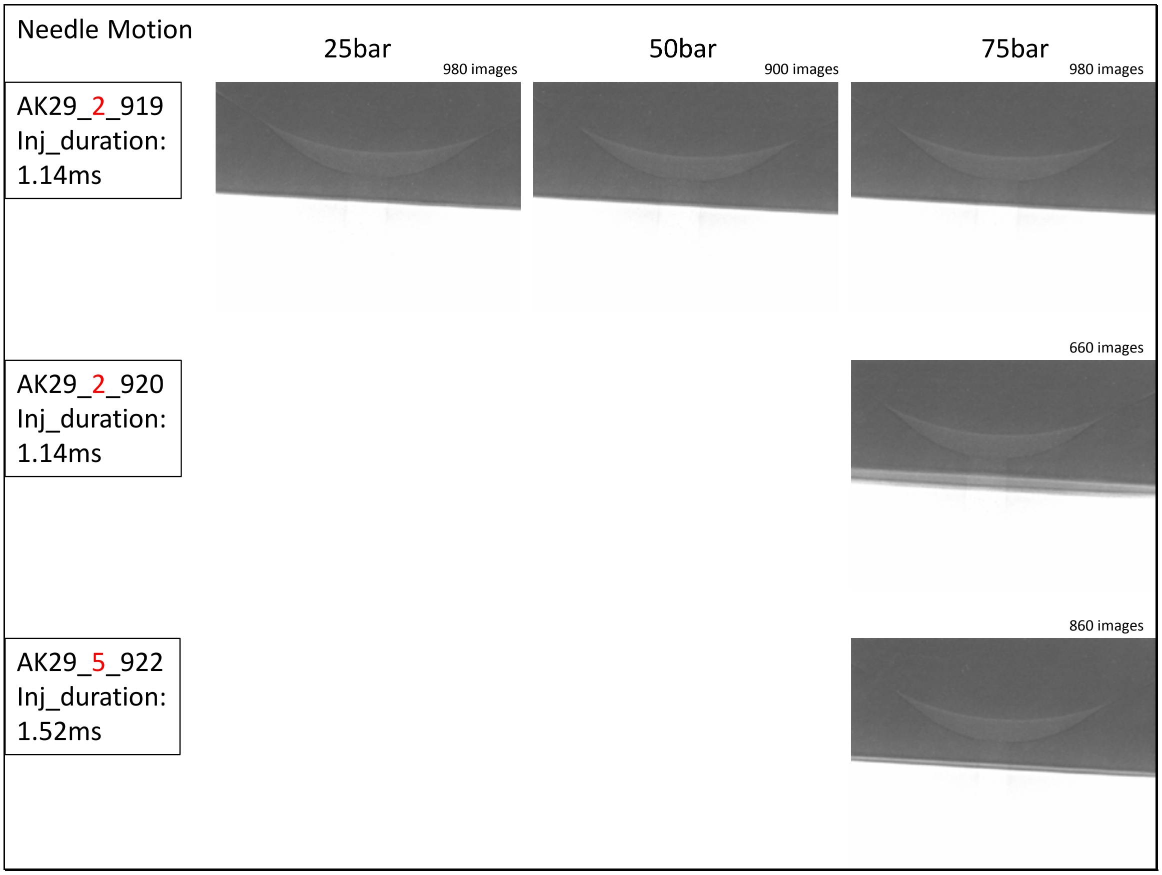
Needle Motion
25bar
980 images
50bar
900 images
75bar
980 images
AK29_2_919
Inj_duration:
1.14ms
660 images
AK29_2_920
Inj_duration:
1.14ms
860 images
AK29_5_922
Inj_duration:
1.52ms

# APPENDIX E SHADOWGRAPH IMAGES

High speed Shadowgraph Images (432 images) of Spray plumes from side view, Luxembourg Spray lab

| Image # | Seat # | d (mm) | β | l/d | (l+L) /d | D/d | Inj. Pres. | View Angle | Shadowgraph Time Images (μs) |
|---|---|---|---|---|---|---|---|---|---|
| 1-6 | AK29-3-001 | ≈.20 | 0° | 1.1 | na | na | 10MPa | 0° | 320,360,400,440,470,520 |
| 7-12 | AK29-3-001 | ≈.20 | 0° | 1.1 | na | na | 10MPa | 0° | 560,600,640,680,720,760 |
| 13-18 | AK29-3-001 | ≈.20 | 0° | 1.1 | na | na | 10MPa | 0° | 800,840,880,920,960,1000 |
| 19-24 | AK29-3-001 | ≈.20 | 0° | 1.1 | na | na | 10MPa | 0° | 1040,1080,1120,1160,1200,1240 |
| 1-6 | AK29-3-001 | ≈.20 | 0° | 1.1 | na | na | 20MPa | 0° | 280,320,360,400,440,480 |
| 7-12 | AK29-3-001 | ≈.20 | 0° | 1.1 | na | na | 20MPa | 0° | 520,560,600,640,680,720 |
| 13-18 | AK29-3-001 | ≈.20 | 0° | 1.1 | na | na | 20MPa | 0° | 760,800,840,880,920,960 |
| 19-24 | AK29-3-001 | ≈.20 | 0° | 1.1 | na | na | 20MPa | 0° | 1000,1040,1080,1120,1160,1200 |
| 1-6 | AK29-3-002 | ≈.20 | 0° | 1.1 | na | na | 10MPa | 0° | 280,320,360,400,440,480 |
| 7-12 | AK29-3-002 | ≈.20 | 0° | 1.1 | na | na | 10MPa | 0° | 520,560,600,640,680,720 |
| 13-18 | AK29-3-002 | ≈.20 | 0° | 1.1 | na | na | 10MPa | 0° | 760,800,840,880,920,960 |
| 19-24 | AK29-3-002 | ≈.20 | 0° | 1.1 | na | na | 10MPa | 0° | 1000,1040,1080,1120,1160,1200 |
| 1-6 | AK29-3-002 | ≈.20 | 0° | 1.1 | na | na | 20MPa | 0° | 280,320,360,400,440,480 |
| 7-12 | AK29-3-002 | ≈.20 | 0° | 1.1 | na | na | 20MPa | 0° | 520,560,600,640,680,720 |
| 13-18 | AK29-3-002 | ≈.20 | 0° | 1.1 | na | na | 20MPa | 0° | 760,800,840,880,920,960 |
| 19-24 | AK29-3-002 | ≈.20 | 0° | 1.1 | na | na | 20MPa | 0° | 1000,1040,1080,1120,1160,1200 |
| 1-6 | AK29-6-002 | ≈.15 | 0° | 1.1 | na | na | 10MPa | 0° | 320,360,400,440,470,520 |
| 7-12 | AK29-6-002 | ≈.15 | 0° | 1.1 | na | na | 10MPa | 0° | 560,600,640,680,720,760 |
| 13-18 | AK29-6-002 | ≈.15 | 0° | 1.1 | na | na | 10MPa | 0° | 800,840,880,920,960,1000 |
| 19-24 | AK29-6-002 | ≈.15 | 0° | 1.1 | na | na | 10MPa | 0° | 1040,1080,1120,1160,1200,1240 |
| 1-6 | AK29-6-002 | ≈.15 | 0° | 1.1 | na | na | 20MPa | 0° | 240,280,320,360,400,440 |
| 7-12 | AK29-6-002 | ≈.15 | 0° | 1.1 | na | na | 20MPa | 0° | 480,520,560,600,640,680 |
| 13-18 | AK29-6-002 | ≈.15 | 0° | 1.1 | na | na | 20MPa | 0° | 760,800,840,880,920,960 |
| 19-24 | AK29-6-002 | ≈.15 | 0° | 1.1 | na | na | 20MPa | 0° | 1000,1040,1080,1120,1160,1200 |
| 1-8 | AK29-9-001 | ≈.20 | 30° | 1.1 | na | na | 10MPa | 0° | 280,320,360,400,440,480,520,560 |
| 9-16 | AK29-9-001 | ≈.20 | 30° | 1.1 | na | na | 10MPa | 0° | 600,640,680,720,760,800,840,880 |
| 17-24 | AK29-9-001 | ≈.20 | 30° | 1.1 | na | na | 10MPa | 0° | 920,1000,1080,1160,1240,1320, 1400,1480 |
| 1-8 | AK29-9-001 | ≈.20 | 30° | 1.1 | na | na | 10MPa | 90° | 280,320,360,400,440,480,520,560 |
| 9-16 | AK29-9-001 | ≈.20 | 30° | 1.1 | na | na | 10MPa | 90° | 600,640,680,720,760,800,840,880 |
| 17-24 | AK29-9-001 | ≈.20 | 30° | 1.1 | na | na | 10MPa | 90° | 920,1000,1080,1160,1240,1320, 1400,1480 |
| 1-8 | AK29-9-001 | ≈.20 | 30° | 1.1 | na | na | 20MPa | 0° | 280,320,360,400,440,480,520,560 |
| 9-16 | AK29-9-001 | ≈.20 | 30° | 1.1 | na | na | 20MPa | 0° | 600,640,680,720,760,800,840,880 |
| 17-24 | AK29-9-001 | ≈.20 | 30° | 1.1 | na | na | 20MPa | 0° | 920,1000,1080,1160,1240,1320, 1400,1480 |
| 1-8 | AK29-9-001 | ≈.20 | 30° | 1.1 | na | na | 20MPa | 90° | 280,320,360,400,440,480,520,560 |
| 9-16 | AK29-9-001 | ≈.20 | 30° | 1.1 | na | na | 20MPa | 90° | 600,640,680,720,760,800,840,880 |
| 17-24 | AK29-9-001 | ≈.20 | 30° | 1.1 | na | na | 20MPa | 90° | 920,1000,1080,1160,1240,1320, 1400,1480 |

| | | | | | | | | | |
|---|---|---|---|---|---|---|---|---|---|
| 1-8 | AK29-10-3-003 | ≈.15 | 30° | 1.1 | 3.96 | 2.5 | 10MPa | 0° | 320,340,400,440,480,520,560,600 |
| 9-16 | AK29-10-3-003 | ≈.15 | 30° | 1.1 | 3.96 | 2.5 | 10MPa | 0° | 640,680,720,760,800,840,880,920 |
| 17-24 | AK29-10-3-003 | ≈.15 | 30° | 1.1 | 3.96 | 2.5 | 10MPa | 0° | 1000,1080,1160,1240,1320,1400, 1480,1560 |
| 1-8 | AK29-10-3-003 | ≈.15 | 30° | 1.1 | 3.96 | 2.5 | 10MPa | 90° | 320,340,400,440,480,520,560,600 |
| 9-16 | AK29-10-3-003 | ≈.15 | 30° | 1.1 | 3.96 | 2.5 | 10MPa | 90° | 640,680,720,760,800,840,880,920 |
| 17-24 | AK29-10-3-003 | ≈.15 | 30° | 1.1 | 3.96 | 2.5 | 10MPa | 90° | 1000,1080,1160,1240,1320,1400, 1480,1560 |
| 1-8 | AK29-10-3-003 | ≈.15 | 30° | 1.1 | 3.96 | 2.5 | 20MPa | 0° | 280,320,360,400,440,480,520,560 |
| 9-16 | AK29-10-3-003 | ≈.15 | 30° | 1.1 | 3.96 | 2.5 | 20MPa | 0° | 600,640,680,720,760,800,840,880 |
| 17-24 | AK29-10-3-003 | ≈.15 | 30° | 1.1 | 3.96 | 2.5 | 20MPa | 0° | 920,1000,1080,1160,1240,1320, 1400,1480 |
| 1-8 | AK29-10-3-003 | ≈.15 | 30° | 1.1 | 3.96 | 2.5 | 20MPa | 90° | 280,320,360,400,440,480,520,560 |
| 9-16 | AK29-10-3-003 | ≈.15 | 30° | 1.1 | 3.96 | 2.5 | 20MPa | 90° | 600,640,680,720,760,800,840,880 |
| 17-24 | AK29-10-3-003 | ≈.15 | 30° | 1.1 | 3.96 | 2.5 | 20MPa | 90° | 920,1000,1080,1160,1240,1320, 1400,1480 |
| 1-8 | AK29-11-3-002 | ≈.15 | 30° | 3.96 | na | na | 10MPa | 0° | 320,340,400,440,480,520,560,600 |
| 9-16 | AK29-11-3-002 | ≈.15 | 30° | 3.96 | na | na | 10MPa | 0° | 640,680,720,760,800,840,880,920 |
| 17-24 | AK29-11-3-002 | ≈.15 | 30° | 3.96 | na | na | 10MPa | 0° | 1000,1080,1160,1240,1320,1400, 1480,1560 |
| 1-8 | AK29-11-3-002 | ≈.15 | 30° | 3.96 | na | na | 10MPa | 90° | 320,340,400,440,480,520,560,600 |
| 9-16 | AK29-11-3-002 | ≈.15 | 30° | 3.96 | na | na | 10MPa | 90° | 640,680,720,760,800,840,880,920 |
| 17-24 | AK29-11-3-002 | ≈.15 | 30° | 3.96 | na | na | 10MPa | 90° | 1000,1080,1160,1240,1320,1400, 1480,1560 |
| 1-8 | AK29-11-3-002 | ≈.15 | 30° | 3.96 | na | na | 20MPa | 0° | 280,320,360,400,440,480,520,560 |
| 9-16 | AK29-11-3-002 | ≈.15 | 30° | 3.96 | na | na | 20MPa | 0° | 600,640,680,720,760,800,840,880 |
| 17-24 | AK29-11-3-002 | ≈.15 | 30° | 3.96 | na | na | 20MPa | 0° | 920,1000,1080,1160,1240,1320, 1400,1480 |
| 1-8 | AK29-11-3-002 | ≈.15 | 30° | 3.96 | na | na | 20MPa | 90° | 280,320,360,400,440,480,520,560 |
| 9-16 | AK29-11-3-002 | ≈.15 | 30° | 3.96 | na | na | 20MPa | 90° | 600,640,680,720,760,800,840,880 |
| 17-24 | AK29-11-3-002 | ≈.15 | 30° | 3.96 | na | na | 20MPa | 90° | 920,1000,1080,1160,1240,1320, 1400,1480 |

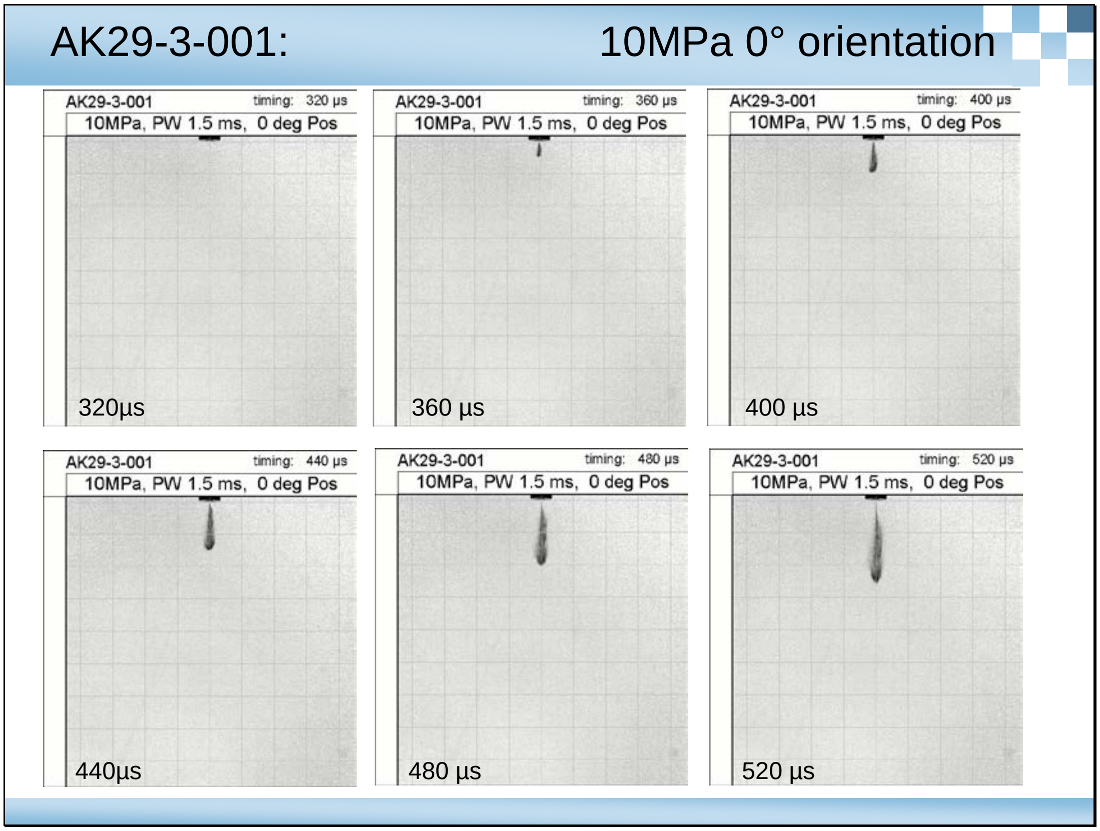
AK29-3-001:
10MPa 0° orientation
AK29-3-001 timing: 320 µs
10MPa, PW 1.5 ms, 0 deg Pos
320µs
AK29-3-001 timing: 360 µs
10MPa, PW 1.5 ms, 0 deg Pos
360 µs
AK29-3-001 timing: 400 µs
10MPa, PW 1.5 ms, 0 deg Pos
400 µs
AK29-3-001 timing: 440 µs
10MPa, PW 1.5 ms, 0 deg Pos
440µs
AK29-3-001 timing: 480 µs
10MPa, PW 1.5 ms, 0 deg Pos
480 µs
AK29-3-001 timing: 520 µs
10MPa, PW 1.5 ms, 0 deg Pos
520 µs

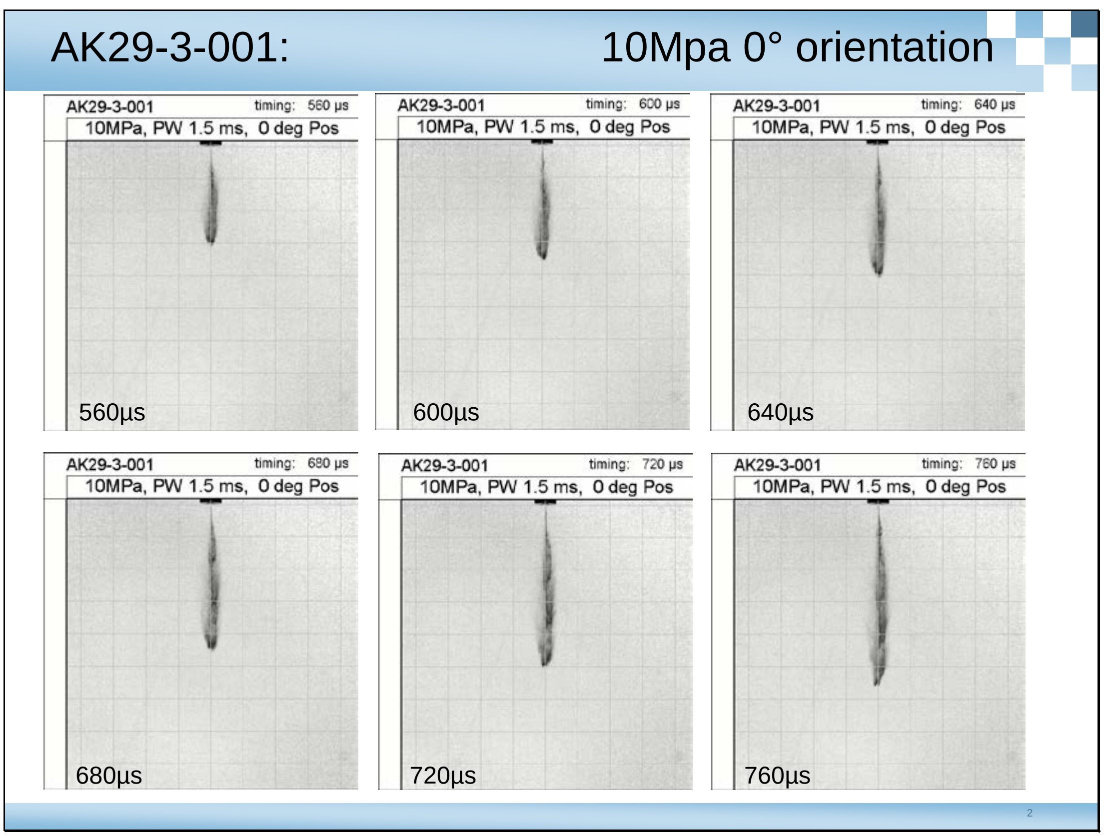
AK29-3-001:
10Mpa 0° orientation
AK29-3-001 timing: 560 µs
10MPa, PW 1.5 ms, 0 deg Pos
560µs
AK29-3-001 timing: 600 µs
10MPa, PW 1.5 ms, 0 deg Pos
600µs
AK29-3-001 timing: 640 µs
10MPa, PW 1.5 ms, 0 deg Pos
640µs
AK29-3-001 timing: 680 µs
10MPa, PW 1.5 ms, 0 deg Pos
680µs
AK29-3-001 timing: 720 µs
10MPa, PW 1.5 ms, 0 deg Pos
720µs
AK29-3-001 timing: 760 µs
10MPa, PW 1.5 ms, 0 deg Pos
760µs

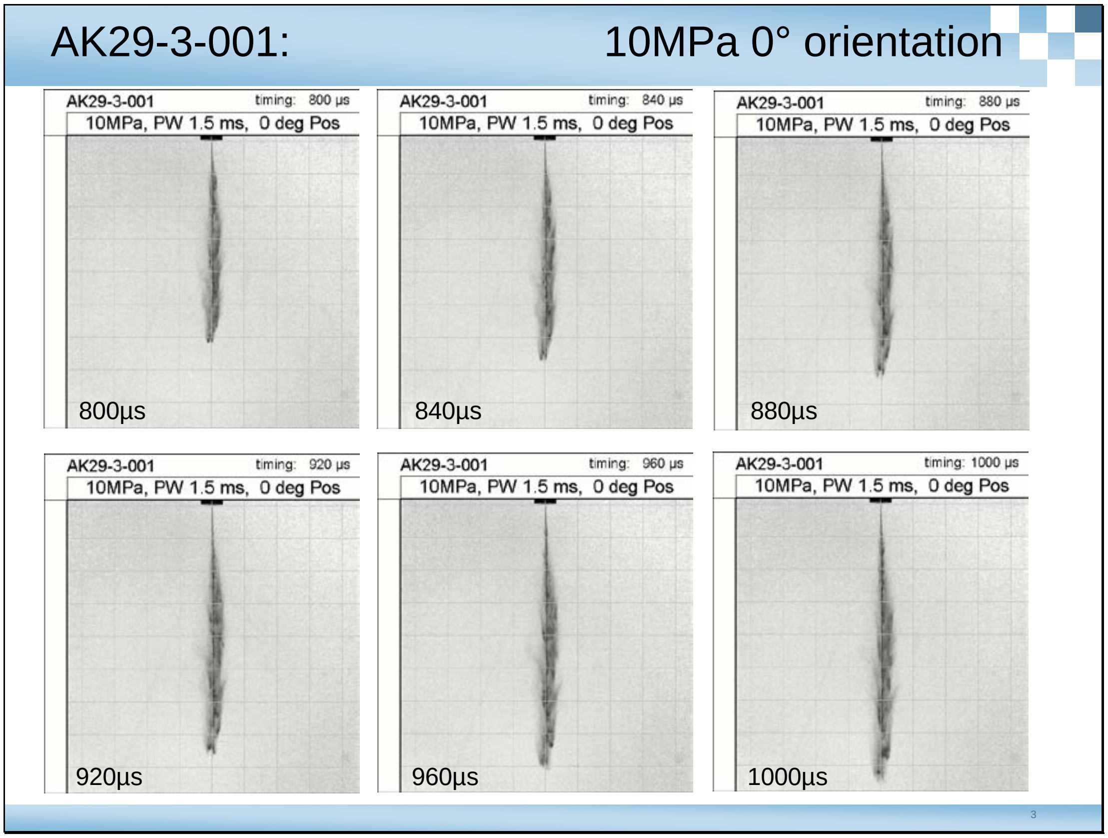
AK29-3-001:
10MPa 0° orientation
AK29-3-001
timing: 800 µs
10MPa, PW 1.5 ms, 0 deg Pos
800µs
AK29-3-001
timing: 840 µs
10MPa, PW 1.5 ms, 0 deg Pos
840µs
AK29-3-001
timing: 880 µs
10MPa, PW 1.5 ms, 0 deg Pos
880µs
AK29-3-001
timing: 920 µs
10MPa, PW 1.5 ms, 0 deg Pos
920µs
AK29-3-001
timing: 960 µs
10MPa, PW 1.5 ms, 0 deg Pos
960µs
AK29-3-001
timing: 1000 µs
10MPa, PW 1.5 ms, 0 deg Pos
1000µs

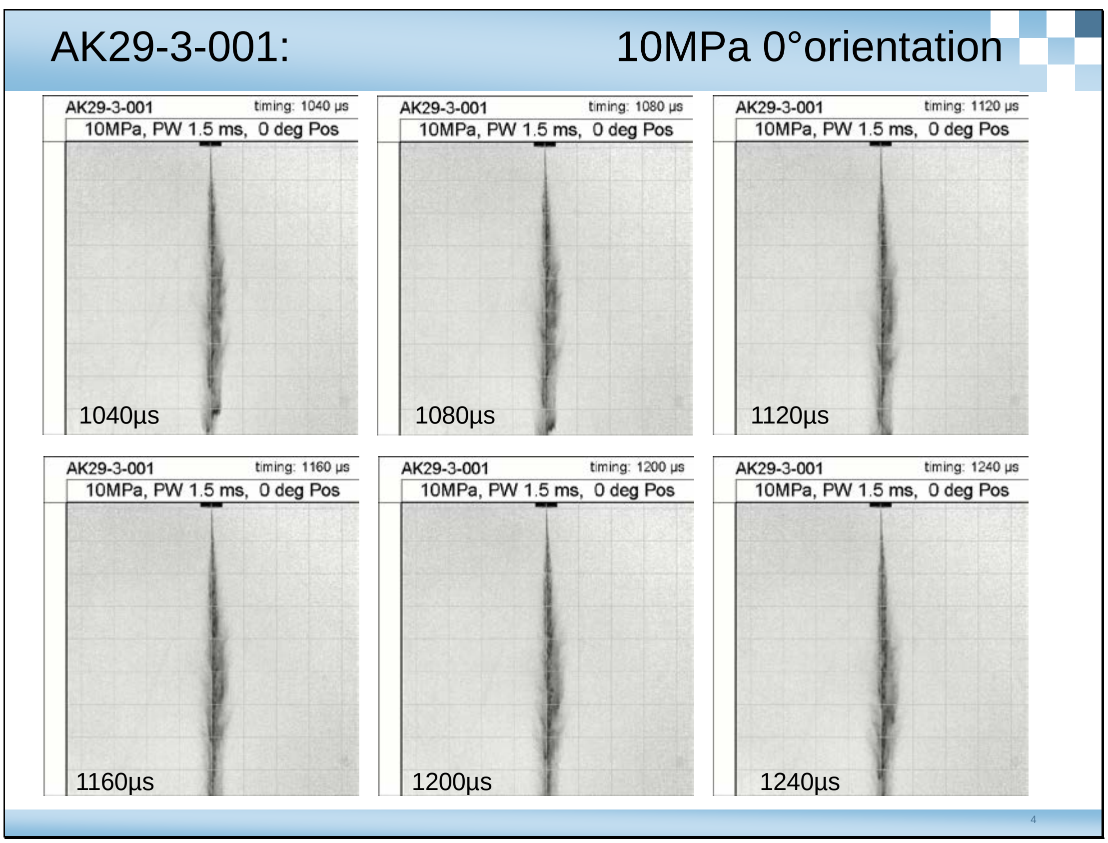
AK29-3-001:
10MPa 0°orientation
AK29-3-001
timing: 1040 µs
10MPa, PW 1.5 ms, 0 deg Pos
1040µs
AK29-3-001
timing: 1080 µs
10MPa, PW 1.5 ms, 0 deg Pos
1080µs
AK29-3-001
timing: 1120 µs
10MPa, PW 1.5 ms, 0 deg Pos
1120µs
AK29-3-001
timing: 1160 µs
10MPa, PW 1.5 ms, 0 deg Pos
1160µs
AK29-3-001
timing: 1200 µs
10MPa, PW 1.5 ms, 0 deg Pos
1200µs
AK29-3-001
timing: 1240 µs
10MPa, PW 1.5 ms, 0 deg Pos
1240µs

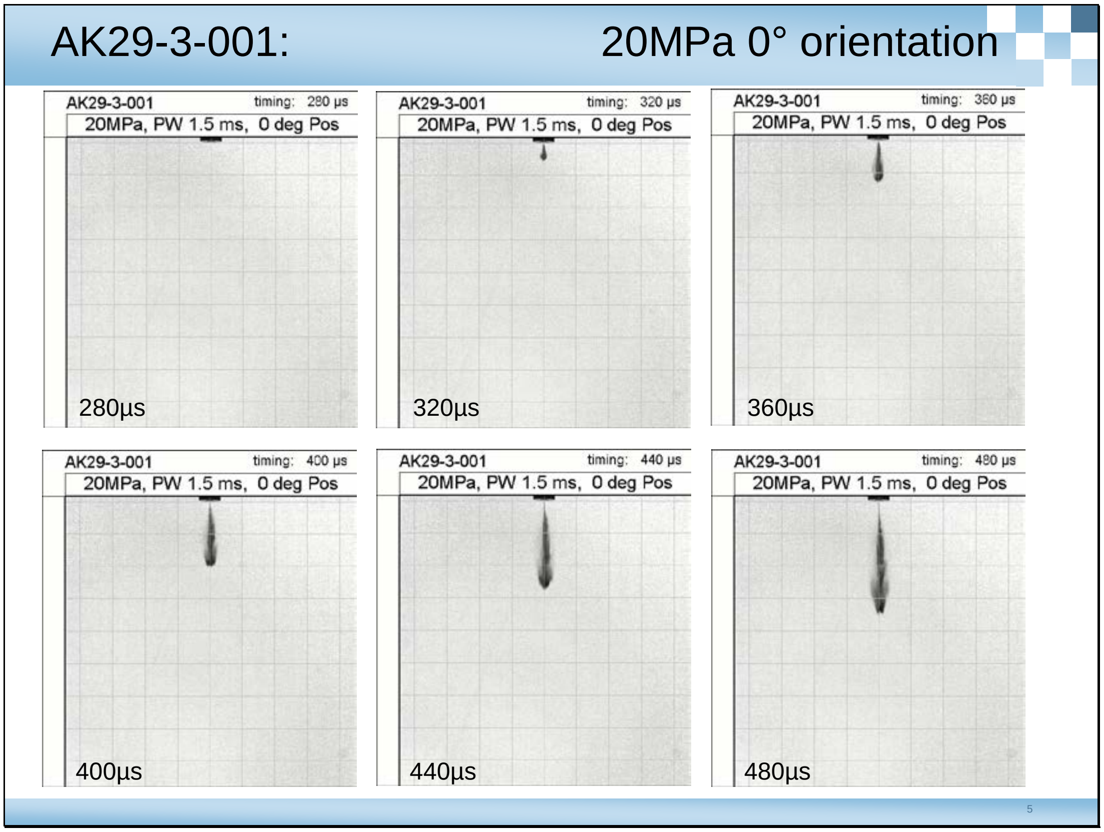
AK29-3-001:
20MPa 0° orientation
AK29-3-001 timing: 280 µs
20MPa, PW 1.5 ms, 0 deg Pos
280µs
AK29-3-001 timing: 320 µs
20MPa, PW 1.5 ms, 0 deg Pos
320µs
AK29-3-001 timing: 360 µs
20MPa, PW 1.5 ms, 0 deg Pos
360µs
AK29-3-001 timing: 400 µs
20MPa, PW 1.5 ms, 0 deg Pos
400µs
AK29-3-001 timing: 440 µs
20MPa, PW 1.5 ms, 0 deg Pos
440µs
AK29-3-001 timing: 480 µs
20MPa, PW 1.5 ms, 0 deg Pos
480µs
5

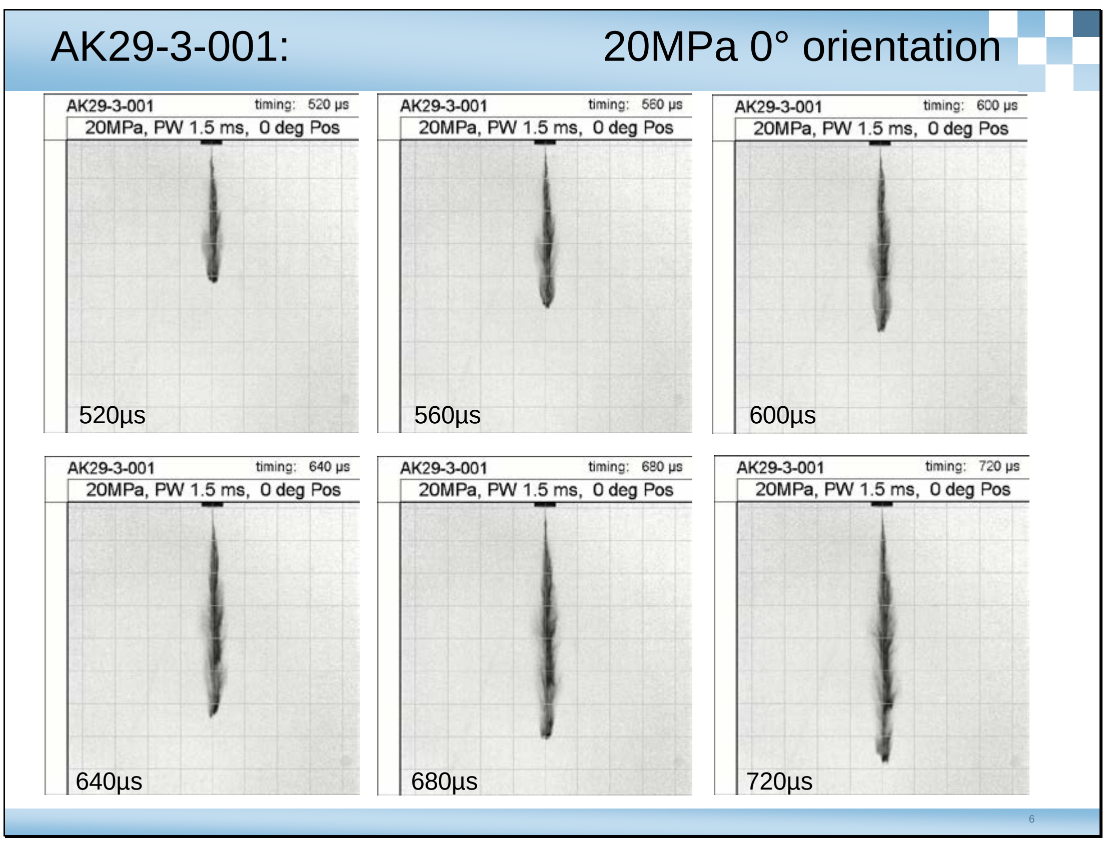
AK29-3-001:
20MPa 0° orientation
AK29-3-001 timing: 520 µs
20MPa, PW 1.5 ms, 0 deg Pos
520µs
AK29-3-001 timing: 560 µs
20MPa, PW 1.5 ms, 0 deg Pos
560µs
AK29-3-001 timing: 600 µs
20MPa, PW 1.5 ms, 0 deg Pos
600µs
AK29-3-001 timing: 640 µs
20MPa, PW 1.5 ms, 0 deg Pos
640µs
AK29-3-001 timing: 680 µs
20MPa, PW 1.5 ms, 0 deg Pos
680µs
AK29-3-001 timing: 720 µs
20MPa, PW 1.5 ms, 0 deg Pos
720µs
6

## AK29-3-001: 20MPa 0° orientation

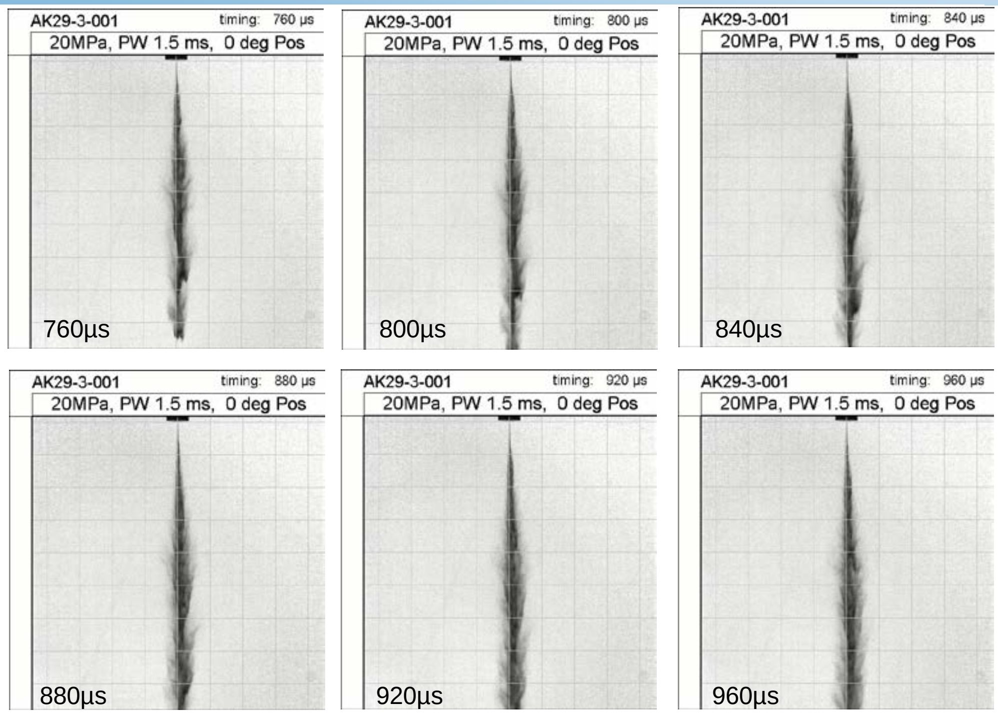


## AK29-3-001: 20MPa 0° orientation

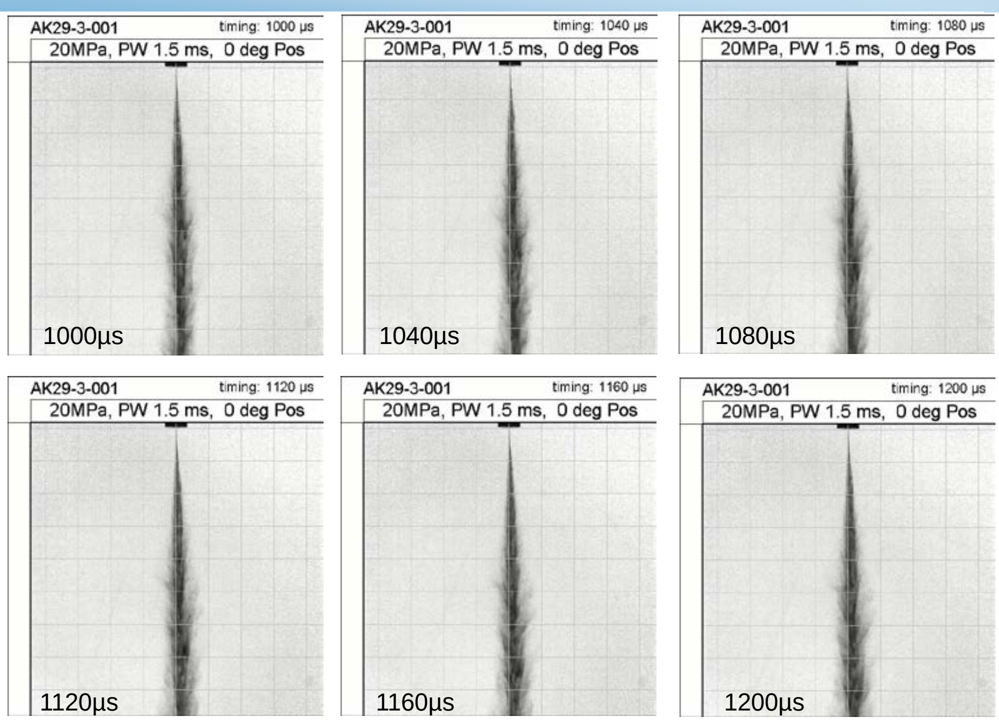

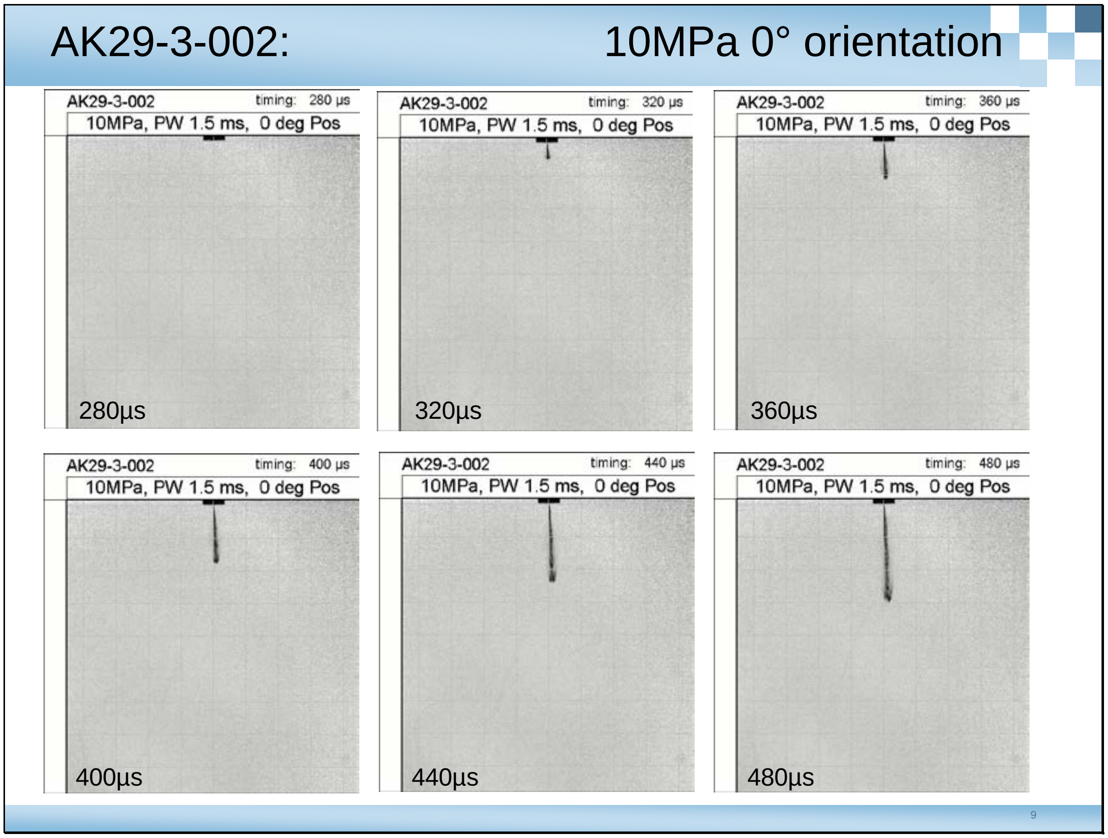
AK29-3-002:
10MPa 0° orientation
AK29-3-002 timing: 280 µs
10MPa, PW 1.5 ms, 0 deg Pos
280µs
AK29-3-002 timing: 320 µs
10MPa, PW 1.5 ms, 0 deg Pos
320µs
AK29-3-002 timing: 360 µs
10MPa, PW 1.5 ms, 0 deg Pos
360µs
AK29-3-002 timing: 400 µs
10MPa, PW 1.5 ms, 0 deg Pos
400µs
AK29-3-002 timing: 440 µs
10MPa, PW 1.5 ms, 0 deg Pos
440µs
AK29-3-002 timing: 480 µs
10MPa, PW 1.5 ms, 0 deg Pos
480µs
9

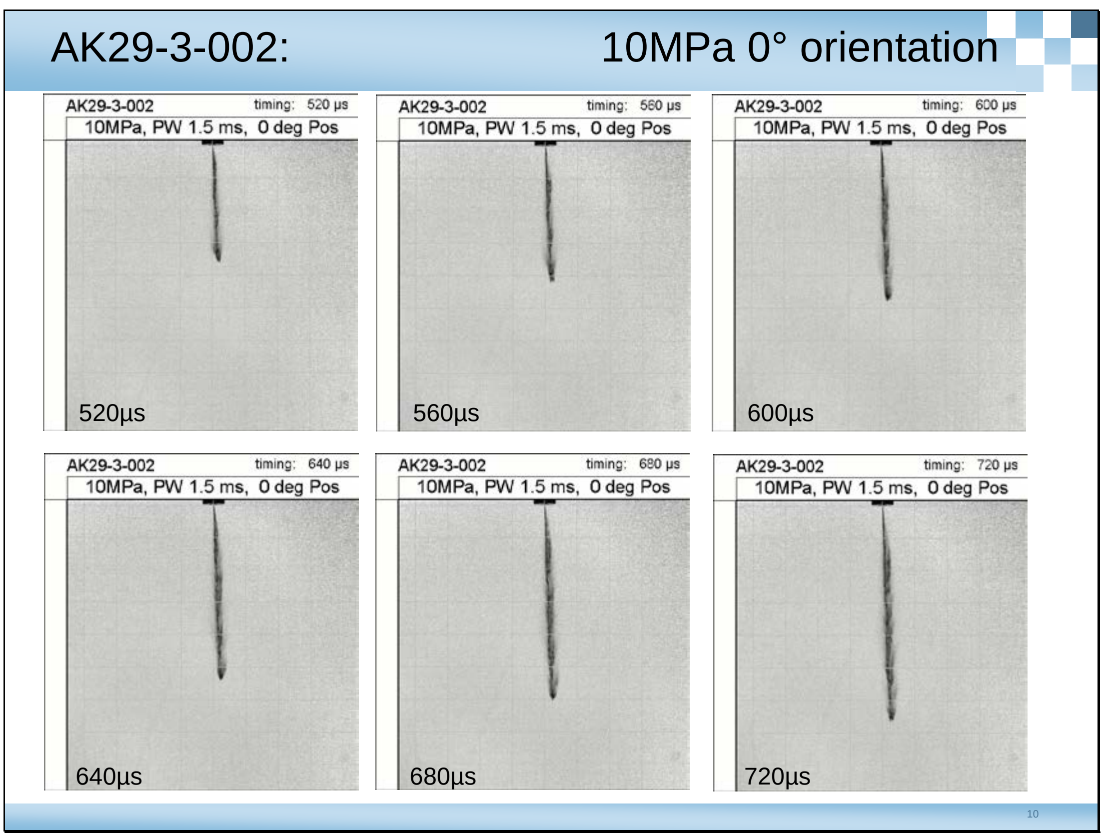
AK29-3-002:
10MPa 0° orientation
AK29-3-002 timing: 520 µs
10MPa, PW 1.5 ms, 0 deg Pos
520µs
AK29-3-002 timing: 560 µs
10MPa, PW 1.5 ms, 0 deg Pos
560µs
AK29-3-002 timing: 600 µs
10MPa, PW 1.5 ms, 0 deg Pos
600µs
AK29-3-002 timing: 640 µs
10MPa, PW 1.5 ms, 0 deg Pos
640µs
AK29-3-002 timing: 680 µs
10MPa, PW 1.5 ms, 0 deg Pos
680µs
AK29-3-002 timing: 720 µs
10MPa, PW 1.5 ms, 0 deg Pos
720µs
10

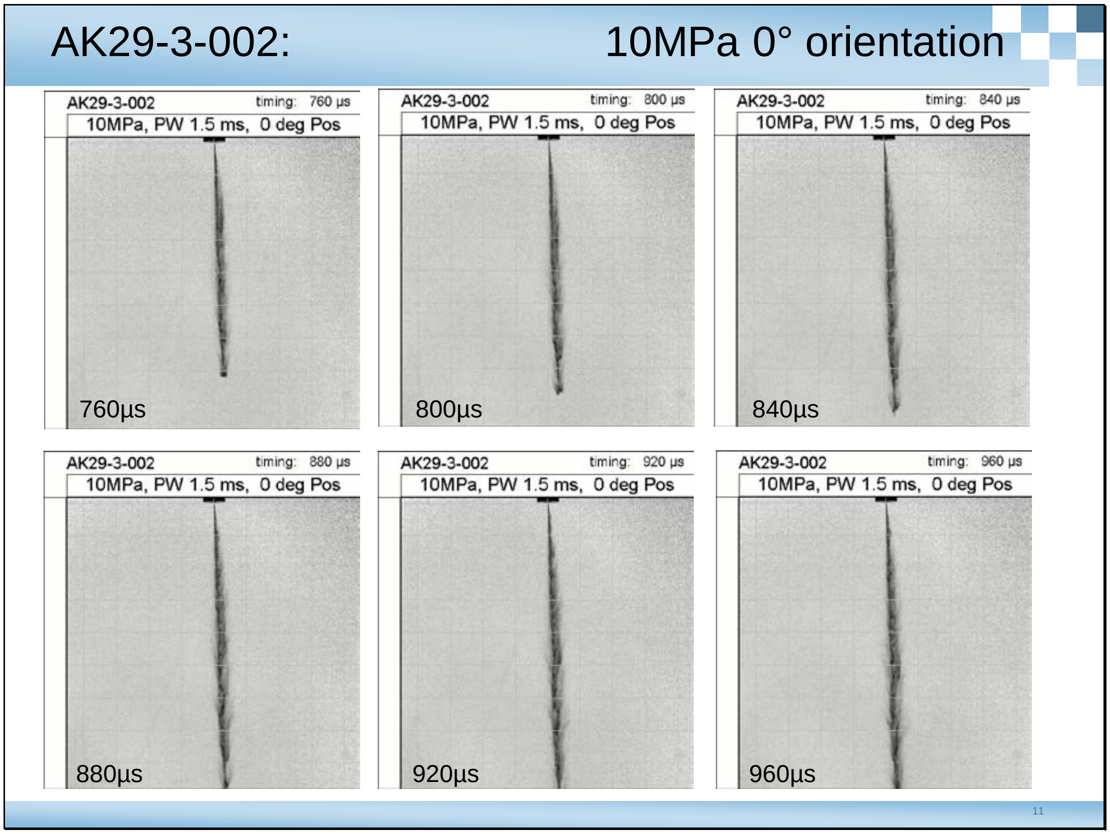
AK29-3-002:
10MPa 0° orientation
AK29-3-002 timing: 760 µs
10MPa, PW 1.5 ms, 0 deg Pos
760µs
AK29-3-002 timing: 800 µs
10MPa, PW 1.5 ms, 0 deg Pos
800µs
AK29-3-002 timing: 840 µs
10MPa, PW 1.5 ms, 0 deg Pos
840µs
AK29-3-002 timing: 880 µs
10MPa, PW 1.5 ms, 0 deg Pos
880µs
AK29-3-002 timing: 920 µs
10MPa, PW 1.5 ms, 0 deg Pos
920µs
AK29-3-002 timing: 960 µs
10MPa, PW 1.5 ms, 0 deg Pos
960µs
11

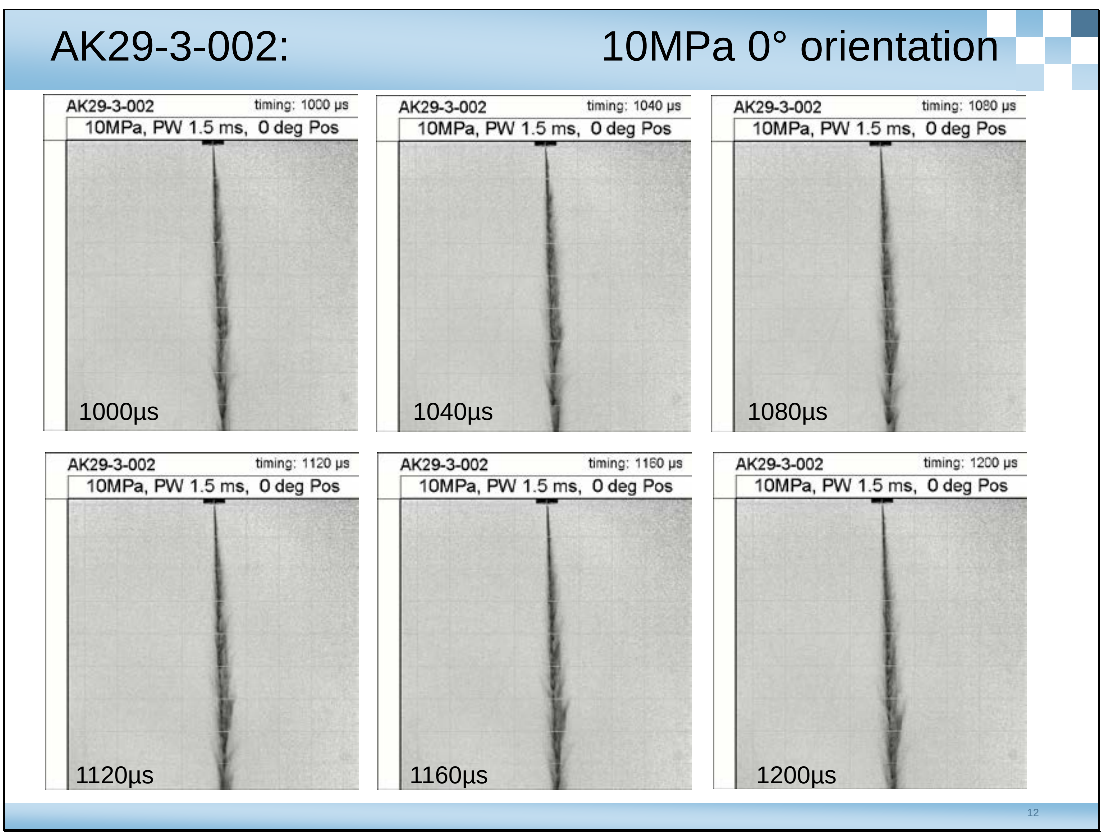
AK29-3-002:
10MPa 0° orientation
AK29-3-002 timing: 1000 µs
10MPa, PW 1.5 ms, 0 deg Pos
1000µs
AK29-3-002 timing: 1040 µs
10MPa, PW 1.5 ms, 0 deg Pos
1040µs
AK29-3-002 timing: 1080 µs
10MPa, PW 1.5 ms, 0 deg Pos
1080µs
AK29-3-002 timing: 1120 µs
10MPa, PW 1.5 ms, 0 deg Pos
1120µs
AK29-3-002 timing: 1160 µs
10MPa, PW 1.5 ms, 0 deg Pos
1160µs
AK29-3-002 timing: 1200 µs
10MPa, PW 1.5 ms, 0 deg Pos
1200µs
12

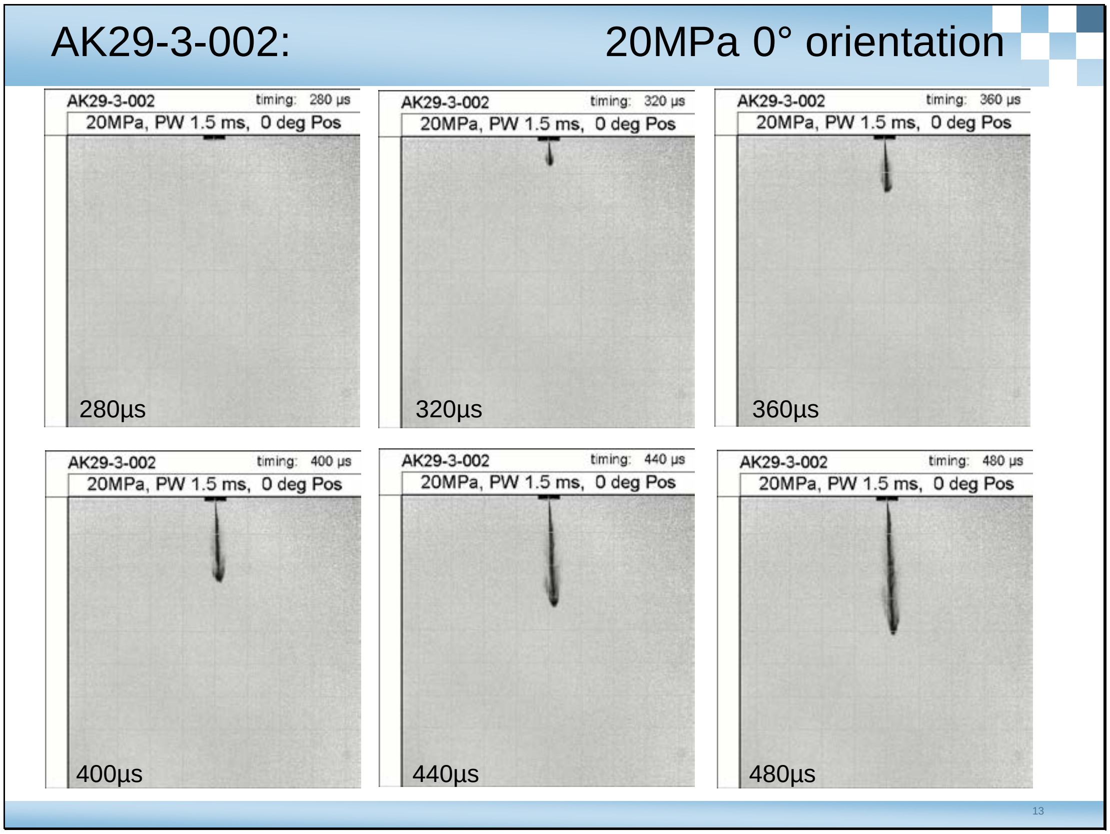
AK29-3-002:
20MPa 0° orientation
AK29-3-002 timing: 280 µs
20MPa, PW 1.5 ms, 0 deg Pos
280µs
AK29-3-002 timing: 320 µs
20MPa, PW 1.5 ms, 0 deg Pos
320µs
AK29-3-002 timing: 360 µs
20MPa, PW 1.5 ms, 0 deg Pos
360µs
AK29-3-002 timing: 400 µs
20MPa, PW 1.5 ms, 0 deg Pos
400µs
AK29-3-002 timing: 440 µs
20MPa, PW 1.5 ms, 0 deg Pos
440µs
AK29-3-002 timing: 480 µs
20MPa, PW 1.5 ms, 0 deg Pos
480µs

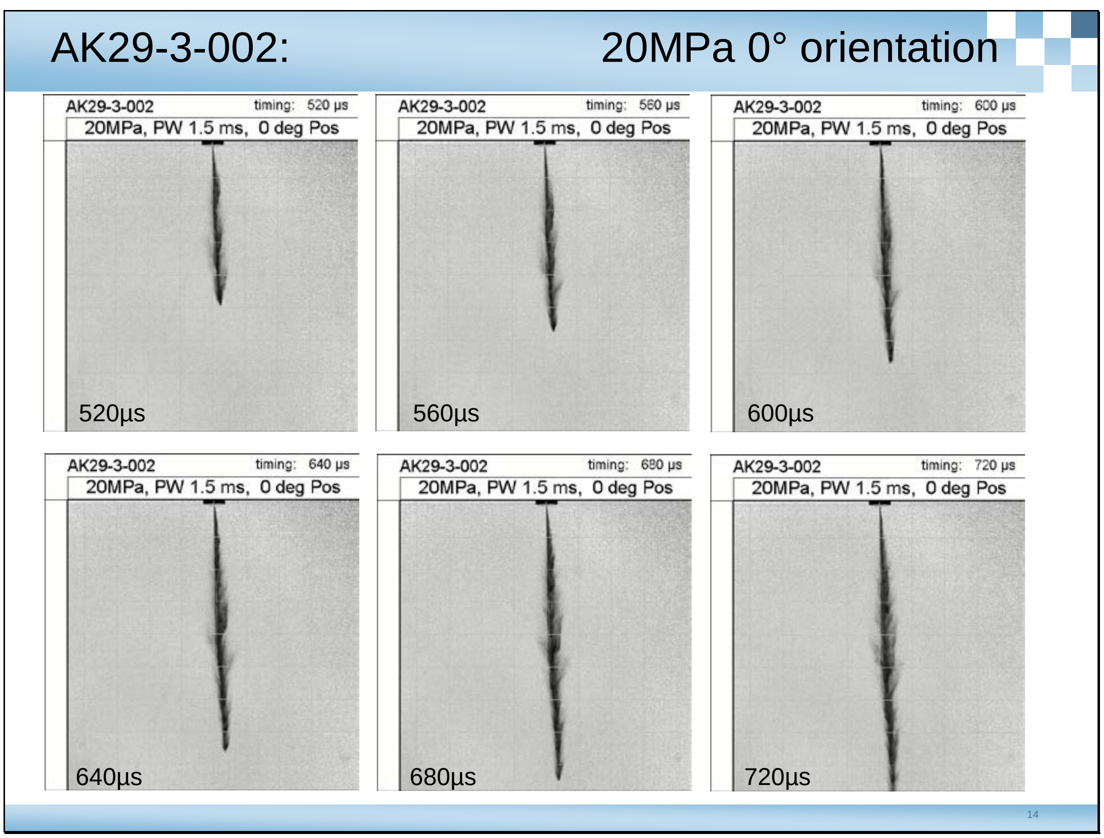
AK29-3-002:
20MPa 0° orientation
AK29-3-002 timing: 520 µs
20MPa, PW 1.5 ms, 0 deg Pos
520µs
AK29-3-002 timing: 560 µs
20MPa, PW 1.5 ms, 0 deg Pos
560µs
AK29-3-002 timing: 600 µs
20MPa, PW 1.5 ms, 0 deg Pos
600µs
AK29-3-002 timing: 640 µs
20MPa, PW 1.5 ms, 0 deg Pos
640µs
AK29-3-002 timing: 680 µs
20MPa, PW 1.5 ms, 0 deg Pos
680µs
AK29-3-002 timing: 720 µs
20MPa, PW 1.5 ms, 0 deg Pos
720µs

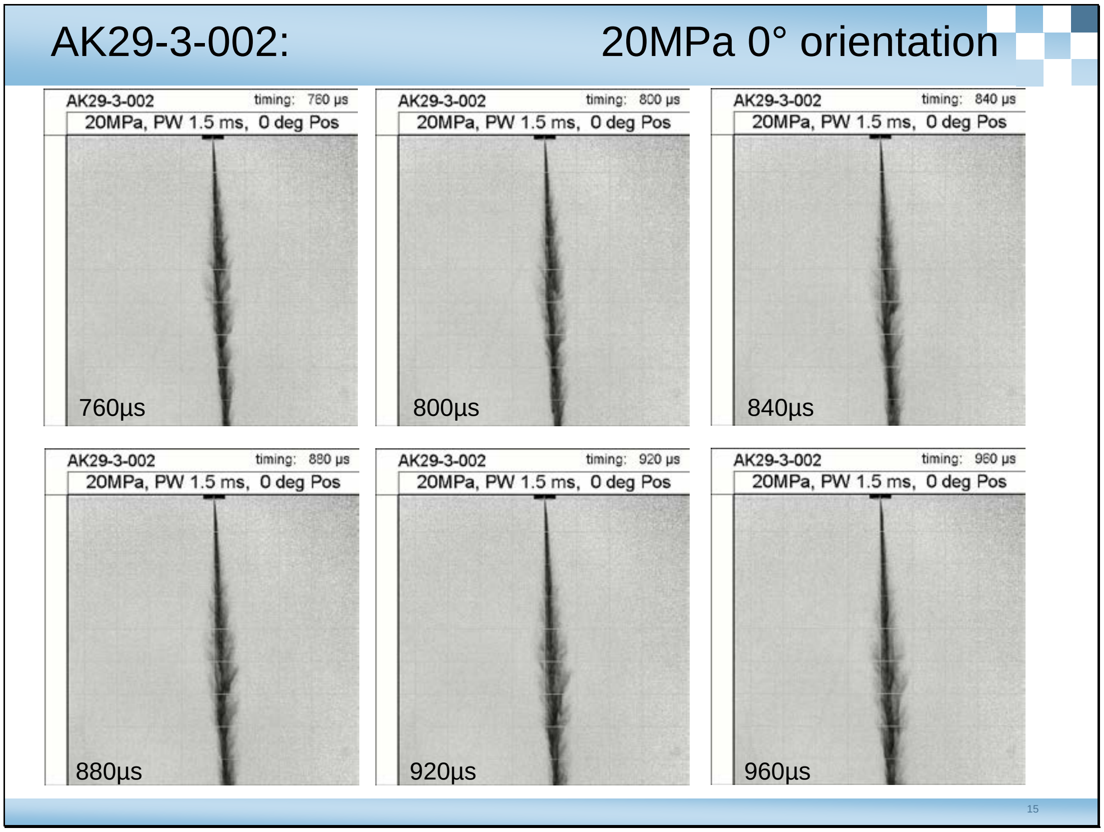
AK29-3-002:
20MPa 0° orientation
AK29-3-002 timing: 760 µs
20MPa, PW 1.5 ms, 0 deg Pos
760µs
AK29-3-002 timing: 800 µs
20MPa, PW 1.5 ms, 0 deg Pos
800µs
AK29-3-002 timing: 840 µs
20MPa, PW 1.5 ms, 0 deg Pos
840µs
AK29-3-002 timing: 880 µs
20MPa, PW 1.5 ms, 0 deg Pos
880µs
AK29-3-002 timing: 920 µs
20MPa, PW 1.5 ms, 0 deg Pos
920µs
AK29-3-002 timing: 960 µs
20MPa, PW 1.5 ms, 0 deg Pos
960µs
15

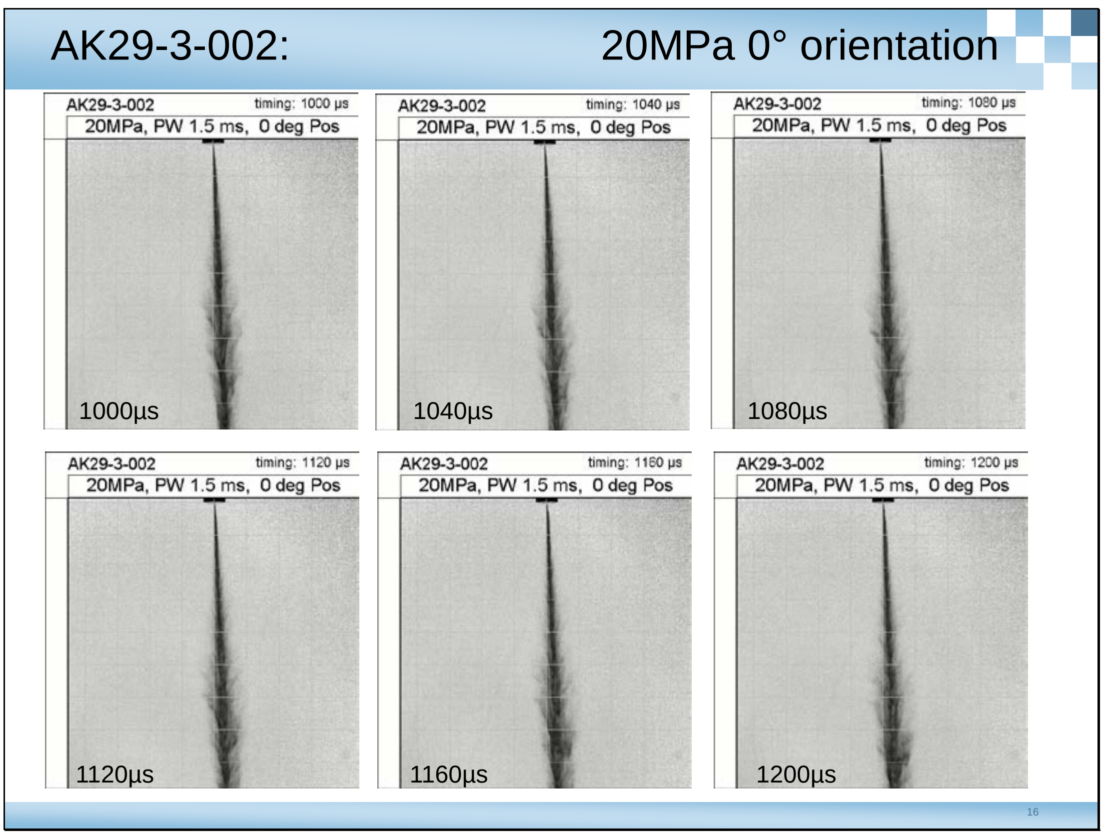
AK29-3-002:
20MPa 0° orientation
AK29-3-002 timing: 1000 µs
20MPa, PW 1.5 ms, 0 deg Pos
1000µs
AK29-3-002 timing: 1040 µs
20MPa, PW 1.5 ms, 0 deg Pos
1040µs
AK29-3-002 timing: 1080 µs
20MPa, PW 1.5 ms, 0 deg Pos
1080µs
AK29-3-002 timing: 1120 µs
20MPa, PW 1.5 ms, 0 deg Pos
1120µs
AK29-3-002 timing: 1160 µs
20MPa, PW 1.5 ms, 0 deg Pos
1160µs
AK29-3-002 timing: 1200 µs
20MPa, PW 1.5 ms, 0 deg Pos
1200µs
16

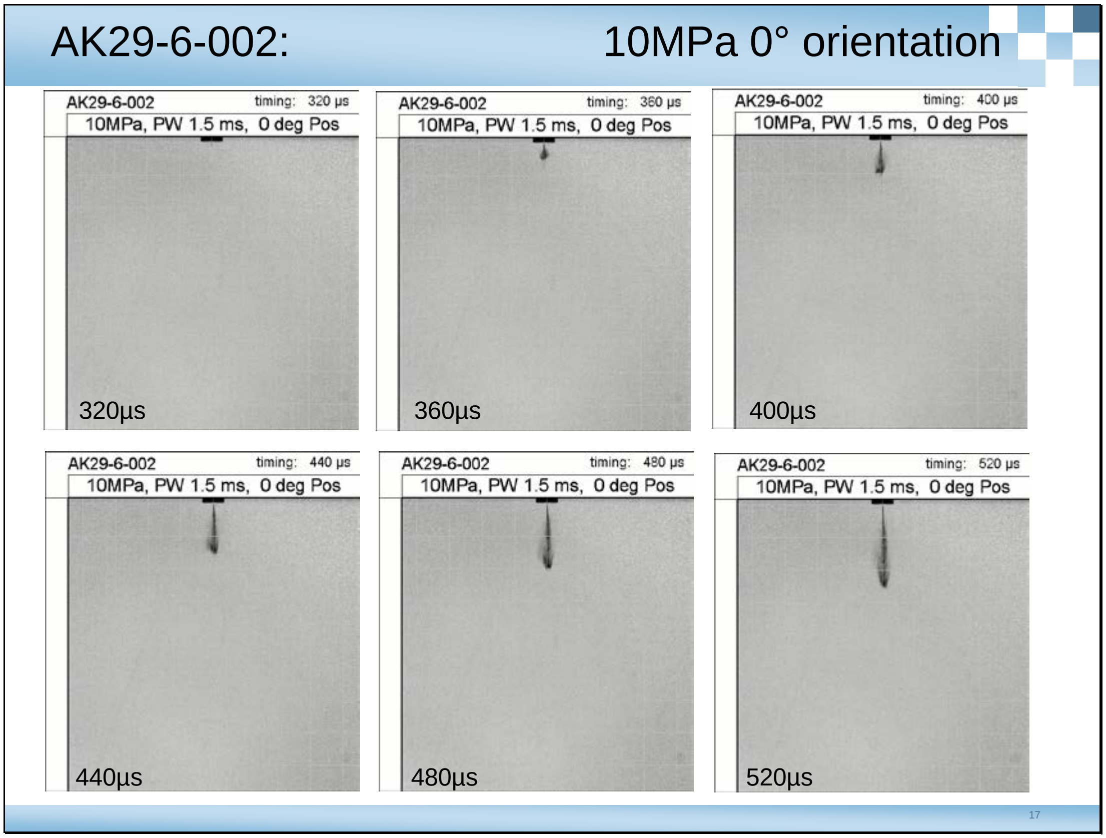
AK29-6-002:
10MPa 0° orientation
AK29-6-002 timing: 320 µs
10MPa, PW 1.5 ms, 0 deg Pos
320µs
AK29-6-002 timing: 360 µs
10MPa, PW 1.5 ms, 0 deg Pos
360µs
AK29-6-002 timing: 400 µs
10MPa, PW 1.5 ms, 0 deg Pos
400µs
AK29-6-002 timing: 440 µs
10MPa, PW 1.5 ms, 0 deg Pos
440µs
AK29-6-002 timing: 480 µs
10MPa, PW 1.5 ms, 0 deg Pos
480µs
AK29-6-002 timing: 520 µs
10MPa, PW 1.5 ms, 0 deg Pos
520µs
17

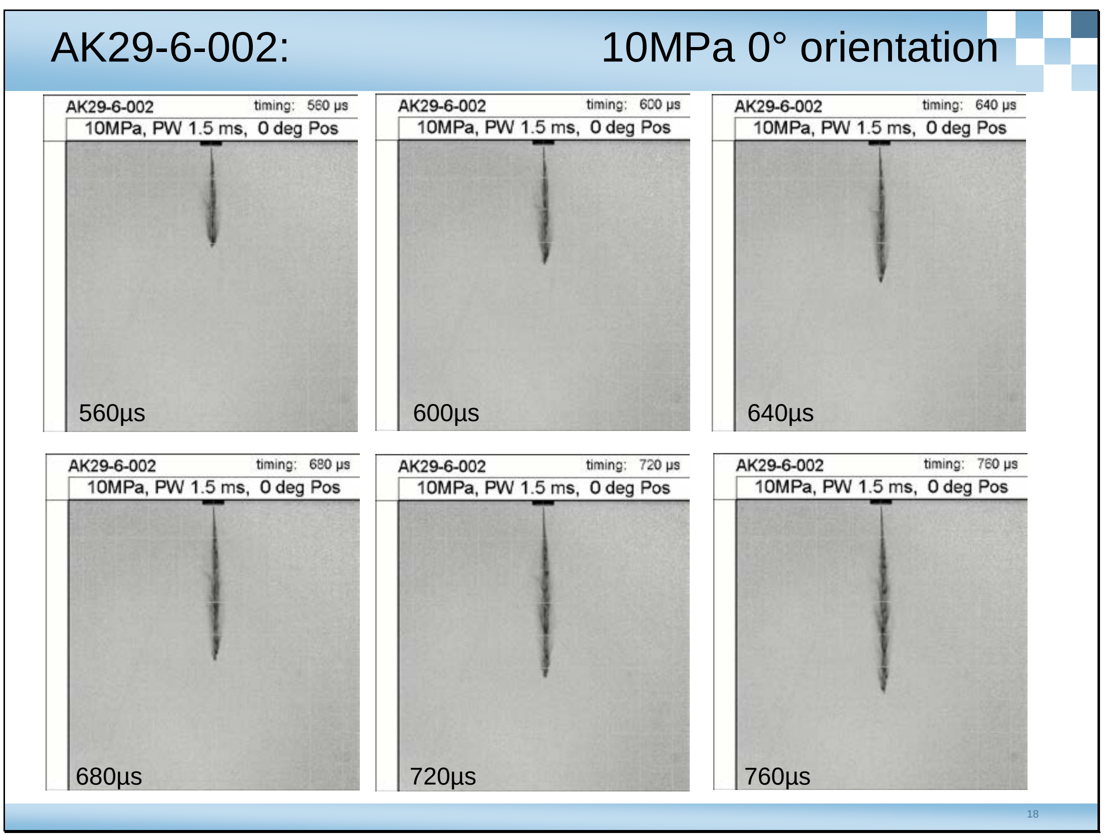
AK29-6-002:
10MPa 0° orientation
AK29-6-002 timing: 560 µs
10MPa, PW 1.5 ms, 0 deg Pos
560µs
AK29-6-002 timing: 600 µs
10MPa, PW 1.5 ms, 0 deg Pos
600µs
AK29-6-002 timing: 640 µs
10MPa, PW 1.5 ms, 0 deg Pos
640µs
AK29-6-002 timing: 680 µs
10MPa, PW 1.5 ms, 0 deg Pos
680µs
AK29-6-002 timing: 720 µs
10MPa, PW 1.5 ms, 0 deg Pos
720µs
AK29-6-002 timing: 760 µs
10MPa, PW 1.5 ms, 0 deg Pos
760µs
18

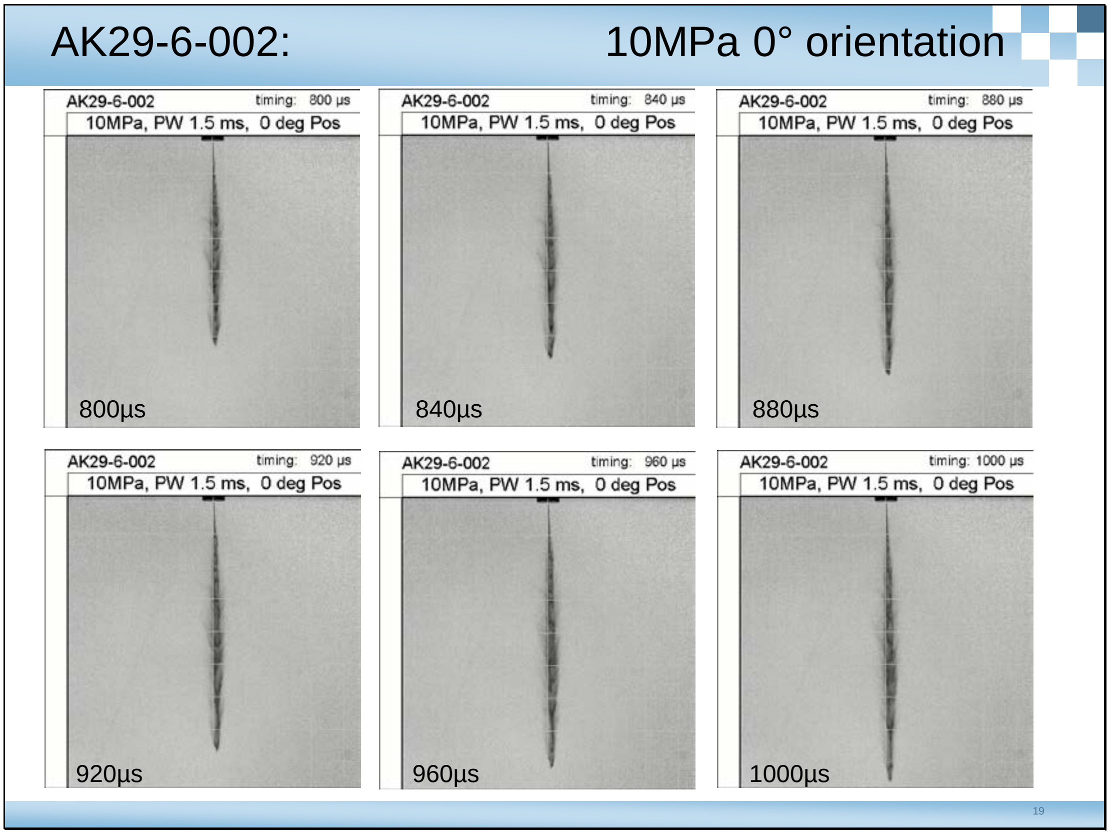
AK29-6-002:
10MPa 0° orientation
AK29-6-002 timing: 800 µs
10MPa, PW 1.5 ms, 0 deg Pos
800µs
AK29-6-002 timing: 840 µs
10MPa, PW 1.5 ms, 0 deg Pos
840µs
AK29-6-002 timing: 880 µs
10MPa, PW 1.5 ms, 0 deg Pos
880µs
AK29-6-002 timing: 920 µs
10MPa, PW 1.5 ms, 0 deg Pos
920µs
AK29-6-002 timing: 960 µs
10MPa, PW 1.5 ms, 0 deg Pos
960µs
AK29-6-002 timing: 1000 µs
10MPa, PW 1.5 ms, 0 deg Pos
1000µs
19

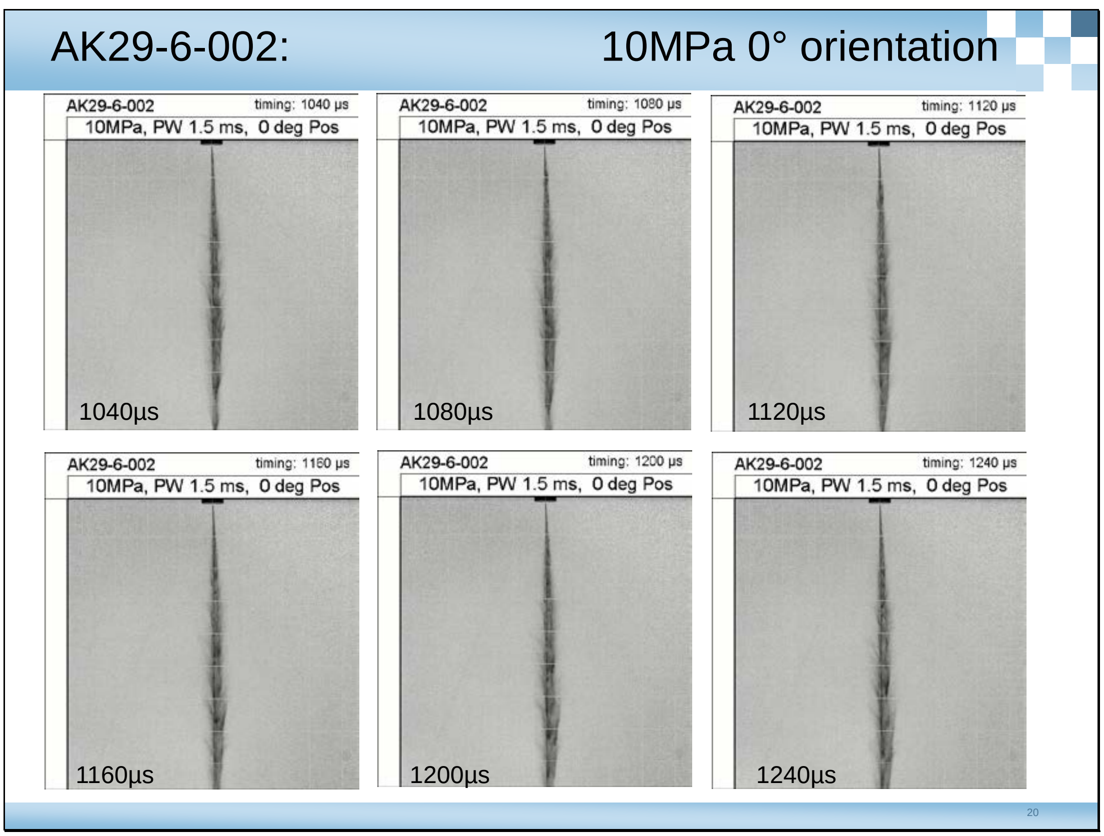
AK29-6-002:
10MPa 0° orientation
AK29-6-002 timing: 1040 µs
10MPa, PW 1.5 ms, 0 deg Pos
1040µs
AK29-6-002 timing: 1080 µs
10MPa, PW 1.5 ms, 0 deg Pos
1080µs
AK29-6-002 timing: 1120 µs
10MPa, PW 1.5 ms, 0 deg Pos
1120µs
AK29-6-002 timing: 1160 µs
10MPa, PW 1.5 ms, 0 deg Pos
1160µs
AK29-6-002 timing: 1200 µs
10MPa, PW 1.5 ms, 0 deg Pos
1200µs
AK29-6-002 timing: 1240 µs
10MPa, PW 1.5 ms, 0 deg Pos
1240µs
20

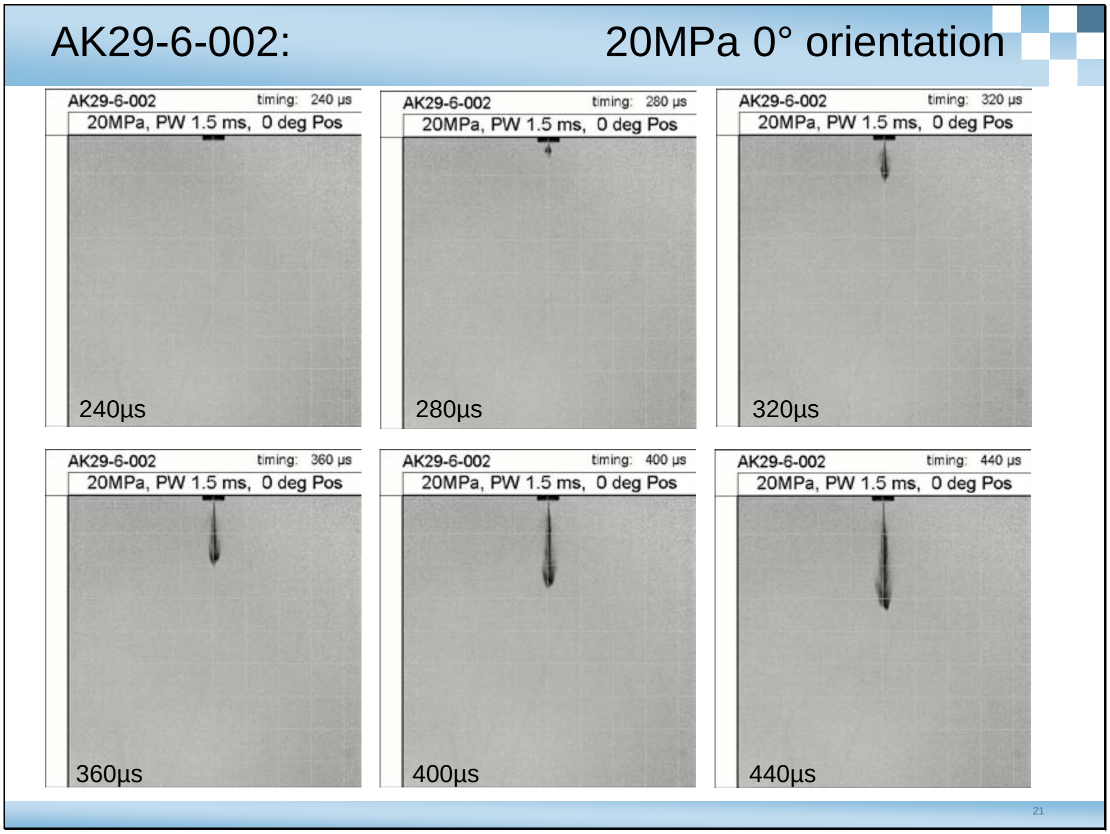
AK29-6-002:
20MPa 0° orientation
AK29-6-002 timing: 240 µs
20MPa, PW 1.5 ms, 0 deg Pos
240µs
AK29-6-002 timing: 280 µs
20MPa, PW 1.5 ms, 0 deg Pos
280µs
AK29-6-002 timing: 320 µs
20MPa, PW 1.5 ms, 0 deg Pos
320µs
AK29-6-002 timing: 360 µs
20MPa, PW 1.5 ms, 0 deg Pos
360µs
AK29-6-002 timing: 400 µs
20MPa, PW 1.5 ms, 0 deg Pos
400µs
AK29-6-002 timing: 440 µs
20MPa, PW 1.5 ms, 0 deg Pos
440µs
21

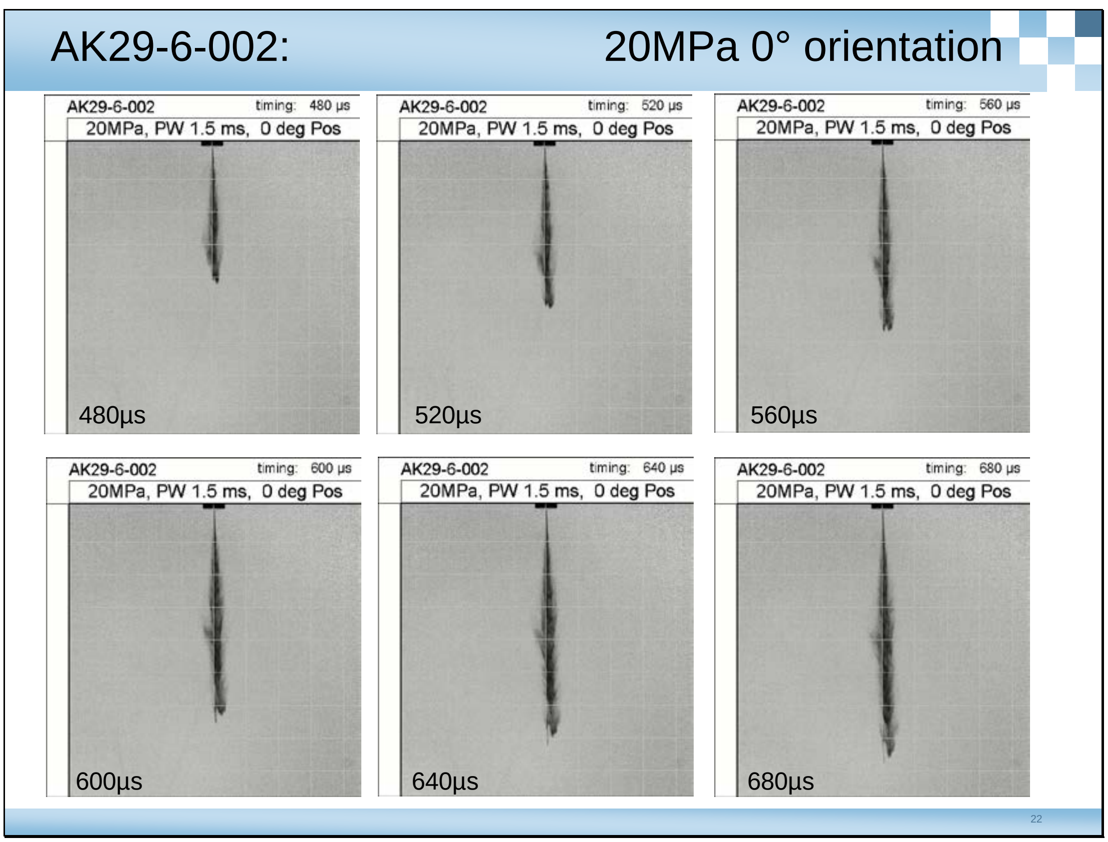
AK29-6-002:
20MPa 0° orientation
AK29-6-002 timing: 480 µs
20MPa, PW 1.5 ms, 0 deg Pos
480µs
AK29-6-002 timing: 520 µs
20MPa, PW 1.5 ms, 0 deg Pos
520µs
AK29-6-002 timing: 560 µs
20MPa, PW 1.5 ms, 0 deg Pos
560µs
AK29-6-002 timing: 600 µs
20MPa, PW 1.5 ms, 0 deg Pos
600µs
AK29-6-002 timing: 640 µs
20MPa, PW 1.5 ms, 0 deg Pos
640µs
AK29-6-002 timing: 680 µs
20MPa, PW 1.5 ms, 0 deg Pos
680µs
22

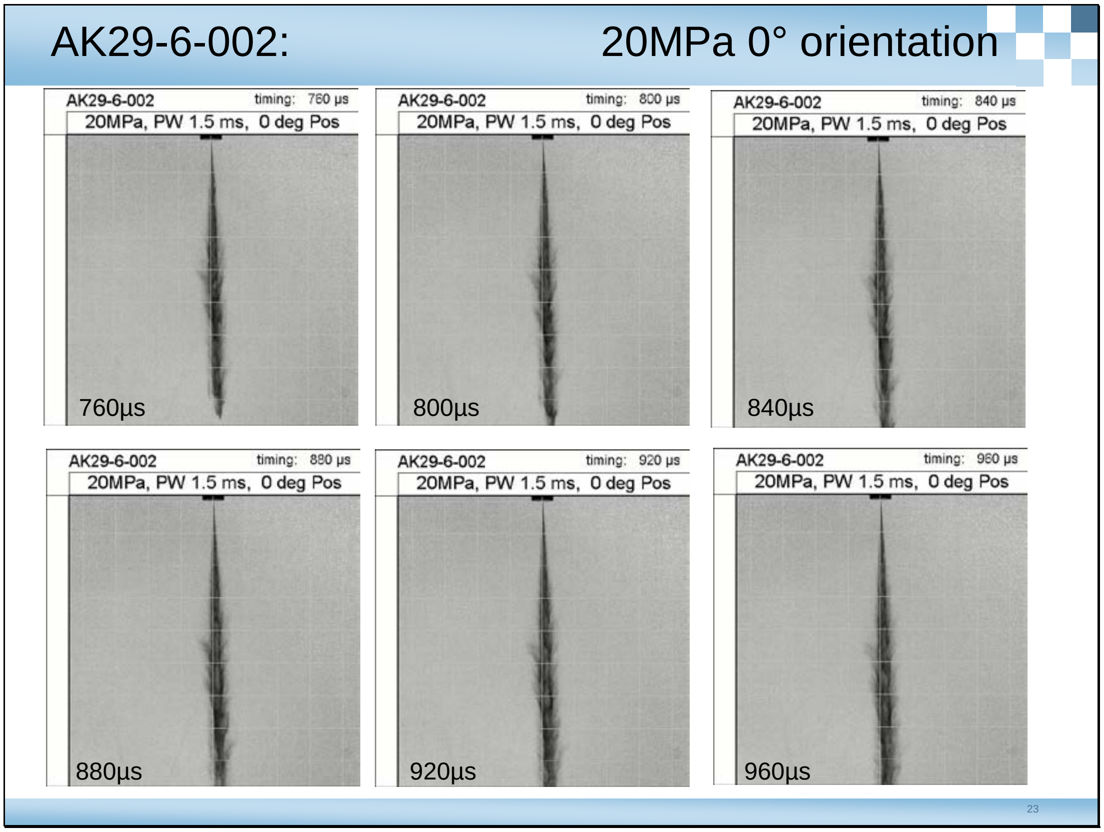
AK29-6-002:
20MPa 0° orientation
AK29-6-002 timing: 760 µs
20MPa, PW 1.5 ms, 0 deg Pos
760µs
AK29-6-002 timing: 800 µs
20MPa, PW 1.5 ms, 0 deg Pos
800µs
AK29-6-002 timing: 840 µs
20MPa, PW 1.5 ms, 0 deg Pos
840µs
AK29-6-002 timing: 880 µs
20MPa, PW 1.5 ms, 0 deg Pos
880µs
AK29-6-002 timing: 920 µs
20MPa, PW 1.5 ms, 0 deg Pos
920µs
AK29-6-002 timing: 960 µs
20MPa, PW 1.5 ms, 0 deg Pos
960µs
23

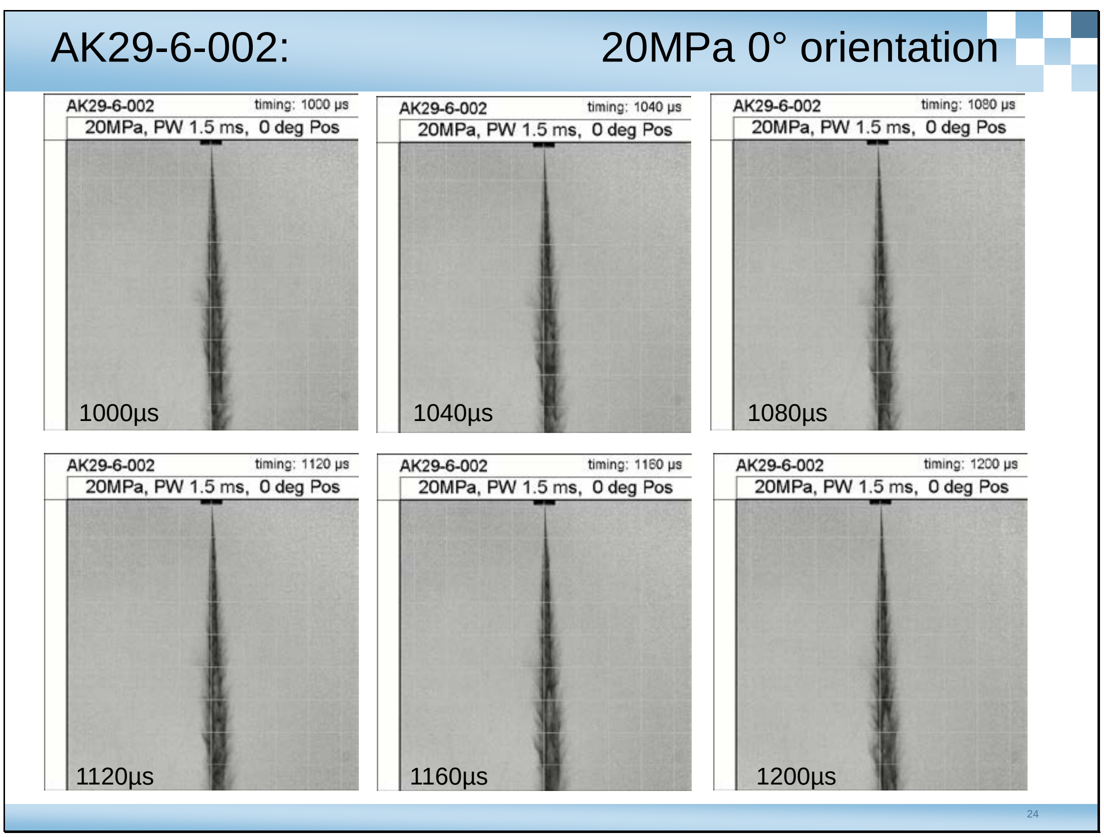
AK29-6-002:
20MPa 0° orientation
AK29-6-002 timing: 1000 µs
20MPa, PW 1.5 ms, 0 deg Pos
1000µs
AK29-6-002 timing: 1040 µs
20MPa, PW 1.5 ms, 0 deg Pos
1040µs
AK29-6-002 timing: 1080 µs
20MPa, PW 1.5 ms, 0 deg Pos
1080µs
AK29-6-002 timing: 1120 µs
20MPa, PW 1.5 ms, 0 deg Pos
1120µs
AK29-6-002 timing: 1160 µs
20MPa, PW 1.5 ms, 0 deg Pos
1160µs
AK29-6-002 timing: 1200 µs
20MPa, PW 1.5 ms, 0 deg Pos
1200µs
24

## Shadow spray image 90° orientation

Shadow spray images for 90 degree orientation show similar behavior, so not shown.



## AK29-9-001: 10MPa 0° orientation

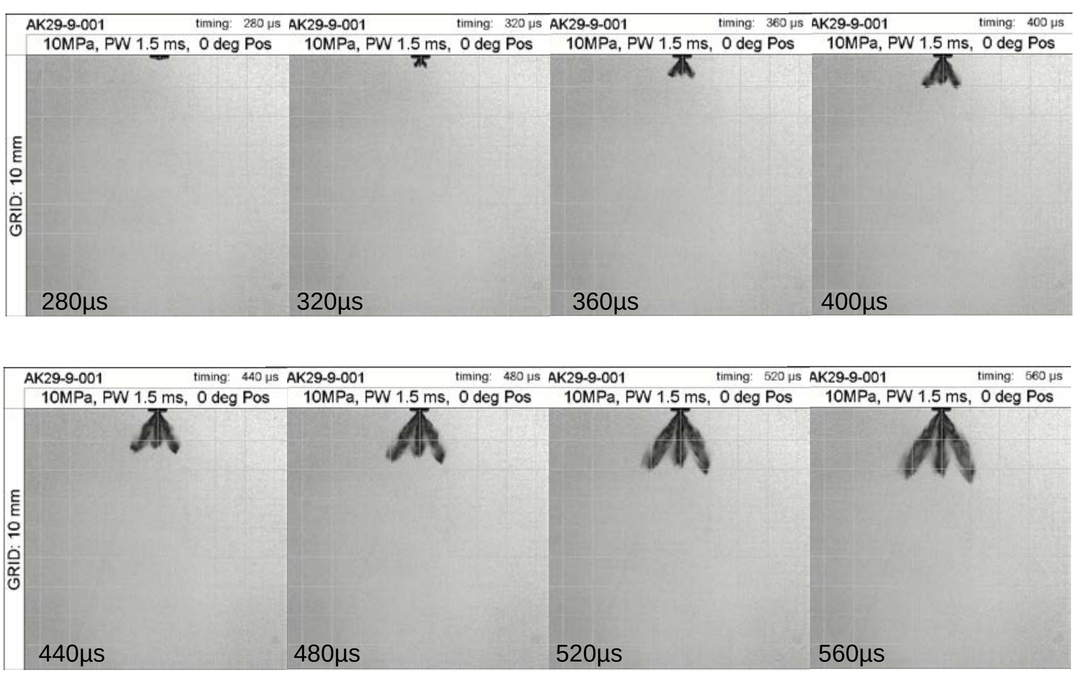

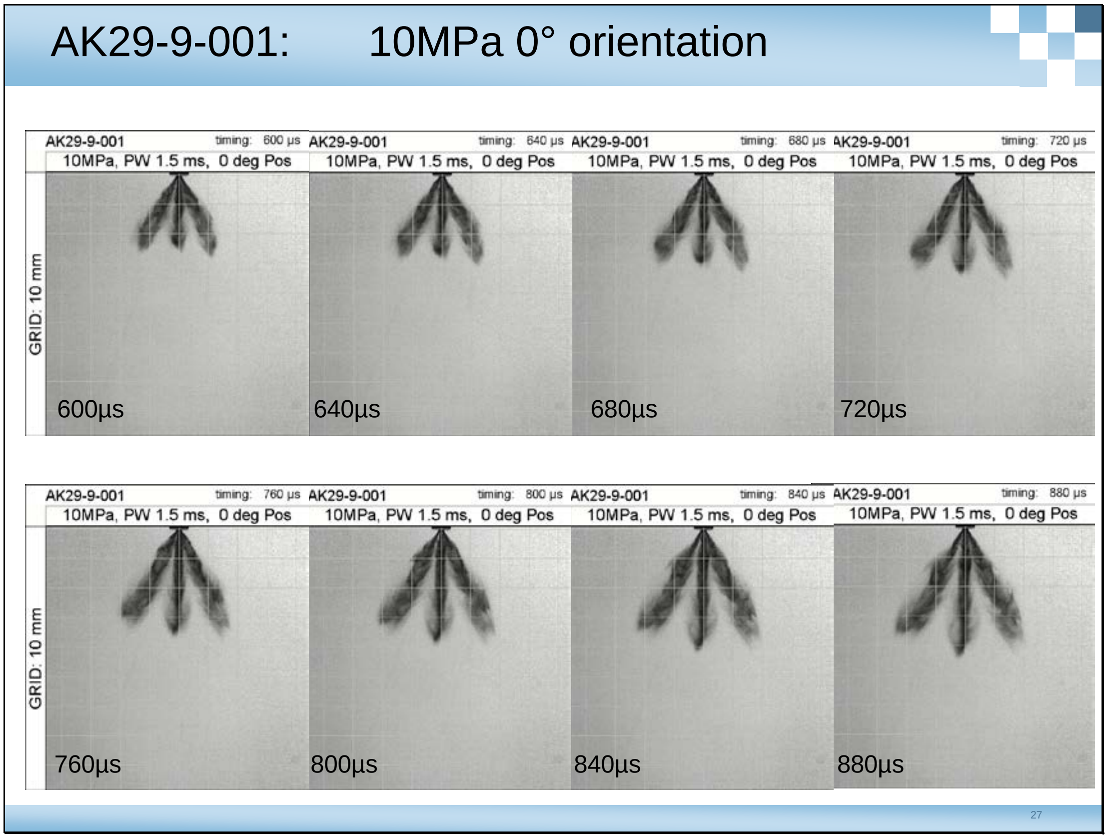
AK29-9-001: 10MPa 0° orientation
AK29-9-001
10MPa, PW 1.5 ms, 0 deg Pos
GRID: 10 mm
600µs
640µs
680µs
720µs
760µs
800µs
840µs
880µs
27

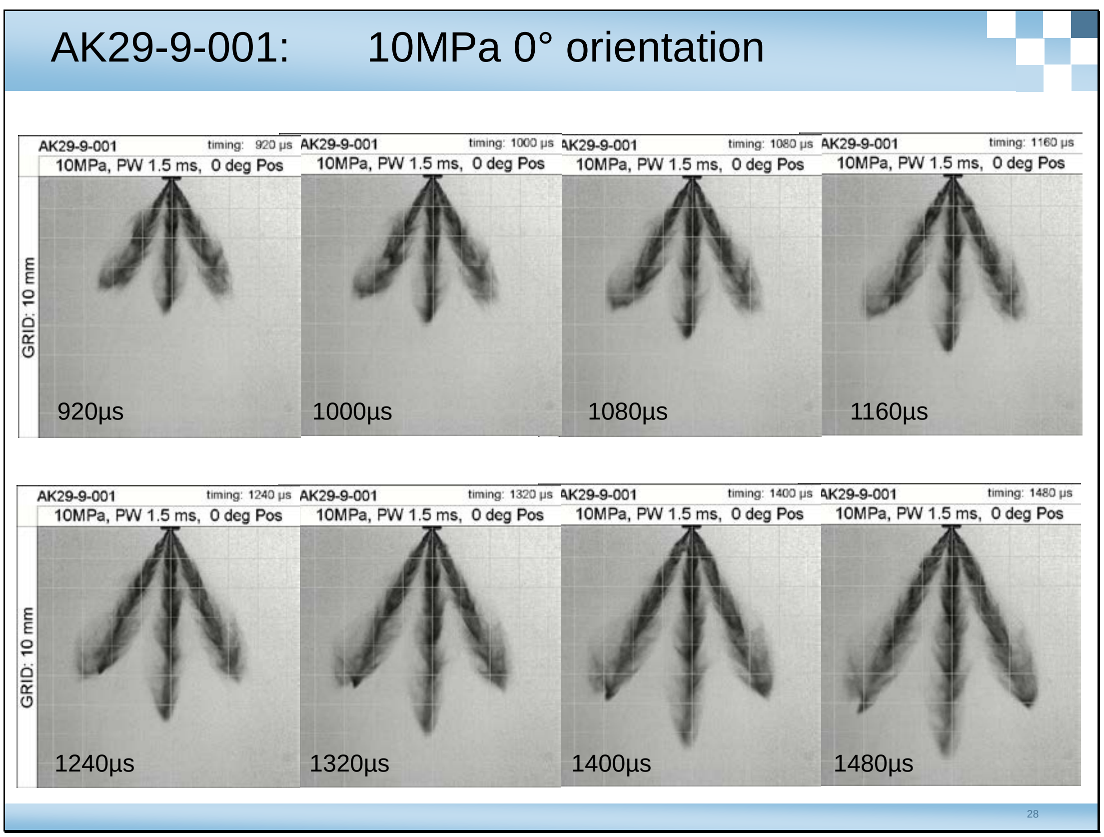
AK29-9-001: 10MPa 0° orientation
AK29-9-001
10MPa, PW 1.5 ms, 0 deg Pos
GRID: 10 mm
920µs
1000µs
1080µs
1160µs
1240µs
1320µs
1400µs
1480µs
28

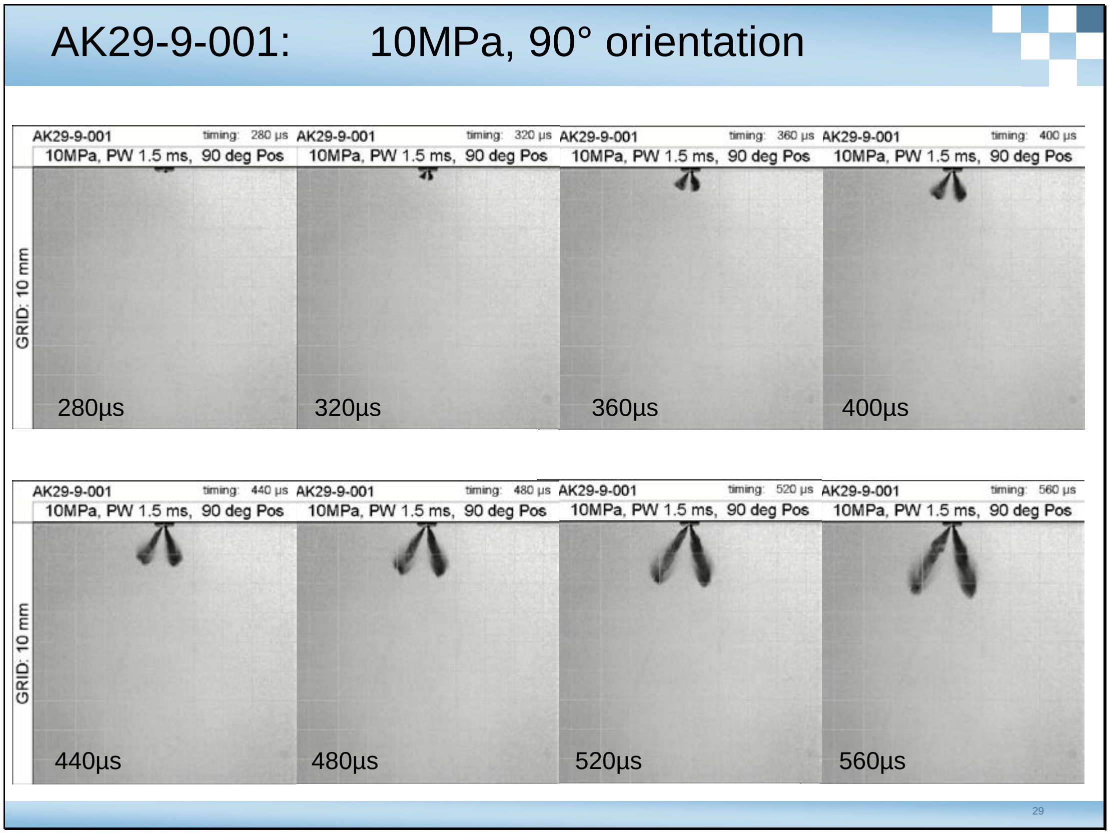
AK29-9-001: 10MPa, 90° orientation
AK29-9-001 timing: 280 µs 10MPa, PW 1.5 ms, 90 deg Pos
AK29-9-001 timing: 320 µs 10MPa, PW 1.5 ms, 90 deg Pos
AK29-9-001 timing: 360 µs 10MPa, PW 1.5 ms, 90 deg Pos
AK29-9-001 timing: 400 µs 10MPa, PW 1.5 ms, 90 deg Pos
GRID: 10 mm
280µs
320µs
360µs
400µs
AK29-9-001 timing: 440 µs 10MPa, PW 1.5 ms, 90 deg Pos
AK29-9-001 timing: 480 µs 10MPa, PW 1.5 ms, 90 deg Pos
AK29-9-001 timing: 520 µs 10MPa, PW 1.5 ms, 90 deg Pos
AK29-9-001 timing: 560 µs 10MPa, PW 1.5 ms, 90 deg Pos
GRID: 10 mm
440µs
480µs
520µs
560µs
29

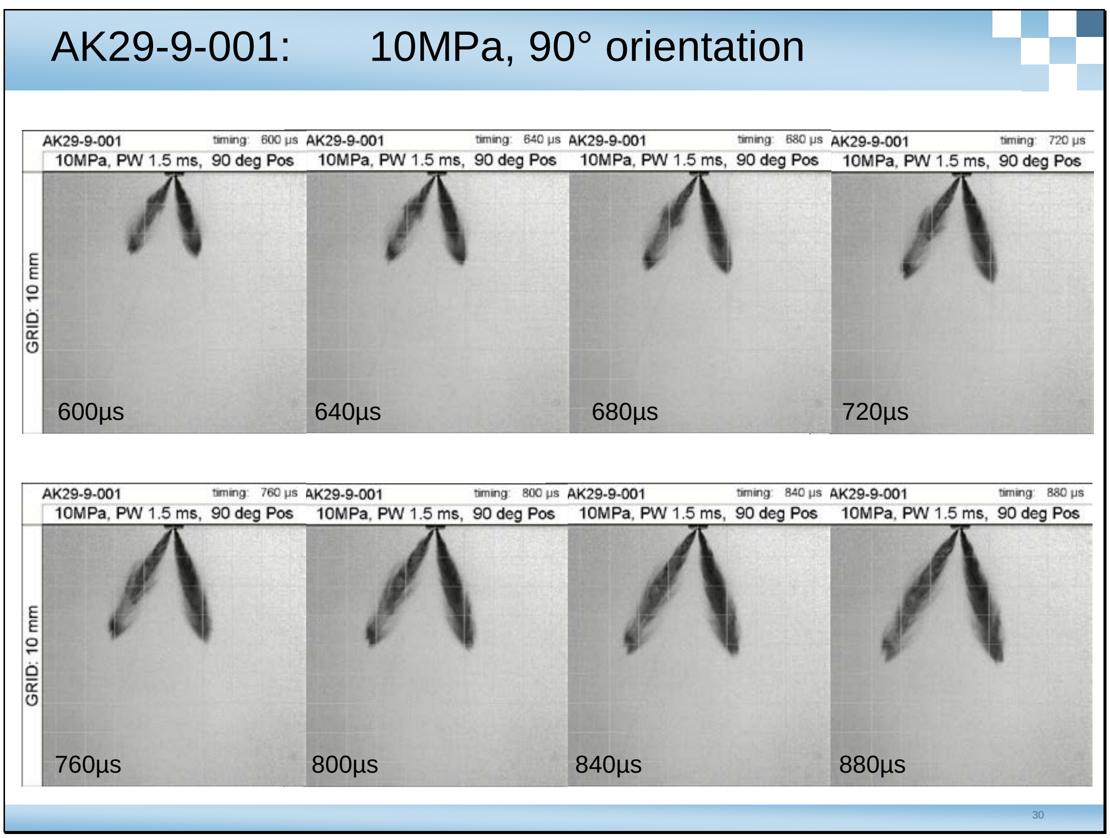
AK29-9-001: 10MPa, 90° orientation
AK29-9-001 timing: 600 µs 10MPa, PW 1.5 ms, 90 deg Pos
AK29-9-001 timing: 640 µs 10MPa, PW 1.5 ms, 90 deg Pos
AK29-9-001 timing: 680 µs 10MPa, PW 1.5 ms, 90 deg Pos
AK29-9-001 timing: 720 µs 10MPa, PW 1.5 ms, 90 deg Pos
GRID: 10 mm
600µs
640µs
680µs
720µs
AK29-9-001 timing: 760 µs 10MPa, PW 1.5 ms, 90 deg Pos
AK29-9-001 timing: 800 µs 10MPa, PW 1.5 ms, 90 deg Pos
AK29-9-001 timing: 840 µs 10MPa, PW 1.5 ms, 90 deg Pos
AK29-9-001 timing: 880 µs 10MPa, PW 1.5 ms, 90 deg Pos
GRID: 10 mm
760µs
800µs
840µs
880µs
30

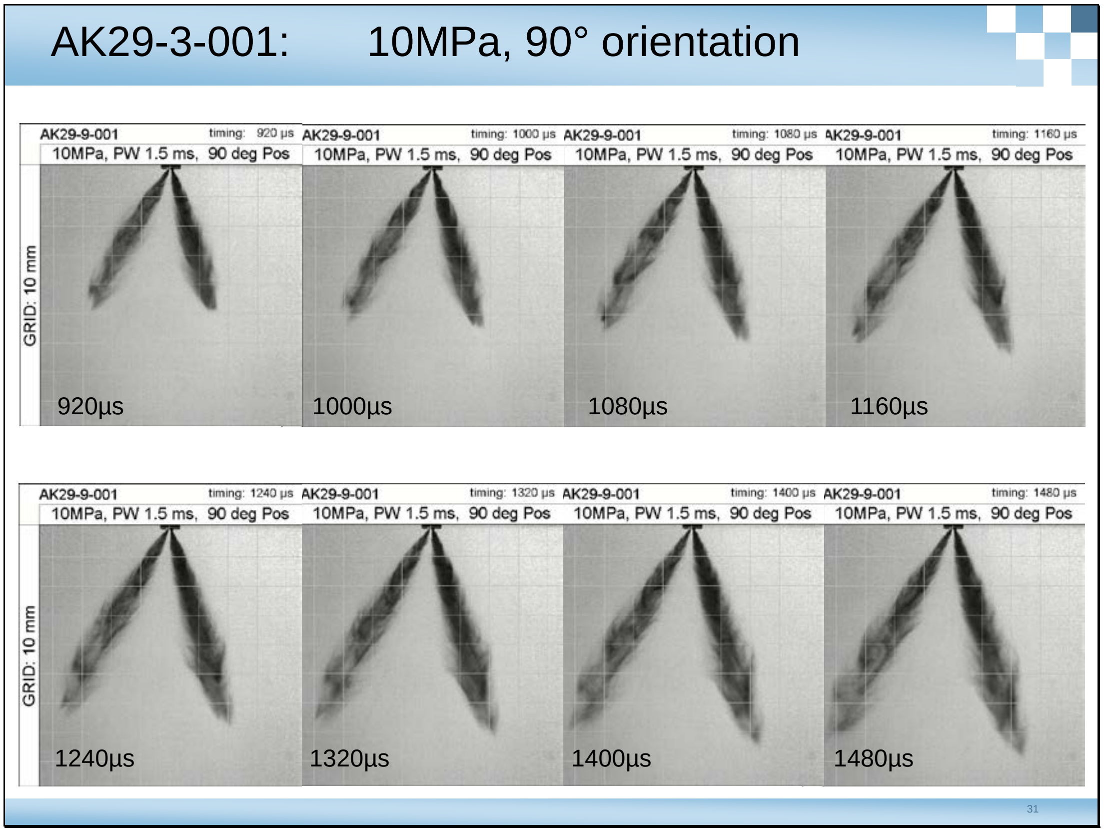
AK29-3-001: 10MPa, 90° orientation
AK29-9-001
timing: 920 µs
10MPa, PW 1.5 ms, 90 deg Pos
timing: 1000 µs
timing: 1080 µs
timing: 1160 µs
timing: 1240 µs
timing: 1320 µs
timing: 1400 µs
timing: 1480 µs
GRID: 10 mm
920µs
1000µs
1080µs
1160µs
1240µs
1320µs
1400µs
1480µs
31

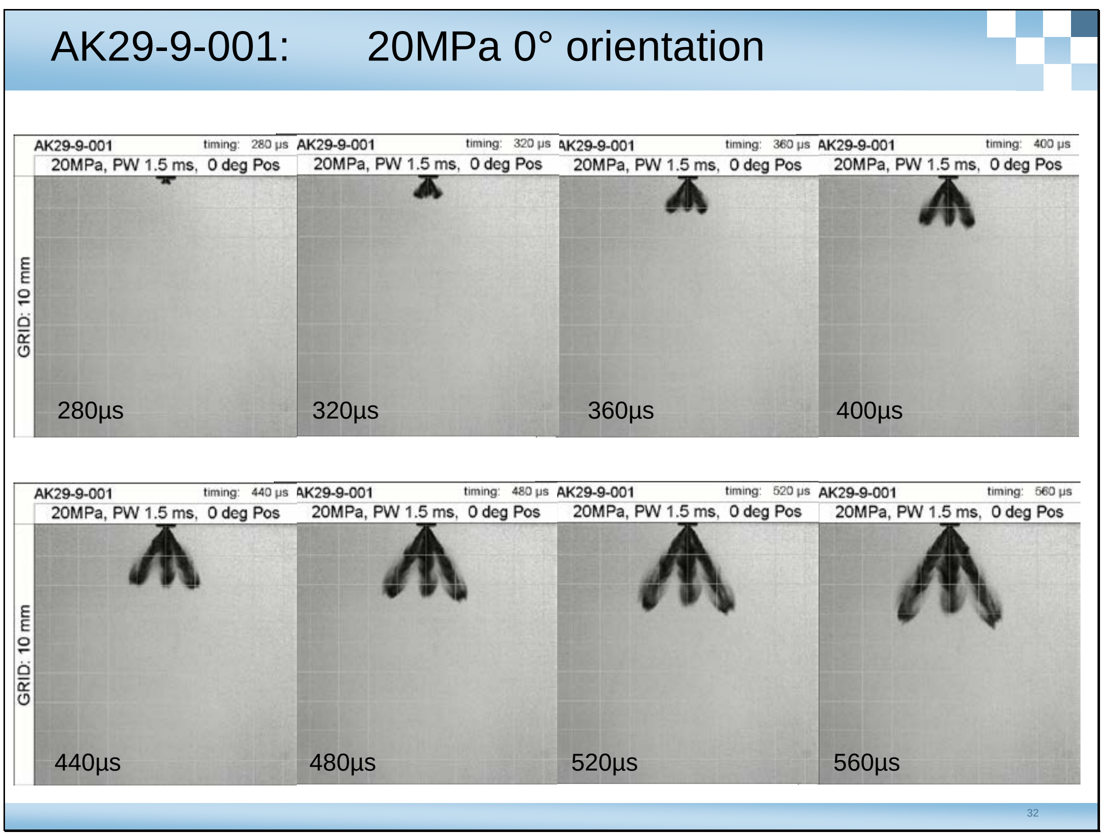
AK29-9-001: 20MPa 0° orientation
AK29-9-001
timing: 280 µs
20MPa, PW 1.5 ms, 0 deg Pos
timing: 320 µs
timing: 360 µs
timing: 400 µs
timing: 440 µs
timing: 480 µs
timing: 520 µs
timing: 560 µs
GRID: 10 mm
280µs
320µs
360µs
400µs
440µs
480µs
520µs
560µs
32

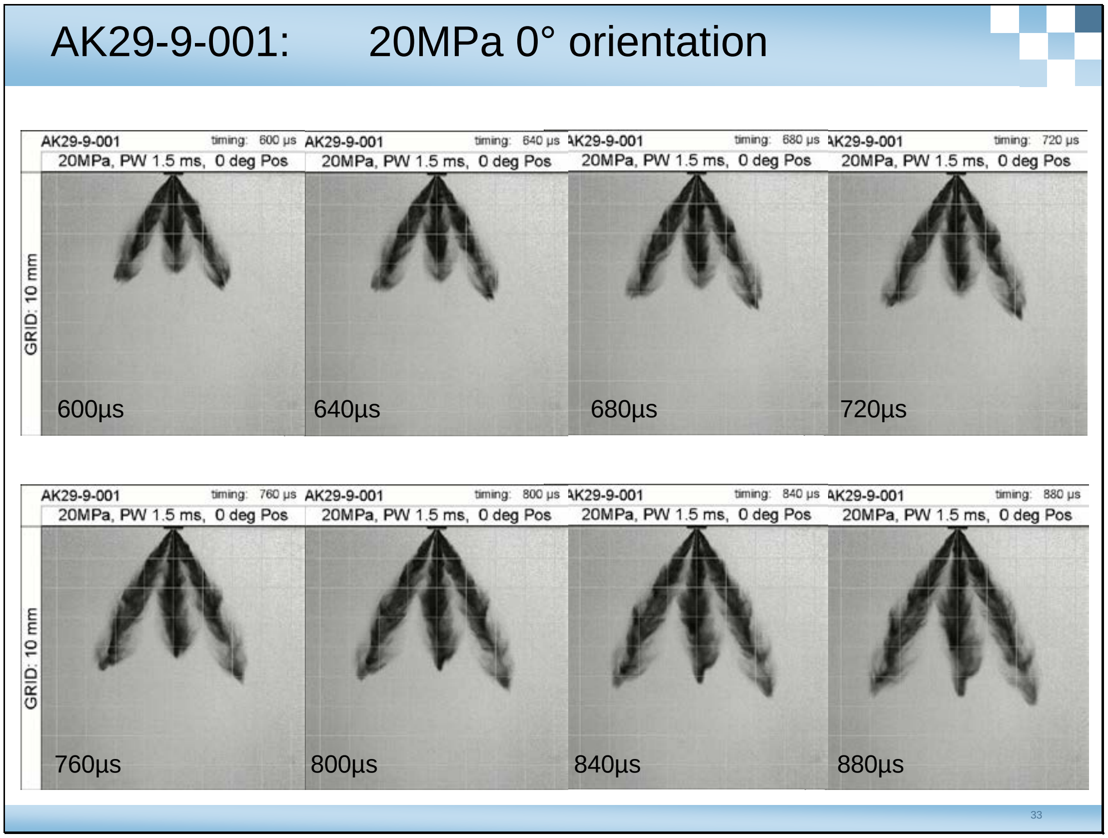
AK29-9-001: 20MPa 0° orientation
AK29-9-001 timing: 600 µs 20MPa, PW 1.5 ms, 0 deg Pos
AK29-9-001 timing: 640 µs 20MPa, PW 1.5 ms, 0 deg Pos
AK29-9-001 timing: 680 µs 20MPa, PW 1.5 ms, 0 deg Pos
AK29-9-001 timing: 720 µs 20MPa, PW 1.5 ms, 0 deg Pos
GRID: 10 mm
600µs
640µs
680µs
720µs
AK29-9-001 timing: 760 µs 20MPa, PW 1.5 ms, 0 deg Pos
AK29-9-001 timing: 800 µs 20MPa, PW 1.5 ms, 0 deg Pos
AK29-9-001 timing: 840 µs 20MPa, PW 1.5 ms, 0 deg Pos
AK29-9-001 timing: 880 µs 20MPa, PW 1.5 ms, 0 deg Pos
GRID: 10 mm
760µs
800µs
840µs
880µs
33

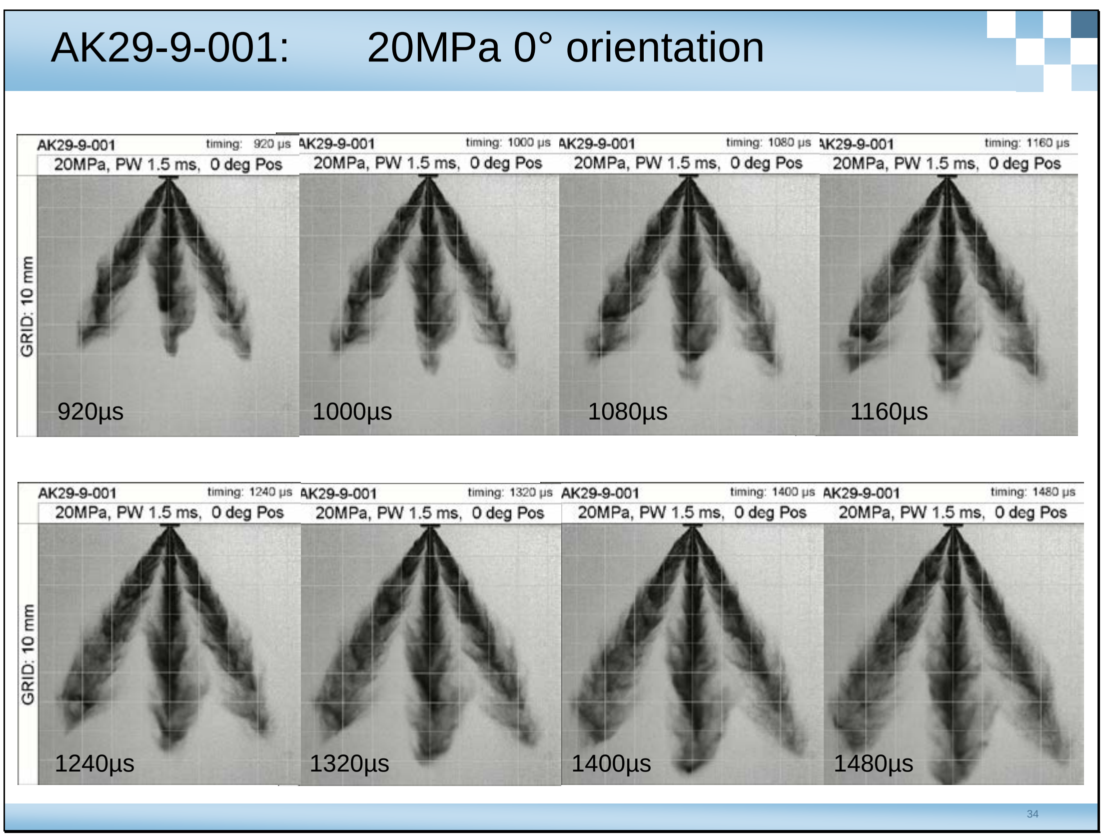
AK29-9-001: 20MPa 0° orientation
AK29-9-001 timing: 920 µs 20MPa, PW 1.5 ms, 0 deg Pos
AK29-9-001 timing: 1000 µs 20MPa, PW 1.5 ms, 0 deg Pos
AK29-9-001 timing: 1080 µs 20MPa, PW 1.5 ms, 0 deg Pos
AK29-9-001 timing: 1160 µs 20MPa, PW 1.5 ms, 0 deg Pos
GRID: 10 mm
920µs
1000µs
1080µs
1160µs
AK29-9-001 timing: 1240 µs 20MPa, PW 1.5 ms, 0 deg Pos
AK29-9-001 timing: 1320 µs 20MPa, PW 1.5 ms, 0 deg Pos
AK29-9-001 timing: 1400 µs 20MPa, PW 1.5 ms, 0 deg Pos
AK29-9-001 timing: 1480 µs 20MPa, PW 1.5 ms, 0 deg Pos
GRID: 10 mm
1240µs
1320µs
1400µs
1480µs
34

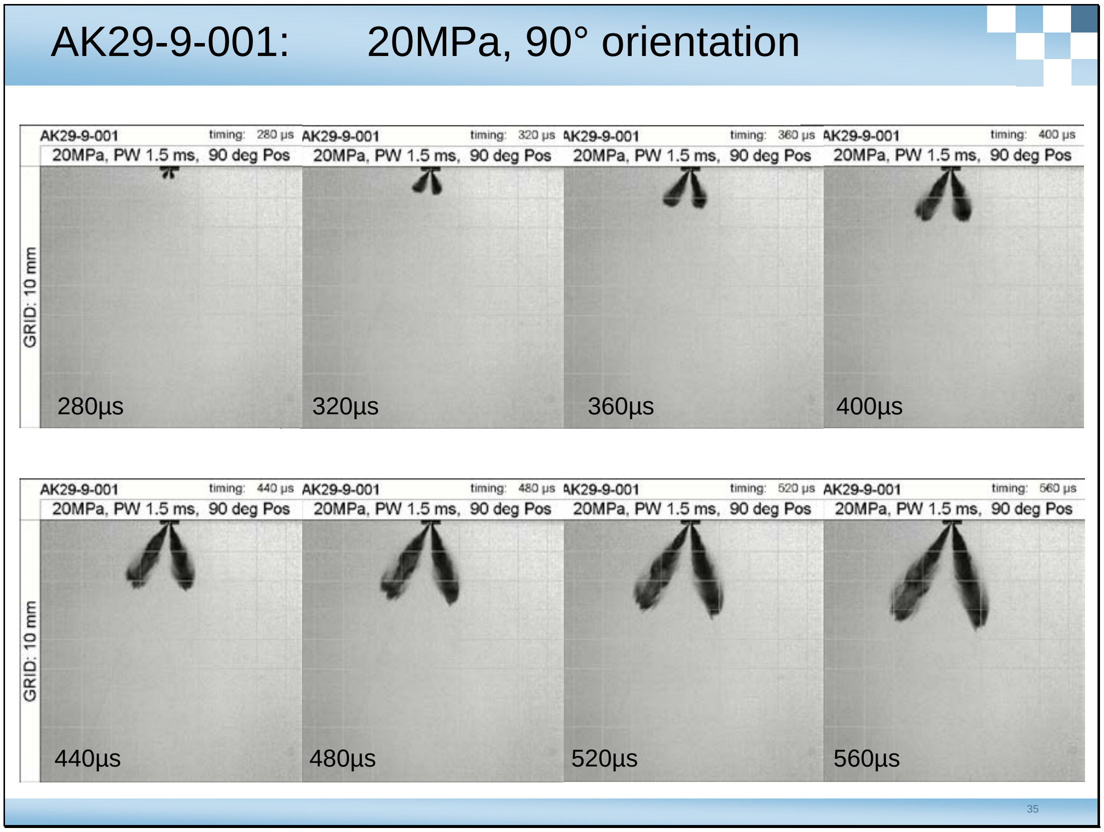
AK29-9-001: 20MPa, 90° orientation
AK29-9-001
20MPa, PW 1.5 ms, 90 deg Pos
GRID: 10 mm
280µs
320µs
360µs
400µs
440µs
480µs
520µs
560µs
35

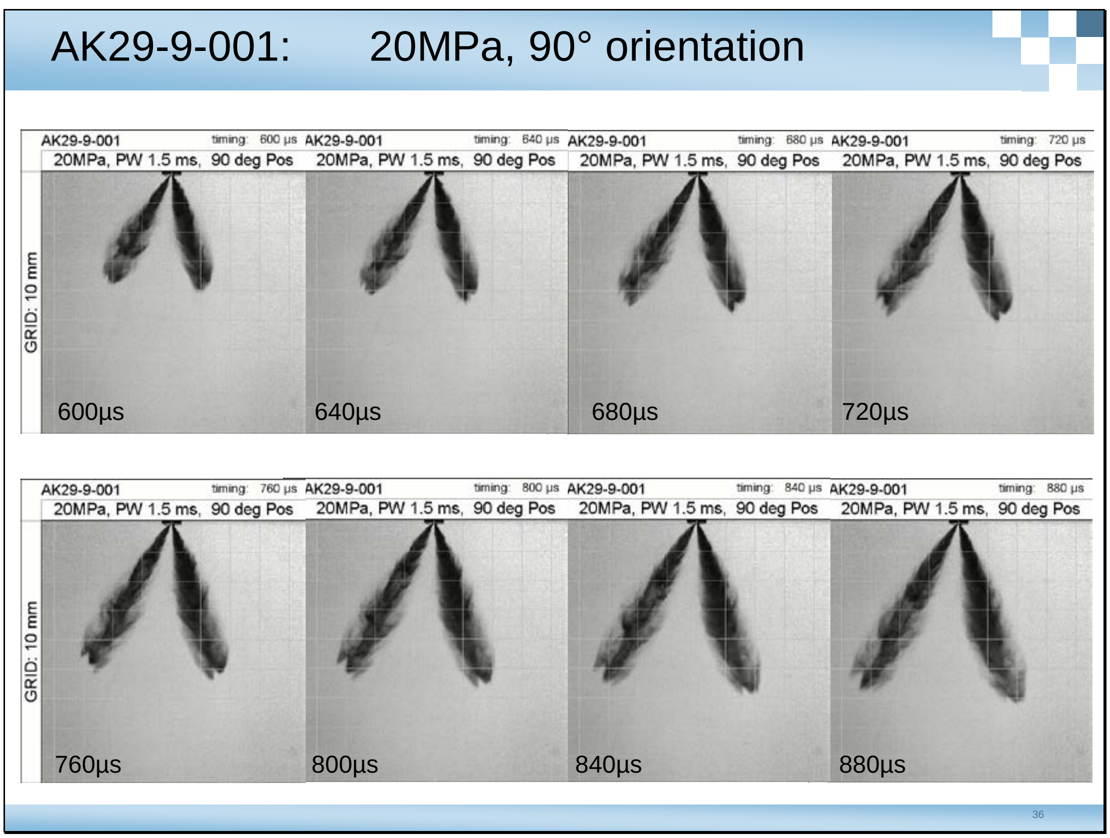
AK29-9-001: 20MPa, 90° orientation
AK29-9-001
20MPa, PW 1.5 ms, 90 deg Pos
GRID: 10 mm
600µs
640µs
680µs
720µs
760µs
800µs
840µs
880µs
36

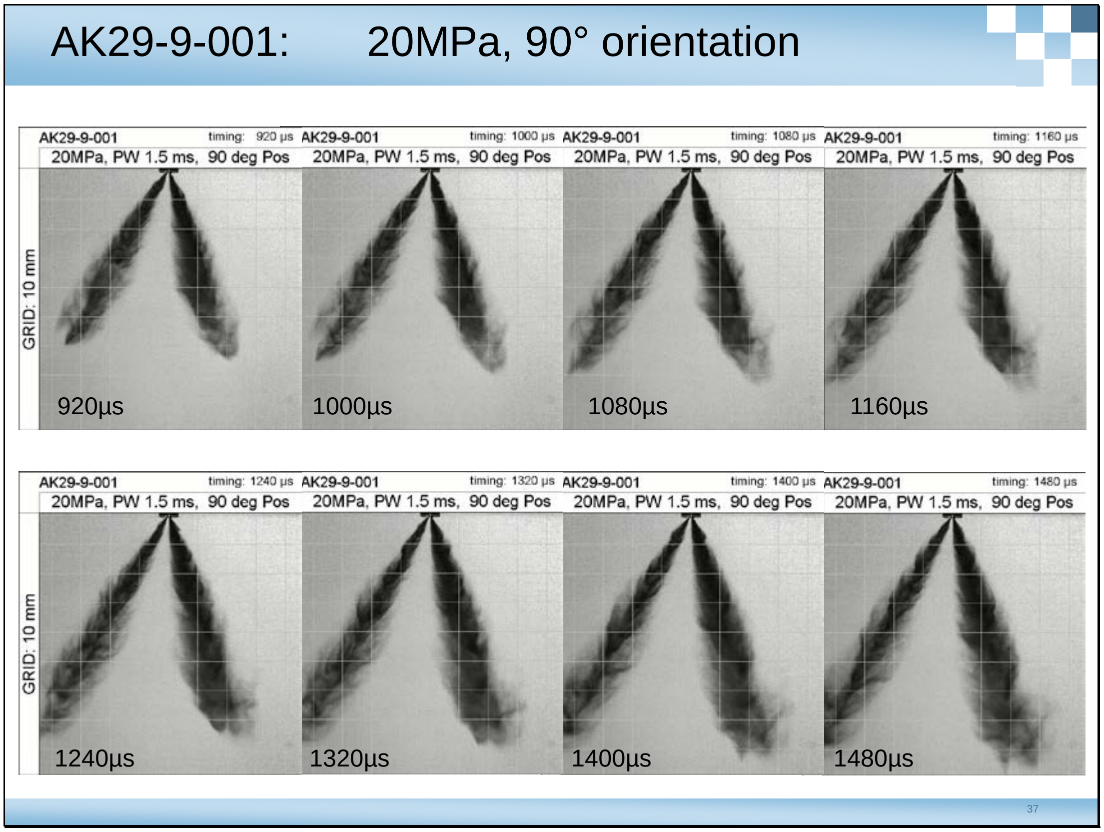
AK29-9-001: 20MPa, 90° orientation
AK29-9-001
20MPa, PW 1.5 ms, 90 deg Pos
GRID: 10 mm
timing: 920 µs
timing: 1000 µs
timing: 1080 µs
timing: 1160 µs
timing: 1240 µs
timing: 1320 µs
timing: 1400 µs
timing: 1480 µs
920µs
1000µs
1080µs
1160µs
1240µs
1320µs
1400µs
1480µs
37

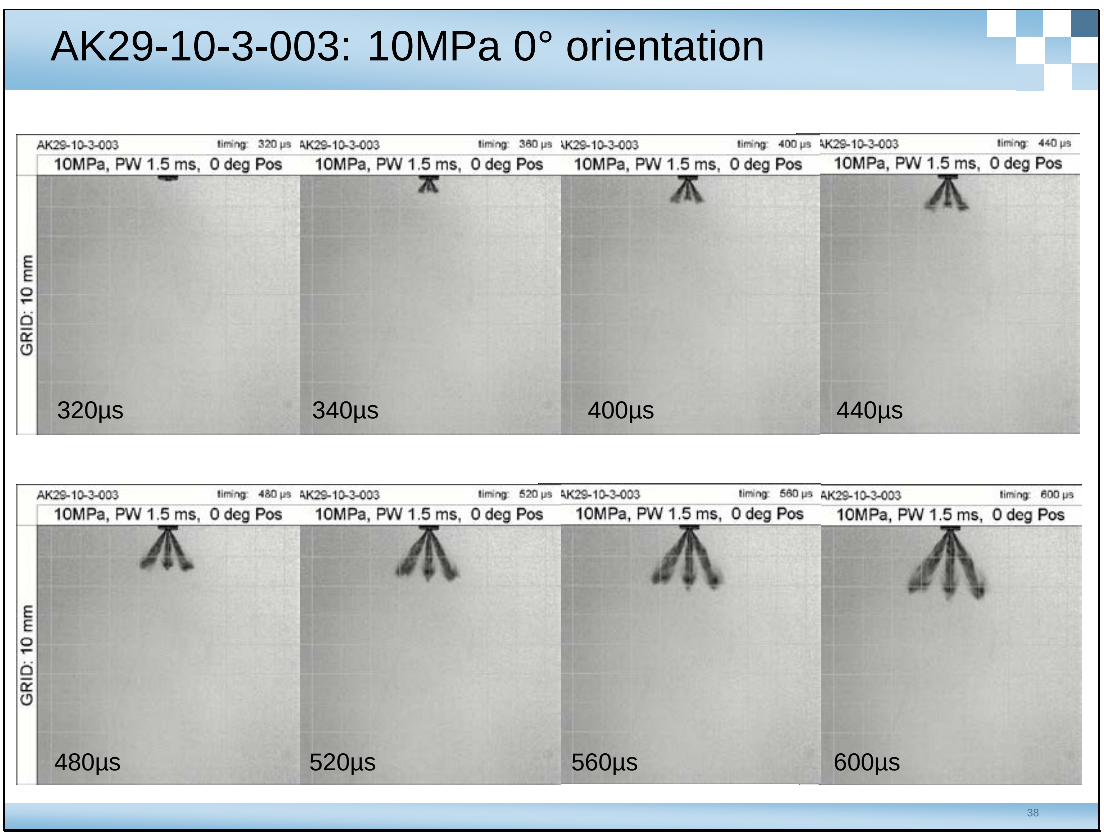
AK29-10-3-003: 10MPa 0° orientation
AK29-10-3-003
10MPa, PW 1.5 ms, 0 deg Pos
GRID: 10 mm
timing: 320 µs
timing: 360 µs
timing: 400 µs
timing: 440 µs
timing: 480 µs
timing: 520 µs
timing: 560 µs
timing: 600 µs
320µs
340µs
400µs
440µs
480µs
520µs
560µs
600µs
38

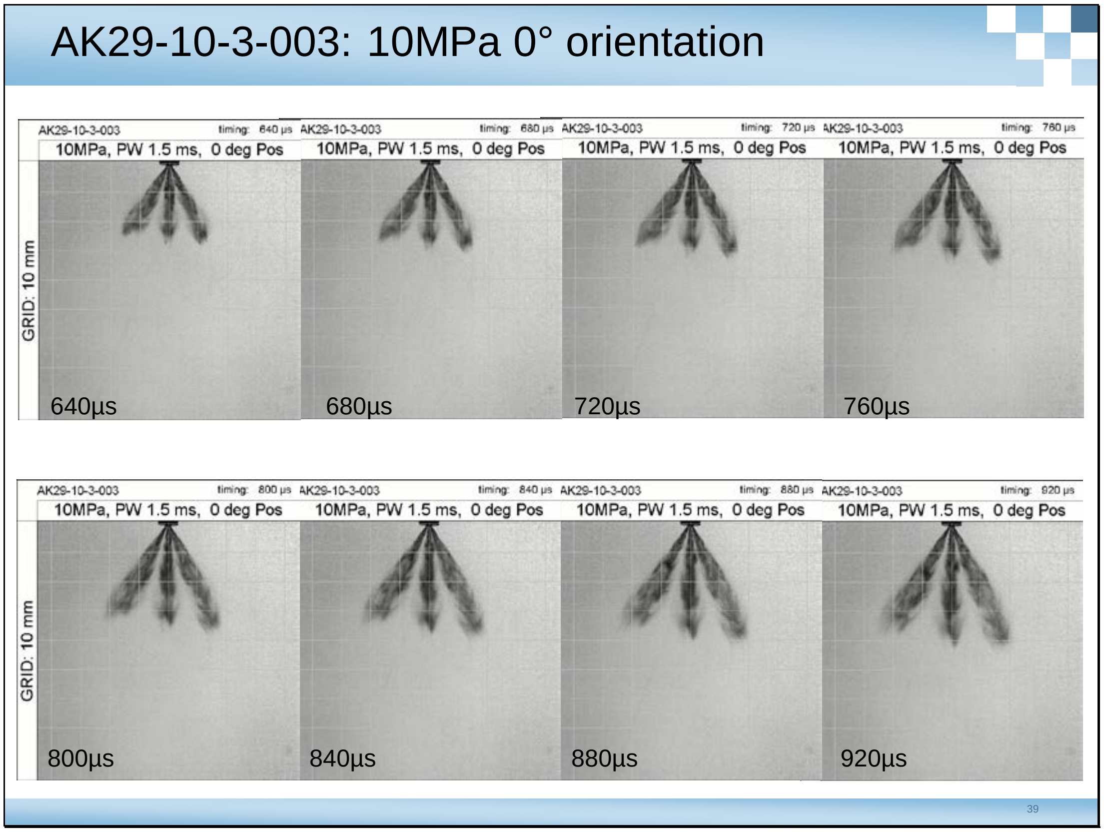
AK29-10-3-003: 10MPa 0° orientation
AK29-10-3-003
10MPa, PW 1.5 ms, 0 deg Pos
GRID: 10 mm
640µs
680µs
720µs
760µs
800µs
840µs
880µs
920µs
39

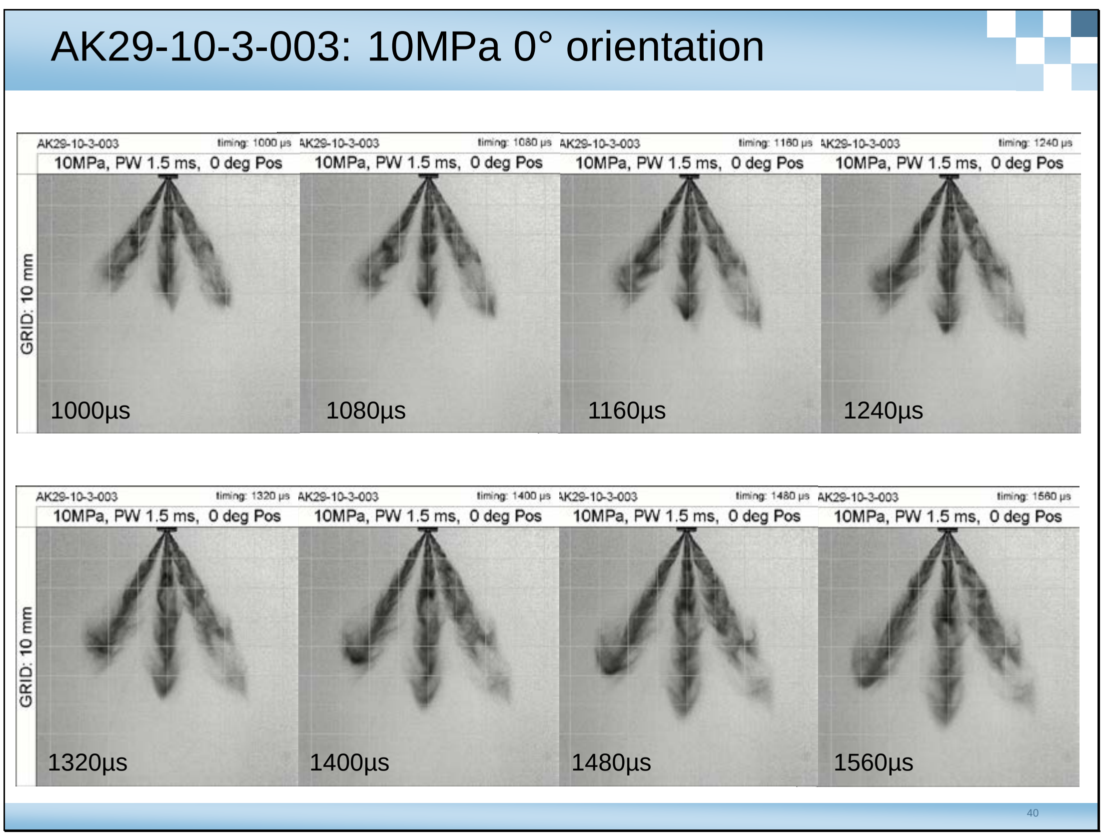
AK29-10-3-003: 10MPa 0° orientation
AK29-10-3-003
10MPa, PW 1.5 ms, 0 deg Pos
GRID: 10 mm
1000µs
1080µs
1160µs
1240µs
1320µs
1400µs
1480µs
1560µs
40

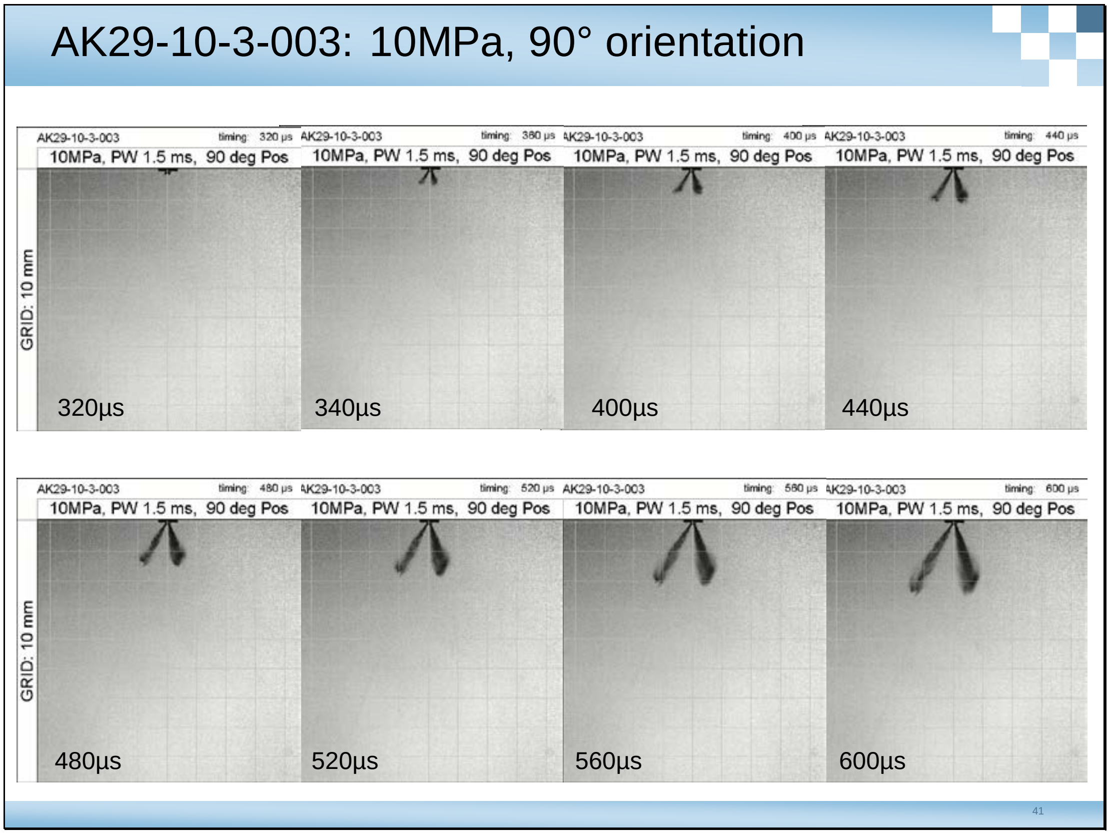
AK29-10-3-003: 10MPa, 90° orientation
AK29-10-3-003
10MPa, PW 1.5 ms, 90 deg Pos
GRID: 10 mm
320µs
340µs
400µs
440µs
480µs
520µs
560µs
600µs
41

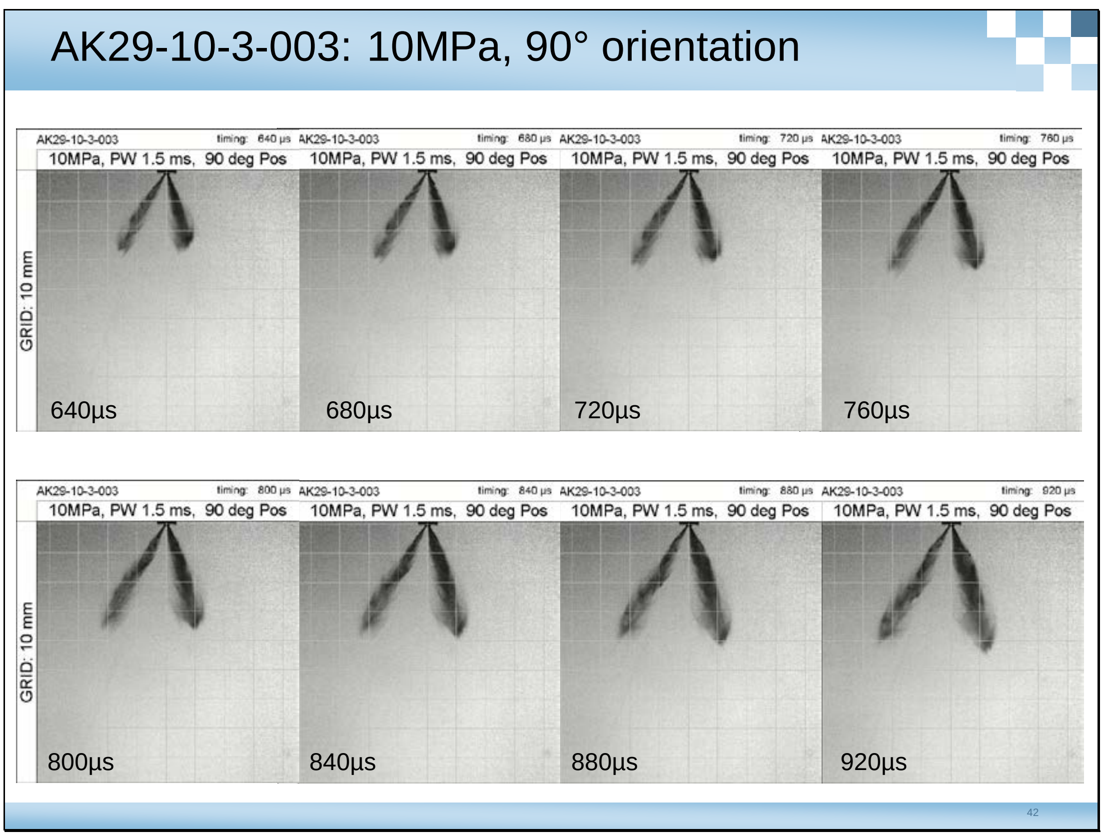
AK29-10-3-003: 10MPa, 90° orientation
AK29-10-3-003
10MPa, PW 1.5 ms, 90 deg Pos
GRID: 10 mm
640µs
680µs
720µs
760µs
800µs
840µs
880µs
920µs
42

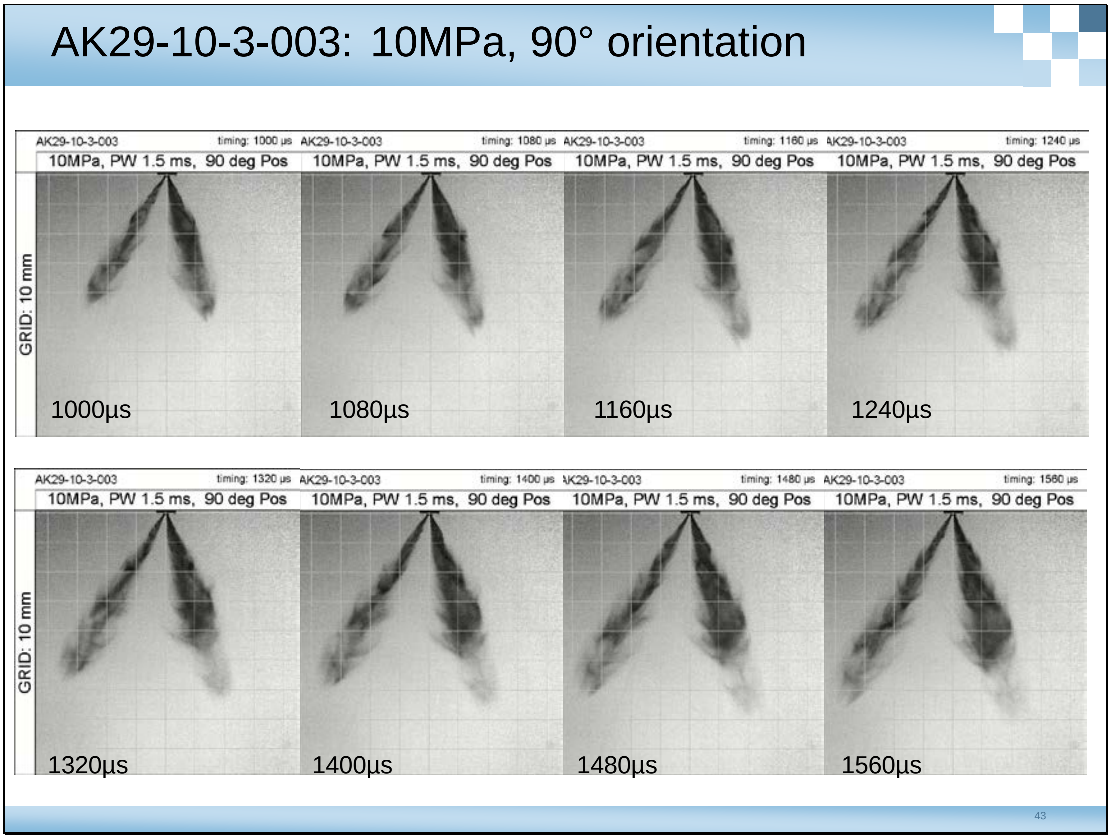
AK29-10-3-003: 10MPa, 90° orientation
10MPa, PW 1.5 ms, 90 deg Pos
GRID: 10 mm
1000µs
1080µs
1160µs
1240µs
1320µs
1400µs
1480µs
1560µs
43

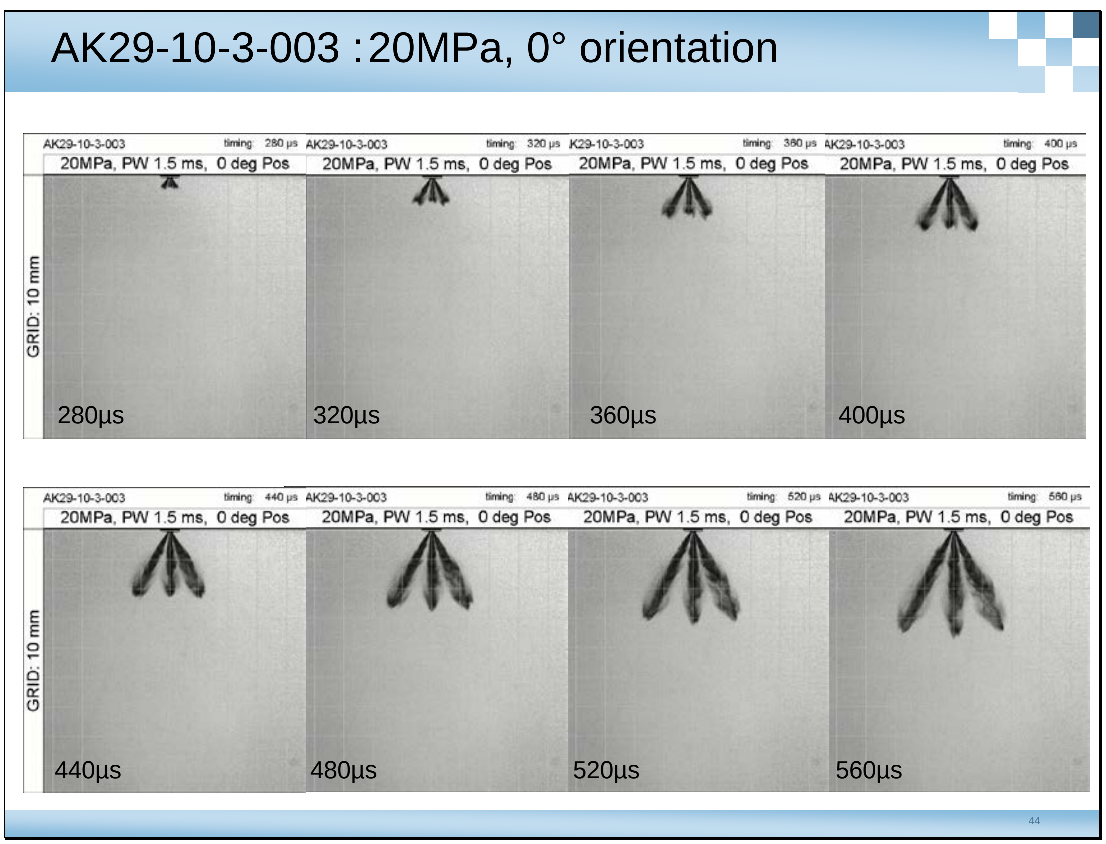
AK29-10-3-003 :20MPa, 0° orientation
20MPa, PW 1.5 ms, 0 deg Pos
GRID: 10 mm
280µs
320µs
360µs
400µs
440µs
480µs
520µs
560µs
44

## AK29-10-3-003 :20MPa, 0° orientation

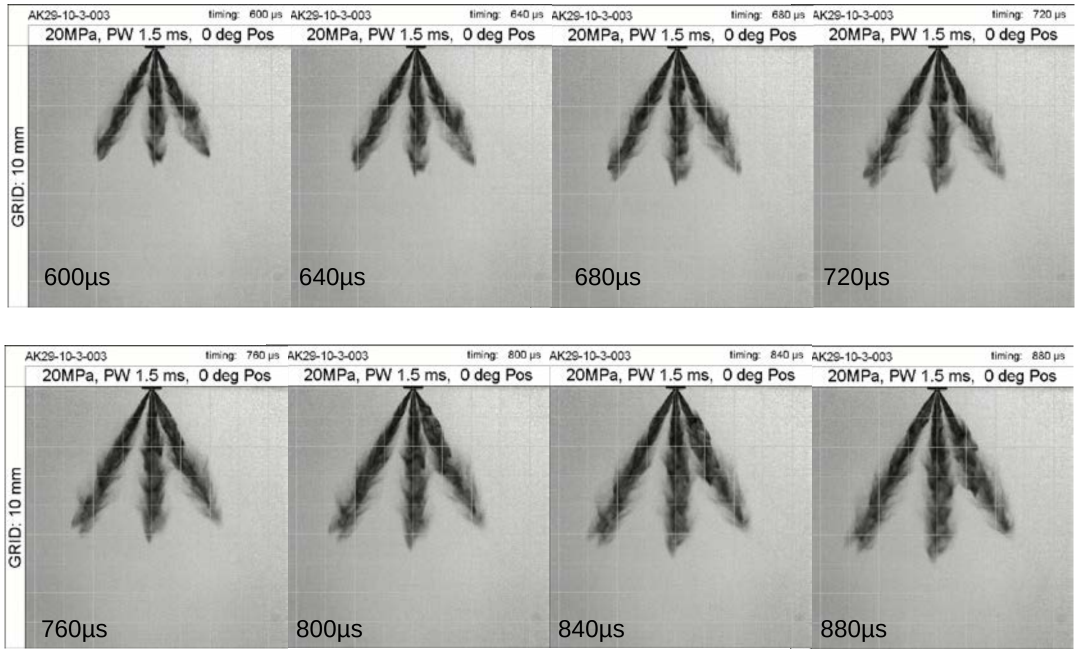


45

## AK29-10-3-003: 20MPa, 0° orientation

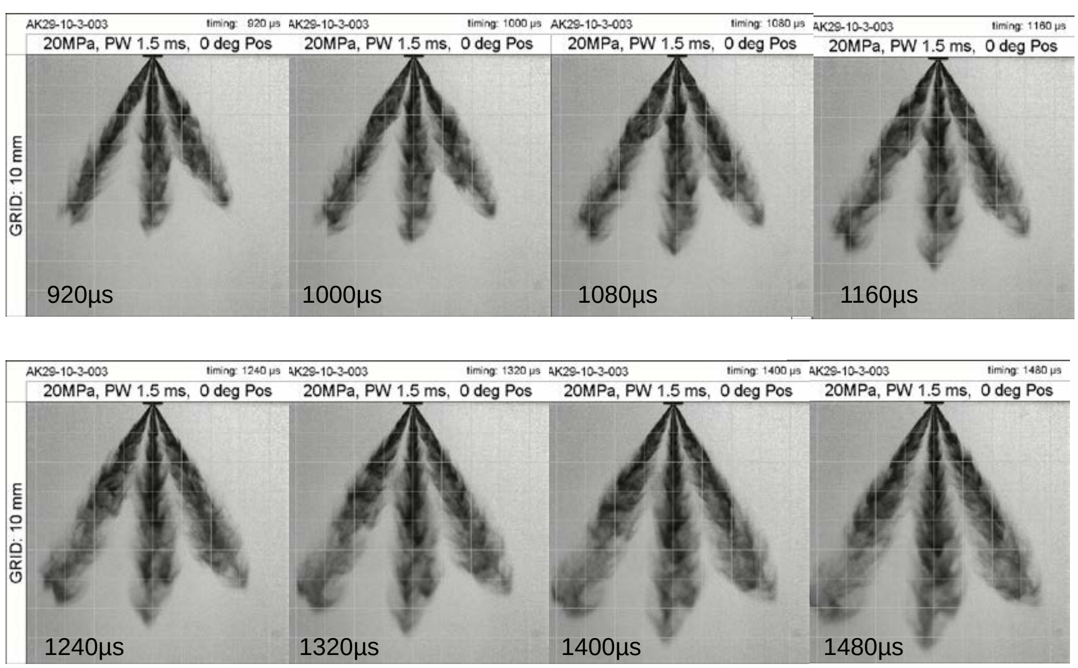


46

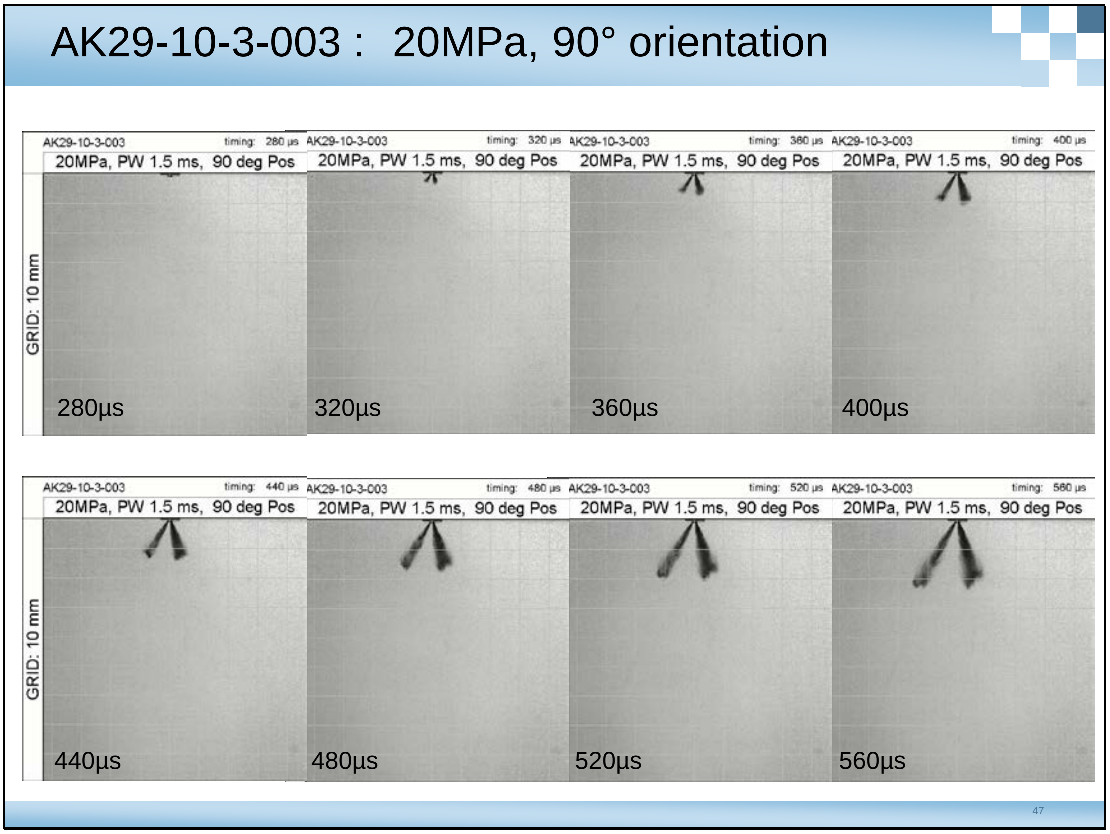
AK29-10-3-003 : 20MPa, 90° orientation
AK29-10-3-003
20MPa, PW 1.5 ms, 90 deg Pos
GRID: 10 mm
280µs
320µs
360µs
400µs
440µs
480µs
520µs
560µs
47

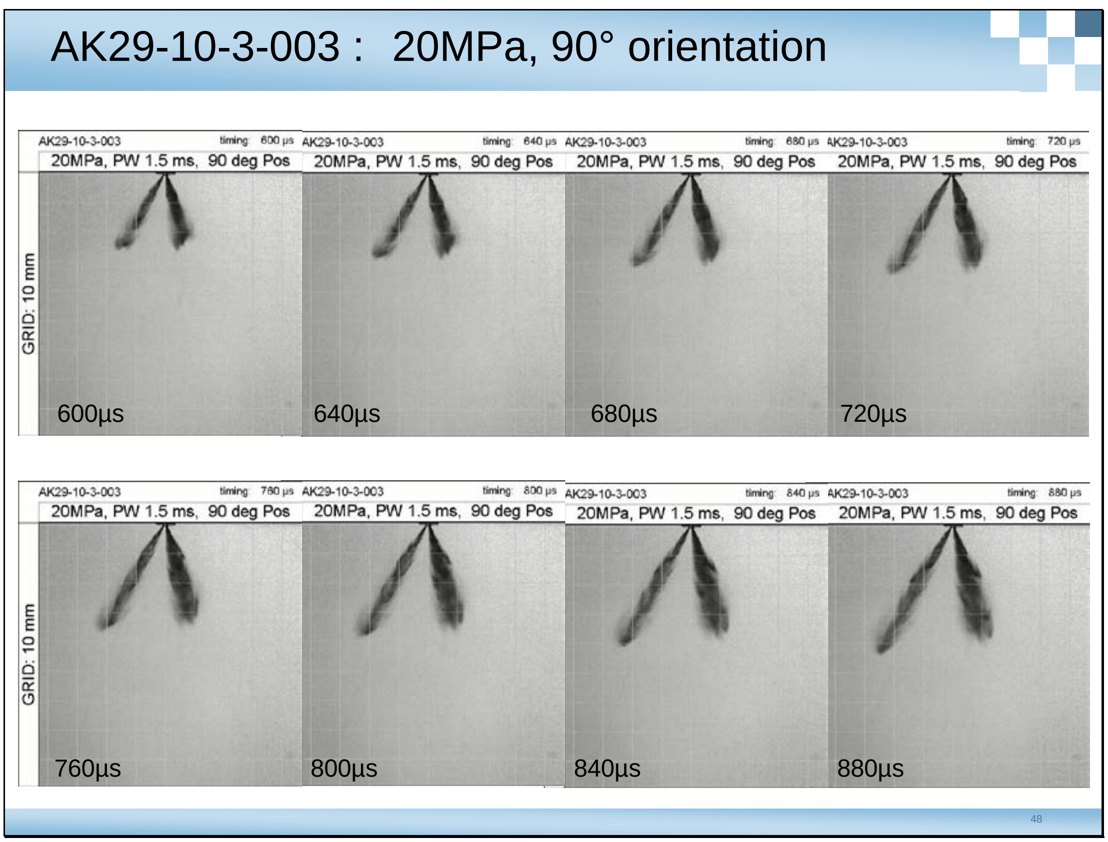
AK29-10-3-003 : 20MPa, 90° orientation
AK29-10-3-003
20MPa, PW 1.5 ms, 90 deg Pos
GRID: 10 mm
600µs
640µs
680µs
720µs
760µs
800µs
840µs
880µs
48

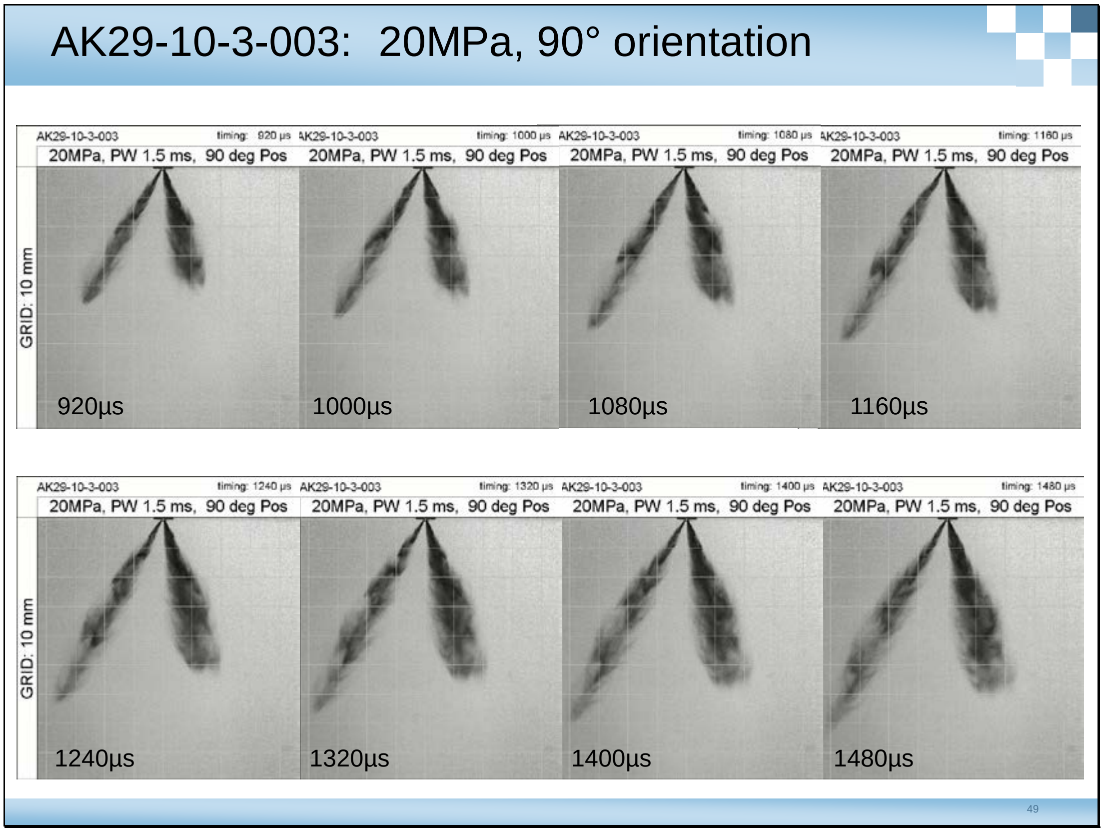
AK29-10-3-003: 20MPa, 90° orientation
20MPa, PW 1.5 ms, 90 deg Pos
GRID: 10 mm
920µs
1000µs
1080µs
1160µs
1240µs
1320µs
1400µs
1480µs
49

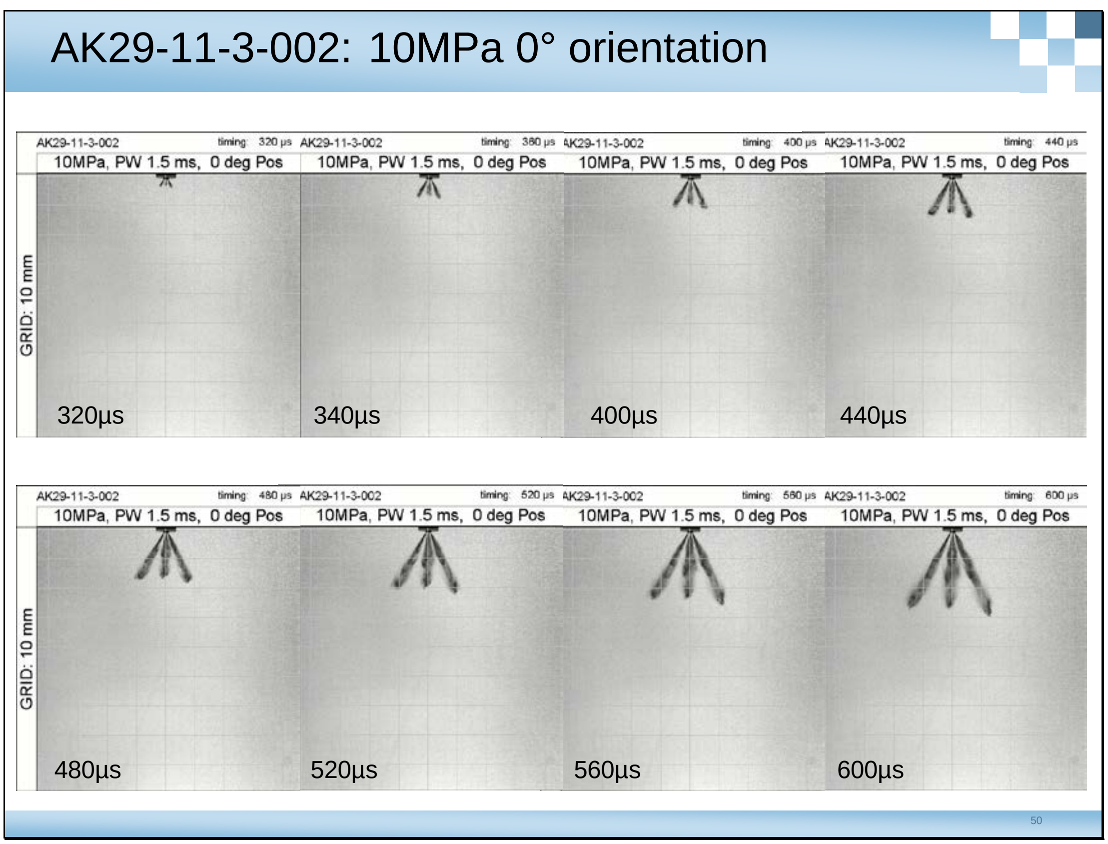
AK29-11-3-002: 10MPa 0° orientation
10MPa, PW 1.5 ms, 0 deg Pos
GRID: 10 mm
320µs
340µs
400µs
440µs
480µs
520µs
560µs
600µs
50

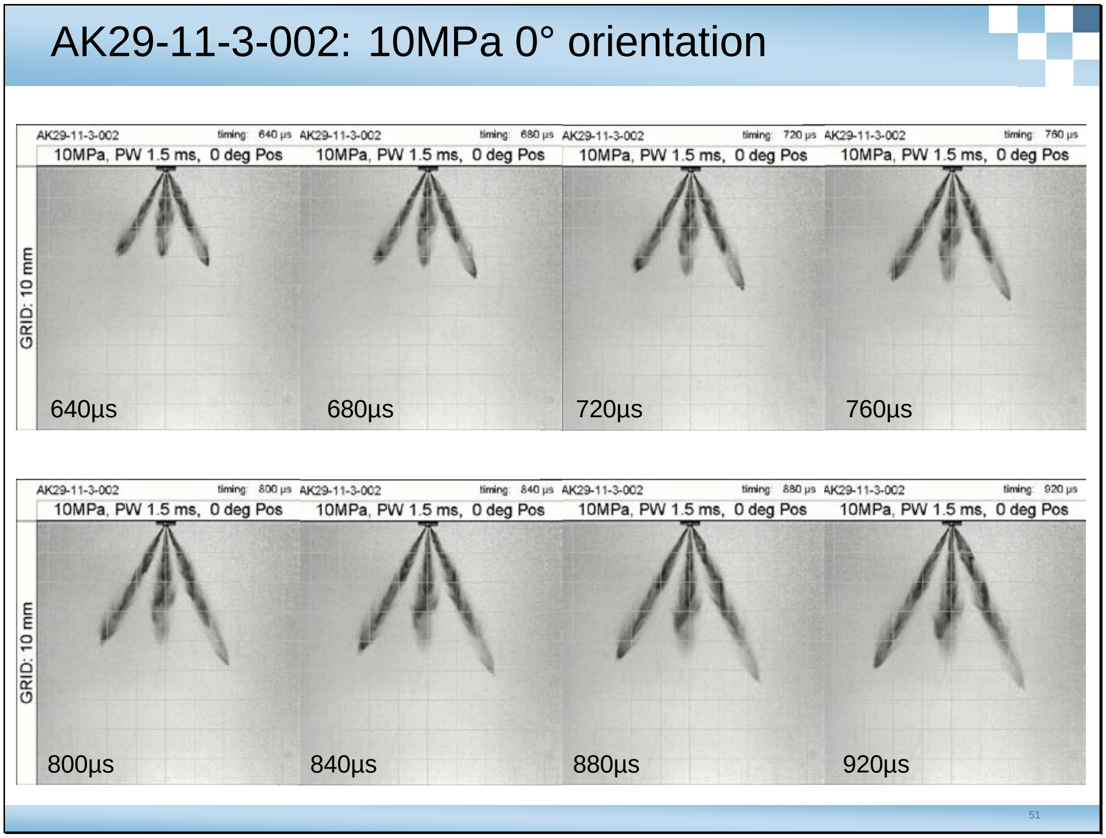
AK29-11-3-002: 10MPa 0° orientation
10MPa, PW 1.5 ms, 0 deg Pos
GRID: 10 mm
640µs
680µs
720µs
760µs
800µs
840µs
880µs
920µs
51

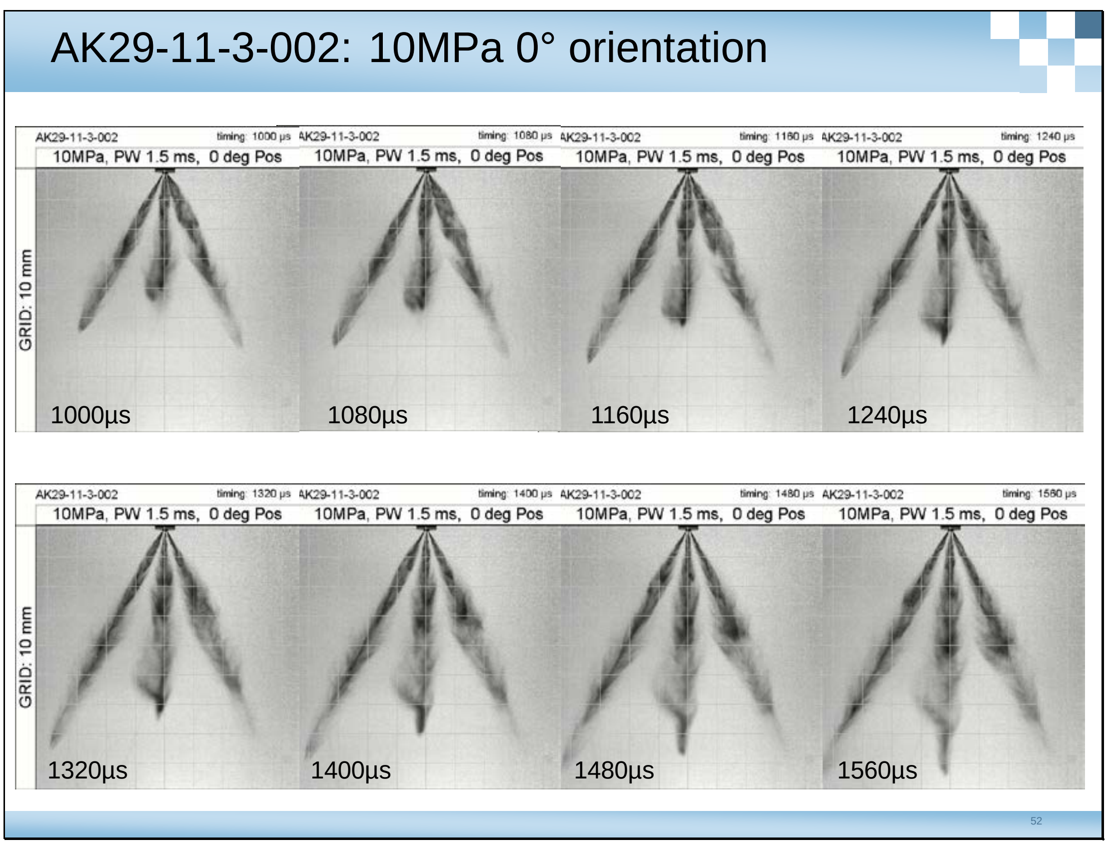
AK29-11-3-002: 10MPa 0° orientation
10MPa, PW 1.5 ms, 0 deg Pos
GRID: 10 mm
1000µs
1080µs
1160µs
1240µs
1320µs
1400µs
1480µs
1560µs
52

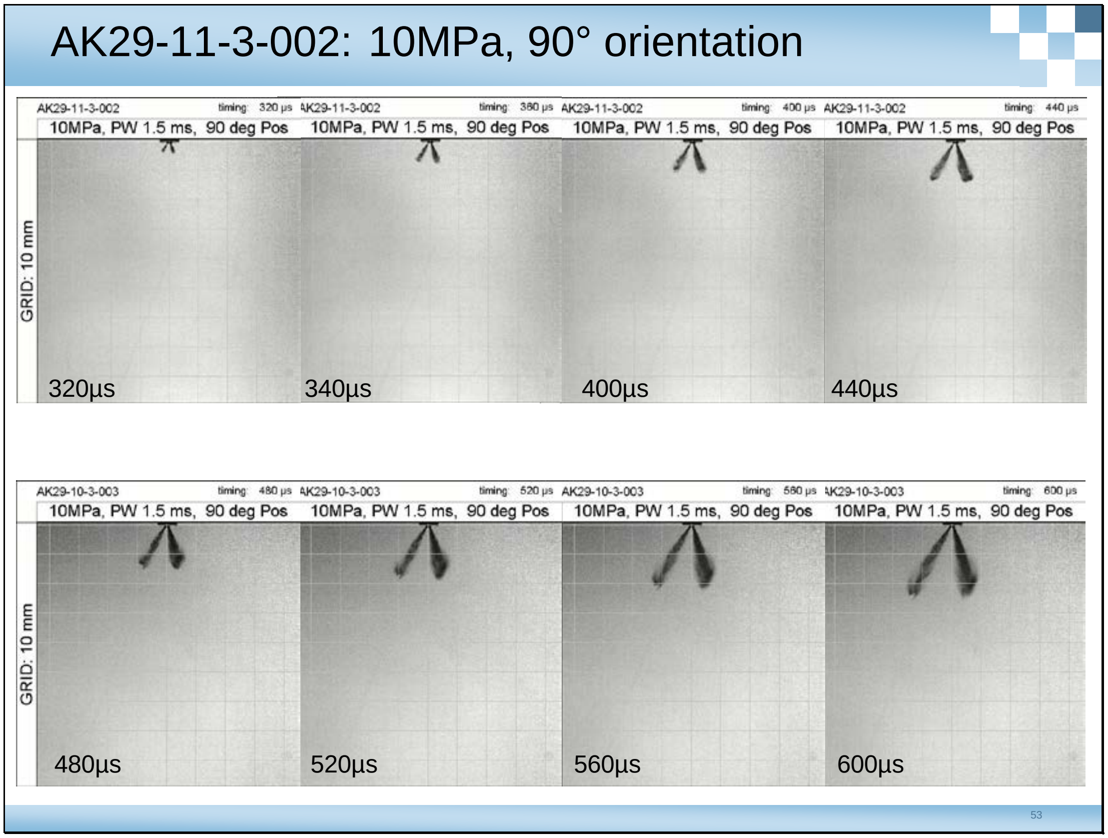
AK29-11-3-002: 10MPa, 90° orientation
AK29-11-3-002
10MPa, PW 1.5 ms, 90 deg Pos
AK29-10-3-003
10MPa, PW 1.5 ms, 90 deg Pos
GRID: 10 mm
320µs
340µs
400µs
440µs
480µs
520µs
560µs
600µs
53

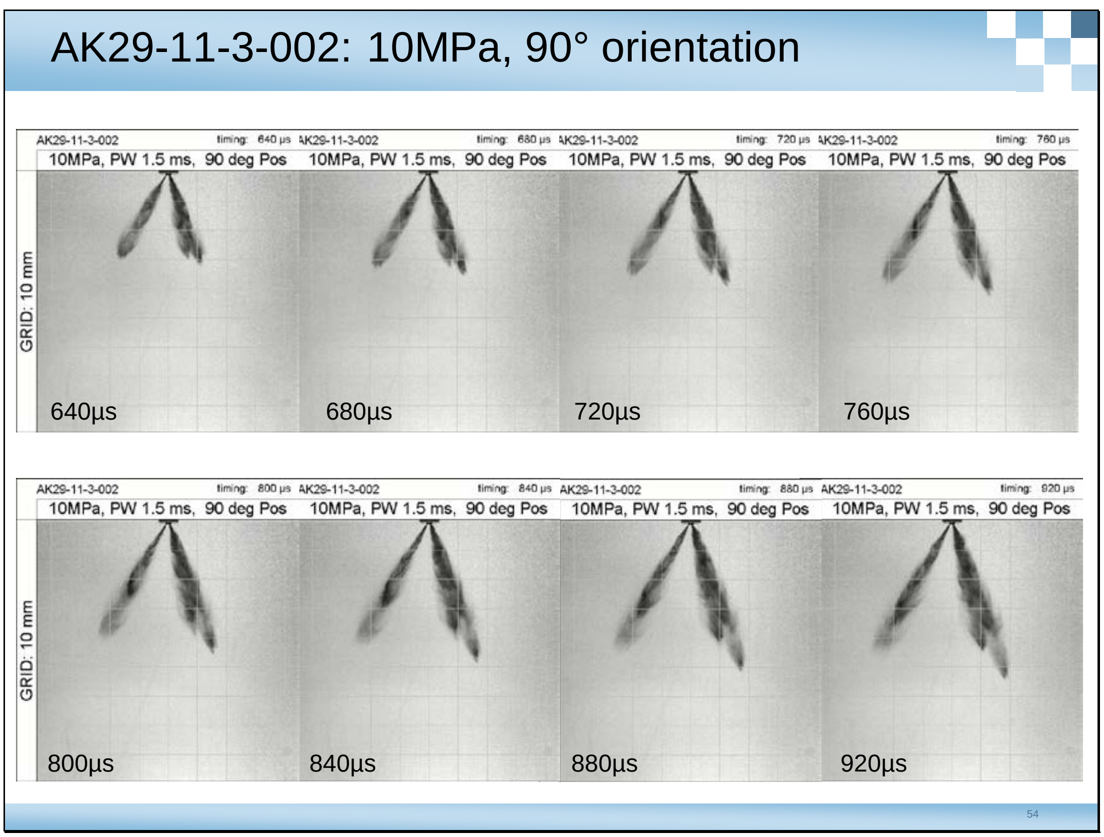
AK29-11-3-002: 10MPa, 90° orientation
AK29-11-3-002
10MPa, PW 1.5 ms, 90 deg Pos
GRID: 10 mm
640µs
680µs
720µs
760µs
800µs
840µs
880µs
920µs
54

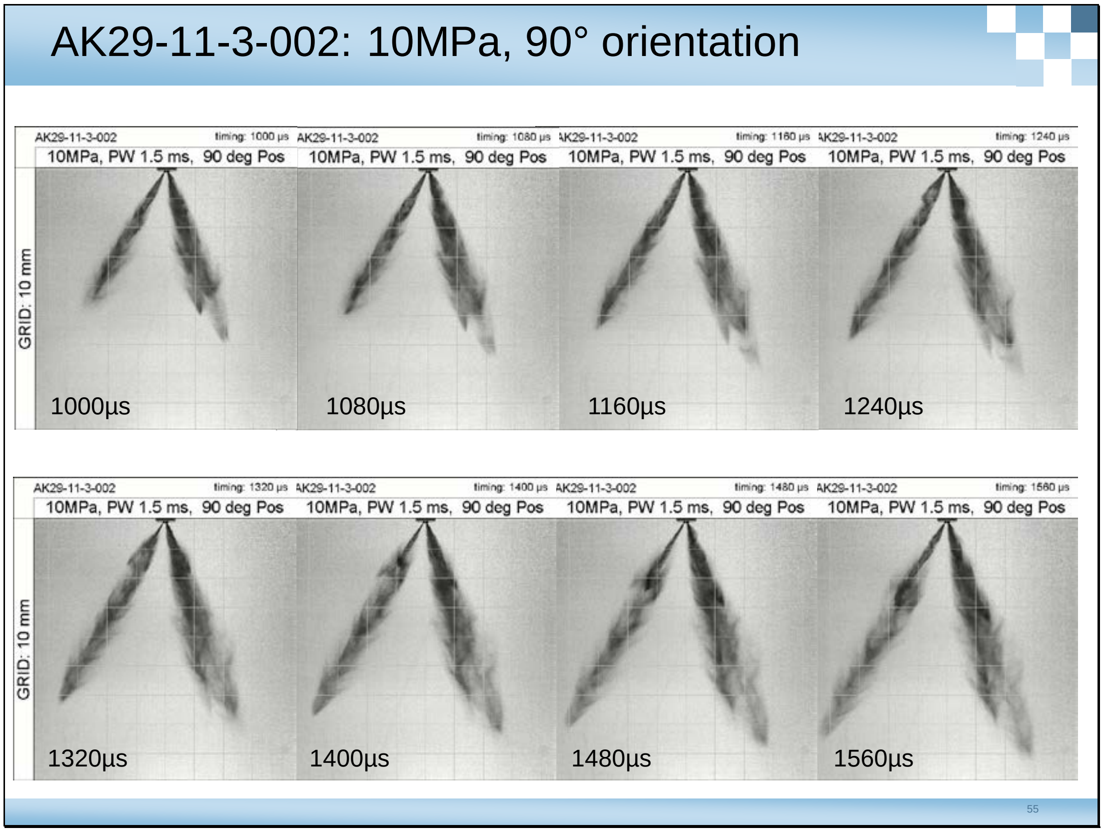
AK29-11-3-002: 10MPa, 90° orientation
AK29-11-3-002 timing: 1000 µs
10MPa, PW 1.5 ms, 90 deg Pos
AK29-11-3-002 timing: 1080 µs
10MPa, PW 1.5 ms, 90 deg Pos
AK29-11-3-002 timing: 1160 µs
10MPa, PW 1.5 ms, 90 deg Pos
AK29-11-3-002 timing: 1240 µs
10MPa, PW 1.5 ms, 90 deg Pos
GRID: 10 mm
1000µs
1080µs
1160µs
1240µs
AK29-11-3-002 timing: 1320 µs
10MPa, PW 1.5 ms, 90 deg Pos
AK29-11-3-002 timing: 1400 µs
10MPa, PW 1.5 ms, 90 deg Pos
AK29-11-3-002 timing: 1480 µs
10MPa, PW 1.5 ms, 90 deg Pos
AK29-11-3-002 timing: 1560 µs
10MPa, PW 1.5 ms, 90 deg Pos
GRID: 10 mm
1320µs
1400µs
1480µs
1560µs
55

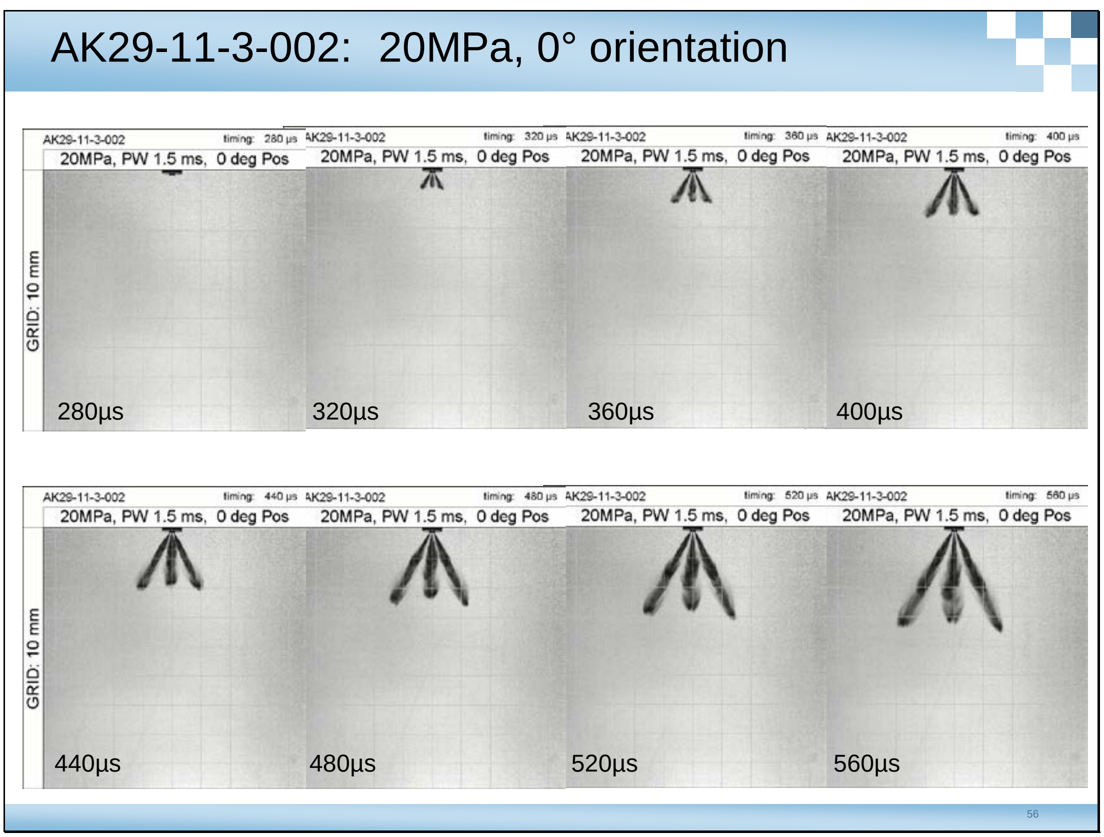
AK29-11-3-002: 20MPa, 0° orientation
AK29-11-3-002 timing: 280 µs
20MPa, PW 1.5 ms, 0 deg Pos
AK29-11-3-002 timing: 320 µs
20MPa, PW 1.5 ms, 0 deg Pos
AK29-11-3-002 timing: 360 µs
20MPa, PW 1.5 ms, 0 deg Pos
AK29-11-3-002 timing: 400 µs
20MPa, PW 1.5 ms, 0 deg Pos
GRID: 10 mm
280µs
320µs
360µs
400µs
AK29-11-3-002 timing: 440 µs
20MPa, PW 1.5 ms, 0 deg Pos
AK29-11-3-002 timing: 480 µs
20MPa, PW 1.5 ms, 0 deg Pos
AK29-11-3-002 timing: 520 µs
20MPa, PW 1.5 ms, 0 deg Pos
AK29-11-3-002 timing: 560 µs
20MPa, PW 1.5 ms, 0 deg Pos
GRID: 10 mm
440µs
480µs
520µs
560µs
56

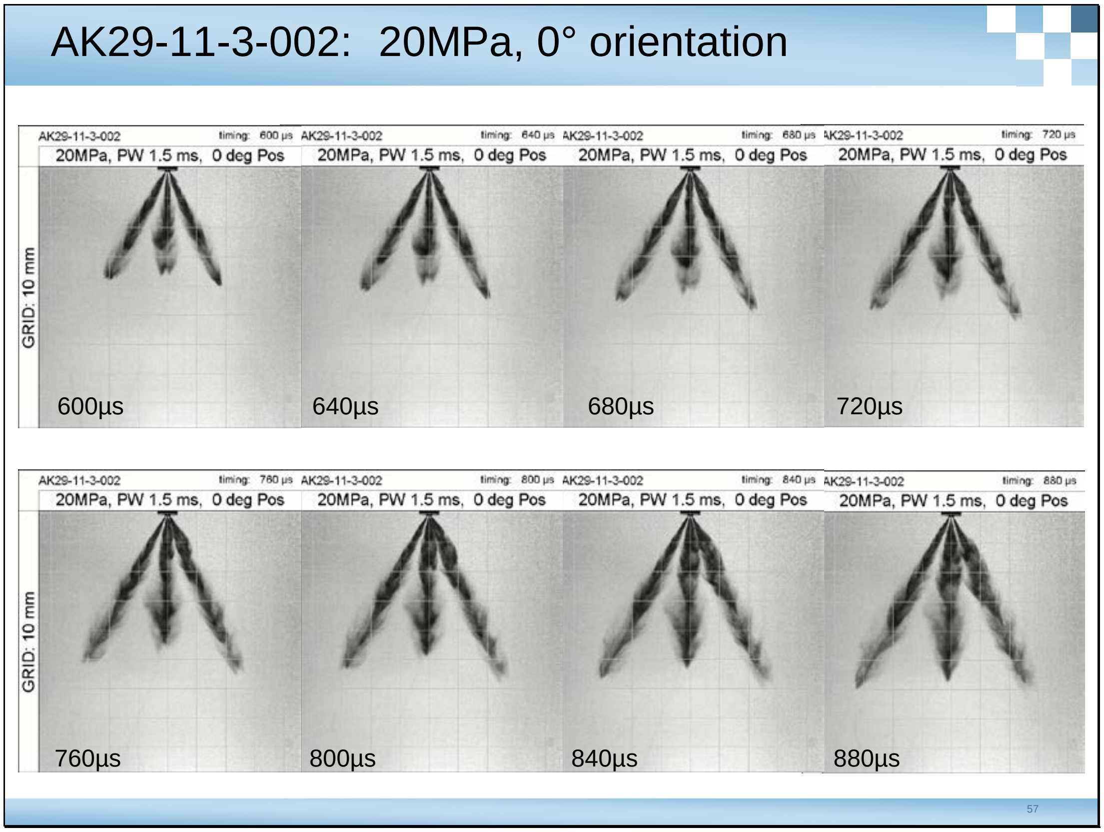
AK29-11-3-002: 20MPa, 0° orientation
AK29-11-3-002
20MPa, PW 1.5 ms, 0 deg Pos
GRID: 10 mm
600µs
640µs
680µs
720µs
760µs
800µs
840µs
880µs
57

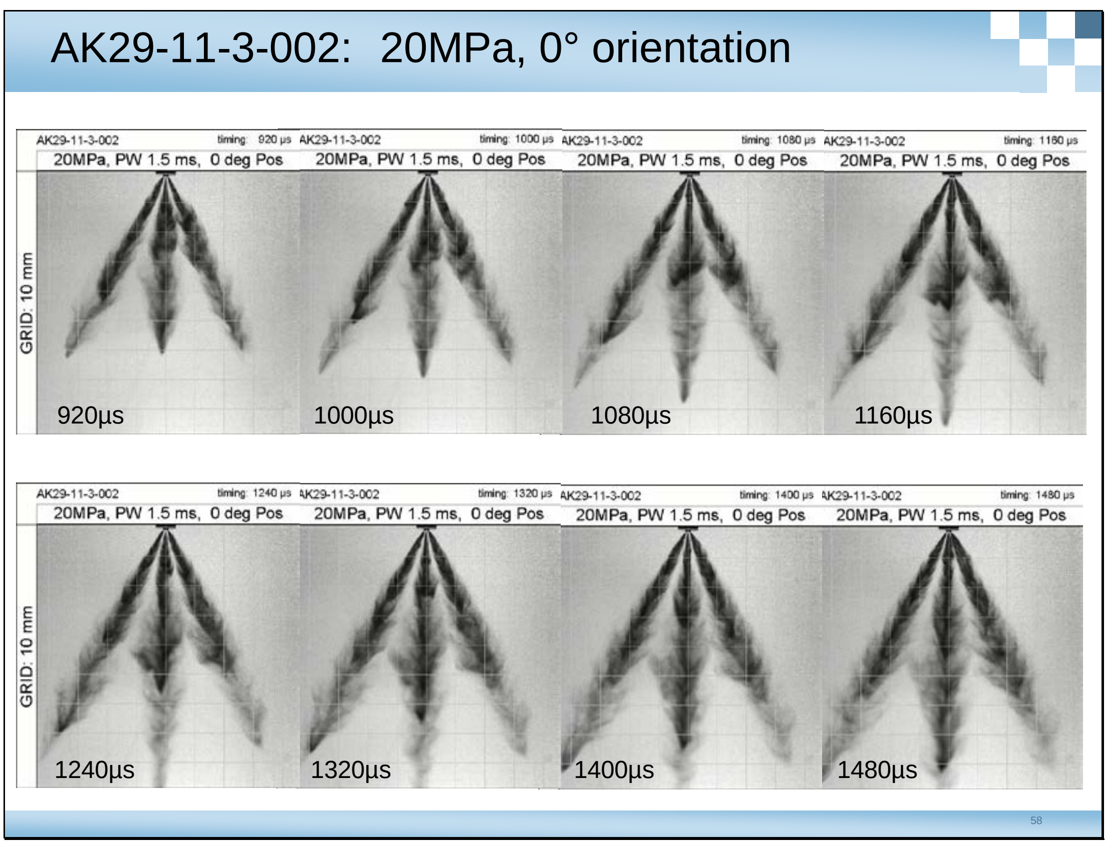
AK29-11-3-002: 20MPa, 0° orientation
AK29-11-3-002
20MPa, PW 1.5 ms, 0 deg Pos
GRID: 10 mm
920µs
1000µs
1080µs
1160µs
1240µs
1320µs
1400µs
1480µs
58

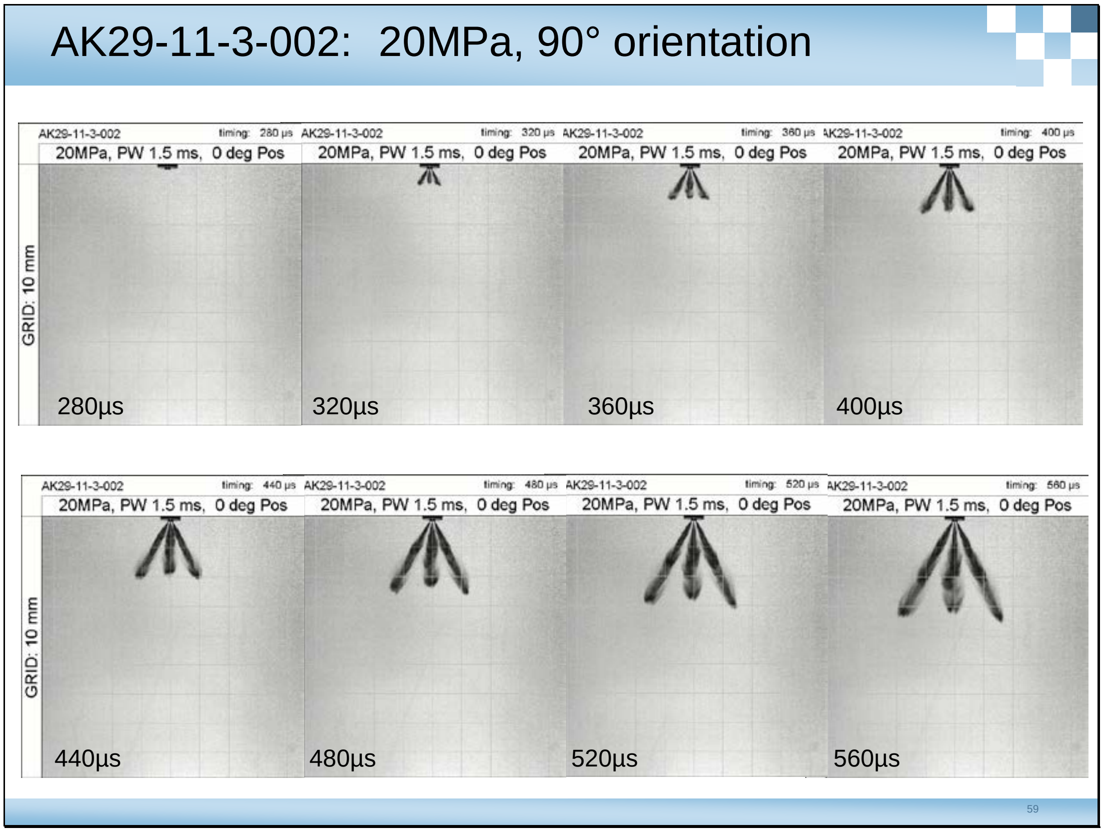
AK29-11-3-002: 20MPa, 90° orientation
AK29-11-3-002 timing: 280 µs
20MPa, PW 1.5 ms, 0 deg Pos
AK29-11-3-002 timing: 320 µs
20MPa, PW 1.5 ms, 0 deg Pos
AK29-11-3-002 timing: 360 µs
20MPa, PW 1.5 ms, 0 deg Pos
AK29-11-3-002 timing: 400 µs
20MPa, PW 1.5 ms, 0 deg Pos
GRID: 10 mm
280µs
320µs
360µs
400µs
AK29-11-3-002 timing: 440 µs
20MPa, PW 1.5 ms, 0 deg Pos
AK29-11-3-002 timing: 480 µs
20MPa, PW 1.5 ms, 0 deg Pos
AK29-11-3-002 timing: 520 µs
20MPa, PW 1.5 ms, 0 deg Pos
AK29-11-3-002 timing: 560 µs
20MPa, PW 1.5 ms, 0 deg Pos
GRID: 10 mm
440µs
480µs
520µs
560µs
59

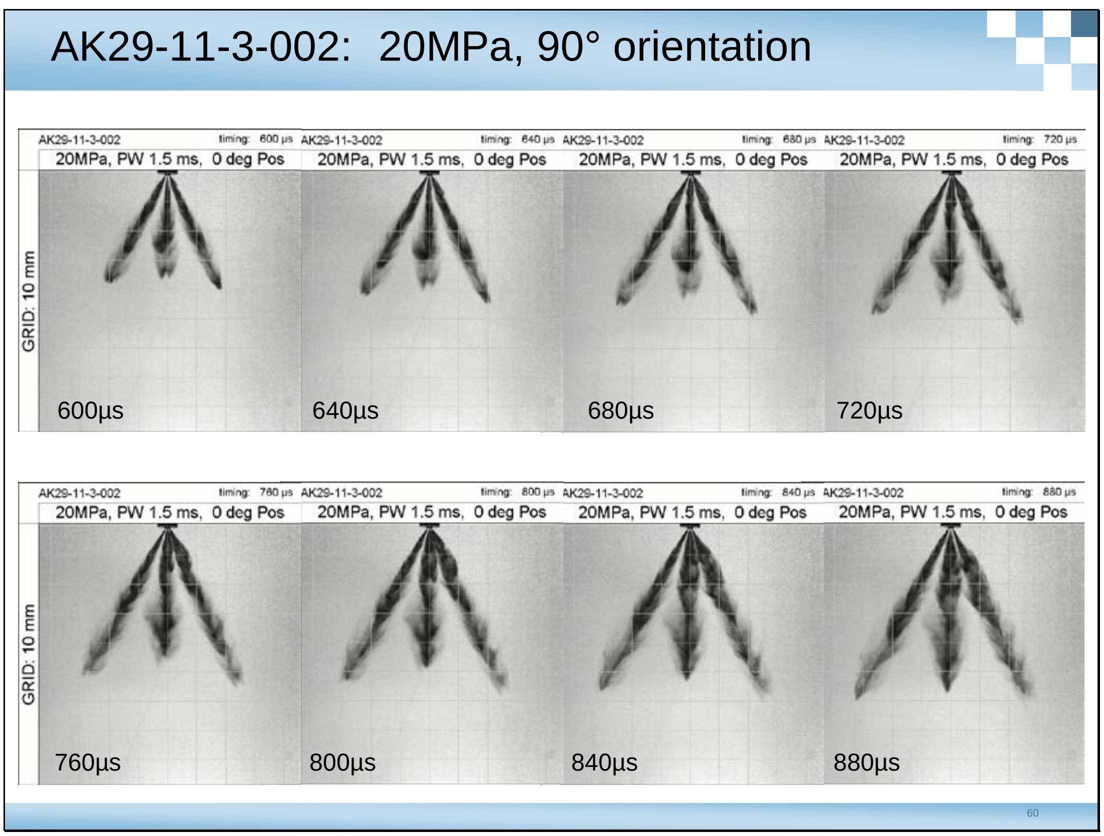
AK29-11-3-002: 20MPa, 90° orientation
AK29-11-3-002 timing: 600 µs
20MPa, PW 1.5 ms, 0 deg Pos
AK29-11-3-002 timing: 640 µs
20MPa, PW 1.5 ms, 0 deg Pos
AK29-11-3-002 timing: 680 µs
20MPa, PW 1.5 ms, 0 deg Pos
AK29-11-3-002 timing: 720 µs
20MPa, PW 1.5 ms, 0 deg Pos
GRID: 10 mm
600µs
640µs
680µs
720µs
AK29-11-3-002 timing: 760 µs
20MPa, PW 1.5 ms, 0 deg Pos
AK29-11-3-002 timing: 800 µs
20MPa, PW 1.5 ms, 0 deg Pos
AK29-11-3-002 timing: 840 µs
20MPa, PW 1.5 ms, 0 deg Pos
AK29-11-3-002 timing: 880 µs
20MPa, PW 1.5 ms, 0 deg Pos
GRID: 10 mm
760µs
800µs
840µs
880µs
60

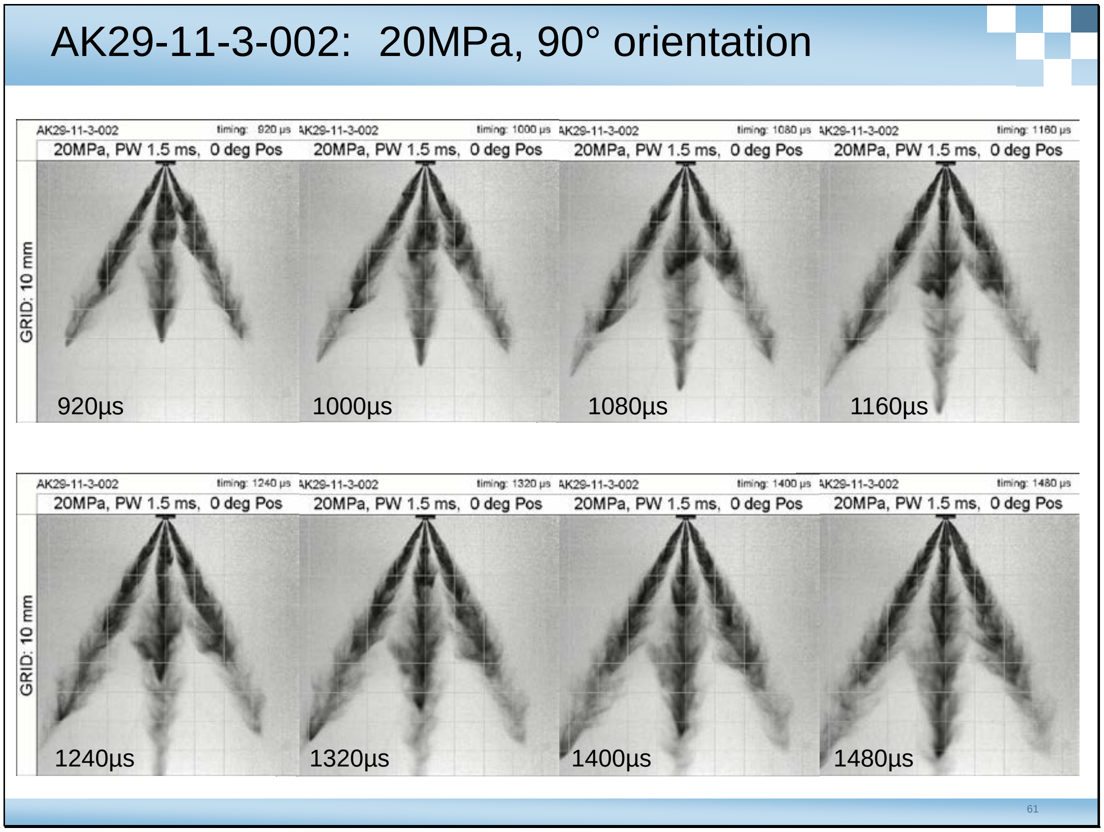
AK29-11-3-002: 20MPa, 90° orientation
AK29-11-3-002
timing: 920 µs
20MPa, PW 1.5 ms, 0 deg Pos
timing: 1000 µs
timing: 1080 µs
timing: 1160 µs
timing: 1240 µs
timing: 1320 µs
timing: 1400 µs
timing: 1480 µs
GRID: 10 mm
920µs
1000µs
1080µs
1160µs
1240µs
1320µs
1400µs
1480µs
61

# APPENDIX F MIE SCATTER IMAGES, SIDE VIEW

High speed Mie Imaging (408 images) of Spray plumes from side view, Luxembourg Spray lab

| Image # | Seat # | d (mm) | β | l/d | (l+L) /d | D/d | Inj. Pres. | View Angle | Mie Scatter Time Images (µs) |
|---|---|---|---|---|---|---|---|---|---|
| 1-6 | AK29-3-001 | ≈.20 | 0° | 1.1 | na | na | 10MPa | 0° | 320,360,400,440,470,520 |
| 7-12 | AK29-3-001 | ≈.20 | 0° | 1.1 | na | na | 10MPa | 0° | 560,600,640,680,720,760 |
| 13-18 | AK29-3-001 | ≈.20 | 0° | 1.1 | na | na | 10MPa | 0° | 800,840,880,920,960,1000 |
| 19-24 | AK29-3-001 | ≈.20 | 0° | 1.1 | na | na | 10MPa | 0° | 1040,1080,1120,1160,1200,1240 |
| 1-6 | AK29-3-001 | ≈.20 | 0° | 1.1 | na | na | 20MPa | 0° | 280,320,360,400,440,480 |
| 7-12 | AK29-3-001 | ≈.20 | 0° | 1.1 | na | na | 20MPa | 0° | 520,560,600,640,680,720 |
| 13-18 | AK29-3-001 | ≈.20 | 0° | 1.1 | na | na | 20MPa | 0° | 760,800,840,880,920,960 |
| 19-24 | AK29-3-001 | ≈.20 | 0° | 1.1 | na | na | 20MPa | 0° | 1000,1040,1080,1120,1160,1200 |
| 1-6 | AK29-3-002 | ≈.20 | 0° | 1.1 | na | na | 10MPa | 0° | 320,360,400,440,470,520 |
| 7-12 | AK29-3-002 | ≈.20 | 0° | 1.1 | na | na | 10MPa | 0° | 560,600,640,680,720,760 |
| 13-18 | AK29-3-002 | ≈.20 | 0° | 1.1 | na | na | 10MPa | 0° | 800,840,880,920,960,1000 |
| 19-24 | AK29-3-002 | ≈.20 | 0° | 1.1 | na | na | 10MPa | 0° | 1040,1080,1120,1160,1200,1240 |
| 1-6 | AK29-3-002 | ≈.20 | 0° | 1.1 | na | na | 20MPa | 0° | 280,320,360,400,440,480 |
| 7-12 | AK29-3-002 | ≈.20 | 0° | 1.1 | na | na | 20MPa | 0° | 520,560,600,640,680,720 |
| 13-18 | AK29-3-002 | ≈.20 | 0° | 1.1 | na | na | 20MPa | 0° | 760,800,840,880,920,960 |
| 19-24 | AK29-3-002 | ≈.20 | 0° | 1.1 | na | na | 20MPa | 0° | 1000,1040,1080,1120,1160,1200 |
| 1-6 | AK29-6-002 | ≈.15 | 0° | 1.1 | na | na | 10MPa | 0° | 320,360,400,440,470,520 |
| 7-12 | AK29-6-002 | ≈.15 | 0° | 1.1 | na | na | 10MPa | 0° | 560,600,640,680,720,760 |
| 13-18 | AK29-6-002 | ≈.15 | 0° | 1.1 | na | na | 10MPa | 0° | 800,840,880,920,960,1000 |
| 19-24 | AK29-6-002 | ≈.15 | 0° | 1.1 | na | na | 10MPa | 0° | 1040,1080,1120,1160,1200,1240 |
| 1-6 | AK29-6-002 | ≈.15 | 0° | 1.1 | na | na | 20MPa | 0° | 240,280,320,360,400,440 |
| 7-12 | AK29-6-002 | ≈.15 | 0° | 1.1 | na | na | 20MPa | 0° | 480,520,560,600,640,680 |
| 13-18 | AK29-6-002 | ≈.15 | 0° | 1.1 | na | na | 20MPa | 0° | 720,760,800,840,880,920 |
| 19-24 | AK29-6-002 | ≈.15 | 0° | 1.1 | na | na | 20MPa | 0° | 960,1000,1040,1080,1120,1160 |
| 1-8 | AK29-9-001 | ≈.20 | 30° | 1.1 | na | na | 10MPa | 0° | 320,360,400,440,470,520,560,600 |
| 9-16 | AK29-9-001 | ≈.20 | 30° | 1.1 | na | na | 10MPa | 0° | 640,680,720,760,800,840,880,920 |
| 17-24 | AK29-9-001 | ≈.20 | 30° | 1.1 | na | na | 10MPa | 0° | 1000,1080,1160,1240,1320,1400,1 480,1560 |
| 1-8 | AK29-9-001 | ≈.20 | 30° | 1.1 | na | na | 10MPa | 90° | 320,360,400,440,470,520,560,600 |
| 9-16 | AK29-9-001 | ≈.20 | 30° | 1.1 | na | na | 10MPa | 90° | 640,680,720,760,800,840,880,920 |
| 17-24 | AK29-9-001 | ≈.20 | 30° | 1.1 | na | na | 10MPa | 90° | 1000,1080,1160,1240,1320,1400,1 480,1560 |
| 1-8 | AK29-9-001 | ≈.20 | 30° | 1.1 | na | na | 20MPa | 0° | 280,320,360,400,440,480,520,560 |
| 9-16 | AK29-9-001 | ≈.20 | 30° | 1.1 | na | na | 20MPa | 0° | 600,640,680,720,760,800,840,880 |
| 17-24 | AK29-9-001 | ≈.20 | 30° | 1.1 | na | na | 20MPa | 0° | 920,1000,1080,1160,1240,1320, 1400,1480 |
| 1-8 | AK29-9-001 | ≈.20 | 30° | 1.1 | na | na | 20MPa | 90° | 280,320,360,400,440,480,520,560 |
| 9-16 | AK29-9-001 | ≈.20 | 30° | 1.1 | na | na | 20MPa | 90° | 600,640,680,720,760,800,840,880 |
| 17-24 | AK29-9-001 | ≈.20 | 30° | 1.1 | na | na | 20MPa | 90° | 920,1000,1080,1160,1240,1320, 1400,1480 |
| 1-8 | AK29-10-3-003 | ≈.15 | 30° | 1.1 | 3.96 | 2.5 | 10MPa | 0° | 320,340,400,440,480,520,560,600 |

| | | | | | | | | | |
|---|---|---|---|---|---|---|---|---|---|
| 9-16 | AK29-10-3-003 | ≈.15 | 30° | 1.1 | 3.96 | 2.5 | 10MPa | 0° | 640,680,720,760,800,840,880,920 |
| 17-24 | AK29-10-3-003 | ≈.15 | 30° | 1.1 | 3.96 | 2.5 | 10MPa | 0° | 1000,1080,1160,1240,1320,1400,1480,1560 |
| 1-8 | AK29-10-3-003 | ≈.15 | 30° | 1.1 | 3.96 | 2.5 | 10MPa | 90° | 320,340,400,440,480,520,560,600 |
| 9-16 | AK29-10-3-003 | ≈.15 | 30° | 1.1 | 3.96 | 2.5 | 10MPa | 90° | 640,680,720,760,800,840,880,920 |
| 17-24 | AK29-10-3-003 | ≈.15 | 30° | 1.1 | 3.96 | 2.5 | 10MPa | 90° | 1000,1080,1160,1240,1320,1400,1480,1560 |
| 1-8 | AK29-10-3-003 | ≈.15 | 30° | 1.1 | 3.96 | 2.5 | 20MPa | 0° | 280,320,360,400,440,480,520,560 |
| 9-16 | AK29-10-3-003 | ≈.15 | 30° | 1.1 | 3.96 | 2.5 | 20MPa | 0° | 600,640,680,720,760,800,840,880 |
| 17-24 | AK29-10-3-003 | ≈.15 | 30° | 1.1 | 3.96 | 2.5 | 20MPa | 0° | 920,1000,1080,1160,1240,1320,1400,1480 |
| 1-8 | AK29-10-3-003 | ≈.15 | 30° | 1.1 | 3.96 | 2.5 | 20MPa | 90° | 280,320,360,400,440,480,520,560 |
| 9-16 | AK29-10-3-003 | ≈.15 | 30° | 1.1 | 3.96 | 2.5 | 20MPa | 90° | 600,640,680,720,760,800,840,880 |
| 17-24 | AK29-10-3-003 | ≈.15 | 30° | 1.1 | 3.96 | 2.5 | 20MPa | 90° | 920,1000,1080,1160,1240,1320,1400,1480 |
| 1-8 | AK29-11-3-002 | ≈.15 | 30° | 3.96 | na | na | 10MPa | 0° | 320,340,400,440,480,520,560,600 |
| 9-16 | AK29-11-3-002 | ≈.15 | 30° | 3.96 | na | na | 10MPa | 0° | 640,680,720,760,800,840,880,920 |
| 17-24 | AK29-11-3-002 | ≈.15 | 30° | 3.96 | na | na | 10MPa | 0° | 1000,1080,1160,1240,1320,1400,1480,1560 |
| 1-8 | AK29-11-3-002 | ≈.15 | 30° | 3.96 | na | na | 10MPa | 90° | 320,340,400,440,480,520,560,600 |
| 9-16 | AK29-11-3-002 | ≈.15 | 30° | 3.96 | na | na | 10MPa | 90° | 640,680,720,760,800,840,880,920 |
| 17-24 | AK29-11-3-002 | ≈.15 | 30° | 3.96 | na | na | 10MPa | 90° | 1000,1080,1160,1240,1320,1400,1480,1560 |
| 1-8 | AK29-11-3-002 | ≈.15 | 30° | 3.96 | na | na | 20MPa | 0° | 280,320,360,400,440,480,520,560 |
| 9-16 | AK29-11-3-002 | ≈.15 | 30° | 3.96 | na | na | 20MPa | 0° | 600,640,680,720,760,800,840,880 |
| 17-24 | AK29-11-3-002 | ≈.15 | 30° | 3.96 | na | na | 20MPa | 0° | 920,1000,1080,1160,1240,1320,1400,1480 |
| 1-8 | AK29-11-3-002 | ≈.15 | 30° | 3.96 | na | na | 20MPa | 90° | 280,320,360,400,440,480,520,560 |
| 9-16 | AK29-11-3-002 | ≈.15 | 30° | 3.96 | na | na | 20MPa | 90° | 600,640,680,720,760,800,840,880 |
| 17-24 | AK29-11-3-002 | ≈.15 | 30° | 3.96 | na | na | 20MPa | 90° | 920,1000,1080,1160,1240,1320,1400,1480 |

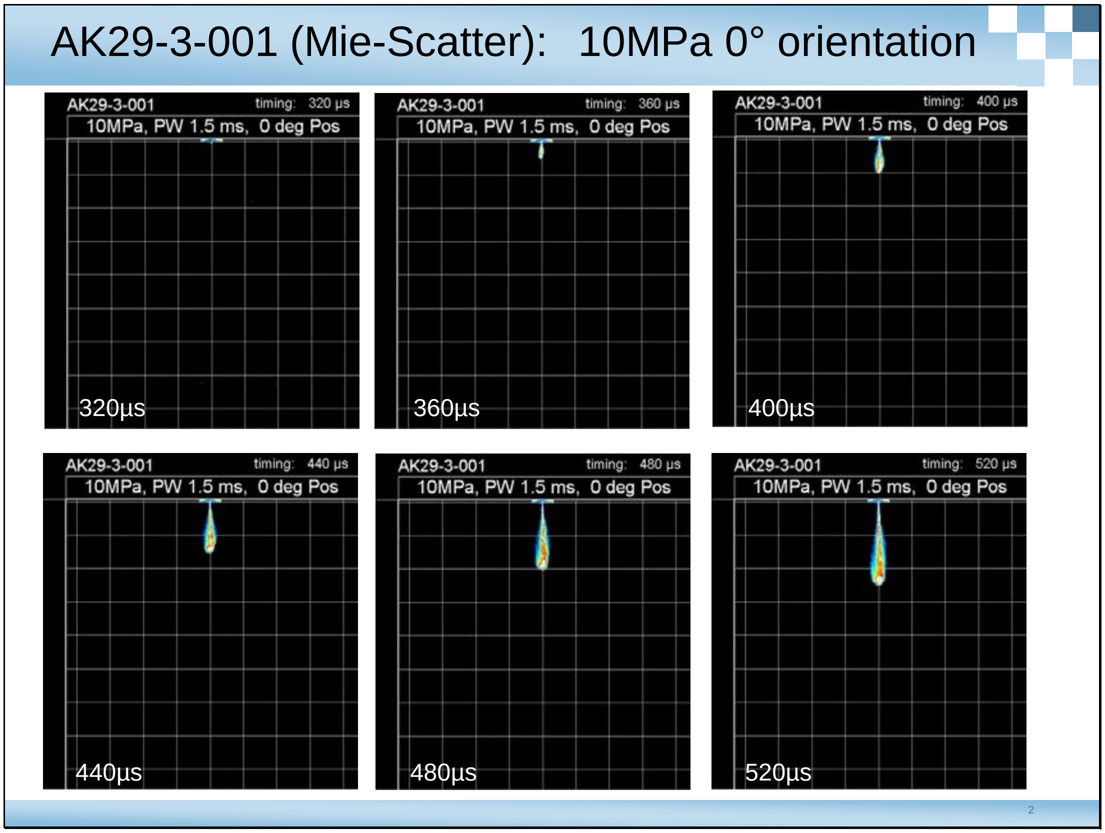
AK29-3-001 (Mie-Scatter): 10MPa 0° orientation
AK29-3-001 timing: 320 µs
10MPa, PW 1.5 ms, 0 deg Pos
320µs
AK29-3-001 timing: 360 µs
10MPa, PW 1.5 ms, 0 deg Pos
360µs
AK29-3-001 timing: 400 µs
10MPa, PW 1.5 ms, 0 deg Pos
400µs
AK29-3-001 timing: 440 µs
10MPa, PW 1.5 ms, 0 deg Pos
440µs
AK29-3-001 timing: 480 µs
10MPa, PW 1.5 ms, 0 deg Pos
480µs
AK29-3-001 timing: 520 µs
10MPa, PW 1.5 ms, 0 deg Pos
520µs
2

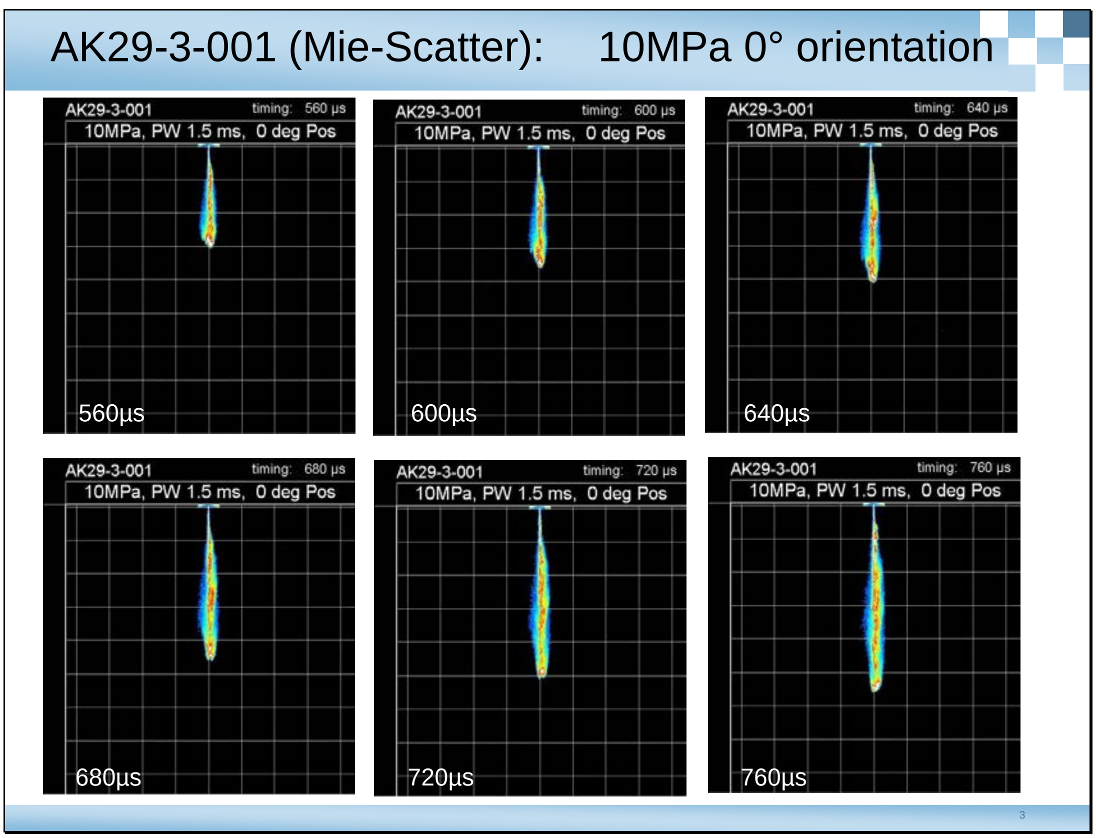
AK29-3-001 (Mie-Scatter): 10MPa 0° orientation
AK29-3-001 timing: 560 µs
10MPa, PW 1.5 ms, 0 deg Pos
560µs
AK29-3-001 timing: 600 µs
10MPa, PW 1.5 ms, 0 deg Pos
600µs
AK29-3-001 timing: 640 µs
10MPa, PW 1.5 ms, 0 deg Pos
640µs
AK29-3-001 timing: 680 µs
10MPa, PW 1.5 ms, 0 deg Pos
680µs
AK29-3-001 timing: 720 µs
10MPa, PW 1.5 ms, 0 deg Pos
720µs
AK29-3-001 timing: 760 µs
10MPa, PW 1.5 ms, 0 deg Pos
760µs
3

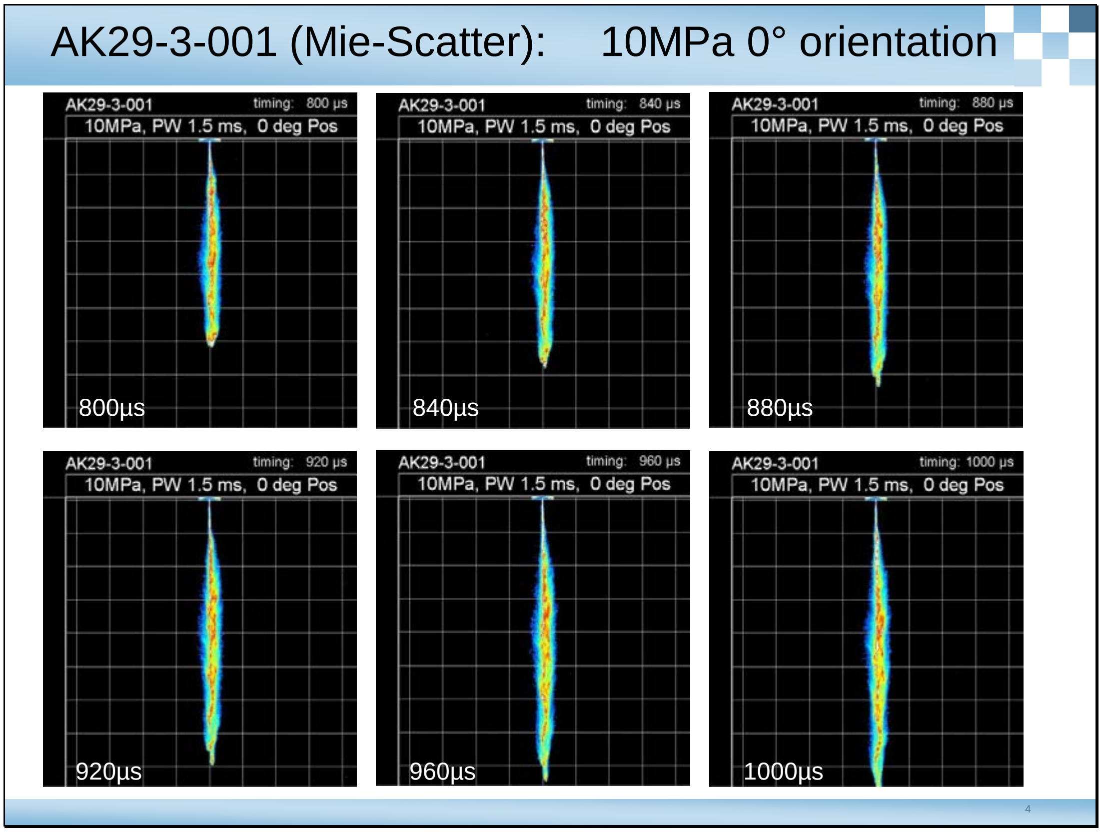
AK29-3-001 (Mie-Scatter): 10MPa 0° orientation
AK29-3-001 timing: 800 µs
10MPa, PW 1.5 ms, 0 deg Pos
800µs
AK29-3-001 timing: 840 µs
10MPa, PW 1.5 ms, 0 deg Pos
840µs
AK29-3-001 timing: 880 µs
10MPa, PW 1.5 ms, 0 deg Pos
880µs
AK29-3-001 timing: 920 µs
10MPa, PW 1.5 ms, 0 deg Pos
920µs
AK29-3-001 timing: 960 µs
10MPa, PW 1.5 ms, 0 deg Pos
960µs
AK29-3-001 timing: 1000 µs
10MPa, PW 1.5 ms, 0 deg Pos
1000µs

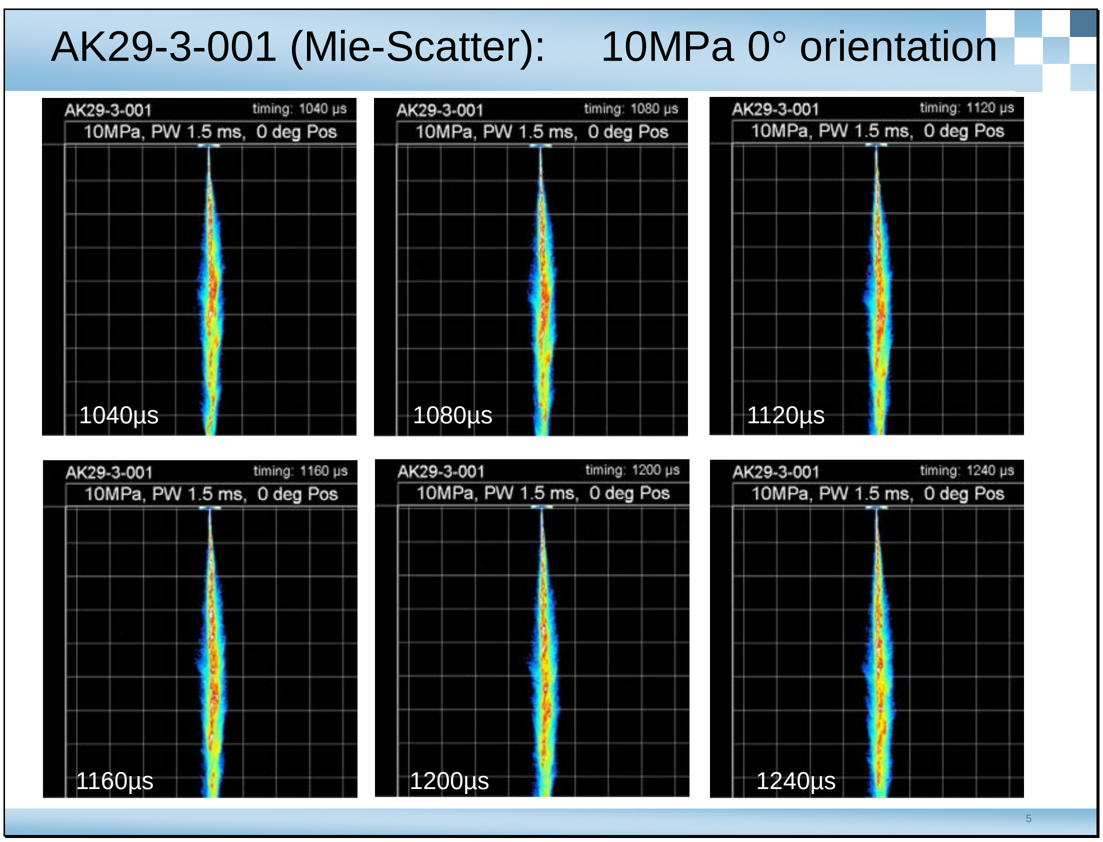
AK29-3-001 (Mie-Scatter): 10MPa 0° orientation
AK29-3-001 timing: 1040 µs
10MPa, PW 1.5 ms, 0 deg Pos
1040µs
AK29-3-001 timing: 1080 µs
10MPa, PW 1.5 ms, 0 deg Pos
1080µs
AK29-3-001 timing: 1120 µs
10MPa, PW 1.5 ms, 0 deg Pos
1120µs
AK29-3-001 timing: 1160 µs
10MPa, PW 1.5 ms, 0 deg Pos
1160µs
AK29-3-001 timing: 1200 µs
10MPa, PW 1.5 ms, 0 deg Pos
1200µs
AK29-3-001 timing: 1240 µs
10MPa, PW 1.5 ms, 0 deg Pos
1240µs

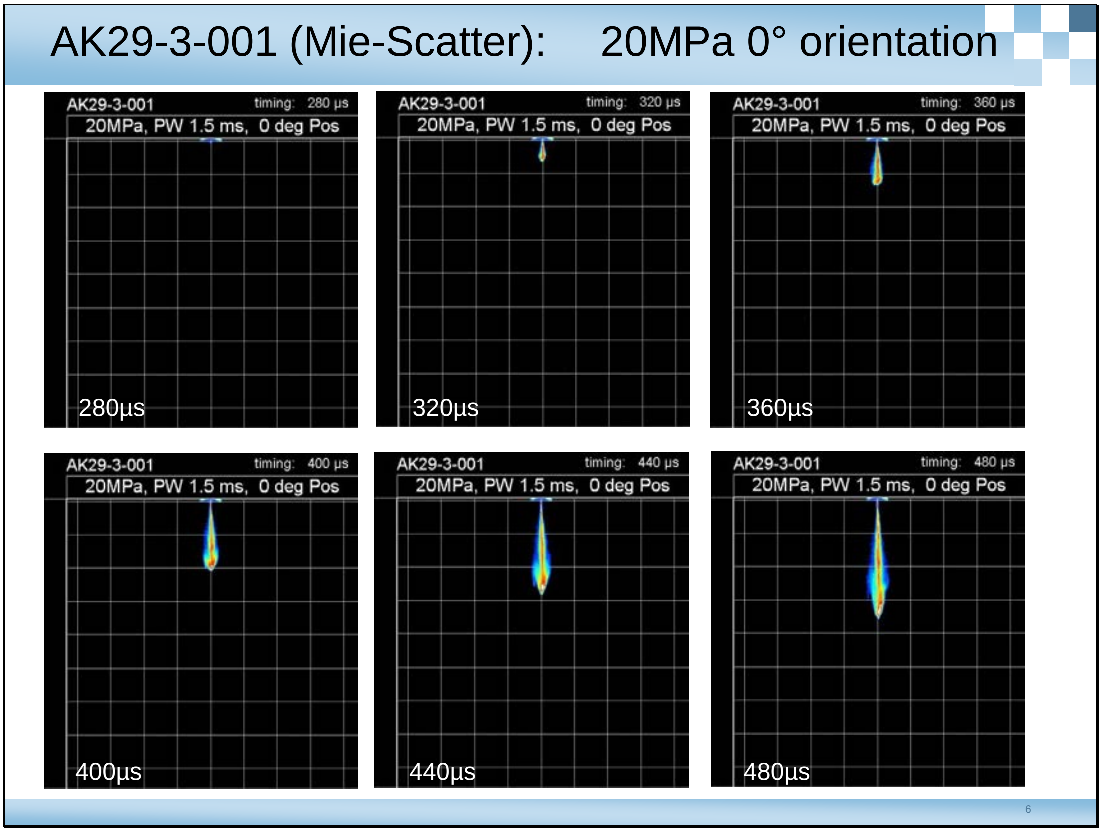
AK29-3-001 (Mie-Scatter): 20MPa 0° orientation
AK29-3-001 timing: 280 µs
20MPa, PW 1.5 ms, 0 deg Pos
280µs
AK29-3-001 timing: 320 µs
20MPa, PW 1.5 ms, 0 deg Pos
320µs
AK29-3-001 timing: 360 µs
20MPa, PW 1.5 ms, 0 deg Pos
360µs
AK29-3-001 timing: 400 µs
20MPa, PW 1.5 ms, 0 deg Pos
400µs
AK29-3-001 timing: 440 µs
20MPa, PW 1.5 ms, 0 deg Pos
440µs
AK29-3-001 timing: 480 µs
20MPa, PW 1.5 ms, 0 deg Pos
480µs

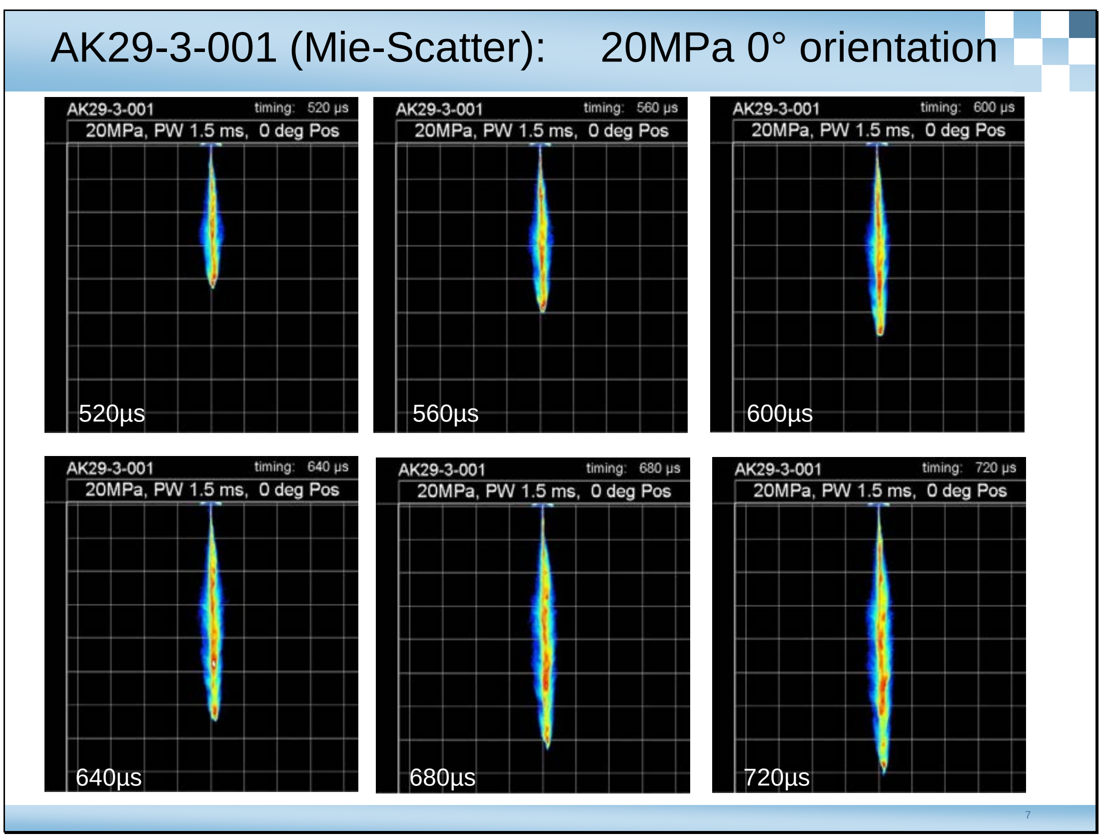
AK29-3-001 (Mie-Scatter): 20MPa 0° orientation
AK29-3-001 timing: 520 µs
20MPa, PW 1.5 ms, 0 deg Pos
520µs
AK29-3-001 timing: 560 µs
20MPa, PW 1.5 ms, 0 deg Pos
560µs
AK29-3-001 timing: 600 µs
20MPa, PW 1.5 ms, 0 deg Pos
600µs
AK29-3-001 timing: 640 µs
20MPa, PW 1.5 ms, 0 deg Pos
640µs
AK29-3-001 timing: 680 µs
20MPa, PW 1.5 ms, 0 deg Pos
680µs
AK29-3-001 timing: 720 µs
20MPa, PW 1.5 ms, 0 deg Pos
720µs

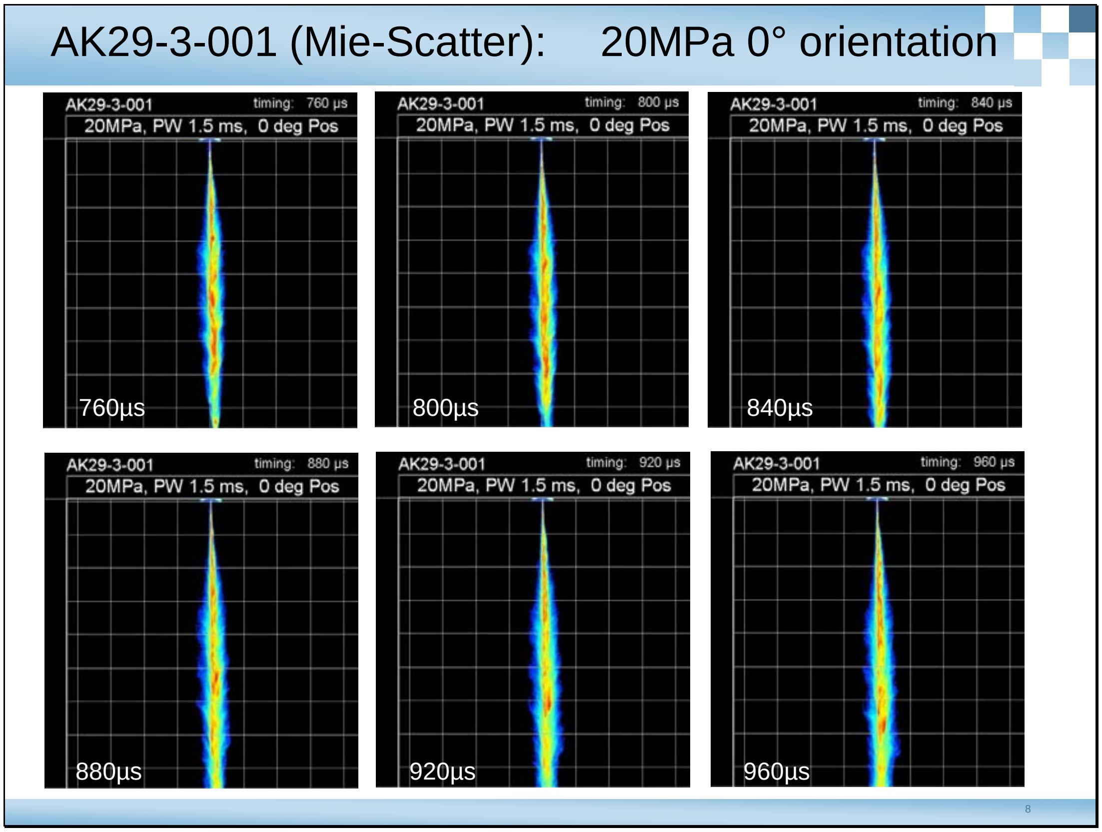
AK29-3-001 (Mie-Scatter): 20MPa 0° orientation
AK29-3-001 timing: 760 µs
20MPa, PW 1.5 ms, 0 deg Pos
760µs
AK29-3-001 timing: 800 µs
20MPa, PW 1.5 ms, 0 deg Pos
800µs
AK29-3-001 timing: 840 µs
20MPa, PW 1.5 ms, 0 deg Pos
840µs
AK29-3-001 timing: 880 µs
20MPa, PW 1.5 ms, 0 deg Pos
880µs
AK29-3-001 timing: 920 µs
20MPa, PW 1.5 ms, 0 deg Pos
920µs
AK29-3-001 timing: 960 µs
20MPa, PW 1.5 ms, 0 deg Pos
960µs
8

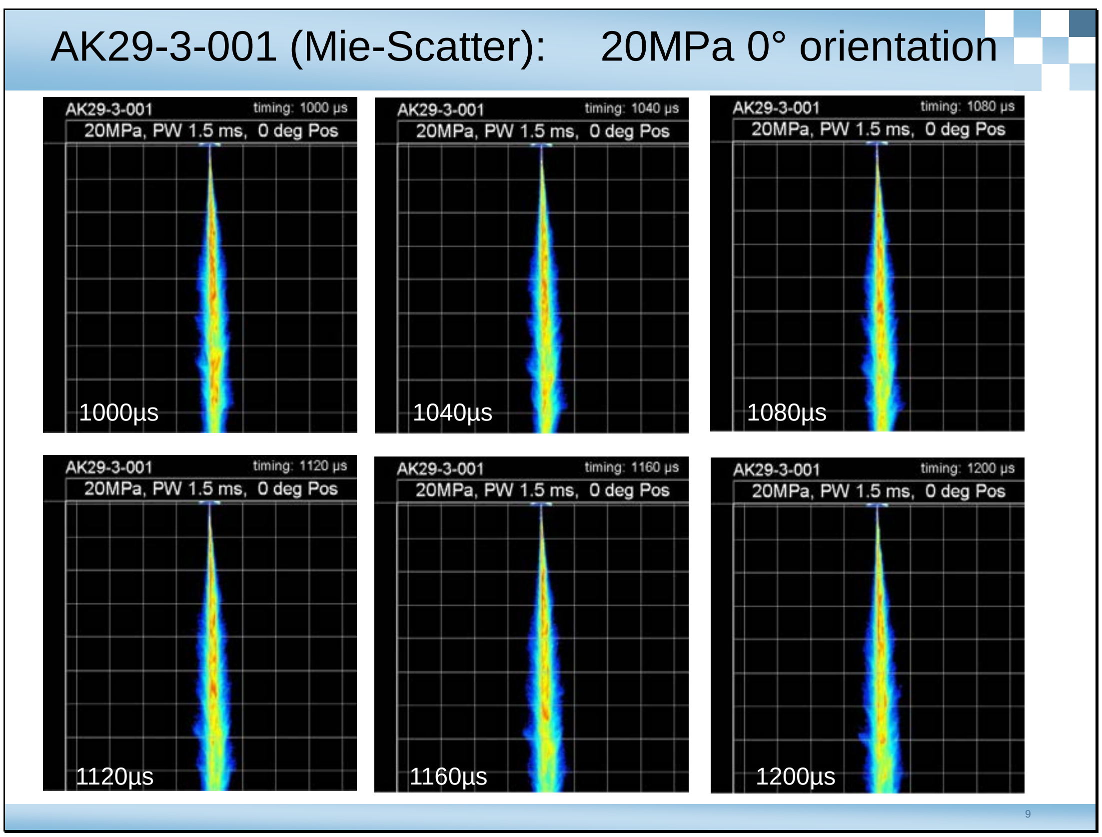
AK29-3-001 (Mie-Scatter): 20MPa 0° orientation
AK29-3-001 timing: 1000 µs
20MPa, PW 1.5 ms, 0 deg Pos
1000µs
AK29-3-001 timing: 1040 µs
20MPa, PW 1.5 ms, 0 deg Pos
1040µs
AK29-3-001 timing: 1080 µs
20MPa, PW 1.5 ms, 0 deg Pos
1080µs
AK29-3-001 timing: 1120 µs
20MPa, PW 1.5 ms, 0 deg Pos
1120µs
AK29-3-001 timing: 1160 µs
20MPa, PW 1.5 ms, 0 deg Pos
1160µs
AK29-3-001 timing: 1200 µs
20MPa, PW 1.5 ms, 0 deg Pos
1200µs
9

## AK29-3-002 (Mie-Scatter): 10MPa 0° orientation

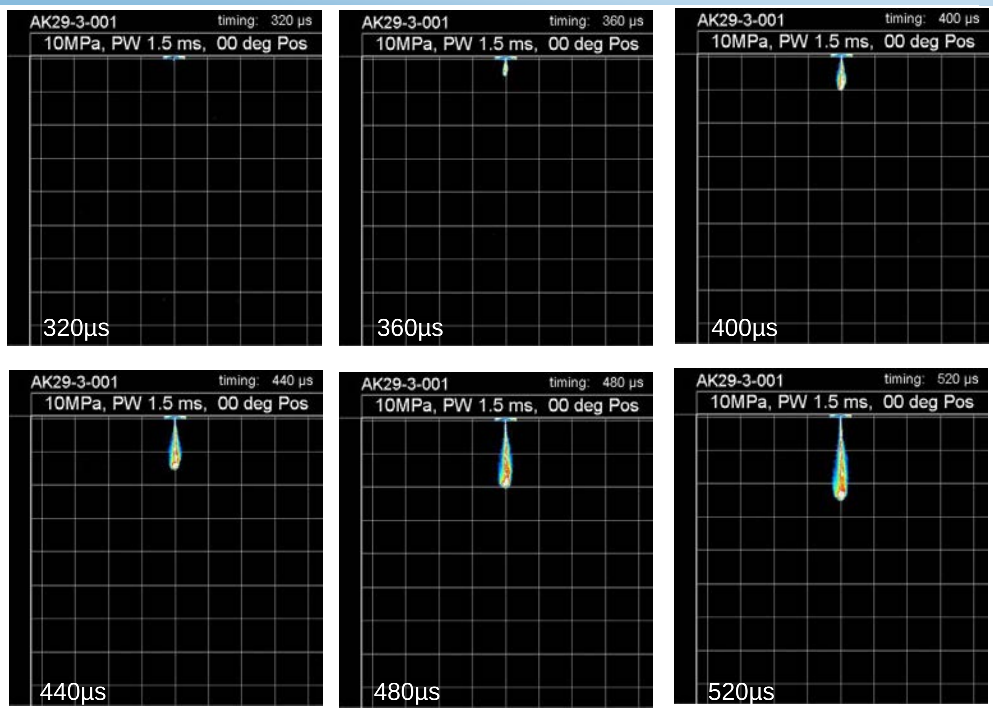


10

## AK29-3-002 (Mie-Scatter): 10MPa 0° orientation

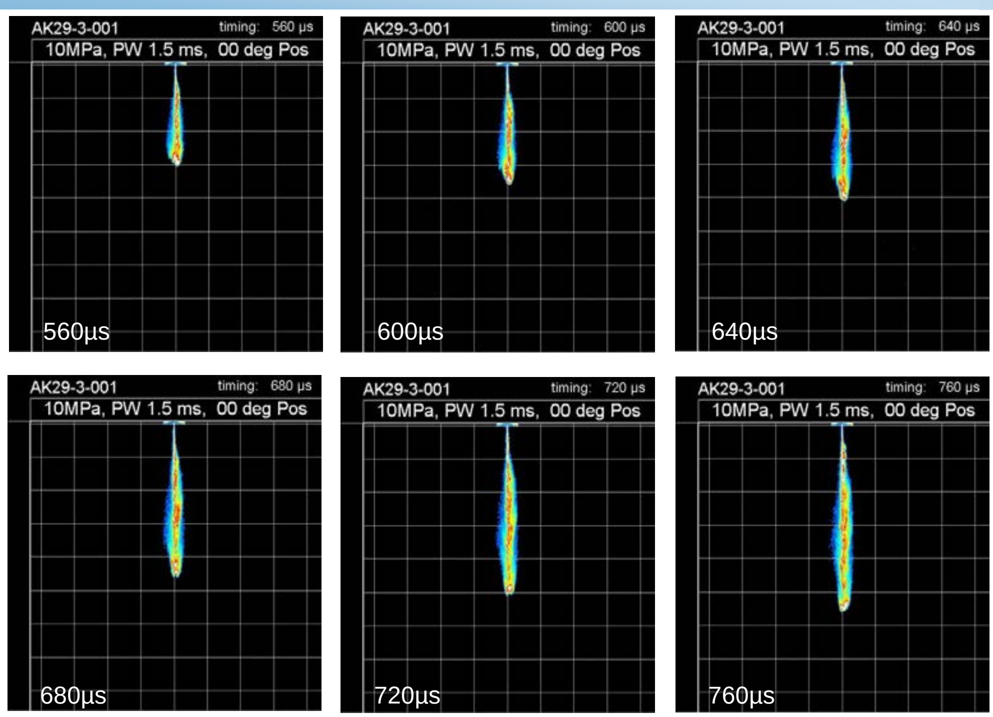


11

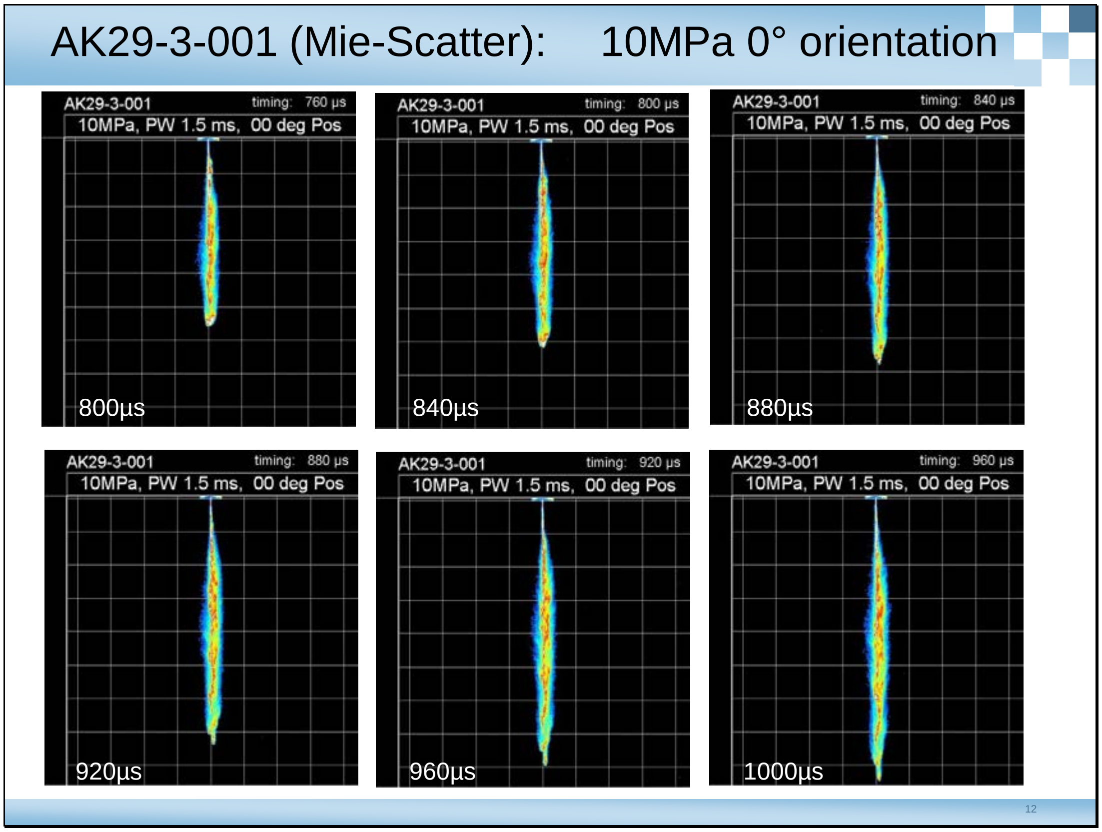
AK29-3-001 (Mie-Scatter): 10MPa 0° orientation
AK29-3-001 timing: 760 µs
10MPa, PW 1.5 ms, 00 deg Pos
800µs
AK29-3-001 timing: 800 µs
10MPa, PW 1.5 ms, 00 deg Pos
840µs
AK29-3-001 timing: 840 µs
10MPa, PW 1.5 ms, 00 deg Pos
880µs
AK29-3-001 timing: 880 µs
10MPa, PW 1.5 ms, 00 deg Pos
920µs
AK29-3-001 timing: 920 µs
10MPa, PW 1.5 ms, 00 deg Pos
960µs
AK29-3-001 timing: 960 µs
10MPa, PW 1.5 ms, 00 deg Pos
1000µs
12

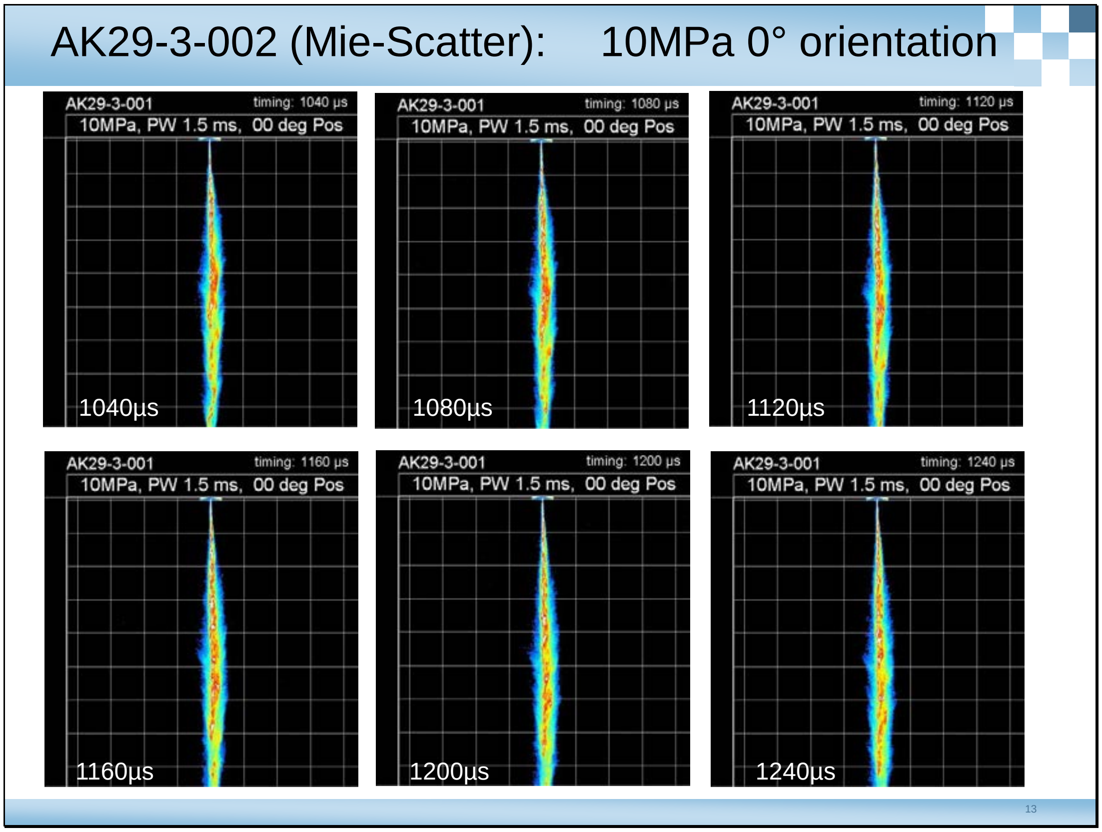
AK29-3-002 (Mie-Scatter): 10MPa 0° orientation
AK29-3-001 timing: 1040 µs
10MPa, PW 1.5 ms, 00 deg Pos
1040µs
AK29-3-001 timing: 1080 µs
10MPa, PW 1.5 ms, 00 deg Pos
1080µs
AK29-3-001 timing: 1120 µs
10MPa, PW 1.5 ms, 00 deg Pos
1120µs
AK29-3-001 timing: 1160 µs
10MPa, PW 1.5 ms, 00 deg Pos
1160µs
AK29-3-001 timing: 1200 µs
10MPa, PW 1.5 ms, 00 deg Pos
1200µs
AK29-3-001 timing: 1240 µs
10MPa, PW 1.5 ms, 00 deg Pos
1240µs
13

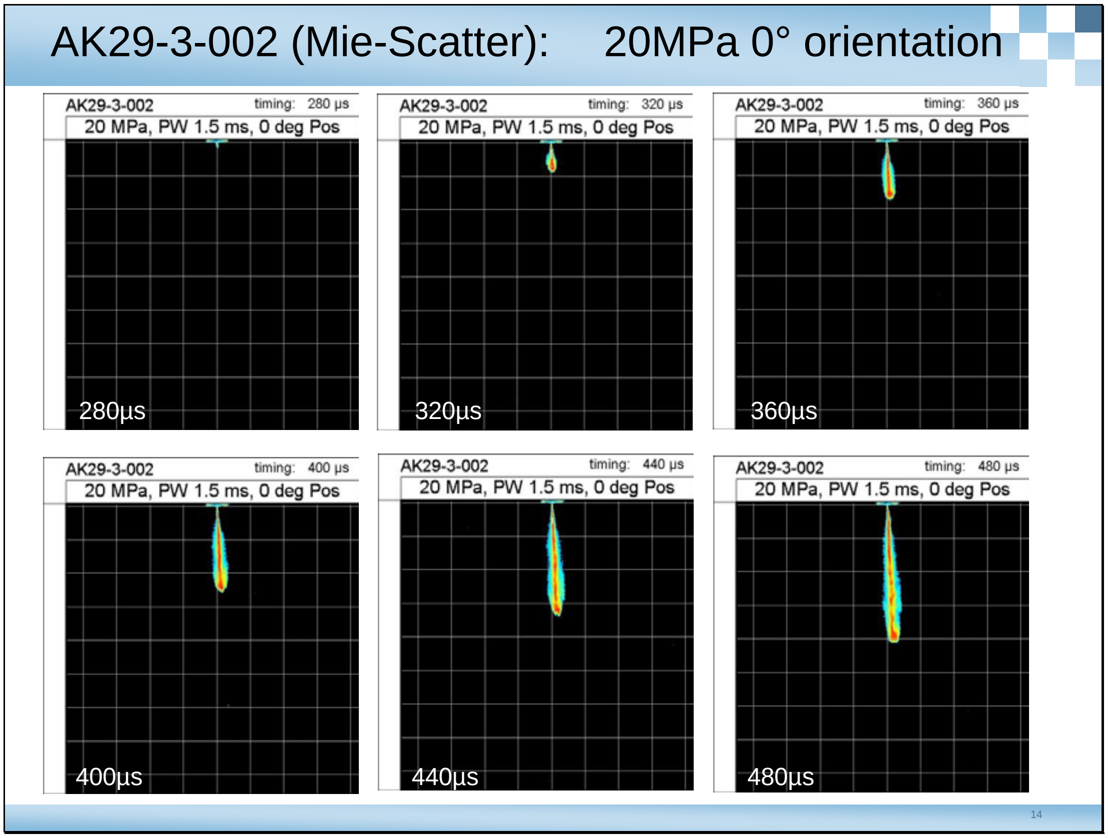
AK29-3-002 (Mie-Scatter): 20MPa 0° orientation
AK29-3-002 timing: 280 µs
20 MPa, PW 1.5 ms, 0 deg Pos
280µs
AK29-3-002 timing: 320 µs
20 MPa, PW 1.5 ms, 0 deg Pos
320µs
AK29-3-002 timing: 360 µs
20 MPa, PW 1.5 ms, 0 deg Pos
360µs
AK29-3-002 timing: 400 µs
20 MPa, PW 1.5 ms, 0 deg Pos
400µs
AK29-3-002 timing: 440 µs
20 MPa, PW 1.5 ms, 0 deg Pos
440µs
AK29-3-002 timing: 480 µs
20 MPa, PW 1.5 ms, 0 deg Pos
480µs
14

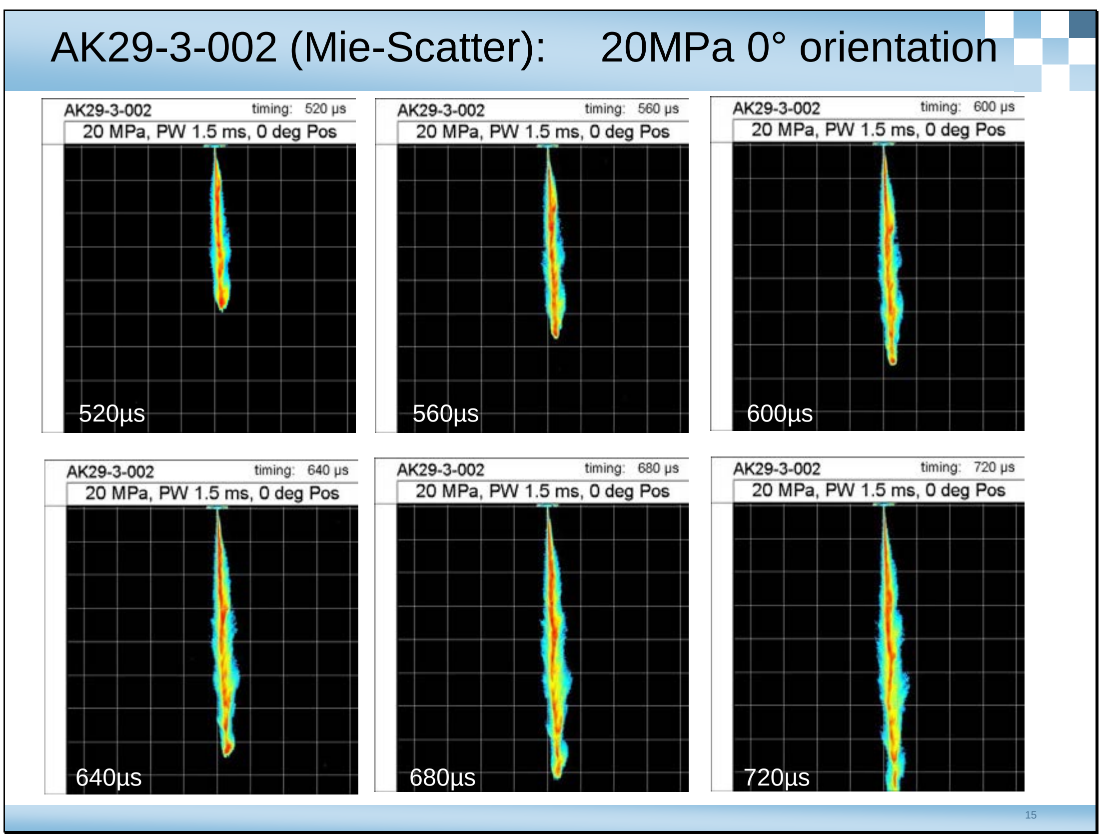
AK29-3-002 (Mie-Scatter): 20MPa 0° orientation
AK29-3-002 timing: 520 µs
20 MPa, PW 1.5 ms, 0 deg Pos
520µs
AK29-3-002 timing: 560 µs
20 MPa, PW 1.5 ms, 0 deg Pos
560µs
AK29-3-002 timing: 600 µs
20 MPa, PW 1.5 ms, 0 deg Pos
600µs
AK29-3-002 timing: 640 µs
20 MPa, PW 1.5 ms, 0 deg Pos
640µs
AK29-3-002 timing: 680 µs
20 MPa, PW 1.5 ms, 0 deg Pos
680µs
AK29-3-002 timing: 720 µs
20 MPa, PW 1.5 ms, 0 deg Pos
720µs
15

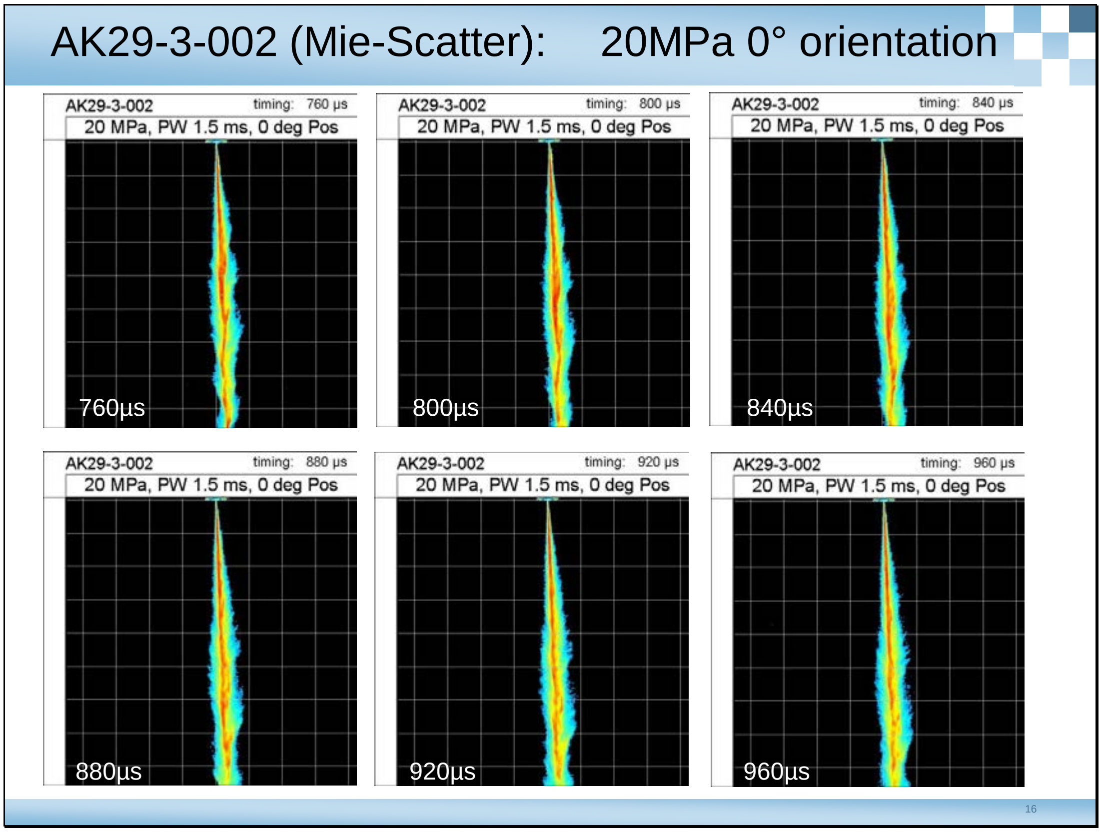
AK29-3-002 (Mie-Scatter): 20MPa 0° orientation
AK29-3-002 timing: 760 µs
20 MPa, PW 1.5 ms, 0 deg Pos
760µs
AK29-3-002 timing: 800 µs
20 MPa, PW 1.5 ms, 0 deg Pos
800µs
AK29-3-002 timing: 840 µs
20 MPa, PW 1.5 ms, 0 deg Pos
840µs
AK29-3-002 timing: 880 µs
20 MPa, PW 1.5 ms, 0 deg Pos
880µs
AK29-3-002 timing: 920 µs
20 MPa, PW 1.5 ms, 0 deg Pos
920µs
AK29-3-002 timing: 960 µs
20 MPa, PW 1.5 ms, 0 deg Pos
960µs
16

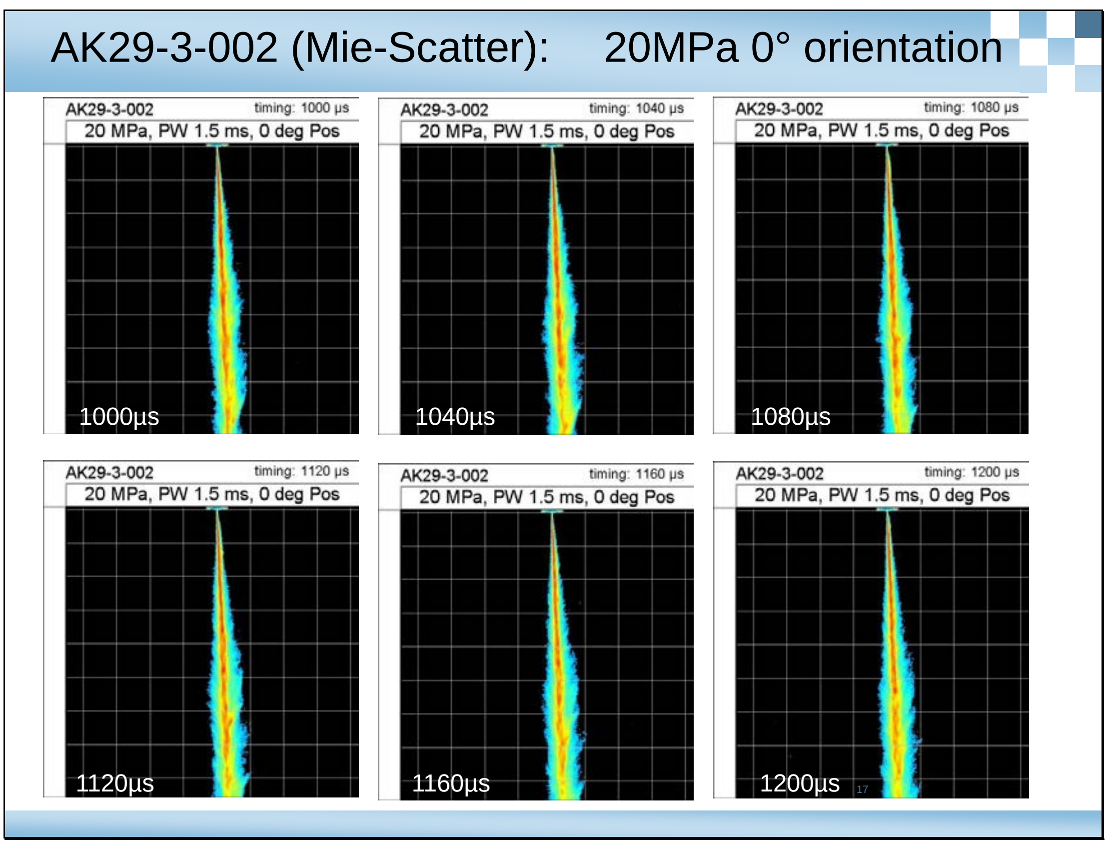
AK29-3-002 (Mie-Scatter): 20MPa 0° orientation
AK29-3-002 timing: 1000 µs
20 MPa, PW 1.5 ms, 0 deg Pos
1000µs
AK29-3-002 timing: 1040 µs
20 MPa, PW 1.5 ms, 0 deg Pos
1040µs
AK29-3-002 timing: 1080 µs
20 MPa, PW 1.5 ms, 0 deg Pos
1080µs
AK29-3-002 timing: 1120 µs
20 MPa, PW 1.5 ms, 0 deg Pos
1120µs
AK29-3-002 timing: 1160 µs
20 MPa, PW 1.5 ms, 0 deg Pos
1160µs
AK29-3-002 timing: 1200 µs
20 MPa, PW 1.5 ms, 0 deg Pos
1200µs
17

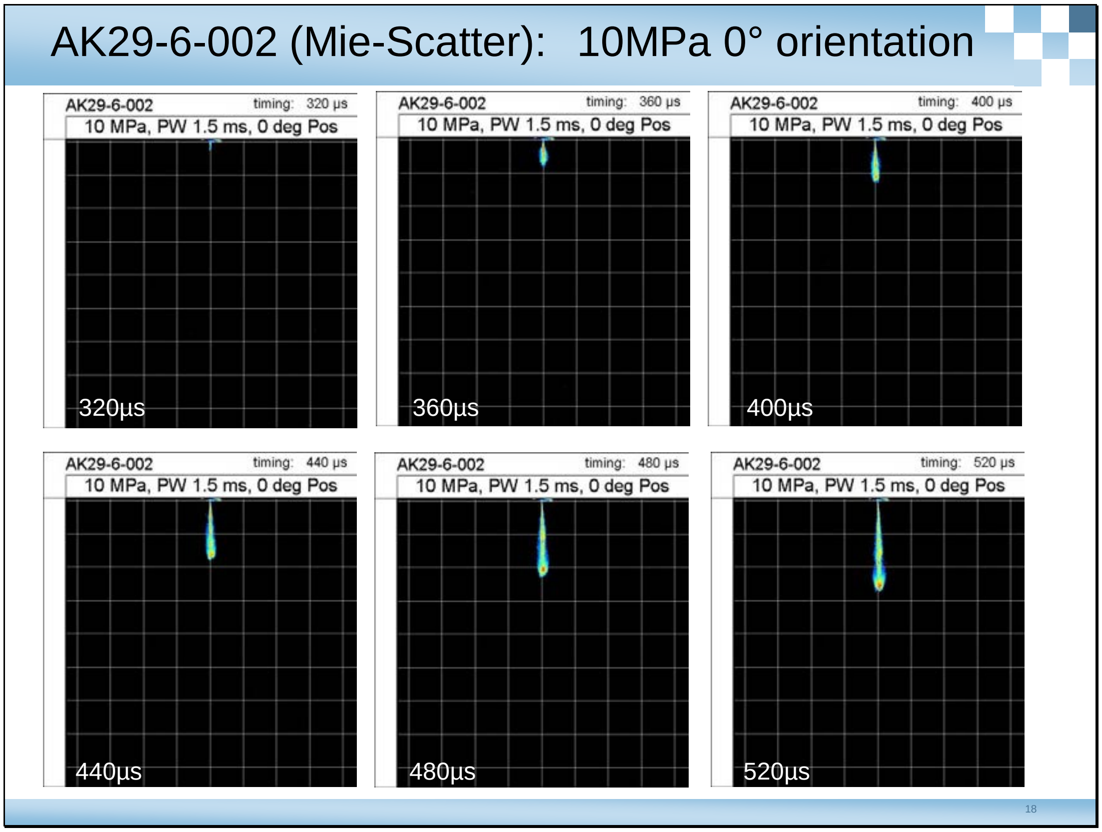
AK29-6-002 (Mie-Scatter): 10MPa 0° orientation
AK29-6-002 timing: 320 µs
10 MPa, PW 1.5 ms, 0 deg Pos
320µs
AK29-6-002 timing: 360 µs
10 MPa, PW 1.5 ms, 0 deg Pos
360µs
AK29-6-002 timing: 400 µs
10 MPa, PW 1.5 ms, 0 deg Pos
400µs
AK29-6-002 timing: 440 µs
10 MPa, PW 1.5 ms, 0 deg Pos
440µs
AK29-6-002 timing: 480 µs
10 MPa, PW 1.5 ms, 0 deg Pos
480µs
AK29-6-002 timing: 520 µs
10 MPa, PW 1.5 ms, 0 deg Pos
520µs
18

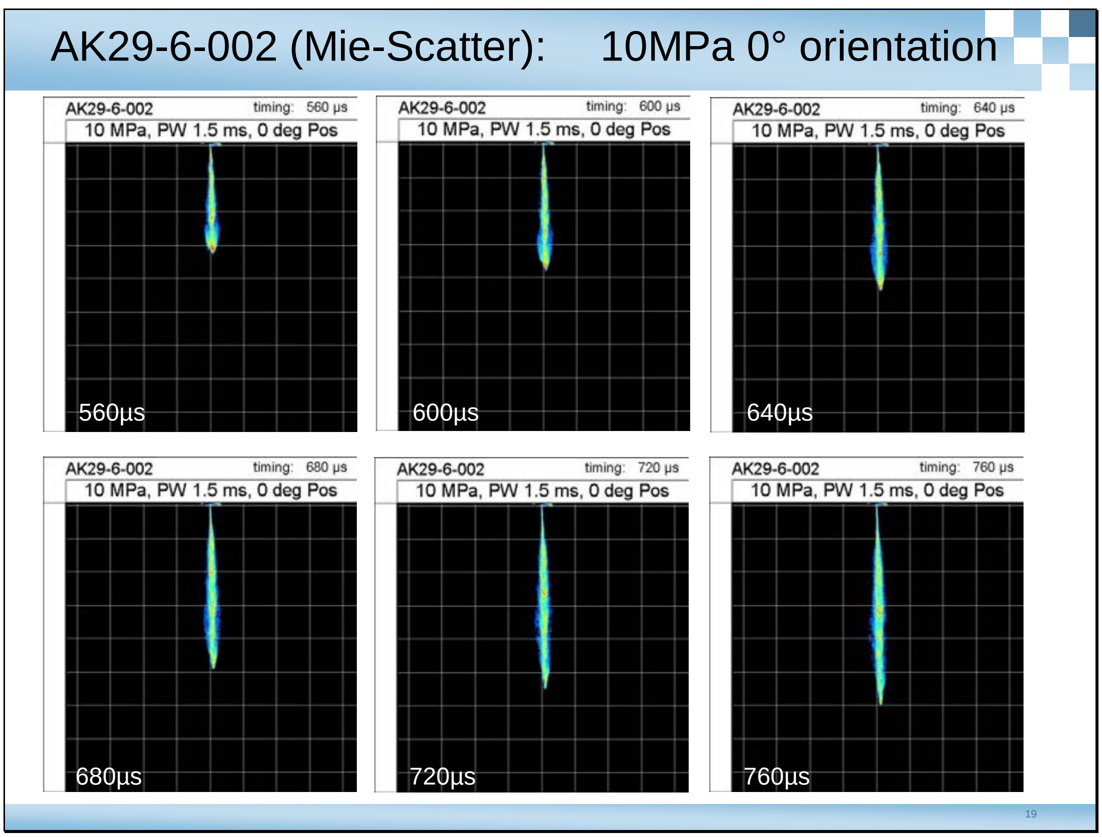
AK29-6-002 (Mie-Scatter): 10MPa 0° orientation
AK29-6-002 timing: 560 µs
10 MPa, PW 1.5 ms, 0 deg Pos
560µs
AK29-6-002 timing: 600 µs
10 MPa, PW 1.5 ms, 0 deg Pos
600µs
AK29-6-002 timing: 640 µs
10 MPa, PW 1.5 ms, 0 deg Pos
640µs
AK29-6-002 timing: 680 µs
10 MPa, PW 1.5 ms, 0 deg Pos
680µs
AK29-6-002 timing: 720 µs
10 MPa, PW 1.5 ms, 0 deg Pos
720µs
AK29-6-002 timing: 760 µs
10 MPa, PW 1.5 ms, 0 deg Pos
760µs
19

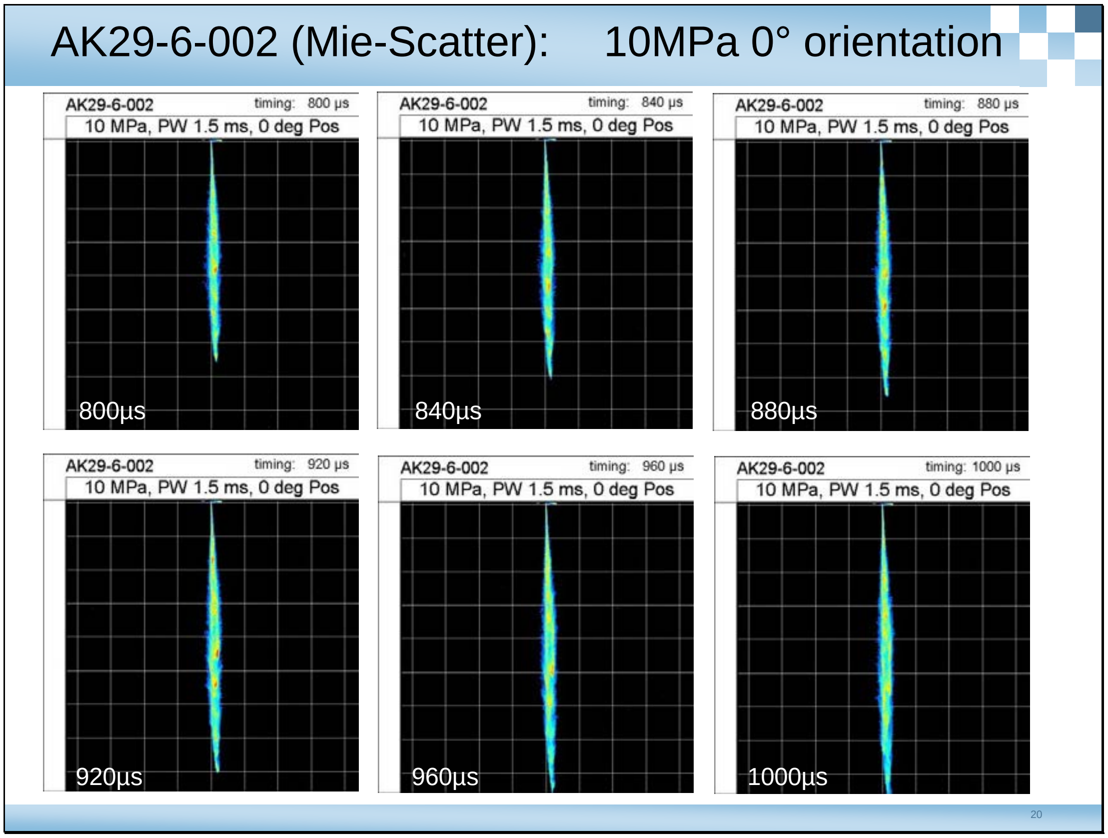
AK29-6-002 (Mie-Scatter): 10MPa 0° orientation
AK29-6-002 timing: 800 μs
10 MPa, PW 1.5 ms, 0 deg Pos
800μs
AK29-6-002 timing: 840 μs
10 MPa, PW 1.5 ms, 0 deg Pos
840μs
AK29-6-002 timing: 880 μs
10 MPa, PW 1.5 ms, 0 deg Pos
880μs
AK29-6-002 timing: 920 μs
10 MPa, PW 1.5 ms, 0 deg Pos
920μs
AK29-6-002 timing: 960 μs
10 MPa, PW 1.5 ms, 0 deg Pos
960μs
AK29-6-002 timing: 1000 μs
10 MPa, PW 1.5 ms, 0 deg Pos
1000μs
20

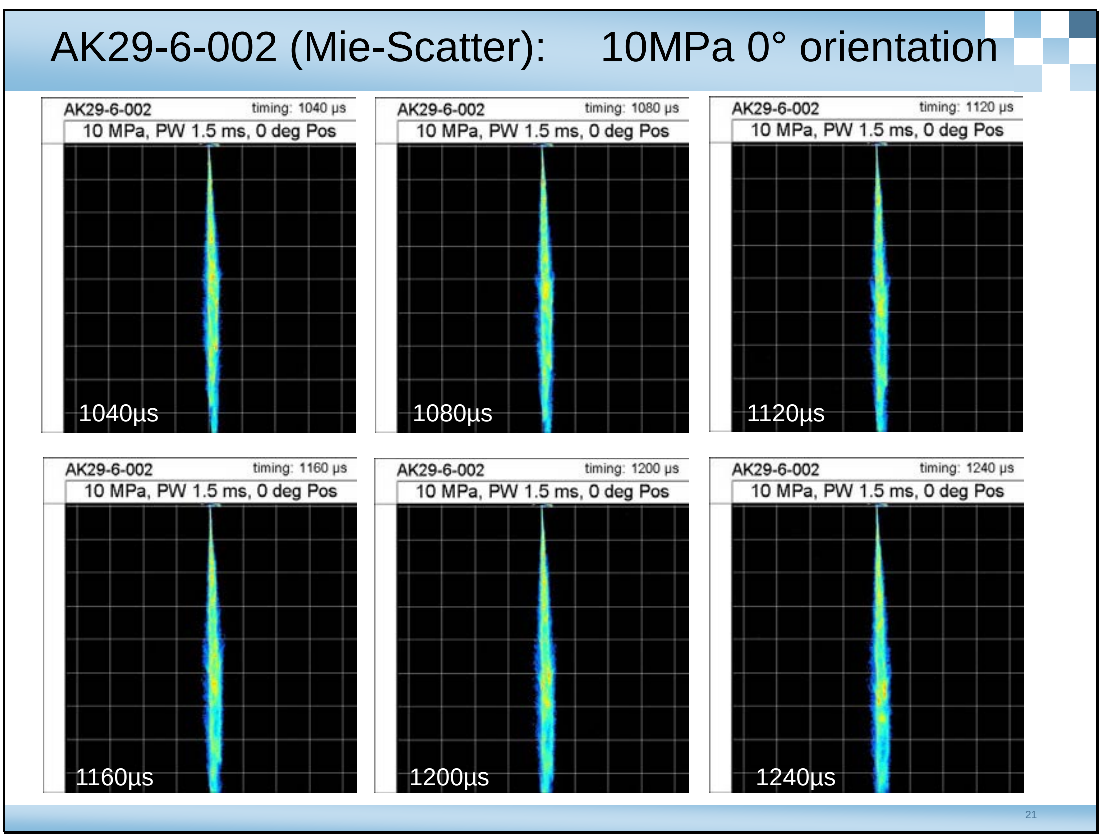
AK29-6-002 (Mie-Scatter): 10MPa 0° orientation
AK29-6-002 timing: 1040 μs
10 MPa, PW 1.5 ms, 0 deg Pos
1040μs
AK29-6-002 timing: 1080 μs
10 MPa, PW 1.5 ms, 0 deg Pos
1080μs
AK29-6-002 timing: 1120 μs
10 MPa, PW 1.5 ms, 0 deg Pos
1120μs
AK29-6-002 timing: 1160 μs
10 MPa, PW 1.5 ms, 0 deg Pos
1160μs
AK29-6-002 timing: 1200 μs
10 MPa, PW 1.5 ms, 0 deg Pos
1200μs
AK29-6-002 timing: 1240 μs
10 MPa, PW 1.5 ms, 0 deg Pos
1240μs
21

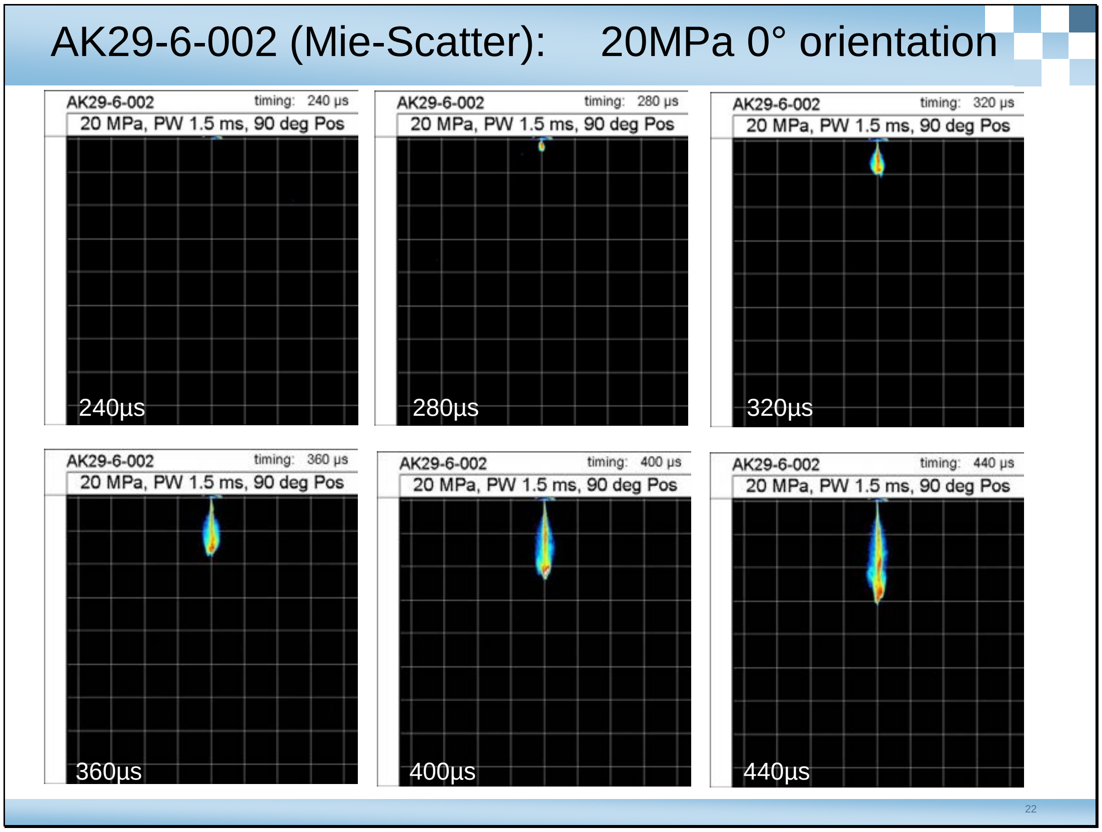
AK29-6-002 (Mie-Scatter): 20MPa 0° orientation
AK29-6-002 timing: 240 µs
20 MPa, PW 1.5 ms, 90 deg Pos
240µs
AK29-6-002 timing: 280 µs
20 MPa, PW 1.5 ms, 90 deg Pos
280µs
AK29-6-002 timing: 320 µs
20 MPa, PW 1.5 ms, 90 deg Pos
320µs
AK29-6-002 timing: 360 µs
20 MPa, PW 1.5 ms, 90 deg Pos
360µs
AK29-6-002 timing: 400 µs
20 MPa, PW 1.5 ms, 90 deg Pos
400µs
AK29-6-002 timing: 440 µs
20 MPa, PW 1.5 ms, 90 deg Pos
440µs
22

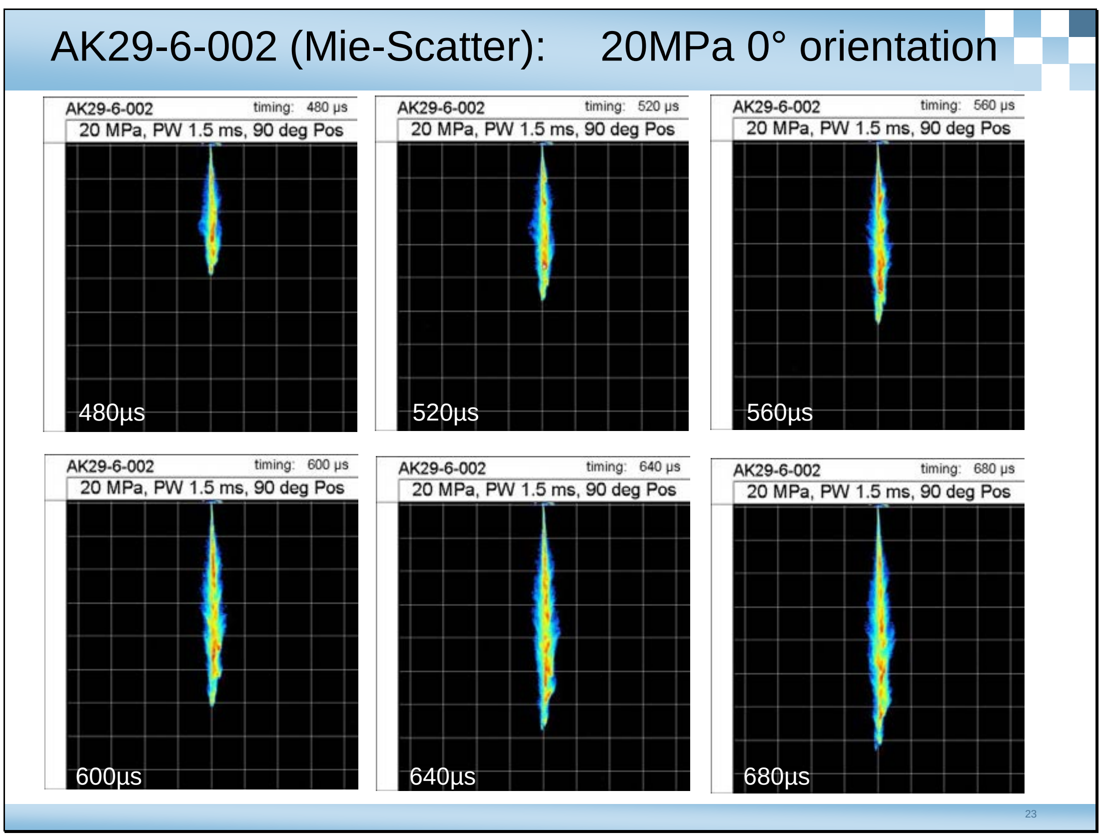
AK29-6-002 (Mie-Scatter): 20MPa 0° orientation
AK29-6-002 timing: 480 µs
20 MPa, PW 1.5 ms, 90 deg Pos
480µs
AK29-6-002 timing: 520 µs
20 MPa, PW 1.5 ms, 90 deg Pos
520µs
AK29-6-002 timing: 560 µs
20 MPa, PW 1.5 ms, 90 deg Pos
560µs
AK29-6-002 timing: 600 µs
20 MPa, PW 1.5 ms, 90 deg Pos
600µs
AK29-6-002 timing: 640 µs
20 MPa, PW 1.5 ms, 90 deg Pos
640µs
AK29-6-002 timing: 680 µs
20 MPa, PW 1.5 ms, 90 deg Pos
680µs
23

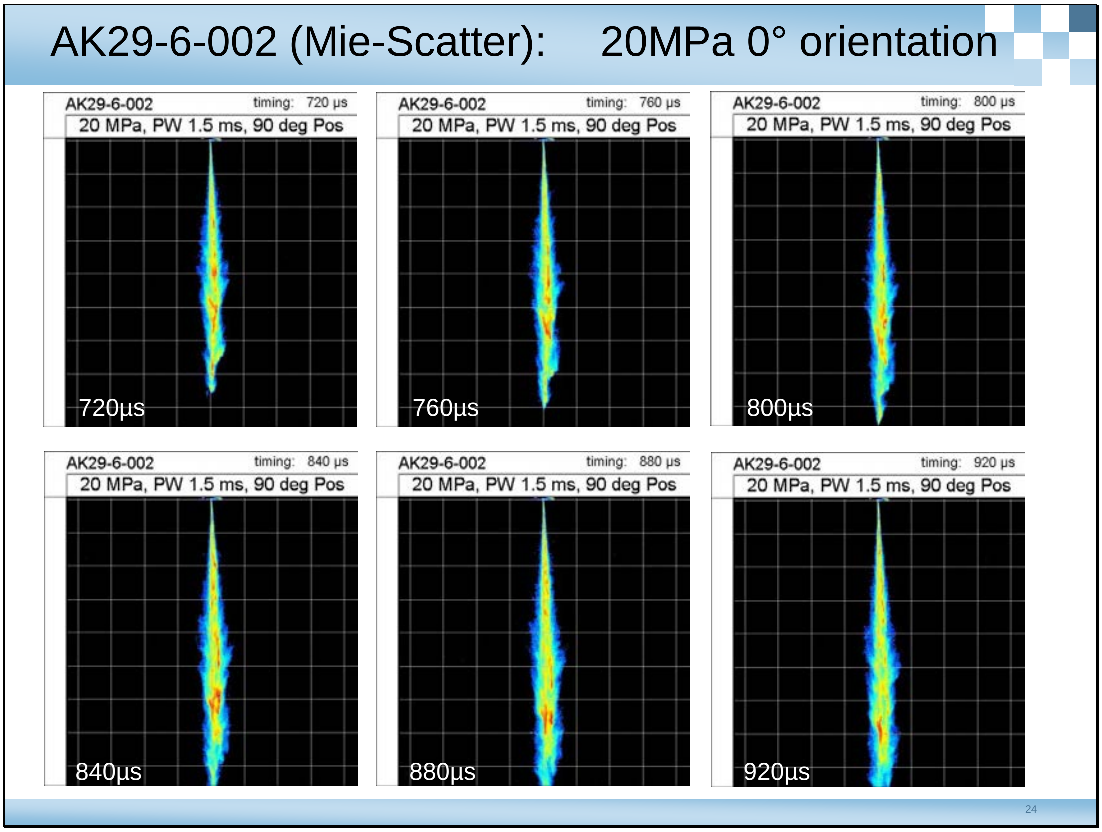
AK29-6-002 (Mie-Scatter): 20MPa 0° orientation
AK29-6-002 timing: 720 µs
20 MPa, PW 1.5 ms, 90 deg Pos
720µs
AK29-6-002 timing: 760 µs
20 MPa, PW 1.5 ms, 90 deg Pos
760µs
AK29-6-002 timing: 800 µs
20 MPa, PW 1.5 ms, 90 deg Pos
800µs
AK29-6-002 timing: 840 µs
20 MPa, PW 1.5 ms, 90 deg Pos
840µs
AK29-6-002 timing: 880 µs
20 MPa, PW 1.5 ms, 90 deg Pos
880µs
AK29-6-002 timing: 920 µs
20 MPa, PW 1.5 ms, 90 deg Pos
920µs
24

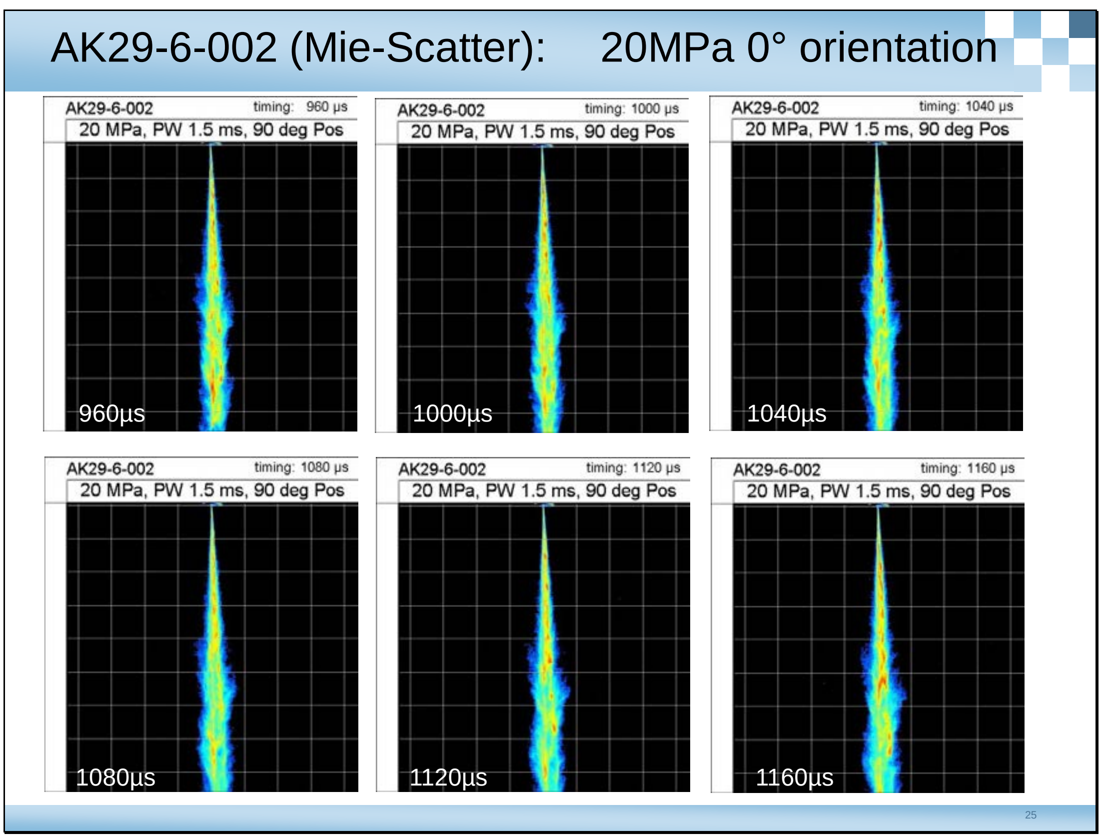
AK29-6-002 (Mie-Scatter): 20MPa 0° orientation
AK29-6-002 timing: 960 µs
20 MPa, PW 1.5 ms, 90 deg Pos
960µs
AK29-6-002 timing: 1000 µs
20 MPa, PW 1.5 ms, 90 deg Pos
1000µs
AK29-6-002 timing: 1040 µs
20 MPa, PW 1.5 ms, 90 deg Pos
1040µs
AK29-6-002 timing: 1080 µs
20 MPa, PW 1.5 ms, 90 deg Pos
1080µs
AK29-6-002 timing: 1120 µs
20 MPa, PW 1.5 ms, 90 deg Pos
1120µs
AK29-6-002 timing: 1160 µs
20 MPa, PW 1.5 ms, 90 deg Pos
1160µs
25

## Mie spray images 90° orientation

Mie Scatter spray images for 90 degree orientation show similar behavior, therefore not shown here.

26

## AK29-9-001 (Mie-Scatter): 10MPa, 0° orientation

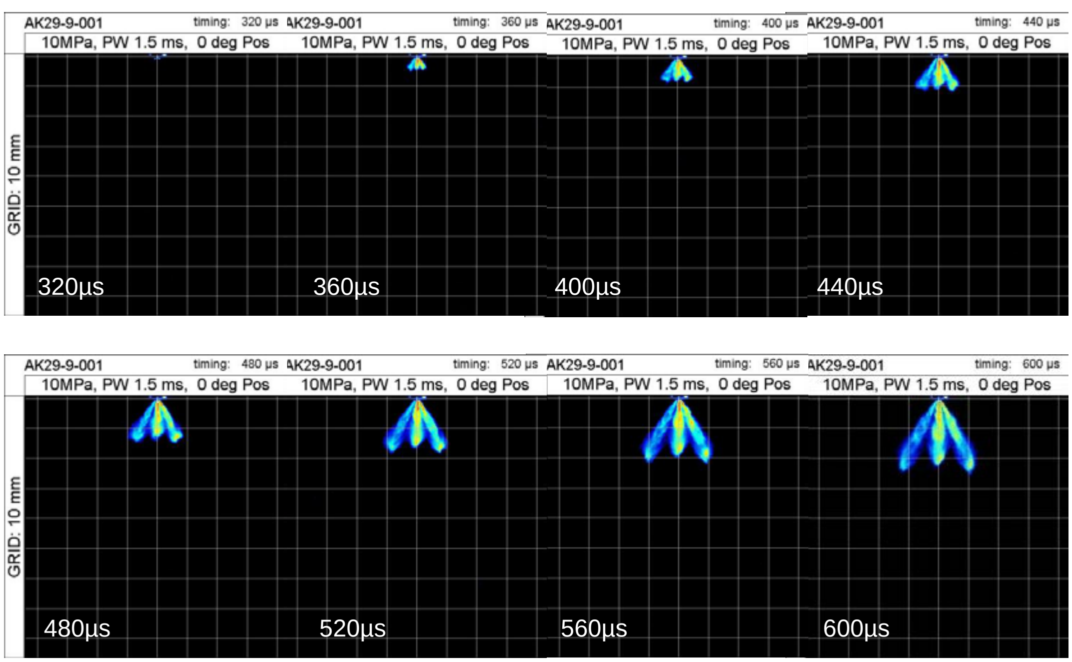


27

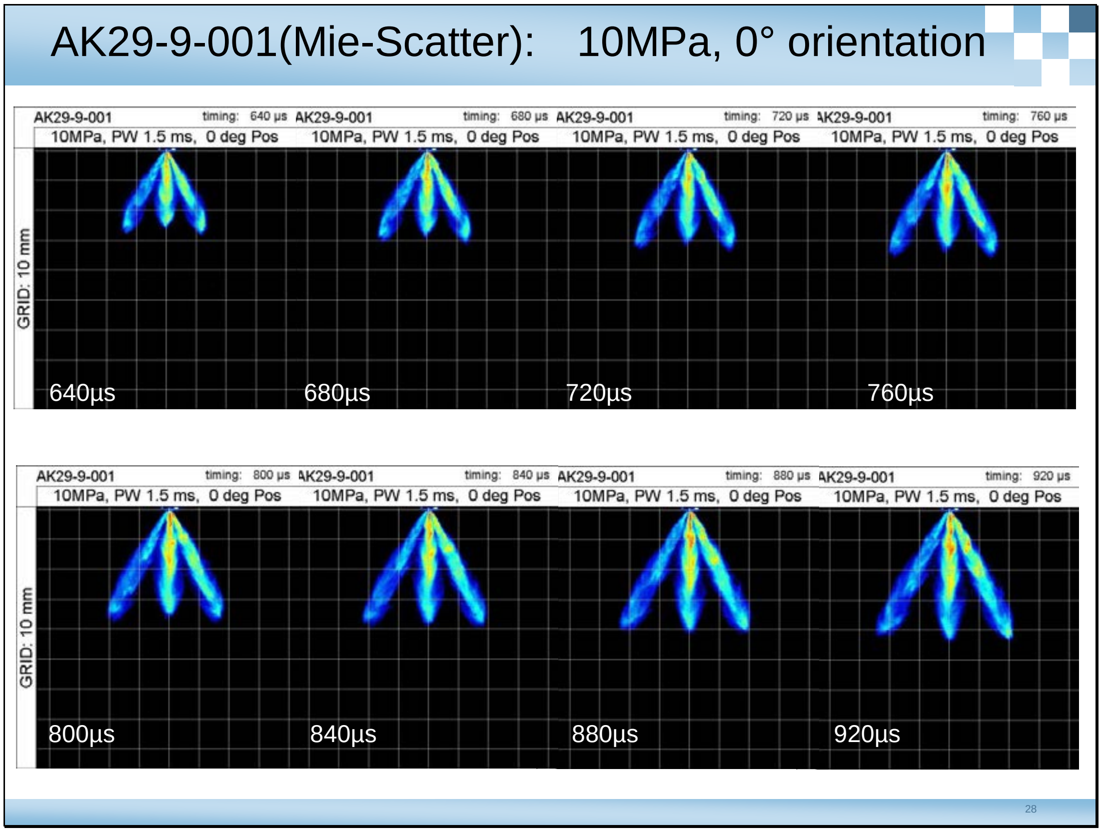
AK29-9-001(Mie-Scatter): 10MPa, 0° orientation
AK29-9-001
10MPa, PW 1.5 ms, 0 deg Pos
GRID: 10 mm
640µs
680µs
720µs
760µs
800µs
840µs
880µs
920µs
28

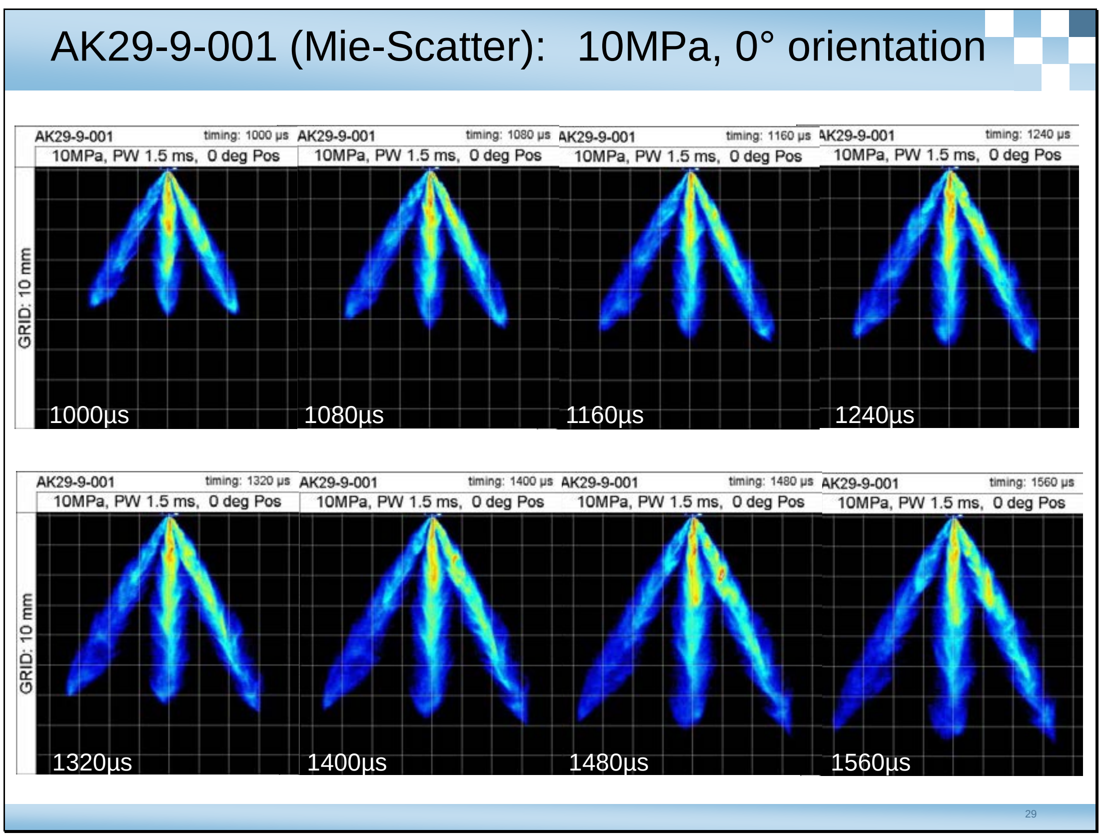
AK29-9-001 (Mie-Scatter): 10MPa, 0° orientation
AK29-9-001
10MPa, PW 1.5 ms, 0 deg Pos
GRID: 10 mm
1000µs
1080µs
1160µs
1240µs
1320µs
1400µs
1480µs
1560µs
29

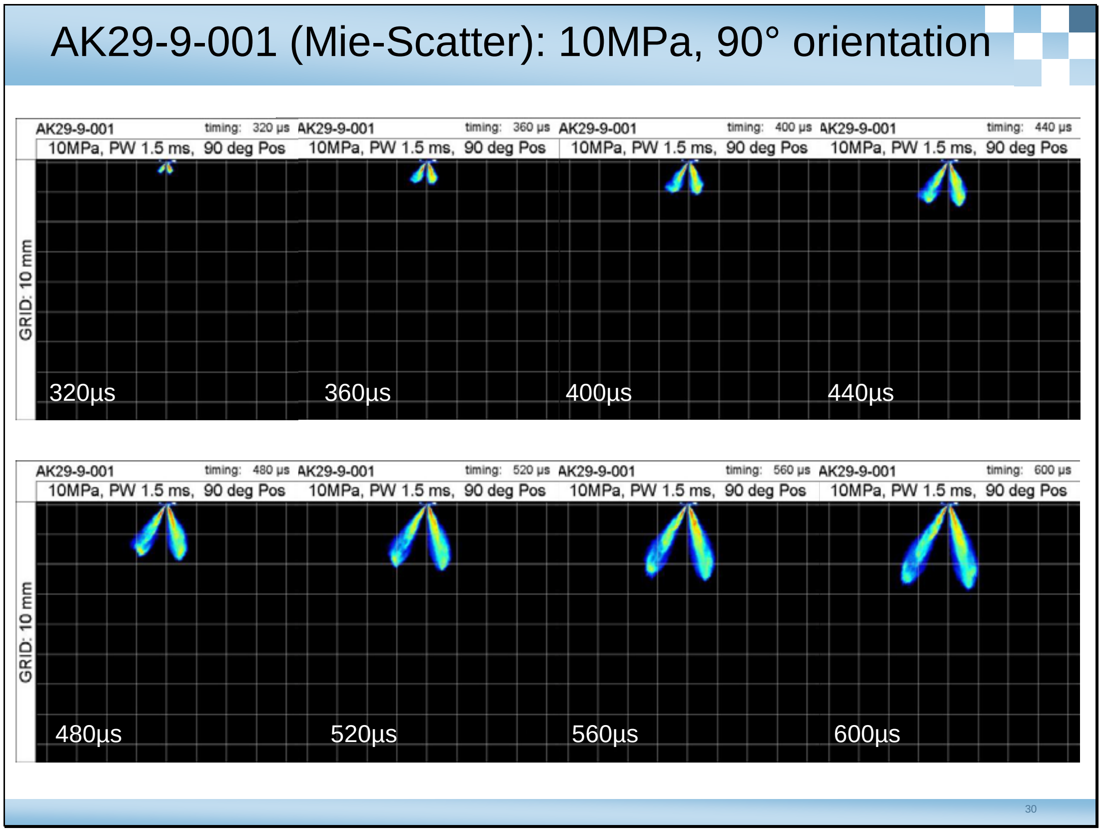
AK29-9-001 (Mie-Scatter): 10MPa, 90° orientation
AK29-9-001 timing: 320 µs
10MPa, PW 1.5 ms, 90 deg Pos
AK29-9-001 timing: 360 µs
10MPa, PW 1.5 ms, 90 deg Pos
AK29-9-001 timing: 400 µs
10MPa, PW 1.5 ms, 90 deg Pos
AK29-9-001 timing: 440 µs
10MPa, PW 1.5 ms, 90 deg Pos
GRID: 10 mm
320µs
360µs
400µs
440µs
AK29-9-001 timing: 480 µs
10MPa, PW 1.5 ms, 90 deg Pos
AK29-9-001 timing: 520 µs
10MPa, PW 1.5 ms, 90 deg Pos
AK29-9-001 timing: 560 µs
10MPa, PW 1.5 ms, 90 deg Pos
AK29-9-001 timing: 600 µs
10MPa, PW 1.5 ms, 90 deg Pos
GRID: 10 mm
480µs
520µs
560µs
600µs
30

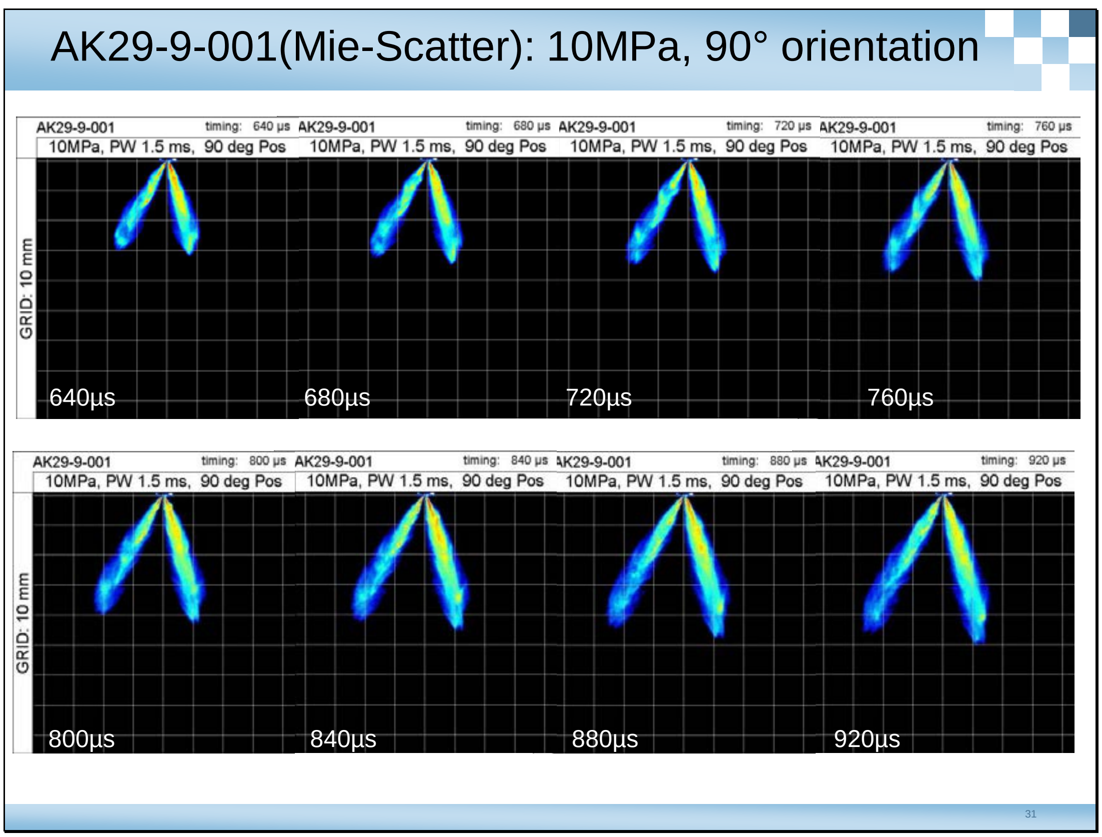
AK29-9-001(Mie-Scatter): 10MPa, 90° orientation
AK29-9-001 timing: 640 µs
10MPa, PW 1.5 ms, 90 deg Pos
AK29-9-001 timing: 680 µs
10MPa, PW 1.5 ms, 90 deg Pos
AK29-9-001 timing: 720 µs
10MPa, PW 1.5 ms, 90 deg Pos
AK29-9-001 timing: 760 µs
10MPa, PW 1.5 ms, 90 deg Pos
GRID: 10 mm
640µs
680µs
720µs
760µs
AK29-9-001 timing: 800 µs
10MPa, PW 1.5 ms, 90 deg Pos
AK29-9-001 timing: 840 µs
10MPa, PW 1.5 ms, 90 deg Pos
AK29-9-001 timing: 880 µs
10MPa, PW 1.5 ms, 90 deg Pos
AK29-9-001 timing: 920 µs
10MPa, PW 1.5 ms, 90 deg Pos
GRID: 10 mm
800µs
840µs
880µs
920µs
31

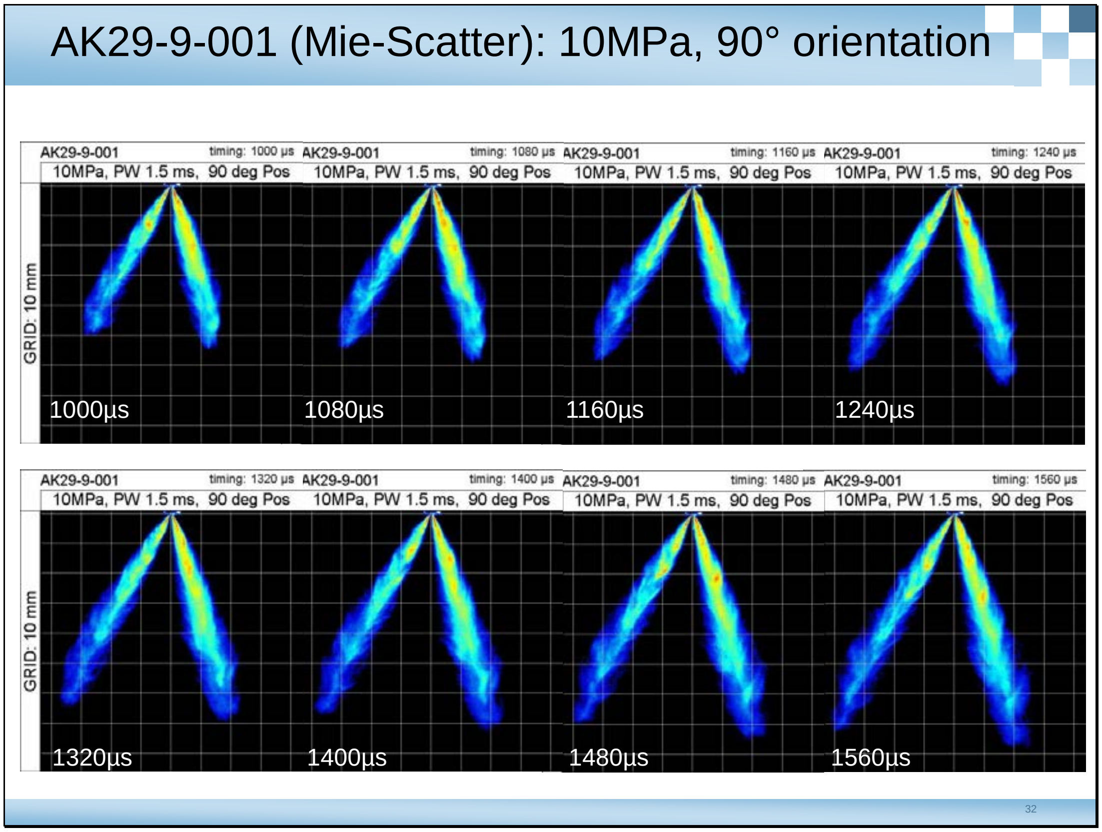
AK29-9-001 (Mie-Scatter): 10MPa, 90° orientation
AK29-9-001 timing: 1000 µs
10MPa, PW 1.5 ms, 90 deg Pos
AK29-9-001 timing: 1080 µs
10MPa, PW 1.5 ms, 90 deg Pos
AK29-9-001 timing: 1160 µs
10MPa, PW 1.5 ms, 90 deg Pos
AK29-9-001 timing: 1240 µs
10MPa, PW 1.5 ms, 90 deg Pos
GRID: 10 mm
1000µs
1080µs
1160µs
1240µs
AK29-9-001 timing: 1320 µs
10MPa, PW 1.5 ms, 90 deg Pos
AK29-9-001 timing: 1400 µs
10MPa, PW 1.5 ms, 90 deg Pos
AK29-9-001 timing: 1480 µs
10MPa, PW 1.5 ms, 90 deg Pos
AK29-9-001 timing: 1560 µs
10MPa, PW 1.5 ms, 90 deg Pos
GRID: 10 mm
1320µs
1400µs
1480µs
1560µs
32

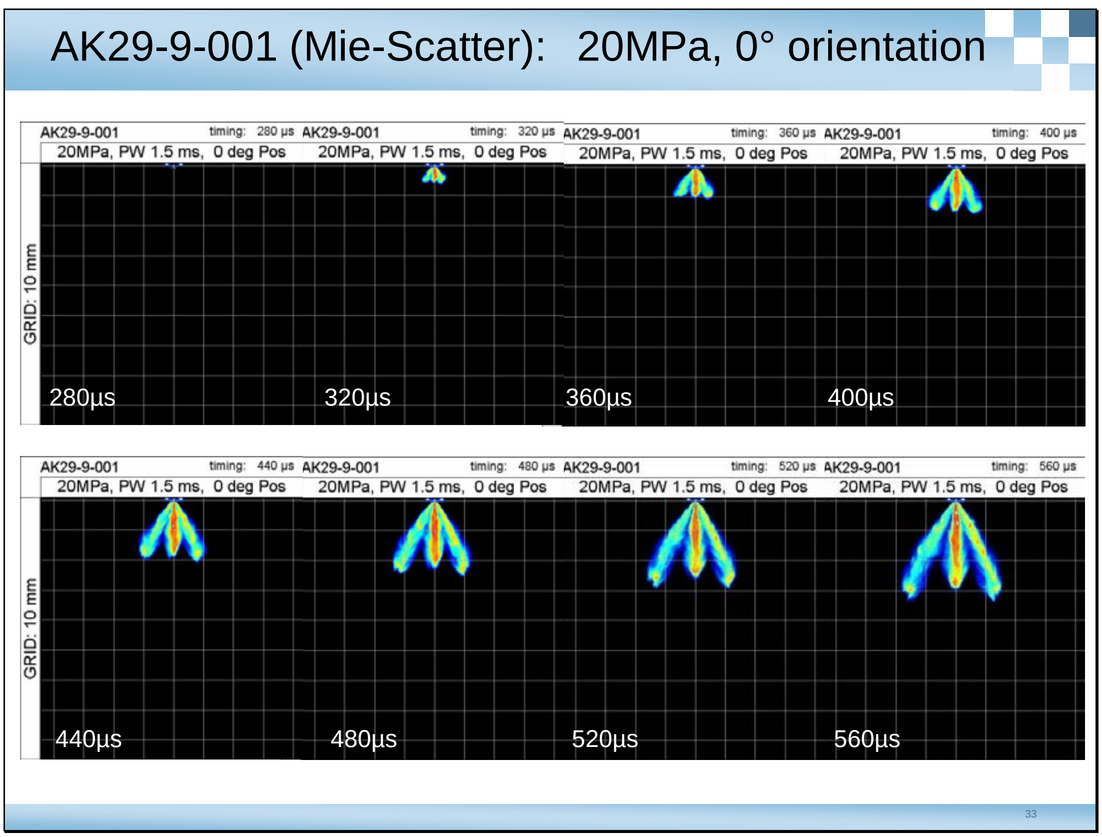
AK29-9-001 (Mie-Scatter): 20MPa, 0° orientation
AK29-9-001 timing: 280 µs
20MPa, PW 1.5 ms, 0 deg Pos
AK29-9-001 timing: 320 µs
20MPa, PW 1.5 ms, 0 deg Pos
AK29-9-001 timing: 360 µs
20MPa, PW 1.5 ms, 0 deg Pos
AK29-9-001 timing: 400 µs
20MPa, PW 1.5 ms, 0 deg Pos
GRID: 10 mm
280µs
320µs
360µs
400µs
AK29-9-001 timing: 440 µs
20MPa, PW 1.5 ms, 0 deg Pos
AK29-9-001 timing: 480 µs
20MPa, PW 1.5 ms, 0 deg Pos
AK29-9-001 timing: 520 µs
20MPa, PW 1.5 ms, 0 deg Pos
AK29-9-001 timing: 560 µs
20MPa, PW 1.5 ms, 0 deg Pos
GRID: 10 mm
440µs
480µs
520µs
560µs
33

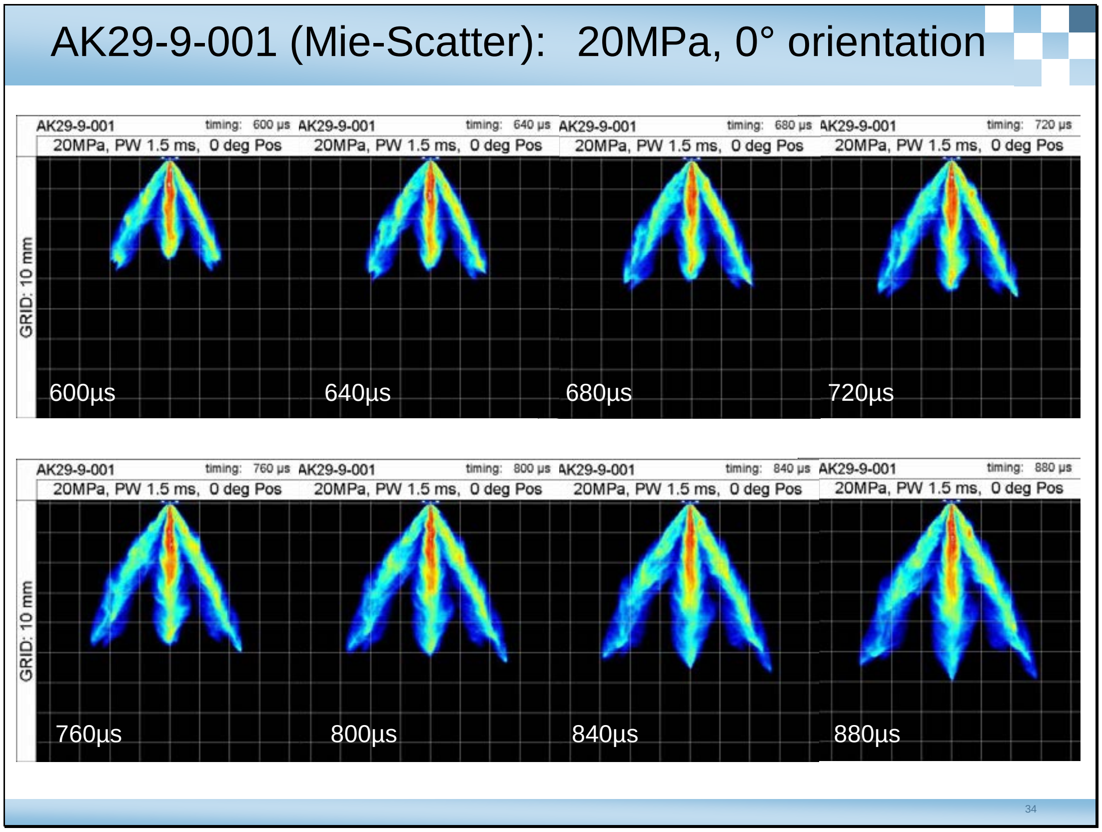
AK29-9-001 (Mie-Scatter): 20MPa, 0° orientation
AK29-9-001
20MPa, PW 1.5 ms, 0 deg Pos
GRID: 10 mm
600µs
640µs
680µs
720µs
760µs
800µs
840µs
880µs
34

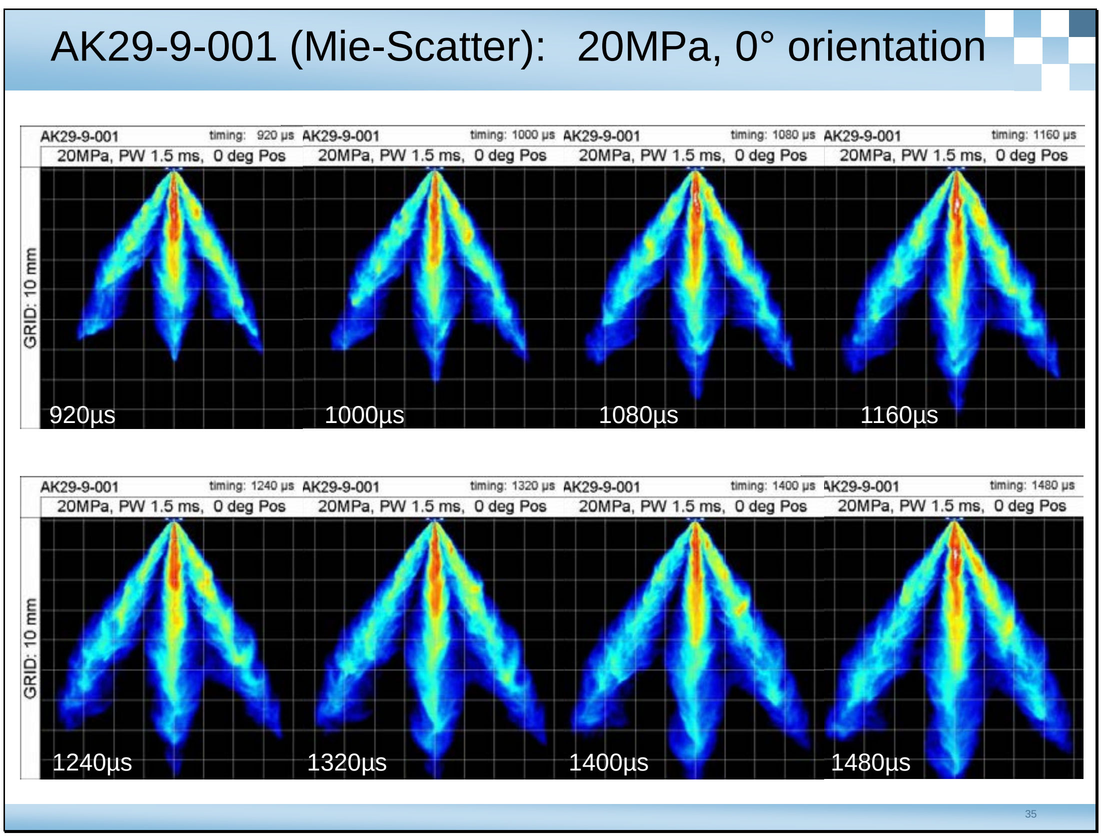
AK29-9-001 (Mie-Scatter): 20MPa, 0° orientation
AK29-9-001
20MPa, PW 1.5 ms, 0 deg Pos
GRID: 10 mm
920µs
1000µs
1080µs
1160µs
1240µs
1320µs
1400µs
1480µs
35

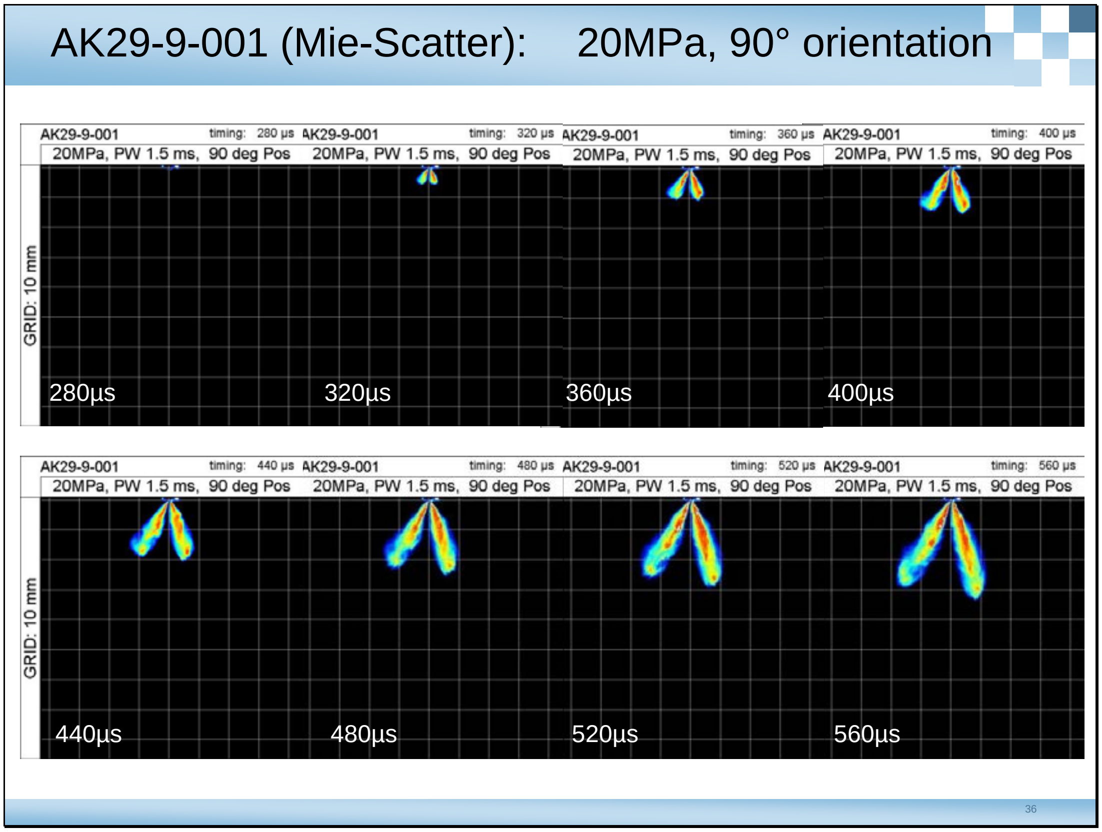
AK29-9-001 (Mie-Scatter): 20MPa, 90° orientation
AK29-9-001
20MPa, PW 1.5 ms, 90 deg Pos
GRID: 10 mm
280µs
320µs
360µs
400µs
440µs
480µs
520µs
560µs
36

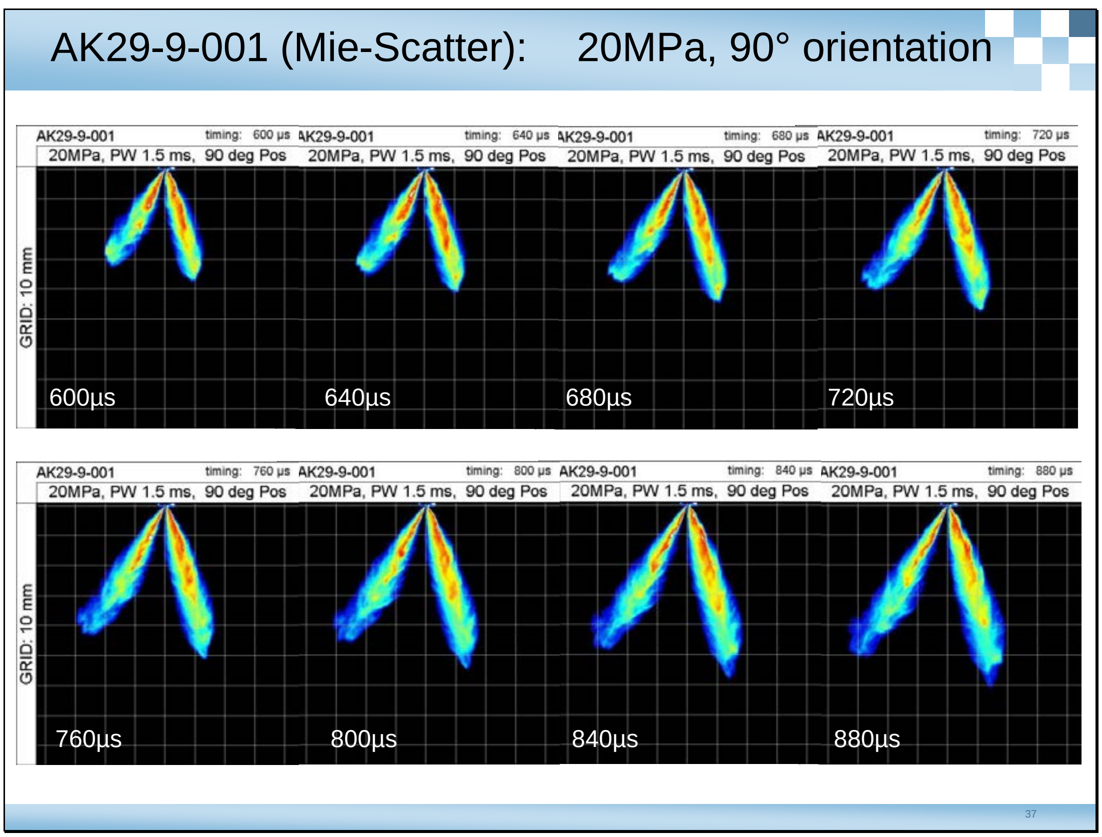
AK29-9-001 (Mie-Scatter): 20MPa, 90° orientation
AK29-9-001
20MPa, PW 1.5 ms, 90 deg Pos
GRID: 10 mm
600µs
640µs
680µs
720µs
760µs
800µs
840µs
880µs
37

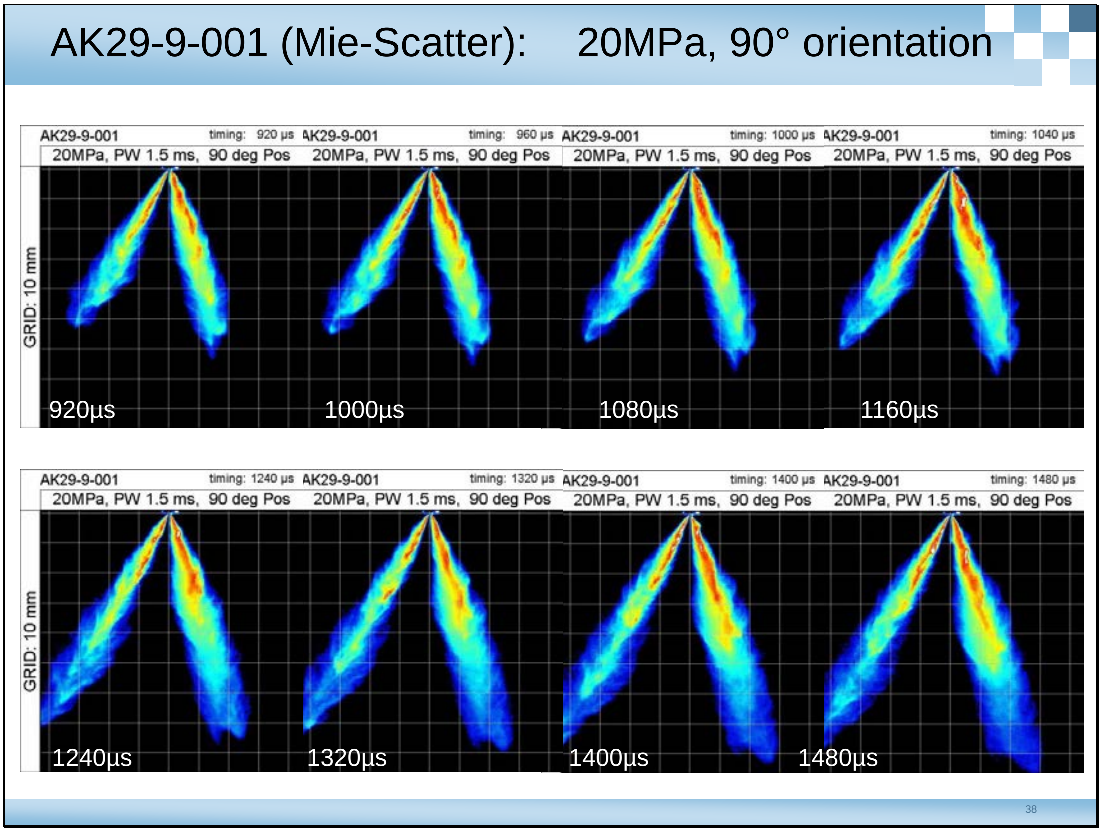
AK29-9-001 (Mie-Scatter): 20MPa, 90° orientation
AK29-9-001
20MPa, PW 1.5 ms, 90 deg Pos
GRID: 10 mm
920µs
1000µs
1080µs
1160µs
1240µs
1320µs
1400µs
1480µs
38

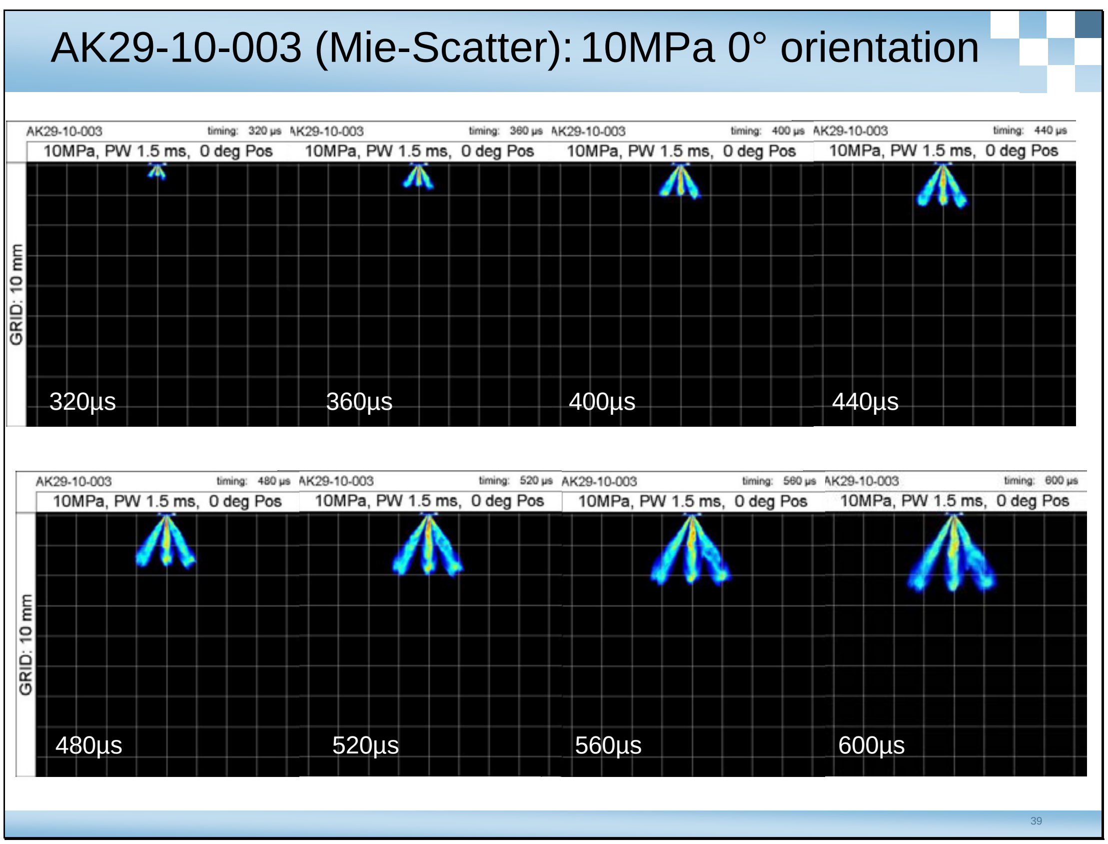
AK29-10-003 (Mie-Scatter): 10MPa 0° orientation
AK29-10-003
10MPa, PW 1.5 ms, 0 deg Pos
GRID: 10 mm
320µs
360µs
400µs
440µs
480µs
520µs
560µs
600µs
39

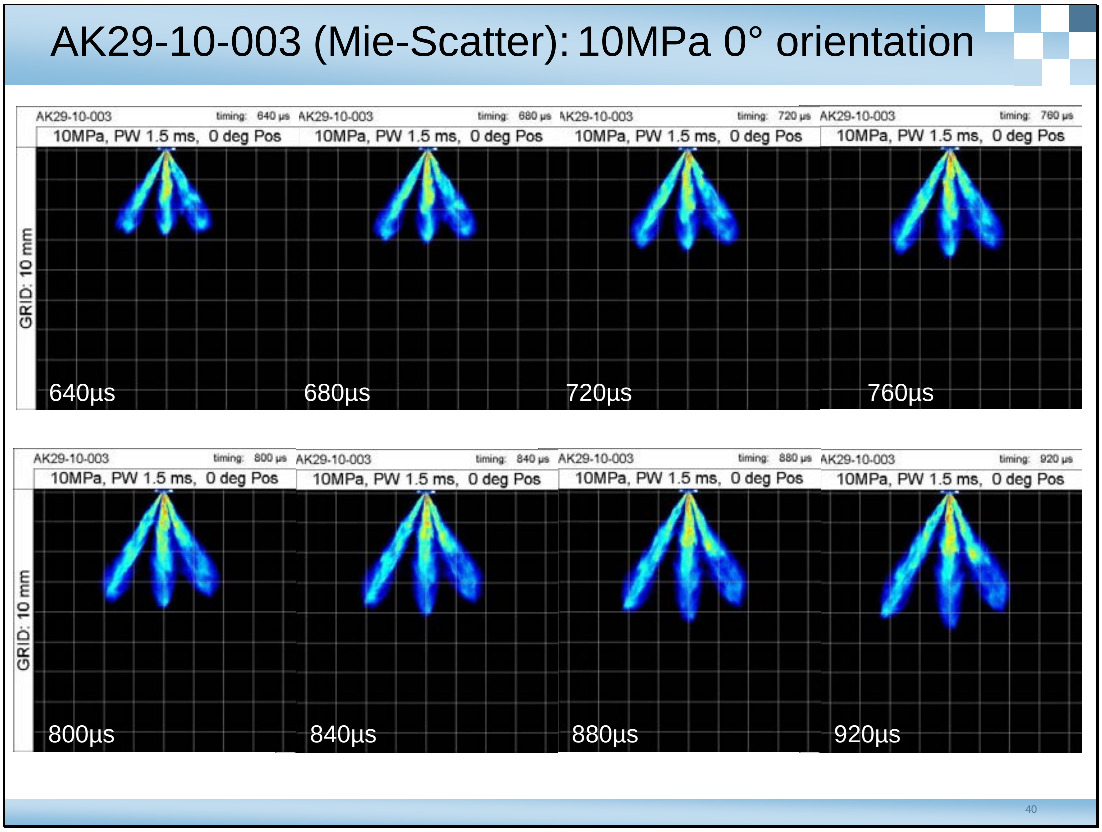
AK29-10-003 (Mie-Scatter): 10MPa 0° orientation
AK29-10-003
10MPa, PW 1.5 ms, 0 deg Pos
GRID: 10 mm
640µs
680µs
720µs
760µs
800µs
840µs
880µs
920µs
40

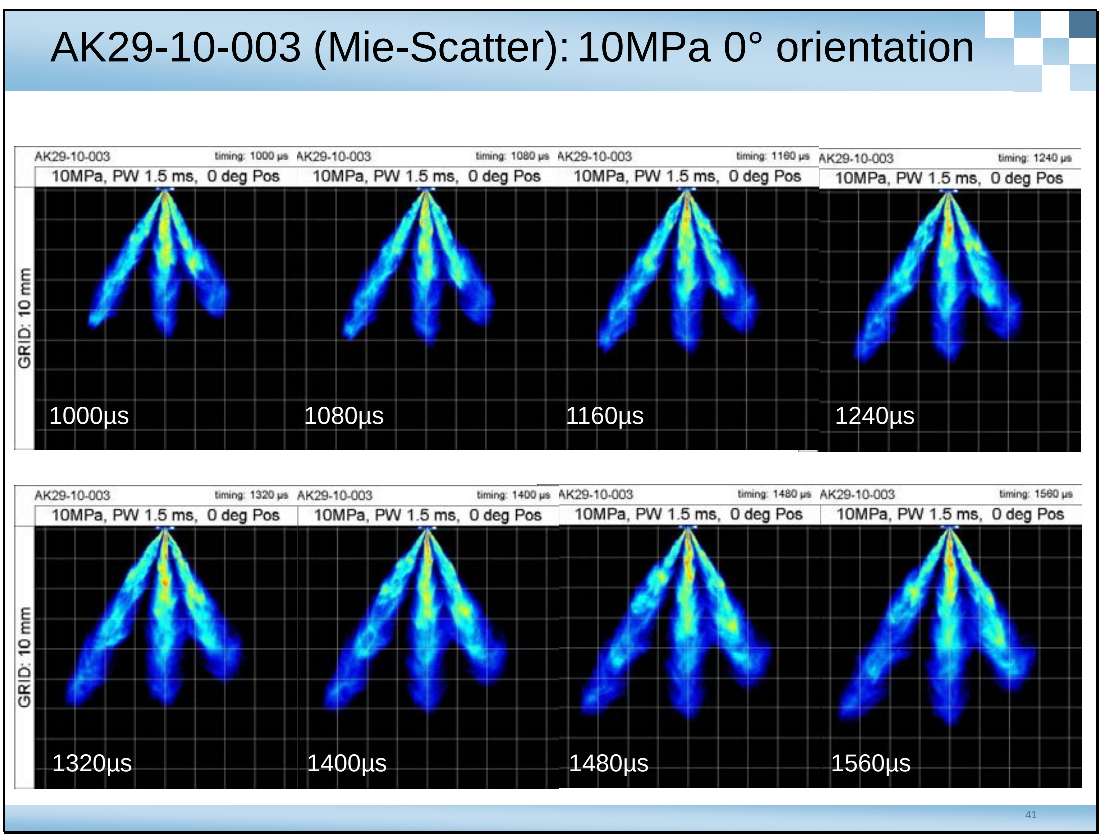
AK29-10-003 (Mie-Scatter): 10MPa 0° orientation
AK29-10-003
10MPa, PW 1.5 ms, 0 deg Pos
GRID: 10 mm
1000µs
1080µs
1160µs
1240µs
1320µs
1400µs
1480µs
1560µs
41

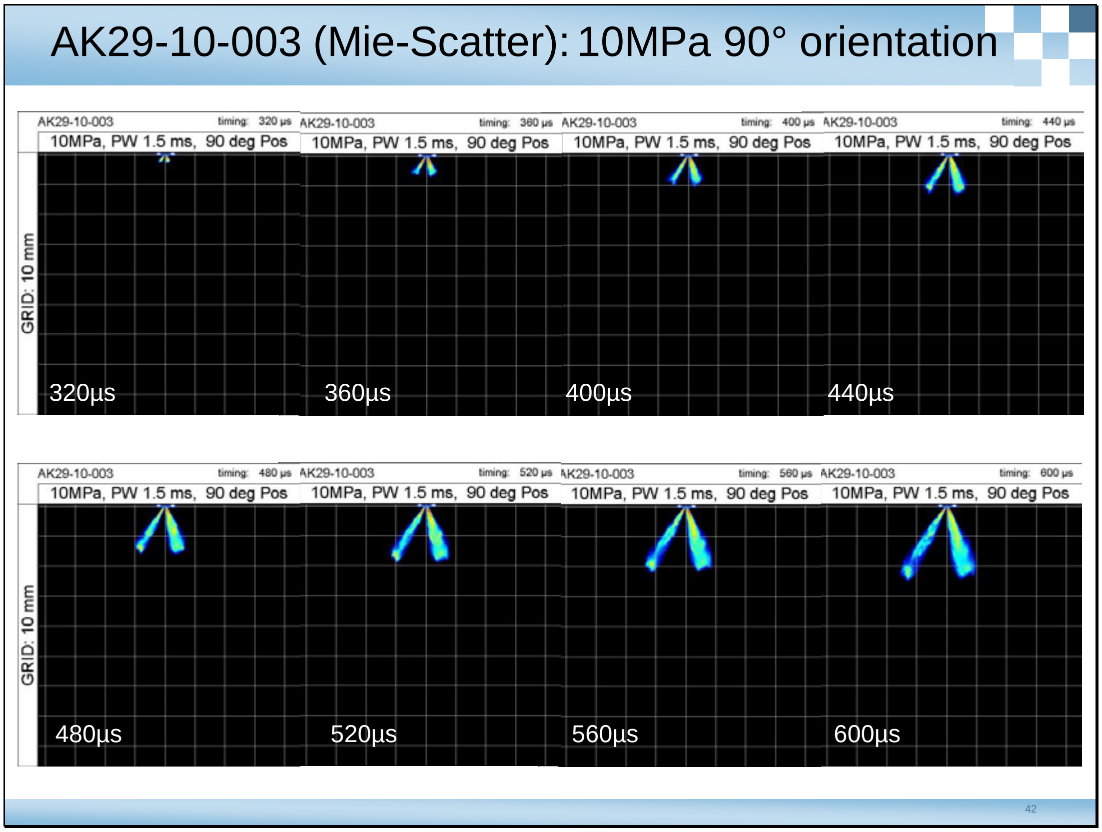
AK29-10-003 (Mie-Scatter): 10MPa 90° orientation
AK29-10-003
10MPa, PW 1.5 ms, 90 deg Pos
GRID: 10 mm
320µs
360µs
400µs
440µs
480µs
520µs
560µs
600µs
42

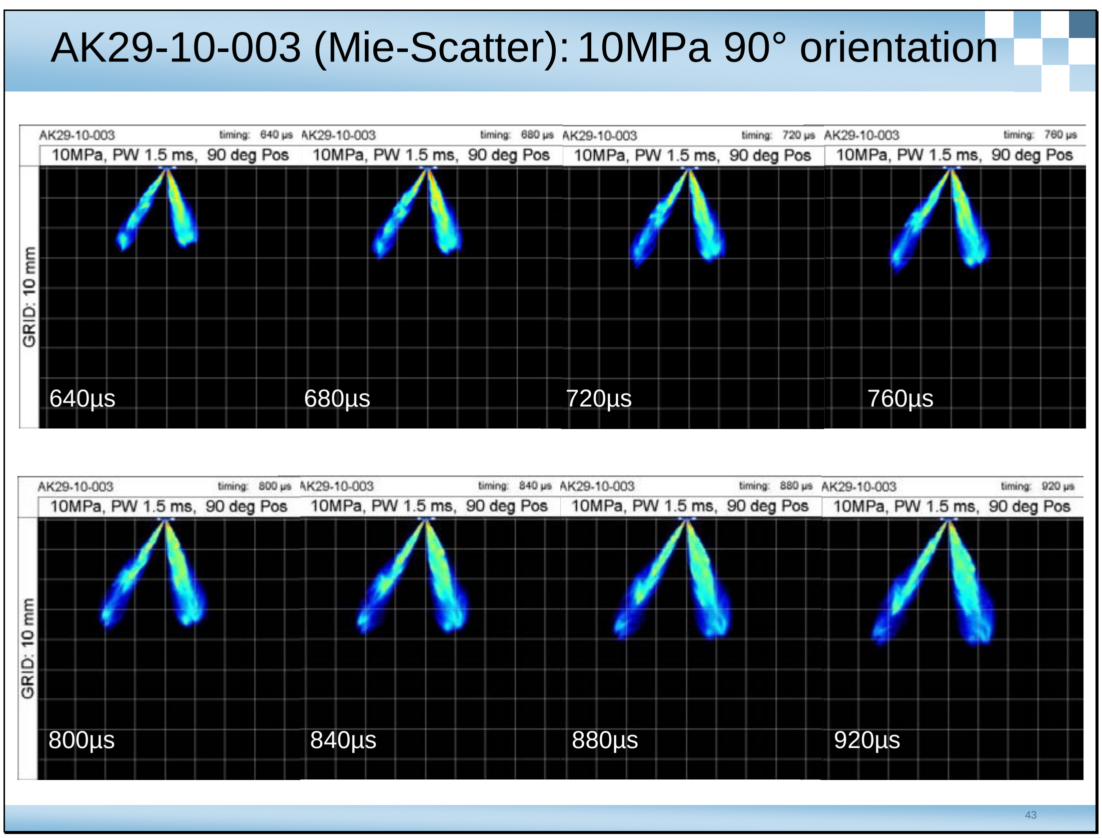
AK29-10-003 (Mie-Scatter): 10MPa 90° orientation
AK29-10-003
10MPa, PW 1.5 ms, 90 deg Pos
GRID: 10 mm
640µs
680µs
720µs
760µs
800µs
840µs
880µs
920µs
43

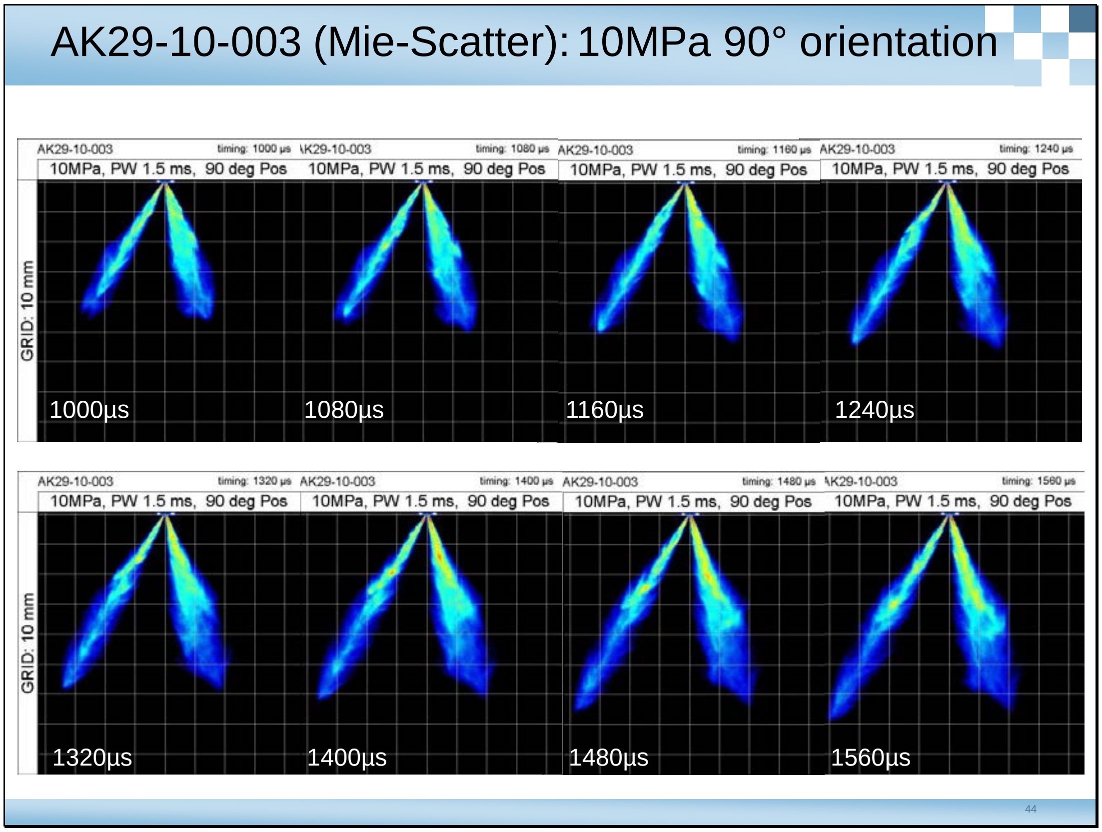
AK29-10-003 (Mie-Scatter): 10MPa 90° orientation
AK29-10-003
10MPa, PW 1.5 ms, 90 deg Pos
GRID: 10 mm
1000µs
1080µs
1160µs
1240µs
1320µs
1400µs
1480µs
1560µs
44

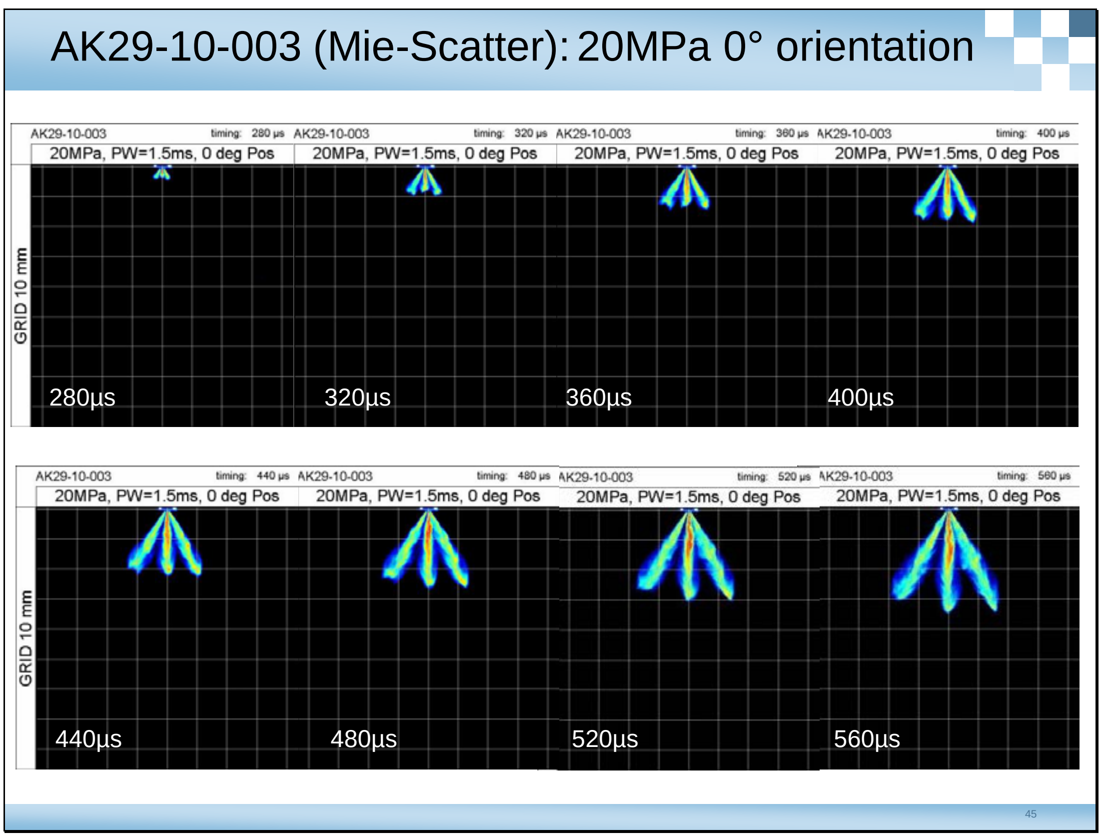
AK29-10-003 (Mie-Scatter): 20MPa 0° orientation
AK29-10-003
20MPa, PW=1.5ms, 0 deg Pos
GRID 10 mm
280µs
320µs
360µs
400µs
440µs
480µs
520µs
560µs
45

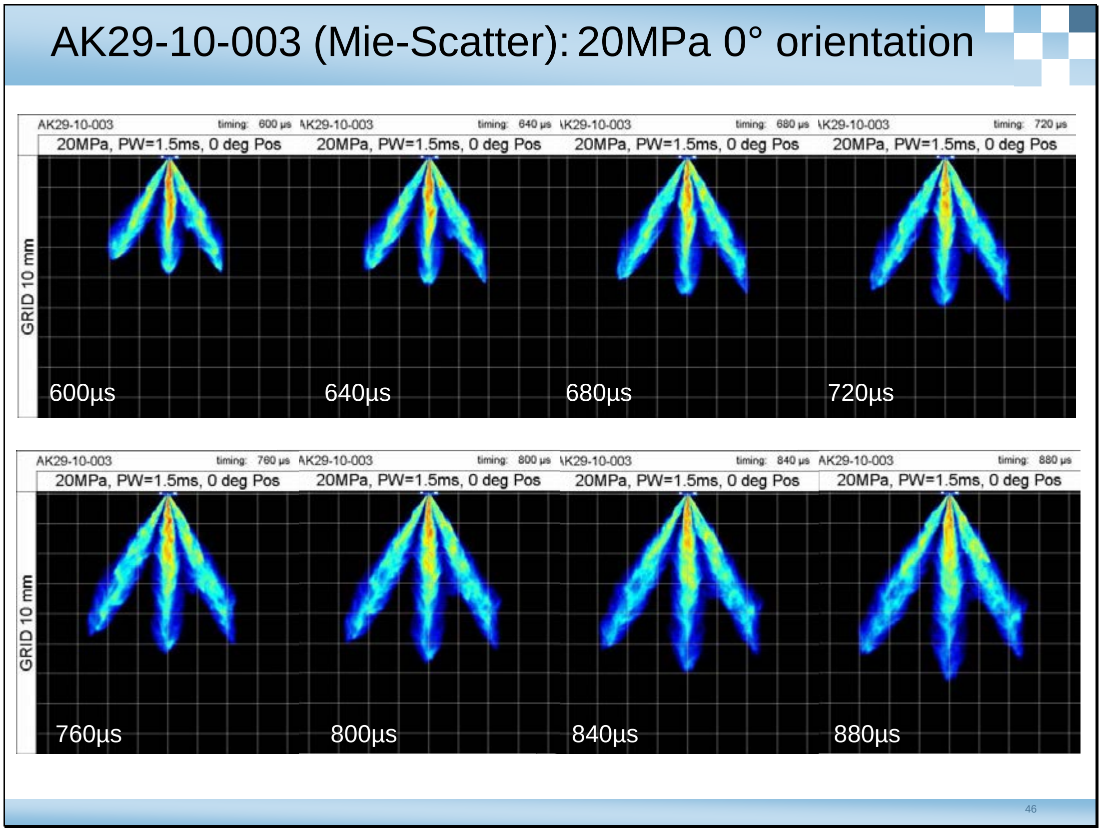
AK29-10-003 (Mie-Scatter): 20MPa 0° orientation
AK29-10-003
20MPa, PW=1.5ms, 0 deg Pos
GRID 10 mm
600µs
640µs
680µs
720µs
760µs
800µs
840µs
880µs
46

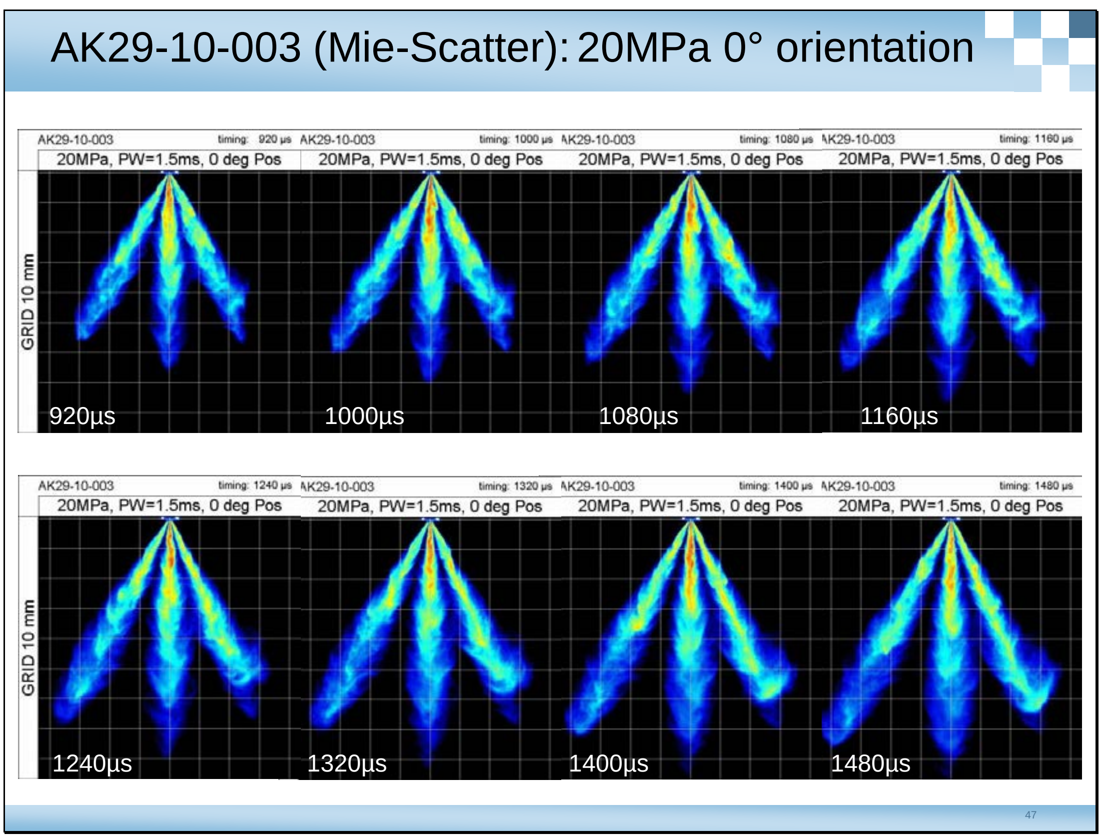
AK29-10-003 (Mie-Scatter): 20MPa 0° orientation
AK29-10-003
20MPa, PW=1.5ms, 0 deg Pos
GRID 10 mm
920µs
1000µs
1080µs
1160µs
1240µs
1320µs
1400µs
1480µs
47

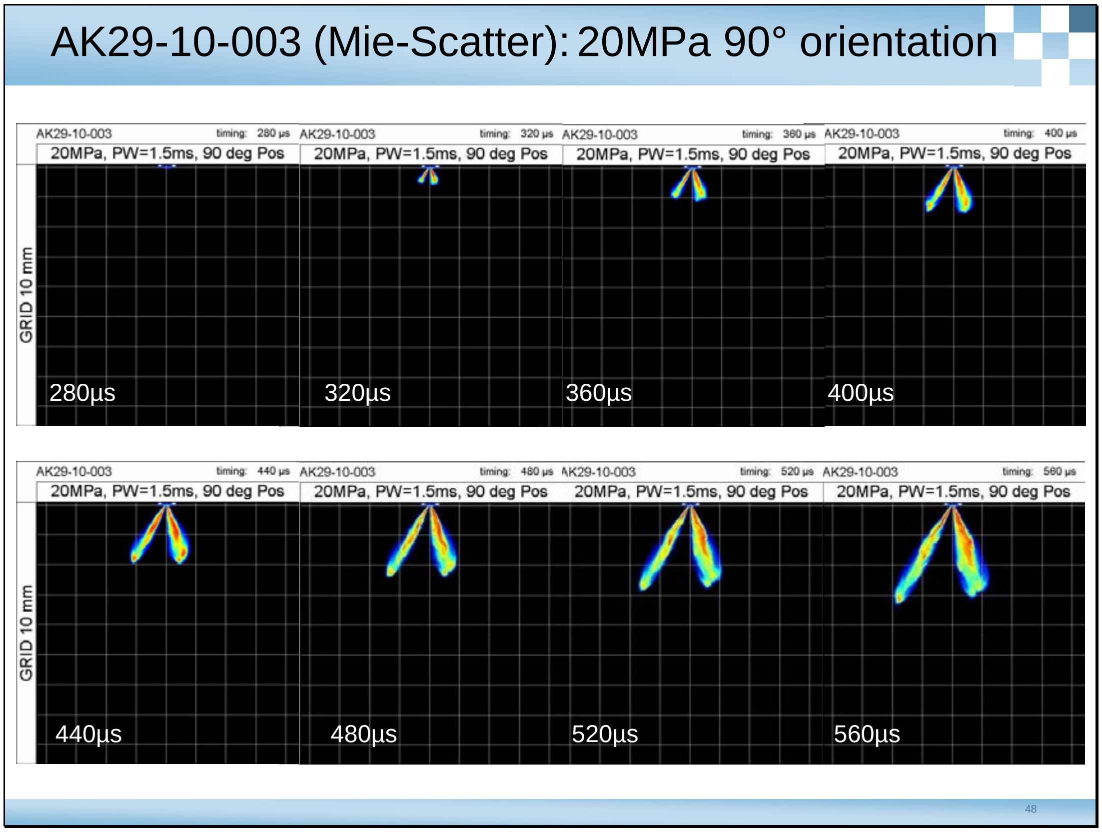
AK29-10-003 (Mie-Scatter): 20MPa 90° orientation
AK29-10-003
20MPa, PW=1.5ms, 90 deg Pos
GRID 10 mm
280µs
320µs
360µs
400µs
440µs
480µs
520µs
560µs
48

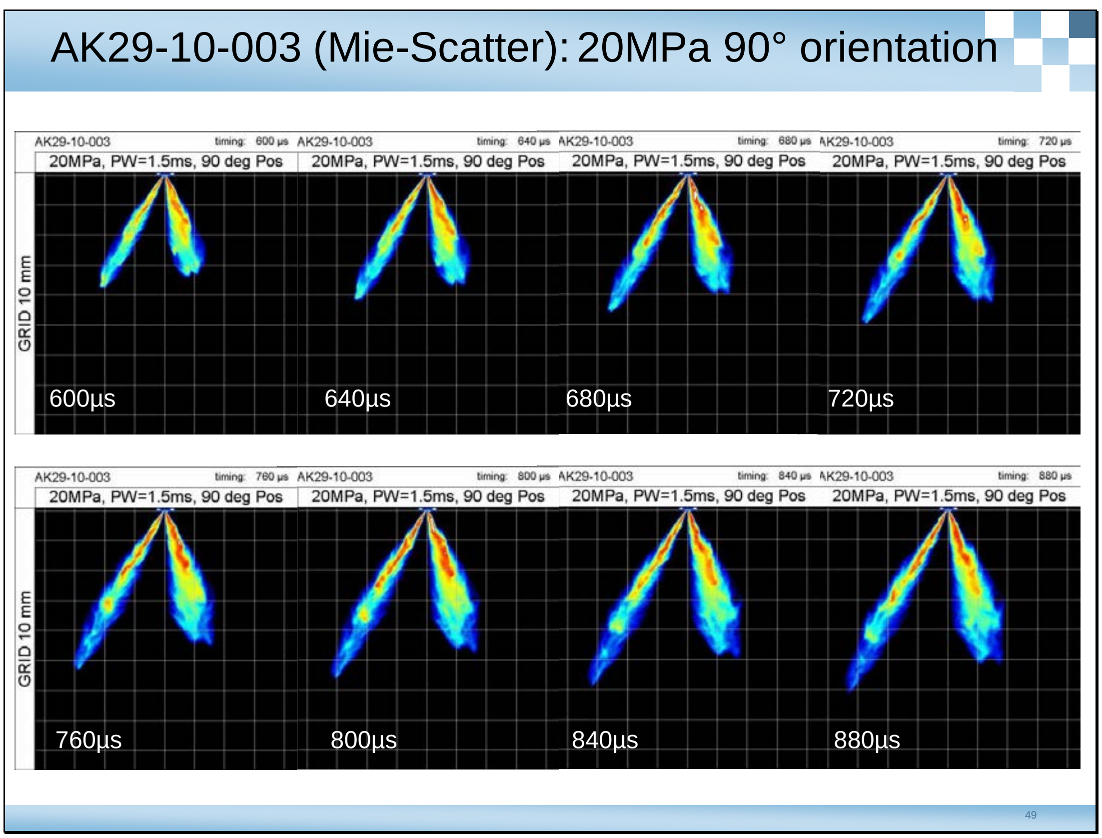
AK29-10-003 (Mie-Scatter): 20MPa 90° orientation
AK29-10-003
20MPa, PW=1.5ms, 90 deg Pos
GRID 10 mm
600µs
640µs
680µs
720µs
760µs
800µs
840µs
880µs
49

## AK29-10-003 (Mie-Scatter): 20MPa 90° orientation

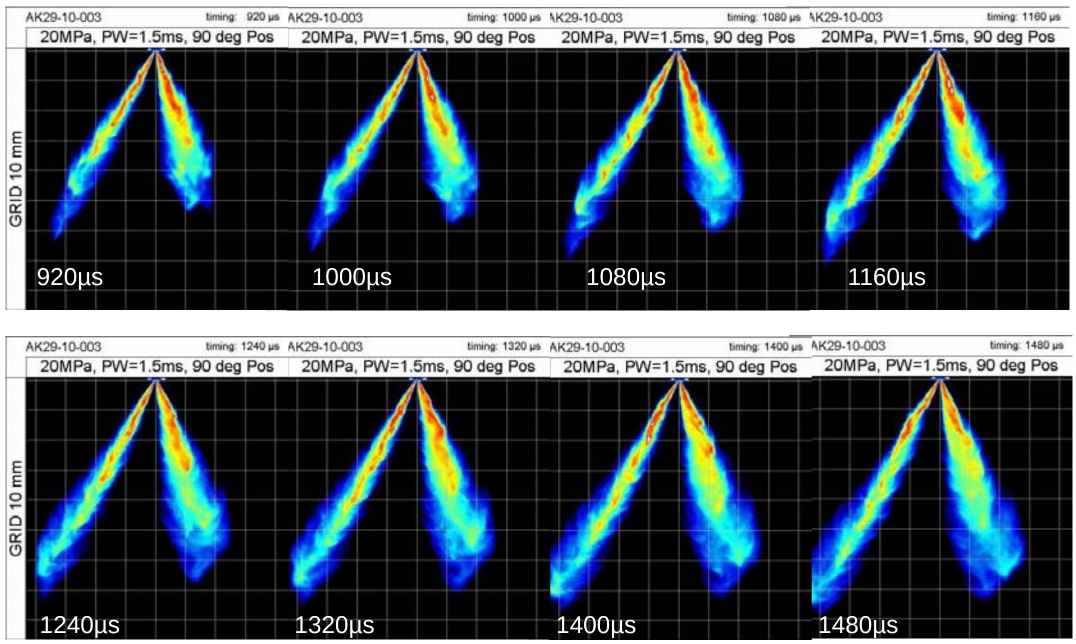




## AK29-11-3-002 (Mie-Scatter): 10MPa, 0°orientation

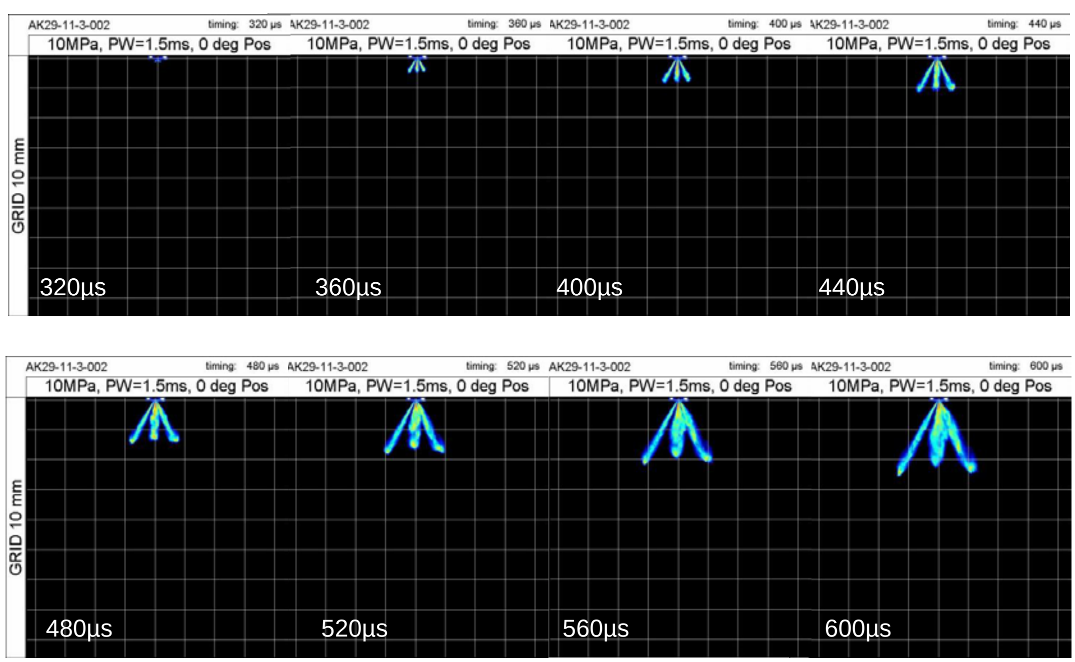

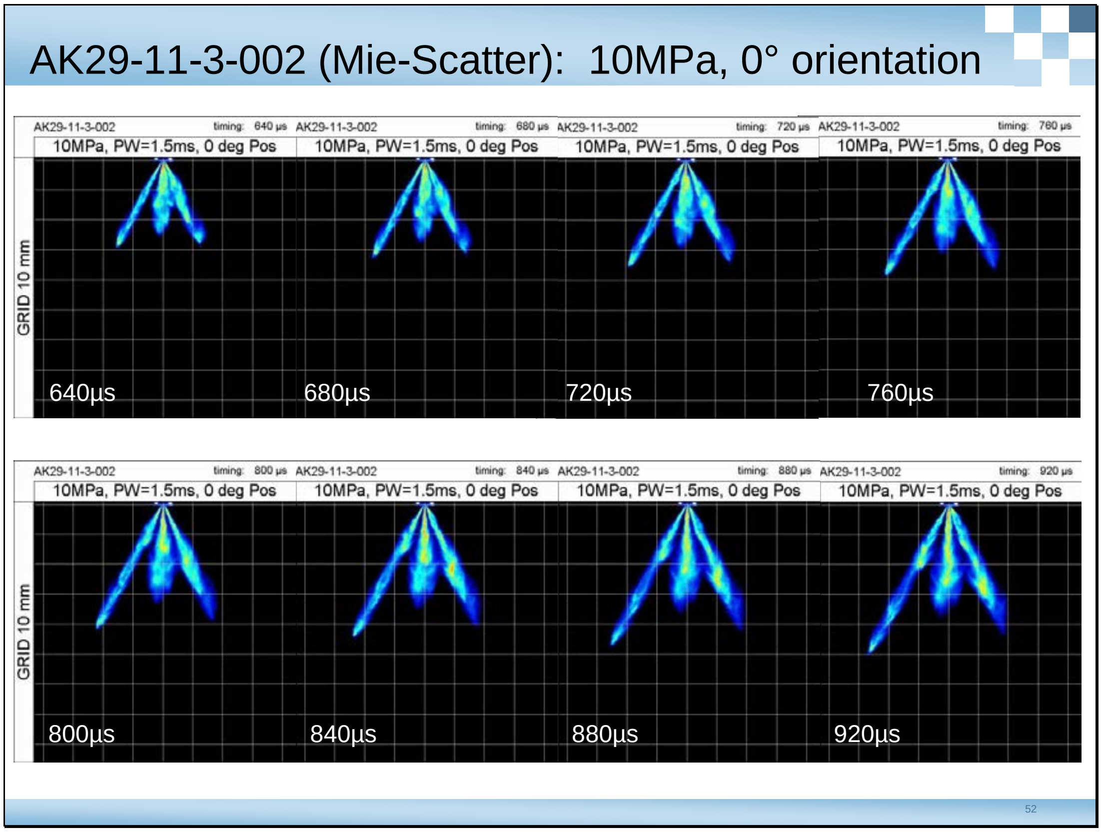
AK29-11-3-002 (Mie-Scatter): 10MPa, 0° orientation
AK29-11-3-002
10MPa, PW=1.5ms, 0 deg Pos
GRID 10 mm
640µs
680µs
720µs
760µs
800µs
840µs
880µs
920µs
52

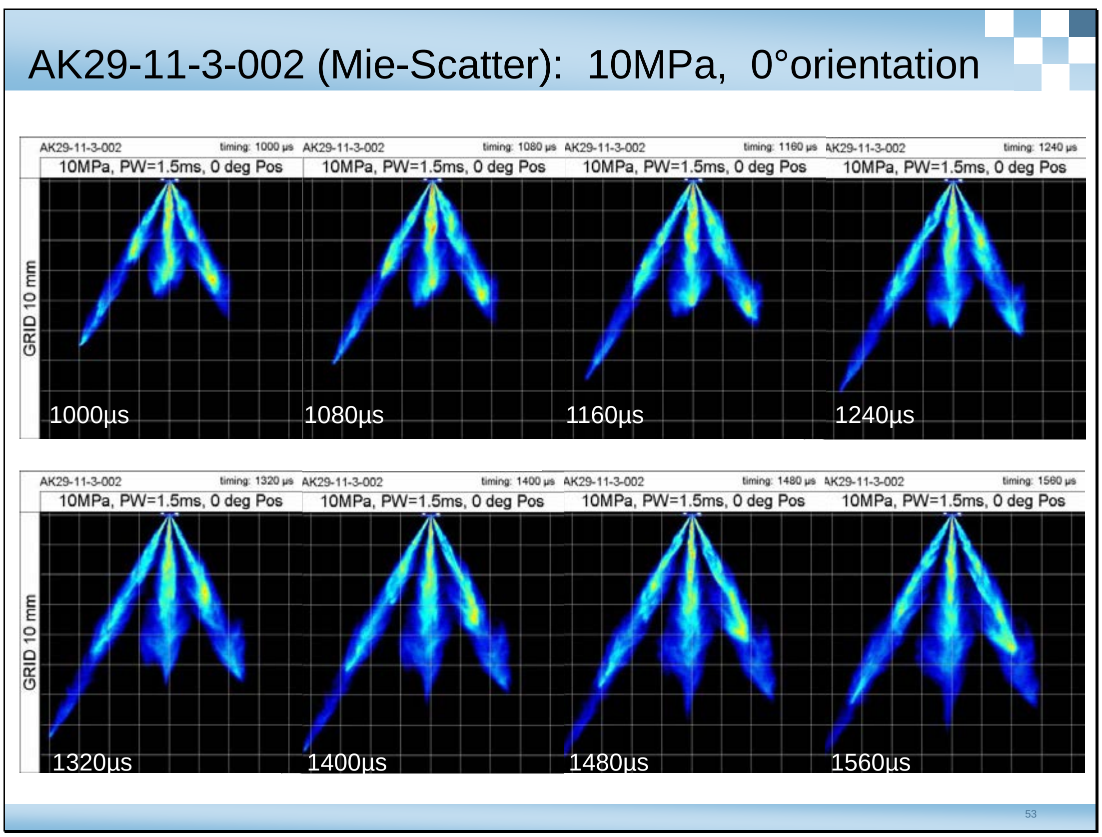
AK29-11-3-002 (Mie-Scatter): 10MPa, 0°orientation
AK29-11-3-002
10MPa, PW=1.5ms, 0 deg Pos
GRID 10 mm
1000µs
1080µs
1160µs
1240µs
1320µs
1400µs
1480µs
1560µs
53

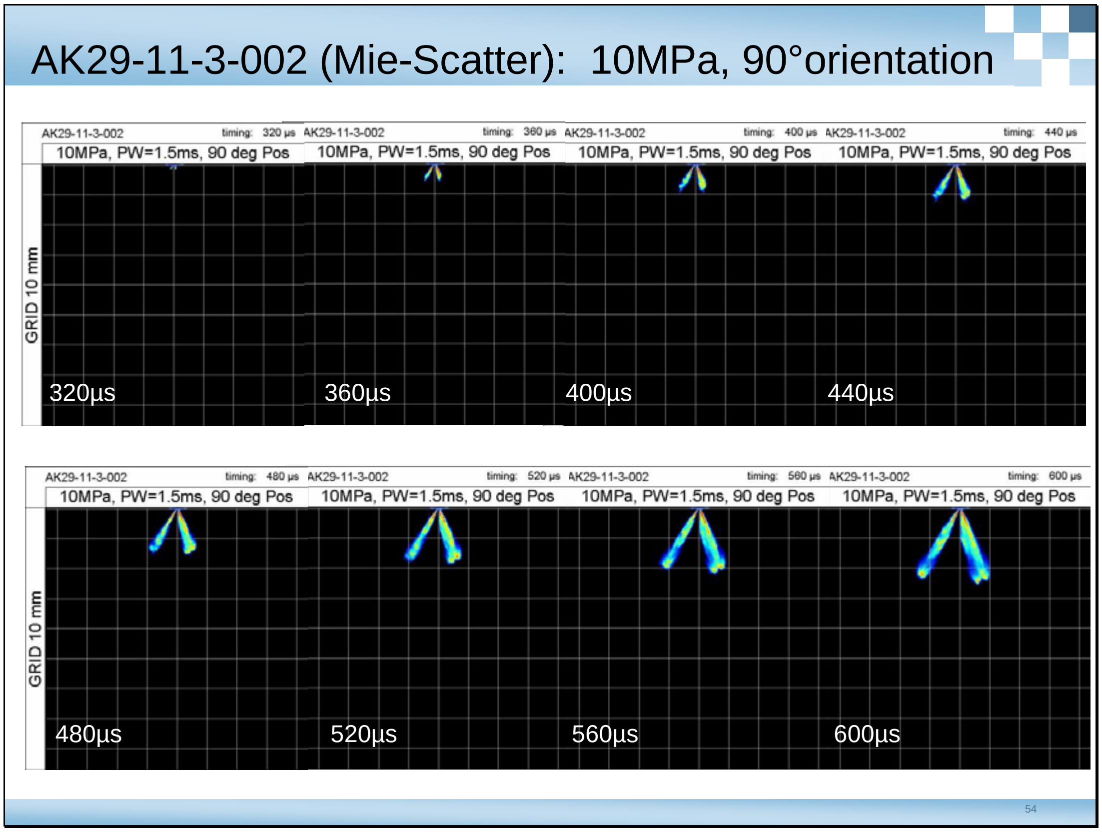
AK29-11-3-002 (Mie-Scatter): 10MPa, 90°orientation
10MPa, PW=1.5ms, 90 deg Pos
GRID 10 mm
320µs
360µs
400µs
440µs
480µs
520µs
560µs
600µs
54

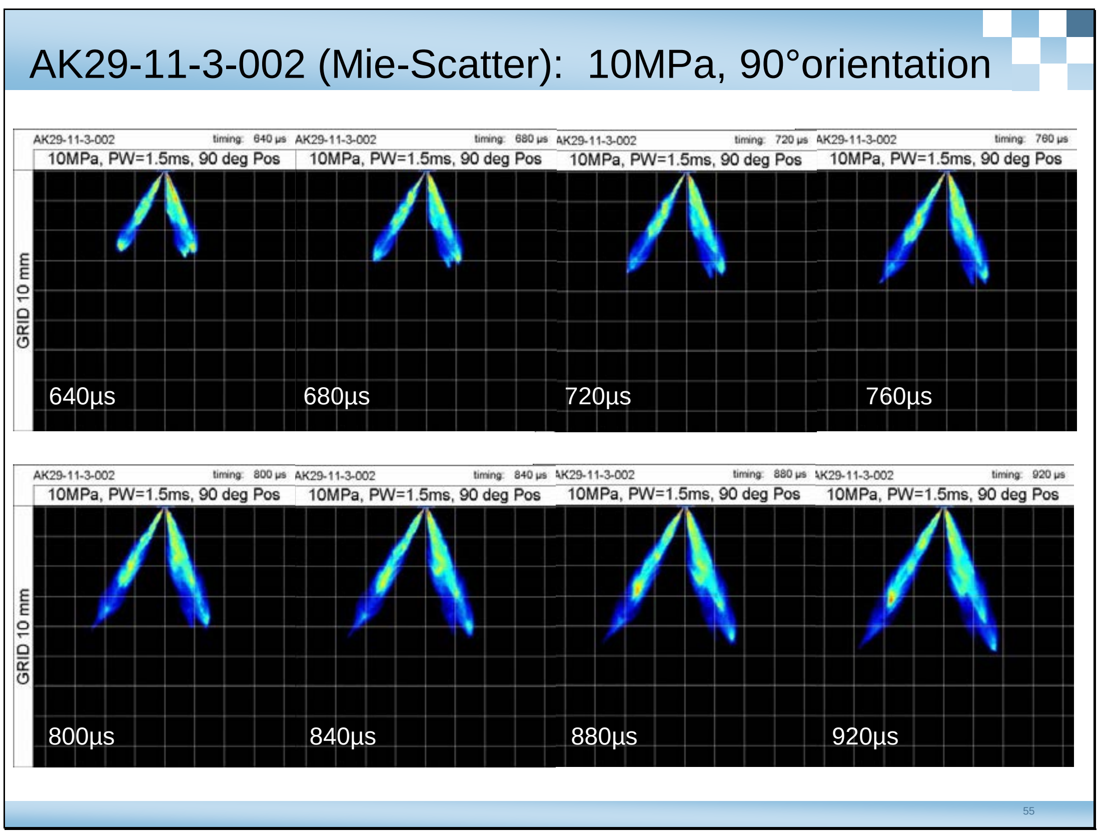
AK29-11-3-002 (Mie-Scatter): 10MPa, 90°orientation
10MPa, PW=1.5ms, 90 deg Pos
GRID 10 mm
640µs
680µs
720µs
760µs
800µs
840µs
880µs
920µs
55

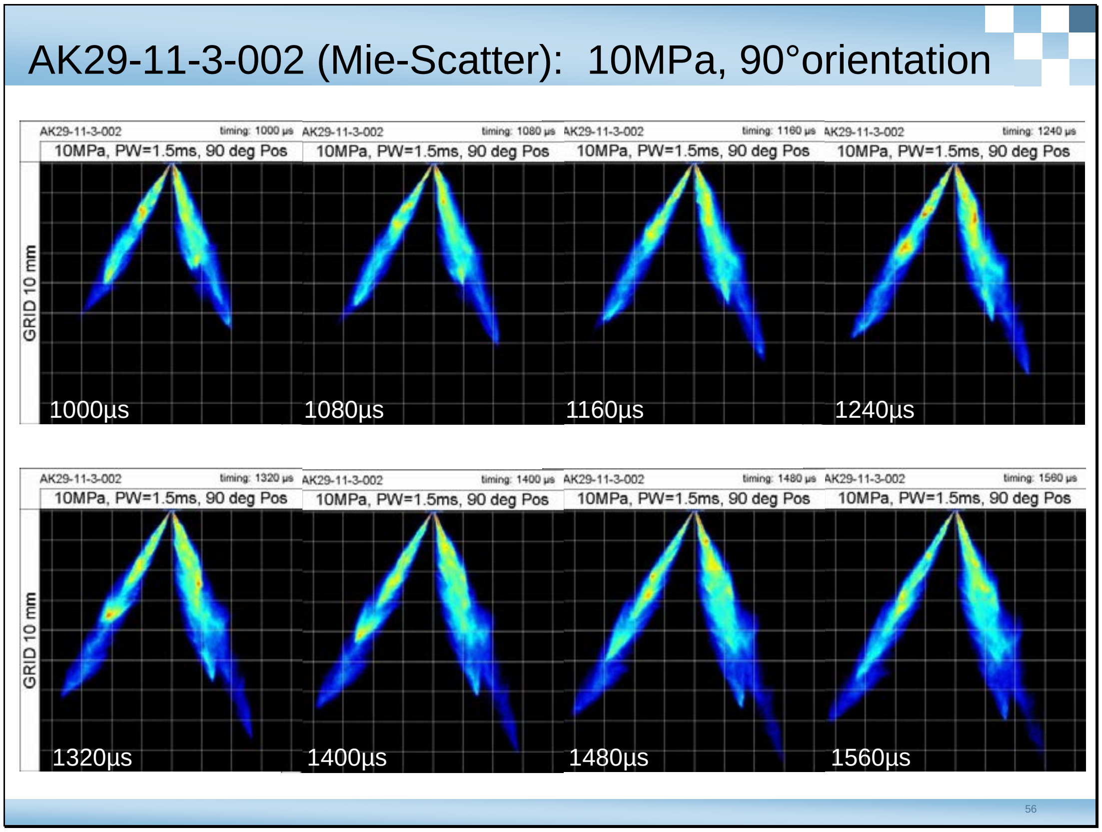
AK29-11-3-002 (Mie-Scatter): 10MPa, 90°orientation
10MPa, PW=1.5ms, 90 deg Pos
GRID 10 mm
1000µs
1080µs
1160µs
1240µs
1320µs
1400µs
1480µs
1560µs
56

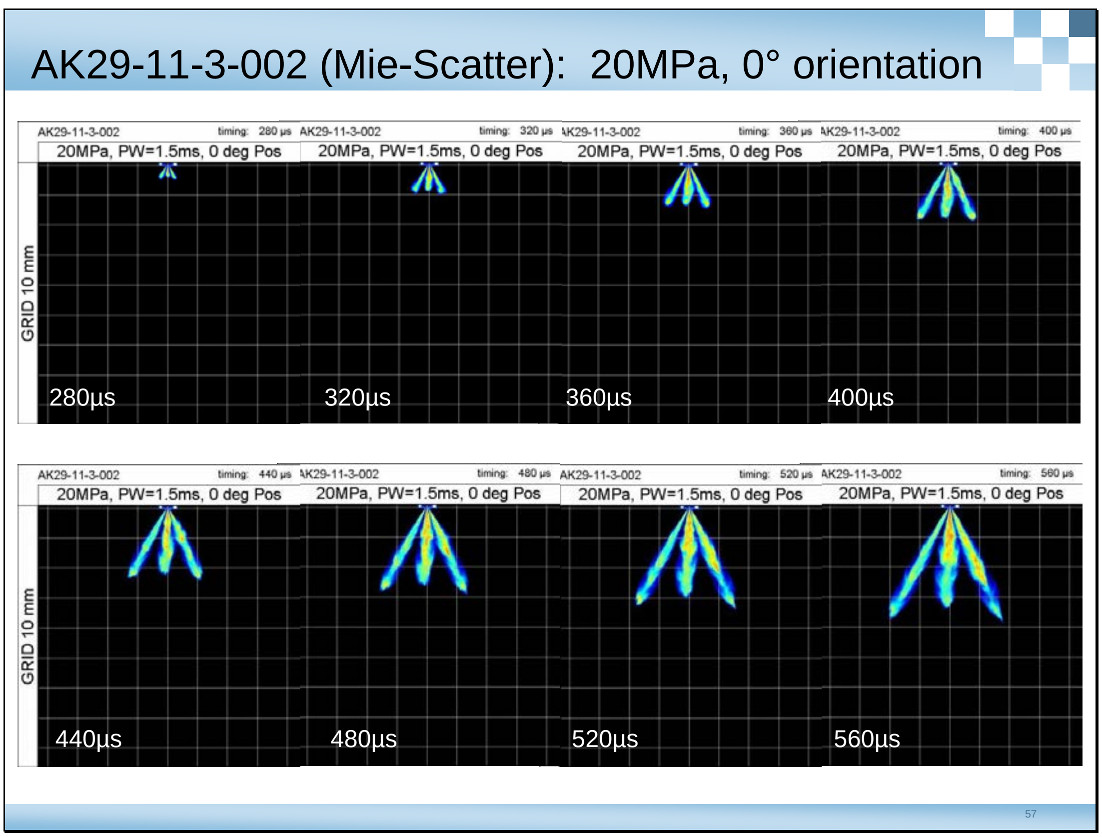
AK29-11-3-002 (Mie-Scatter): 20MPa, 0° orientation
20MPa, PW=1.5ms, 0 deg Pos
GRID 10 mm
280µs
320µs
360µs
400µs
440µs
480µs
520µs
560µs
57

## AK29-11-3-002 (Mie-Scatter): 20MPa, 0° orientation

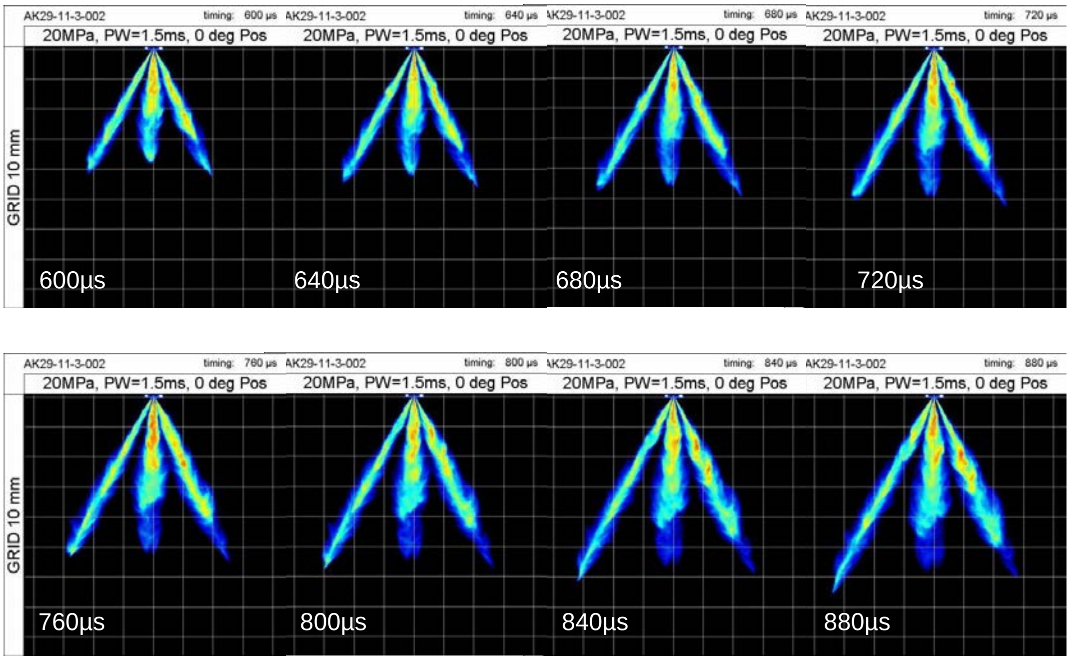


58

## AK29-11-3-002 (Mie-Scatter): 20MPa, 0°orientation

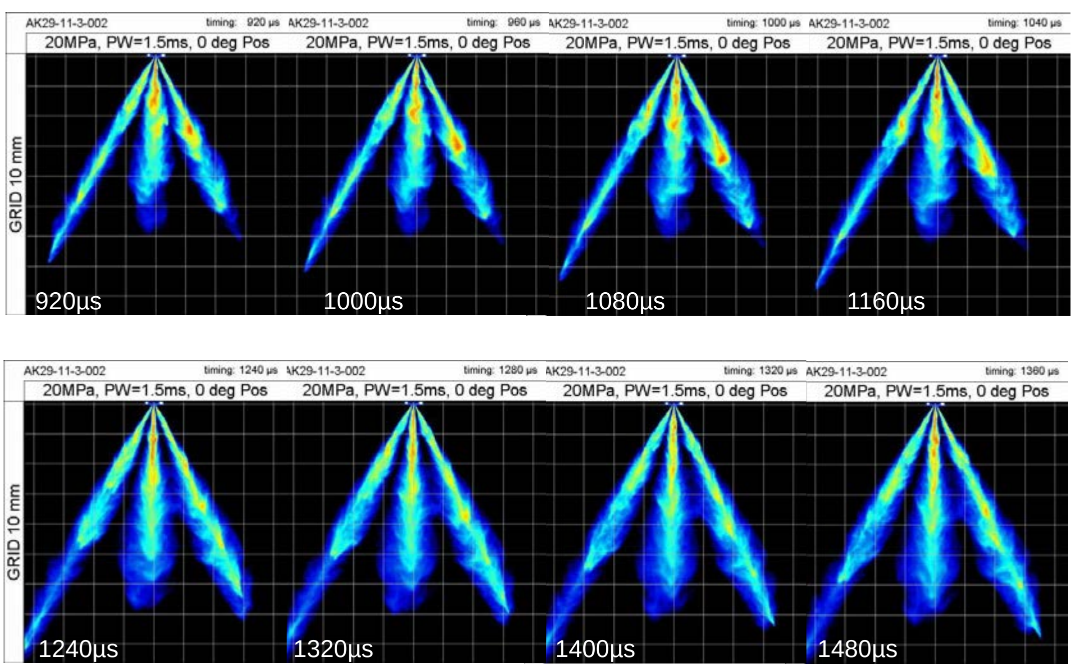


59

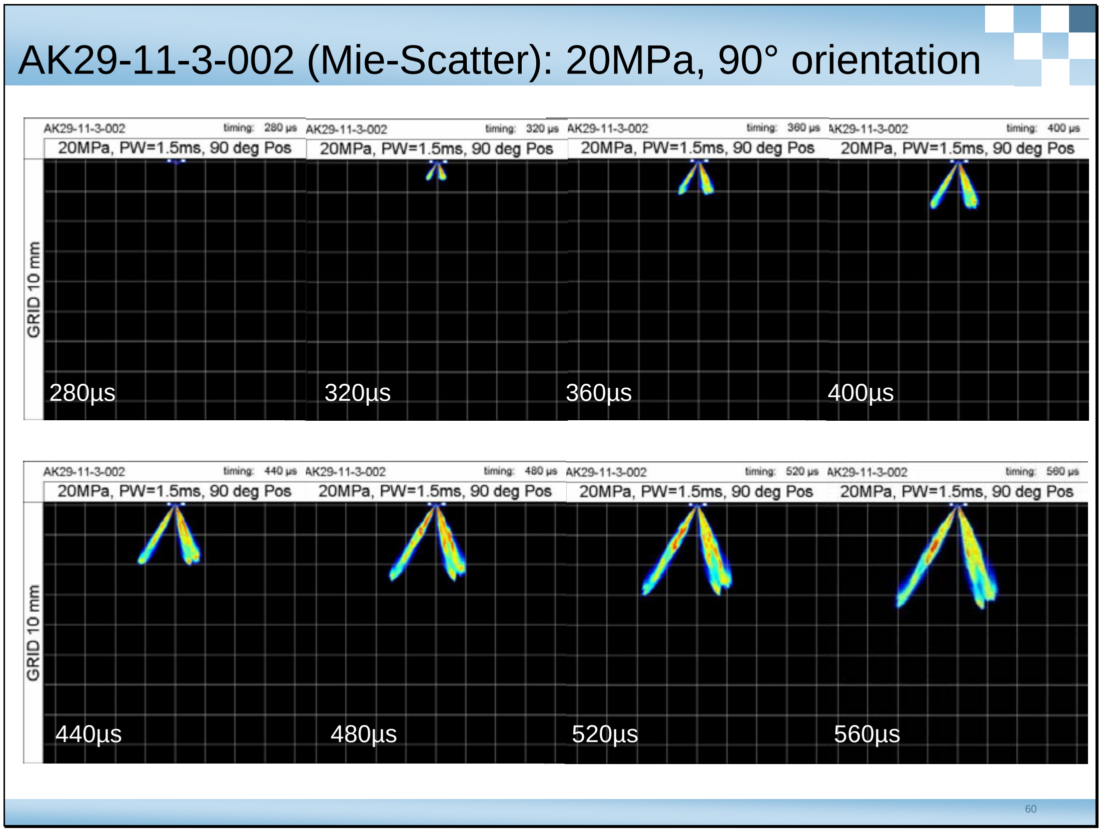
AK29-11-3-002 (Mie-Scatter): 20MPa, 90° orientation
AK29-11-3-002 timing: 280 µs
20MPa, PW=1.5ms, 90 deg Pos
AK29-11-3-002 timing: 320 µs
20MPa, PW=1.5ms, 90 deg Pos
AK29-11-3-002 timing: 360 µs
20MPa, PW=1.5ms, 90 deg Pos
AK29-11-3-002 timing: 400 µs
20MPa, PW=1.5ms, 90 deg Pos
GRID 10 mm
280µs
320µs
360µs
400µs
AK29-11-3-002 timing: 440 µs
20MPa, PW=1.5ms, 90 deg Pos
AK29-11-3-002 timing: 480 µs
20MPa, PW=1.5ms, 90 deg Pos
AK29-11-3-002 timing: 520 µs
20MPa, PW=1.5ms, 90 deg Pos
AK29-11-3-002 timing: 560 µs
20MPa, PW=1.5ms, 90 deg Pos
GRID 10 mm
440µs
480µs
520µs
560µs
60

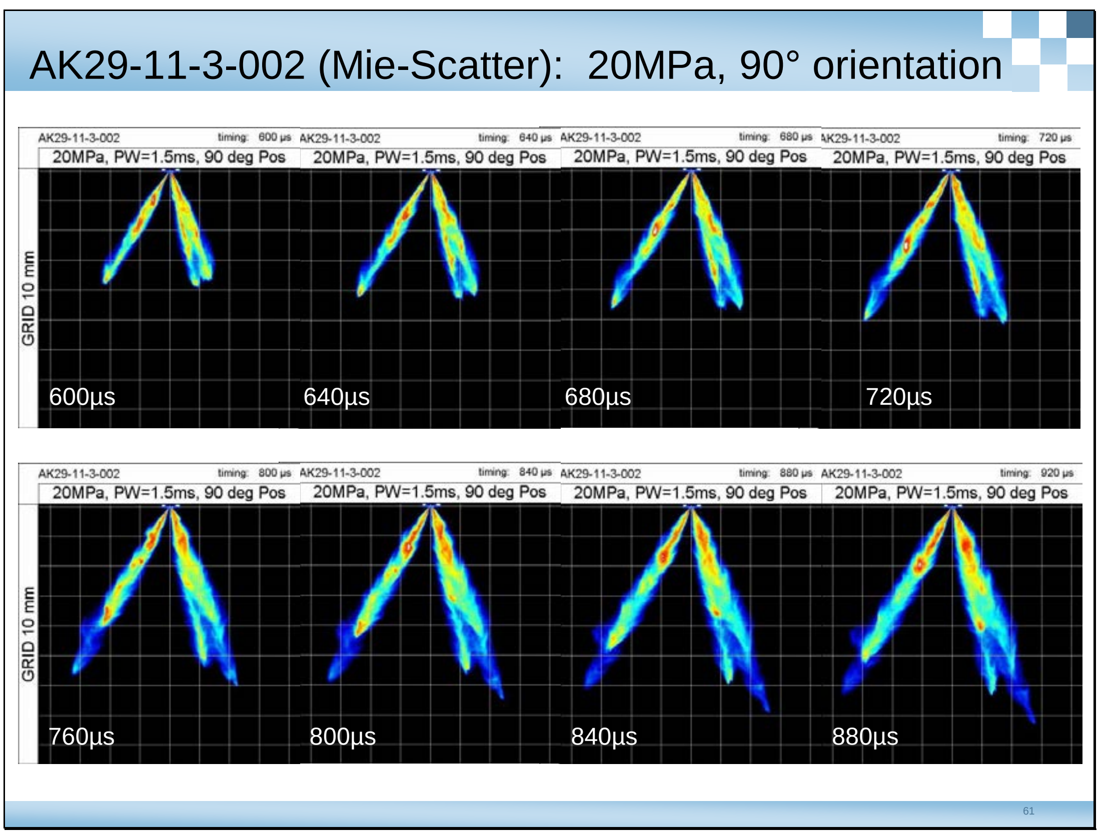
AK29-11-3-002 (Mie-Scatter): 20MPa, 90° orientation
AK29-11-3-002 timing: 600 µs
20MPa, PW=1.5ms, 90 deg Pos
AK29-11-3-002 timing: 640 µs
20MPa, PW=1.5ms, 90 deg Pos
AK29-11-3-002 timing: 680 µs
20MPa, PW=1.5ms, 90 deg Pos
AK29-11-3-002 timing: 720 µs
20MPa, PW=1.5ms, 90 deg Pos
GRID 10 mm
600µs
640µs
680µs
720µs
AK29-11-3-002 timing: 800 µs
20MPa, PW=1.5ms, 90 deg Pos
AK29-11-3-002 timing: 840 µs
20MPa, PW=1.5ms, 90 deg Pos
AK29-11-3-002 timing: 880 µs
20MPa, PW=1.5ms, 90 deg Pos
AK29-11-3-002 timing: 920 µs
20MPa, PW=1.5ms, 90 deg Pos
GRID 10 mm
760µs
800µs
840µs
880µs
61

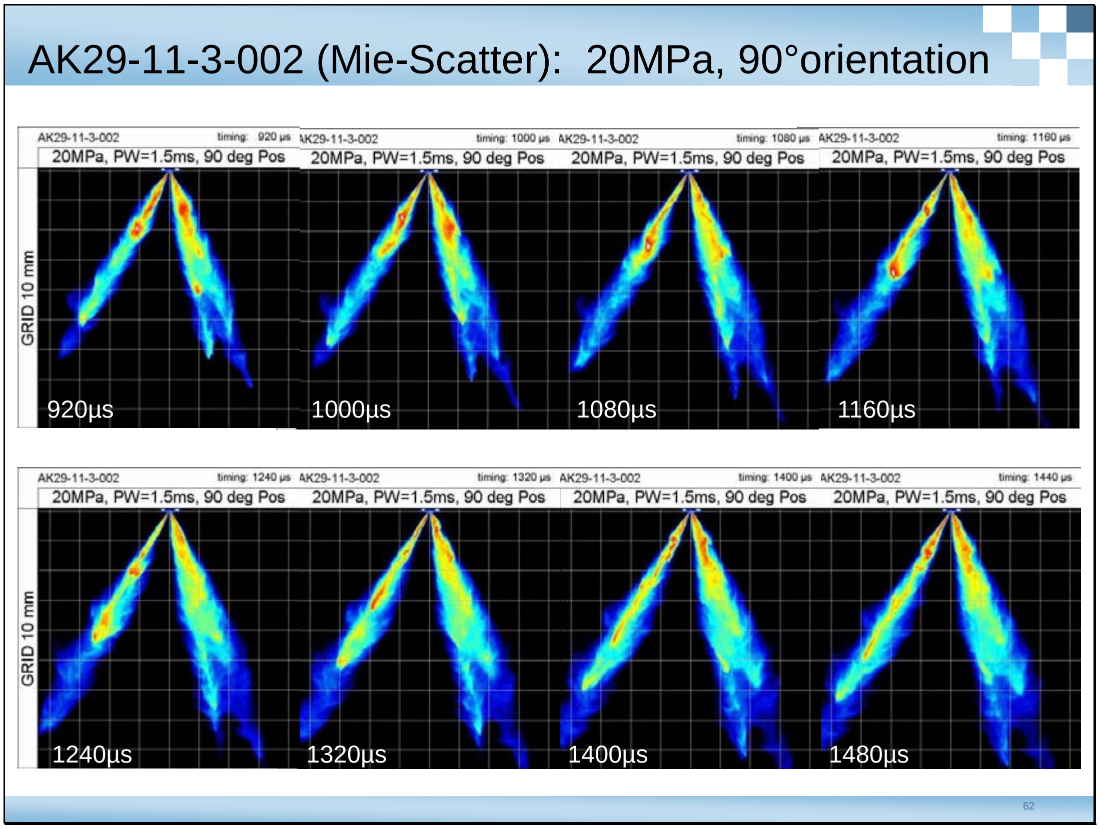
AK29-11-3-002 (Mie-Scatter): 20MPa, 90°orientation
20MPa, PW=1.5ms, 90 deg Pos
GRID 10 mm
920µs
1000µs
1080µs
1160µs
1240µs
1320µs
1400µs
1480µs
62

# APPENDIX G MIE SCATTER IMAGES, SIDE VIEW

High speed Mie Imaging (144 images) of Spray plumes from bottom view, Luxembourg Spray lab

| Image # | Seat # | d (mm) | β | l/d | (l+L) /d | D/d | Inj. Pres. | Mie Scatter Time Images (μs) |
|---|---|---|---|---|---|---|---|---|
| 1-8 | AK29-9-001 | ≈.20 | 30° | 1.1 | na | na | 10MPa | 320,360,400,440,470,520,560,600 |
| 9-16 | AK29-9-001 | ≈.20 | 30° | 1.1 | na | na | 10MPa | 640,680,720,760,800,840,880,920 |
| 17-24 | AK29-9-001 | ≈.20 | 30° | 1.1 | na | na | 10MPa | 1000,1080,1160,1240,1320,1400, 1480, 1560 |
| 1-8 | AK29-9-001 | ≈.20 | 30° | 1.1 | na | na | 20MPa | 320,360,400,440,470,520,560,600 |
| 9-16 | AK29-9-001 | ≈.20 | 30° | 1.1 | na | na | 20MPa | 640,680,720,760,800,840,880,920 |
| 17-24 | AK29-9-001 | ≈.20 | 30° | 1.1 | na | na | 20MPa | 1000,1080,1160,1240,1320,1400, 1480, 1560 |
| 1-8 | AK29-10-3-003 | ≈.15 | 30° | 1.1 | 3.96 | 2.5 | 10MPa | 320,340,400,440,480,520,560,600 |
| 9-16 | AK29-10-3-003 | ≈.15 | 30° | 1.1 | 3.96 | 2.5 | 10MPa | 640,680,720,760,800,840,880,920 |
| 17-24 | AK29-10-3-003 | ≈.15 | 30° | 1.1 | 3.96 | 2.5 | 10MPa | 1000,1080,1160,1240,1320,1400, 1480, 1560 |
| 1-8 | AK29-10-3-003 | ≈.15 | 30° | 1.1 | 3.96 | 2.5 | 20MPa | 320,340,400,440,480,520,560,600 |
| 9-16 | AK29-10-3-003 | ≈.15 | 30° | 1.1 | 3.96 | 2.5 | 20MPa | 640,680,720,760,800,840,880,920 |
| 17-24 | AK29-10-3-003 | ≈.15 | 30° | 1.1 | 3.96 | 2.5 | 20MPa | 1000,1080,1160,1240,1320,1400, 1480, 1560 |
| 1-8 | AK29-11-3-002 | ≈.15 | 30° | 3.96 | na | na | 10MPa | 320,340,400,440,480,520,560,600 |
| 9-16 | AK29-11-3-002 | ≈.15 | 30° | 3.96 | na | na | 10MPa | 640,680,720,760,800,840,880,920 |
| 17-24 | AK29-11-3-002 | ≈.15 | 30° | 3.96 | na | na | 10MPa | 1000,1080,1160,1240,1320,1400, 1480, 1560 |
| 1-8 | AK29-11-3-002 | ≈.15 | 30° | 3.96 | na | na | 20MPa | 320,340,400,440,480,520,560,600 |
| 9-16 | AK29-11-3-002 | ≈.15 | 30° | 3.96 | na | na | 20MPa | 640,680,720,760,800,840,880,920 |
| 17-24 | AK29-11-3-002 | ≈.15 | 30° | 3.96 | na | na | 20MPa | 1000,1080,1160,1240,1320,1400, 1480, 1560 |

## AK29-9-001 (Mie-Scatter Plume): 10MPa

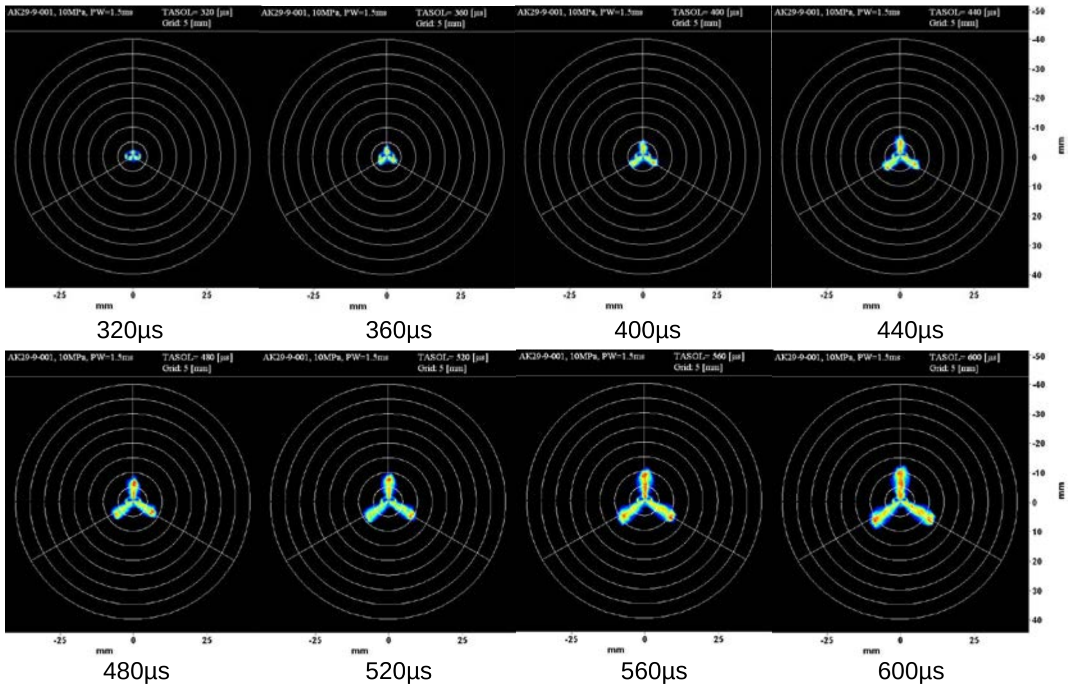




## AK29-9-001 (Mie-Scatter Plume): 10MPa

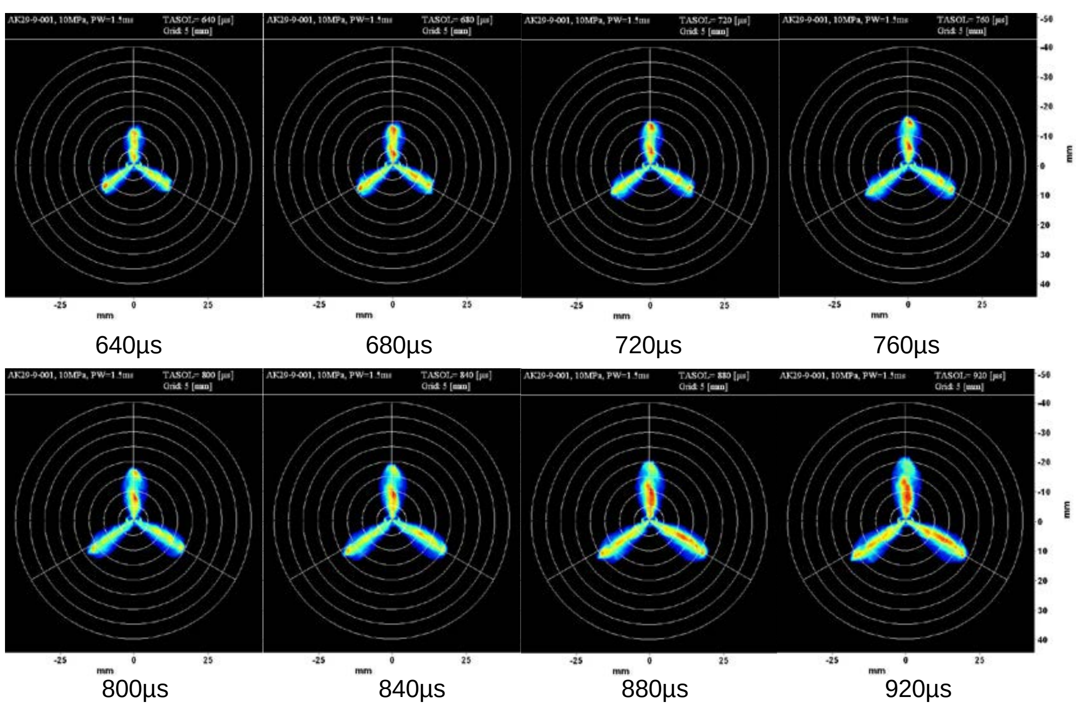

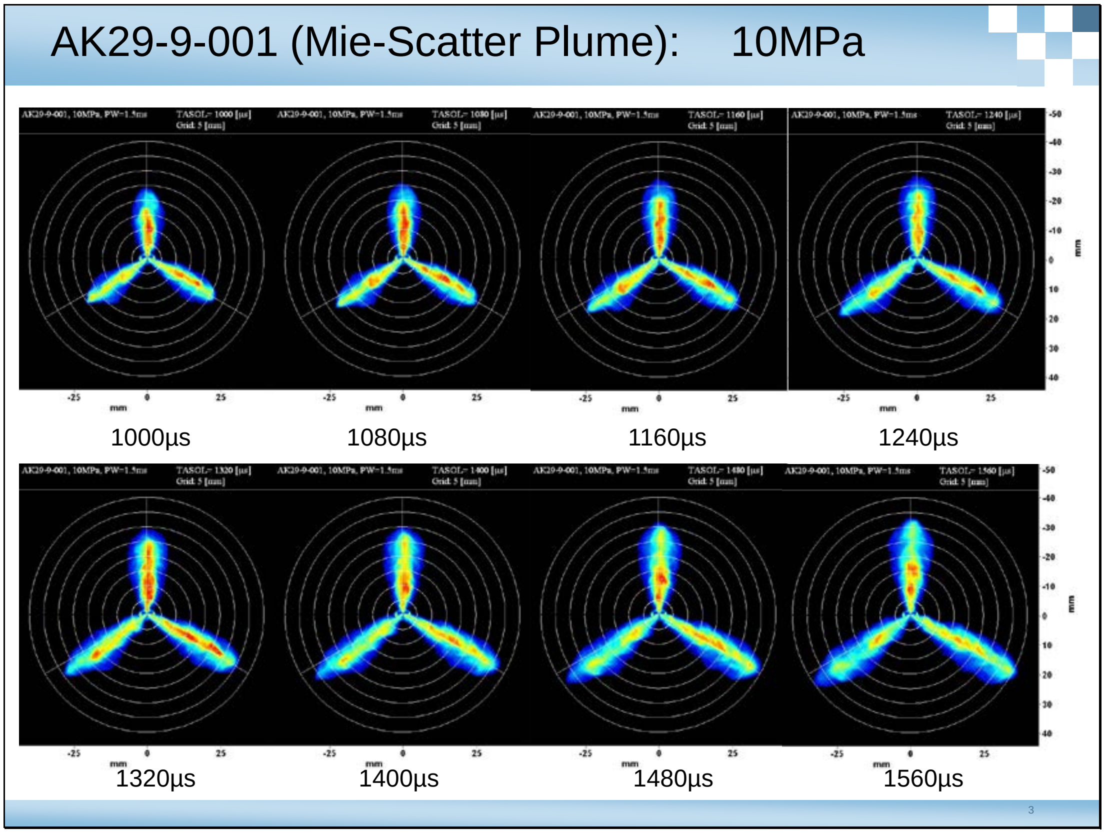
AK29-9-001 (Mie-Scatter Plume): 10MPa
1000µs
1080µs
1160µs
1240µs
1320µs
1400µs
1480µs
1560µs

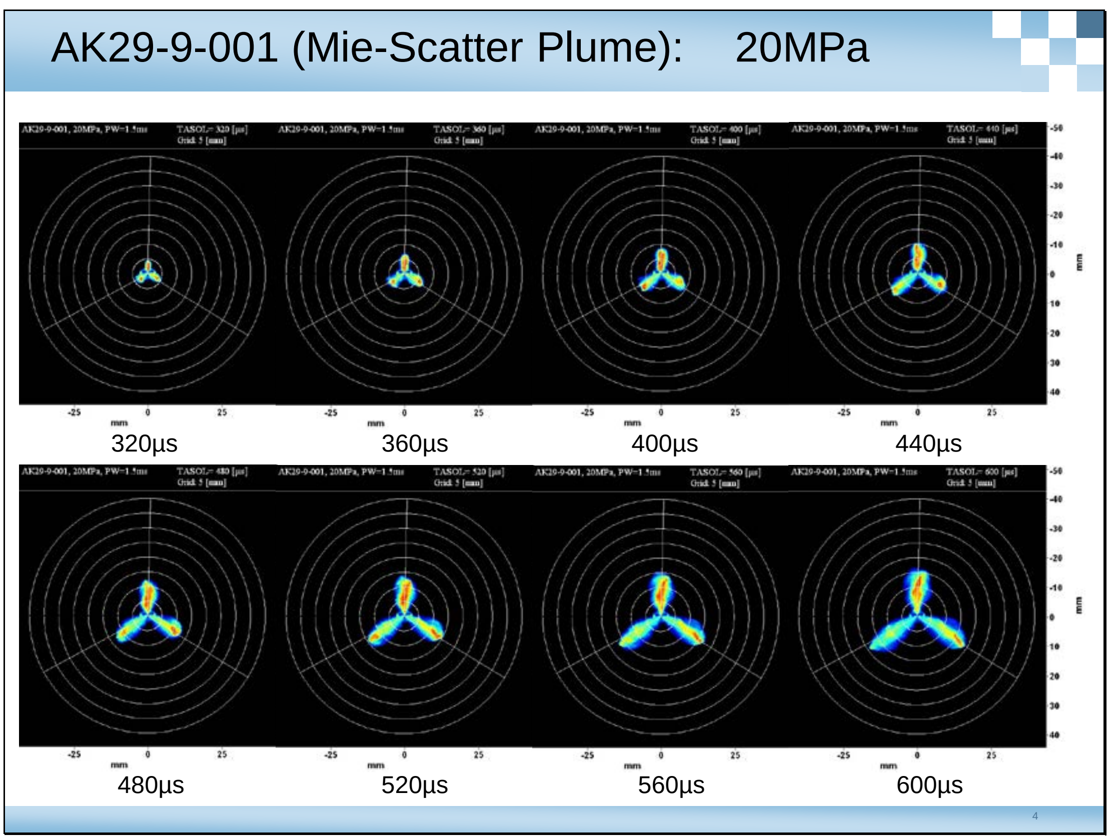
AK29-9-001 (Mie-Scatter Plume): 20MPa
320µs
360µs
400µs
440µs
480µs
520µs
560µs
600µs

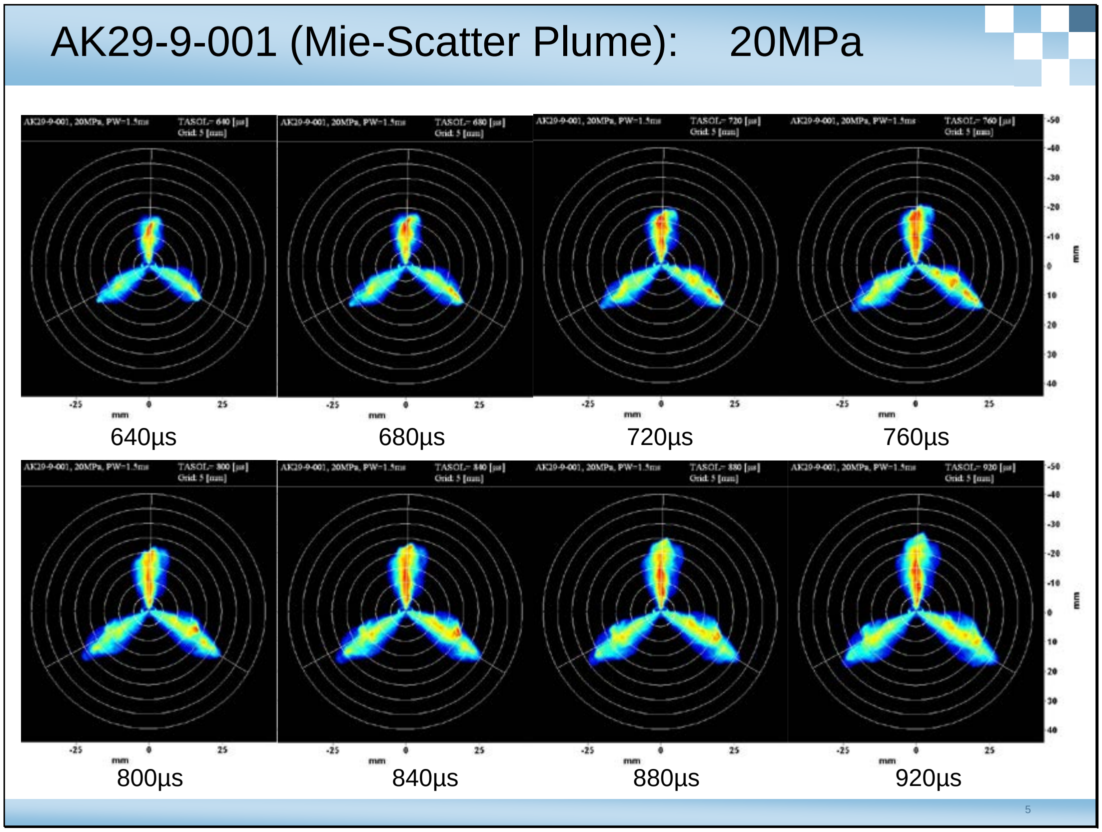
AK29-9-001 (Mie-Scatter Plume): 20MPa
640µs
680µs
720µs
760µs
800µs
840µs
880µs
920µs
5

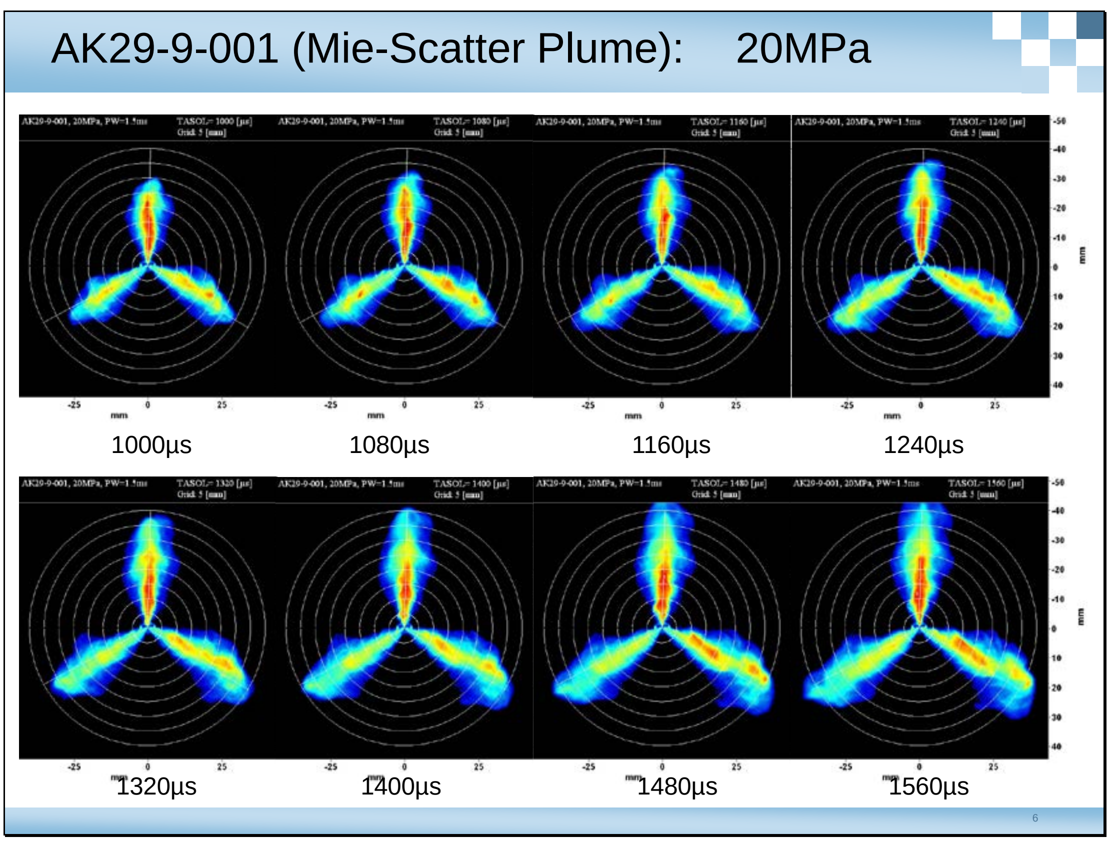
AK29-9-001 (Mie-Scatter Plume): 20MPa
1000µs
1080µs
1160µs
1240µs
1320µs
1400µs
1480µs
1560µs
6

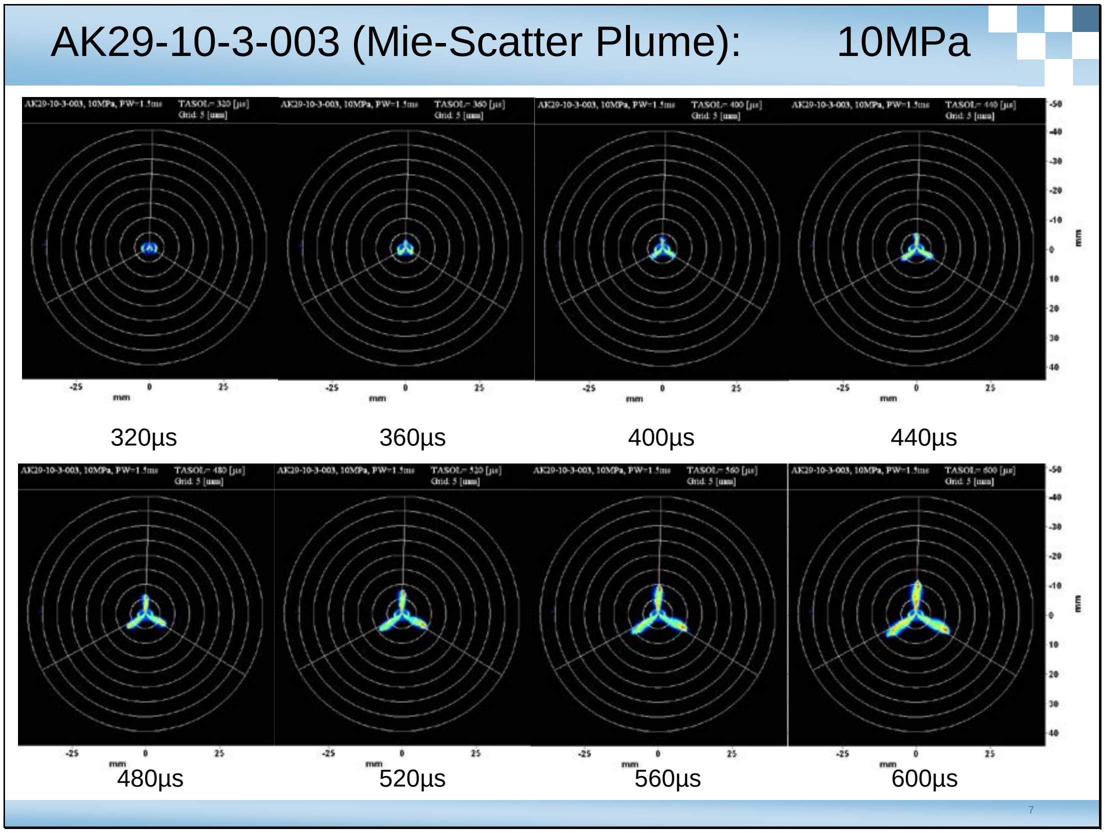
AK29-10-3-003 (Mie-Scatter Plume): 10MPa
320µs
360µs
400µs
440µs
480µs
520µs
560µs
600µs

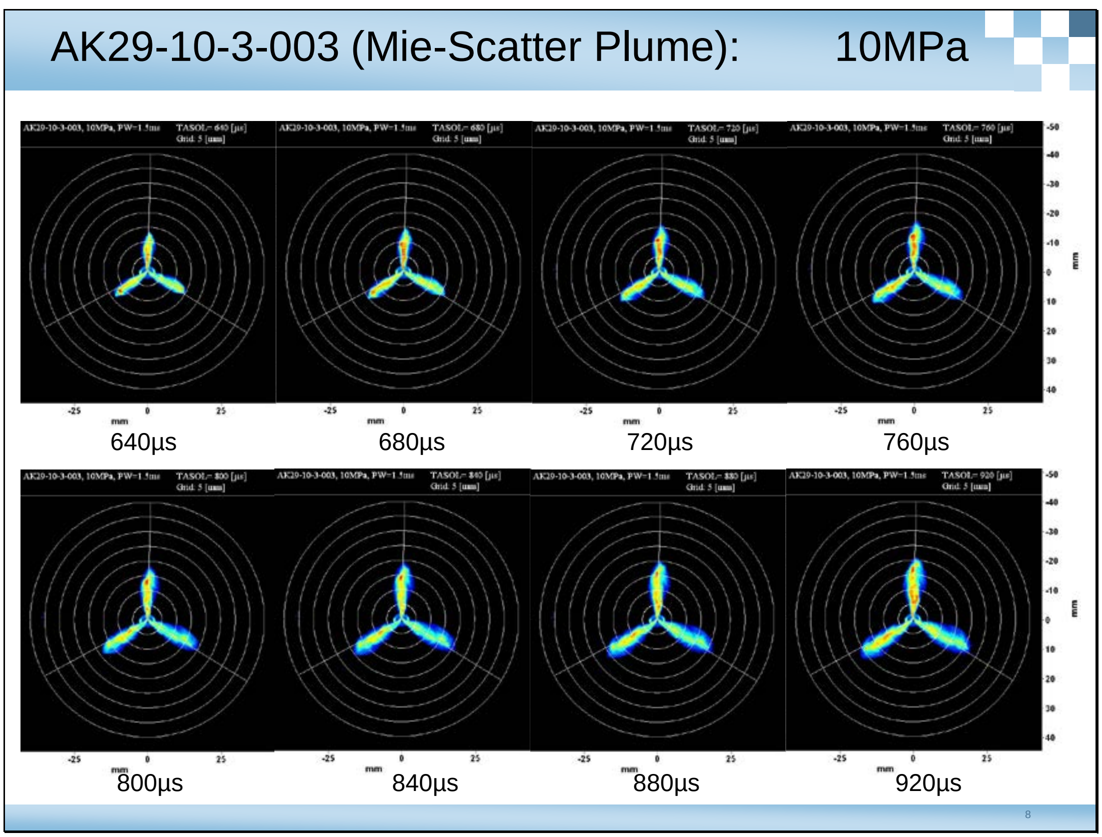
AK29-10-3-003 (Mie-Scatter Plume): 10MPa
640µs
680µs
720µs
760µs
800µs
840µs
880µs
920µs

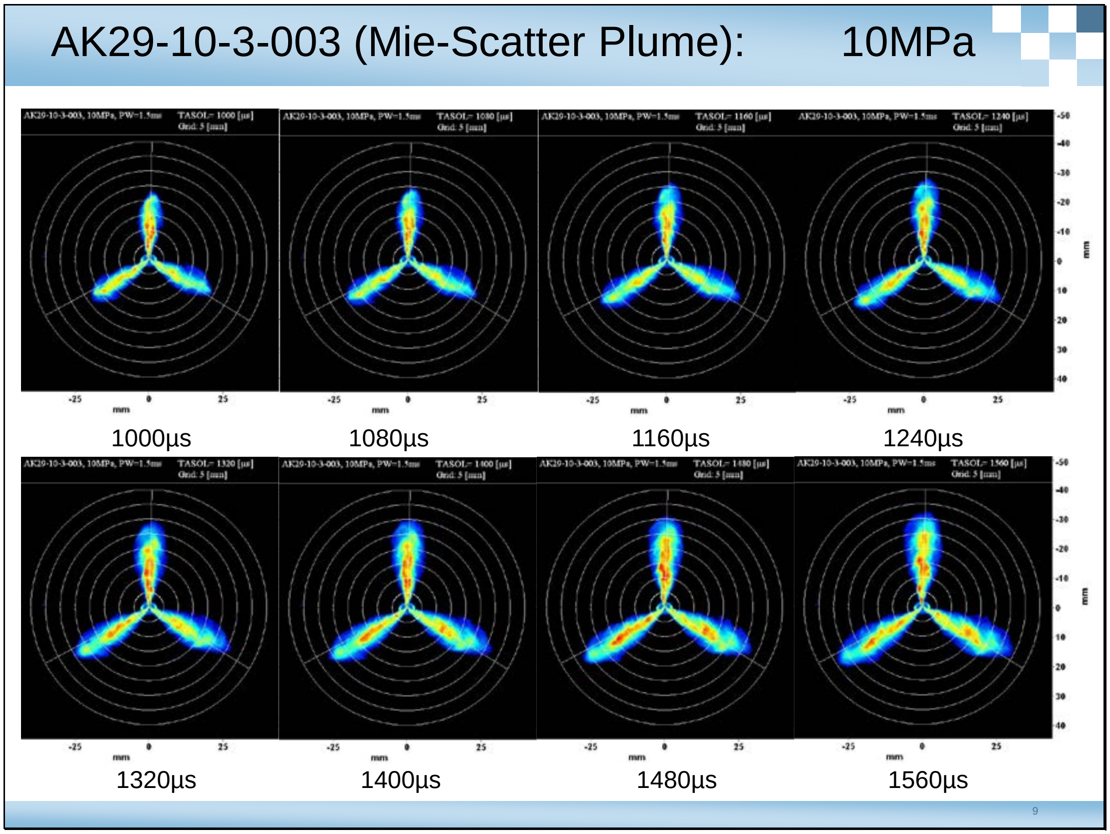
AK29-10-3-003 (Mie-Scatter Plume): 10MPa
1000µs
1080µs
1160µs
1240µs
1320µs
1400µs
1480µs
1560µs
mm
9

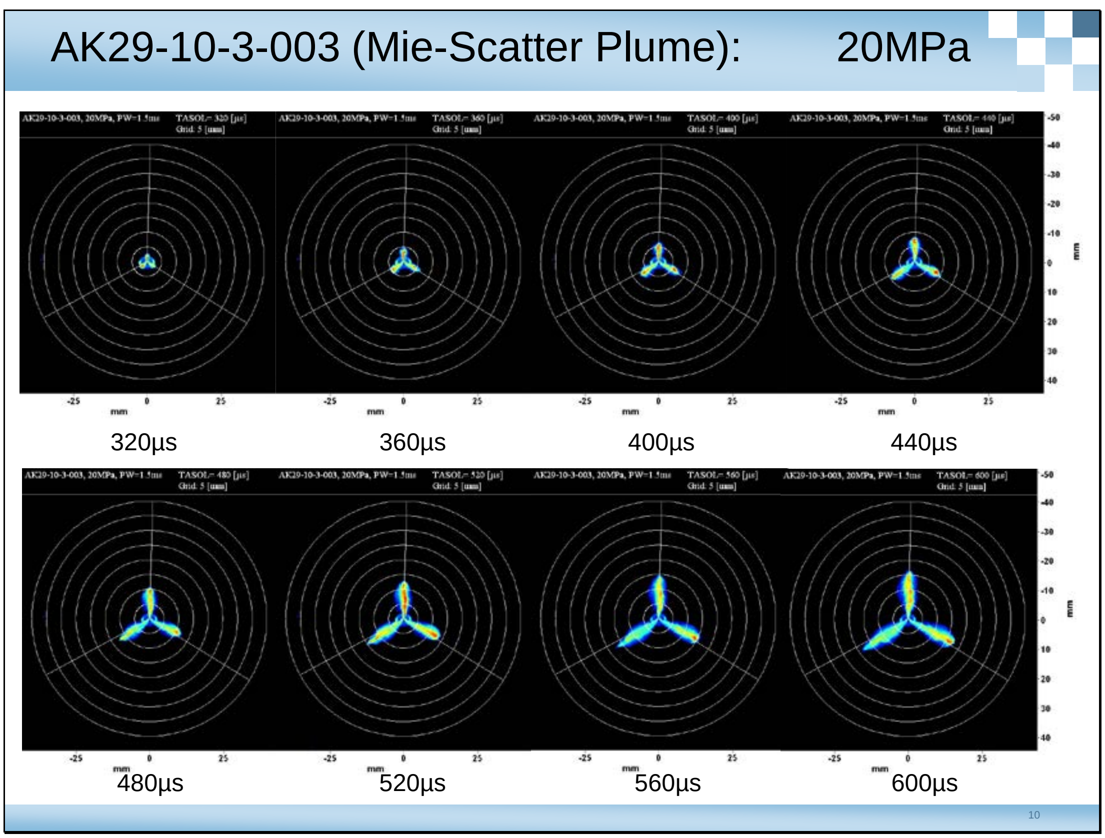
AK29-10-3-003 (Mie-Scatter Plume): 20MPa
320µs
360µs
400µs
440µs
480µs
520µs
560µs
600µs
mm
10

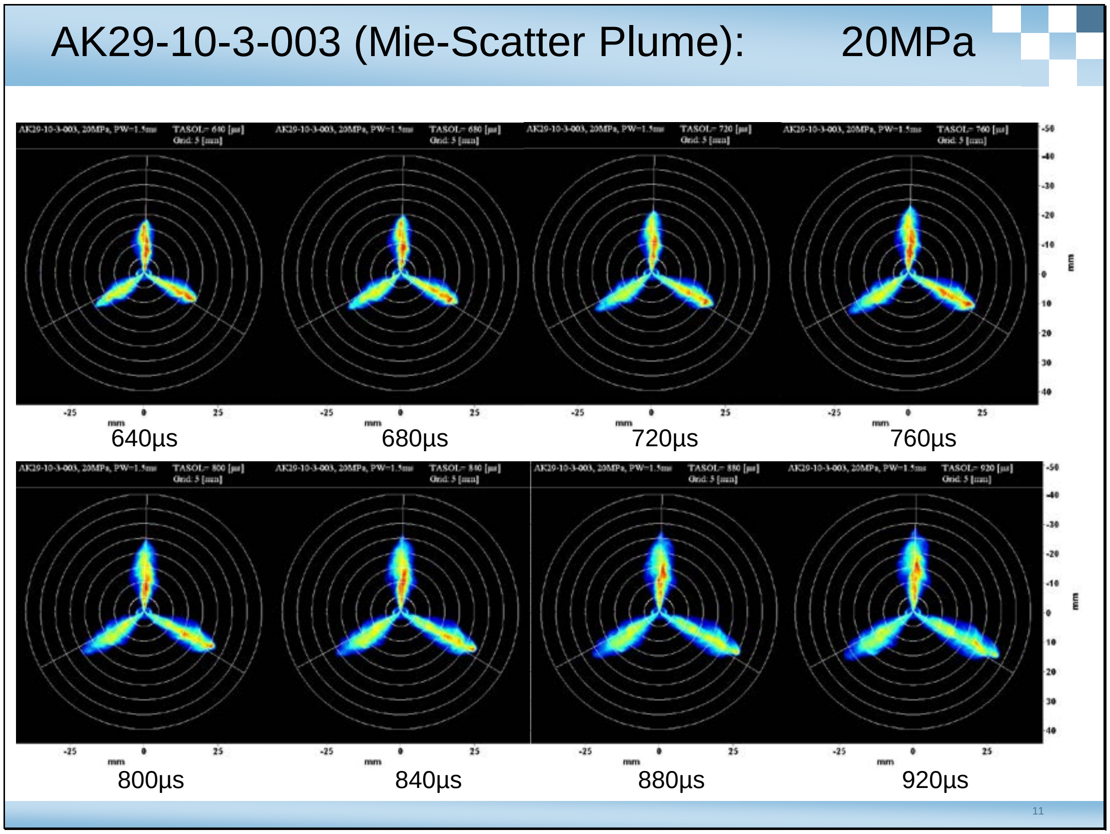
AK29-10-3-003 (Mie-Scatter Plume): 20MPa
640µs
680µs
720µs
760µs
800µs
840µs
880µs
920µs
11

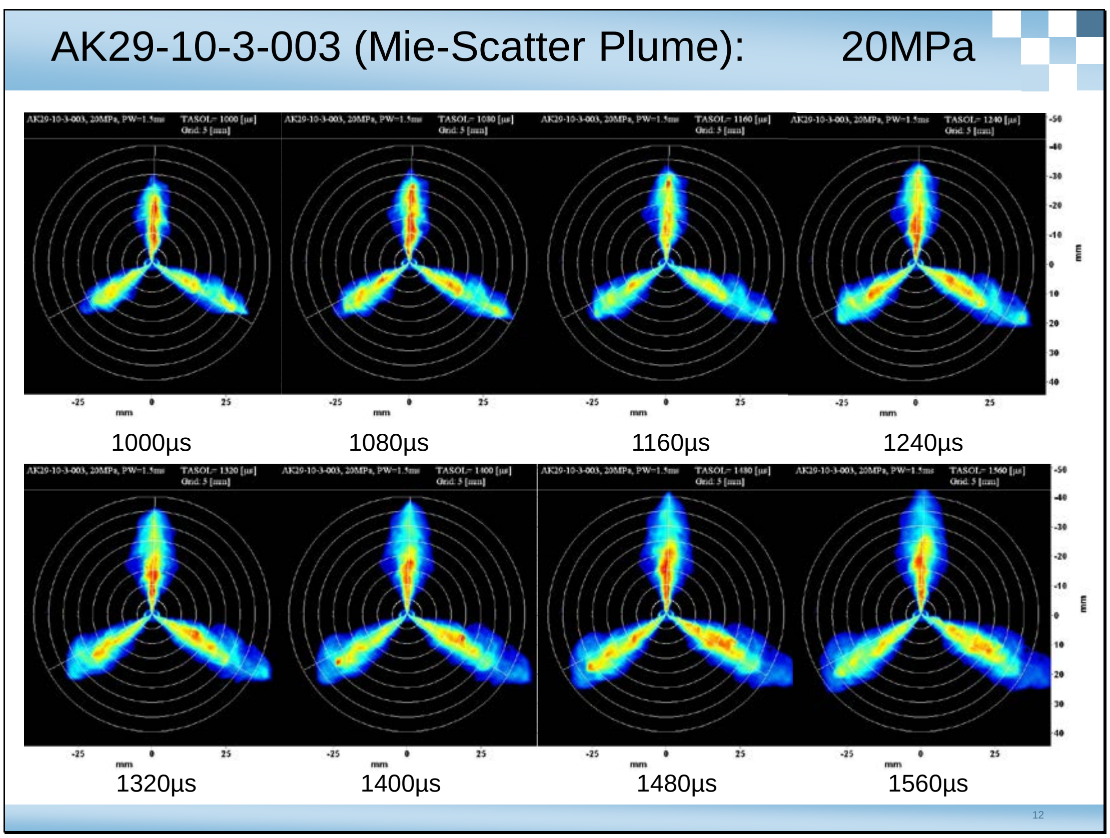
AK29-10-3-003 (Mie-Scatter Plume): 20MPa
1000µs
1080µs
1160µs
1240µs
1320µs
1400µs
1480µs
1560µs
12

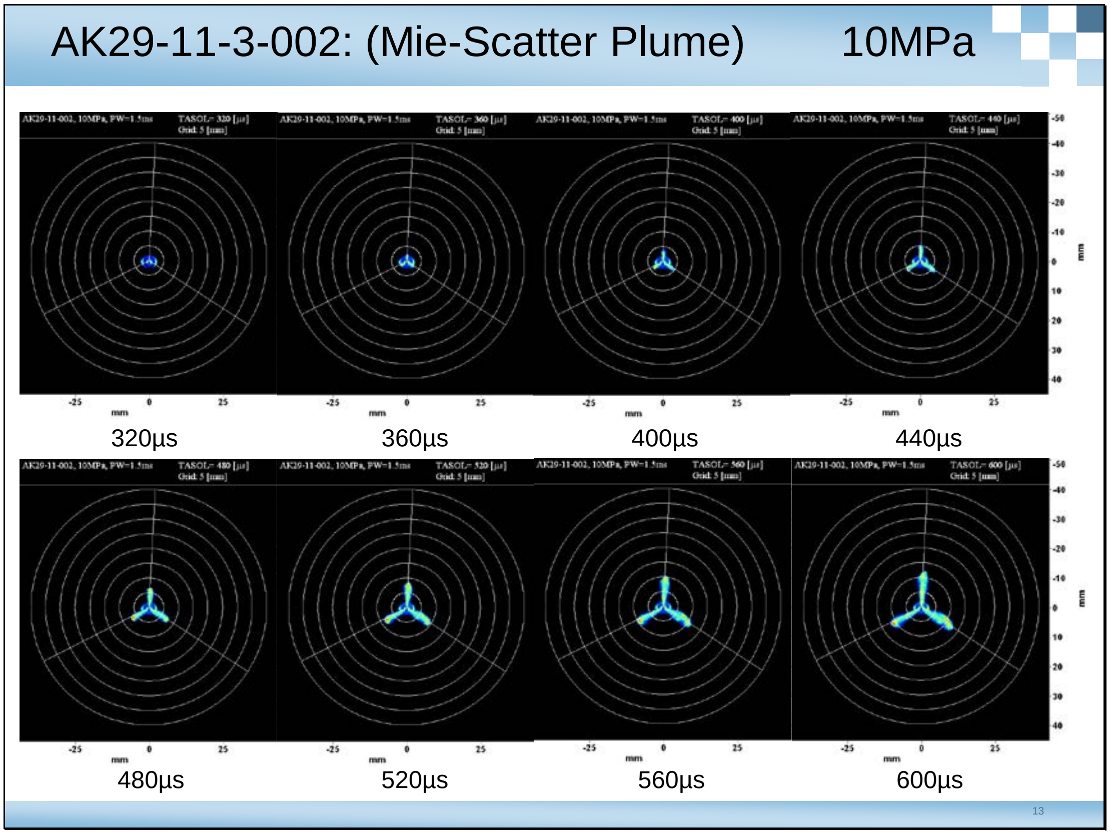
AK29-11-3-002: (Mie-Scatter Plume)
10MPa
320µs
360µs
400µs
440µs
480µs
520µs
560µs
600µs
13

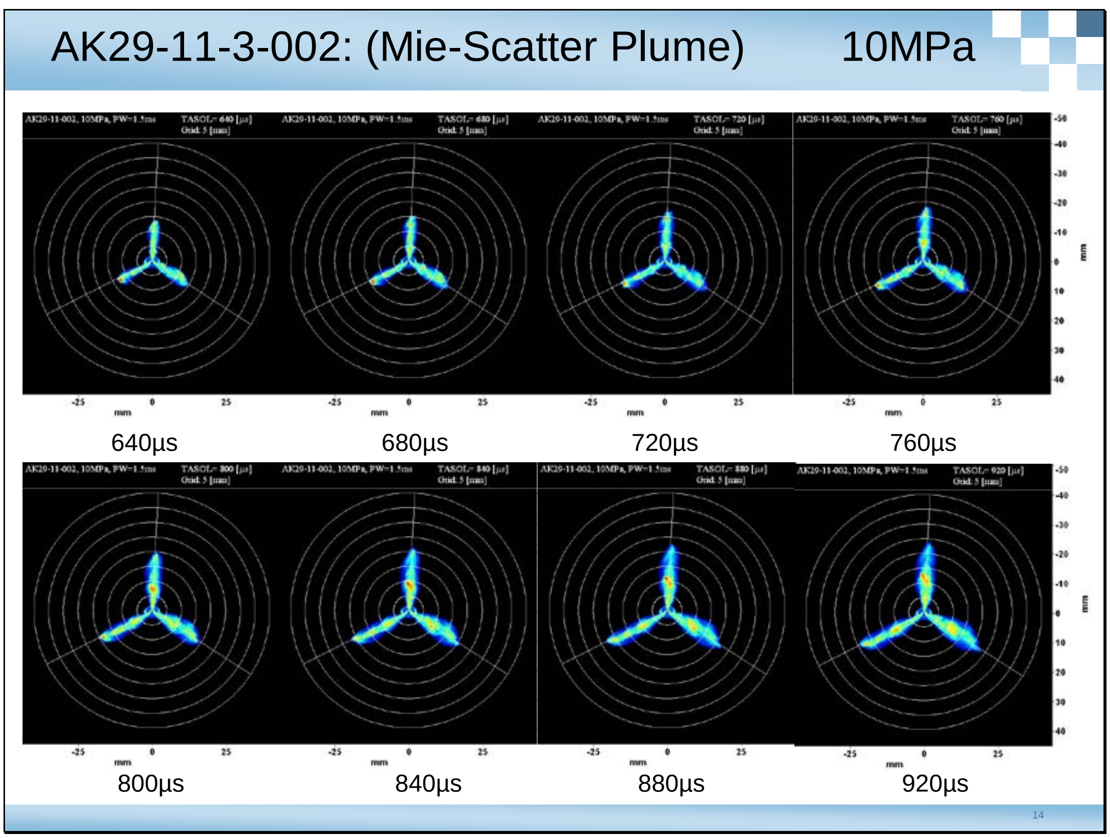
AK29-11-3-002: (Mie-Scatter Plume)
10MPa
640µs
680µs
720µs
760µs
800µs
840µs
880µs
920µs
14

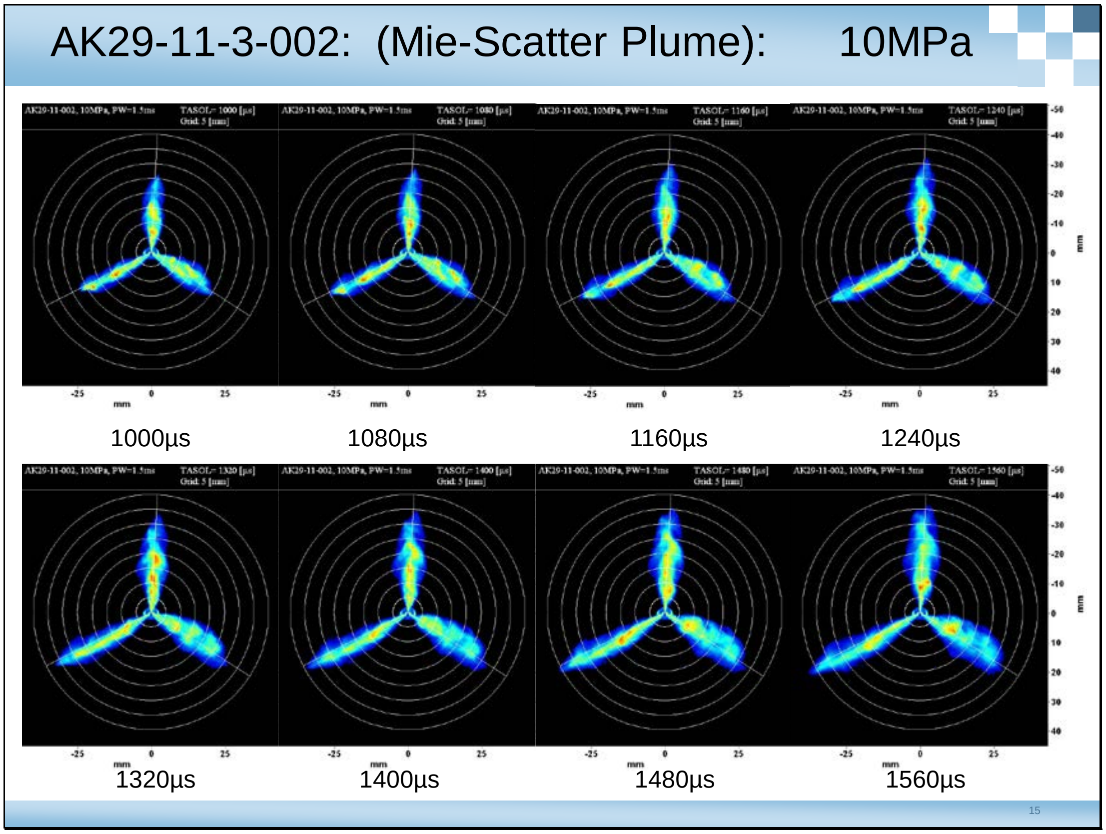
AK29-11-3-002: (Mie-Scatter Plume): 10MPa
1000µs
1080µs
1160µs
1240µs
1320µs
1400µs
1480µs
1560µs
15

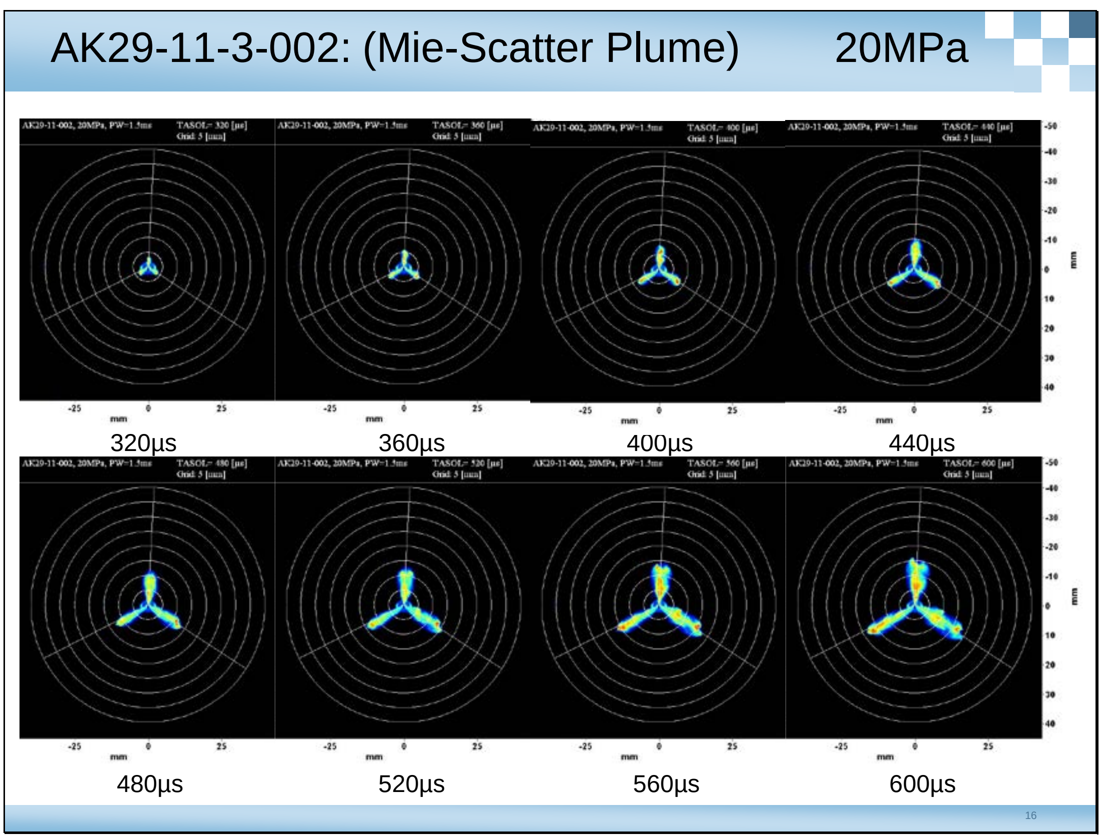
AK29-11-3-002: (Mie-Scatter Plume) 20MPa
320µs
360µs
400µs
440µs
480µs
520µs
560µs
600µs
16

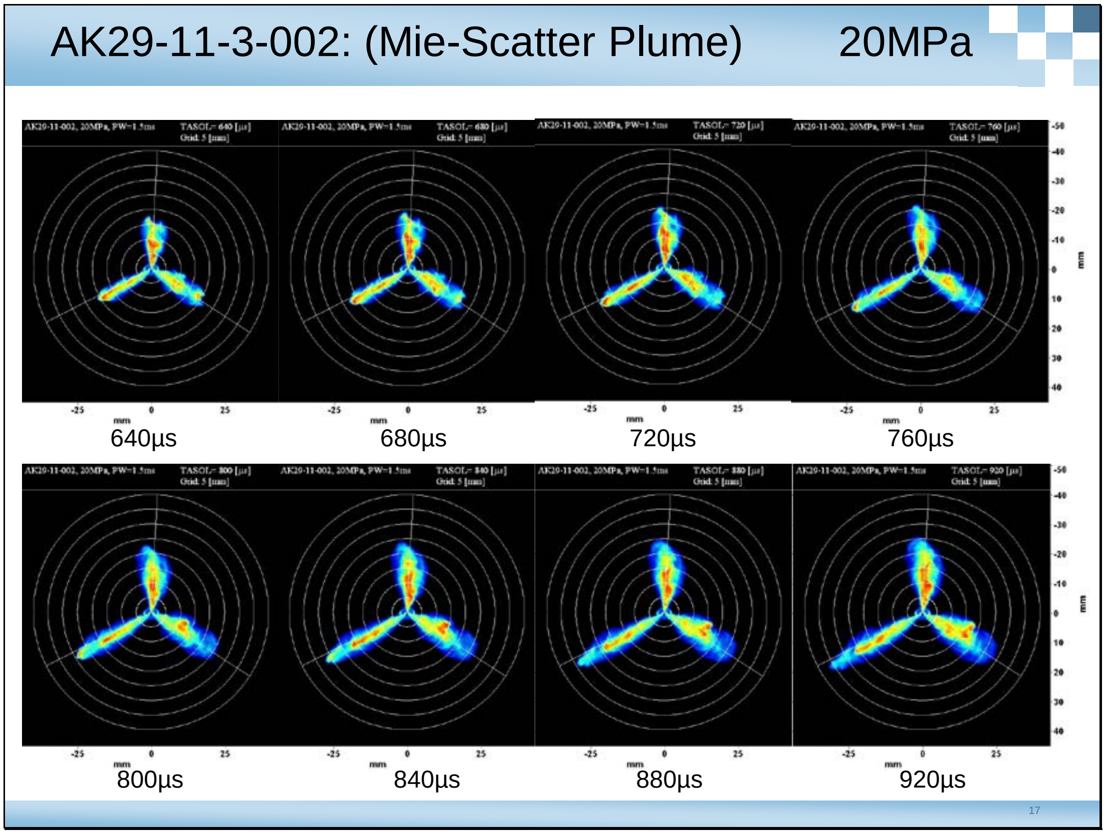
AK29-11-3-002: (Mie-Scatter Plume)
20MPa
640µs
680µs
720µs
760µs
800µs
840µs
880µs
920µs
17

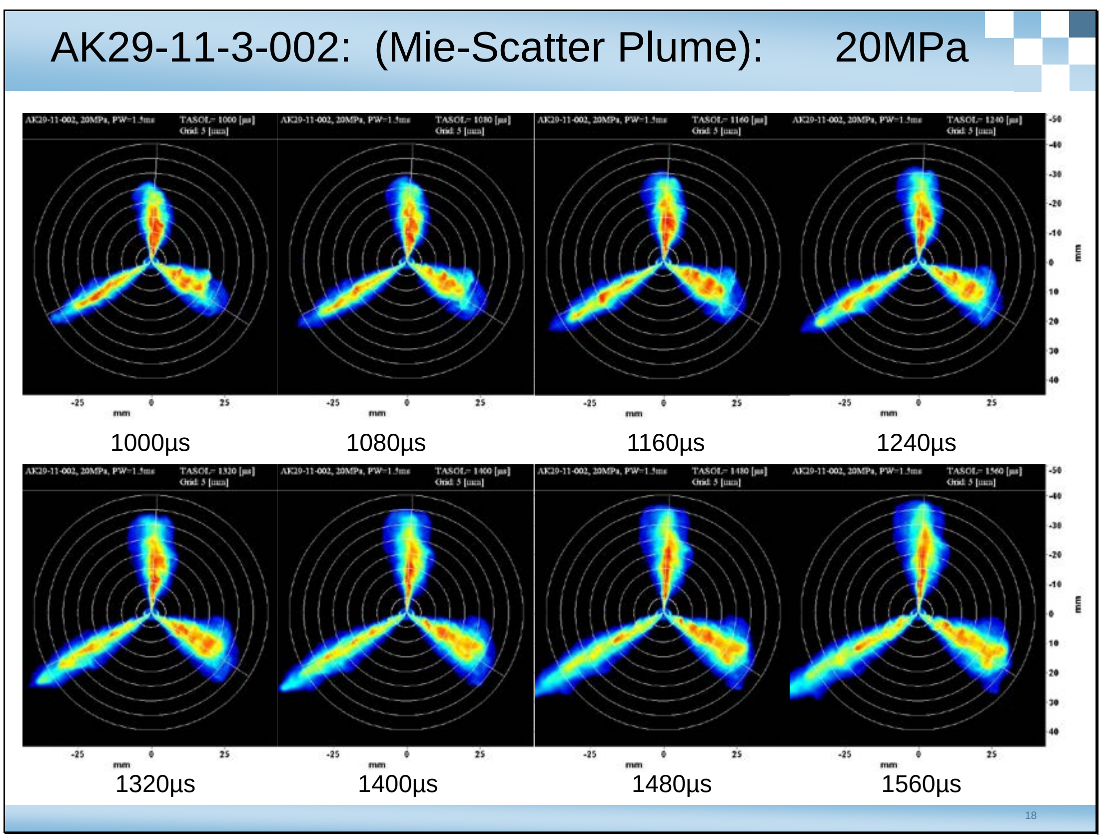
AK29-11-3-002: (Mie-Scatter Plume):
20MPa
1000µs
1080µs
1160µs
1240µs
1320µs
1400µs
1480µs
1560µs
18

# APPENDIX H MIE SCATTER IMAGES, BOTTOM VIEW

High speed Mie Imaging of near-field injector spray from side view, Luxembourg Spray lab

| Image # | Seat # | d (mm) | β | l/d | (l+L) /d | D/d | Inj. Pres. | Pulse Width | Mie Scatter Time Images (µs) |
|---|---|---|---|---|---|---|---|---|---|
| 1-18 | AK29-3-001 | ≈.20 | 0° | 1.1 | na | na | 20MPa | 1 ms | 310,313,317,320,323,327, 330,333,337,340,343,347, 350,353,357,360,363,367 |
| 19-26 | AK29-3-001 | ≈.20 | 0° | 1.1 | na | na | 20MPa | 1 ms | 370,373,377,380,383,387, 390,393,397,400,403,407, 410,413,417,420,423,427 |
| 27-44 | AK29-3-001 | ≈.20 | 0° | 1.1 | na | na | 20MPa | 1 ms | 430,433,437,440,443,447, 450,453,457,460,463,467, 470,473,477,480,483,487 |
| 45-62 | AK29-3-001 | ≈.20 | 0° | 1.1 | na | na | 20MPa | 1 ms | 1300,1310,1320,1330,1340, 1350,1360,1370,1380,1390, 1400,1410,1420,1430,1440, 1450,1460,1470 |
| 63-90 | AK29-3-001 | ≈.20 | 0° | 1.1 | na | na | 20MPa | 1 ms | 1480,1490,1500,1510,1520, 1530,1540,1550,1560,1570, 1580,1590,1600,1610,1620, 1630,1640,1650 |

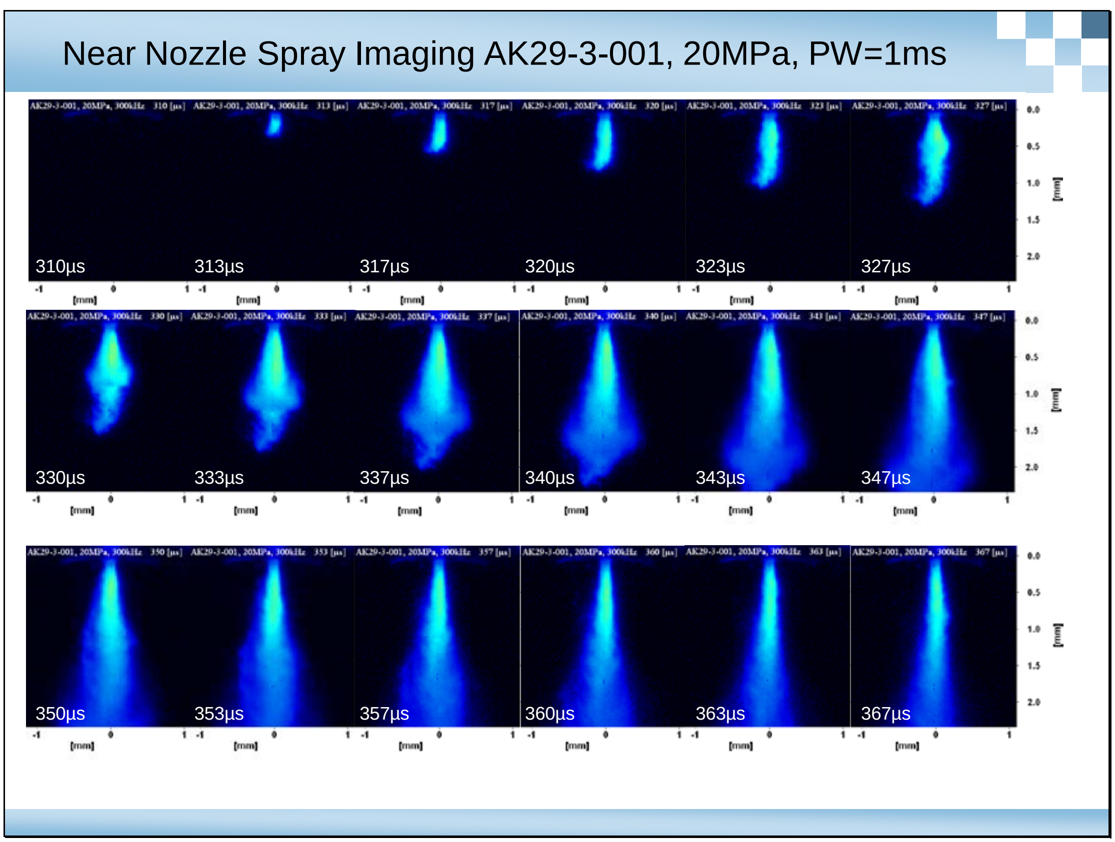

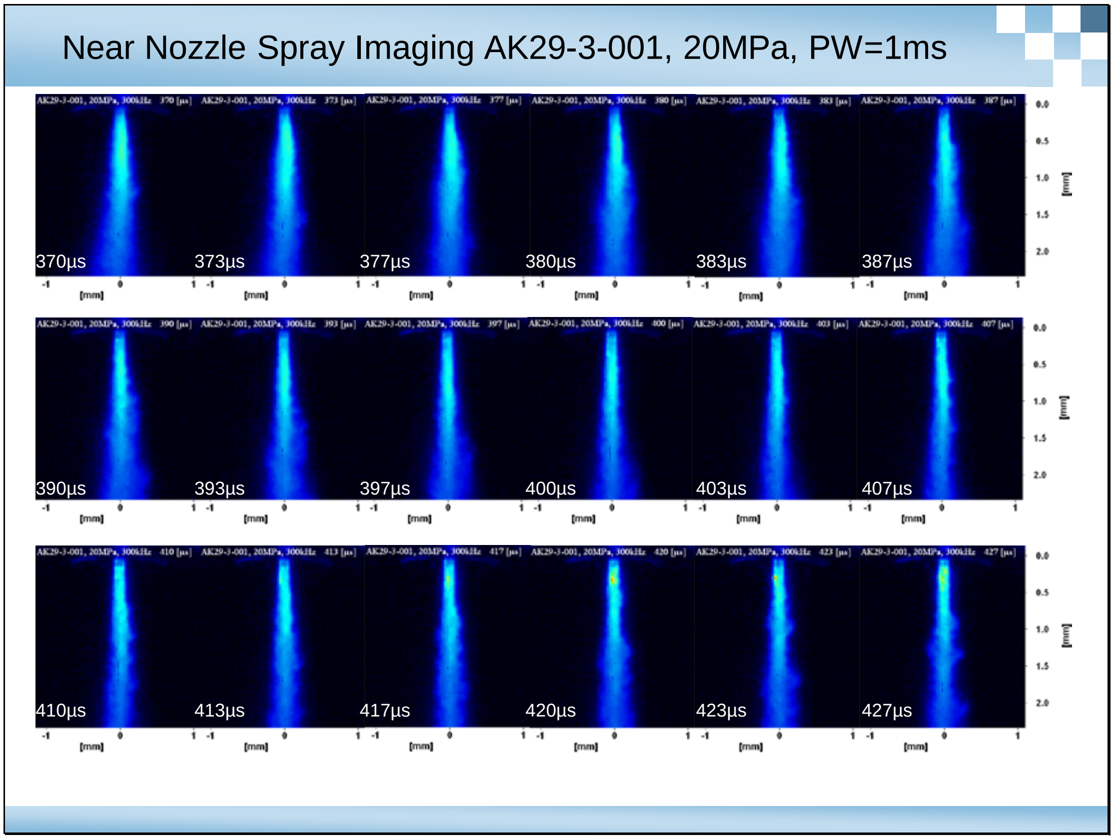
Near Nozzle Spray Imaging AK29-3-001, 20MPa, PW=1ms
370µs
373µs
377µs
380µs
383µs
387µs
390µs
393µs
397µs
400µs
403µs
407µs
410µs
413µs
417µs
420µs
423µs
427µs
[mm]

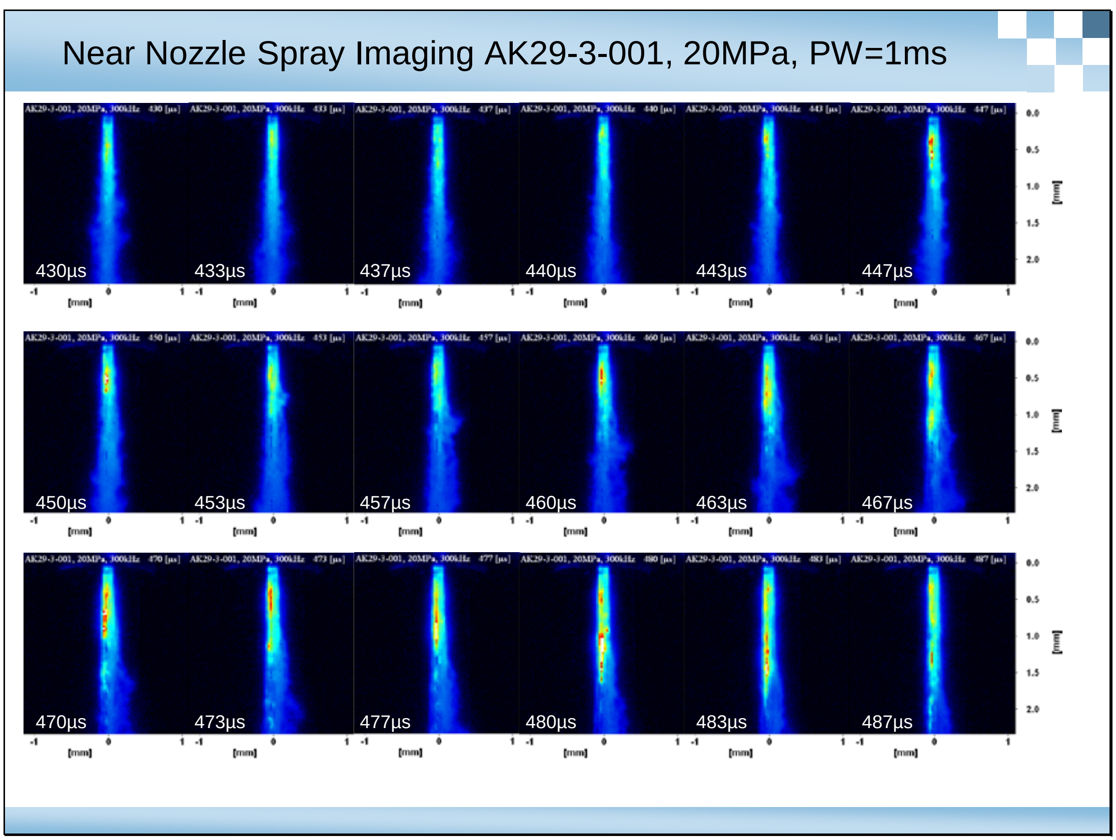
Near Nozzle Spray Imaging AK29-3-001, 20MPa, PW=1ms
430µs
433µs
437µs
440µs
443µs
447µs
450µs
453µs
457µs
460µs
463µs
467µs
470µs
473µs
477µs
480µs
483µs
487µs
[mm]

## Near Nozzle Spray Imaging AK29-3-001, 20MPa, PW=1ms
## Closing Behavior

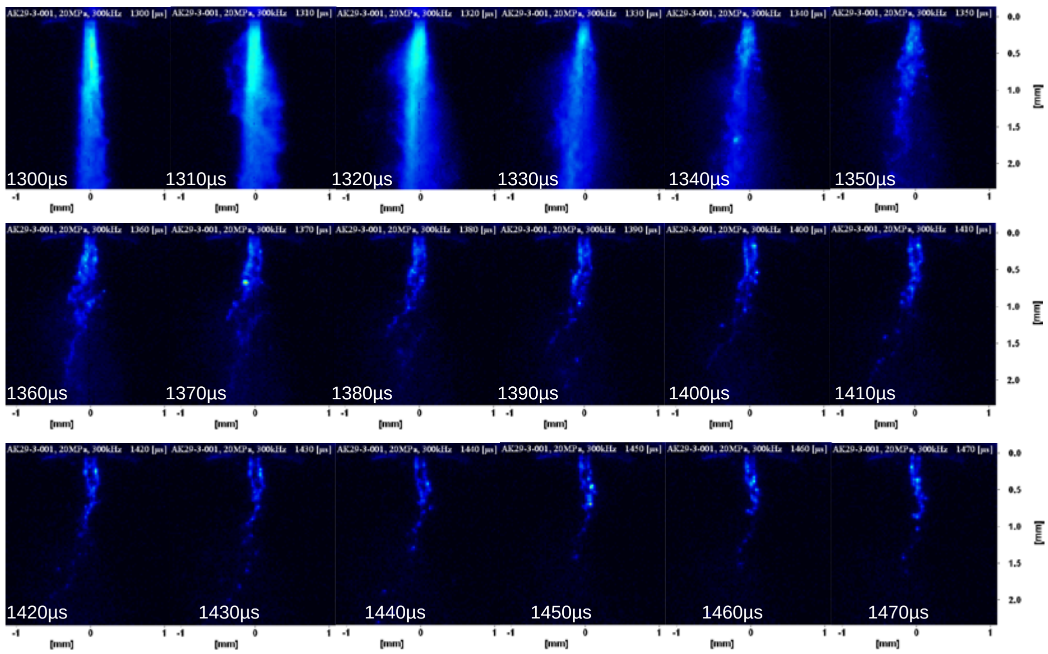


## Near Nozzle Spray Imaging AK29-3-001, 20MPa, PW=1ms
## Closing Behavior

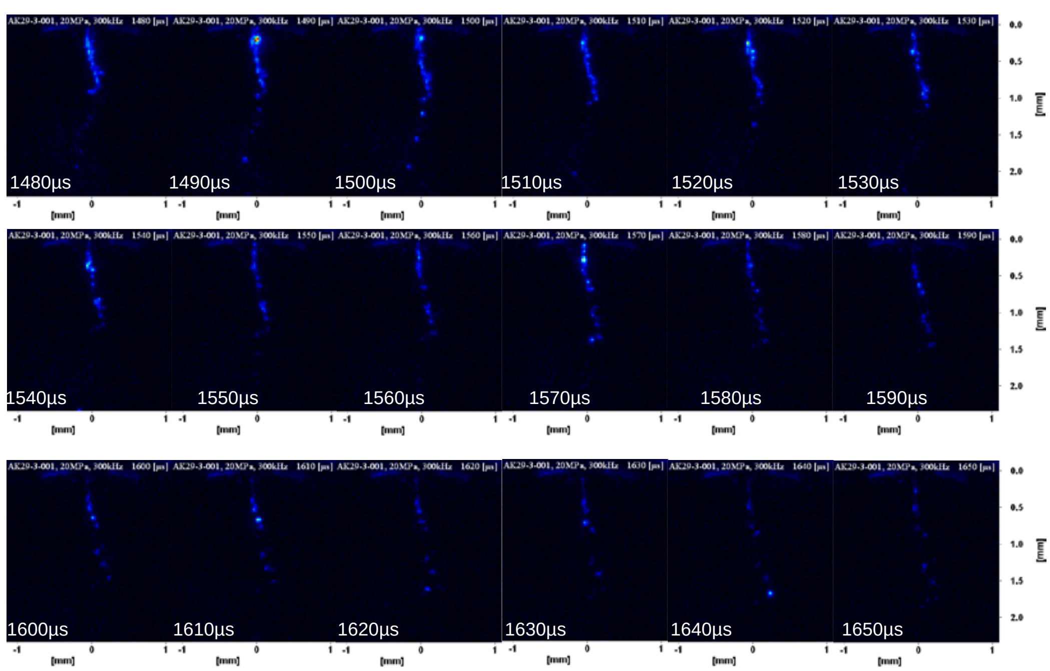

# APPENDIX I PHASE-CONTRAST X-RAY IMAGES

Phase Contrast X-ray image mosaics (100 mosaics) from Argonne testing 3-hole injectors

Each image is comprised of a mosaic of 4-5 image captures selected for spatial and temporal coherence to represent spray

| Mosaic # | Seat # | Hole # | d (mm) | β | l/d | (l+L) /d | D/d | Inj. Pres. | View Angle | X-ray Time Images (μs) |
|---|---|---|---|---|---|---|---|---|---|---|
| 1-10 | AK29-9-001 | 1 | ≈.20 | 30° | 1.1 | na | na | 10MPa | 0° | 0,50,100,150,200, 250,300,350,400, 450 |
| 1-10 | AK29-9-001 | 2 | ≈.20 | 30° | 1.1 | 2.95 | 2.5 | 10MPa | 0° | 0,50,100,150,200, 250,300,350,400, 450 |
| 1-10 | AK29-9-002 | 1 | ≈.20 | 30° | 1.1 | na | na | 10MPa | 0° | 0,50,100,150,200, 250,300,350,400, 450 |
| 1-10 | AK29-9-002 | 2 | ≈.20 | 30° | 1.1 | 2.95 | 2.5 | 10MPa | 0° | 0,50,100,150,200, 250,300,350,400, 450 |
| 1-10 | AK29-9-002 | 1 | ≈.20 | 30° | 1.1 | na | na | 5MPa | 0° | 0,50,100,150,200, 250,300,350,400, 450 |
| 1-10 | AK29-9-002 | 2 | ≈.20 | 30° | 1.1 | 2.95 | 2.5 | 5MPa | 0° | 0,50,100,150,200, 250,300,350,400, 450 |
| 1-10 | AK29-10-3-002 | | ≈.15 | 30° | 1.1 | 3.96 | 2.5 | 5MPa | 0° | 0,50,100,150,200, 250,300,350,400, 450 |
| 1-10 | AK29-10-3-002 | | ≈.15 | 30° | 1.1 | 3.96 | 2.5 | 10MPa | 0° | 0,50,100,150,200, 250,300,350,400, 450 |
| 1-10 | AK29-11-3-002 | | ≈.15 | 30° | 3.96 | na | na | 5MPa | 0° | 0,50,100,150,200, 250,300,350,400, 450 |
| 1-10 | AK29-11-3-002 | | ≈.15 | 30° | 3.96 | na | na | 10MPa | 0° | 0,50,100,150,200, 250,300,350,400, 450 |

| AK29-9-001 | |
|---|---|
| Injection Pressure | 10 MPa |
| Time Sequence | 1.30 ms |
| Time Step | 0.05 ms |
| Repeat Times | 10 times |

| AK29 | 09 |
|---|---|
| Proposed X-ray nozzle test nozzles | 19-Dec-11 |
| | 3HN3(short) |
| d(mm) | ≈0.20 |
| β | ~30° |
| l/d | 1.1 |
| (l+L)/d | grnd |
| D/d | na |
| Effects of | c-bore |
| # of Holes | 3 |


1.74 mm

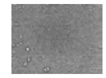

1.32 mm

ASOI: 0 µs 50 µs 100 µs 150 µs 200 µs

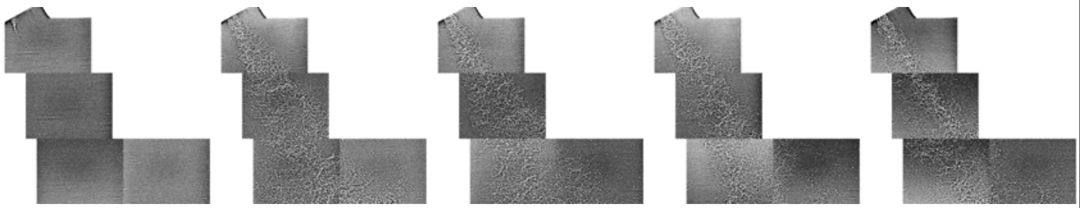

250 µs 300 µs 350 µs 400 µs 450 µs

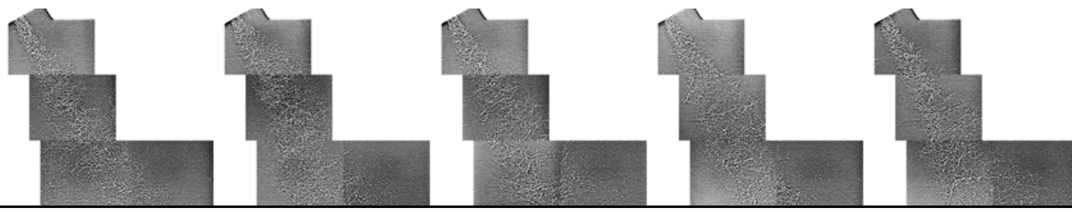

| AK29-9-001 | |
|---|---|
| Injection Pressure | 10 MPa |
| Time Sequence | 1.30 ms |
| Time Step | 0.05 ms |
| Repeat Times | 10 times |

| AK29 | 09 |
|---|---|
| Proposed X-ray nozzle test nozzles | 19-Dec-11 |
| | 3HN3(short) |
| d(mm) | ≈0.20 |
| β | ~30° |
| l/d | 1.1 |
| (l+L)/d | 2.95 |
| D/d | 2.5 |
| Effects of | c-bore |
| # of Holes | 3 |


ASOI: 0 µs 50 µs 100 µs 150 µs 200 µs

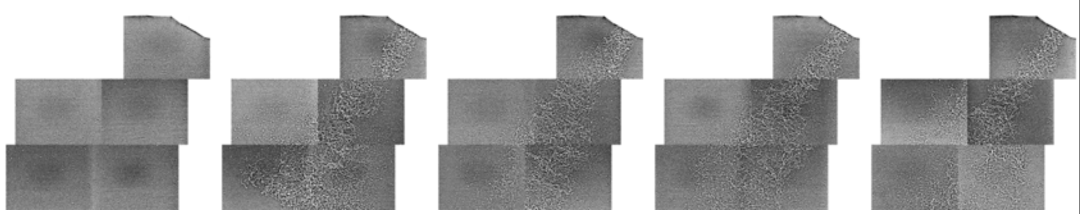

250 µs 300 µs 350 µs 400 µs 450 µs

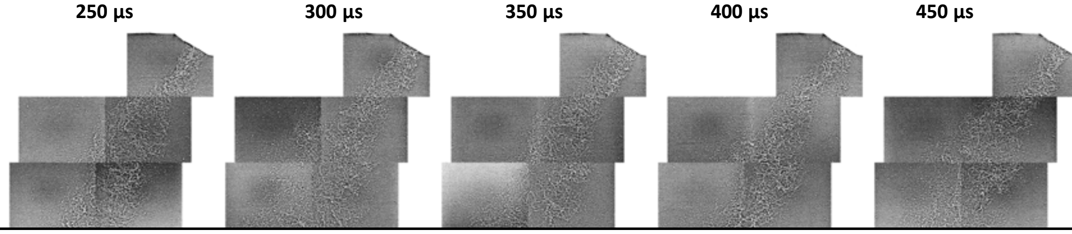

| *AK29-9-002* | |
|---|---|
| Injection Pressure | **10 MPa** |
| Time Sequence | 2.30 ms |
| Time Step | 0.05 ms |
| Repeat Times | 10 times |

| **AK29** | **09** |
|---|---|
| Proposed X-ray nozzle test nozzles | 19-Dec-11 |
| | 3HN3(short) |
| d(mm) | ≈0.20 |
| β | ~30° |
| **l/d** | **1.1** |
| **(l+L)/d** | **grnd** |
| **D/d** | **na** |
| **Effects of** | c-bore |
| **# of Holes** | 3 |


**ASOI: 0 µs 50 µs 100 µs 150 µs 200 µs**

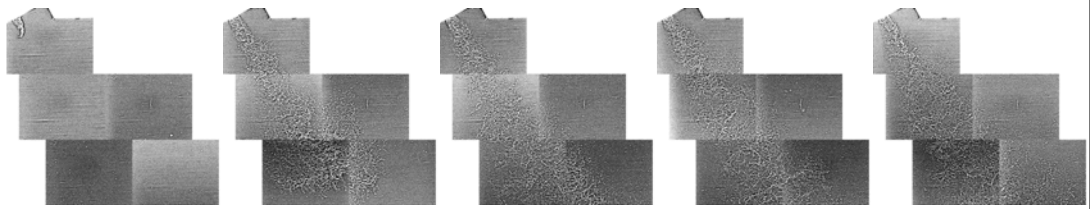

**250 µs 300 µs 350 µs 400 µs 450 µs**

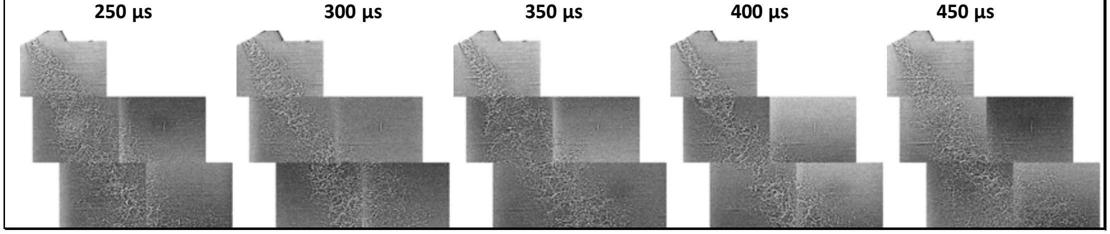

| *AK29-9-002* | |
|---|---|
| Injection Pressure | **10MPa** |
| Time Sequence | 2.30 ms |
| Time Step | 0.05 ms |
| Repeat Times | 10 times |

| **AK29** | **09** |
|---|---|
| Proposed X-ray nozzle test nozzles | 19-Dec-11 |
| | 3HN3(short) |
| d(mm) | ≈0.20 |
| β | ~30° |
| **l/d** | **1.1** |
| **(l+L)/d** | **2.95** |
| **D/d** | **2.5** |
| **Effects of** | c-bore |
| **# of Holes** | 3 |


**ASOI: 0 µs 50 µs 100 µs 150 µs 200 µs**

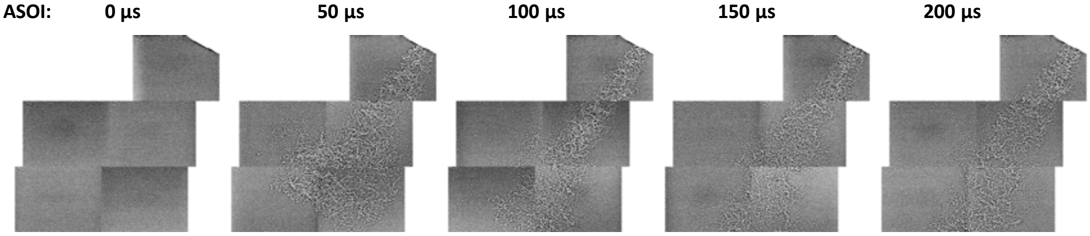

**250 µs 300 µs 350 µs 400 µs 450 µs**

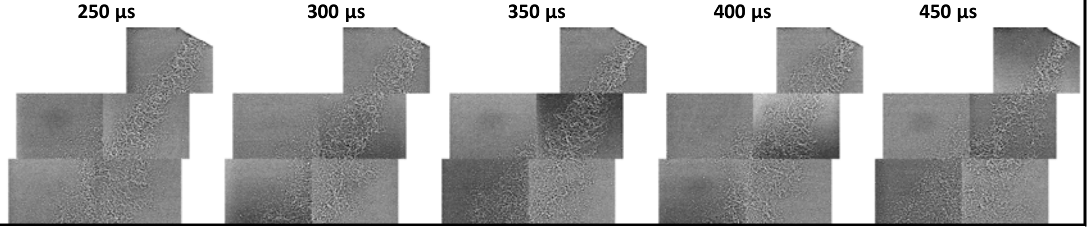

| *AK29-9-002* | |
|---|---|
| Injection Pressure | **5 MPa** |
| Time Sequence | 1.10 ms |
| Time Step | 0.05 ms |
| Repeat Times | 10 times |

| **AK29** | **09** |
|---|---|
| Proposed X-ray nozzle test nozzles | 19-Dec-11 |
| | 3HN3(short) |
| d(mm) | ≈0.20 |
| β | ~30˚ |
| **l/d** | **1.1** |
| **(l+L)/d** | **grnd** |
| **D/d** | **na** |
| **Effects of** | c-bore |
| **# of Holes** | 3 |


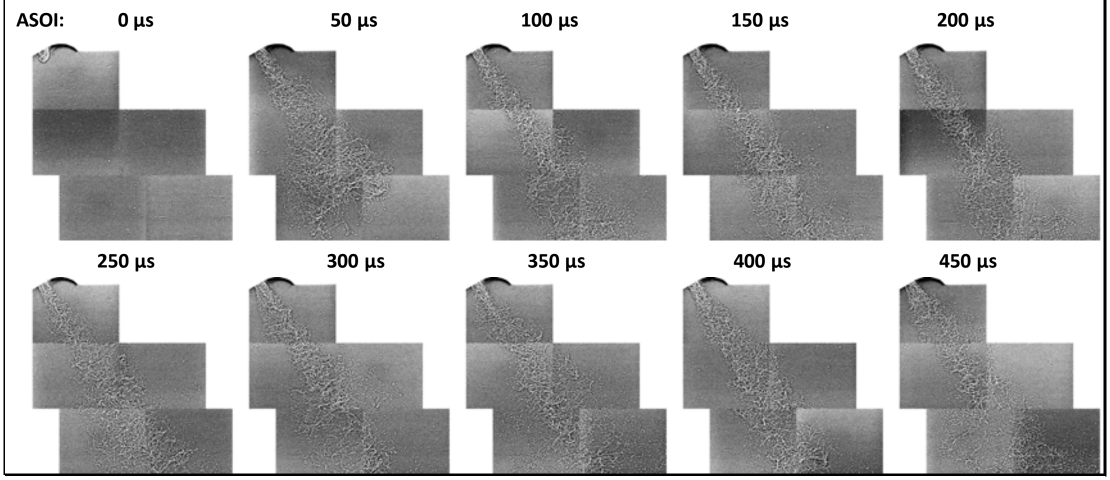


| *AK29-9-002* | |
|---|---|
| Injection Pressure | **5 MPa** |
| Time Sequence | 1.10 ms |
| Time Step | 0.05 ms |
| Repeat Times | 10 times |

| **AK29** | **09** |
|---|---|
| Proposed X-ray nozzle test nozzles | 19-Dec-11 |
| | 3HN3(short) |
| d(mm) | ≈0.20 |
| β | ~30˚ |
| **l/d** | **1.1** |
| **(l+L)/d** | **2.95** |
| **D/d** | **2.5** |
| **Effects of** | c-bore |
| **# of Holes** | 3 |


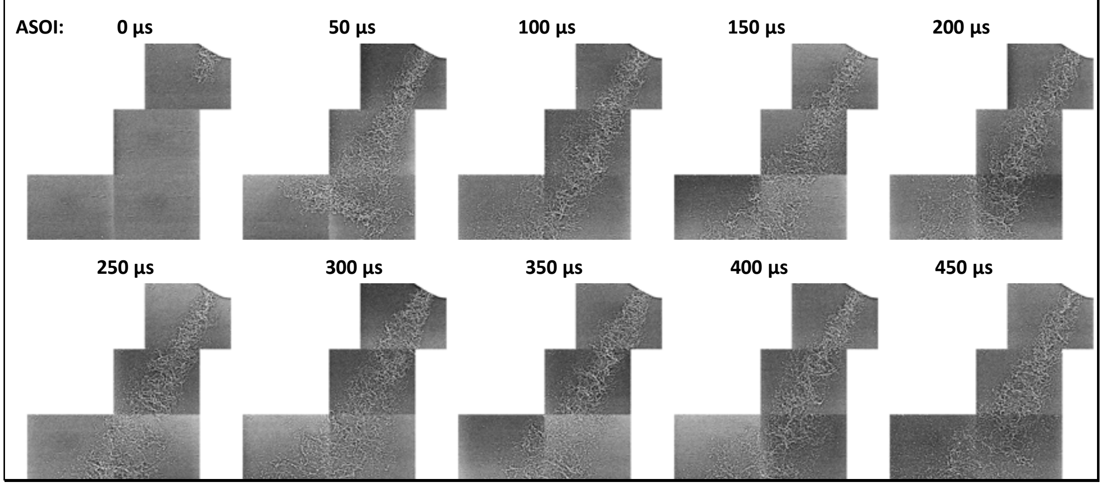

| *AK29-10-3-002* | |
|---|---|
| Injection Pressure | **10 MPa** |
| Time Sequence | 2.10 ms |
| Time Step | 0.05 ms |
| Repeat Times | 10 times |

| **AK29** | **10** |
|---|---|
| Proposed X-ray nozzle test nozzles | 1-Aug-11 |
| | SHN4(small) |
| d(mm) | ≈0.15 |
| β | ~30° |
| **l/d** | **1.10** |
| **(l+L)/d** | **3.96** |
| **D/d** | **2.50** |
| **Effects of** | |
| **# of Holes** | 1 |

**ASOI:** **0 µs** **50 µs** **100 µs** **150 µs** **200 µs**

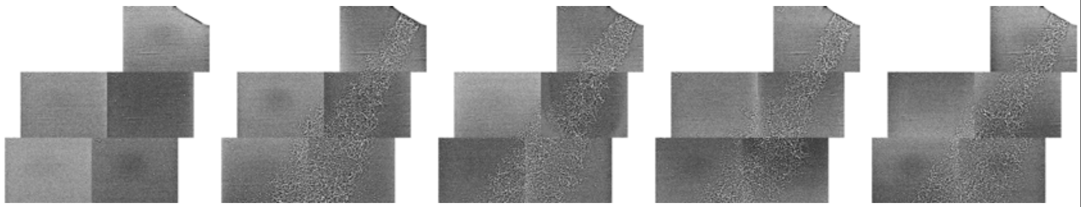

**250 µs** **300 µs** **350 µs** **400 µs** **450 µs**

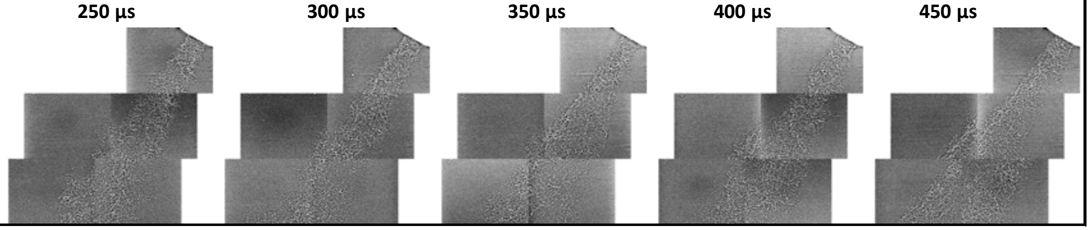

| *AK29-11-3-002* | |
|---|---|
| Injection Pressure | **5 MPa** |
| Time Sequence | 1.15 ms |
| Time Step | 0.05 ms |
| Repeat Times | 10 times |

| **AK29** | **11** |
|---|---|
| Proposed X-ray nozzle test nozzles | 1-Aug-11 |
| | SHN5(s-L) |
| d(mm) | ≈0.15 |
| β | ~30° |
| **l/d** | **3.96** |
| **(l+L)/d** | **na** |
| **D/d** | **na** |
| **Effects of** | |
| **# of Holes** | 3 |

**ASOI:** **0 µs** **50 µs** **100 µs** **150 µs** **200 µs**

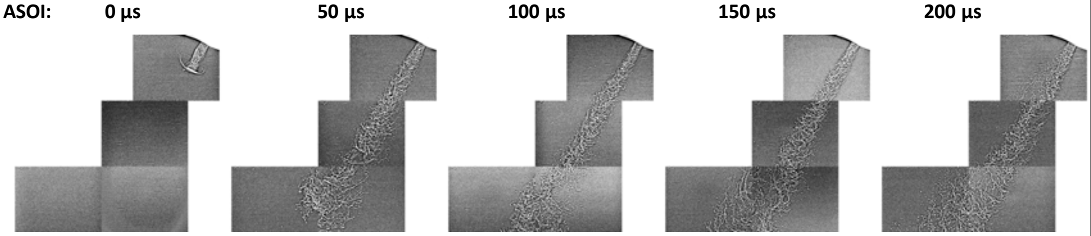

**250 µs** **300 µs** **350 µs** **400 µs** **450 µs**

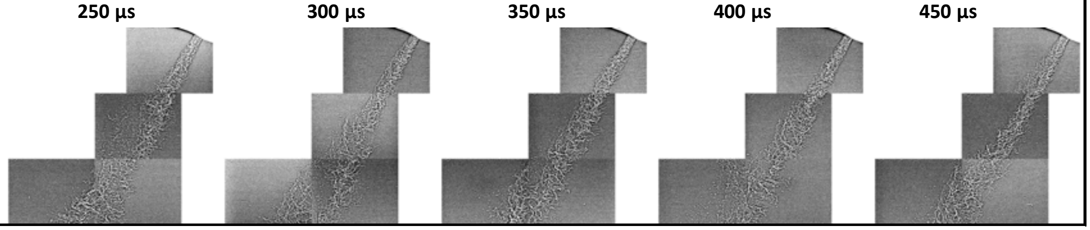

| *AK29-11-3-002* | |
|---|---|
| Injection Pressure | **10 MPa** |
| Time Sequence | 2.10 ms |
| Time Step | 0.05 ms |
| Repeat Times | 10 times |

| **AK29** | **11** |
|---|---|
| Proposed X-ray nozzle test nozzles | 1-Aug-11 |
| | SHN5(s-L) |
| d(mm) | ≈0.15 |
| β | ~30° |
| **l/d** | **3.96** |
| **(l+L)/d** | **na** |
| **D/d** | **na** |
| **Effects of** | |
| **# of Holes** | 3 |

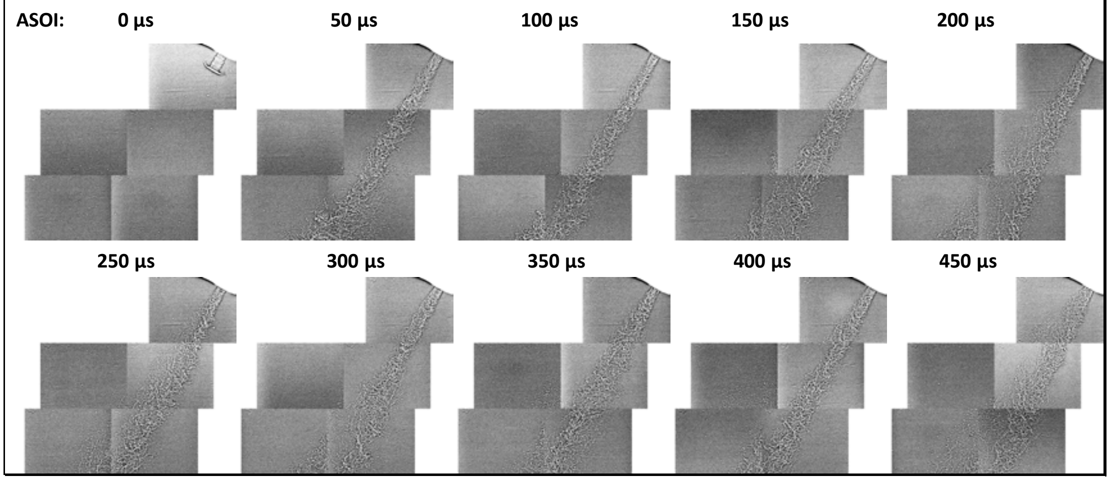

# REFERENCES

[1] Yi, J., Wooldridge, S., Coulson, G., Hilditch, J. et al., "Development and Optimization of the Ford 3.5L V6 EcoBoost Combustion System," *SAE Int. J. Engines 2*, pp. 1388-1407, 2009.

[2] Kirwan, J., Shost, M., Roth, G., and Zizelman, J., "3-Cylinder Turbocharged Gasoline Direct Injection: A High Value Solution for Low CO2 and NOx Emissions," *SAE Int. J. Engines 3(1),* pp. 355-371, 2010.

[3] Bakker, A., "Applied Computational Fluid Dynamics, Lecture 8 – Turbulence," 2006.

[4] Reynolds, O., "On the dynamical theory of turbulent incompressible viscous fluids and the detremination of the sriterion," *Phil. Trans. Royal Soc. London A v. 186,* pp. 123-164, 1894.

[5] Richardson, L., F., "Weather Prediction by Numerical Process," 1922.

[6] Kolmogorov, A.,"The local structure of turbulence in incompressible viscous fluid," *Dokl. Akad. Nauk., Vol. 30,* pp. 301-305, 1941.

[7] Reitz, R., D., and Bracco F., V., "Mechanism of Atomization of a Liquid Jet," *Phys. Fluids, 25,* p. 1730 – 1742, 1982.

[8] Reitz, R., D., "Modeling Atomization Processes in High-Pressure Vaporizing Sprays," *Atom. & Spray Tech., 3,* pp. 309-337, 1987.

[9] Lin, S., P. and Reitz, R., D., "Drop and Spray Formation from a Liquid Jet," *Annu. Rev. Fluid Mech., 30,* pp. 85-105, 1998.

[10] O'Rourke, P.J., and Amsden, A.A., "The TAB Method for Numerical Calculation of Spray Droplet Breakup," *SAE Technical Paper 872089*, 1987.

[11] Smagorinsky, J., "General Circulation Experiments with the Primitive Equations," *Monthly Weather Review, 91*, 1963.

[12] Deardorff, J., W., "A Numerical study of three-dimensional turbulent channel flow at large Reynolds numbers," *J. Fluid Mech. 41,* p. 453, 1970.

[13] Bakker, A., "Applied Fluid Dynamics, Lecture 12 - LES," [Online].

[14] Boussinesq, J., "Essai sur la Th´eorie des Eaux Courantes," *M´em. pr´es. par div.*, vol. 23, pp. 1-680, 1877.

[15] Schmitt, F., G., "About Boussinesq's turbulent viscosity hypothesis: historical remarks and a direct evaluation of its validity," *Comptes Rendus Mécanique,* vol. 335, no. 9-10, pp. 617-627, 2007.

[16] Prandtl, L., "Bericht uber Untersuchungen zur ausgebildeten Turbulenz," *Zs. agnew. Math. Mech. 5,* pp. 136-139, 1925.

[17] Wilcox, D., "Turbulence Modeling for CFD," DCW Industries, Inc, LA Canada, CA, 1993.

[18] Saguat, P., Large Eddy Simulation for Incompressible Flows, 3rd edition, Springer, 2005.

[19] Leonard, A., "Energy cascade in large-eddy simulations of turbulent fluid flows," *Adv. in Geophys. A 18,* pp. 237-248, 1974.

[20] Germano, M., "Turbulence : the filtering approach," *J . Fluid Mech.*, vol. 238, pp. 325-336, 1992.

[21] Lilly, D., K.,"A proposed modification of the Germano subgrid-scale closure method," *Physics of Fluids*, pp. 633-636, 1992.

[22] Yoshizawa, A. and Horiuti, K., "A Statistically-Derived Subgrid-Scale Kinetic Energy Model for the Large Eddy Simulation of Turbulent Flows," *J. Phys. Soc. Japan, 54 (8),* pp.

2834-2839, 1985.

[23] Weller, H.G., Tabor, G., Jasak, C.,Fureby, C., "A tensorial approach to computational continuum mechanics using object-oriented techniques," *Journal of Computational Physics,* vol. 12, no. 6, pp. 56-74, 1998.

[24] Arai, M., Shimizu, M. and Hiroyasu, H., "Break-up Length and Spray Angle of a High Speed Jet," *Proceedings of ICLASS '85, Paper IB/4,* July 1985.

[25] Soteriou, C., E. and Andrews, R., J., "Cavitation Hydraulic Flip and Atomization in Direct Injection Diesel Sprays," *Proceedings of IMechE, Paper C465/051/93,* 1993.

[26] Chaves, H., Knapp, M., Kubitzek, A., Obermeier, F., et. al., "Experimental Study of Cavitation in the Nozzle Hole of Diesel Injectors Using Transparent Nozzles," *SAE Technical Paper 950290,* 1995.

[27] Lai, M., Wang, T., Xie, X., Han, J. et al., "Microscopic Characterization of Diesel Sprays at VCO Nozzle Exit," *SAE Technical Paper 982542,* 1998.

[28] Wu, P., K., Miranda, R., F., and Faeth, G., M., "Effects of Initial Flow Conditions on Primary Breakup of Non Turbulent and Turbulent Round Liquid Jets," *Atomiz. Sprays,* 1995.

[29] Andriotis A., Gavaises, M., and Arcoumanis, C., "Vortex Flow and Cavitation in Diesel Injector Nozzles," *J. Fluid Maechanics, 610 (1),* pp. 195-215, 2008.

[30] Andriotis A. and Gavaises, M., "Influence of Vortex flow and Cavitation on Near-Nozzle Diesel Spray Dispersion Angle," *Atomi Spraysts, 19(3),* 2009.

[31] Lai, M.C., Zheng, Y., Xie, X., Moon, S. et. al., "Characterization of the Near-Field Spray and Internal Flow of Single-Hole and Multi-Hole Sac Nozzles Using Phase Contrast X-ray

Imaging and CFD," *SAE Int. J. Engines 4(1),* pp. 703-719, 2011.

[32] Das, S., Chang, S., and Kirwan, J., "Spray Pattern Recognition for Multi-Hole Gasoline Direct Injectors Using CFD Modeling," *SAE Technical Paper 2009-01-1488,* 2009.

[33] Befrui, B., Corbinelli, G., D'Onofrio, M., and Varble, D., "GDI Multi-Hole Injector Internal Flow and Spray Analysis," *SAE Technical Paper 2011-01-1211,* 2011.

[34] Lai, M., Zheng, Y., Shost, M., Xie, X. et al, "Characterization of Internal Flow and Spray of Multihole DI gasoline Spray using X-ray Imaging and CFD," *SAE Technical Paper 2011-01-1881,* 2011.

[35] Albina, F.O., Muzaferija, S., Peric, M., "Numerical Simulation of Jet Instabilities," *Proceedings of ILASS-Europe 2000, Darmstadt (Germany), Sep. 2000,* 2000.

[36] Klein, M. and Janika, J., "Large-eddy Simulation of the primary Breakup of a Spatially Developing Liquid Film," *Proceedings of International Conference on Atomization and Sprays (ICLASS), Sorrento (Italy), July 2003,* 2003.

[37] Klein, M., "Direct Numerical Simulation of a Spatially Developing Water Sheet at Moderate Reynolds Number," *Int. J. Heat Fluid Flow, 26,* pp. 722-731, 2005.

[38] Sander, W. and Weigand, B., Direct Numerical Simulation of Primary Breakup Phenomena in liquid Sheets in Science and Engineering, Springer, 2007, p. 223 – 236.

[39] Sander, W. and Weigand, B., "Direct numerical simulation and analysis of instability enhancing parameters in liquid sheets at moderate Reynolds numbers," *Phys. Fluids 20,* 2008.

[40] Befrui, B., Corbinelli, G., Robart, D., Reckers, W., et. al., "LES Simulation of the Internal Flow and Near-Field Spray Structure of an Outward-Opening GDi Injector and Comparison

with Imaging Data," *SAE Technical Paper 2008-01-0137*, 2008.

[41] Corbinelli, G., Befrui, B., and Reckers, W., "Large Eddy Simulation and Optical Studies of the Primary Break-up of a Thin Planar-Sheet Liquid Jet," *SAE Int. J. Fuels Lubr. 3(1),* pp. 266-276, 2010.

[42] Hung, D., Harrington, D., Gandhi, A., Markle, L., et. al., "Gasoline Fuel Injector Spray Measurement and Characterization - A New SAE J2715 Recommended Practice," *SAE Int. J. Fuels Lubr. 1(1),* pp. 534-548, 2009.

[43] Rivera, E., Mastro, N., Zizelman, J., Kirwan, J. et. al., "Development of Injector for the Direct Injection Homogeneous Market using Design for Six Sigma," *SAE Technical Paper 2010-01-0594,* 2010.

[44] Malvern Instruments, "www.Malvern.com," 15 9 2014. [Online]. Available: www.malvern.com. [Accessed 15 9 2014].

[45] de Villiers, E., Gosman, A., and Weller, H., "Large Eddy Simulation of Primary Diesel Atomization," *SAE Technical Paper 2004-01-0100,* 2004.

[46] de Villiers, E., *The Potential of Large Eddy Simulation for the Modeling of Wall Bounded Flows PhD Thesis,* London: Imperial College of Science, Technology and Medicine, 2006.

[47] Brackbill, J. U., Kothe, D. B., Zemach, C., "A Continuum Method for Modelling surface Tension," *J. Comp. Phys., 100,* pp. 335-354, 1992.

[48] Ubbink, O., *Numerical Prediction of Two Fluid Systems with Sharp Interfaces,* University of London, 1997.

[49] Weller, H., *A New Approach to VOF-based Interface Capturing Methods for Incompressible and Compressible Flows,* 2008.

[50] Gomaa, H., Kumar, S., Huber, C., Weigand, B. and Peters, B., "Numerical Comparison of 3D Jet Breakup Using a Compression Scheme and an Interface Reconstruction Based VOF," in *Proceedings ILASS – Europe 2011, 24th European Conference on Liquid Atomization and Spray Systems*, Estoril, Portugal, 2011.

[51] Jasak, H., Weller, H., G., Gosman, A., D., "High Resolution NVD Differencing Scheme forArbitrary Unstructure Meshes," *Int. J. Numer. Math Fluids,* vol. 31, pp. 431-449, 1999.

[52] Jeong, J. and Hussain, F., "On the identification of a vortex," *J. Fluid Mechanics,* vol. 285, pp. 69-94, 1995.

[53] Hunt, J., C., R., Wray, A., A. and Moin, P., "Eddies, Stream and Convergence Zones in Turbulent Flows," *Center for Turbulence Research Report S88, 193,* p. 193, 1998.

[54] "OpenCFD Ltd., OpenFOAM – User Guide,," 2010. [Online]. Available: http://www.opencfd.com.

[55] Issa, R.I., "Solution of the Implicitly Discretized Fluid Flow Equations by Operator Splitting," *J. Comp. Phys. 62,* pp. 40-65, 1986.

[56] Befrui, B., Corbinelli, G., Spiekermann, P., Shost, M., Lai, M-C., et. al., "Large Eddy Simulation of GDI Single-Hole Flow and Near-Field Spray," *SAE Int. J. Fuels Lubr. 5(2),* pp. 620-636, 2012.

[57] Payri, R., Salvador, F. J., Gimeno, J., Zapata, L. D., "Diesel Nozzle Geometry Influence on Spray Liquid Phase Fuel Penetration in Evaporative Conditions," *J. Fuel , 87 (7),* pp. 1165 - 1176, 2008.

[58] Kong, J. and Bae, C., "Effect of Tapered Nozzle Hole on Spray Characteristics of High Pressure Diesel Injection," in *11th International Annual Conference on Liquid Atomization*

*and Spray Systems*, Vail, Colorado, 2009.

[59] Som, S., Ramirez, A.I., Longman, D. E., Aggarwal,S.K., "Effect of Nozzle Orifice Geometry on Spray, Combustion and Emission Characteristics under Diesel Engine Conditions," *J Fuel, 90,* pp. 1267-1276, 2011.

[60] Befrui, B., Aye, A., Spiekermann, P., Varble, D. Shost, M., Lai, M-C., et. al., "GDi Skew-Angled Nozzle Flow and Near-Field Spray," *SAE Technical Paper 2013-01-0255*, 2013.

[61] Shi, J.,M., Wenzlawski, K., Helie,J., Nuglisch, H., Cousin, J., "URANS & SAS analysis of flow dynamics in a GDI nozzle," in *ILASS- Europe 23rd Annual Conference on Liquid Atomization and Spray Systems*, Brno (Czech Republic), 2010.

[62] Pitcher, G., Wigley, G., "The Droplet Dynamics of Diesel Fuel Sprays under Ambient and Engine Conditions," *ASME,* vol. 2, pp. 571-586, 1991.

[63] Xie, X., Lai, M.-C., Moon, S., Liu, Z., Gao, J., Dufresne, E., Fezza, K., Wang, J., "Ultrafast X-ray Phase-Contrast Imaging of High-Speed Fule SPrays from a Two-Hole Diesel Nozzle," in *ILASS Americas 22nd Annual Conference on Liquid Atomization and Spray Systems*, Cincinnati, OH, 2010.

[64] Gao, J., Reitz, R., D., Ghandhi, J., B., Wang, J., Liu, Z., P., "A Study of the Primary Breakup Process and Macroscale Characterictics of Impinging Diesel Spray Nozzles," in *ICLASS 11th Triennial International Annual Conference on Liquid Atomization and Spray Systems*, Vail CO, 2009.

[65] Gao, J., Liu, Z., Moon, S., Xie, X., Dufresne, E., et. al., "Morphology of Diesel sprays from single-Orifice Micronozzles," in *ILASS Americas 22nd Annual Conference on Liquid Atomization and Spray Systems*, Cincinnati, oH, 2010.

[66] Mitroglou, N., *Multi-Hole Injectors for Direct Injection gasoline Engines, PhD Thesis,* London, UK: The City University of London, 2006.

[67] Papoulias, D., Giannadakis, E., Mitroglou, N., Gavaises, M., et. al., "Cavitation in Fuel Injection Systems for Spray-Guided Direct Injection Gasoline Engines," SAE Technical Paper 2007-01-1418, 2007.

[68] Shost, M., Lai, M., Befrui, B., Spiekermann, P., et. al., "GDi Nozzle Parameter Studies Using LES and Spray Imaging Methods," *SAE Technical Paper 2014-01-1434,*, 2014.

[69] Befrui, B., Spikermann, P., Shost, M., Lai, M., -C., "VoF-LES Studies of GDi Multi-Hole Nozzle Plume Primary Breakup and Comparison with Imaging Data," in *ILASS-Europe 25th European Conference on Liquid Atomization and Spray Systems,* chania, Greece, 2013.

[70] Befrui, B. and D'Onofrio, M., "Primary Atomization of a GDi Multi-Hole Plume Using VOF-LES Method," *SAE Technical Paper 2014-01-1125*, 2014.

# ABSTRACT

## EVALUATION OF NOZZLE GEOMETRY ON HIGH PRESSURE GASOLINE DIRECT INJECTION SPRAY ATOMIZATION

by

**MARK ANTHONY SHOST**

**December 2014**

**Advisor:** Professor Ming-Chai Lai

**Major:** Mechanical Engineering

**Degree:** Doctor of Philosophy

This research presents a critical study of injector nozzle geometry on high-pressure Gasoline Direct Injection, GDi, injector spray morphology. The study was conducted with the aid of multi-fluid Volume-of-Fluid, Large-Eddy-Simulation, VOF-LES, method. Alternative nozzle geometries, that are the subject of current interest including varying nozzle hole length to diameter ratio, counterbore presence and nozzle-hole skew-angle geometry, are studied in detail in order to provide insight into their specific influence on spray plume targeting and jet primary breakup characteristics. A comparison of the simulation results with near-field shadowgraph and Mie scatter imaging as well as phase-contrast X-ray imaging is provided. When near-field experimental imaging validated the simulation results further investigation of the fundamental flow mechanism internal to the injector was studied using VOF-LES to gain insight to the cause of spray morphology changes within the injector valve group. The complementary analysis of Computational Fluid Dynamics method and empirical data supported definitive conclusions on nozzle design parameter effects for l/d, skew angle, counterbore for varying injection pressure as well as provided an understanding of the underlying physical mechanisms involved to engender the resulting spray plume characteristics.

## AUTOBIOGRAPHICAL STATEMENT

Mark A. Shost, currently Director of Powertrain Application Engineering at Chrysler, responsible for Powertrain Engine and Transmission calibration, On-Board-Diagnostic calibration, CARB certification, corporate criteria emissions planning and exhaust aftertreatment specification.

2012-2013, Vice President of Powertrain Engineering at Tula, Led engineering activities to create and integrate real-time cylinder-event-based powertrain controls with advanced signal processing, resulting in a unique, digital engine that achieves the best possible fuel efficiency over the engine's speed and load operating conditions.

2009-2012, Product Line Executive and European Regional Director residing in Luxembourg for Gasoline Engine Management Systems for Delphi Powertrain, this General Management position was P&L responsible for air & fuel systems, electronic controllers and full gasoline ems. The product portfolio generates $800M in revenue supported by 1,200 salaried and 2,500 hourly employees worldwide. Global responsibilities included board member for Korean Joint Venture.

1985-2009, Joined GM and held engineering positions of increasing responsibility to Director for engine management systems portfolio generating $3B in revenue. Established integrated technology plans including; operating budgets, and capital spending, balancing business growth and cost. Direct reports included 12 product-line chief engineers in seven global technical centers leading an organization of 3,100 employees. Led Mexico Technical Center growth to 2,500 engineers and held various chief engineer roles. R&D leadership for product development and innovation utilizing; robust engineering, Extensive background in manufacturing, program management, and product launch, as well as quality improvement and cost reduction initiatives using Six Sigma DFSS, Shainin Red X & Green Y, and Value Engineering tools.

**Inventor on 16 United States Patents**

5,033,327 5,090,364 5,129,373 5,588,404 6,392,406 6,463,951 6,467,495 6,595,485
6,766,819 6,788,054 6,830,232 6,851,306 6,889,546 7,279,133 7,800,379 8,464,690

**The Pennsylvania State University**
BSME, Engineering, 1981–1985

•Activities and Societies: Tau Beta Pi - The Engineering Honor Society, Pi Tau Sigma Treasurer - Mechanical Engineering Honor Society

**University of Rochester - William E. Simon Graduate School of Business Administration**
MBA, Business Administration, 1990–1992

• Attended under General Motors Fellowship
• Activities and Societies: Beta Gamma Sigma - The International Honor Society Recognizing Business Excellence

**Wayne State University**
MSME, Mechanical Engineering, 2006-2009

• 2009–2014 Achieved Doctoral Candidacy Status towards Ph.D. in Mechanical Engineering, dissertation study of GDi injector spray, completion planned in 2014